Analysis and Interpretation of Clustered Microseismicity at Geothermal and Petroleum Reservoirs

by

Shirley A. Rieven

Submitted to the Department of
Earth, Atmospheric, and Planetary Sciences
in partial fulfillment of the requirements
for the degree of
Doctor of Philosophy in Geophysics

at the

MASSACHUSETTS INSTITUTE OF TECHNOLOGY

February, 1999

Signature of Author .....
Department of Earth, Atmospheric, and Planetary Sciences
February 17, 1999

Certified by .....
Professor M. Nafi Toksöz
Professor of Geophysics
Thesis Advisor

Accepted by .....
Professor Ronald Prinn
Department Chair

Analysis and Interpretation of Clustered Microseismicity at Geothermal and Petroleum Reservoirs

by

Shirley A. Rieven

Submitted to the Department of Earth, Atmospheric, and Planetary Sciences
on February 17, 1999 in partial fulfillment of the requirements
for the degree of Doctor of Philosophy in Geophysics

ABSTRACT

This thesis presents the analysis and interpretation of four microearthquake clusters near geothermal and petroleum reservoirs. One cluster was induced during a controlled hydraulic fracture experiment conducted by Atlantic Richfield Corporation (ARCO). The other three clusters occurred near geothermal fields in western Italy during condensate reinjection.

Analysis of events induced during ARCO's Deep Well Treatment and Injection project demonstrated "real-time" hypocenter modeling for hydraulic fracture diagnostics. The injection produced a hydraulic fracture that exhibited strong spatial asymmetry. Analysis of the results suggest that the phenomenon of "screenout" may be one mechanism contributing to the observed seismicity's spatial and temporal characteristics and the direction of the asymmetric failure may be related to heterogeneities in formation depositional structures.

A swarm of events in 1993 near the northern boundary of the Larderello Geothermal field occurred just below an important regional seismic reflector known as the "K" horizon. The distribution of events suggests that seismic slip on steeply dipping, northwest-southeast striking Tortonian age normal faults could account for the observations and that high pressure fluids circulating in the fracture zone of the "K" horizon cause stress changes and slip on localized patches of the faults. Due to the relative depth of this swarm, compared to

reservoir depths, this cluster was attributed to the natural geodynamics of this complex area.

Analysis of a set of events from the LAGO seismogenic zone in the Larderello Geothermal field again showed a spatial association with the seismic "K" horizon and a lateral NW-SE linear distribution that correlated well with the direction of regional extension.

Finally, this thesis reports the results of the relative event relocation for a 1997 swarm of events from the Monte Amiata geothermal field. The hypocenters are located very near a northwest-southeast striking fault at depths correlated with the deeper of two actively producing fracture zones of the Piancastagnaio field.

Thesis supervisor: M. Nafi Toksöz
Title: Professor of Geophysics

DEDICATION

For my mother... in hope

and my father... in dreams.

ACKNOWLEDGMENT

This thesis would not have been possible without the support of many, many people and I would like to thank as many as I can and acknowledge all they have done for me.

The work described herein was accomplished because my advisor, Professor M. Nafi Toksöz, helped me to reach a lifelong goal. First, he recognized in me some potential as a scientist, offered me a place to work and access to the seemingly boundless creative and material resources of ERL and MIT, and then appropriately (and figuratively) told me to get to work. Over the years, he has subtly and caringly directed, and sometimes redirected, me as I struggled to find my thoughts and the words to express them. Not an easy task. I cannot begin to describe my gratitude to him; for his technical advice, for his personal understanding during some of my rougher moments, and most importantly, for giving me the opportunity to try. Thank you so much.

Professor Dale Morgan has also been a great help to me. On various occasions, he has contributed to the work described in this thesis by illuminating several sources of error in hypocenter estimation and I thank him for his valued technical advice. I also want to thank him for a number of very enjoyable and enlightening conversations about the goals and philosophy of science.

Professor Ted Madden and Dr. Randy Mackie eased my transition from the environmental consulting business into the MIT environment. I chose as my first project, to work with them on processing, modeling and interpreting magnetotelluric data collected at the Larderello geothermal field. Ted and Randy inspired me with their extraordinary technical expertise and their personal excitement about the nitty-gritty of scientific discovery. I especially want to thank Randy for saying one thing in particular. After viewing a rather confused plot I had created, he shook his head, furrowed his brow and said "No, no, no... Stop a minute... Stand back... Look at the BIIIIG picture..." I will never, ever forget that.

Shortly after I became familiar with Ted and Randy's work, I began working with another of ERL's truly exceptional scientists, Dr. William Rodi. Bill's careful work sets a professional standard in the lab that I have attempted to uphold in my work. Bill is extraordinary in more than just his scientific abilities. He is an exceptionally warm and caring person who offers his time and advice to all of the students in the lab. It is, in great part, because of him that I have completed this thesis. I look forward to our continued collaboration and friendship.

Together with Professors Toksöz and Morgan, and Dr. Rodi, three non-ERL professors served on my thesis defense committee and deserve particular note; Professor Chris Marone, defense committee chairman (MIT/EAPS), Professor Clark Burchfiel (MIT/EAPS), and Professor Michel Bouchon (University of Grenoble, France). I would like to thank each of them for offering their time and energy while reviewing the manuscript, serving on the committee, and advising me during the preparation of the thesis.

My thesis benefitted greatly by the interest and support of several individuals representing the petroleum and geothermal communities. First, I would like to acknowledge the huge contributions of Dr. Robert Withers and Dr. Richard Keck (both from ARCO). The time I spent working as a student intern under Robert's direction inspired me to pursue passive seismic monitoring as a thesis topic. His enthusiasm for the subject was contagious. Dr. Richard Keck has continued to encourage my interests, offering insights from an engineering perspective, pointing out excellent references and introducing me to a host of fracture engineers, and hydrofrac monitoring experts associated with SPE. This has been particularly helpful to me. I would like to thank both Robert and Richard for their support and encouragement while also acknowledging ARCO, as a corporation, for making the DWTI data set available for study and allowing me to continue the work started during my summer with them.

The portions of the thesis focusing on geothermal seismicity could not have been produced without the generous support of ENEL (the Italian Electricity Board). ENEL and Dr. Gian Mauro Cameli made the three data sets available for analysis and interpretation. The Tuscany geothermal fields are very interesting and I have found considerable enjoyment exploring their many facets. Dr. Adolfo Fiordelisi (ENEL) and Dr. Adele Manzella (IIRG) were instrumental in teaching me about the Tuscany reservoirs and I thank them for their expert technical advice. My sincere thanks go to ENEL for letting me work on their data.

Several others contributed to the successful completion of this thesis through their generous advice, support and in helping me keep my eye on the ball. I appreciated their gentle pats on the back and words of encouragement. Dr. Arthur Cheng (Western Atlas) and Dr. Dan Burns (ERL) were always willing to offer their practical insights or lend an ear when things overwhelmed me. Their support is warmly remembered. Likewise, Dr. John Queen (CONOCO), never failed to put me through my paces (whenever he got the chance) but always made sure that I left the conversation positively challenged and enthusiastic. Thank you, John. Chuck Doll (ERL) patiently taught me the practicalities of seismicity monitoring and never seemed to mind when I watched over his shoulder while he carefully maintained the New England Seismic Network. His enthusiasm and love for seismology made working with him a great honor for me and I am glad he let me help out from time to time. I am also honored to say that I received generous advice on the subject of clustered seismicity and passive monitoring from the wonderful scientists at the Los Alamos National Laboratory (LANL) and Tohoku University, Sendai, Japan. My heartfelt thanks go to Dr. W. Scott Phillips (LANL), Dr. Jim Rutledge (LANL), Dr. Leigh House (LANL), Dr. Mike Fehler (LANL), Professor Hiroaki Niitsuma (Tohoku), Dr. Hirokazu Moriya (Tohoku) and Dr. Kazuhiko Tezuka (JAPEX).

ERL is fortunate to have a staff of superb administrative professionals, and graphic artists who make sure that the lab functions smoothly and that the fruits of everybody's labor are polished and professional. Sara Brydges, Liz Henderson, Sue Turbak, and Kate Jesdale keep us all sane by directing and activating the lab functions that allow all of us to complete our objectives. Naida Buckingham was, for too brief a time, also invaluable in helping me write understandable text and translating works from my Italian colleagues. I look forward

to thanking her personally, if I can catch up with her! Jane Maloof expertly administers ERL's complex computer resources and patiently teaches the ERL students and staff how to navigate in the ether without too much pain and agony. I am sure it must feel like herding kittens to her and my hat is off to her important contribution. Over all, I surely could not have successfully completed this thesis without their expert advice and emotional support. I am grateful for having had the opportunity to work with each of them during the past six years and look forward to many more years of friendship, fun, and perhaps professional interaction.

I was also fortunate to have the advice of several counsellors who helped me evaluate my motives, resolve my conflicts, and refresh my commitment. My sincere thanks go to Bonnie Broe, Rich Goldhammer, Dawn Metcalf, Dan Burns, Scott Sewell and most especially, Lynn Roberson and Uli Dettling. Each of these gifted individuals helped me find my way and I am very grateful for their assistance.

In directing ERL, Professor Toksöz has brought together talented students, post-docs, research scientists (both visiting and in residence) and support staff to make the lab a place of creative discovery and lively interactions. Through those interactions I have built important professional and personal relationships. My student colleagues have, on many occasions, proven to be not only insightful scientists in their own right, but wise and caring confidants. Several people in particular spent countless hours supporting me with wise counsel and a strong shoulder. Chantal Chauvelier exhibited extraordinary emotional strength and professional integrity during her stay at ERL and I cherish both her friendship and her example as a talented scientist. Dr. Bob Greaves and I started at the same time and spent many hours over homework for the same classes. Lunches with Bob were always a highlight of my time here and the comraderie was greatly appreciated. And then there is Dr. Oleg Mikhailov. What can I say about Oleg that can possibly do justice to his good humor and radiant personality? He brightened my day every time he came to visit my office and I can only say that I hope that someday we will work side by side on a project that we both love. What a treat and honor that would be for me. I can't wait! David Cist has also been a close friend during my stay at the lab and I would like to thank him for being a breath of fresh air. His uncommon grace is no less than an inspiration and I am pleased to call him a friend.

I wish that I had all of the room in the world to thank each of the ERL students and staff who have walked with me. Let me just say thank you to: Dr. Matthijs Haartsen and Dr. Matthias Imhof (my first office mates), Dr. Joe Matarese (for his extensive computer help), Dr. Bob Cicerone (for his wise counsel and warm friendship), Abdulfattah Al-Dajani (for knocking on my door....often), Dr. John Olson (for his wisdom and enthusiasm), Dr. Rob Reilinger (for his consistent support, conversation and coffee breaks), Dr. Roger Turpening (for his contagious confidence and joyous outlook on life), and Phil Reppert (for his vision and his companionship on the train). My heartfelt thanks also go to Stacey Frangos, Dr. Weiqun Shi, Dr. Jie Zhang, Xiaojun Huang, Jonathan Kane, Mary Krasovec, Dr. John Sogade, Dr. Shen Feng, Dr. David Harkrider, Dr. Rama Rao, Dr. Zhenya Zhu, Carolynn Bischoff, Margaret Edie, Dr. Felix Herrmann, Jesus Sierra, Youshun Sun, Yervant

Vichabian, Muhammad Al-Saggaf, Koichi Hayashi, and Hafiz Alshammery.

Some people who have helped me I am only beginning to get to know. I look forward to working with Jim Lewkowicz, Dr. Delaine Reiter, and the rest of the talented people at Weston Geophysical. They have been so patient in waiting for me to finish. I thank them for welcoming me so enthusiastically!

It is traditional to thank family members and close personal friends last and this is their rightful place. Because it is their contribution to this thesis that has the deepest roots, it is justified that their names should echo on after the last words from this page are read.

First, I am deeply indebted to Janet Burge, Chuck Jones, Mark Mezger, Rich Dickey, Ken Leach, and Coleman Joyce for their consistent support throughout my thesis efforts. They never faltered in expressing their confidence, especially when I needed it most. I also thank them for not giving up on me when I had to turn down their offers of "fun stuff to do". I thank them all for standing by me.

I'd like to thank Mr. Kaye Berigan for teaching me how to be comfortable with myself. A long time ago (and, hopefully, today as well) he created the most beautiful music and I had the opportunity to be there, to hear it, feel it and understand what it meant to be a part of it. His main objective, I think, was to teach each of us to be the best musicians we could be. I want him to know now that it was in his classroom that I learned to be the best PERSON I could be. He was always calm and he spoke quietly with a tone that always made me feel that he had really thought about what he was saying and that he meant it. I trusted him and from that trust I gained an important insight about who I was and about the value of my contribution to the world. From him I learned that if I cared about what I was doing and paid attention, anything I tried would be made of love and it would be as beautiful as the music those children were learning to play back then. His acceptance of us as individuals and our music, no matter how rough hewn, was the key to my ability to perservere when I was afraid of failing. I cannot tell you, or him, how important that is to me now and how I will cherish it in the future. But knowing him, I suspect that he may be able to guess....

And so I come to my family. My family is, perhaps, unaware that they have always been in my thoughts. I have traveled away from them in my pursuit of experiences and I know that this has been hard for them...seeing me go. Despite their sadness due to my absense they have continued to support and encourage me and that has touched me deeply. It is in our current closeness that I can now see how we have grown from, and perhaps triumphed over, our shared personal tragedies. Our victories will outlast any tears we have shed. I can only say thankyou for staying with me and for keeping a deep and abiding faith that we all stand stronger if we stand together. I am deeply indebted to my mother, June Tendick for teaching me responsibility, committent and courage, to my sister Diane Ammerman, for teaching me gentleness and humility, to my brother, Eric Tendick, for teaching me an appreciation for beauty and precision, to my sister Leslie Wilson, for teaching me quiet strength and compassion, and to my late father, for teaching me the meaning of sacrifice

and consequences.

There is one more person I wish to thank; my past, my present and my future; my husband, Steve. He has been, throughout our long association, a creative force of such power and brightness that it can seem unreal at times. During my stay at ERL I was often humbled by his ability to enter into a problem I was having in my research and to assimilate the information immediately. He would reorganize the problem and synthesize a solution, apparently without effort! In many ways, he is my ideal scientist, and I have often pondered his way of seeing the world. It still eludes me, but now I often just sit back and watch how beautiful his work is. Because of his insatiable curiosity and his tremendous technical range, he allowed me to come home each evening and read my books and research ideas aloud. Or, maybe it was just because he loved me... In either case, I am so glad he has chosen to be by my side. He is truely remarkable and I love him for everything that he has been, is, and will be.

Thank you every one....

Biographical Note

Shirley Ann Rieven was born September 6th, 1962 in Milwaukee, Wisconsin to June and Leonard Tendick. She attended Milwaukee Public Schools for her primary education and graduated from James Madison Senior High School in 1980. She received her Bachelor degree in Applied Geophysics from Michigan Technological University (Houghton, MI) in May, 1986 (under her married name of Danke). After completing her undergraduate education, she taught physical and historical geology at Ferris State College in Big Rapids, Michigan during the Fall of 1986 and Spring of 1987. In May 1987, she accepted a position with NUS Corporation (later, Halliburton NUS Environmental Corporation) where she attained the position of project manager for Hazard Ranking System (HRS) scoring for hazardous waste sites being evaluated for inclusion on the National Priority List (as defined under the Comprehensive Environmental Response, Compensation and Liability Act (CERCLA, or "Superfund") (as amended)). In September, 1992 (under her remarried name of Rieven), she was accepted by the Earth, Atmospheric and Planetary Sciences department of the Massachusetts Institute of Technology as a graduate student in geophysics working in the Earth Resources Laboratory under the direction of Professor M. Nafi Toksöz. This thesis, completed in partial fullfillment of the requirements for the degree of Doctor of Philosophy in Geophysics, was successfully defended on December 16th, 1998. February 1, 1999 she will begin working with Weston Geophysical Corporation of Northboro, Massachusetts as a research seismologist.

Contents

1 Introduction **16**

1.1 Introduction and Definition of Terms 16

1.1.1 Placing this work in Context: Current State of the Art and the History of Microseismic Observation and Monitoring at Reservoirs . . . 17

1.2 How the work in this thesis contributes 27

1.3 Outline 28

2 Case Descriptions **32**

2.1 Introduction to the Case Studies 32

2.1.1 Monitoring Microseismicity during a Hydraulic Injection Experiment in Eastern Texas 32

2.1.2 Monitoring Microseismicity During Production at Geothermal Fields in Western Tuscany 38

2.2 Sensor Array geometries and Example Waveforms 43

2.2.1 Sensor Array and Seismic Record Display for the DWTI MEQ data 43

2.2.2 Sensor Array and Example Seismic Records for the LAGO Cluster . 45

2.2.3 Sensor Array and Example Seismic Records for the Larderello 1993 Swarm 46

2.2.4 Sensor Array and Example Seismic Records for the Monte Amiata 1997 Swarm 46

2.3 Geologic and Seismic Velocity Model Estimation 47

2.3.1 DWTI Velocity Model 47

2.3.2 The Larderello Geothermal Field Velocity Model 48

2.3.3 The Monte Amiata Geothermal Field Velocity Model 49

3 Analysis **68**

3.1 Hypocenter Modeling of the DWTI Induced Microearthquakes 68

3.1.1 Non-Linear Least-Squares Inversion of Microearthquake Arrival Time Data 71

3.2 Hypocenter Modeling of the Tuscany Geothermal Field Microearthquakes . 74

3.2.1 Data Processing for Absolute Hypocenter Modeling: Process steps 1 - 5 75

3.2.2 Absolute Event Hypocenter Modeling: Process Steps 6-8 76

3.2.3 High Resolution Relative Event Relocation 78

4 Interpretation **142**

4.1 Interpretation Objectives 142

4.2 Interpretation of the DWTI Hydraulic Fracture Induced Microearthquakes . 146

4.2.1 Cluster Identification 146

4.2.2 Cluster Source Process Evaluation 147

4.2.3 Process Diagnostics 147

4.2.4 Follow-on Analysis: Implications and Technology Evaluation 157

4.3 Interpretation of the Tuscany Geothermal Field Microearthquake Clusters . 158

4.3.1 The Larderello 1993 MEQ Swarm 158

4.3.2 Follow-on Analysis: Implications and Impact on Production Related Processes 164

4.3.3 The LAGO MEQ Cluster 165

4.3.4 Follow-on Analysis: Implications and Impact on Production Related Processes 170

4.3.5 The Monte Amiata MEQ Swarm 171

4.3.6 Follow-on Analysis: Implications and Impact on Production Related Processes 173

5 Discussion and Conclusions **190**

5.1 Discussion 190

5.2 Conclusions 191

A Review of the Natural Resources and Geology of Texas and the Gulf of Mexico Basin **194**

A.1 Introduction 194

A.2 Introduction to the Natural Resources of the Texas Gulf Coast 195

A.3 Review of the Geology and Geodynamics of the Gulf of Mexico Basin . . . 197

A.3.1 Sedimentary Structures of the Texas Gulf Coast 199

A.4 Hydrocarbon and Geopressured Geothermal Resources 202

B Review of the Energy Resources and Geology of Tuscany and the Tyrrhenian Back-Arc Basin **205**

B.1 Introduction to Energy Production in the Geothermal Fields of Tuscany . . 205

B.2 Review of the geology and geodynamics of Italy and the Alpine-Mediterranean Region 208

B.2.1 Geodynamics of the Alpine-Mediteranean Region 209

B.2.2 The Geology and Geodynamics of Italy - The Apennine Orogeny . . 214

B.3 The Tuscan Geothermal Fields 220

B.3.1 Local Geology 220

B.3.2 The Larderello Hydrothermal Reservoir 220

C Confidence region estimation for ARCO's DWTI Demonstration Project Induced MEQs **226**

C.0.3 Conclusions 229

D Animations **243**

Chapter 1

Introduction

1.1 Introduction and Definition of Terms

This thesis presents the analysis and interpretation of microearthquakes near petroleum and geothermal reservoirs. The work focuses on spatially and temporally related events from three geographic areas, one associated with petroleum operations (a waste disposal simulation), and two from geothermal (steam) reservoirs. The interpretation of the event characteristics increases our understanding of the seismic response of these geologic structures to natural and man-made stress perturbations within and around the reservoirs. This information can be used in future reservoir management plans and during real-time field operations. Before proceeding on to a discussion of the data analysis and results, I will define several terms used throughout the text. This brief review is intended to provide a common vocabulary for expanded discussion in the later sections.

Microearthquake monitoring is the practice of recording, analyzing, and interpreting earthquakes with local magnitudes $M_L \leq 2.5$. The practice shares its fundamental physical principles with global and regional earthquake seismology but differs somewhat in application due to the data acquisition criteria for small events. Local networks, like the ones installed at geothermal fields, are designed and instrumented specifically for recording the

short period seismic signals emitted by small, nearby disturbances. Never the less, these networks are also capable of detecting events exceeding the $M_L = 2.5$ upper bound (albeit, perhaps not optimally) and often do, providing a useful cross-reference for calibration purposes.

Regardless of the network scale, all seismic stations are subject to some degree of noise. These signals, which were traditionally referred to as "microseisms", are produced by non-earthquake related ground motions, particularly those produced by wind or wave action. The definition specifies microseisms as seismic disturbances with characteristic spectral frequencies of less than 1 Hz (Bates and Jackson, 1984; Lay and Wallace, 1995). However, literature on the subject of induced MEQs, commonly includes the term "microseismicity" where it is used synonymously with the phrase "microearthquakes". I will adopt this convention and avoid the somewhat ambiguous term "microseism" in favor of the more general term "noise".

In discussing groups of events, several descriptors are commonly encountered. The term "earthquake swarm" refers to a temporal series of events that are spatially correlated but not associated with an identified main shock and this is how it will be used here (Lay and Wallace, 1995). To differentiate swarms from groups of events that are spatially but not necessarily temporally correlated I will use the terms "cluster" or "subcluster".

1.1.1 Placing this work in Context: Current State of the Art and the History of Microseismic Observation and Monitoring at Reservoirs

Microseismic monitoring of oil, gas and geothermal reservoirs evolved slowly over a period of nearly 80 years. Its history is an excellent example of how developments in technology are driven by the needs of society, facilitated by advances in other technologies and tempered by the limits of scientific understanding. In the case of MEQ monitoring of petroleum and, eventually, geothermal production operations, the driving force was society's rapidly growing energy consumption at the beginning of the century. Figure 1-1 presents a timeline of

important developments in the history of seismicity studies near petroleum and geothermal reservoirs. One of the facilitating technologies was the development of the portable Galitzin and Wood-Anderson Seismometers, introduced in 1914 and 1922, capable of being deployed in temporary seismic networks (Lay and Wallace, 1995). By the early 1920s, hydrocarbon production was well underway in many US states including Texas and California while production of electricity was beginning at the Larderello geothermal field in Western Italy. Massive extraction of oil and natural gas at a number of fields were producing measurable surface subsidence. A number of small, "felt" earthquakes in the 1920s at the Goose Creek oil field in Southern Texas were the first reported incidences of seismicity related to on-site production processes (Figure 1-1) (Segall, 1989; Kovach, 1974; Nicholson and Wesson, 1992). Although these felt events were apparently not recorded seismically, they mark the beginning of the movement toward active monitoring programs.

During the years following the observations at Goose Creek, product recovery at hydrocarbon fields continued to climb. At the Wilmington Oil Field near Long Beach, California, the rate of extraction rose rapidly after 1946 eventually reaching its peak production at the end of 1951 (Kovach, 1974). A series of earthquakes with magnitudes ranging from 2.4 to 3.3 M_L occurred at the Wilmington Field in 1947, 1949, 1951, 1955 and 1961 (Figure 1-1). These extremely shallow events were recorded at seismographic stations in Riverside and Pasadena where they produced seismograms exhibiting large amplitude surface waves (Kovach, 1974). The events were attributed to displacements of 20 cm due to horizontal shear at the Wilmington Oil Field, a conclusion corroborated by direct observation from cores drilled at the site. Production wells at the site were damaged by the dislocations, some unrecoverably. Extraction related pore pressure reductions and the subsequent impact on production at hydrocarbon reservoirs motivated the introduction in 1943 of water injection as a means of pressure maintenance during late stage primary recovery operations (Muskat, 1981). Subsidence at Wilmington was eventually stopped by the use of this technology (Kovach, 1974).

The ever increasing demand for oil and gas and the need to improve deliverability led to the introduction of hydraulic fracturing as a secondary recovery technology at Hugoton Gas

field, Grant County Kansas in July, 1947 (Figure 1-1) (Veatch *et al.*, 1989). This technology utilized high pressure injection of water and/or other fluids to "stimulate" production in the reservoir by creating fractures and thereby producing new flow conduits. This technology would become extremely important in increasing the total recoverable hydrocarbon reserves, eventually being applied at more than 30 percent of the oil wells and 50 percent of the gas wells in the U.S. (Wolhart *et al.*, 1998).

In the years following the introduction of the injection technologies, determining the underlying causes of anomalous seismicity at reservoirs became more difficult because both extraction and injection were possible causes. Segall (1989) described the poroelastic behavior of reservoir rocks undergoing fluid extraction and illustrated how a reduction of reservoir pore pressure produces contraction near the extraction point and zones of high stress in the surrounding rock mass. This "remote" shear failure is manifested as earthquakes with normal and reverse type focal mechanisms along the flanks of the reservoir (Segall, 1989). The alternative cause of seismicity, injection of fluids, can also modify the reservoir stress conditions by increasing pore pressure near the injection point and Segall (1989) states that this increase reduces the effective normal stresses in the near formation allowing affected faults to fail under ambient shear stresses.

A number of excellent journal articles present detailed analyses and interpretations of the seismicity where both extraction and injection were potential causes. Some of the most cited studies focused on event clusters that were either known to have been induced or were strongly suspected. Good examples include observations at the Lacq gas field in France, various hydrocarbon fields in the Central Basin Platform of West Texas (War-Wink, Odessa, and Keystone), the Rangely Oil Field in Northwest Colorado, and the Gazli Gas Field in Uzbekistan (Figure 1-1) (Grasso and Feignier, 1990; Simpson and Leith, 1985; Bredehoeft *et al.*, 1974; Rogers and Malkiel, 1979). The Gazli events are important because they represent an example where the proximity of a production facility to a number of isolated high intensity earthquakes produced considerable attention and concern for public safety. However, attributing these events to a specific source process is complicated by the existence of active regional tectonics and so remains a topic of continued study. The Lacq gas field

and the West Texas studies are illustrative of general production related seismicity while the Rangely oil field was the site of an important experiment demonstrating the correlation between injection pressure and seismicity. I will review two of these cases, specifically the Lacq gas field events and the Rangely oil field experiment, as brief but illustrative examples of induced seismicity case studies.

Grasso and Feignier (1990) describe the results of ten years of seismic monitoring at the Lacq Gas Field. They report the results of locating over 800 earthquakes with magnitudes ranging from 1.0 to 4.2 and conclude that the majority of these events originated in a very small volume near the center of the field. The network of seismic receivers included an array of seven surface sensors and one analog three component borehole sensor with telemetry data transfer. Production programs at the Lacq field began in 1950 with the extraction of oil and the injection of water. In 1959, the production of gas from an anticline controlled trap overtook the production of oil at the site. Seismicity began to be observed in 1969 and the monitoring program was initiated in the early 1970s (Grasso and Feignier, 1990; Feignier and Grasso, 1990).

Feignier and Grasso (1990) expanded the analysis of 120 of these earthquakes by calculating composite focal mechanisms. The authors analyzed the spatial and temporal variations of the failure planes and compared the results to known structures at the field. They concluded that 20 years of production and the subsequent reduction in reservoir pressure by up to 50 MPa caused compaction of the central portion of the reservoir which, in turn, reactivated pre-existing faults at the edges of the field and stratigraphic interfaces in the central portions of the anticline. They concluded that in the Lacq gas field the effects of extraction were more important than the effects of either wastewater reinjection or regional tectonics in determining the spatial distribution of seismicity and that the failure occurred on pre-existing planes of weakness which were favorably oriented with respect to the resultant local stresses (Feignier and Grasso, 1990; Grasso and Feignier, 1990).

Seismicity monitoring at the Rangely Oil Field was undertaken in 1967 in a joint venture between the U.S. Geological Survey (USGS) and Chevron Oil Company, the operator of the

field. A USGS seismic station in Utah recorded an unusual amount of seismicity located near the waterflood area of the field. In an effort to understand this phenomenon, a three-phase program was undertaken in 1969 to monitor the seismicity during a controlled series of waterfloods. The program, which ran for four years, demonstrated that the induced seismicity could be "controlled" directly by variations in hydraulic injection fluid pressure. The authors state that under the favorable geologic conditions at the site, the seismicity was noticibly reduced by decreasing the injection pressure during phase 1 of the experiment. Increases in injection fluid pressure during phase 2 reactivated local faults and reinitiated observable amounts of seismicity (Figure 1-1) (Bredehoeft *et al.*, 1974).

During the late 1950s and early 1960s, when the application of hydraulic fracturing was expanding and becoming a major technological contributor in increasing recoverable hydrocarbon reserves, a number of international geothermal programs were initiated. The U.S. brought the Geysers Steam Field online, while New Zealand began production at Wairakei and Japan initiated operations at the Matsukawa field (See Figure 1-1) (DiPippo, 1985; Thain, 1985; Mori, 1985). Geothermal operations require the extraction of hot fluids from the formation (steam, hot water, or a combination) in order to generate electricity (Garnish, 1985). Typically, these fluids are extracted without reinjection as long as the reservoir maintains pressure. After pressure decline, for preventative pressure maintenance and for general reservoir fluid replenishment, water or condensate reinjection is commonly initiated. For most of the geothermal fields brought online during the sixties (and earlier in the case of Larderello), water reinjection programs were not employed until the mid 1970s or later (Figure 1-1) (Ferrara *et al.*, 1985; Duprat and Ungemach, 1985; Eberhart-Phillips and Oppenheimer, 1984). In some cases, water reinjection programs were applied intermittently due to concerns about the potential environmental impact (Thain, 1985; Mori, 1985).

The areas of the crust where geothermal resources exist commonly exhibit a certain amount of naturally occurring "felt" seismicity. Thus, seismic observations near geothermal fields were historically conducted as a matter of course as soon as seismic networks began being installed (in some cases, network installation preceeded establishment of the geothermal production facilities). Figure 1-1 shows the relationship between the beginnings of production

at various geothermal fields and the development of seismic data acquisition systems.

Many of the worlds geothermal fields benefited from the proximity of federally funded seismographic stations as well as university operated arrays of portable, temporary sensors deployed directly at the site. For instance, seismicity studies addressing activity near the Geysers steam field in northern California utilized seismic records from various networks. For instance, in 1966, the USGS established the Central California Seismic Network (CALNET). Eberhart-Phillips and Oppenheimer (1984) used the catalog of events from 40 sensors from this network to complete a spatial and temporal analysis of events recorded from 1975 to 1982 (Eberhart-Phillips and Oppenheimer, 1984; Lay and Wallace, 1995). Young and Ward (1977) published an analysis of seismicity recorded by a portable array of 14 three component sensors operated by the USGS in the Clear Lake area near the Geysers field. Similarly, O'Connel and Johnson (1982) cite data from a nine station array of 3-component digital recorders in the area of the main production which they used to determine a more accurate velocity model and source mechanisms for the observed events.

In addition to having recordings from USGS (and for non-US fields, other nationally funded networks) many geothermal fields, like the Geysers, continued to supplement their own local networks for ongoing monitoring. Using whatever records were available, public or private, various organizations began publishing the results of seismologic studies near geothermal fields in the early 1970s. Evaluations of event statistics and source parameters were published for seismicity at the Salton Sea Geothermal field in the Imperial Valley of California (Lee, 1976; Jarpe *et al.*, 1989), the Coso Geothermal field, also in southern California (Roquemore and Zellmer, 1982; Pavlis and Booker, 1983), Cerro Prieto in Mexico (Albores *et al.*, 1977; Grannell *et al.*, 1982) and later, for Hengill in Iceland (Julian *et al.*, 1993), Chipilapa in El Salvador (Fabriol *et al.*, 1992) and Kakkonda in Japan (Niitsuma *et al.*, 1985b).

The success of the international geothermal projects paired with an awareness of the world's growing energy consumption heralded a transition in the history of microseismic monitoring at energy production operations. In 1970, the Los Alamos Laboratory applied for a U.S.

patent for the process of recovering heat from a Hot, Dry Rock (HDR) geothermal reservoir by hydraulically fracturing the formation and injecting water for later extraction as a heat transfer fluid. In 1974, the U.S. HDR Geothermal Energy Development Program began with the first HDR hydraulic fracture conducted at the Fenton Hill site in northern New Mexico (Duchane and Albright, 1996). This program incorporated the specific application of microseismic monitoring as a means of delineating the new fractures and demonstrated its potential by recording over 10,000 microseismic events during various injection experiments conducted over the 20 year life of the project (Potter and Dennis, 1974; Fehler *et al.*, 1987; Albright, 1976; Li *et al.*, 1995). In 1978-1979, the International Energy Agency (IEA) including representatives of Germany, Japan, Sweden, Switzerland, the UK and the USA, collaborated in a program to evaluate alternate methods of heat mining. The conclusion supported the application of hydraulic fracturing as the best option (Garnish, 1985). Those countries also initiated HDR programs, specifically, the UK's Camborne School of Mines (CSM) site at Rosemanowes in Cornwall, Germany's Falkenberg site, Le Mayet de Montagne and Soultz-Sous-Forêts (in the Rhine Graben) France, Hijiori in Japan, and Fjallbäcka in Sweden. Many of these included microseismic monitoring programs to provide information about the hydraulic fracture and the effectiveness of the stimulations. The application of microseismic monitoring to hydraulic injection at these sites contributed important insights into the technology of hydraulic fracture in crystalline rock and provided opportunities to design and test downhole seismic arrays (Garnish, 1985; Bachelor, 1996; Kuriyagawa *et al.*, 1996; Sato and Abé, 1996; Heineman-Glutsch and Kappelmayer, 1996; Baria *et al.*, 1996; Wallroth and Dyer, 1996).

While geothermal energy production technologies continued to develop and HDR projects came online, hydrocarbon production was requiring increasingly sophisticated methods of recovery. Significant research efforts were made refining secondary recovery methods and developing EOR (enhanced oil recovery) technologies such as steam or hot water drives, and CO_2 recovery. These new technologies would require improved diagnostic tools for assessing the results of the stimulation treatments (Moritis, 1998).

In 1986, Sandia National Laboratories conducted a hydraulic fracture of a tight gas (perme-

abilities k, $0.1 \leq$ *millidarcies*), fluvial sand formation at the US Department of Energy's "Multiwell" (MWX) experiment site (Figure 1-1). They demonstrated Sandia's Borehole Seismic System (BSS) for monitoring the fracture by recording microseismicity using three downhole seismic receivers in each of two wells (Thorne and Morris, 1988). Over 100 MEQs were recorded during the 22,000 gallon foam and 32,500 lb proppant stimulation. Twenty-nine of these events were recorded with sufficient quality to be located using hypocenter inversion methods (Thorne and Morris, 1988). The authors state that the MEQ hypocenters delineated the fracture well enough that an azimuth could be determined with a *"fairly high level of confidence"*, but that dependence on observations from a single well could lead to erroneous azimuths in inhomogeneous and anisotropic formations. They also indicate that fracture height was not determined due to *"the near total absence of microseisms near the bottom of the fracture"*.

Vinegar *et al.* (1992) published the results of a fracture stimulation conducted by Shell Oil Company in the Belridge Diatomite Formation, California. The very tight well spacings specified in the reservoir engineering designs required strict fracture geometry parameter estimation. Length and azimuth of the fracture had to be determined as precisely as possible to optimize resource recovery. Thus, a microseismic monitoring program was designed, instrumented and completed. The data acquisition system recorded seismic signals from 56 downhole receivers (from a string of 150) in two monitoring wells and the treatment well. 132 events were recorded with sufficient quality to be used for hypocenter location. The results indicated a fracture with complicated geometry, showing growth both upward and downward in two of the higher permeability zones of the target formation. The authors stated that *"Classic pressure decline analysis cannot predict where fractures will occur or handle the case of multiple fractures in a single stimulation"*. They continue, adding that *"These processes are neither well understood nor included in current hydraulic fracture models"* (Vinegar *et al.*, 1992).

The spatial and temporal distribution of seismicity recorded during other monitoring programs indicated complex stress distributions as well, particularly the results from the Fenton Hill HDR site (Fehler, 1989; Dreesen *et al.*, 1987; Fehler *et al.*, 1987). In fact, each of the

HDR sites shown in Figure 1-1 were being monitored for MEQs during circulation and flow tests. The distribution of events in the stimulated volumes and the relationships between the onset of seismicity, pumping rates and volumes were presented at international forums on HDR technologies. In addition to the many published studies conducted by scientists at the Los Alamos National Laboratory regarding the seismicity at the Fenton Hill HDR site, detailed studies have also been published for MEQ swarms during production at the Ogachi, Soultz-sous-Fôrets, and Hijiori HDR reservoir developments (Willis-Richards *et al.*, 1996; Moriya *et al.*, 1996; Jones *et al.*, 1996; Helm and Hoang-Trong, 1996; Sasaki, 1996).

These examples from the petroleum and HDR fields illuminate circumstances where production decisions are directly impacted by the application of microseismic monitoring during extraction, injection or both. Hydrothermal sites introduce an additional complication. Specifically, most of the worlds major hydrothermal fields are located in seismically active areas, particularly near convergent plate boundaries where magmatic upwellings provide sources of heat. Natural seismicity associated with the movement of magma in volcanic systems, thermal contraction of the cooling structures, or tectonic processes related to plate motions, can mask the occurrence of production related seismicity. Eberhart-Phillips and Oppenheimer (1984) reported that reinjection was being conducted at the Geysers as early as 1980 and a reinjection program was initiated at the Larderello field in 1981 (Ferrara *et al.*, 1985). The combination of natural seismicity coupled with the potential for production related events expands the goals of microseismic monitoring from fracture diagnostics to include event type descrimination as well.

A number of important complications affect monitoring programs at the major geothermal fields. High formation temperatures and harsh fluid chemistry has thus far limited the installation of borehole monitoring systems. Subsequently, local networks have been limited to traditional surface arrays. Additionally, the geologic environments where geothermal resources exist are inherently complex and this produces complex seismic signals and imposes a variety of specific data processing needs such as more sophisticated seismic velocity models and inversion techniques. In contrast, production from HDR reservoirs often utilize heat from within fairly homogeneous granite masses where the conditions are less inhospitable to

the acquisition equipment. Monitoring programs at these sites have subsequently been able to install borehole sensor arrays which allows much better coverage of the MEQ activity.

Additionally, MEQ monitoring can be used to assess the efficacy of various other hydraulic injection related technologies. For instance, brine and other industrial process fluids and solids have been injected into hydrologically isolated formations as a means of waste disposal. In some cases, this injection has lead to reactivation of local faults. This was shown to be the case following a brine injection during salt mining near Attica-Dale, NY (Figure 1-1) (Fletcher and Sykes, 1977). The spatial correlation of the injection and a nearby fault was discovered after an increase in seismicity occurred near the facility. In this case, the seismicity was associated with high rates of fluid injection very near the fault zone. Fortunately, MEQ monitoring can also be used as a diagnostic tool in careful waste disposal operations. In this case, the objective is to delineate the distribution of disposed materials in the formation and provide information regarding deviations from expected behavior during the procedure. The successful application of this technology was demonstrated in 1993 by ARCO. The seismicity data recorded during this simulated waste disposal in a major petroleum bearing formation in East Texas provides one of the case studies for this thesis. The details of this demonstration will be provided in Chapter 2.

In all of these applications, there is the additional desire to understand the risks posed to public health, safety and property if an induced earthquake of sufficient intensity were to occur. The damaging effects produced by the unintentional inducement of events at the Wilmington, California field and the long-standing controversy surrounding three high magnitude events near the Gazli Field in Uzbekistan highlight the concern for safety and the need for the reduction of risk and potential liability. In this regard, Cypser and Davis (1995) addressed the possible legal ramifications regarding the generation of induced and damaging seismicity from production facilities and urged that the potential for increased public scrutiny be strongly considered during the development of reservoir management plans.

Through this review we can see that MEQ monitoring at reservoirs has evolved from a no-

tation of spatial correlation during general seismicity studies to an active production technology. The advantages are clear for its use as a fracture treatment diagnostics method, as a health and safety monitoring tool, and in its more classic application as an interpretive aid for general reservoir behavior assessment. However, several problems have existed until recently that limit its widespread application during either petroleum or geothermal operations.

In both venues, it would be useful to apply the technology during invasive procedures in real-time as a means to feedback reservoir response parameters to the operators. For this application to be practical, it requires the development of data acquisition systems that provide adequate sensor coverage, and fast, portable computer hardware with adequate memory to deal with real-time data rates. Likewise, it requires high-speed data processing and analysis tools. These must be provided at a cost that is competetive with other stimulation diagnostic tools, such as tilt-meter analysis, pressure testing, or radioactive tracer technologies. The cost of installing a seismic sensor array for MEQ monitoring remains prohibitive for most common production activities although the development of microelectronics and a movement toward smaller, slim-hole tools and high-temperature sensors is encouraging in this regard.

In addition to having the ability to instrument the site for active production monitoring, we must demonstrate that MEQ hypocenter analysis produces results with adequate resolution to answer production questions. Use of the technology will increase when successful applications have been completed and reported.

1.2 How the work in this thesis contributes

The general objectives of the work described in this thesis were to:

- demonstrate that "Real-Time" MEQ hypocenter modeling can be used to characterize the spatial and temporal nature of hydraulically induced rock failure.

- demonstrate the application of relative event hypocenter inversion for clustered MEQs in geologically complex geothermal reservoirs and show how the results can be used to characterize relationships between the seismicity and either natural or production related causes.

The specific objectives completed in support of the general goals were to:

1. **Expand and adapt** pre-existing absolute and relative earthquake hypocenter modeling methods to meet the two general goals stated above. The computer codes and methods worked on included:
   - A "Real-Time" hypocenter location program for monitoring induced seismicity associated with hydraulic fracture stimulation.
   - A multiple event location program used to determine high resolution hypocenter estimates by the inversion of differential traveltimes between event pairs.
2. **Apply** the aforementioned processing methods to clustered microseismicity data collected in reservoirs undergoing active production and/or stimulation, specifically for clusters occurring near two geothermal fields in western Italy, and one waste disposal site in east Texas.
3. **Interpret** the spatial and temporal characteristics of the hypocenter locations in light of site specific geologic conditions for each of the field cases addressed.

1.3 Outline

The contents of this thesis are presented in five chapters and four appendices. Chapter 1 contains an overview of the history of seismicity monitoring at petroleum and geothermal reservoirs and a statement of the objectives of this thesis.

Chapter 2 presents descriptions of the four case studies, including seismic sensor array geometry, experiment designs and objectives, and fundamental geologic descriptions for the

areas being monitored. The basic geologic descriptions in this chapter refer to appendices containing detailed summaries of current literature on the geology and geodynamics for the regions. The appendices are offered as a means of providing a common understanding of geologic and geodynamic models for the sites and may be read according to the need of the reader.

Chapter 3 presents a full description of all pertinent aspects of data analyses, including selected elements of data acquisition, P and S phase arrival determination, forward travel time modeling, velocity models used, inverse modeling of absolute arrival times, multiplet analysis, differential travel time calculation, and inverse modeling of differential travel times. The results of each step of analysis for each of the cases studied are presented during the description of the analytical techniques in consecutive order. This is done as a way of highlighting similarities and differences between the case data sets. Final results are presented at the end of this chapter.

Chapter 4 presents detailed individual case interpretations using the results offered in chapter 3. The interpretations are developed by integrating the chapter 3 results with the those of previous studies for events from the same data sets or, if appropriate, with pertinent results from studies of data from other sites of similar nature.

Chapter 5 presents a joint case discussion, placing the results from this thesis in the context of the larger problem of microseismicity monitoring at production sites. This discussion combines elements of chapters 1 and 4 to focus attention on possible future research directions. Finally, this chapter closes with a summary of the present findings for each of the studies and a revisiting of the original stated objectives.

Sources for Figure 1-1: (Baria *et al.*, 1996; Sato and Abé, 1996; Willis-Richards *et al.*, 1996; Glowacka and Nava, 1996; Rutledge *et al.*, 1995; Phillips *et al.*, 1995; Grasso *et al.*, 1995; Bard *et al.*, 1995; Gomez *et al.*, 1995; Console and Rosini, 1995; Kirkpatrick *et al.*, 1995; Feng and Lees, 1995; Fehler and House, 1995; Sasaki, 1995; Matasova *et al.*, 1995; Li *et al.*, 1995; Lay and Wallace, 1995; Tezuka and Niitsuma, 1995; Vinegar *et al.*, 1992; Keck and Withers, 1994; Truby *et al.*, 1994; Keck *et al.*, 1996; Withers *et al.*, 1996; Atlantic Richfield Corporation, 1994; Segall, 1989; Veatch *et al.*, 1989; Thorne and Morris, 1988; Niitsuma *et al.*, 1985a; Ceccarelli *et al.*, 1987; Mori, 1985; Garnish, 1985; Ferrara *et al.*, 1985; DiPippo, 1985; Thain, 1985; Wetmiller, 1986; Simpson and Leith, 1985; Muskat, 1981; Rogers and Malkiel, 1979; Fletcher and Sykes, 1977; Kovach, 1974; Bredehoeft *et al.*, 1974; Potter and Dennis, 1974)

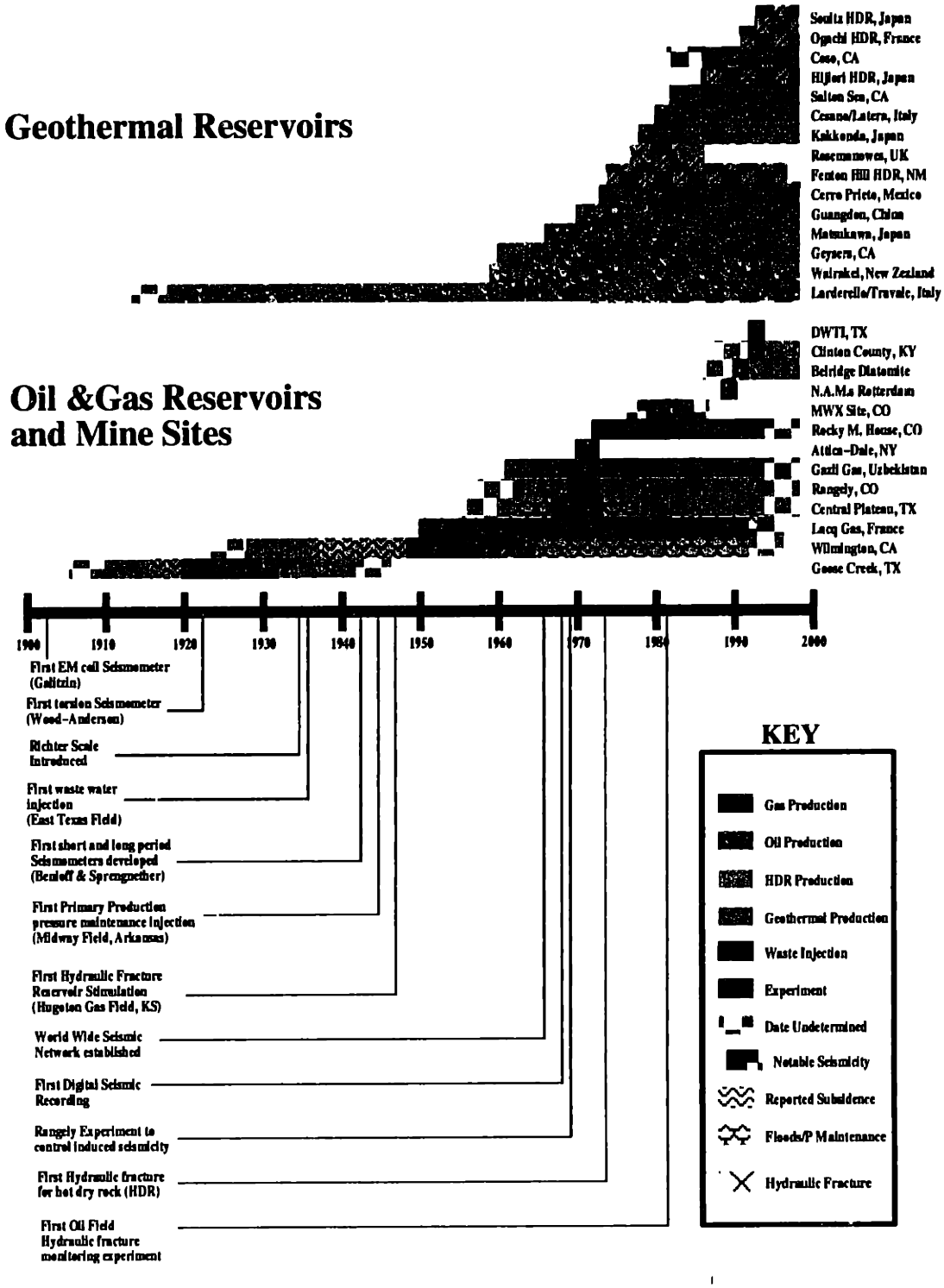

Figure 1-1: Timeline of significant events in the history of induced seismicity studies.

Chapter 2

Case Descriptions

2.1 Introduction to the Case Studies

The methodologies described in this thesis were applied to data from four clusters of microearthquakes from three different geographic locations, including induced events from a hydraulic fracture waste disposal simulation in Jasper, Texas, two distinct clusters of MEQs from the Larderello Geothermal field in Western Tuscany, Italy, and one cluster of events from the Monte Amiata Geothermal field, also in Western Tuscany. I will begin by providing a basic description (i.e. cluster location, reservoir type, number of events recorded, etc.) of each of the data sets, and a summary of the specific objectives and challenges posed in each case.

2.1.1 Monitoring Microseismicity during a Hydraulic Injection Experiment in Eastern Texas

The first cluster of microseismicity presented in this thesis was recorded during a field technology demonstration project conducted by Atlantic Richfield Corporation (ARCO). The data set represents the type of microseismicity that may be induced during invasive pro-

duction enhancement procedures such as hydraulic fracture stimulation. Although this particular hydraulic fracture was produced as part of a waste disposal technology development program in which petroleum production field conditions were simulated, the information obtained from this experiment is applicable to actively producing reservoirs (petroleum or geothermal) and wherever injection technologies are applied.

This cluster of induced MEQs was recorded using the smallest scale network of the four data sets analyzed for this thesis. That is, the longest dimension, of either the network or the fracture itself did not exceed 1500 feet in any direction. Subsequently, this data set represents the highest sampling data rate and largest total data volume of the four sets.

This cluster is presented first as a way of establishing the fundamentals of microseismic monitoring (in terms of the underlying modeling methodologies for "absolute" hypocenter locations) while demonstrating how these fundamentals can be adapted to the real-time production environment using recent advancements in computer visualization techniques. This data set is also ideal for establishing the fundamental principles because of the high quality of the recordings, the clearly defined seismic phase arrivals, the simple receiver array geometry, and the existence of strong waveform similarity from event to event over the course of the experiment.

The specific objectives of analyzing this cluster included developing and testing a "real time" computer monitoring program for use during hydraulic fracture stimulation. Monitoring objectives called for the estimation of hypocenters for as many of the recorded events as possible. The hypocenter location parameters had to be determined to the highest degree of accuracy possible within the context of real time monitoring.

Design Objectives for ARCO's Deep Well Treatment and Injection Demonstration Project

ARCO proposed that solid waste generated during hydrocarbon recovery operations could be safely disposed by suspending the solids in a bentonite slurry and injecting them into

deeply burried, hydrogeologically isolated formations. The method and its safe application were presented in a Fracture Technology Field Demonstration conducted over a five day period in October, 1993 at the Deep Well Treatment and Injection site (DWTI) in Jasper, Texas (Figure 2-1). During the demonstration, ARCO injected 4 million pounds of sand and bentonite clay and 2.1 million gallons of water into an isolated portion of the Lower Frio Sand, a major petroleum bearing stratigraphic unit in the Texas Gulf coast. The injection was conducted in 4 episodes (segments) designated as cycles 0, 1, 2, and 3. These injection cycles hydraulically fractured the sand while forcing the sand/clay suspension into the fractured zone and surrounding formation. The demonstration specifically addressed two key issues concerning the disposal method; 1) the technique needed to allow disposal of a significant quantity of waste, and 2) the affected zone must be delineated in order to ensure containment of the wastes within the isolated formation. The answer to the first issue was given immediately by the amount of simulated waste injected during the demonstration. The second issue was addressed in two parts. First, ARCO showed that the vertical fracture growth could be monitored in real time by determining the depths of the microseismic events induced by the fracture relative to the string of borehole sensors. Second, they demonstrated, using post-operation processing, that the fracture dimensions determined by microseismic monitoring were in agreement with those predicted by currently available fracture modeling methods. The results from both methods suggested that the fracture had not compromised the integrity of the upper and lower bounding confining layers (Keck and Withers, 1994; Truby *et al.*, 1994; Keck *et al.*, 1996; Withers *et al.*, 1996; Atlantic Richfield Corporation, 1994).

The processing software developed and used to process the DWTI data, the results of which are presented in this thesis, was designed to expand the field capabilities of the monitoring system so that the entire set of hypocenter parameters, not just relative vertical position, could be determined in real time. This functionality allowed the assessment of lateral fracture growth that could be used to ensure fracture containment for stimulations with horizontally limited target formations. The DWTI data set represents the test case for demonstrating the robustness of the processing software while allowing a detailed interpre-

tation of the DWTI experimental fracture configuration.

Data Acquisition during ARCO's Deep Well Treatment and Injection Demonstration Project

ARCO produced the DWTI hydraulic fracture by injecting the simulated waste into an isolated sand layer via a treatment well designated the Field Technology Demonstration Well #2 (FTD #2). Simultaneously, microseismic events were recorded by geophones located in two monitoring wells designated FTD Wells #1 and #3. Figure 2-2 presents the field geometry of the three wells. The injection well (FTD #2) was constructed using standard petroleum field completion with the perforation extending from 4426 feet to 4614 feet. The perforations were chosen such that the geologic unit receiving the waste was a 155 foot thick portion of the Lower Frio Sand (Figure 2-3). This section of the Lower Frio Sand is bounded above by a 130 foot thick layer of shale and below by a 1500 foot thick layer of shale. The Lower Frio Sand is regionally continuous and of large lateral extent. The nearest known fault is at a distance of 5000 feet away from the perforated zone (Keck and Withers, 1994; Truby *et al.*, 1994; Keck *et al.*, 1996; Withers *et al.*, 1996; Atlantic Richfield Corporation, 1994).

ARCO placed 150 30 Hertz geophones in the two monitoring wells to record the microseismic activity during the injection. Two strings of 75 geophones (25 pods, each containing three orthogonally oriented phones) were installed; one string in each of the two monitoring wells (FTD #1 and #3). The 25 pods were located along the strings at 30 foot intervals over a range spanning the target sand layer and portions of the upper and lower bounding shales. The full string of phones provided a total aperture of 720 feet for each well (Figure 2-3). The vertical location of each pod was determined using radioactive tracers but the absolute orientations of the two horizontal phones in each pod were not. The Frio Sand is a permeable, poorly consolidated layer prone to washouts; therefore, the geophone strings were cemented inside the casings.

After installing FTD #1 and #2, ARCO chose the lateral location of FTD #3 based upon the predicted azimuth of the fracture as determined from various lab and field experiments. Hydraulic fractures open "against" (perpendicular to) the minimum principle stress direction and parallel to the maximum and mid valued principal stress directions. In the Jasper field at a depth of 4500 feet, the minimum principal stress direction is thought to be horizontal and therefore the fracture was expected to lie in a vertical plane and to extend as an elliptical crack symmetrically about the wellbore. To optimally place monitoring well FTD #3, an estimate of the fracture azimuth was needed so ARCO conducted three separate laboratory tests on cores from FTD Well #1. These tests included Anelastic Strain Recovery (ASR), Differential Strain Curve Analysis (DSCA), and Velocity Anisotropy (VELAN). ASR predicted a fracture azimuth between N10W and N21E with an average azumuth of N8E plus or minus 10 degrees. DSCA predicted the azimuth to be N12E to N40E, and VELAN predicted the direction to be N35E plus or minus 5 degrees. Televiewer inspection of borehole breakouts indicated a fracture direction of N45E plus or minus 30 degrees, while examination of the strikes of nearby growth faults indicated that the fracture would extend N80E plus or minus 20 degrees. Because of the amount of disagreement between these estimates, ARCO conducted a microfrac test (fracture azimuth injection test). The azimuth of the fracture induced during this test was monitored using a surface array of tiltmeters (Figure 2-2). The final estimate of fracture azimuth was taken to be N40E. Based upon a combination of these test results, the FTD #3 was installed such that the fracture would bisect the two monitoring wells. Despite the preliminary estimates, the DWTI fracture propagated N66E and thus did not bisect the two monitoring wells as expected. Due to the nature of the experiment and the large lateral extent of the Lower Frio Sand unit, the unexpected fracture azimuth had little effect on the objective of the demonstration. These difficulties however, illustrate the challenges of determining accurate fracture propagation parameters.

During the hydraulic fracturing, microseismicity was recorded by 96 of the 150 available geophones via ARCO's Digital Acquisition System (DAS). The data was sampled continuously at a rate of 2000 samples per second and the detected events were isolated and saved

as separate event files. Approximately 2400 individual events were recorded during the 5 day demonstration. In addition to being saved as an independent file, each detected event was examined to determine which geophone along the string triggered first. Based upon the vertical receiver geometry and the concept of minimum travel time, a preliminary estimate of the hypocentral depth was determined. This method allowed an immediate assessment of vertical fracture growth, accurate to 1/2 of the pod spacing (15 feet). This was considered accurate enough (relative to the vertical extent of the bounding shale layers) to determine whether the microseismicity was confined within the sand layer. Onsite interpretation of these estimates suggested that the fracture had, indeed, stayed within the target zone. This assessment was later confirmed by a follow-up study in which ARCO calculated hypocenter locations for the 100 largest magnitude events in the suite of detected events. These hypocenter estimates were determined using a traditional least-squares hypocenter inversion algorithm and standard "record-by-record" phase picks. These hypocenter estimates delineated a cluster of events that were distributed in a laterally narrow band that extending southwest away from the injection well to a distance of approximately 1150 feet. In depth, the hypocenters were found to be located predominantly within the target sand layer with a few being located just outside of the sand in the upper and lower bounding shales. The outliers are all near the sand/shale interface indicating that the injection did not compromise the integrity of the bounding shales layers. The traditional treatment of these 100 hypocenter estimations provided an excellent baseline solution set for later comparisons (Keck and Withers, 1994; Truby *et al.*, 1994; Keck *et al.*, 1996; Withers *et al.*, 1996; Atlantic Richfield Corporation, 1994; House, 1987).

The DWTI demonstration project produced a fracture in the Lower Frio formation. The Frio is a major hydrocarbon producing stratigraphic unit in the eastern section of the Texas Gulf Coast and, as such, is representative of the type of conditions that might be encountered in the producing fields of this oil bearing province. ARCO chose this formation for the demonstration based upon its hydrogeologic isolation, its homogeneous and well documented lithologic characteristics, and its remoteness from potential stress concentrators such as faults and stratigraphic discontinuities. Specific details of the lithology and geo-

logic conditions at the sight will be presented as appropriate in later portions of the thesis, specifically during the discussion of velocity model estimation and again during the interpretation and results sections. However, for those readers unfamiliar with the geology and geodynamic history of the Gulf of Mexico and its rich mineral resources, a review of the currently available literature is provided in Appendix A.

2.1.2 Monitoring Microseismicity During Production at Geothermal Fields in Western Tuscany

The remaining three microearthquake clusters were recorded during continuous and ongoing monitoring of the Larderello and Monte Amiata geothermal fields in western Tuscany. Figure 2-4 presents a regional map indicating the locations of the two fields.

Electric power from geothermal resources in Italy is produced at four major facilities: Larderello, Travale-Radicondoli, Monte Amiata, and Latera. Exploration and development of these resources are primarily conducted by two public agencies; the Ente Nazionale per L'Energia Elettrica of Italy (ENEL) (the governmental utility), and AGIP (the national oil company) (Cataldi *et al.*, 1990; Carella, 1985). The reservoirs are all located along the western coast, northwest of Quaternary age calderas and recently active volcanic areas (Carella, 1985). These igneous structures are associated with dynamic processes acting along the northwest-southeast striking convergent boundary between the Adriatic and Corsica-Sardinia microplates.

The Larderello geothermal field is of the vapor-dominated, hydrothermal type, producing steam from depths of 100-3000m (Batini *et al.*, 1985b; Ferrara *et al.*, 1985; Block, 1991). The Monte Amiata and Travale fields are steam dominated reservoirs (Allegrini *et al.*, 1981). The average depths of the reservoir rocks are: (approximately) 800m (Larderello), 1200m (Travale), 1600m (Monte Amiata), and 2200m (Latera) (Cataldi *et al.*, 1990). The number of wells drilled at each field as of 1989 were: 503 (Larderello), 61 (Travale), 95 (Monte Amiata), and 21 (Latera) (Cataldi *et al.*, 1990). The temperatures for these fields are: 120-

400C (Larderello), 120-250C (Travale), 150-300C (Monte Amiata), and 210C (Latera). In 1989, the installed capacity of these fields were: 408.2 MW (Larderello), 90 MW (Travale), 42 MW (Monte Amiata), and 21 MW (Latera) (Cataldi *et al.*, 1990).

The shallow reservoirs of the Tuscany geothermal fields are primarily associated with Triassic anhydrites (at Larderello) and limestones (Monte Amiata), overlying carbonate formations, and metamorphic basement rocks (phyllites and quartzites) (Allegrini *et al.*, 1981). Figure 2-5 presents an east-west cross-section of the Larderello field indicating the major lithologic units that are typical of the Tuscany geothermal areas (Fiordelisi *et al.*, 1995; Batini *et al.*, 1985b; ENEL-Unita Nazionale Geotermica, 1988). The geothermal source at Larderello is thought to be a granitic type intrusion emplaced during a period of back-arc basin extension during Quaternary time (Batini *et al.*, 1985b; Block, 1991). Neogene age sediments act as cap rock for the shallow reservoir, and fill graben structures associated with Tortonian (Miocene) age extensional faulting (Minissale, 1991).

Cappetti *et al.* (1985) describe exploration and drilling of several deep reservoirs at the Larderello, Travale and Monte Amiata fields beginning in 1978 (at the Sasso 22 Well) and in the Bagnore and Piancastagnaio geothermal areas of the Monte Amiata geothermal field. The deep Sasso 22 Well in the Larderello Field was the first well in Italy reporting temperatures in excess of 400C. This temperature was measured at a depth of 2930 m below sea level. The Monte Amiata wells reported pressures of approximately 200 bars and temperatures of approximately 300C at depths below 2.6 km below sea level. In these fields, the deep reservoirs are associated with fractured zones in the Paleozoic age metamorphic basement rocks.

Cappetti *et al.* (1985) additionally reported the results of deep drilling in the Larderello field at the San Pompeo 2 well. This well was drilled on the basis of the high temperatures found in the Sasso 22 well and was subsequently drilled near the highest temperatures recorded for the Larderello shallow reservoir and over the shallowest surface approach of a strong regional seismic reflector know as the "K" horizon (See Figure 2-5). After traversing the shallow reservoir rocks, this well encountered impermeable phyllites and micaschists at

depths of 2930 meters. At this depth, a fractured zone was penetrated which contained unmeasurably high temperature and pressure fluids (explosions produced caving and borehole backfill). Later tests allowed inference of the deep formation temperatures and pressures to be approximately 400C and 240 bars, respectively Cappetti *et al.* (1985).

Understandably, the seismic "K" horizon continues to be a focus of exploration research as a potential indicator of exploitable reserves. Batini *et al.* (1985b) reported on the results of seismic reflection studies conducted at the Larderello, Travale and Monte Amiata fields indicating that the "K" horizon is a strong regional reflector that is identified at each one of the fields and has its shallowest approach to the surface in the southern Larderello field. This horizon is deeper at the Travale and Monte Amiata fields and in other sections of the Larderello Field. The results of the seismic reflection surveys show that the Tortonian age extentional faults are listric, flattening near or just below the "K" horizon Cameli *et al.* (1993); Batini *et al.* (1985b). Liotta (1991) suggested that the "K" horizon is interupted by the "Piombino-Faenza" line of transform faults (associated with differential crustal extention) which would require a pre-Tortonian age for this regional surface (Cameli *et al.*, 1993).

Various hypotheses have been proposed regarding the physical nature of the "K" horizon, including, a lithologic interface marking the top of the Hercynian age basement granite (Puxeddu, 1984), a zone of fluid bearing fractures and hydrothermal minerals (Batini *et al.*, 1985a), and a thermally controlled, kinematically active rheological boundary delineating the brittle-ductile transition in the mid-crust (Cameli *et al.*, 1993).

For a more complete summary of the regional geology and geodynamics of western Tuscany, the interested reader is referred to Appendix B.

Two of the three clusters presented here were recorded by the Larderello seismic network and the other one was recorded by the Monte Amiata seismic network. Figure 2-6 presents a site map for the Larderello Geothermal Field and indicates the approximate location of each of the microseismic cluster study areas (shaded rectangles). Similarly, Figure 2-7

provides a site map for the Monte Amiata Geothermal Field with the approximate location of the microseismic cluster study area highlighted.

Microseismicity in the LAGO area of the Larderello Geothermal Field

The first cluster of MEQs to be presented is a set of 24 events in the southern section of the Larderello Geothermal field. The original hypocenter estimates for this set (calculated by ENEL) identified the active area as being located near the Larderello seismic network station named LAGO (See Figure 2-6). This set of events will be referred to as the "LAGO" cluster for the remainder of this thesis. The original hypocenter estimates suggested a rough spatial correlation between the events. Their origin times, however, span a period of eight years, between January of 1986 and October of 1994, with small subsets of temporally correlated events. The local magnitudes of events in this cluster ranged from approximately 0.87-2.35. Figure 2-8 (top image, filled circles) presents the temporal charteristics of 24 events from the LAGO cluster.

The events in the LAGO cluster were recorded by the Larderello seismic network, a local array of thirty-one short period seismometers. ENEL provided seismic event records from twenty-five of the thirty-one stations. Twenty-three of these stations were equipped with seismometers that recorded the vertical component of ground motion only. The remaining two stations recorded all three components, i.e. north, east and vertical. Not all of the events were recorded by all twenty-five stations.

The objectives for the analysis of this data set included determining absolute hypocenter locations, identifying multiplets (if they existed), and applying high resolution hypocenter inversion techniques to refine the cluster image provided that the cluster and event characteristics met the minimum requirements for application of the method. In addition, the small number of events in this data set and the limited temporal correlation made this cluster useful for examining temporal waveform variations in a spatially associated cluster.

Ultimately, my goal for this cluster was to produce the best fit estimates of hypocenter

locations and evaluate the results in light of the current structural model for the southern Larderello Field and information regarding concurrent production operations.

The 1993 Microearthquake Swarm in the Northern Larderello Field

Events from the second Tuscany cluster occurred along the northern boundary of the Larderello Field during a 40 hour period between March 20 and March 23, 1993 (See Figures 2-6 and 2-8). The 86 events analyzed for this thesis comprise a consecutive subset of events from a larger cluster of 217 events. Magnitudes ranged from approximately 0.6 to 2.4. The block of events chosen for analysis were selected based upon the number of stations that were actively recording during that time period. Like the LAGO cluster, these events were recorded by the Larderello seismic network. Again, ENEL provided seismic event records from twenty-five of the thirty-one stations. Not all of the events were recorded by all twenty-five stations.

The objectives for this cluster (furthermore referred to as the "Larderello 1993" or "Larderello" cluster), were to relocate the events using the highest resolution techniques possible. Again, if the recorded waveforms meet the minimum characteristic requirements, then multiple relative event relocation would be applied and interpreted. Due, in part, to the "swarm" characteristics of this cluster, an important interpretive goal was to assess the likelihood of association between onsite production activities and these seismic events.

The 1997 Microearthquake Swarm in the Monte Amiata Geothermal Field

The last cluster of microearthquakes to be presented in this thesis occurred as a swarm of 75 events located near the eastern flank of the Monte Amiata Volcano. The events were recorded between March 21 and April 2, 1997 with the majority of events occurring in the first four days. Figure 2-7 indicates the approximate location of the cluster study area with respect to the volcanic cone, the Monte Amiata seismic network, and the three producing geothermal areas that make up the Monte Amiata Geothermal Field (AGF). This cluster

will be referred to as the "Monte Amiata Cluster".

The Monte Amiata seismic network is smaller than the Larderello network, both in terms of the areal coverage and number of receivers. Figure 2-7 shows the locations of the receivers in the Monte Amiata network.

The objectives for the Monte Amiata cluster were similar to those identified for the LAGO and Larderello 1993 clusters, however, the complexity of the velocity model for this cluster exceeded those needed to adequately model the Larderello Field. The development of the velocity models for each one of these clusters will be presented in detail later in this work.

2.2 Sensor Array geometries and Example Waveforms

The following section presents information regarding the data coverage used in the analyses and a few typical example waveforms. For the DWTI cluster, a description of the data display will be provided as well.

2.2.1 Sensor Array and Seismic Record Display for the DWTI MEQ data

Data display, processing and analysis of the DWTI events were completed using a single integrated software tool designed specifically for fracture monitoring. In this thesis, all example records for the DWTI events will be presented using this program's graphics display.

Figure 2-9 shows an annotated display for the DWTI hydraulic fracture data. This layout reflects the user environment as it would be used in real-time during field operations. The figure shows two windows where site information is represented. The large window (shown here in the background) contains the seismic time series recordings coming from the digital acquisition system (DAS). The data was collected as a continuous stream and clipped into smaller files containing individual detected events. This figure presents seismic records from 93 channels of the full DAS complement of 96. These are recordings from a subset of the

150 total available sensors. The large window is referred to as the "display window".

The smaller window (referred to as the "map" window and shown here in the foreground) contains an areal view of the site with symbols indicating the lateral location of the sensors (triangles), other instrumentation such as surface exploration geophones and tiltmeters not used for the hypocenter monitoring (squares or crosses), hypocenter locations (filled and empty circles), and P wave particle motion vectors. This window is used during the processing of the data and will be addressed later in this thesis.

The seismic records shown in the display window show time (in seconds) increasing horizontally across the window. Each horizontal display "slot" can contain up to three overlain seismic records, usually the 3 components from a single reciever pod. Thus, each display slot represents the 3 component seismic information from a particular vertical location along the string. In this figure (and in all DWTI figures presented in this thesis) seismic records from sensors in both monitoring wells will be visible in the display window for the event being processed. In this example, we see records from one of the calibration/primacord shots. The top six display slots (channel IDs 76-93) contain 3 component records from sensors in the well nearest the injection well (the location of the primacord shot). The remaining display slots contain records from sensors in the far well. In this example, the DAS sensor coverage contained a complete set of 25 pods from the far well, but an incomplete set from the near well. Here the DAS sensor coverage for the near well was uniformly decimated to fill the remaining DAS slots.

The seismic sensors record particle velocity and all channels were acquired using identical instrumentation and signal amplification parameters. DAS and instrument response were checked against manufacturers specifications and found to be flat over the appropriate frequency band (DAS sample interval of 0.5 milliseconds). Amplitude outputs are in millivolts per second and are displayed on a constant relative scale for qualitative relative comparison.

Figure 2-10 presents the seismic signals recorded for one event induced during the hydraulic injection. This event was recorded using a DAS channel layout that differed from that used

in the previous example. Most of the recorded events used a DAS coverage similar to the one shown here. The full complement of sensors was decimated to fill the DAS channels so that every other pod in the string was recorded as a full set of 3 components while the intervening pod was represented by only the vertical component (identified in the figure by tracking the channel numbers along the left side of the display slots).

This example is typical of the recording quality for the events induced during the DWTI injection. Most of the 200 events used in this thesis for delineating the fracture were of a similarly excellent quality. Some degradation in signal-to-noise ratio (STN) was encountered as the analysis progressed through the catalog (starting with largest amplitude events first), however, the dense vertical sensor coverage allowed phase arrival picking to be accomplished even when the STN became very low. All events treated here allowed picking of both P and S arrival times with excellent coverage for use in estimating the hypocenter parameters.

2.2.2 Sensor Array and Example Seismic Records for the LAGO Cluster

The microearthquakes of the LAGO cluster were recorded on the Larderello local seismic network. The stations whose records were available during the period of seismic activity are identified in Figure 2-11, although, not all events were detected and recorded at all stations or with sufficient quality for accurate arrival time picking. P and S wave arrival time estimates were generated for most stations and events in this cluster. Stations yielding the best record quality and event coverages are identified in the figure with triangular symbols. An effort was made to use as many records as possible for hypocenter estimation to maximize azimuthal and distance coverage. Recordings from the best stations were analysed and both P and S arrival time estimates were obtained.

Figure 2-12 shows and example of five station recordings for LAGO cluster event number 0236 which occurred on July 29th, 1989 at approximately 10:28 GMT. These records represent the typical data quality for events recorded by the Larderello network. Sample interval for these recordings is 0.004 seconds.

2.2.3 Sensor Array and Example Seismic Records for the Larderello 1993 Swarm

The microearthquakes of the Larderello 1993 MEQ swarm were also recorded by the Larderello local network. Figure 2-13 shows the stations that produced the best recordings (triangles and diamonds). Due to the location of the cluster near the northern edge of the network (See Figure 2-6) the azimuthal coverage is not as good as for the events in the LAGO cluster. Fortunately, the Pomarance station produced excellent recordings of these events and coverage was complete enough for hypocenter estimation. P and S wave arrival time estimates were obtained for nearly all stations and all events in the swarm.

The hypocenters for this swarm of events were modelled using both absolute and relative (high resolution) methods and the symbols used in Figure 2-13 reflect which stations were used in each stage of the processing.

Figure 2-14 presents signal recordings for event 0157 of the 1993 swarm from six representative stations. This event occurred on March 22, 1993 and was eventually used as a reference event for relative hypocenter location. The sample interval was 0.004 seconds.

2.2.4 Sensor Array and Example Seismic Records for the Monte Amiata 1997 Swarm

The MEQs of the Monte Amiata 1997 swarm were recorded by stations of the Monte Amiata local seismic network. Figure 2-15 indicates stations contributing arrival time estimates for use in the hypocenter location modeling. Again, diamond symbols indicate station data used in both the absolute and relative hypocenter modeling calculations. Triangles indicate stations contributing picks to absolute location modeling calculations only. P wave arrival times were determined for all of these stations and used in both the absolute and relative hypocenter modeling. S wave arrivals were assessed for all stations and estimated for seven stations. Approximately 25 percent of the S wave times were incorporated into

the absolute and relative hypocenter determinations, based upon an evaluation of estimated pick reliability and variance.

Figure 2-16 presents example records for Monte Amiata swarm event number 0119, which occurred on March 21, 1997. Approximately 30 percent of the events in this swarm exhibited waveforms similar to those recorded for this event. I used this event as the waveform reference during the relative event hypocenter location calculations. The sample interval for recordings from the Monte Amiata network stations was 0.008 seconds.

2.3 Geologic and Seismic Velocity Model Estimation

The seismic disturbances generated by MEQs propagate away from the source location and travel along a path through the geologic materials. The velocity of their travel is dependent upon the properties of those materials. Consequently, the calculation of accurate hypocenter parameters depends upon the quality of the velocity model used to represent the materials in the modeling calculations. In this section I will describe the velocity models used during the hypocenter modeling and relate them to the local geology.

2.3.1 DWTI Velocity Model

Figure 2-3 showed a cross-section of the formations intersected by the wells at the DWTI site. This interpretation is based upon cores and logs obtained from the injection well and lithologic and formation studies published prior to the experiment (Keck and Withers, 1994; Truby *et al.*, 1994; Keck *et al.*, 1996; Withers *et al.*, 1996; Atlantic Richfield Corporation, 1994; Galloway *et al.*, 1982). ARCO cored a 368 foot section between depths 4332 and 4700 feet, recovering a total of 212 feet of materials. The cores included sections of both the sand and shale layers. Additionally, ARCO obtained standard formation property logs including dual induction, spectral density, dual spaced neutron, gamma ray, cement bond, temperature, caliper logs, low frequency dipole sonic, XY cross dipole sonic, circumferential

acoustic scanning tool, and XY caliper logs (Keck and Withers, 1994; Truby *et al.*, 1994; Keck *et al.*, 1996; Withers *et al.*, 1996; Atlantic Richfield Corporation, 1994). Full wave sonic logs and primacord shots were used to estimate primary and shear wave velocities for these materials. ARCO reported full waveform sonic P wave velocities of 8800 feet/sec in the sands and 8000 feet/sec in the shales. Sonic waveform estimates yielded a Vp/Vs ratio of 2.5 which was qualitatively supported by the poorly consolidated nature of borehole samples. Primacord velocites were estimated as 8100 feet/second average with a Vp/Vs ratio of 2.2. In the hypocenter modeling conducted for the 200 events analysed here, I used a homogeneous velocity model with Vp=8200 feet/second and Vs=3727 feet/second. This velocity model was checked for quality against four callibration/primacord shots, two from just above the target sand interval and two from just below the target sand interval. One example of the fit for this model is shown in Figure 2-9 where the predicted arrival times are indicated by vertical dashes. The homogeneous model fit the observed travel times to within 1-2 miliseconds on average for these shots and also satisfied the practical need for a model that could be calculated analytically. This facilitated the task of calculating the hypocenter parameters in real-time.

2.3.2 The Larderello Geothermal Field Velocity Model

ENEL provided seismic velocity estimates for the geologic sections underlying each of the seismographic stations in the Larderello local seismic network(Batini, 1997). I used these 1-D estimates to produce the pseudo-section velocity model shown in Figure 2-17. This pseudo-section follows no single azimuth but rather shows the individual one-dimensional velocities (by station) according to relative altitude of the station above sea level. This pseudo-section was produced in order to ascertain the degree of variation in velocity contrast interface depths and to aid in the development of appropriately tuned velocity models for use in the hypocenter inversion process.

The pseudo-section shows three general seismic velocity layers. The upper-most layer represents the mantle of neogene sediments and the Liguride flysch unit. The middle layer

is an average velocity for the anhydrites of the Tuscan nappe formations and the quartz-metaconglomerates and phyllites of the Monteciano-Roccastrada unit (the "tectonic slices"). The bottom layer represents the core complex gneisses and amphibolites (Batini, 1997).

The hypocenter inversion software was modified to accomodate multiple 1-D velocity models for different source-receiver paths. The layers exhibiting a range of possible velocities and those stations showing significant variations in interface depths were handled using this functionality.

2.3.3 The Monte Amiata Geothermal Field Velocity Model

ENEL also provided seismic velocity estimates for the geologic sections underlying each of the Monte Amiata seismic network stations(Batini, 1997). The assembled pseudo-section is shown in Figure 2-18. The seismic velocities indicated here are similar to those of the Larderello velocity model. The variations reflect differences in the lithologies of the metamorphic basement rocks (i.e. phyllites and quartzites at the Larderello field versus metagreywacke, metapelite, and marbles at the Monte Amiata field (Cappetti *et al.*, 1985)).

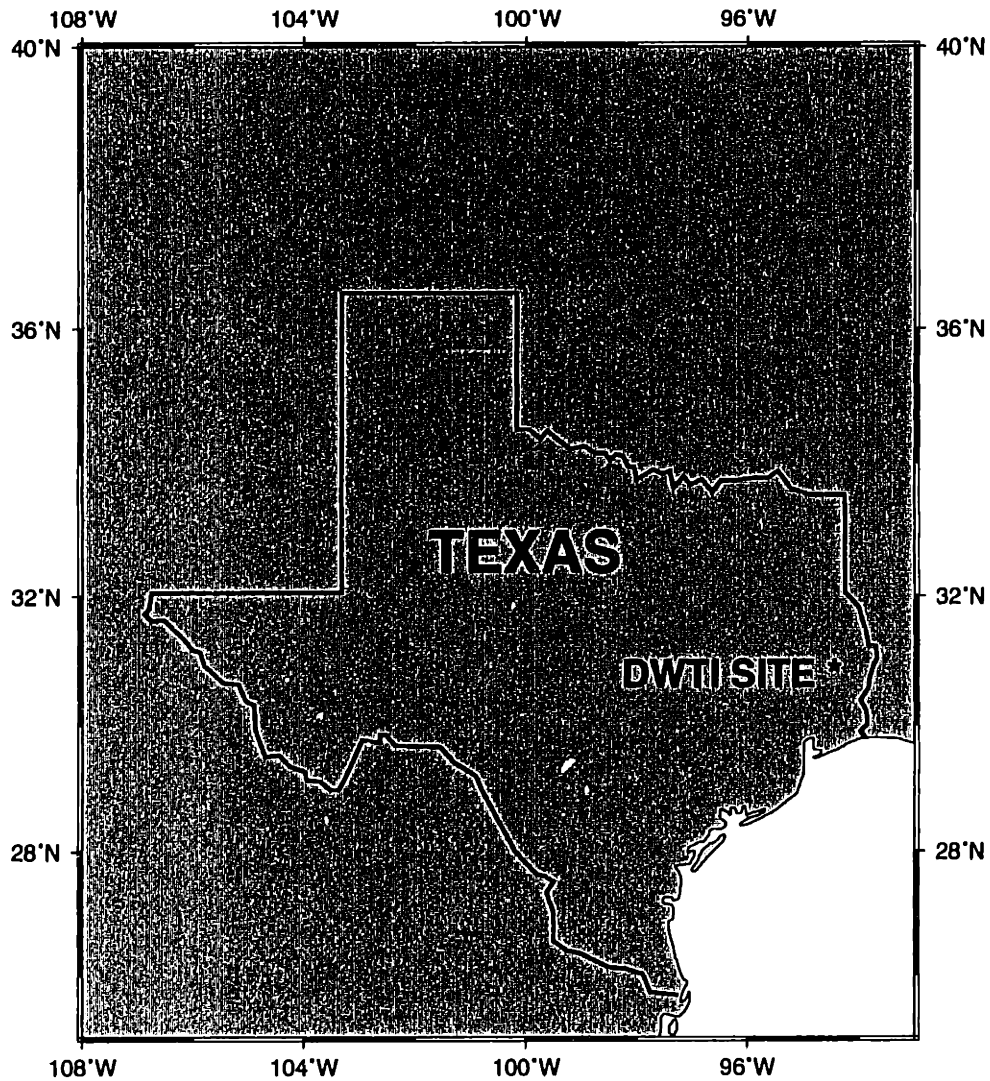

Figure 2-1: Regional map indicating the location of ARCO's 1993 Deep Well Treatment and Injection (DWTI) Demonstration Project in Jasper County, Texas.

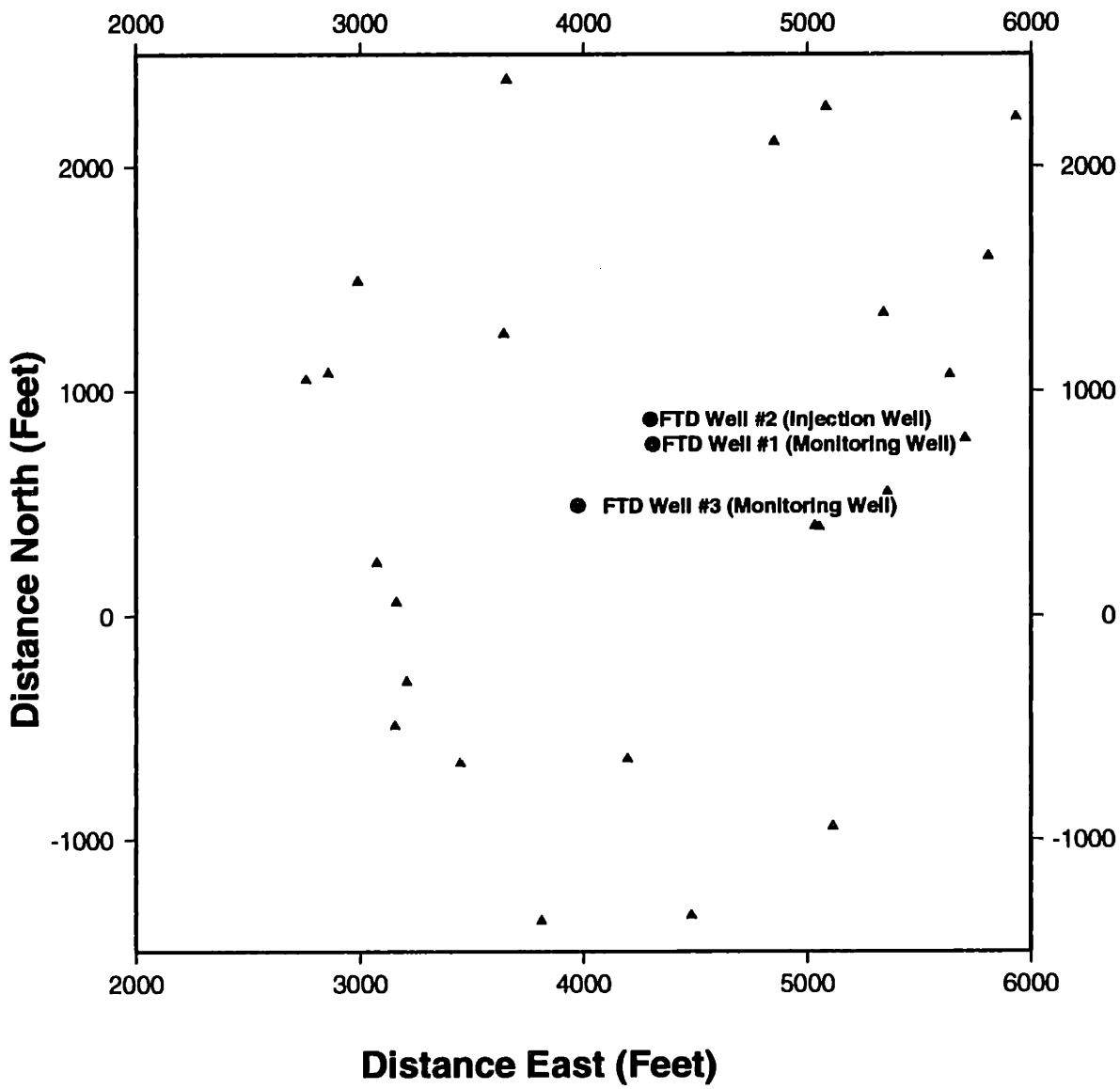

Figure 2-2: Areal view of the DWTI site indicating the locations of the injection well and the two Monitoring Wells (Circles). Triangles represent surface tiltmeters.

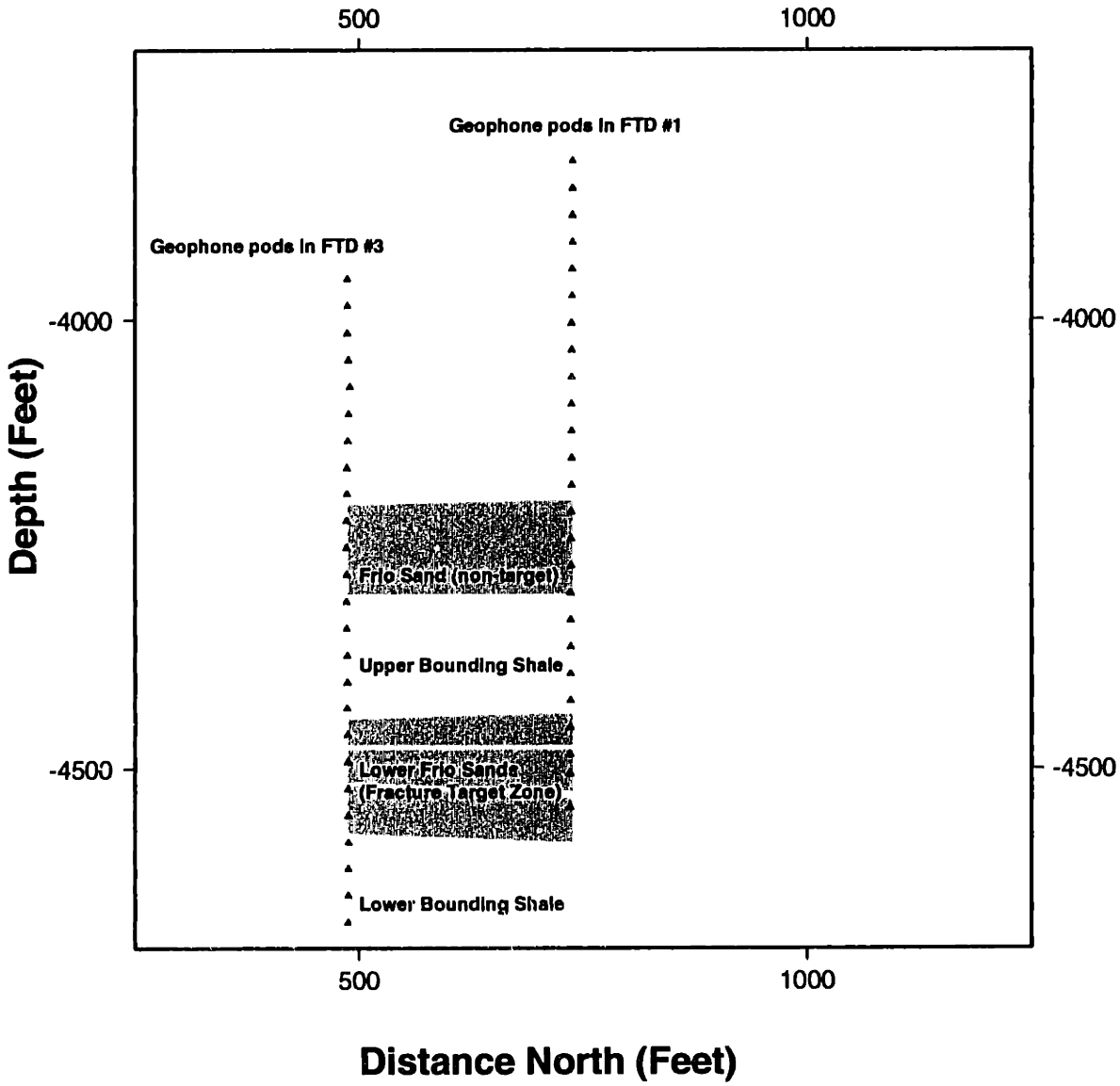

Figure 2-3: Side view of the DWTI site indicating the locations of the downhole three-component geophone pods.

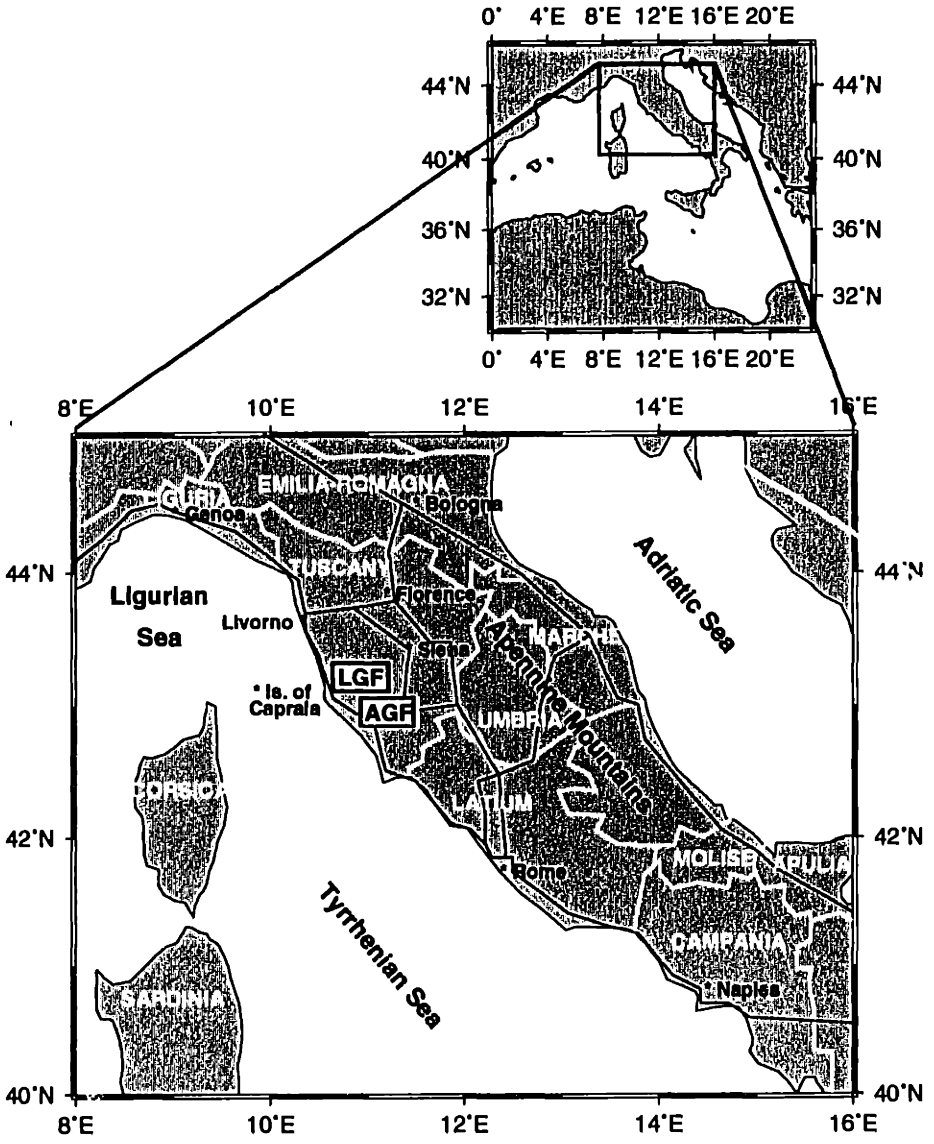

Figure 2-4: Regional map indicating the location of the Larderello (LGF) and Monte Amiata Geothermal (AGF) Fields in Western Tuscany Italy.

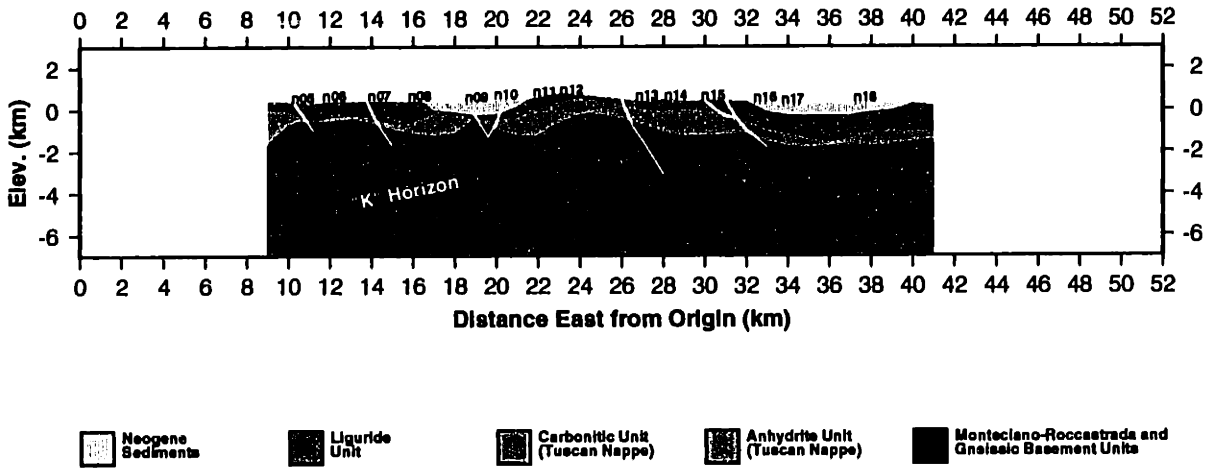

Figure 2-5: Generalized geologic cross-section of the Larderello Geothermal field indicating the relative locations of the major stratigraphic units, the Tortonian age extentional faults and the Seismic "K" horizon. This figure was adapted from (Fiordelisi *et al.*, 1995; Batini *et al.*, 1985b; ENEL-Unita Nazionale Geotermica, 1988)

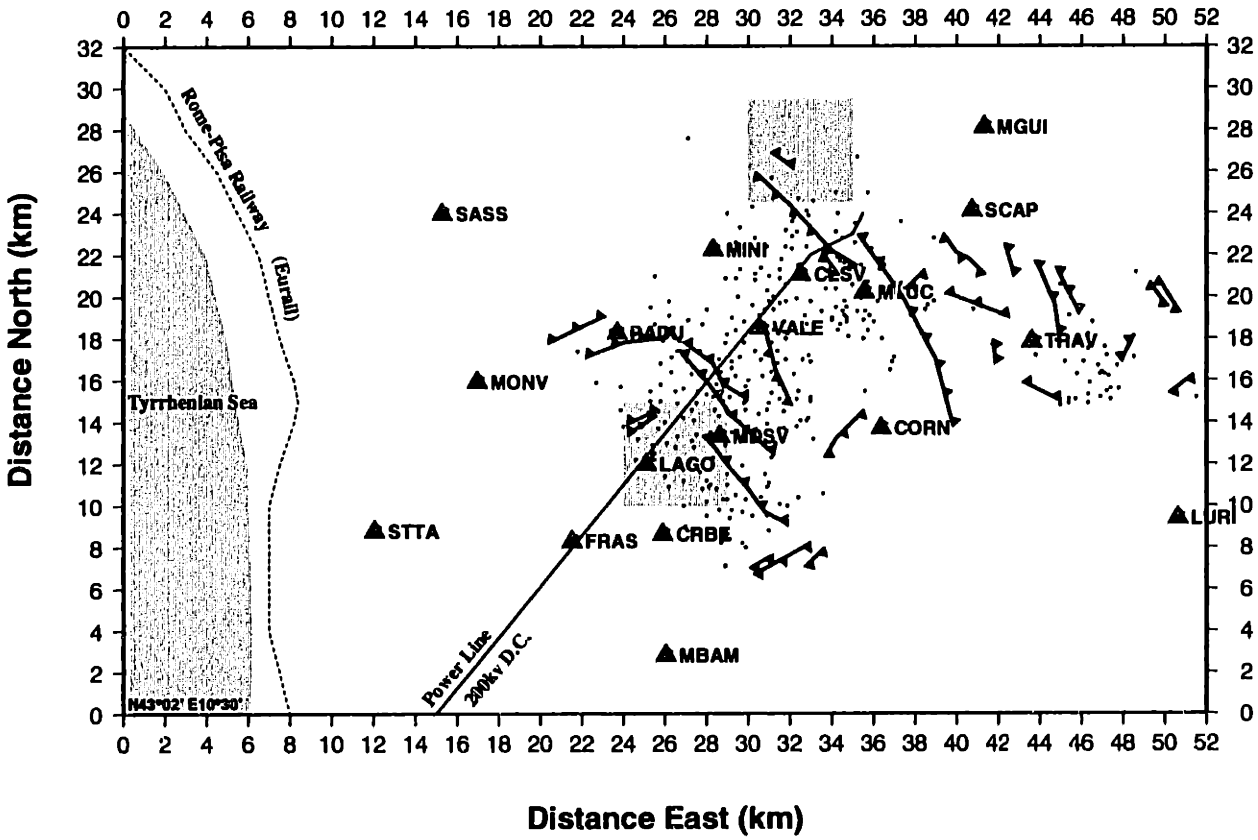

Figure 2-6: Local map of the Larderello Geothermal Field. Dots indicate geothermal wells. Hatchured lines indicate fault traces at depths intersecting the seismic "K" horizon. Shaded blocks indicate the two Larderello MEQ study areas, the Larderello 1993 MEQ swarm area in the north and the LAGO MEQ study area in the south. Triangles represent the Larderello network seismographic stations (excluding the most northerly station, POMA, which is located just off the map north of the MINI and CLSV stations). Sources: (ENEL-Unita Nazionale Geotermica, 1988)

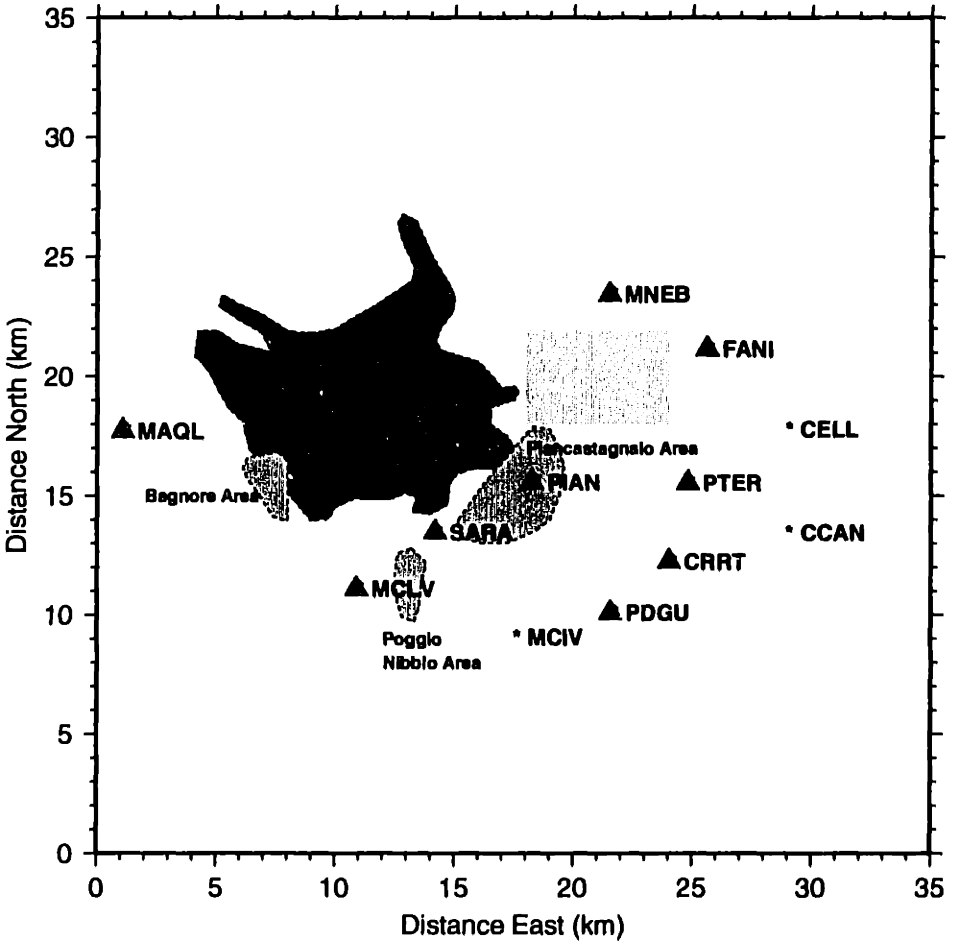

Figure 2-7: Local map of the Monte Amiata Geothermal Field showing the location of the Monte Amiata volcanic cone, the seismographic stations of the Monte Amiata Local Seismic network (triangles) and the three geothermal production areas, Piancastagnaio, Bagnore, and Poggio Nibbio. The shaded block indicates the general location MEQ study area.

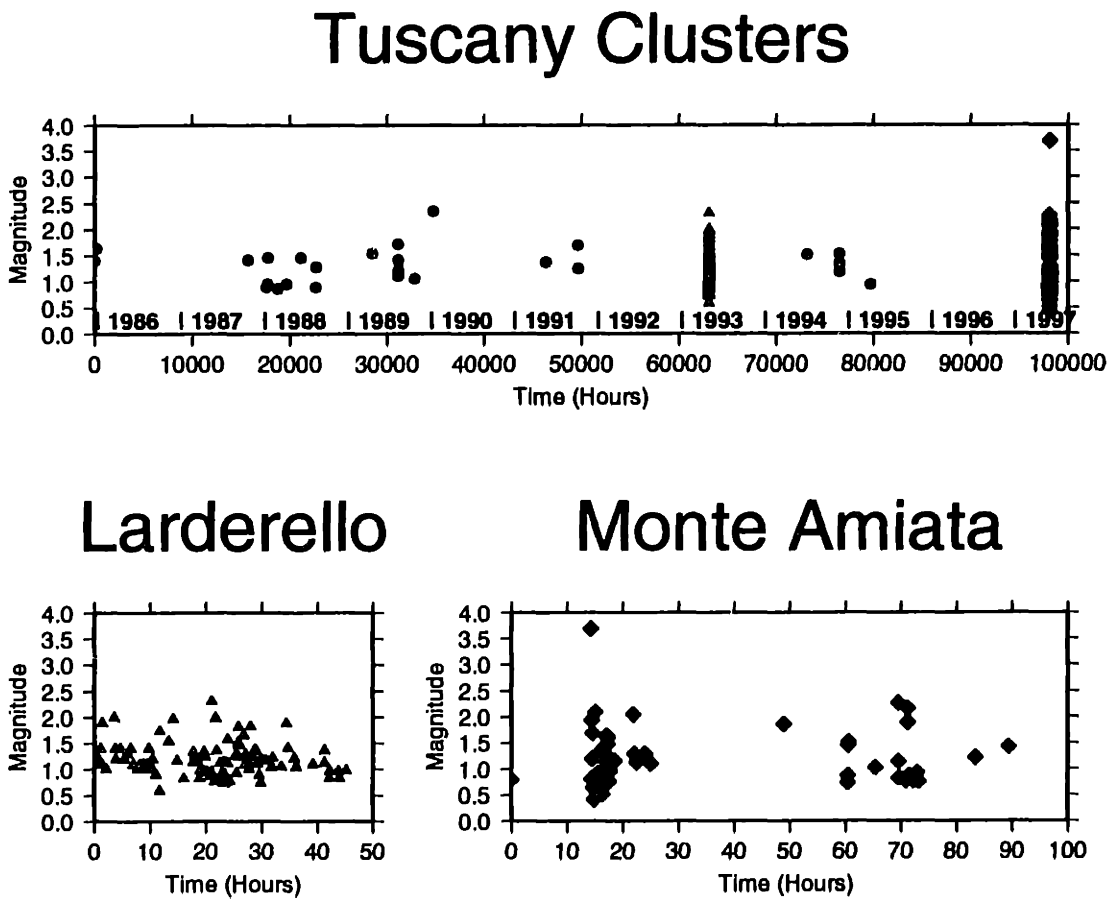

Figure 2-8: Magnitudes versus time for the three Tuscany, Italy MEQ clusters. The top view shows all three sets of events plotted on the LAGO timeline. The bottom two views show the March 20-23 Larderello 1993 and March 21-April 2, 1997 Monte Amiata swarms. Shaded circles are events from the LAGO cluster, Triangles are events from the Larderello 1993 swarm and diamonds are events from the Monte Amiata 1997 swarm.

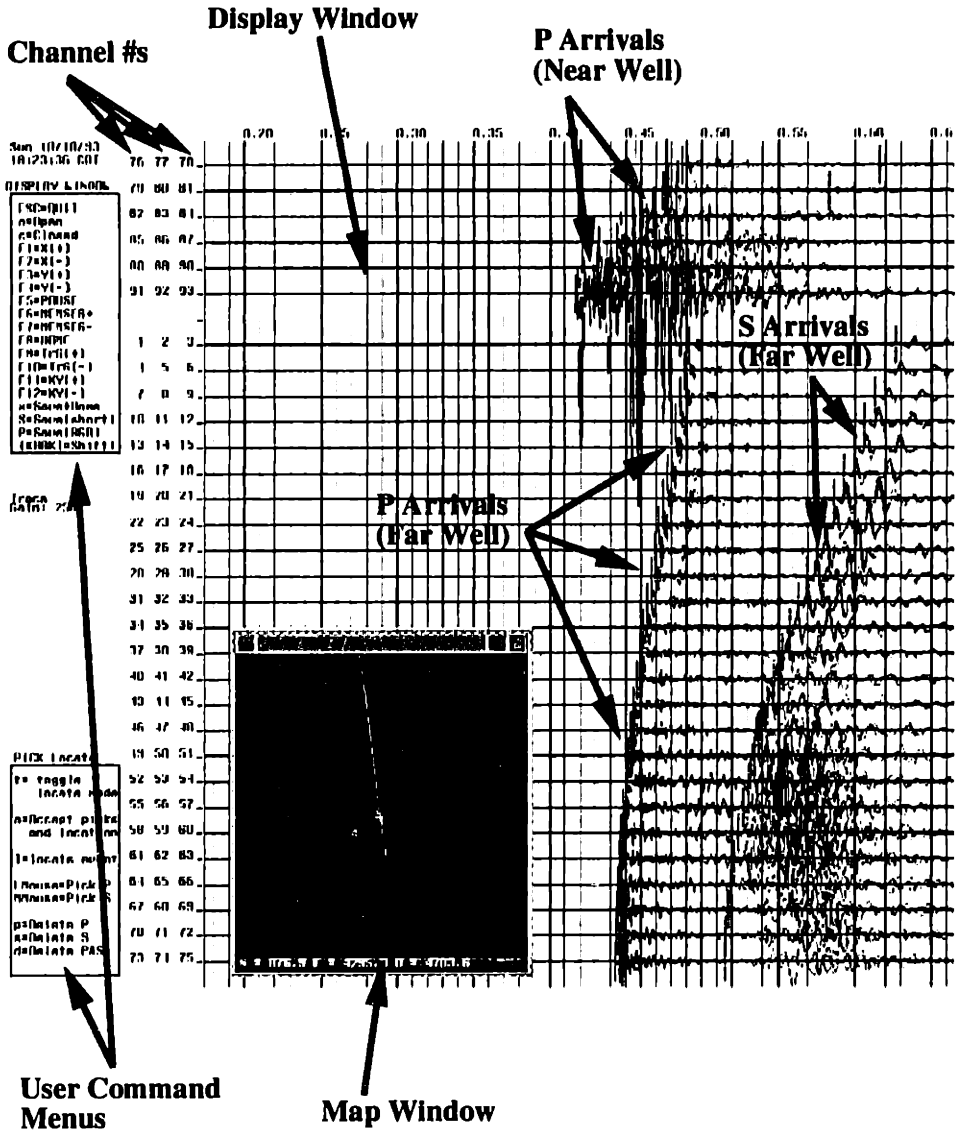

Figure 2-9: User interface for analyzing the DWTI MEQs. This figure shows a "Display Window" (background) and a "Map" window (foreground). The display window shows the 3 component seismic data (3 components per line, see 3 phone ID numbers along left). This figure shows one calibration shot. DAS channels 1-75 were recording data from the well furthest from the shot. Channels 76-93 where recording data from an incomplete set of phones in the far well. The "Map" window shows an areal view of the site with monitoring well locations (triangles), tiltmeter and surface phone positions (x's and squares), hypocenters (dots) and a P Wave particle motion vector from one 3C pod.

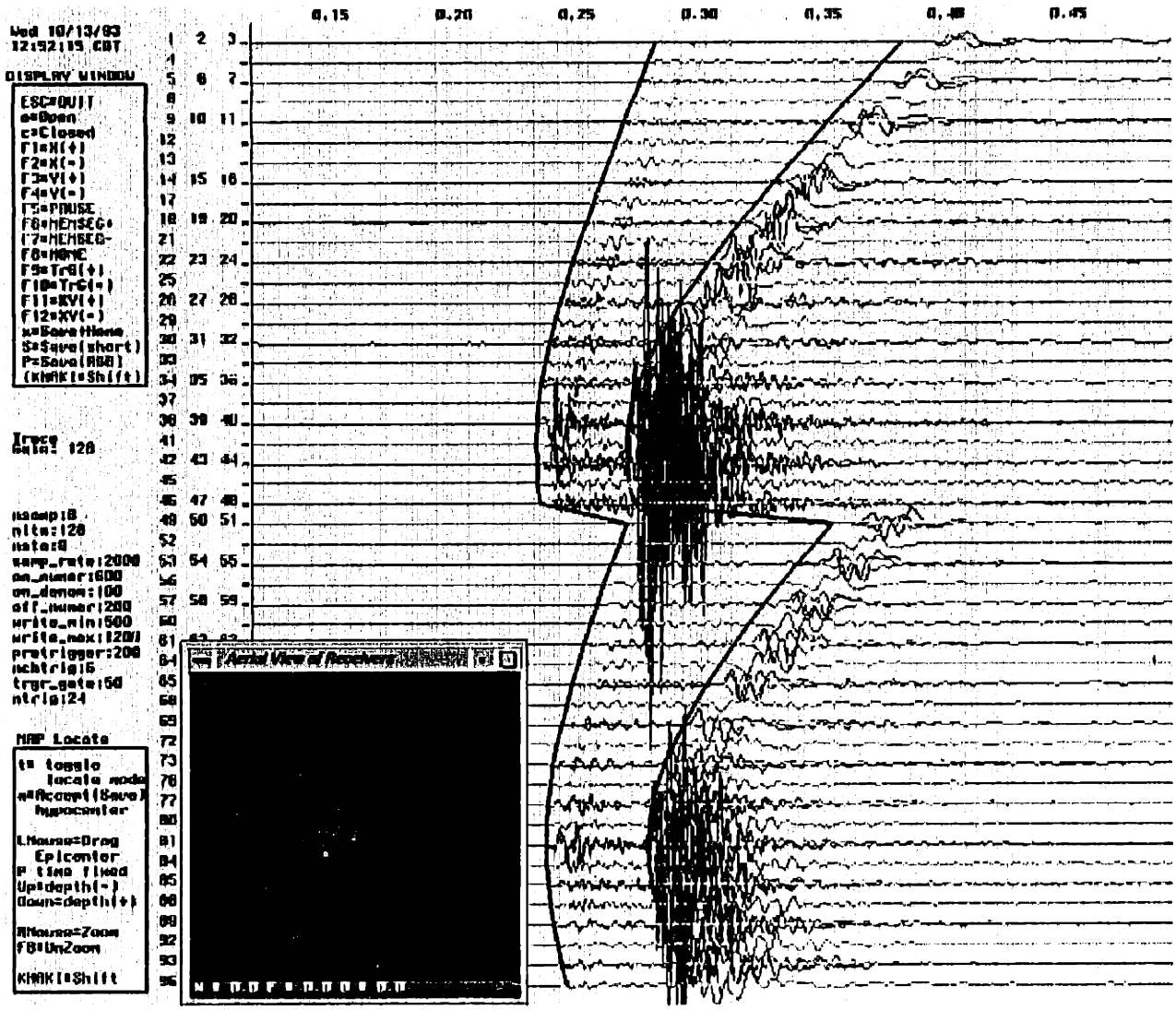

Figure 2-10: An example of a hydraulic fracture induced microearthquake from the DWTI demonstration project.

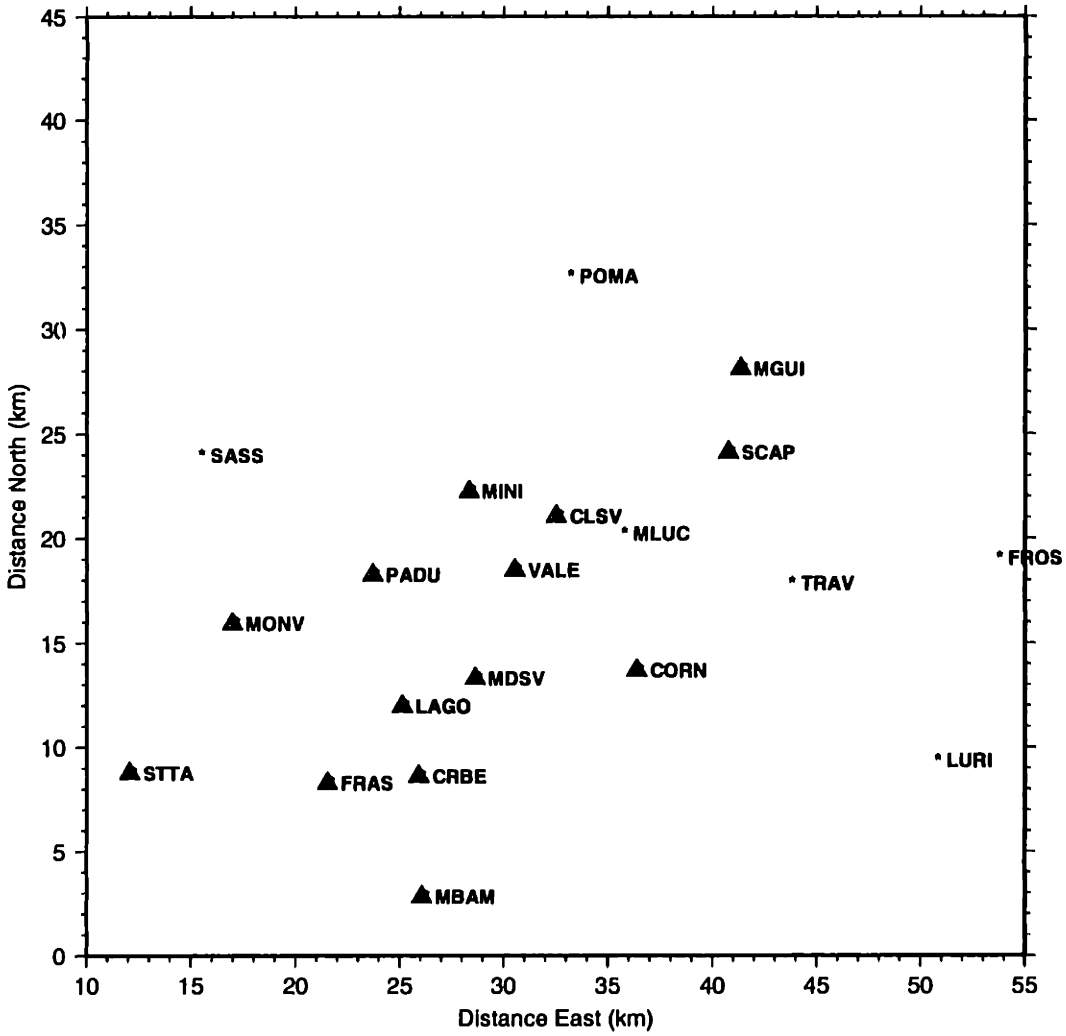

Figure 2-11: Map indicating the location of seismographic stations of the Larderello local Seismic network. Triangles indicate stations contributing P and S wave travel times for inversion of the LAGO cluster absolute hypocenter locations.

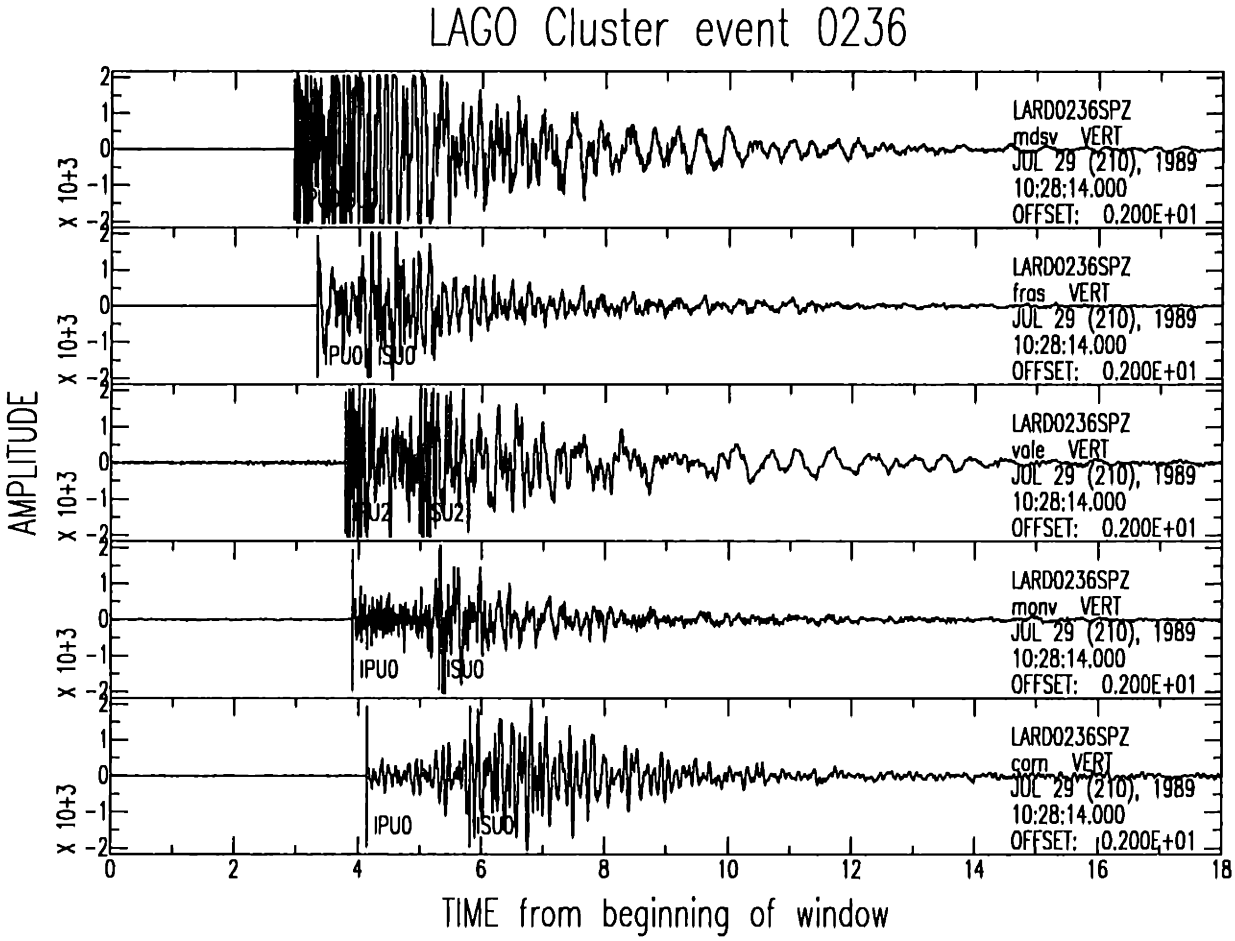

Figure 2-12: Seismic traces from event 0236 in the LAGO cluster.

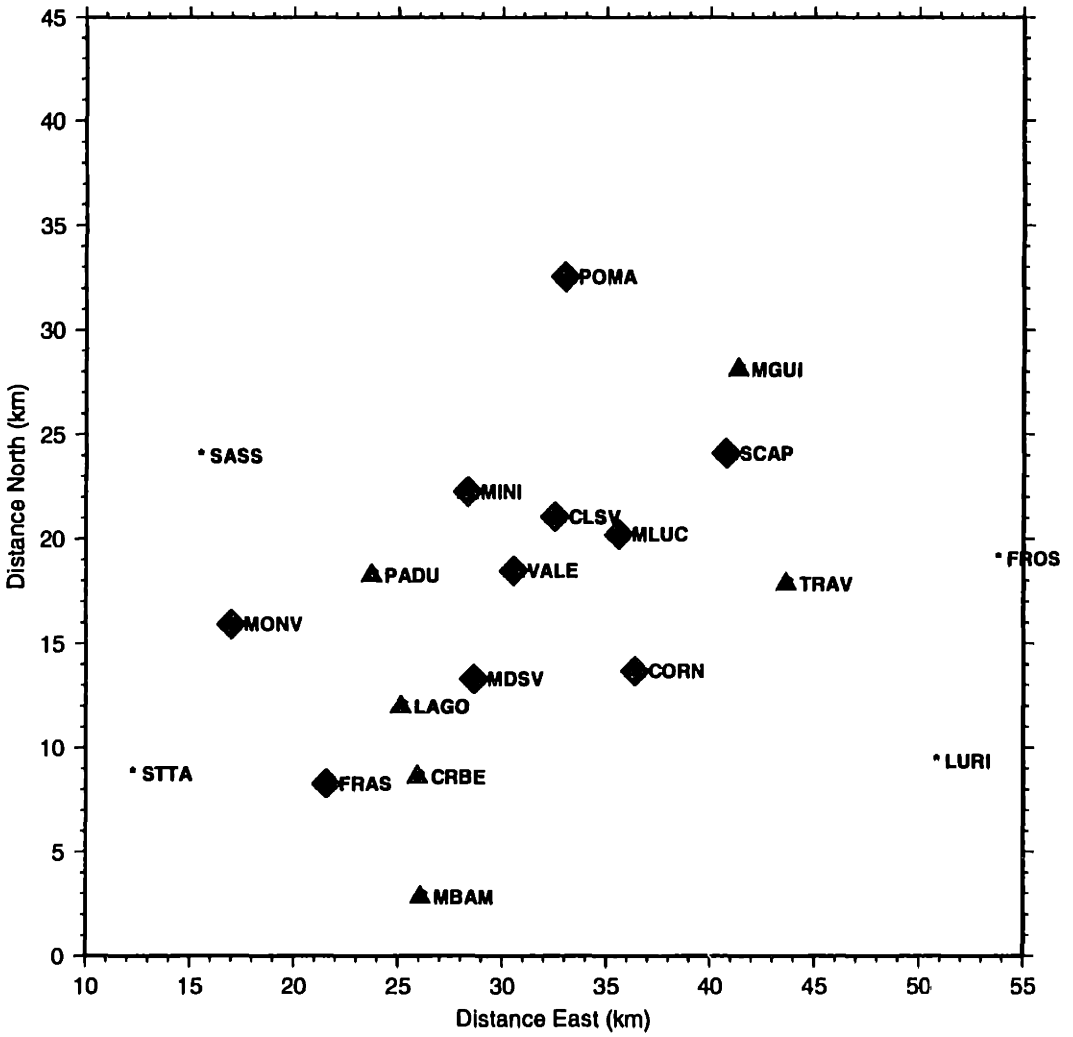

Figure 2-13: Map of the Larderello seismic network. Diamonds indicate stations contributing P and S wave travel times for both absolute and relative travel time inversion for events in the Larderello 1993 cluster. Triangles indicate stations contributing only absolute travel times.

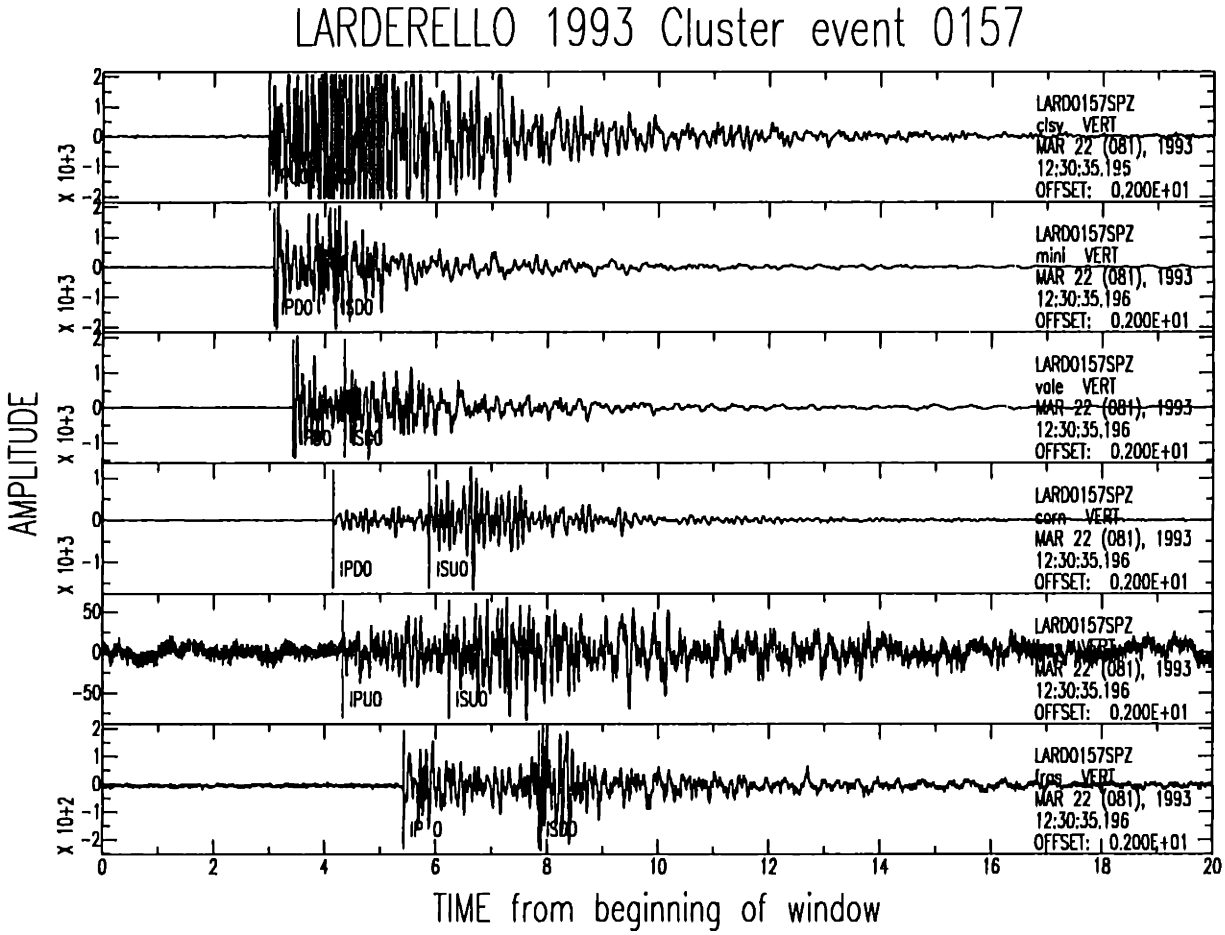

Figure 2-14: Seismic traces from event 0157 in the Larderello 1993 cluster.

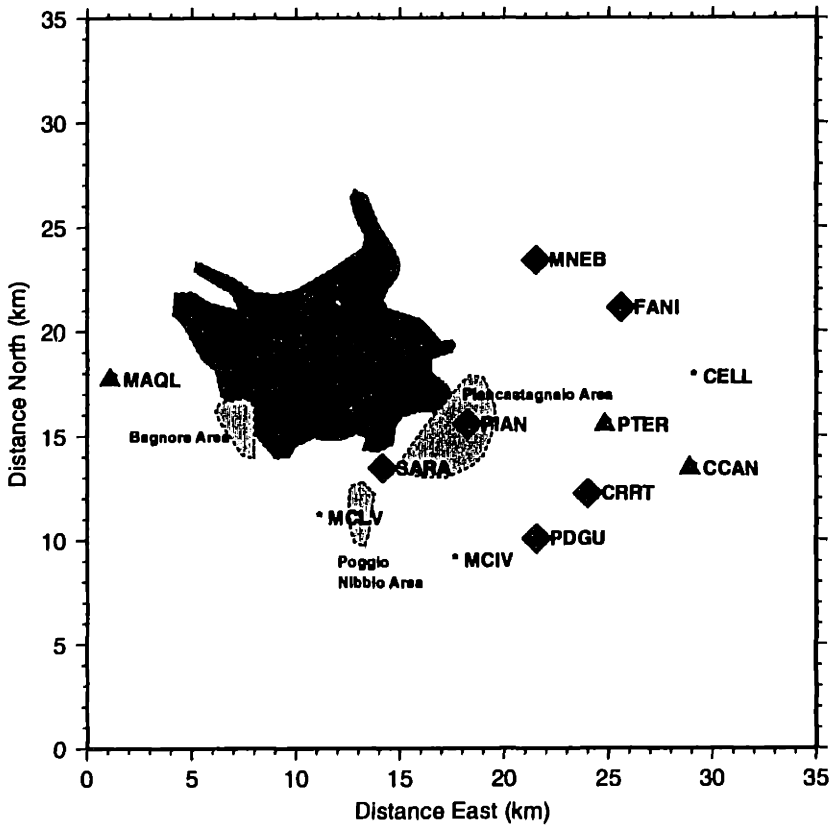

Figure 2-15: Map of the Monte Amiata seismic network. Trangles and diamonds indicate stations contributing P and S wave travel times for absolute and relative traveltime inversion for events in the Monte Amiata cluster. Triangles indicate stations contributing only absolute travel times.

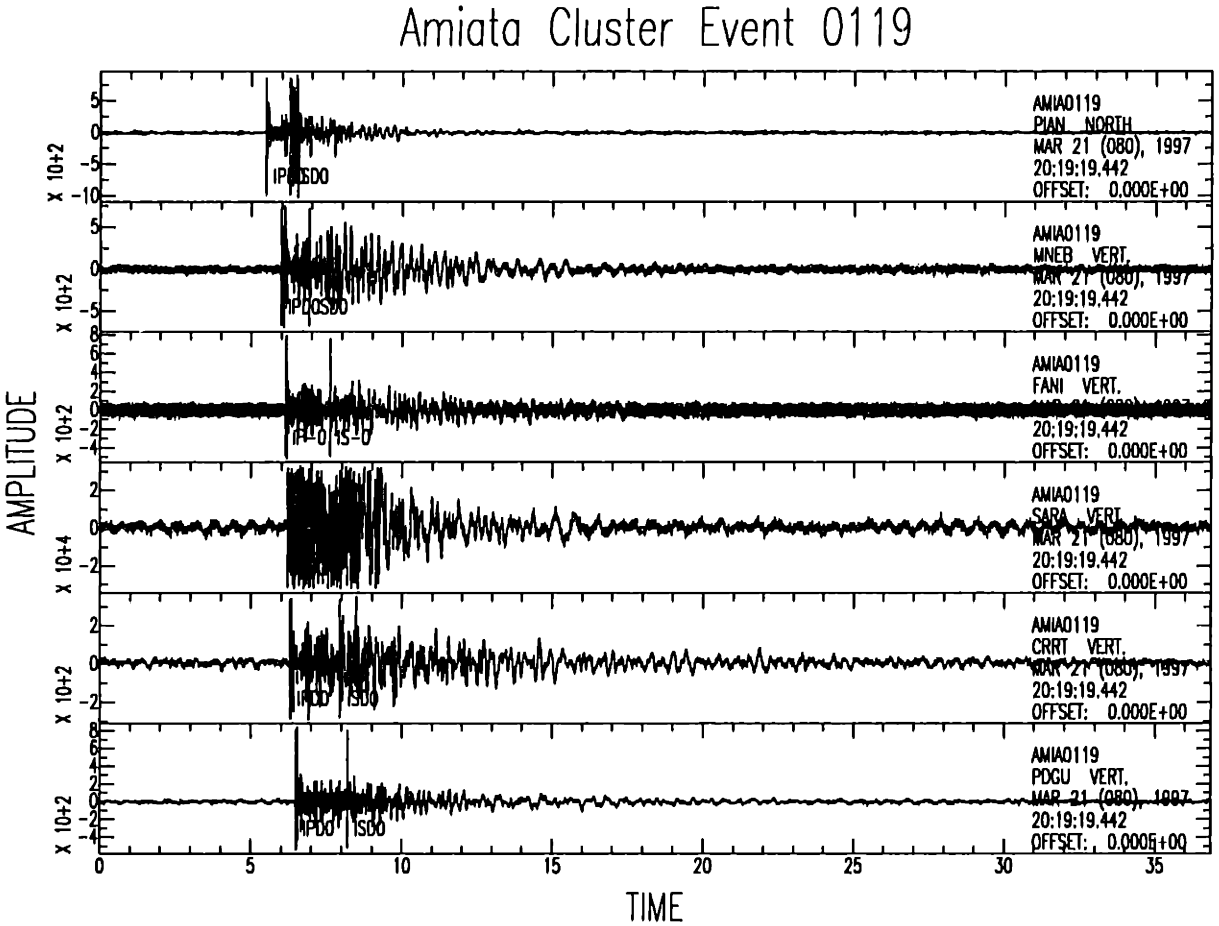

Figure 2-16: Seismic traces for event 0119 in the Monte Amiata cluster.

Velocity Estimates (Larderello)

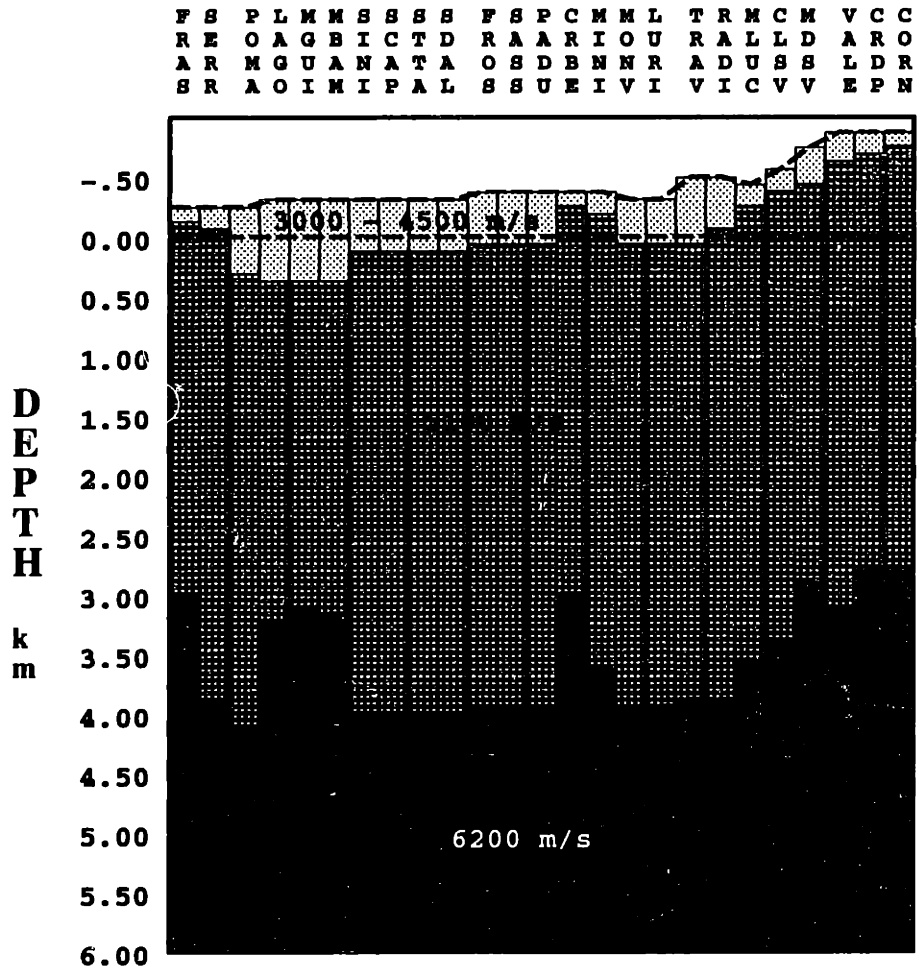

Figure 2-17: Velocity model for the Larderello geothermal field. Vertical strips indicate velocity estimates for materials underlying specific seismographic stations (stations listed across the top of the figure with IDs typed vertically). This display is not a true section. The stations are arranged in order of generally increasing topographic relief. The depths of the velocity contrasts are referenced to sea level. In the inversion, all depths are referenced to the datum level of 886 meters above sea level (keyed to the highest station).

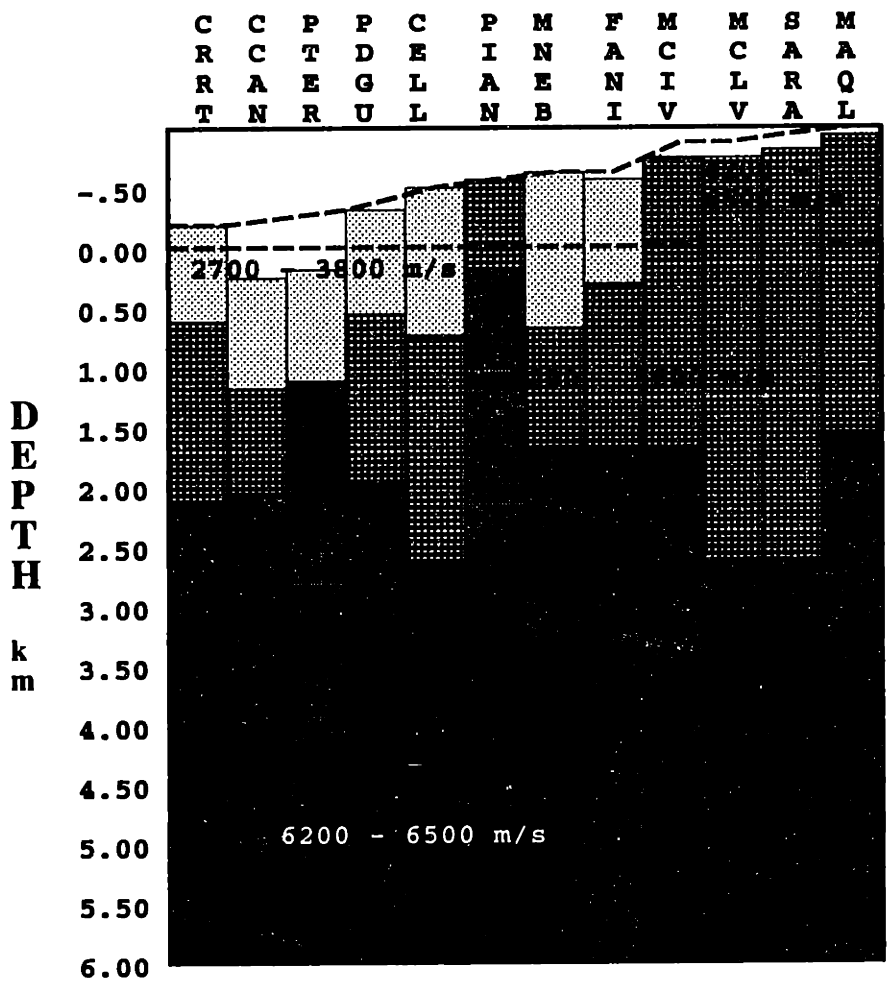

Figure 2-18: Velocity model for the Monte Amiata geothermal field. Vertical strips indicate velocity estimates for materials underlying specific seismographic stations (stations listed across the top of the figure with IDs typed vertically). This display is not a true section. The stations are arranged in order of generally increasing topographic relief. The depths of the velocity contrasts are referenced to sea level. In the inversion, all depths are referenced to the datum level of 1200 meters above sea level (keyed to the highest station).

Chapter 3

Analysis

3.1 Hypocenter Modeling of the DWTI Induced Microearthquakes

The DWTI microearthquakes were analysed using an application software tool designed specifically for use in ARCO's hydraulic fracture monitoring programs. This application package, based upon the original concept of Dr. Robert Withers of ARCO, was developed by myself and members of the ARCO Exploration and Production software department as an extension to their advanced visualization graphics framework established during preparations for the DWTI demonstration.

In field application, seismicity induced by the hydraulic injection is monitored via a "front-end" event detection algorithm. Detected events are clipped and forwarded to the data analysis processing graphics computer. Here, the entire analysis, including seismic phase identification and arrival time picking, forward modeling of the hypocenters, and standard least-squares hypocenter inversion is accomplished, cradle-to-grave. Due to the integration of the modeling procedures with an advanced visualization graphical user interface, the total speed of analysis for each incoming event was reduced from approximately 1 hour (including P and S phase picking for 96 individual records, transfer of the arrival times to a modeling tool and modeling process time using ARCO's previously available standard

processing tools) to approximately 5 minutes for a forward modeled hypocenter estimate or 15 minutes for a carefully picked inversion estimate. This improvement of processing speed makes possible the real-time analysis of injection induced seismicity when the geologic materials can be approximated by simple velocity models for which seismic travel times can be calculated analytically. More complex models, requiring numerical approximations for the travel time calculations, are possible but were not implemented for this study. Utilization of more complex modeling procedures is limited only by available CPU speed.

This analysis program utilizes traditional least-squares inversion to calculate the best estimate of the earthquake hypocenter coordinates given the observable P and S wave arrival times, sensor locations and orientations, and a velocity model. The method can be conceptualized simply as a numerical version of the classic "triangulation" problem and a schematic representation of the principal concept is illustrated in Figures 3-1, 3-2, and 3-3 for a field array geometry similar to that used in the DWTI experiment.

Figure 3-1 shows two vertical wells, each instrumented with seismic sensors (in the interest of graphical clarity only one sensor in each well is indicated here). P and S wave travel time hypocenter inversion for a single sensor will produce a suite of equally valid solutions (a surface) whose shape is dictated by the velocity structure (shown here as a sphere indicating a homogeneous velocity model). When two sensors (one from each well) record P and S arrivals from the same MEQ, the locus of solutions is the intersection of the two sets or in this case, a circle of solutions.

The introduction of additional sensors above and below the expected depth of the hydraulic fracture imposes additional constraints on the solution set, but for P and S travel time inversion, the best that can be accomplished with two wells is a set of two equally valid solutions, and in order to determine these, the arrival times for all sensors must be picked and inverted. The program used to process the DWTI data used an additional constraint (made possible by the vertical string geometry) to temporarily bypass the need for inversion to determine a fast estimate of the hypocenter. Specifically, for simple velocity models the depth of the event can be immediately assertained visually by identifying the sensors

detecting the first seismic disturbance (approximately DAS channel 41 in Figure 2-10). Figure 3-2 shows how the introduction of the depth constraint reduces the number of valid solutions immediately to two. This particular functionality is especially useful when the event has small amplitude or when the signal-to-noise ratio is poor and first arrivals are only visible on a few of the available sensors.

To complete the quick estimate of the hypocenter location (using the forward modeling option), the user graphically "picks" the first P wave arrival on the sensor nearest the event depth and uses the mouse to search the event depth plane (represented graphically in the "Map" window) for the best epicenter (the depth of the hypocenter already being determined). The best estimate is determined by visually fitting a graphical representation of the predicted arrival times to the P and S arrivals visible in the display window (See Figure 2-10).

The final refinement of the fast hypocenter estimate is made by determining which of the two valid solutions is best. This is done by introducing one additional piece of information, specifically, the P wave particle motions as determined from at least one 3-component sensor from each well. Figure 3-3 shows graphically how this additional information reduces the valid solutions from two to one. For this to be possible, the orientation of the 3-component sensors must be known, so that the partical motion vector can be numerically rotated to the north-east coordinate system represented in the user interface. The sensor array used for recording the DWTI MEQs was installed using a flexible cable. Although the 3-components within each pod were orthogonal, the pods themselves could rotate during installation (See Figure 3-4). Interpreting P wave particle motions from an unoriented string would produce incorrect and uncorrelated results for each set of 3-component sensors (See Figure 3-5). The vectors can be numerically corrected for this rotation by determining the compensation angles for each pod using calibration shots from known locations. The DWTI sensors were calibrated using four calibration shots in the injection well, two just above the target formation and two just below. Figures 3-6 and 3-7 present the orientation of the sensors and the P wave particle motion vectors after calibration.

Figures 3-8 and 3-9 present estimates of the hypocenter locations (relative to the target formation) as calculated using the forward modeling method.

The forward modeling as it is implemented here requires picking only one P wave arrival explicitly. However, for a more accurate estimate of the hypocenter parameters, the P and S wave arrivals can be refined individually and then inverted using the non-linear least-squares regression method. Many excellent references are available on this subject, but, to establish the basic methods used to determine the hypocenters for the DWTI and the Tuscany events and to set the stage for later discussion of relative event location, the following summary is provided (based upon the descriptions in (Menke, 1989; Stein, 1989)).

3.1.1 Non-Linear Least-Squares Inversion of Microearthquake Arrival Time Data

To begin, we state that we have a method of calculating the P and S wave travel times and their derivatives, by either analytical or numerical methods, for waves propagating in a medium like the one we wish to investigate. As stated earlier, we used the analytical solution for a homogeneous medium for the DWTI site, but could have used an algorithm for transversely isotropic media, layered media, or other available methods.

We define the seismic arrival times as

$$\mathbf{d}_i = \mathbf{T}_i + t_0 \tag{3.1}$$

where

$\mathbf{d}_i$ = the seismic arrival time for the ith station.

$\mathbf{T}_i$ = the travel time for the ith station.

t_0 = the origin time of the earthquake.

In order to find the best fitting hypocenter, we wish to iteratively try various models with which to calculate synthetic versions of the observables until we find one that maps acceptably close to our target values. In order to do this, we approximate our non-linear function using a first-order Taylor expansion about a center at $\mathbf{m}_j$. The expansion gives

$$\mathbf{d}_i^n(m_j^n) \approx \mathbf{d}_i^0 + \sum_j \frac{\partial \mathbf{d}_i^n(m_j^n)}{\partial m_j}(m_j^{n+1} - m^n) \tag{3.2}$$

where

$\mathbf{d}_i^0$ = represents the observed data

$\mathbf{m_j^n}$ = an estimate of the hypocenter spatial and temporal model parameters, (x,y,z,t), for iteration n

$\mathbf{d}_i^n(m_j^n)$ = represents the calculated data for iteration n (dependent on m_j^n).

Rearranging we get

$$\mathbf{d}_i^n(m_j^n) - \mathbf{d}_i^0 \approx \sum_j \frac{\partial \mathbf{d}_i^n(m_j^n)}{\partial m_j}(m_j^{n+1} - m^n) \tag{3.3}$$

which can be simplified by setting

data residuals, $\delta \mathbf{d}_i^n(m_j^n) = \mathbf{d}_i^n(m_j^n) - \mathbf{d}_i^0$

model parameter change for iteration n, $\delta m_j^{n+1} = (m_j^{n+1} - m^n)$

This gives

$$\delta \mathbf{d}_i^n(m_j^n) \approx \sum_j \frac{\partial \mathbf{d}_i^n(m_j^n)}{\partial m_j} \delta m_j^{n+1} \tag{3.4}$$

The differential term in Equation (3.4) is referred to as the discrete inverse data kernel:

$$\mathbf{G} = \frac{\partial \mathbf{d}_i^n(m_j^n)}{\partial m_j}$$

Simplifying Equation (3.4) leads to the common representation of

$$\mathbf{G}\delta m^{n+1} \approx \delta \mathbf{d}^n \tag{3.5}$$

The least-squares solution of this equation is

$$\mathbf{G}^\mathbf{T}\mathbf{G}\delta m^{n+1} \approx \mathbf{G}^\mathbf{T}\delta \mathbf{d}^n \tag{3.6}$$

The working version of this is

$$\delta m^{n+1} \approx (\mathbf{G}^\mathbf{T}\mathbf{G})^{-1}\mathbf{G}^\mathbf{T}\delta \mathbf{d}^n \tag{3.7}$$

where $(\mathbf{G}^\mathbf{T}\mathbf{G})^{-1}\mathbf{G}^\mathbf{T}$ is the generalized inverse of $\mathbf{G}$.

The analysis software used for estimating the hypocenter parameters for the DWTI MEQs utilizes an algorithm to solve the non-linear least-squares inversion problem originally developed by Dr. Leigh House of Los Alamos National Laboratory (House, 1987). Figures 3-10 and 3-11 present the least-squares hypocentral estimates for the DWTI MEQs using a homogeneous velocity model.

3.2 Hypocenter Modeling of the Tuscany Geothermal Field Microearthquakes

I calculated non-linear, least-squares hypocenter estimates for the Tuscany microearthquakes using one set of data processing and analytical steps for all three clusters. The steps in the process are (in sequential order):

1. P wave identification and arrival time determination
    - P wave arrival time determination by auto-pick algorithm
    - P wave arrival time data quality evaluation and refinement
2. Inverse modeling of absolute hypocenters based on P times and four (station dependent) velocity models $v(z)$
3. Calculation of hypocenter confidence regions for P wave based estimates
4. S wave identification and arrival time determination
    - S wave arrival time determination by visual inspection
    - S wave arrival time data quality evaluation and refinement
        - S wave arrival time estimation using forward modeling from P wave hypocentral locations
        - S wave arrival confirmation using 3-component station data
        - S wave arrival confirmation using moving-window spectrographic analysis
5. Refinement of P and S arrival time data standard error estimates $\mathbf{s}_p, \mathbf{s}_s$
6. Inverse modeling of absolute hypocenters based on P and S times and four (station dependent) velocity models $v(z)$
7. Calculation of hypocenter confidences for P and S wave based estimates
8. Evaluation of hypocenter variance due to model differences

9. Multiplet analysis of each cluster of events using waveform correlation analysis

10. Calculation of differential arrival times for multiplet events using cross-correlation of waveforms (if appropriate after multiplet analysis)

11. Estimation of the differential arrival time standard errors $s_{p_{dt}}, s_{s_{dt}}$ (if appropriate after multiplet analysis)

12. Inverse modeling of relative event hypocenters based on P and S times and one velocity model $v(z)$ (if appropriate after multiplet analysis)

13. Calculation of relative event hypocenter confidences for P and S wave estimates (if appropriate after multiplet analysis)

The following sections describe the major steps in the data processing and analysis. Important concepts will be illustrated using examples from one or another of the three Tuscany clusters, as appropriate. Final results will be presented for all three clusters.

3.2.1 Data Processing for Absolute Hypocenter Modeling: Process steps 1 - 5

High quality hypocenter estimates are dependent on the use of high quality arrival time estimates. Therefore, considerable effort was invested in obtaining good phase arrival times. For all three sets of events from Tuscany, determination of P wave arrivals was routine due to excellent signal-to-noise characteristics of the seismic recordings. In all three cases, P waves were determined using auto-pick routines available in the SAC seismic processing software library (Tapley and Tull, 1991). An initial estimate of the P wave arrival time pick standard errors was therefore made by setting $s_i = 2\delta t$ (two DAS sample intervals). It was expected that this estimate of the standard errors would be refined during the process of the multiple event inversion trials.

Determination of S wave arrivals posed considerably more difficulty. The principal impediments were superposition of the S wave first arrival and the P wave coda caused by

insufficient hypocentral distances, and considerable overlap in spectral content of the two phases. After producing initial S wave arrival time estimates by direct visual inspection of the seismic records (filtered and unfiltered), the arrivals were checked against expected arrival windows calculated from the original P wave hypocenter locations. (This information was used as a general guideline because of the preliminary nature of the P wave hypocenter estimates). Next, the quality of the estimates was checked by applying moving-window spectrographic analysis. For most stations, this method confirmed the visual estimates, however, a few stations required revision of the arrival picks. Information from a few three-component stations were used to add additional constraint on the arrival time estimates.

The spectrographic analysis used in picking the S wave arrivals was also used to refine (establish) the arrival time pick standard errors. Spectral characteristics varied somewhat from event to event and station to station for these clusters, but in general the spectral content included frequencies between 2 and 20 Hz with dominant frequencies between 10 and 20 Hz for P waves and between 2 and 10 Hz for S waves (Figure 3-12). Some events exhibited significant power in frequencies up to 40 Hz and higher. The P wave estimates of arrival time error were increased from the scalar multiple of the sample interval to a percentage of the period of a 17 Hz wave, $s_i \approx 0.012 seconds$, which for a DAS sampling frequency of 250 Hz ($\delta t = 0.004$ seconds) amounts to 3 samples (example for the Larderello Seismic Network stations). Similar estimates of s_{si}, were produced using a percentage of the lowest frequencies in the S wave spectral band.

3.2.2 Absolute Event Hypocenter Modeling: Process Steps 6-8

I calculated single event (absolute) hypocenter estimates by inverting the P and S wave data for all three Tuscany clusters using an inversion program developed by Dr. William Rodi of the Earth Resources Laboratory, MIT (Rodi *et al.*, 1993). This program uses the Polak-Ribiere variant of the conjugate gradient method to solve the non-linear inverse problem described above.

Many combinations of the data and velocity models were inverted to ascertain the sensitivity of the results to various input parameters, including different combinations of stations, different subsets of data, and various versions of the models. Figures 3-13, 3-14 and 3-15 present several of the velocity models used in the inversion trials for the LAGO cluster. Figures 3-16, 3-17, and 3-18 present the results from three of the trials run for 22 events from the LAGO cluster.

Distinctions between the various trial results were assessed according to the data residuals, 90 % confidence regions (lateral dimensions) and 90% confidence intervals (depth). These regions were calculated based upon the method of Jordan and Sverdrup (1981), as implemented by Rodi *et al.* (1993).

The results presented in Figures 3-16, 3-17, and 3-18 exhibit similar hypocentral distributions despite different models and different subsets of data, suggesting that the absolute locations, if not clearly resolvable, are spatially robust. A detailed interpretation of the hypocentral distributions will be taken up in chapter 4 when site specific geologic structures, crustal stress conditions, and geothermal production activities will be jointly considered.

I ran similar trials for 86 events from the Larderello 1993 swarm using the same velocity models as used for the LAGO cluster. These events were best fit when using the layered velocity model. Here I show the results of the P wave absolute estimates (Figure 3-19) which were calculated for the entire set of 86 events. P and S wave solutions were also determined, but for a smaller set of events. These results will be introduced in the section on multiplet analysis. The P wave results shown here will serve as a baseline confidence reference for this swarm.

Similarly, Figures 3-20, 3-21 and 3-22 present some of the velocity models used to calculate estimates of the absolute hypocenters for 75 events in the Monte Amiata MEQ swarm. Figure 3-23 presents results from one of the velocity model trials.

3.2.3 High Resolution Relative Event Relocation

Previous Work: Theoretical Developments

Estimating hypocenter parameters of singular earthquakes using the method of non-linear, least-squares iteratively minimizes the differences between predicted and observed values of the arrival times between one source and an array of receivers. Inherent in the method is the idea that the quality of the results are dependent upon the variance of the observed arrival time errors and how well these variances approximate those of the entire population of arrival times. Reducing the variance and eliminating non-zero means are tasks of the utmost importance if the locations are to be accurate enough to resolve pertinent geologic structures. Some important sources of error affecting the final single event inversion results include:

1. inconsistency of the arrival time estimates due to human error in the visual inspection of the records (which is generally thought to have the characteristics of a normal probability distribution with zero mean)
2. inconsistency of the arrival time estimates due to onset times obscurred by other phase arrivals and backscattered energy, or by non-earthquake related signals (noise)
3. biases in arrival times introduced by inconsistencies in data acquisition from one station to another within the same network (such as clock errors, or uncompensated differences when arrival times from different networks are incorporated into the same inversion
4. inadequate traveltime predictions due to poor choice of velocity model
5. incorrect *a priori* information, such as incorrect hypocentral depth constraints
6. poor sensor array distribution with respect to the event being observed.

Flinn (1965) discussed these issues and presented the fundamentals of error evaluation for single event location given an array of recievers that are adequately distributed to sample

the traveltimes in distance and azimuth. In his work, he discussed the appropriateness of using linear approximations to estimate variances for different relative sizes of confidence regions. He concluded that for regions defining "infinitesimally small" areas around the computed hypocenter, a linear approximation is acceptable. Later, Evernden (1969) amended Flinn's work by demonstrating that fiducial confidence regions (those calculated using the assumption of normally distributed standard errors) depart from estimates of the probable error as the number of stations decreases, greatly over estimating the total size of the confidence regions for sparse networks.

A detailed discussion of confidence region estimation for parameters determined by non-linear regression techniques is not possible within the scope of this work, however, the interested reader is referred to a paper by Sprent (1990) on the history of the development of error measurement models, and standard works on the subject of non-linear regression methods (Draper and Smith Jr., 1981; Seber and Wild, 1989), and multivariate probability distributions (Rencher, 1995; Johnson and Wichern, 1998).

Relative event location methods are a family of techniques that attempt, through various means, to reduce the type and amount of errors in the observed and predicted arrival times. Jordan and Sverdrup (1981) provide summaries of some of the original forms, particularly the homogeneous-station methods in which hypocenters are modeled using only the differences in arrival times between events in an effort to reduce the effects of velocity model errors, and the master-event techniques in which a "master" event is used as a fixed point reference for the locations, again in an effort to apply *a priori* constraints to the errors due to velocity model errors.

In that paper, Jordan and Sverdrup (1981) describe their formulation of a third type, specifically, the method of joint hypocenter determination, in which they simultaneously invert for the hypocentral parameters with respect to a central reference point, thereby minimizing the errors associated with both path and scatter in hypocenter locations. In their implementation, they utilize the centroid as the reference point for their inversion, partitioning their data and model vectors to accomodate individual and differential arrival

times for all events, stations and waves. They additionally offer a method of estimating the confidence regions for the results of their *hypocentroidal decomposition*, which accords the remaining uncompensated errors a normal distribution and assesses their values according to scatter in the hypocentral parameters (Jordan and Sverdrup, 1981).

The computer program I employed for estimating the relative event hypocentral parameters for the Tuscany clusters is an algorithm developed by Rodi for use in regional and local multiple relative event relocation. In his implementation, multiple reference events may be incorporated in the analysis, if it is deemed warranted and necessary for accurate assessment of the clustered events (Rodi *et al.*, 1993)

Previous Work: Case Studies of Relative Event Location Methods

Relative event relocation methods minimize the variance of errors in predicted arrival times because they assume that true velocites in the earth are spatially smooth and slowly varying. In a practical sense, this assumption is taken as appropriate when the events of interest have been previously located using the traditional "absolute" hypocenter inversion techniques and are known to be spatially clustered. Temporal clustering adds additional assurance that the assumptions are met by reducing the likelihood of temporal variations in the velocity model and focal mechanisms.

In the late 1970s and early 1980s, several groups of investigators published articles commenting on the similarity of waveforms for small clusters of events of various magnitudes from numerous locations and geodynamic environments. Early investigations presented the idea that any events exhibiting identical waveforms (including S-P times as well as individual pulse shapes) must be co-located. Thus, the temporal relationships between similar events and large intensity earthquakes or volcanic eruptions began to be assessed for possible precursory indicators.

Those studies reflected concerns from researchers investigating motion along large faults (of various types) including a study of strike-slip events on the San Andreas fault (Geller

and Mueller, 1980), aftershock sequences in the Imperial Valley of California (Pechmann and Kanamori, 1982), and precursor-event-aftershock sequences in the Puerto Rican Trench (Frankel, 1982). These (and other) studies (with the exception of Pechmann and Kanamori (1982)) applied relative event location analysis to small sets of events on which considerable attention was paid to source and signal characteristics in an effort to investigate the physical processes associated with repeated similar events. Several of these investigators commented on the observation that strong waveform similarity was more common in events from foreshock sequences than from aftershock sequences. One common conclusion was that similar events (referred to as doublets, or multiplets) are an indication of stick-slip sliding and the repeated dislocations at points of significant rock strength increases (asperities) (Geller and Mueller, 1980; Frankel, 1982; Poupinet *et al.*, 1984).

Work conducted in the later part of the 1980s and early 1990s included not only similar events from large fault systems (Pechmann and Thorbjarnardottir, 1990), but also larger test cases of earthquake swarms, such as Central Japan (Ito, 1985, 1990), Mount Saint Helens, Washington, (Fremont and Malone, 1987), Kilauea Volcano, Hawaii (James and Savage, 1990) and in the Jura Mountains in northern Switzerland (Deichmann and Garcia-Fernandez, 1992). Also in that time period, method diagnostic studies were offered by researchers from the mining community where the relative event location hypocentral parameter estimates could be compared with the known location and time of mine blasts (Thornjarnardottir and Pechmann, 1987; Israelsson, 1990).

Recently, a few research efforts using relative event location techniques have focused on the imaging of hydraulic fractures during geothermal reservoir stimulation and flow testing. In all of the geothermal case studies the objectives were to image hydraulic fractures induced during production well installation, stimulation or testing rather than for structure identification as had been done in the previous relative event relocation studies. Additionally, all were conducted from sparse borehole networks rather than from surface arrays. Studies have been published from the Fenton Hill HDR site in the Jemez Mountains of New Mexico (Rodi *et al.*, 1993; Li *et al.*, 1995; Phillips *et al.*, 1996), and the Hijiori and Ogachi HDR sites in Japan (Tezuka and Niitsuma, 1995; Moriya *et al.*, 1996). This author has identified only

one published paper regarding the application of relative event relocation at a geothermal steam field, specifically at Kakkonda, Japan (Moriya *et al.*, 1994).

The data processing necessary to apply relative event relocation techniques involves three steps prior to inversion, specifically, steps 9-11 in the list presented at the beginning of this section. The following discussion presents the methods I used in those steps to process the data from the three Tuscany clusters.

Multiplet Analysis for Relative Event Relocation:Process Steps 9-11

The first task in completing relative event relocation is to determine which events in a catalog are similar. Early studies depended upon visual examination of the seismographic records (Geller and Mueller, 1980) and this is still an important aspect of determining the events in the multiplet. Pechmann and Kanamori (1982) were the first to cite the use of time series statistical methods to quantify the degree of similarity. They chose to use time domain cross-correlation series analysis as their quantitative indicator. Poupinet *et al.* (1984) were the first to complete their multiplet analyses using the frequency domain technique of cross-spectral correlation. Of the works reviewed by this author, approximately 60 % of the studies used the time domain methods (Pechmann and Kanamori, 1982; Frankel, 1982; Thornjarnardottir and Pechmann, 1987; Pechmann and Thorbjarnardottir, 1990; Israelsson, 1990; Phillips *et al.*, 1992; Deichmann and Garcia-Fernandez, 1992; Phillips *et al.*, 1996) versus 40 % that applied the frequency domain techniques (Poupinet *et al.*, 1984; Ito, 1985; Fremont and Malone, 1987; Ito, 1990; James and Savage, 1990; Moriya *et al.*, 1994). Although the frequency domain methods allow extremely fine estimations of differential times they are more time costly to apply and tended to be used in studies using a limited number of events, stations, and/or phase arrivals. I chose to apply cross-correlation in the time domain due to the large number of seismic records being processed (2350 records, 4250 phase arrivals).

To evaluate the multiplets for the three Tuscany clusters, I calculated the peak value of

cross-correlation between records of all events (as recorded) from a few stations for each cluster. I based my choice of station on three criteria:

- signal-to-noise ratio (which was very good for most of the stations available at each site)
- the location of the station relative to the location of the absolute hypocentral estimates and the strike of the major geologic structures
- visual identification of similarity

Figures 3-24 through 3-29 present the full cross-correlation matrices for two stations recording the Larderello 1993 cluster. For each of these stations (SCAP and VALE) there are three matrices, each one representing the range of correlations for records truncated for a specific window length. The first matrix in each set is the correlation for a window containing the full signal record from approximately 0.5 seconds before the P wave first arrival to approximately 1-1.5 seconds beyond the S arrival. The second and third matrices represent correlations derived for windows containing either the P arrival or the S arrival. All window lengths were checked to contain enough cycles of the dominant frequencies for that phase so that the correlation would accurately reflect the spectral content of the signal. The values presented in the matrix are represented by shading levels with bright spots representing high values and dark spots representing values below 0.55. This cutoff level was chosen as an initial trial criterion for unfiltered records based upon the minimum cutoff of 0.6 used for filtered data from studies by Pechmann and Kanamori (1982) and Pechmann and Thorbjarnardottir (1990). I anticipated that any events reaching a cutoff criteria of 0.55 unfiltered for all three window lengths would be demonstrating a significant degree of similarity.

In order to represent the matrix as a shaded grid, I fit a suface to the correlation values and contoured the surface. To confirm the fit of the surface to the highly undulating peak-values I confirmed the peak values against the block shading for a variety of events. One example of the peak values for event number 174 (a potential reference, or master, event shown in

rows) cross-correlated against all slave events (shown in columns) is shown running along the bottom of the matrix. Any similar events for this master should also be indicated as a bright spot along the master 174 row in the matrix. (Note that the events are ordered temporally for this cluster from the bottom left up and to the right). An event whose waveform is similar to many other event's waveforms may be designated a "master" event. All events whose waveforms are compared to the master event's waveform may be designated "slave" events.

Not all events were recorded at all stations and therefore the cross-correlation matrices have missing data points. For a fully complete matrix, the diagonal would be completely bright. Where a station is missing a particular master, the block shading is darkened due to smoothing by the surface. This was not a problem in the use of these matrix representations for multiplet identification because it represented the introduction of, at worst, a false positive similarity, which would be identified later in the gathering of the arrivals for the multiplet. The potential for false negatives existed in the initial multiplet scan due to the choice of minimal filtering but was eventually determined to be an unnecessary concern due to the high number of events that met these initial strict match criteria, at least in the case of the Larderello 1993 swarm and the Monte Amiata swarms.

The multiplets were initially identified by searching for bright rows that were consistent from one station and phase to the next. Several potential masters were chosen for follow-up confirmation by a visual inspection of the records. If more than one master event exhibited a reasonable amount of similarity to other events, the tie was resolved by choosing the event with the best event similarity rate. For stations missing S wave picks, S wave correlations were still used by way of the full waveform cross-correlation matrix whose window extended past the expected arrival time for that phase.

Figures 3-24 through 3-29 present the cross-correlation matrices for the Larderello 1993 cluster. For the following discussion, I will refer to Figure 3-28 which exhibits typical characteristics for the Larderello 1993 matrices. The similarity appears disseminated temporally across the events, irregularly alternating irregularly from good similarity to poor similarity.

Macroscopically, it appears that events after number 146 exhibit a stronger degree of similarity than the earlier events, but the values continue to alternate. Figures 3-30 through 3-36 are the matrices for three stations recording the Monte Amiata swarm. The Monte Amiata cross-correlation matrices exhibit a significantly different macroscopic character than those presented for the Larderello 1993 cluster. Here we can see that similar events occurred in large temporal sets separated by events with little similarity to any masters. This suggests a single multiplet temporally interspersed with a series of dissimilar events. For this swarm, I chose event 119 as the master for a single subcluster of similar events which I later relocated using relative event differential travel time hypocenter inversion.

For the Larderello 1993 swarm, I chose events 174 and 157 as masters representing the two alternating multiplets. Event 174 was chosen because it exhibited the highest number of similar slave events for the stations reviewed. The similarity for this master is strongest for the P wave windows and can be viewed easily in Figure 3-28. Although another event from this multiplet, event 154, showed slightly higher correlation values for some events, making its row appear brighter, the number of slaves with acceptable values was slightly higher overall for event 174. Additionally, event 174 was temporally closer to the center of the swarm. Therefore, 174 was chosen as the master for this multiplet. Event 157 was found to represent the alternating multiplet. The difference between these two masters was predominantly in the shear waves and so are more identifiable in matrices containing those phases. Figures 3-24 and 3-26 provide a good example of the differences.

Figures 3-37 through 3-45 represent the cross-correlation matrices for events in the LAGO cluster. Because this cluster of events spanned approximately ten years time, the event ID numbers are not sequentially sequenced. However, the matrices are presented with the events temporally ordered, with the event ID indicated along the left matrix axes.

Similarity for events in this cluster was inconsistent from station to station and phase to phase. The best similarity was exhibited in the P waves, but even this was inconsistent from station to station. A few events appeared to show consistency, however, these subsets of matching events were limited to a few at a time that were temporally correlated. The

lack of a large set of similar results, together with the known temporal span of 10 years and the patchy spatial distributions of hypocenters from the absolute relocation, suggested that this set of events was not similar enough to warrent differential traveltime relative event relocation.

Differential Travel Time Determination for Relative Event Relocation: Process Steps 12-13

Recall our definition of arrival times in equation (3.1). Now we define our observables to be:

$\mathbf{d}_i^s = \mathbf{T}_i^s + t_0^s + \epsilon^s$, the arrival time for the slave event for the ith station (observed)
$\mathbf{d}_i^m = \mathbf{T}_i^m + t_0^m + \epsilon^s$, the arrival time for the master event for the ith station (observed)

where ϵ = errors in the arrival time picks.

Thus, differential travel times are

$$\delta t_i = \mathbf{d}_i^s - \mathbf{d}_i^m \tag{3.8}$$

Substituting in for $\mathbf{d}_i^s$ and $\mathbf{d}_i^m$ we get

$$\delta t_i = \mathbf{T}_i^s + t_0^s + \epsilon^s - (\mathbf{T}_i^m + t_0^m + \epsilon^m) \tag{3.9}$$

But, we can reduce the errors in our differential by using the master event's arrival time pick (in relation to the arrival's waveform) as a reference for the slave event's arrival time pick. We have already noted the similarity of waveform during the multiplet analysis and

can reduce the standard errors in the differential data by using the cross-correlation peak time offset (or lag) to correct our noisy absolute arrival time estimates. This leaves us with our working equation:

$$\delta t_i = \mathbf{T}_i^s + t_0^s + Lag - (\mathbf{T}_i^m + t_0^m + \epsilon^m) \tag{3.10}$$

(Note that the lag applied here is negative due to the order used in the cross-correlation, that is, slave correlated against master).

Thus, the differential times are straight forward to determine, once a master event has been identified for a multiplet. Figure 3-46 presents P wave arrivals for master event 119 for the Monte Amiata swarm plus seven slave event P wave arrivals with a small amount of inconsistency in the picks relative to the wavelet. Cross-correlating the slave event signals against the master we get the records in Figure 3-47. (Note that the top trace is the auto-correlation of the master event and all times are referenced to the beginning of the window). The lags are calculated as the time offset of the slave event's cross-correlation peak from that of the master's auto-correlation peak. The lag times and the normalized cross-correlation peak amplitudes are listed along the left of each trace.

It is important to note here that a high cross-correlation peak value implies a high degree of waveform similarity. The converse assumption however, that a low peak value implies dissimilarity, should be carefully assessed because it can lead to false negatives (if we define a negative to mean inadequate similarity). This can occur if the signal to noise ratio is so poor that the correlation peak can not be identified above the correlation noise floor. If the low correlation peak value is a result of low signal to noise ratio rather than a true dissimilarity in arrival wavelet form, then an appropriate choice of filters can be applied to remedy the situation and improve the contrast.

Window length is also an important factor in producing a representative cross-correlation peak. The window should be long enough to include several cycles of the dominant fre-

quencies in the signal, but not so long as to include secondary arrivals such as converted waves or reflections. Secondary arrivals can produce erroneous lags if it exhibits significant similarity to the master arrival and the noise can not be reduced sufficiently (as might be the case when the noise and signal band overlaps).

Many of the early studies using these techniques applied the process to only a few events. This small sample size forced the investigators to apply extensive signal conditioning in order to prevent losing potentially similar events out of the multiplet due to poor apparent similarity. Heavy filtering of the waveforms allowed the correlation peak values to be maximized, thus ensuring peak clearance of the noise floor. A review of the literature on the subject reveals widely varying cutoff criteria for dissimilarity, ranging from 0.9 to 0.5 for the filtered records. The most widely cited cut-off in the studies I reviewed suggested a lower limit of 0.6 (filtered), based upon the hypothesis of Geller and Mueller (1980) that events exhibiting this level of similarity would be located within 0.25 wavelengths of the master event's hypocentral location. This hypothesis was later corroborated by the results of mine blast studies (Thornjarnardottir and Pechmann, 1987; Israelsson, 1990), however, several authors commented on the rough decrease in peak correlation value with distance, including Thornjarnardottir and Pechmann (1987) who also noted that *"two events have a high average correlation coefficient of 0.69, event though they are 645 m apart, more than six times the maximum separation distance expected for well-correlated events in this passband"*. Ito (1985) also remarked on this issue, concluding that there were two types of similar events, one that is characterized by very short recurance times and a cluster size of less than one wavelength, and another type that occurred intermittently in elongated clusters with maximum dimension much larger than a wavelength.

I set the initial cutoff peak value at 0.5 for the Tuscany data processing because the observations of Thornjarnardottir and Pechmann (1987) and Ito (1985) suggested that setting the initial cutoff too high might unintentionally impose some level of spatial filtering that might impact my ability to characterize geologic structures with dimensions larger than 0.25 wavelength. The integrity of the differential times were ensured by visually inspecting all of the cross-correlation peaks and lags to ensure adequate clearance above the noise floor

and no lag jumping to secondary peaks.

Based upon the results of the initial differential time hypocenter inversion, the cutoff value would be reassessed, and the inversion re-run (if necessary) to ensure an improvement in data misfits (compared to the absolute locations). I calculated differential times for all events in each cluster with respect to each chosen master and then rejected arrivals that did not meet the specified cutoff criteria. 2 - 20 Hz bandpass filters were applied for some stations when unfiltered records produced correlation peaks nearing the noise floor. Window lengths were determined visually to capture at least the first 5 cycles of the phase and were applied consistently for all events recorded by a station. The data used in the inversion included the master events absolute P and S wave arrival times and all slave event's differential travel time that exhibited correlations above the cutoff value.

Figures 3-48 and 3-49 present the absolute and relative locations for two Larderello 1993 multiplets as calculated using the steps just described. The slave events are located relative to their appropriate master. The relative hypocenter locations for the two masters are within 10 meters of their absolute locations. The average peak correlation value for these multiplets were 0.77 (P and S waves) and the RMS data residuals were 0.070 seconds for the absolute and 0.016 seconds for the relative hypocenter estimates.

Figures 3-50, 3-51, and 3-52 present the absolute locations and two trials of relative event results for the Monte Amiata cluster. Three events in the trial represented in Figure 3-51 lost data from a few stations due to peak values below the correlation cutoff. As a separate trial, I lowered the criteria (while still carefully monitoring the behavior of the lag determinations) to bring the network coverage back into balance. The results of that trial are shown in Figure 3-52. As for the Larderello 1993 multiplet, the Monte Amiata slave events are located relative to their master event. The relative hypocenter location is within 25 meters of its absolute location. The average peak correlation value for these multiplets were 0.73 and 0.68 (respectively) and the RMS data residuals were 0.043 seconds for the absolute and 0.020 seconds for the relative hypocenter estimates.

Non–Unique Solution Space for a Two–Observation Point System

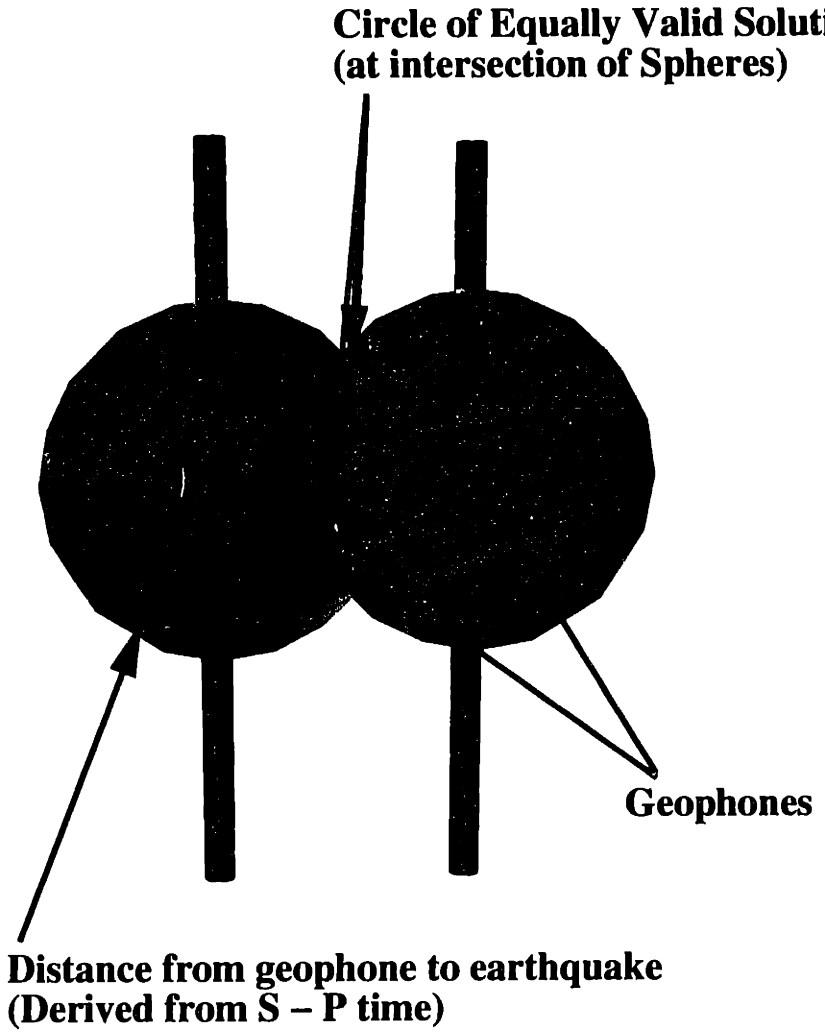

Figure 3-1: Schematic diagram showing the circular loci of solutions for a hypocenter inversion problem using a two observation point sensor array (that is, one sensor in each of the wells, at the center of each sphere).

Non–Unique Solution Space for a Two–Observation Point System

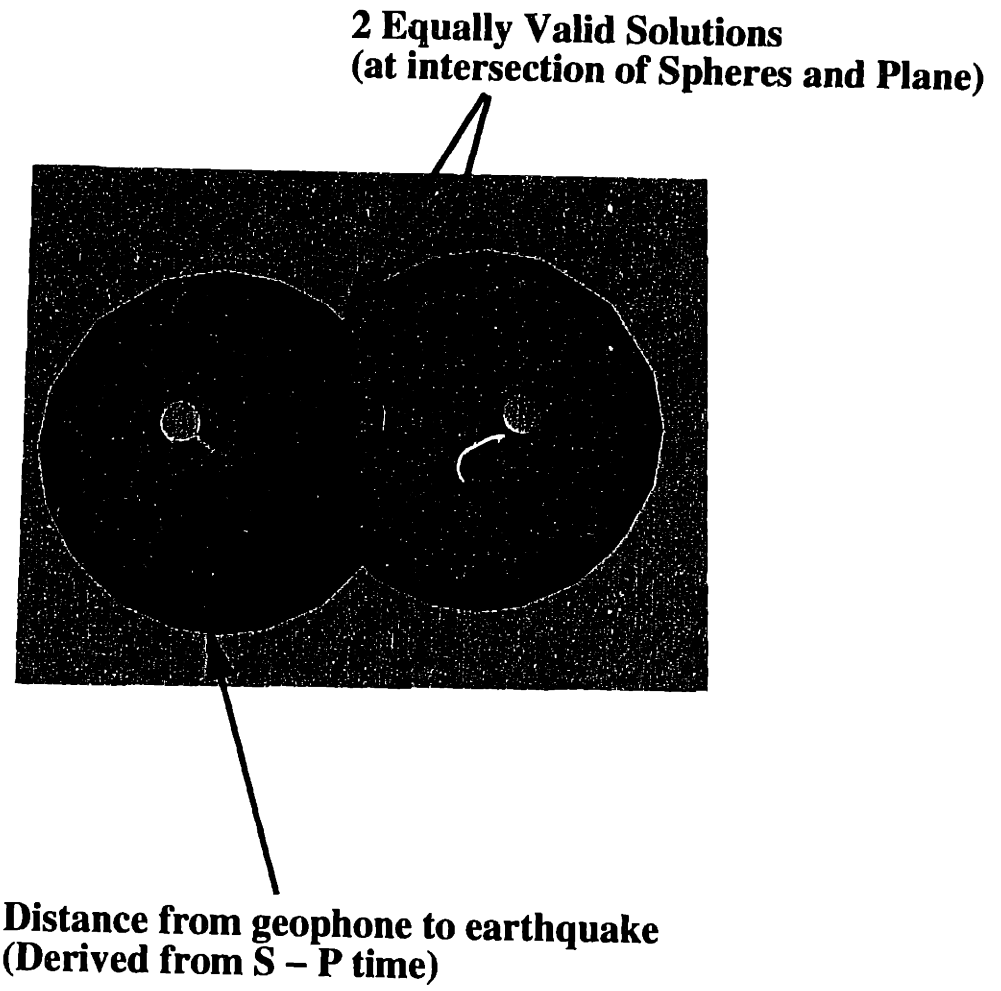

Figure 3-2: Schematic diagram showing the two equally valid solutions for a hypocenter inversion problem using a two observation point sensor array and an imposed depth contraint (indicated by the plane).

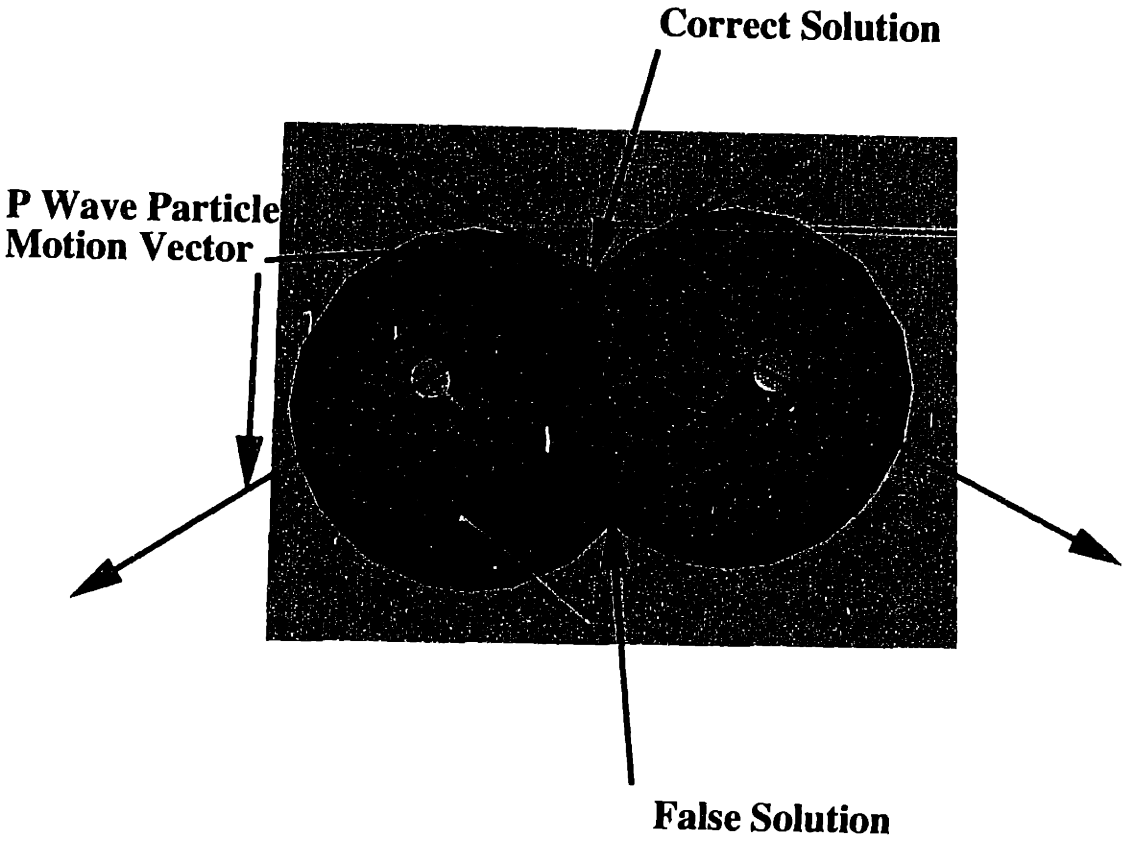

Figure 3-3: Schematic diagram showing the singular valid solution for a hypocenter inversion problem using a two observation point sensor array, an imposed depth contraint, and P wave particle motions from each sensor.

Geophone Configuration
ARCO's DWTI Site, Jasper, TX

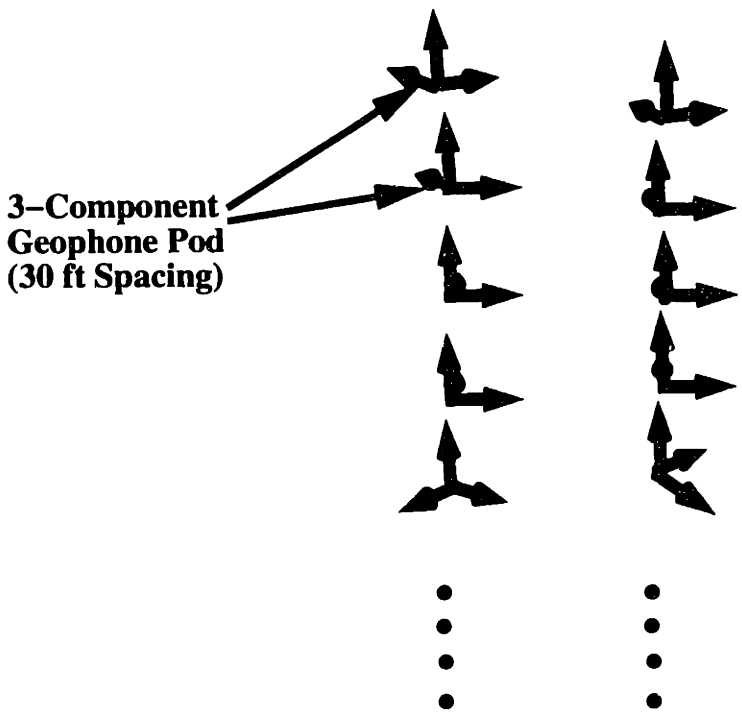

Before rotation of horizontal phones

Figure 3-4: Schematic representation of the geophone configuration for the DWTI experiment.

P Wave Particle Motion Before Geophone Orientation Calibration

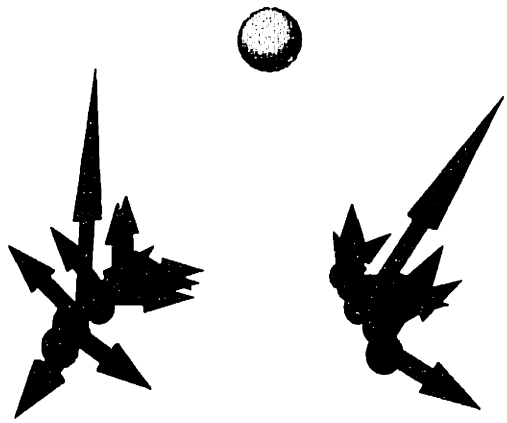

Figure 3-5: Schematic representation of the geophone configuration (areal view) for the DWTI experiment showing P wave particle motions.

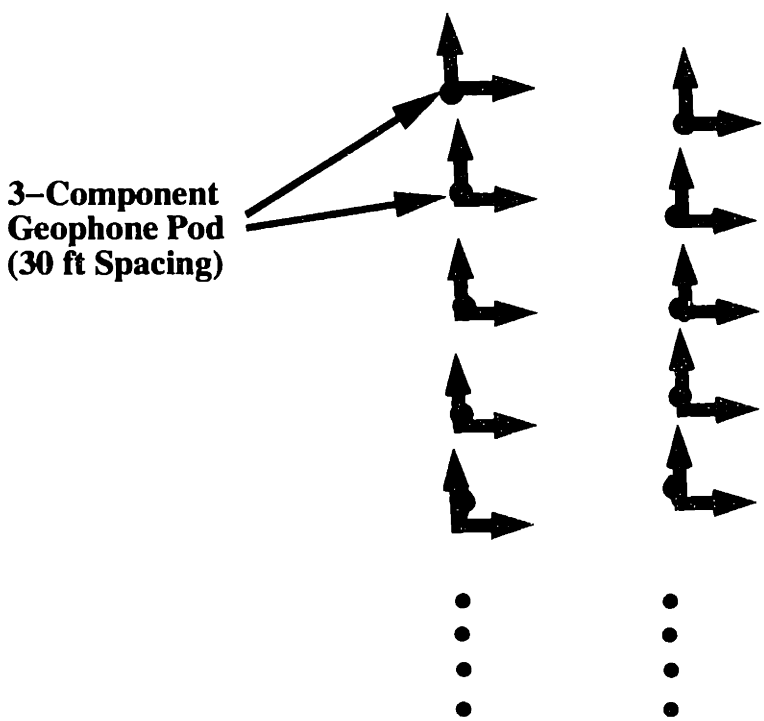

Figure 3-6: Schematic representation of the virtual geophone configuration for the DWTI experiment (that is, after the sensor data had been numerically rotated to correlate with the known location of 4 primacord calibration shots in the injection well).

P Wave Particle Motion After Geophone Orientation Calibration

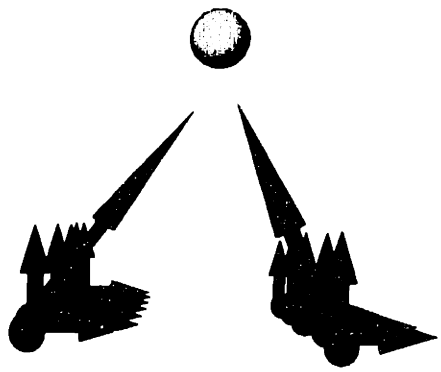

Figure 3-7: Schematic representation of the virtual geophone configuration (areal view) for the DWTI experiment showing P wave particle motions (that is, after numerical rotation to correlate with known location of 4 primacord calibration shots).

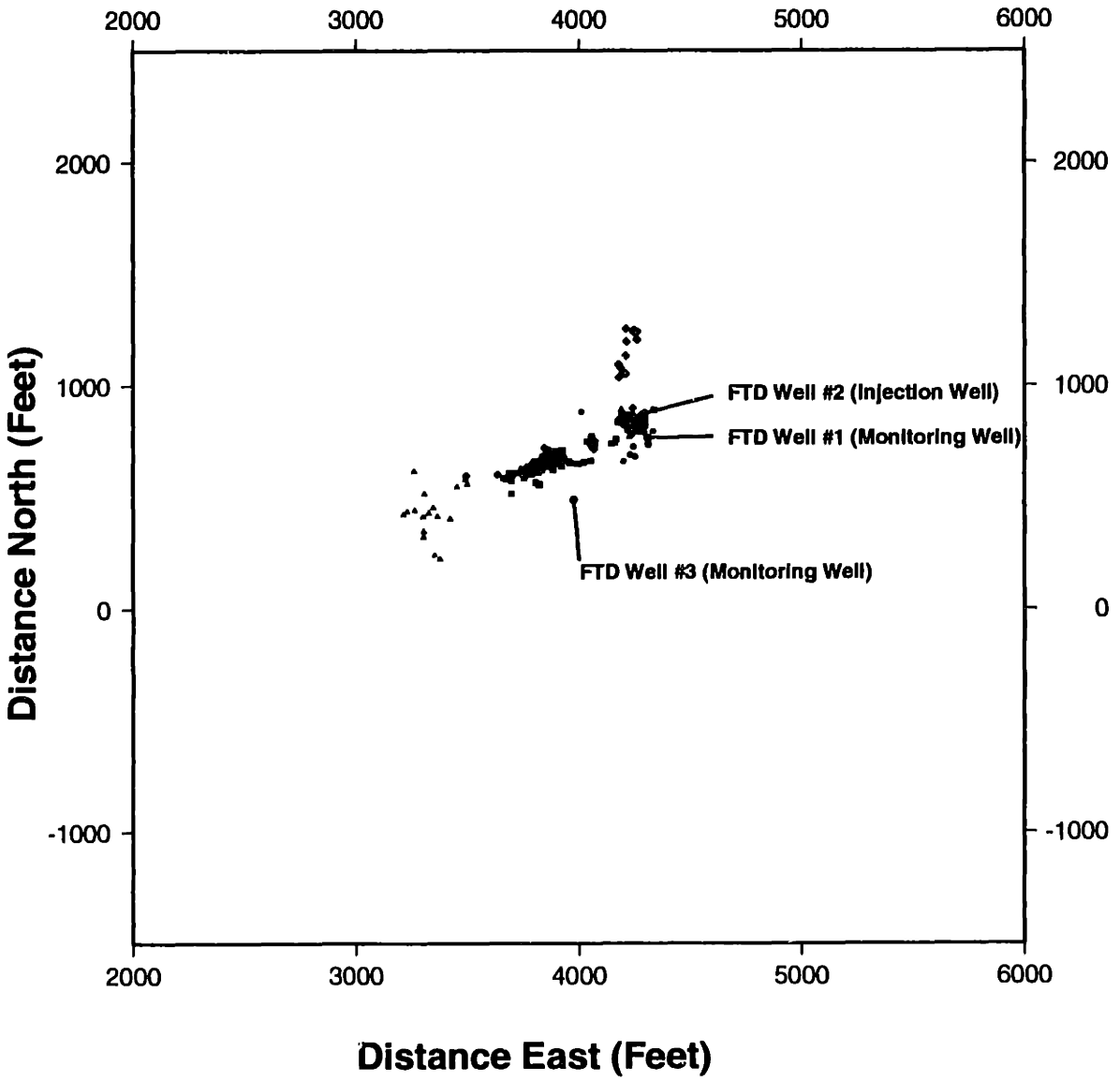

Figure 3-8: Areal view of hypocenters distribution for the DWTI hydraulic injection experiment calculated using forward modeling with depths constrained to that of the nearest sensor. Symbols indicate injection cycle in which the event occurred: Circles = Cycle 0, Squares = Cycle 1, Triangles = Cycle 2, Diamonds = Cycle 3.

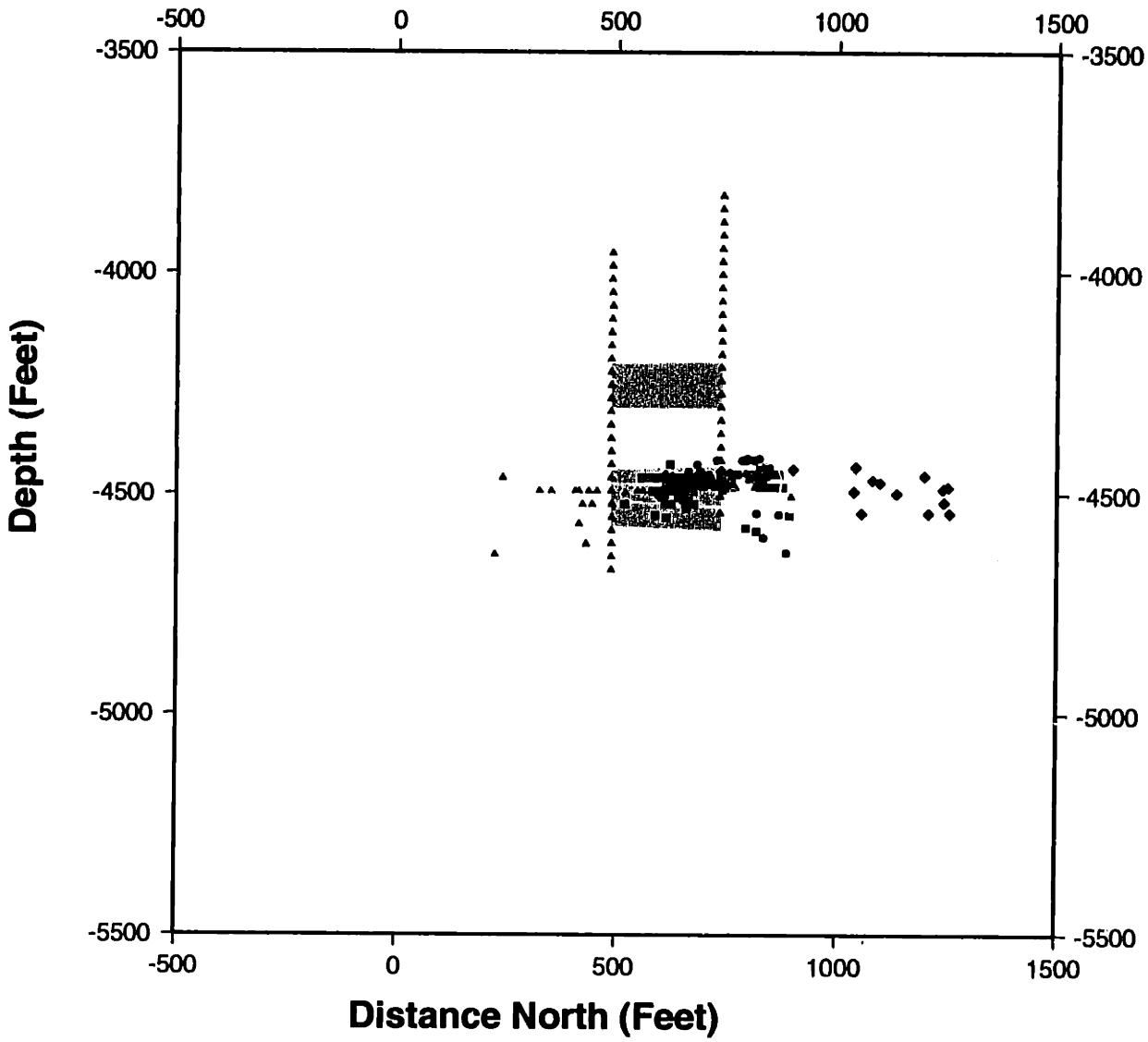

Figure 3-9: Side view (looking west) of hypocenters distribution for the DWTI hydraulic injection experiment calculated using forward modeling with depths constrained to that of the nearest sensor. Symbols indicate injection cycle in which the event occurred: Circles = Cycle 0, Squares = Cycle 1, Triangles = Cycle 2, Diamonds = Cycle 3.

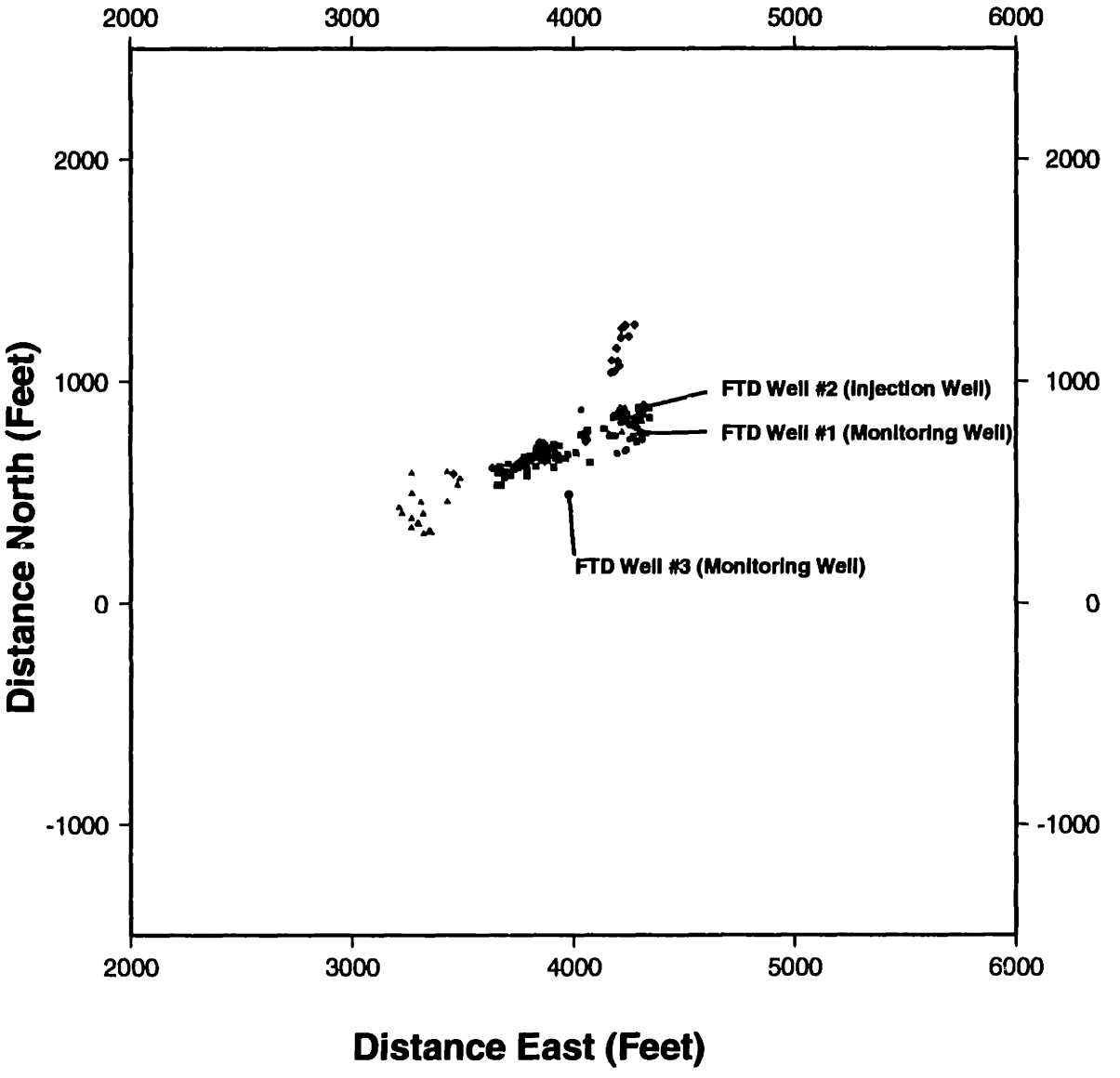

Figure 3-10: Areal view of hypocenters distribution for the DWTI hydraulic injection experiment calculated using least squares inversion with depths free to vary. Symbols indicate injection cycle in which the event occurred: Circles = Cycle 0, Squares = Cycle 1, Triangles = Cycle 2, Diamonds = Cycle 3.

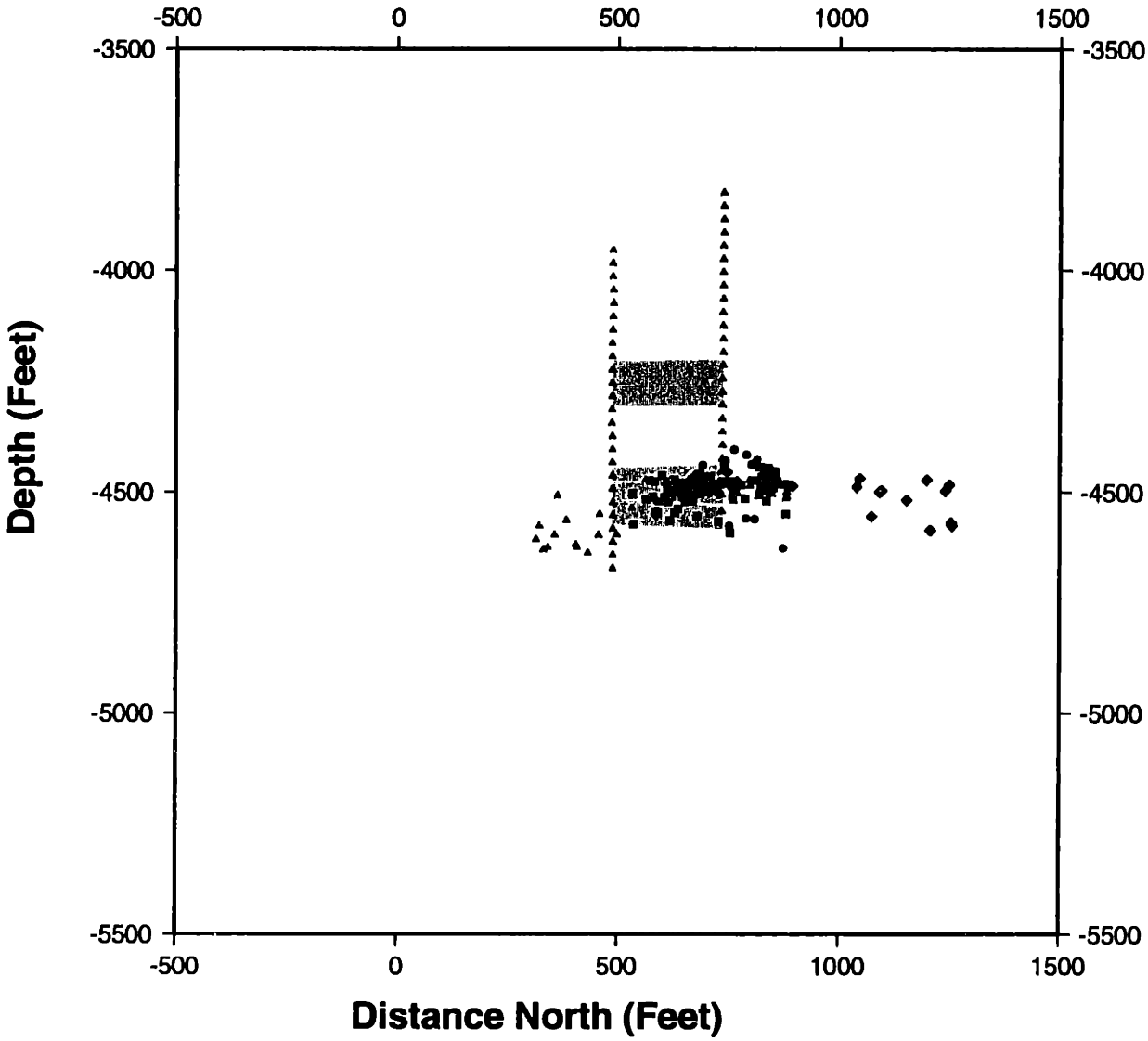

Figure 3-11: Side view (looking west) of hypocenters distribution for the DWTI hydraulic injection experiment calculated using least squares inversion with depths free to vary. Symbols indicate injection cycle in which the event occurred: Circles = Cycle 0, Squares = Cycle 1, Triangles = Cycle 2, Diamonds = Cycle 3.

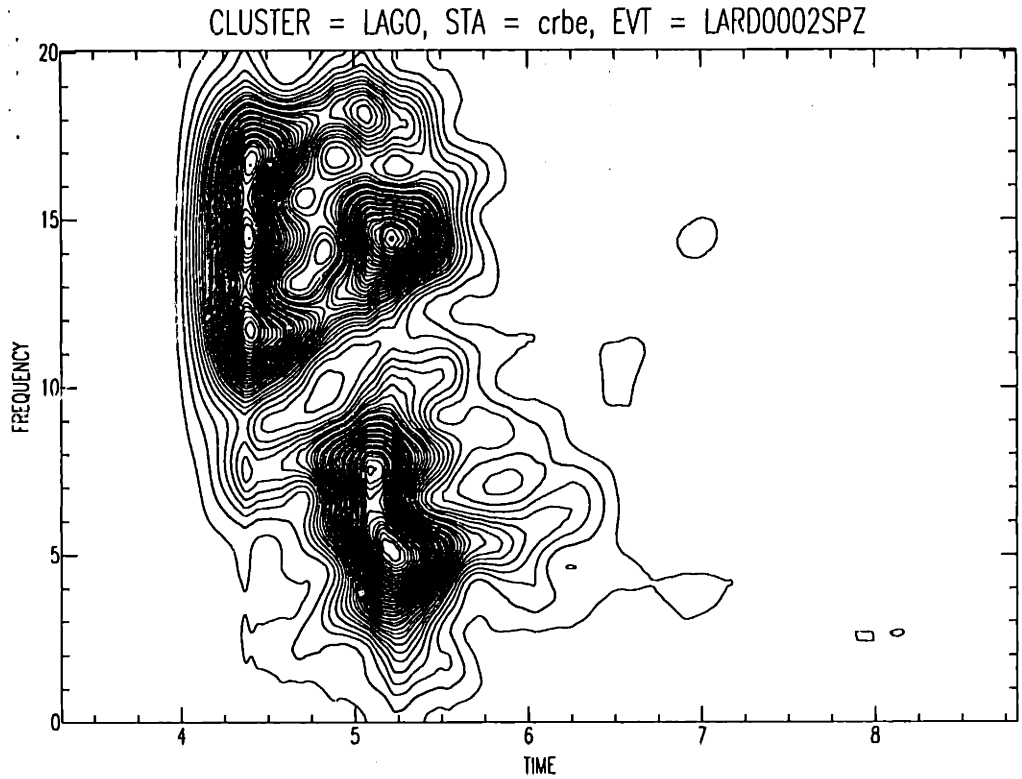

Figure 3-12: Moving-window spectrograph of the signal record for event 002 from station CRBE (LAGO cluster).

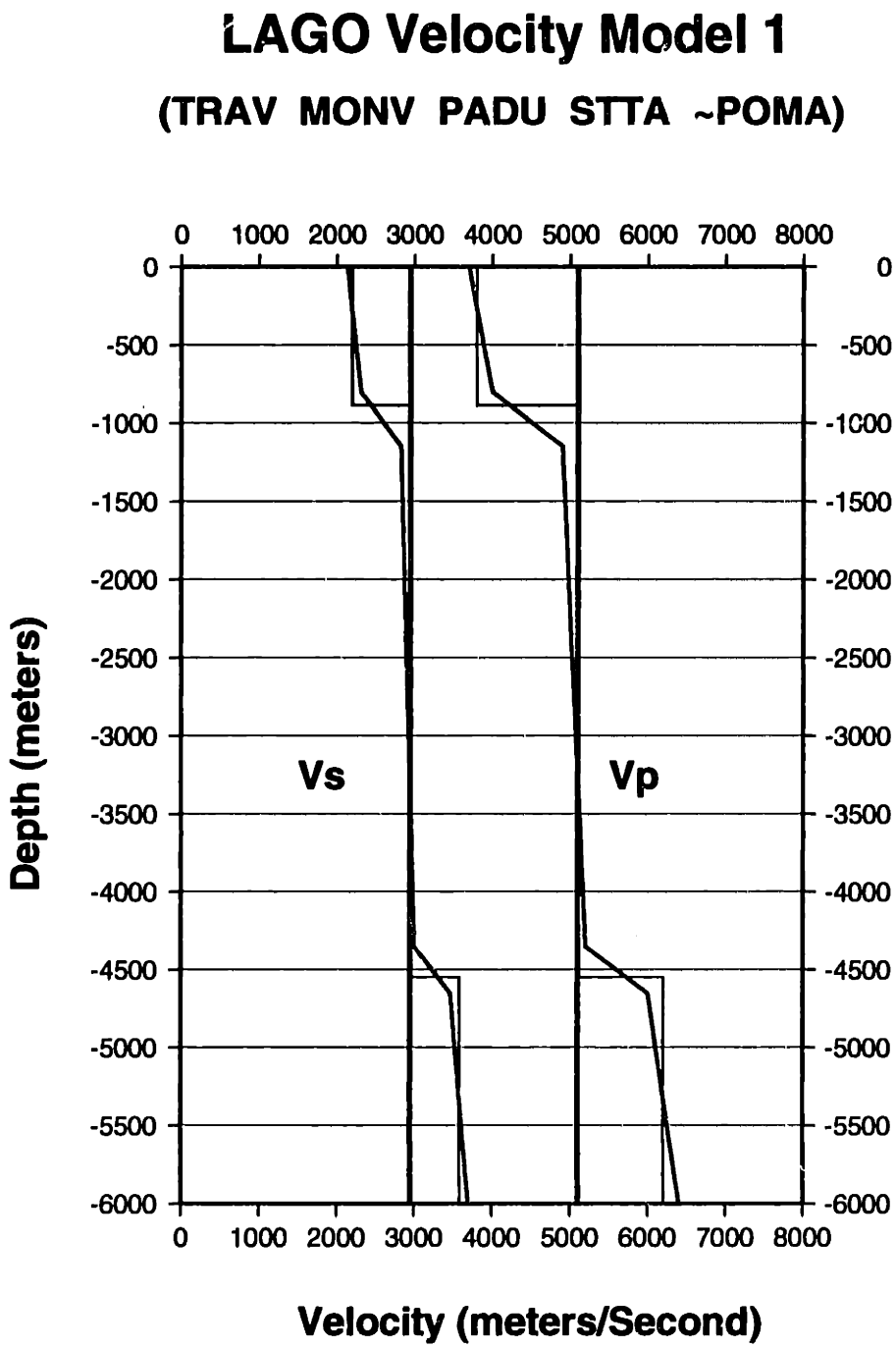

Figure 3-13: Seismic velocity models used for stations TRAV, MONV, PADU, STTA, and POMA of the Larderello Seismic Network. These models were derived from Figure 2-17

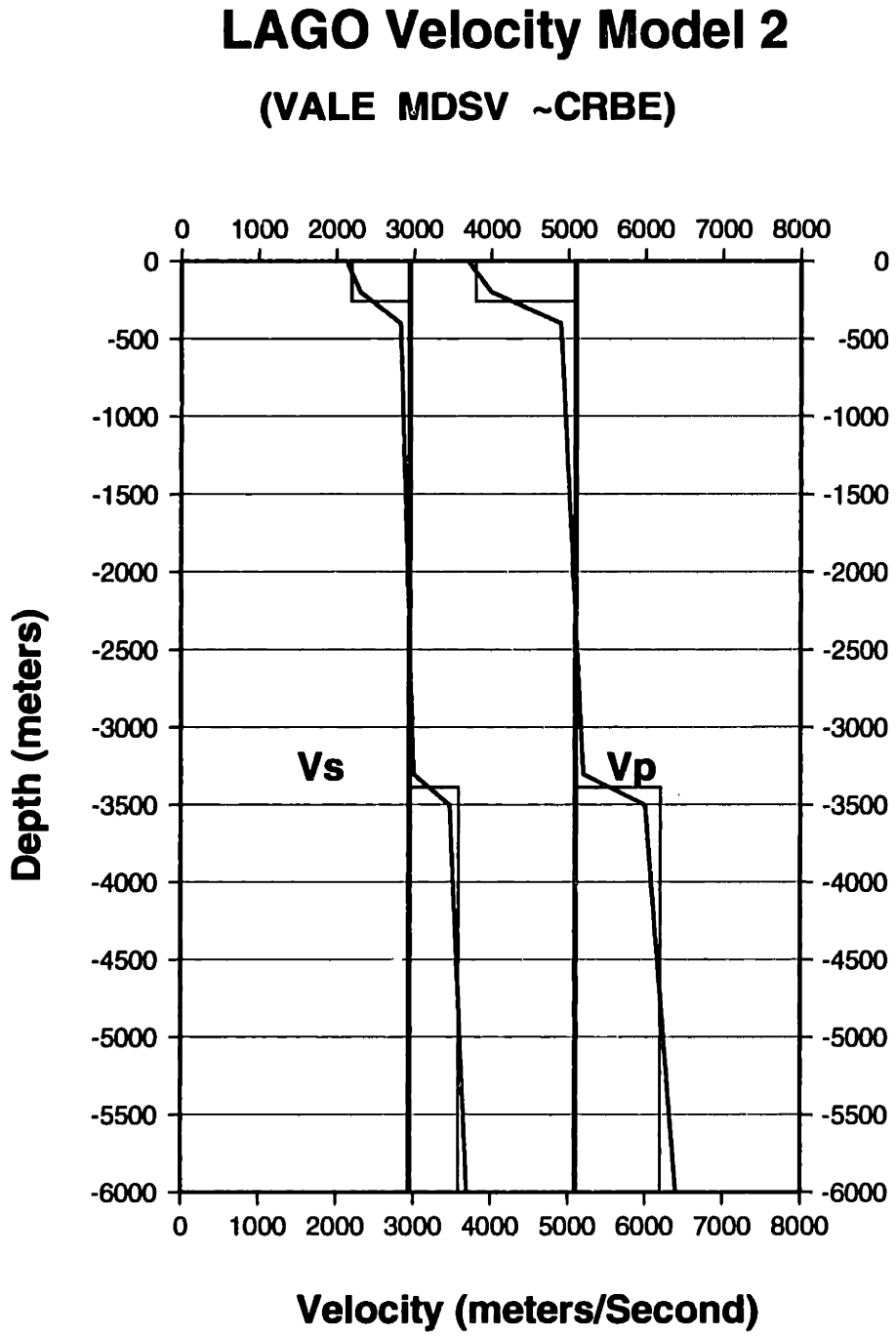

Figure 3-14: Seismic velocity models used for stations VALE, MDSV and CRBE of the Larderello Seismic Network. These models were derived from Figure 2-17

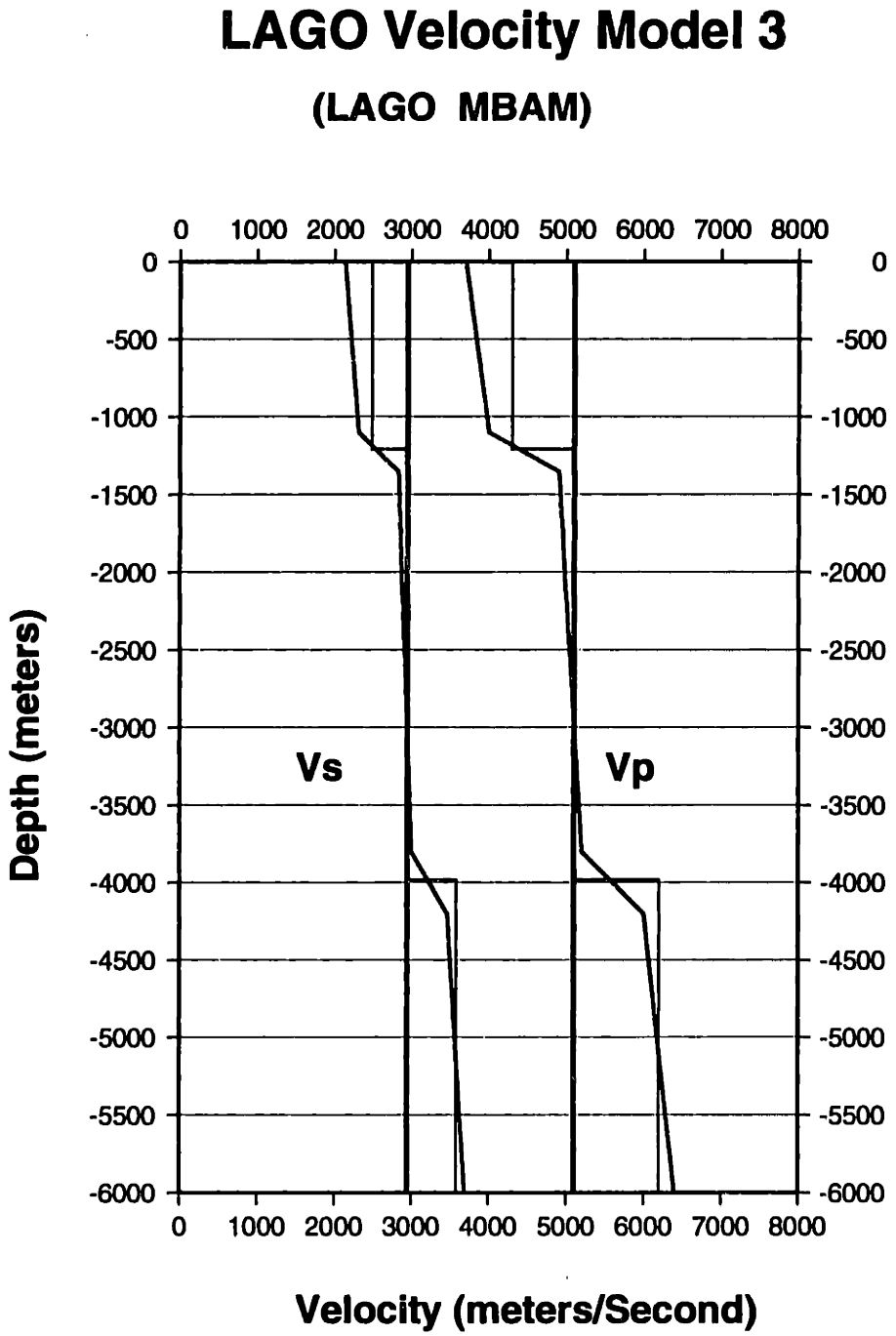

Figure 3-15: Seismic velocity models used for stations LAGO and MBAM of the Larderello Seismic Network. These models were derived from Figure 2-17

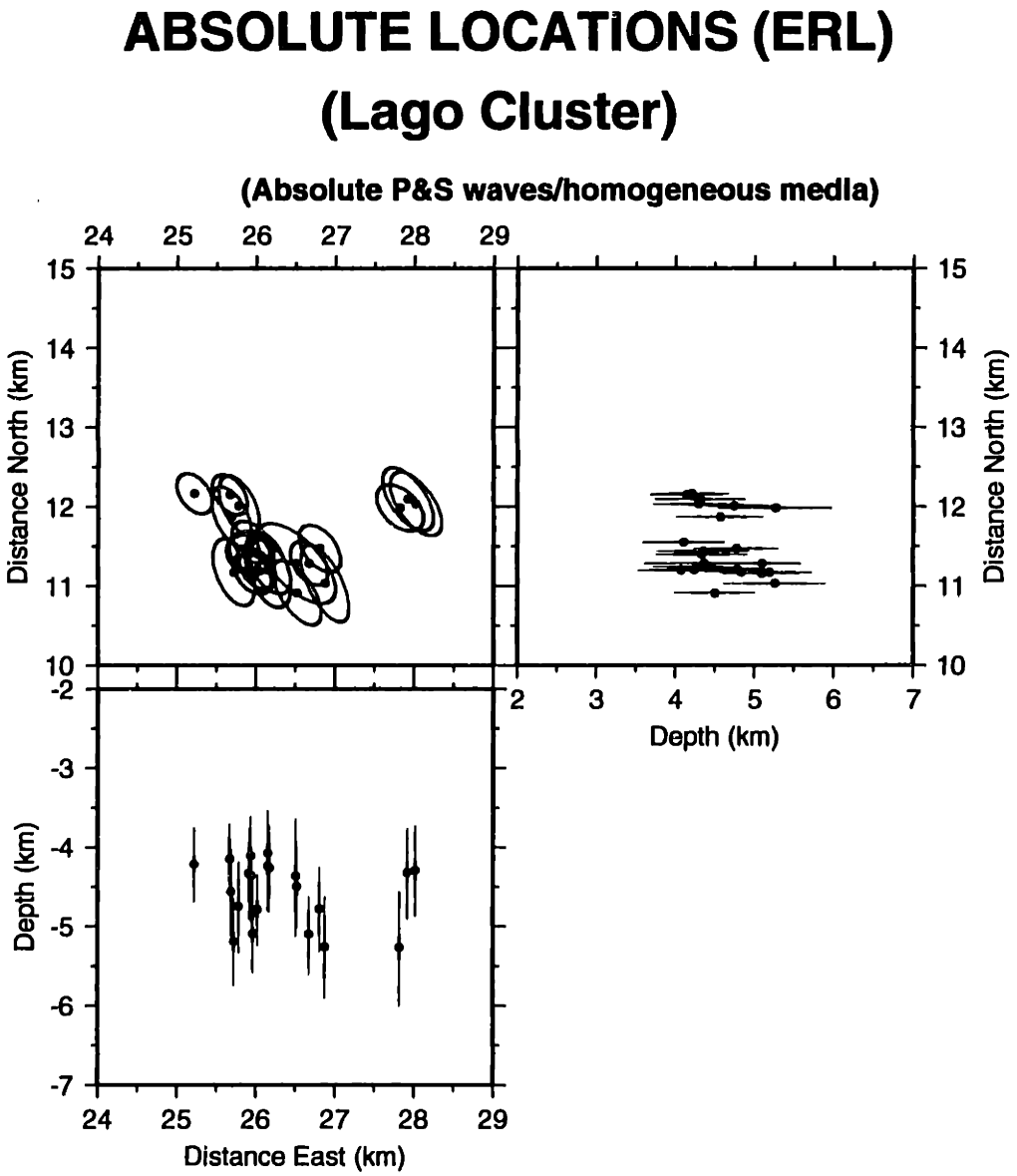

Figure 3-16: Hypocenter location estimates (absolute type) and their 90 percent confidence regions for events of the LAGO microearthquake cluster. These estimates were produced using P and S phase arrivals and a homogeneous velocity model for all stations.

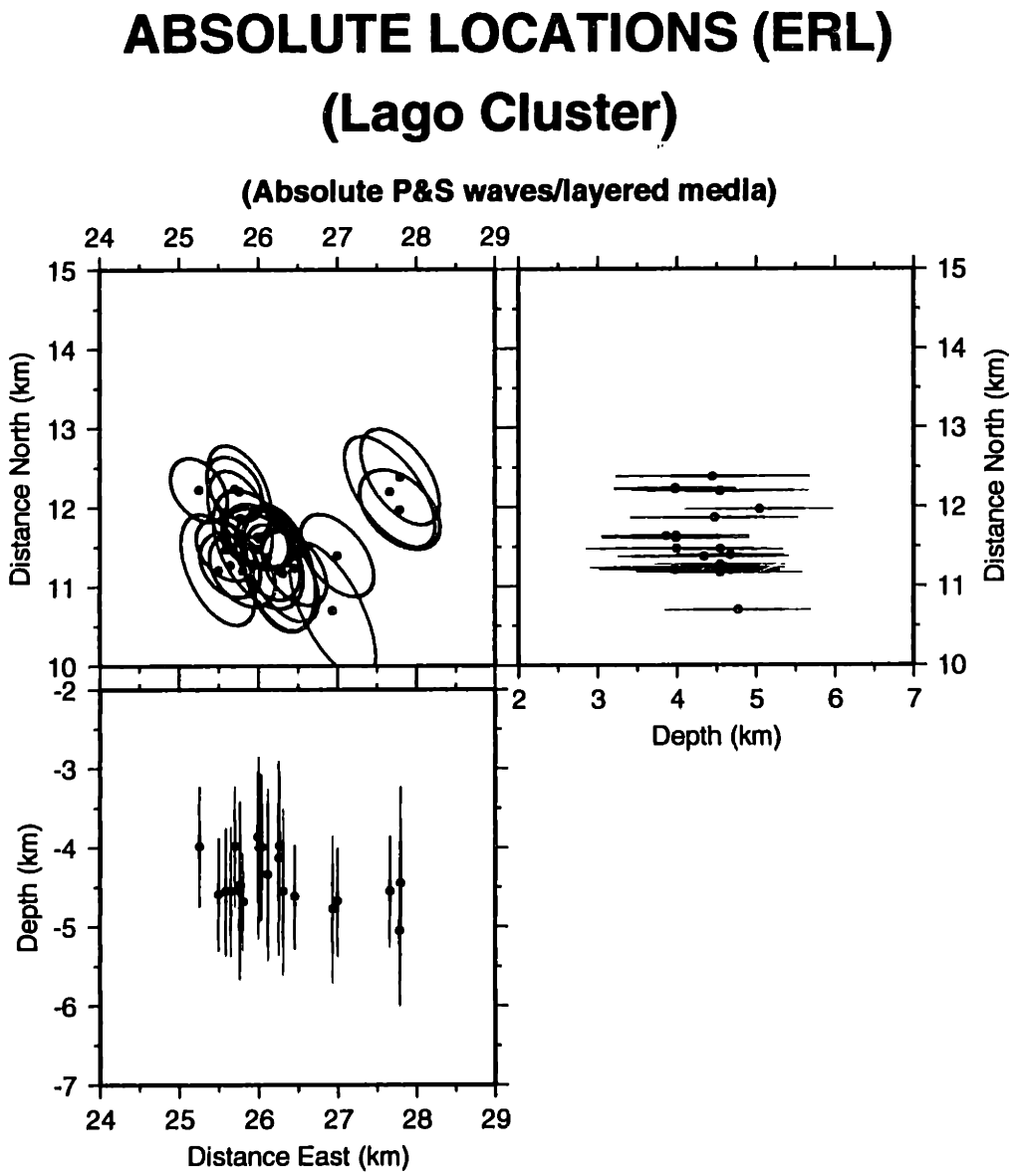

Figure 3-17: Hypocenter location estimates (absolute type) and their 90 percent confidence regions for events of the LAGO microearthquake cluster. These estimates were produced using P and S phase arrivals and station dependent layered velocity models.

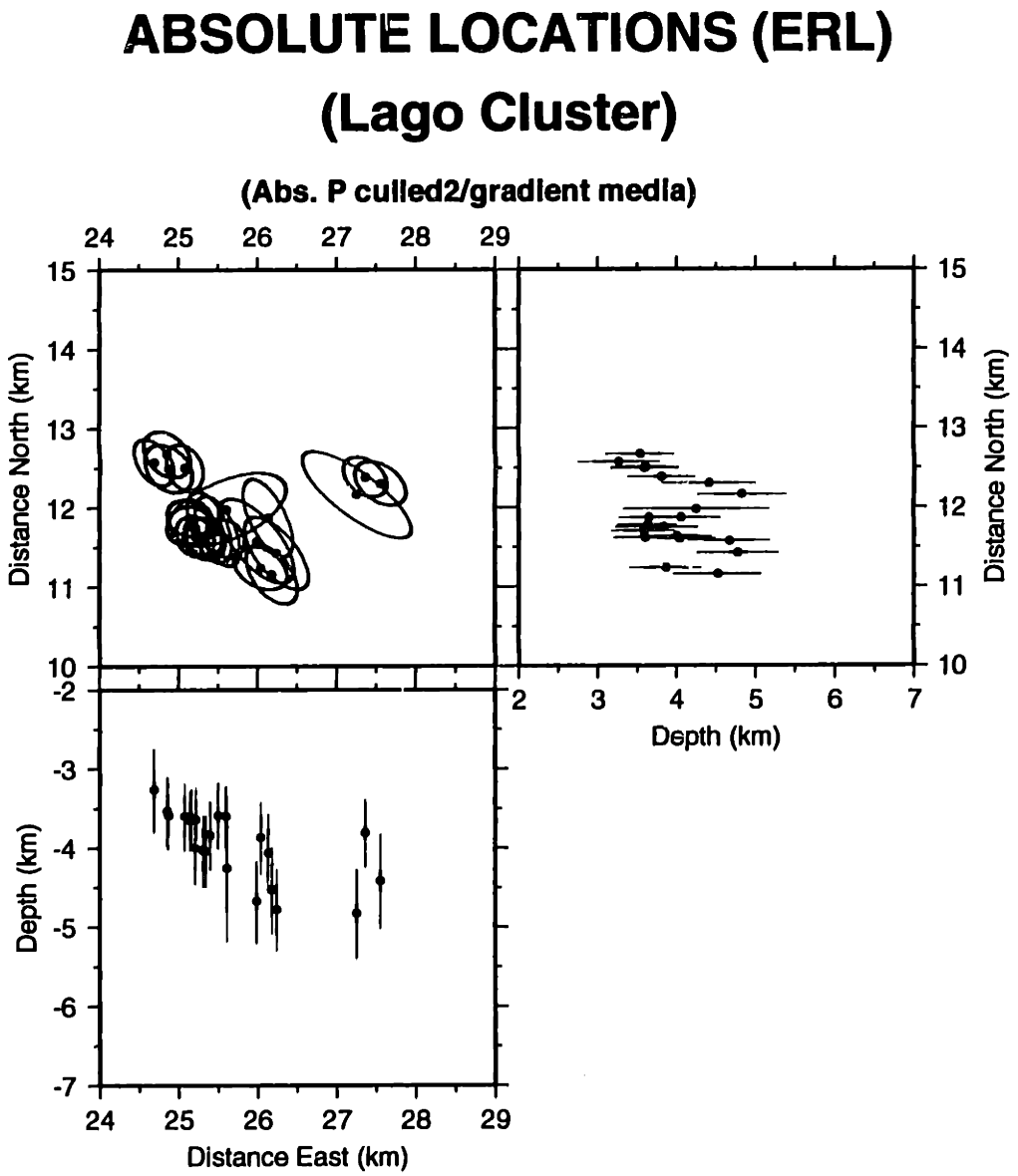

Figure 3-18: Hypocenter location estimates (absolute type) and their 90 percent confidence regions for events of the LAGO microearthquake cluster. These estimates were produced using P wave arrivals and station dependent, piecewise vertical gradient velocity models.

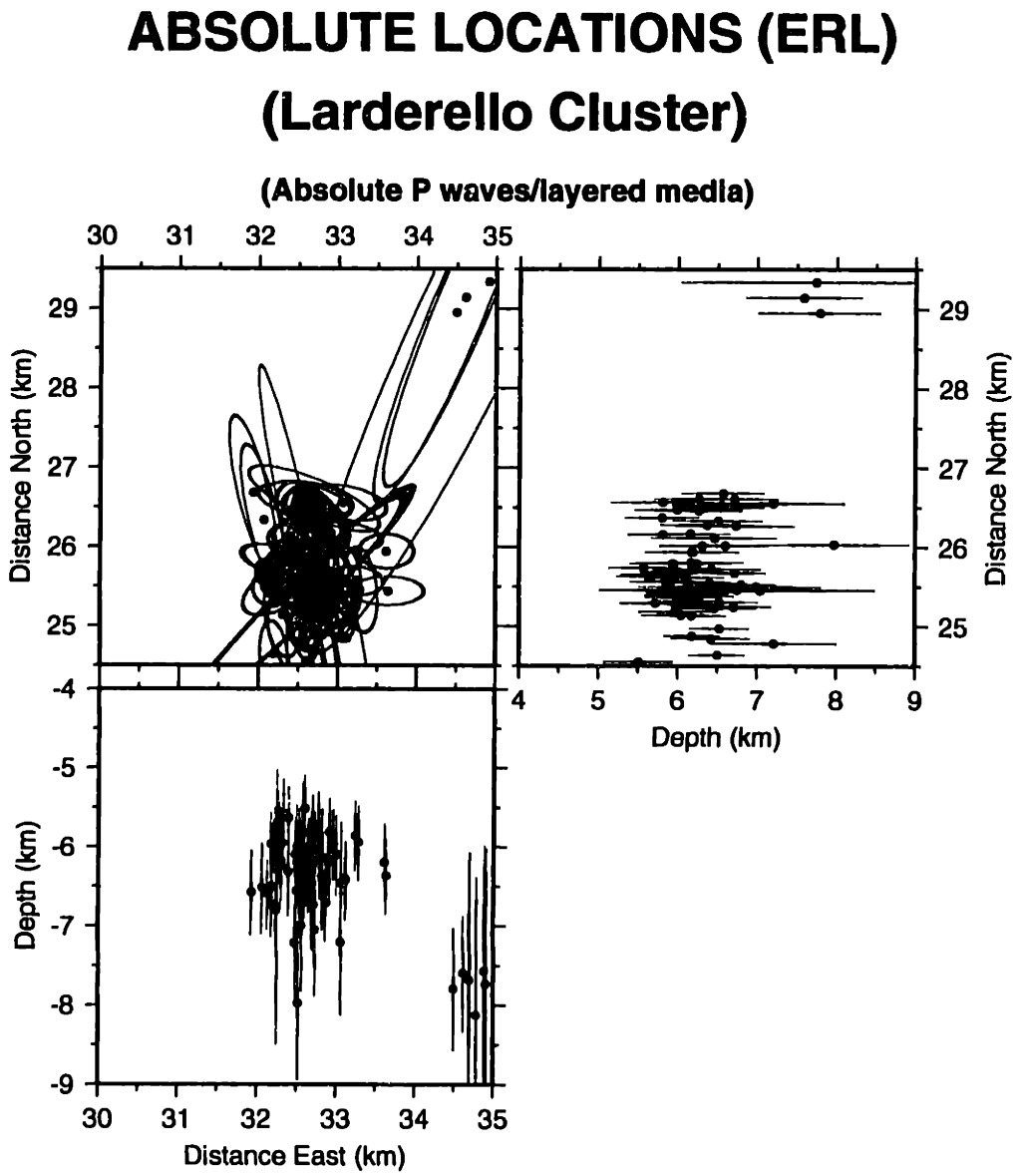

Figure 3-19: Hypocenter location estimates (absolute type) and their 90 percent confidence regions for events of the Larderello 1993 microearthquake swarm. These estimates were produced using P wave arrivals and station dependent layered velocity models.

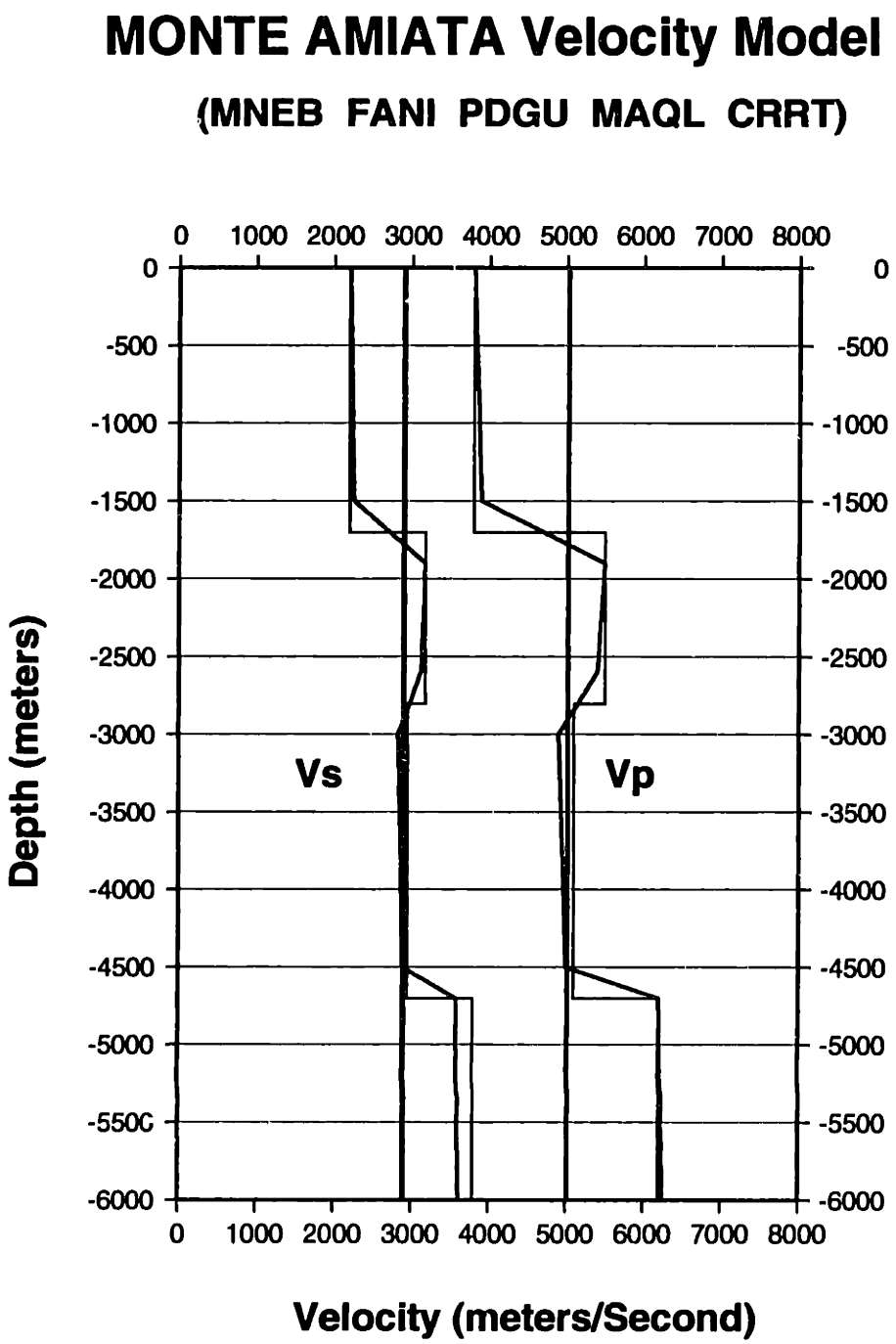

Figure 3-20: Seismic velocity models used for stations MNEB, FANI, PDGU, MAQL and CRRT of the Monte Amiata Seismic Network. These models were derived from Figure 2-18

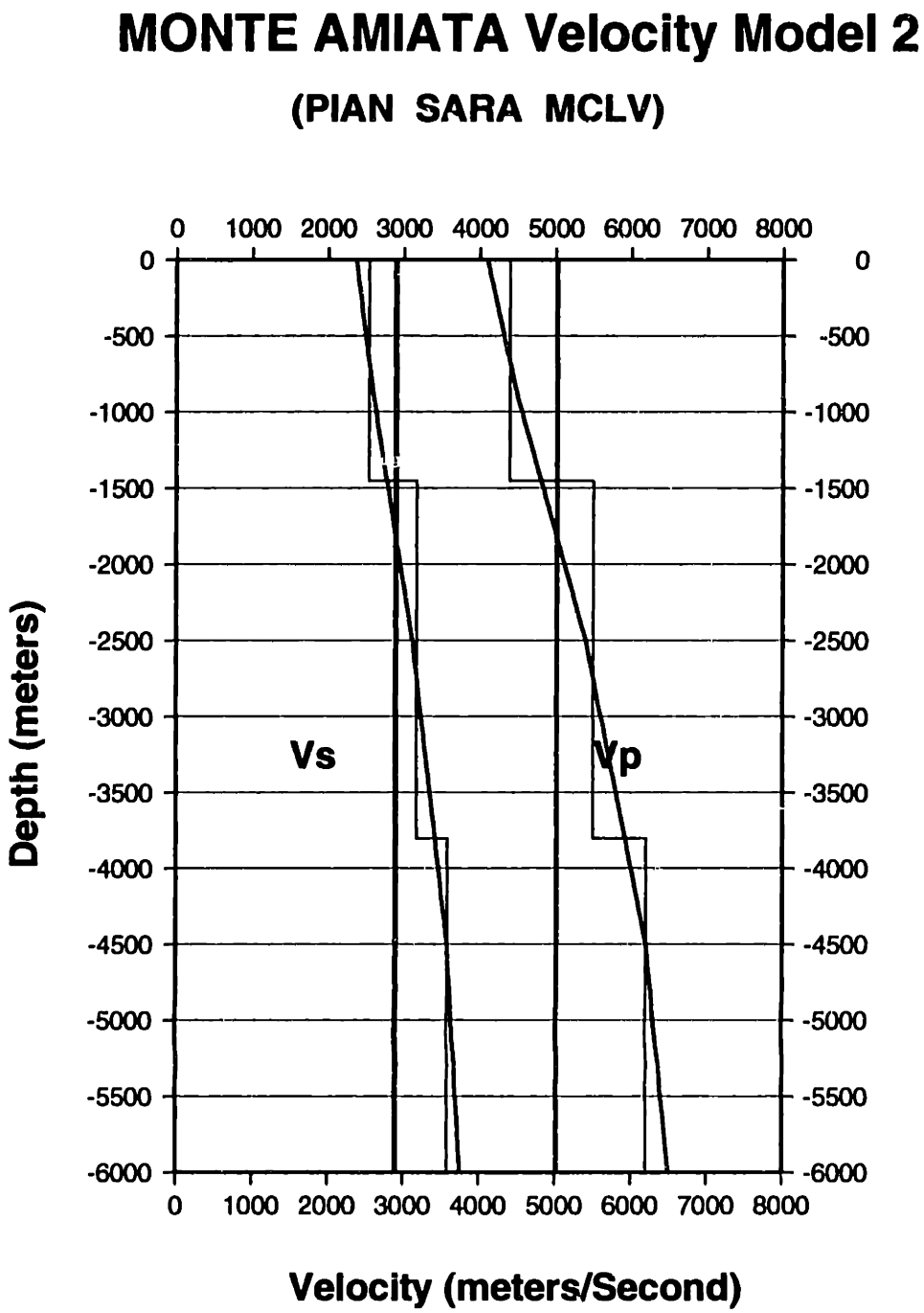

Figure 3-21: Seismic velocity models used for stations PIAN, SARA, and MCLV of the Monte Amiata Seismic Network. These models were derived from Figure 2-18

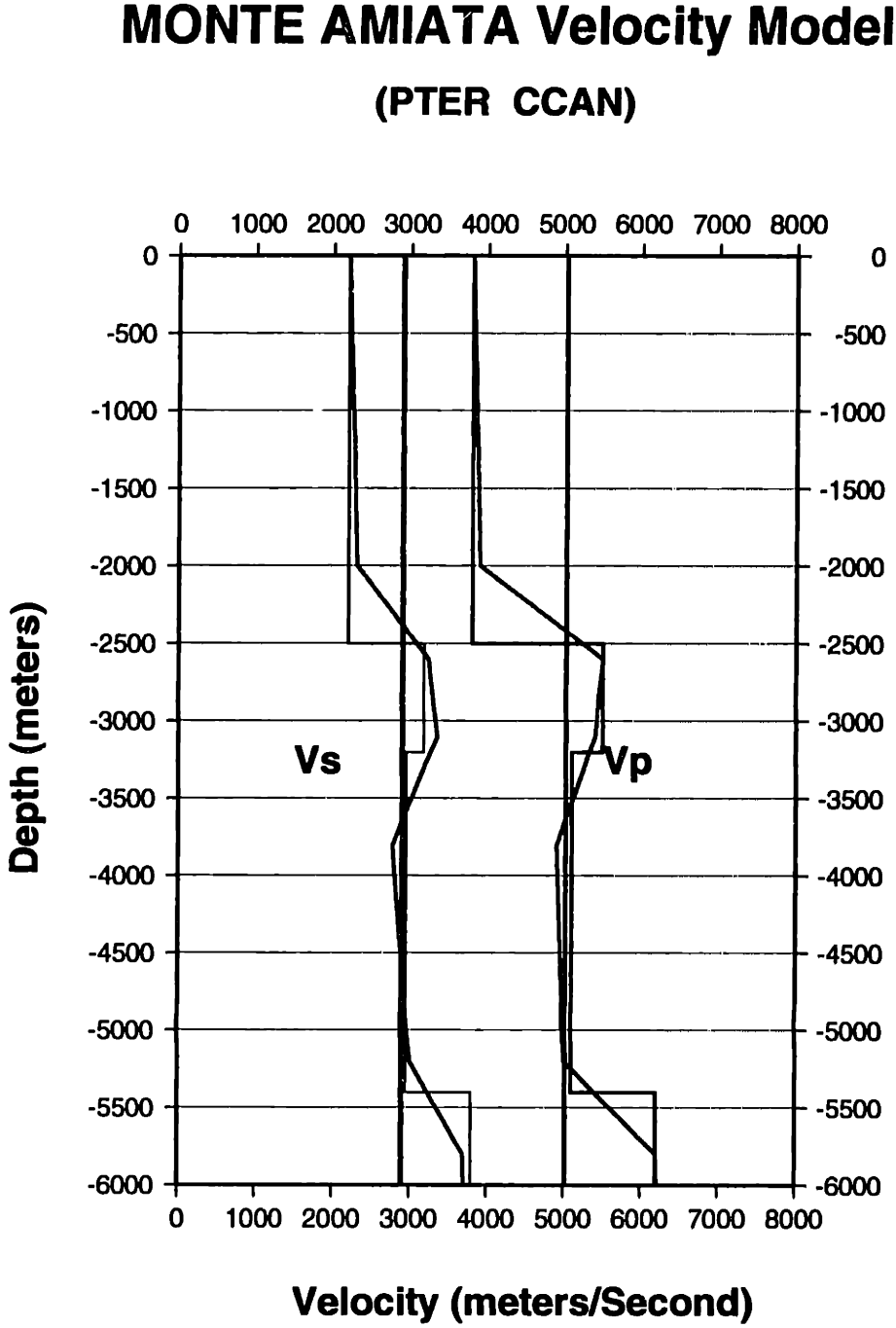

Figure 3-22: Seismic velocity models used for stations PTER and CCAN of the Monte Amiata Seismic Network. These models were derived from Figure 2-18

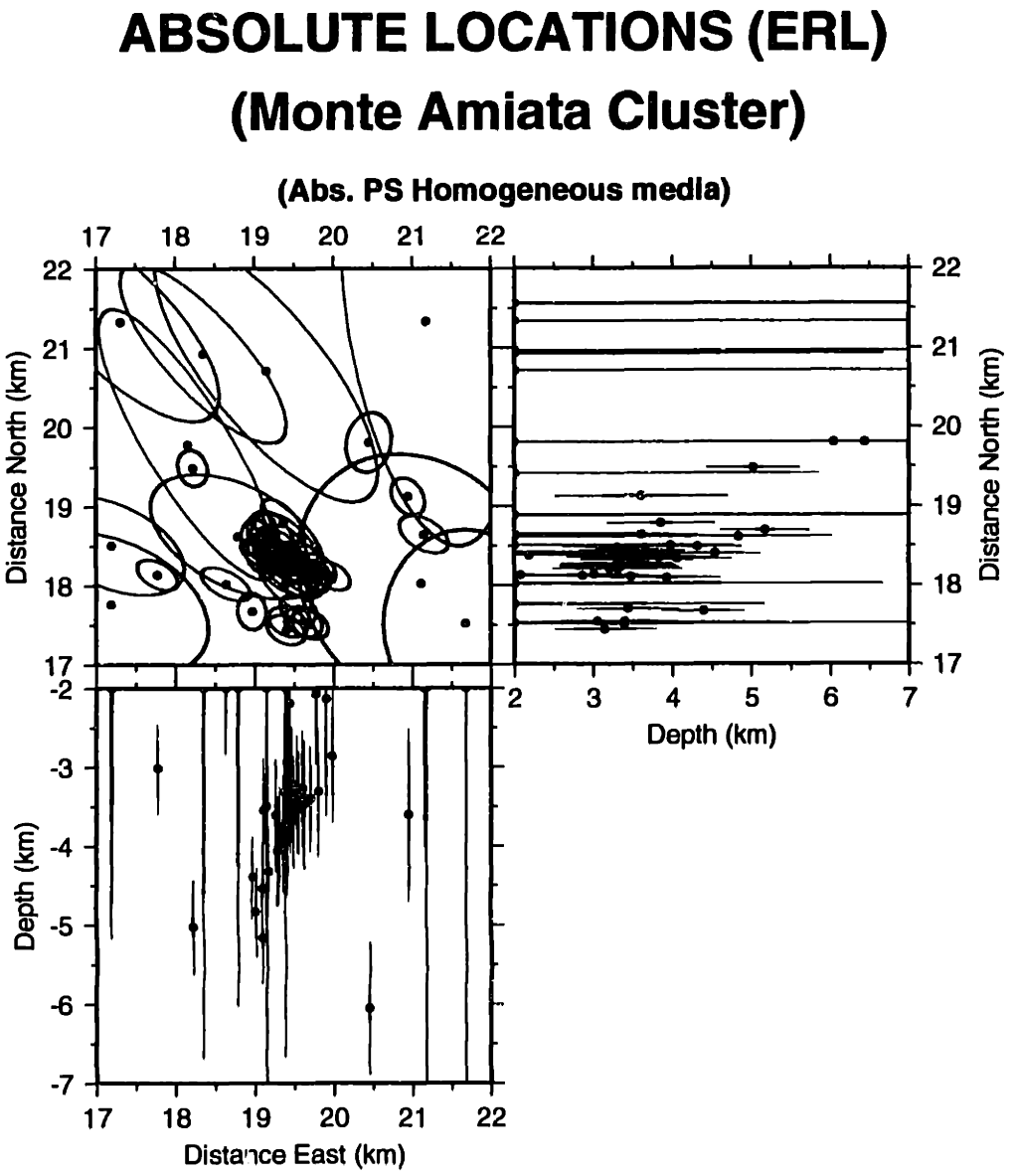

Figure 3-23: Hypocenter location estimates (absolute type) and their 90 percent confidence regions for events of the Monte Amiata microearthquake swarm. These estimates were produced using P and S phase arrivals and a homogeneous velocity model for all stations.

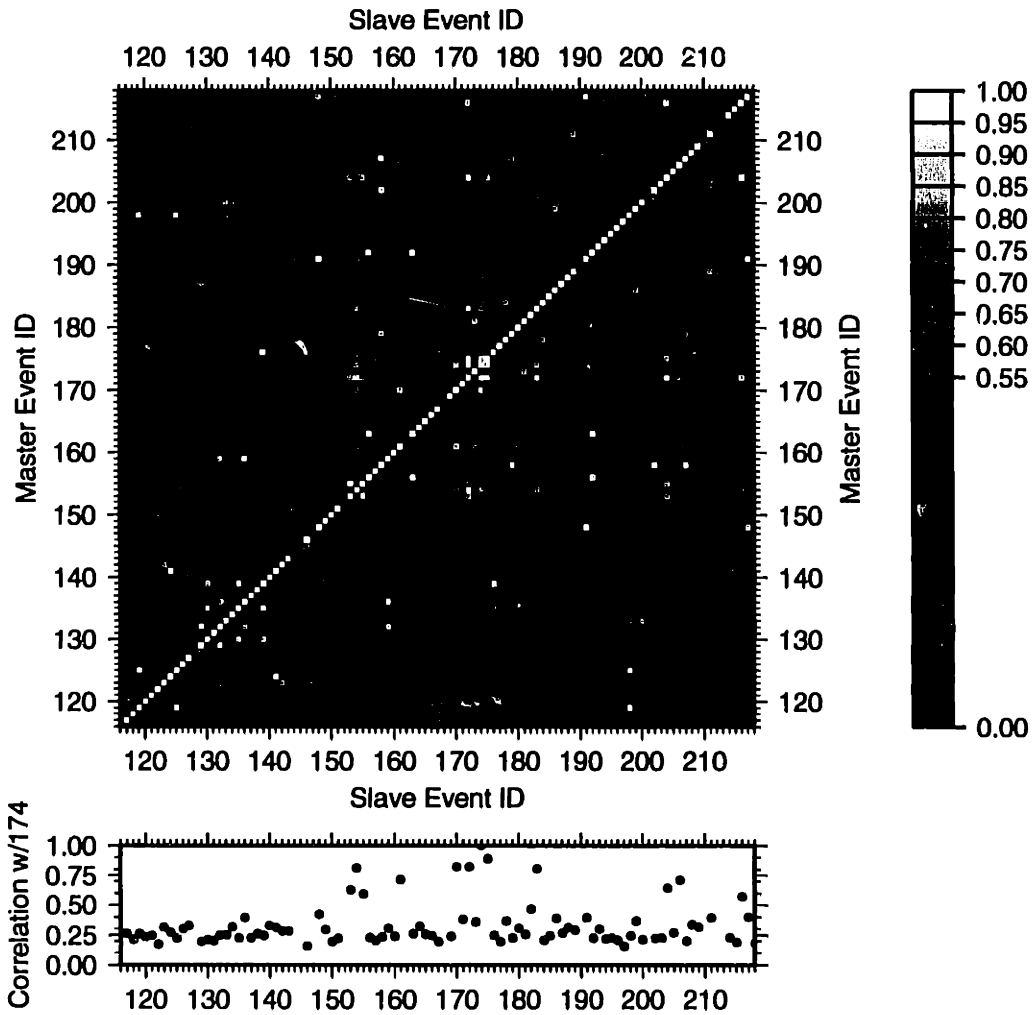

Figure 3-24: Cross (X) correlation matrix (normalized) for a window containing both P and S phase arrivals for events in the Larderello 1993 microearthquake swarm as recorded at station SCAP. Variation off of 1.0 along the diagonal indicates an event that was not recorded at this station.

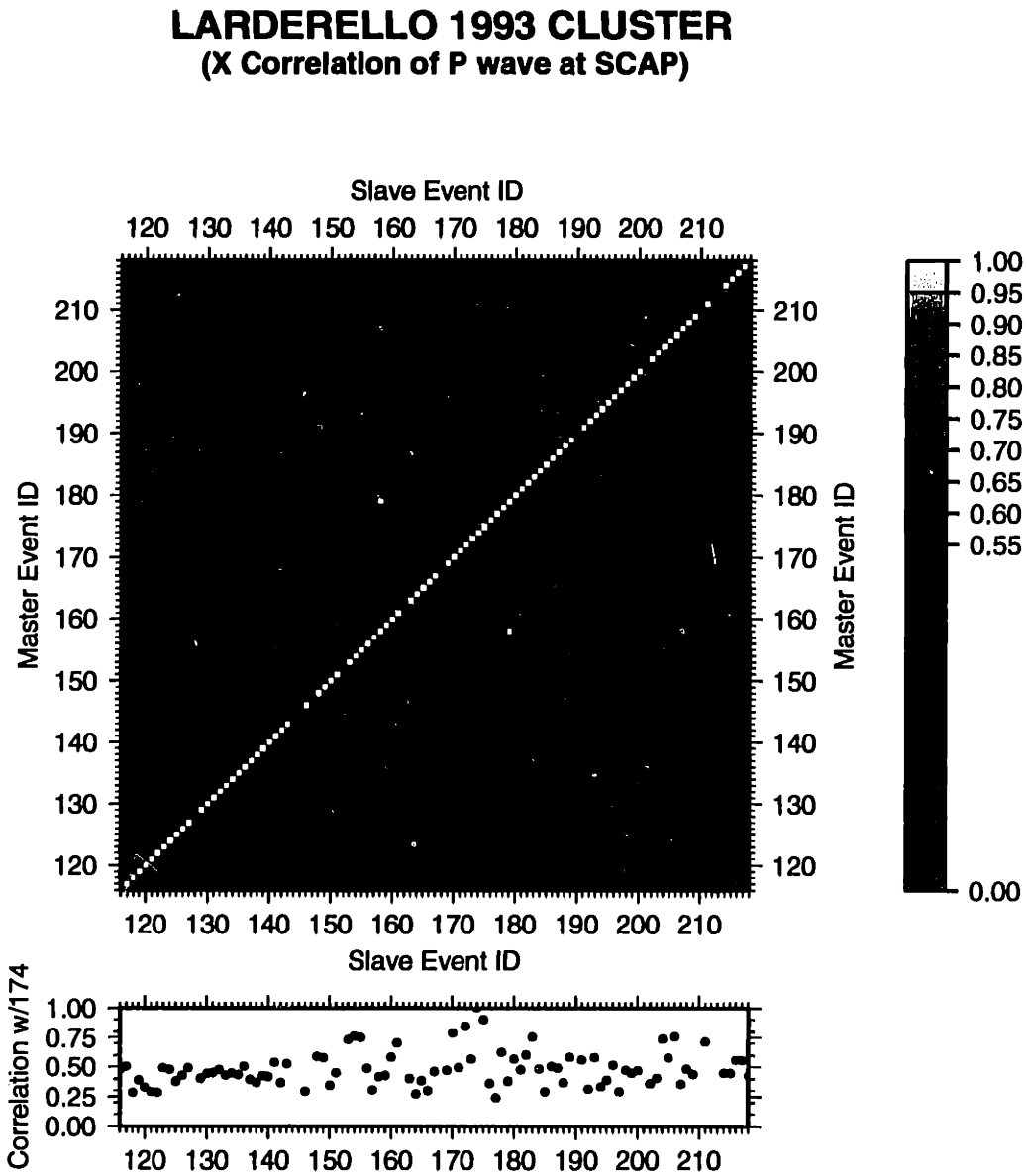

Figure 3-25: Cross (X) correlation matrix (normalized) for a window containing P phase arrivals for events in the Larderello 1993 microearthquake swarm as recorded at station SCAP. Events are ordered temporally left to right. Variation off of 1.0 along the diagonal indicates an event that was not recorded at this station.

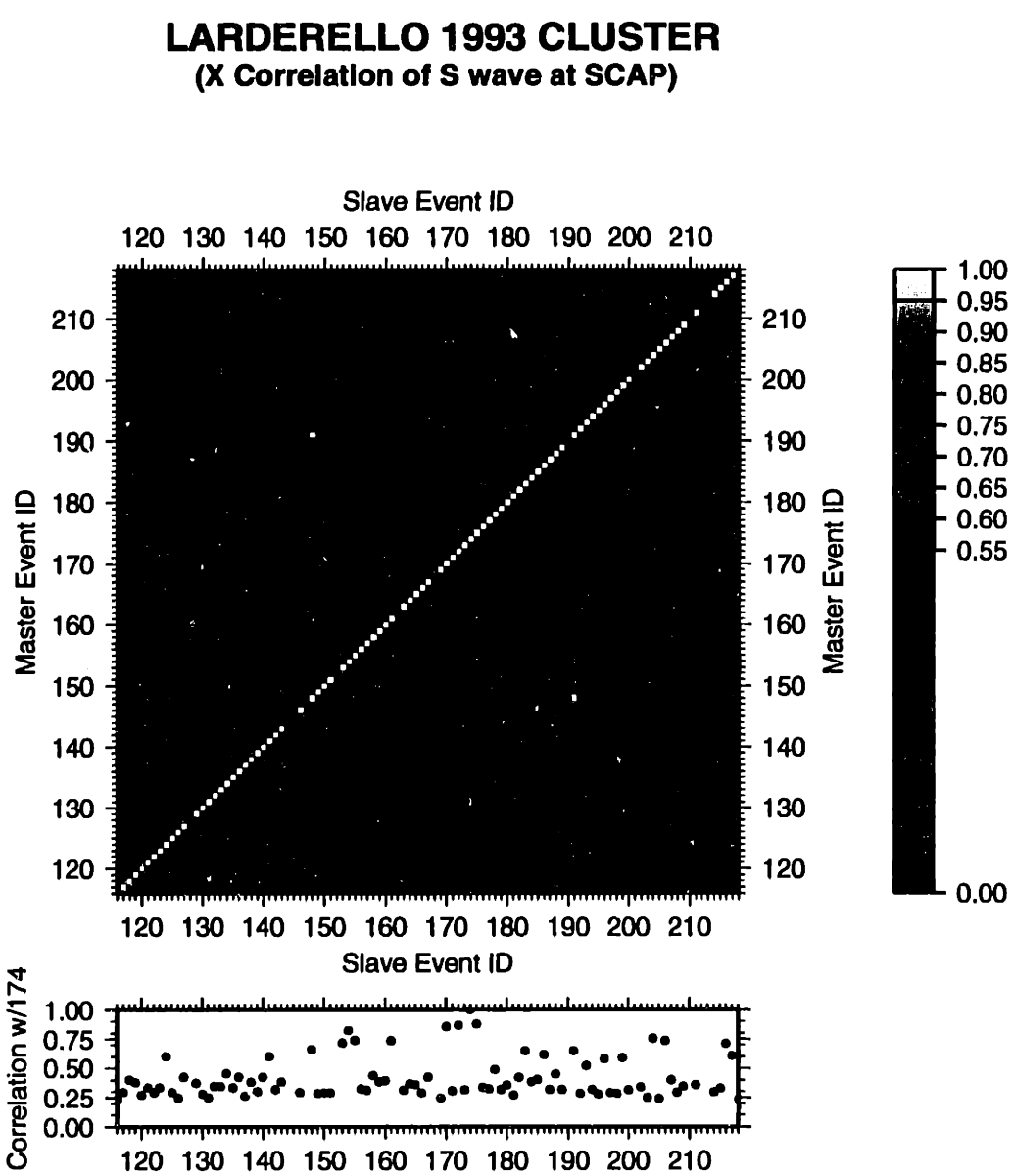

Figure 3-26: Cross (X) correlation matrix (normalized) for a window containing S phase arrivals for events in the Larderello 1993 microearthquake swarm as recorded at station SCAP. Events are ordered temporally left to right. Variation off of 1.0 along the diagonal indicates an event that was not recorded at this station.

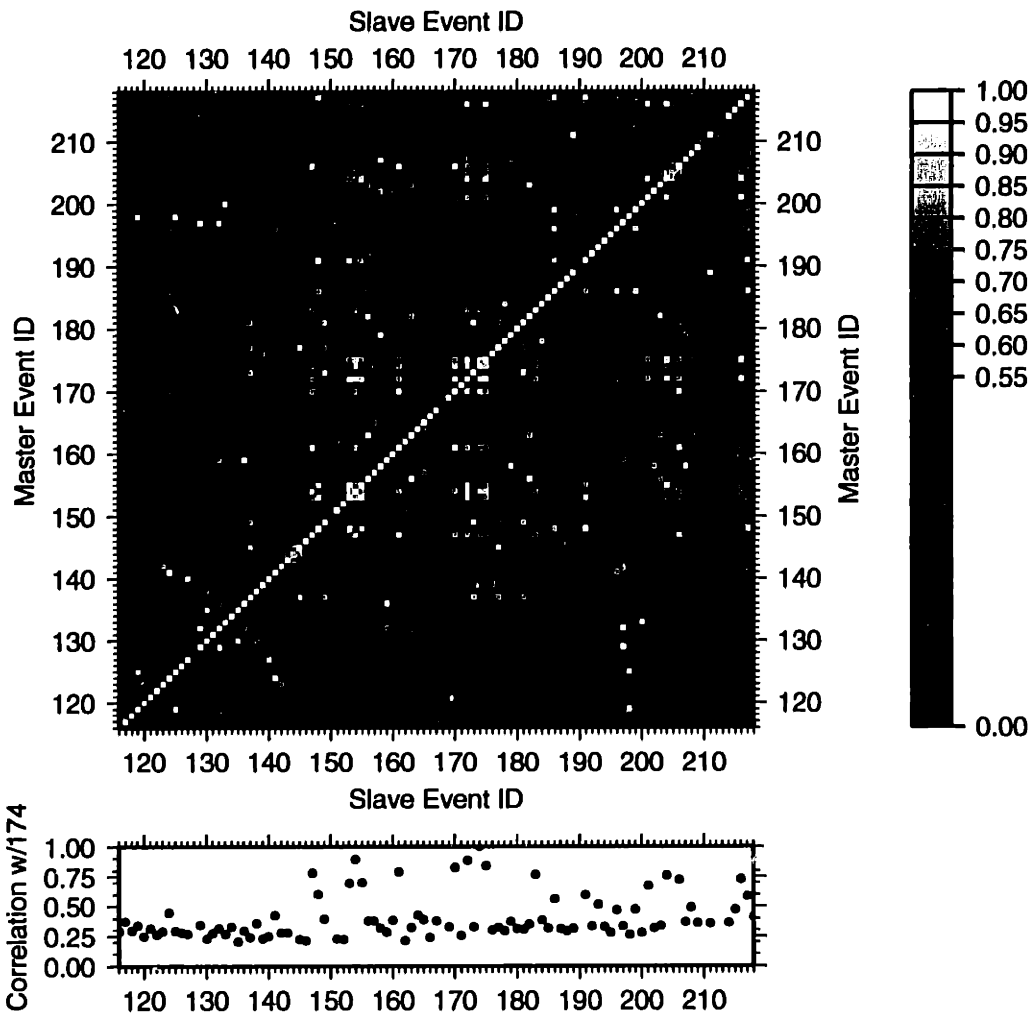

Figure 3-27: Cross (X) correlation matrix (normalized) for a window containing both P and S phase arrivals for events in the Larderello 1993 microearthquake swarm as recorded at station VALE. Events are ordered temporally left to right. Variation off of 1.0 along the diagonal indicates an event that was not recorded at this station.

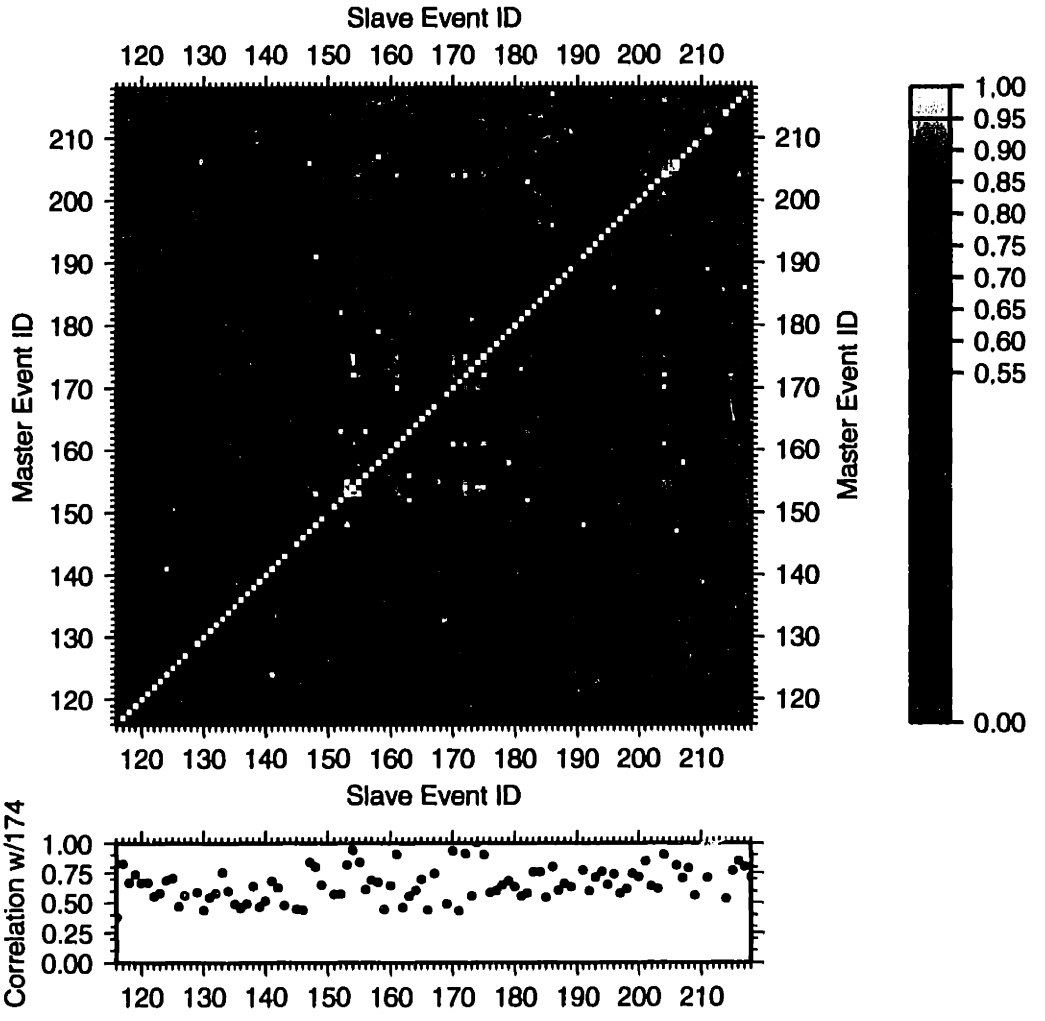

Figure 3-28: Cross (X) correlation matrix (normalized) for a window containing P phase arrivals for events in the Larderello 1993 microearthquake swarm as recorded at station VALE. Events are ordered temporally left to right. Variation off of 1.0 along the diagonal indicates an event that was not recorded at this station.

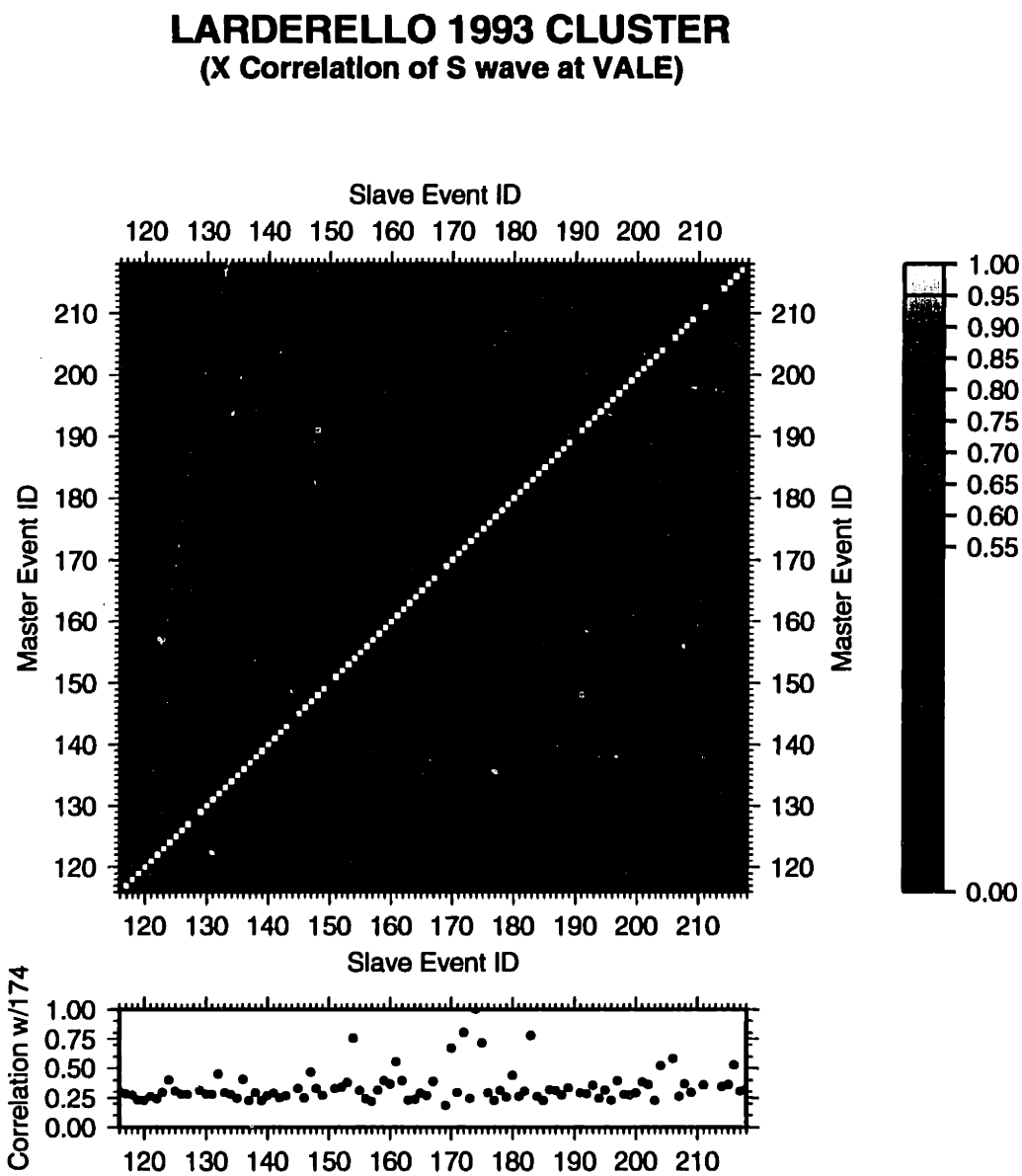

Figure 3-29: Cross (X) correlation matrix (normalized) for a window containing S phase arrivals for events in the Larderello 1993 microearthquake swarm as recorded at station VALE. Events are ordered temporally left to right. Variation off of 1.0 along the diagonal indicates an event that was not recorded at this station.

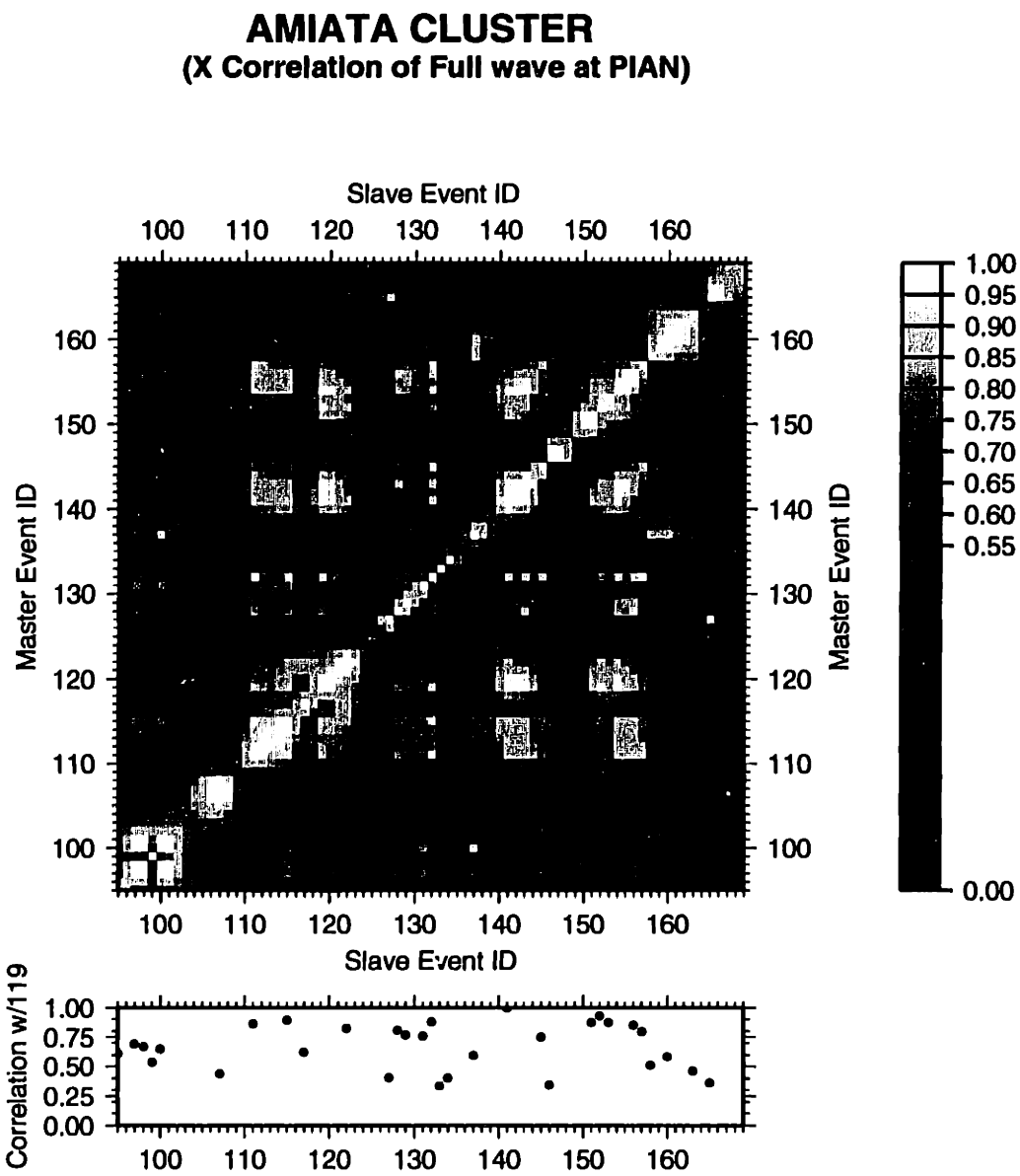

Figure 3-30: Cross (X) correlation matrix (normalized) for a window containing both P and S phase arrivals for events in the Monte Amiata microearthquake swarm as recorded at station PIAN. Events are ordered temporally left to right. Variation off of 1.0 along the diagonal indicates an event that was not recorded at this station.

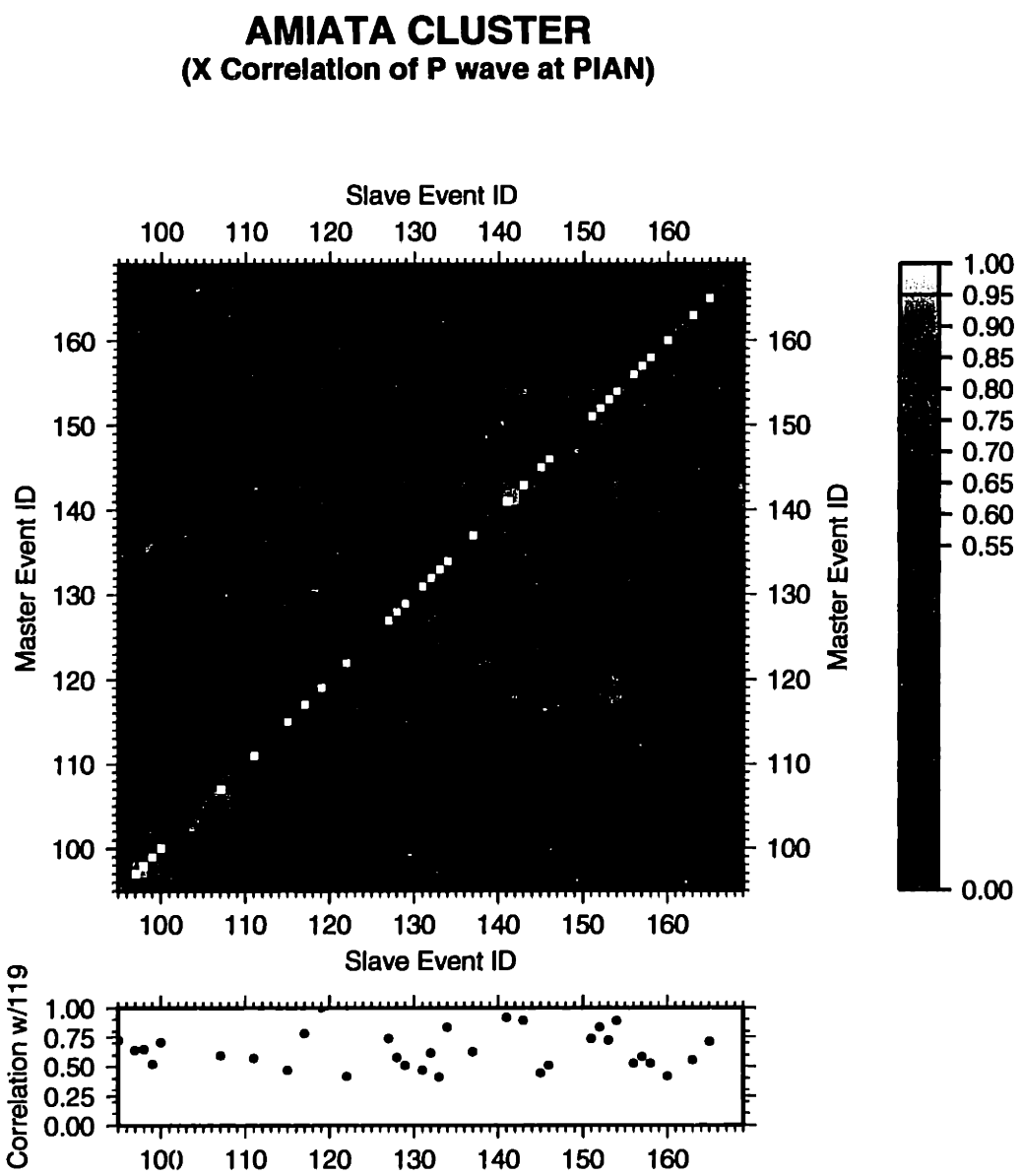

Figure 3-31: Cross (X) correlation matrix (normalized) for a window containing P phase arrivals for events in the Monte Amiata microearthquake swarm as recorded at station PIAN. Events are ordered temporally left to right. Variation off of 1.0 along the diagonal indicates an event that was not recorded at this station.

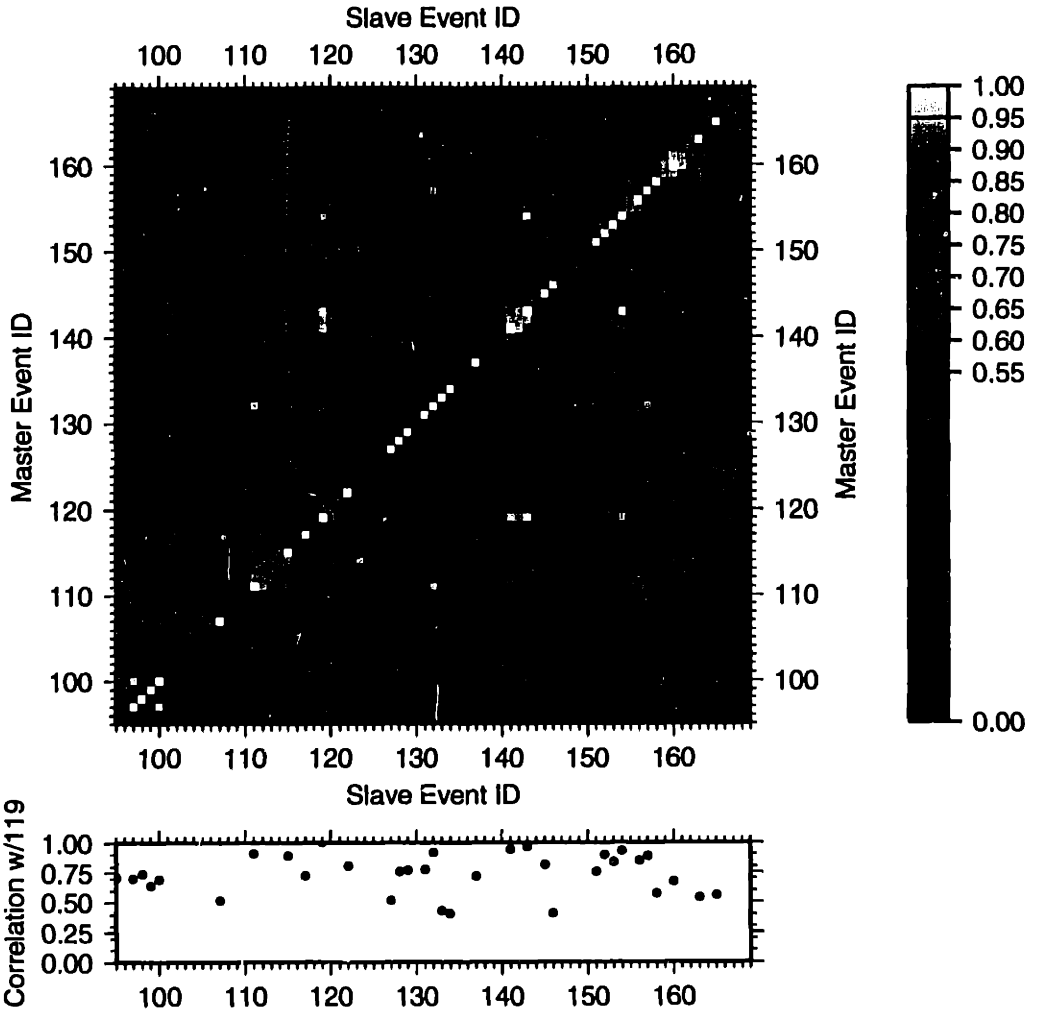

Figure 3-32: Cross (X) correlation matrix (normalized) for a window containing S phase arrivals for events in the Monte Amiata microearthquake swarm as recorded at station PIAN. Events are ordered temporally left to right. Variation off of 1.0 along the diagonal indicates an event that was not recorded at this station.

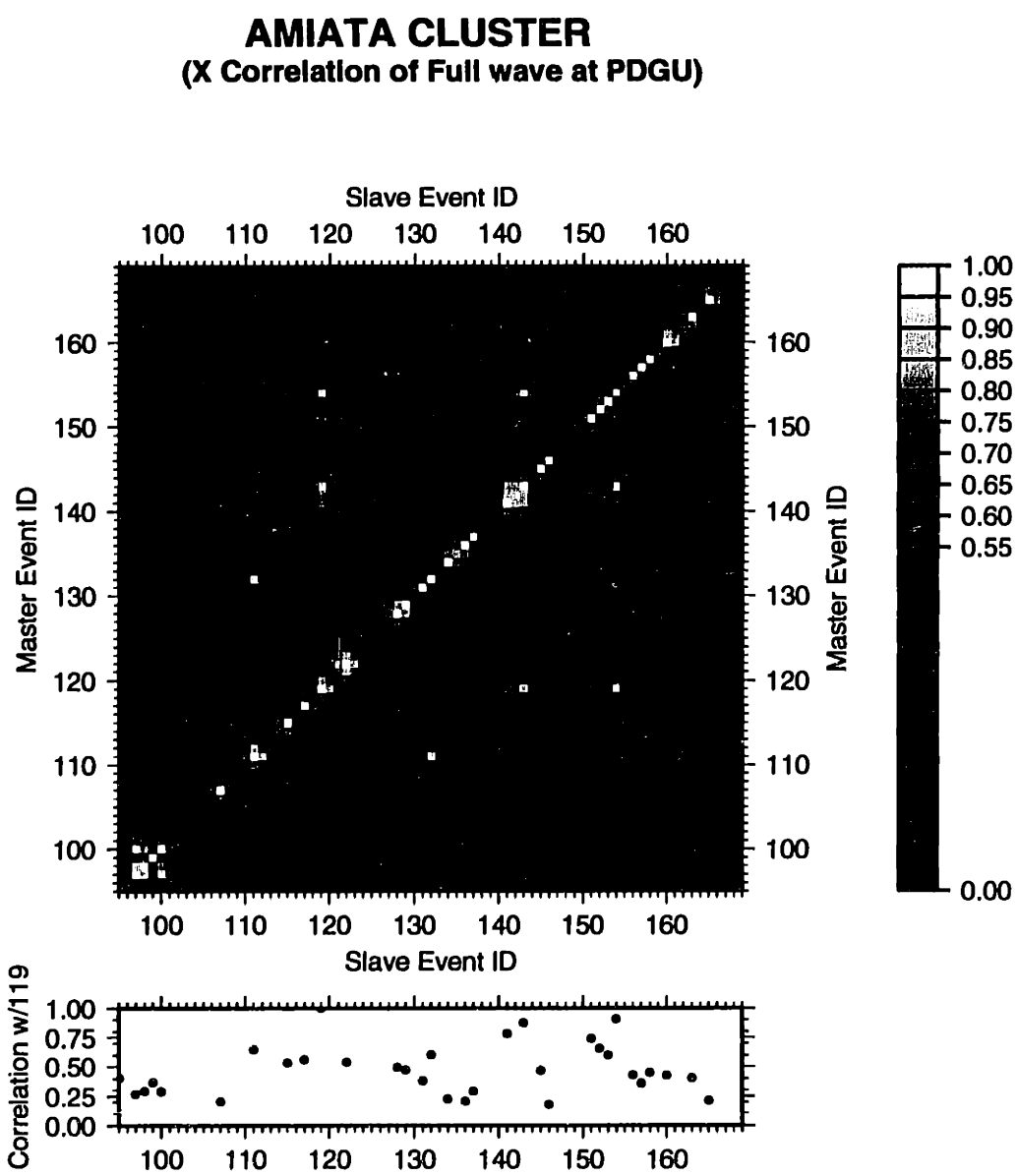

Figure 3-33: Cross (X) correlation matrix (normalized) for a window containing both P and S phase arrivals for events in the Monte Amiata microearthquake swarm as recorded at station PDGU. Events are ordered temporally left to right. Variation off of 1.0 along the diagonal indicates an event that was not recorded at this station.

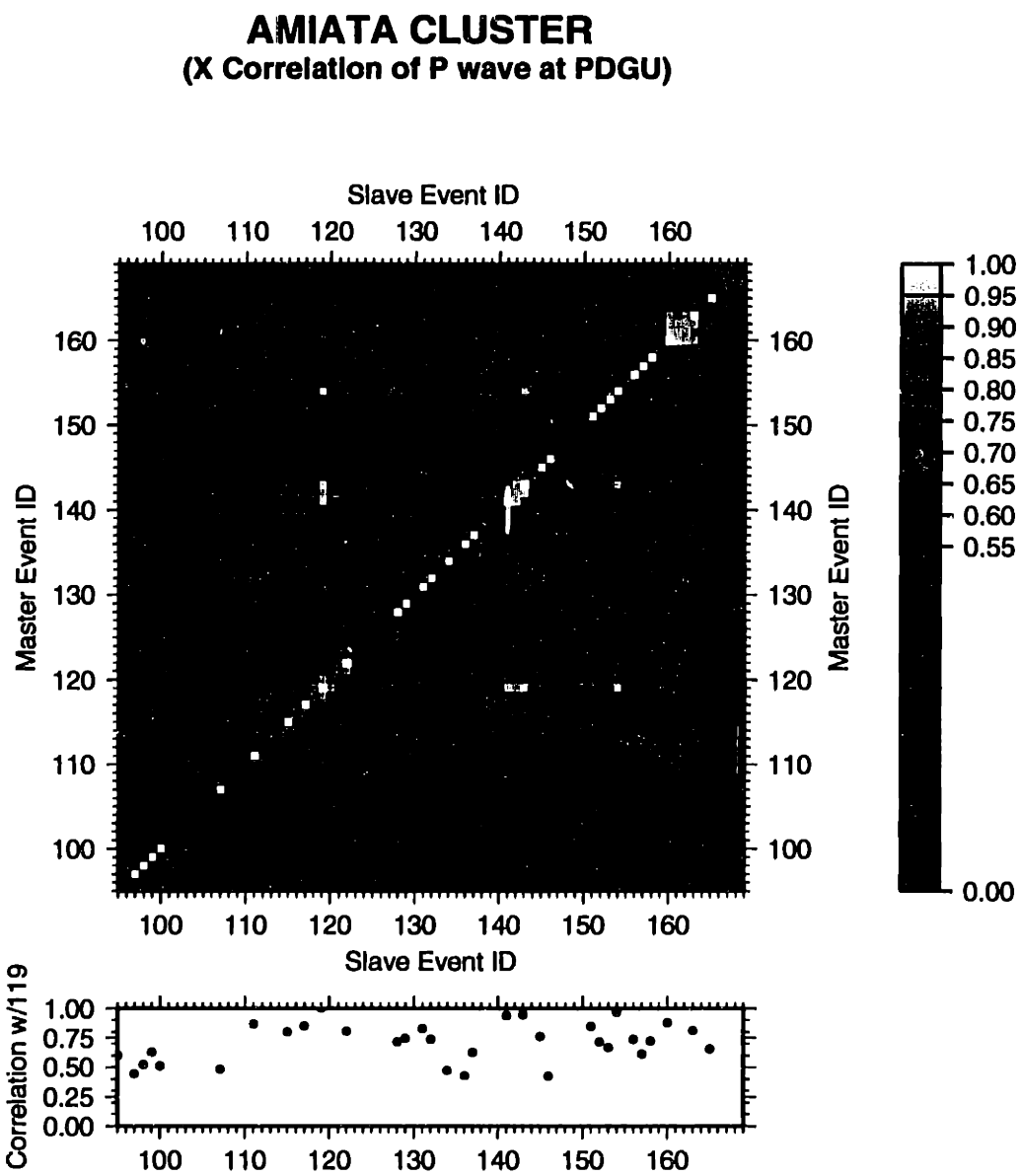

Figure 3-34: Cross (X) correlation matrix (normalized) for a window containing P phase arrivals for events in the Monte Amiata microearthquake swarm as recorded at station PDGU. Events are ordered temporally left to right. Variation off of 1.0 along the diagonal indicates an event that was not recorded at this station.

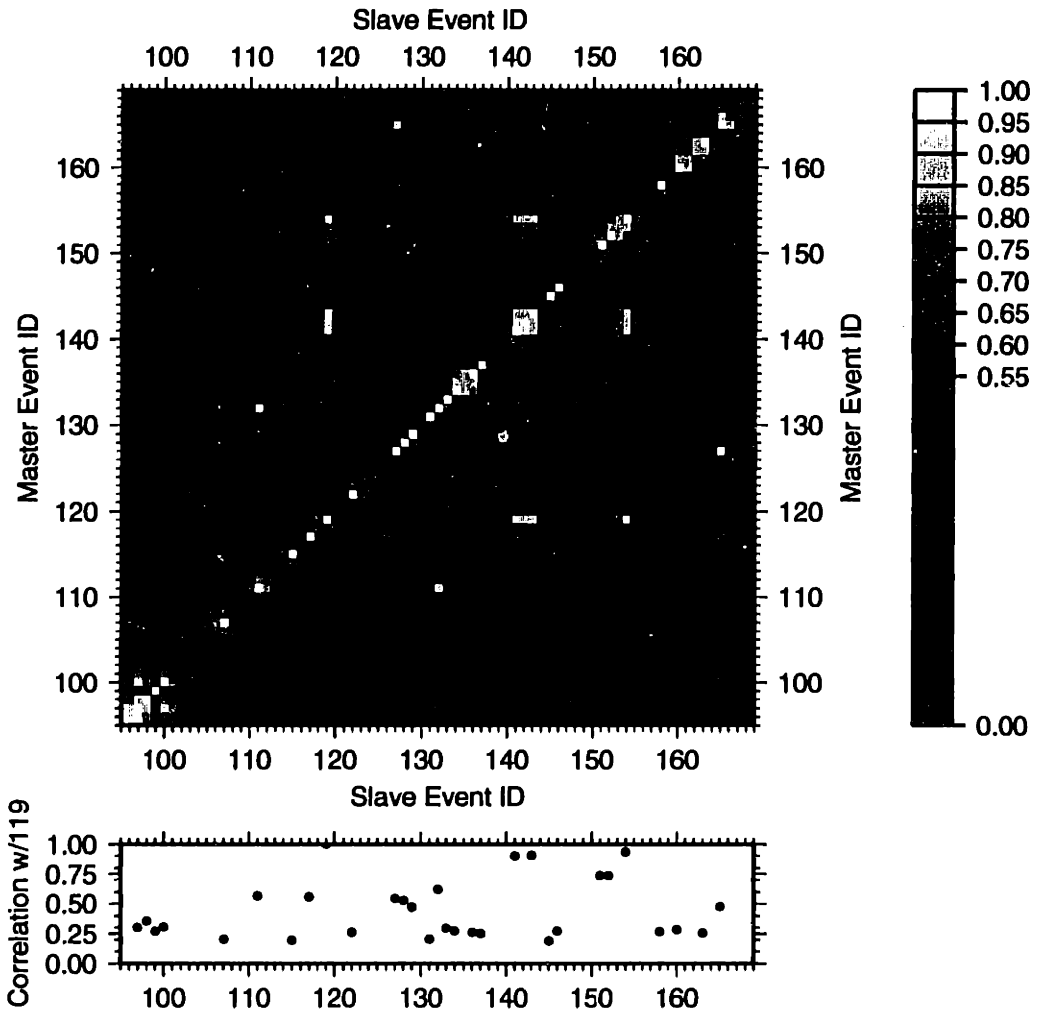

Figure 3-35: Cross (X) correlation matrix (normalized) for a window containing both P and S phase arrivals for events in the Monte Amiata microearthquake swarm as recorded at station MNEB. Events are ordered temporally left to right. Variation off of 1.0 along the diagonal indicates an event that was not recorded at this station.

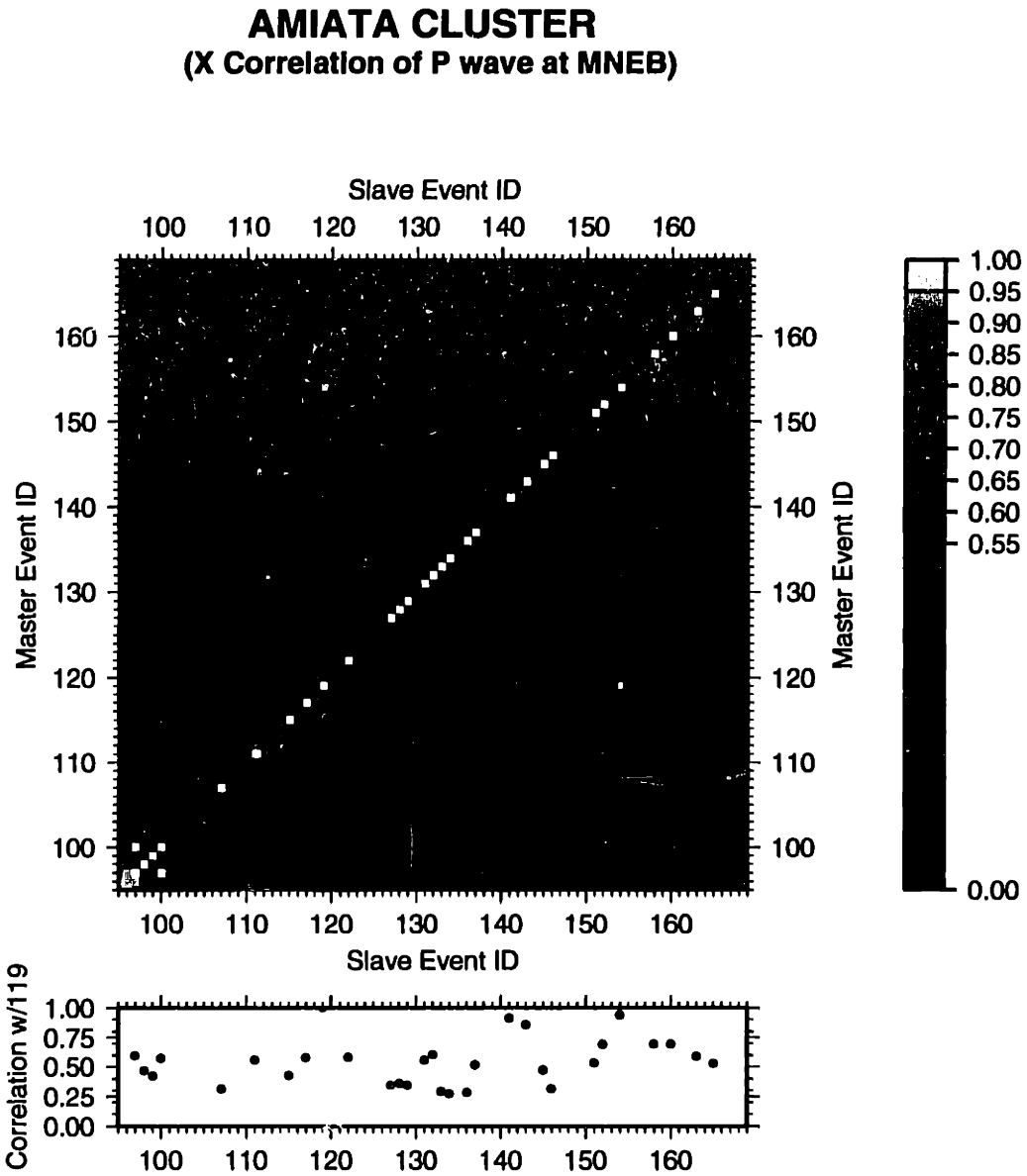

Figure 3-36: Cross (X) correlation matrix (normalized) for a window containing P phase arrivals for events in the Monte Amiata microearthquake swarm as recorded at station MNEB. Events are ordered temporally left to right. Variation off of 1.0 along the diagonal indicates an event that was not recorded at this station.

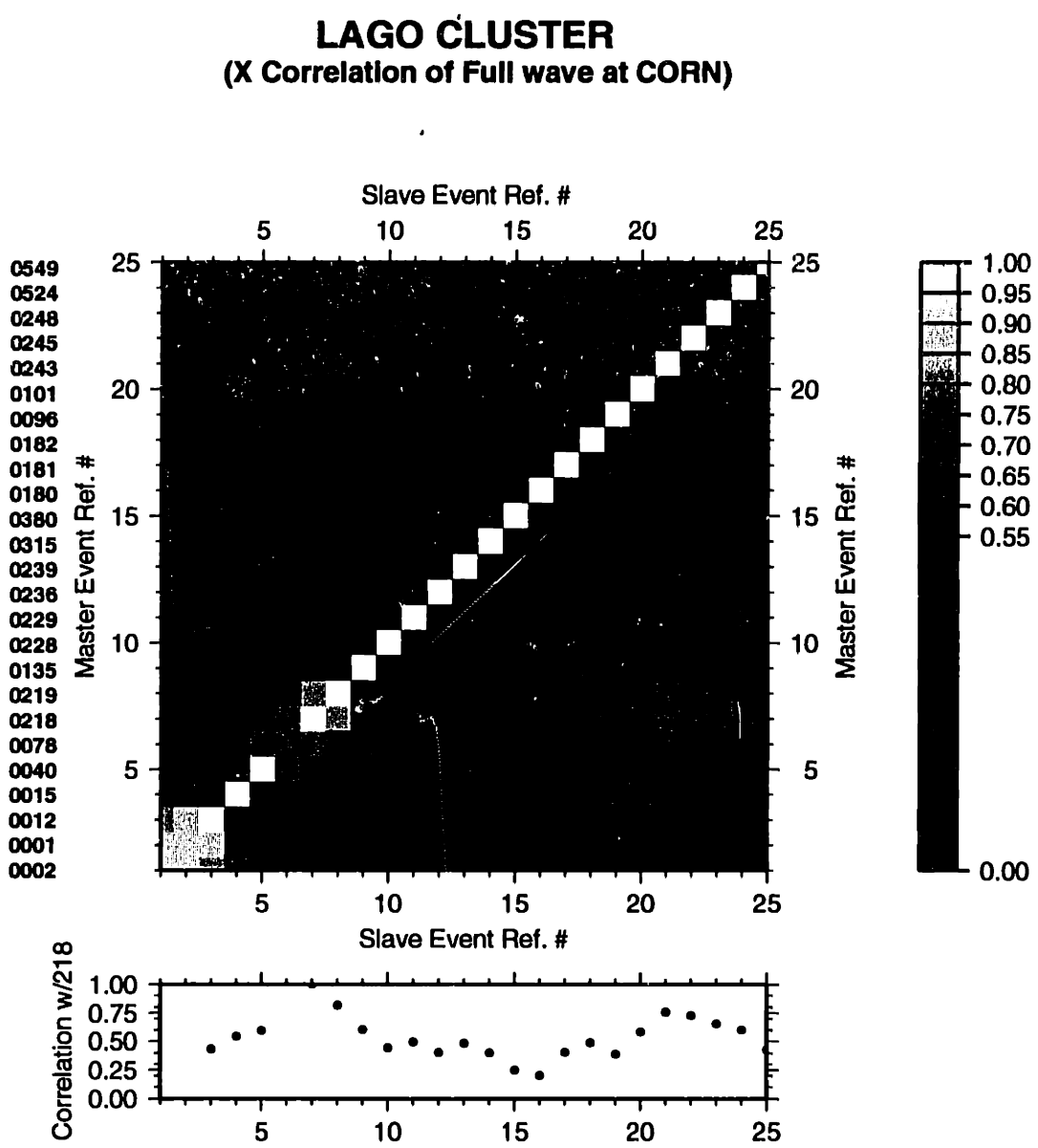

Figure 3-37: Cross (X) correlation matrix (normalized) for a window containing both P and S phase arrivals for events in the LAGO microearthquake cluster as recorded at station CORN. Variation off of 1.0 along the diagonal indicates an event that was not recorded at this station. Events are ordered temporally by ID number.

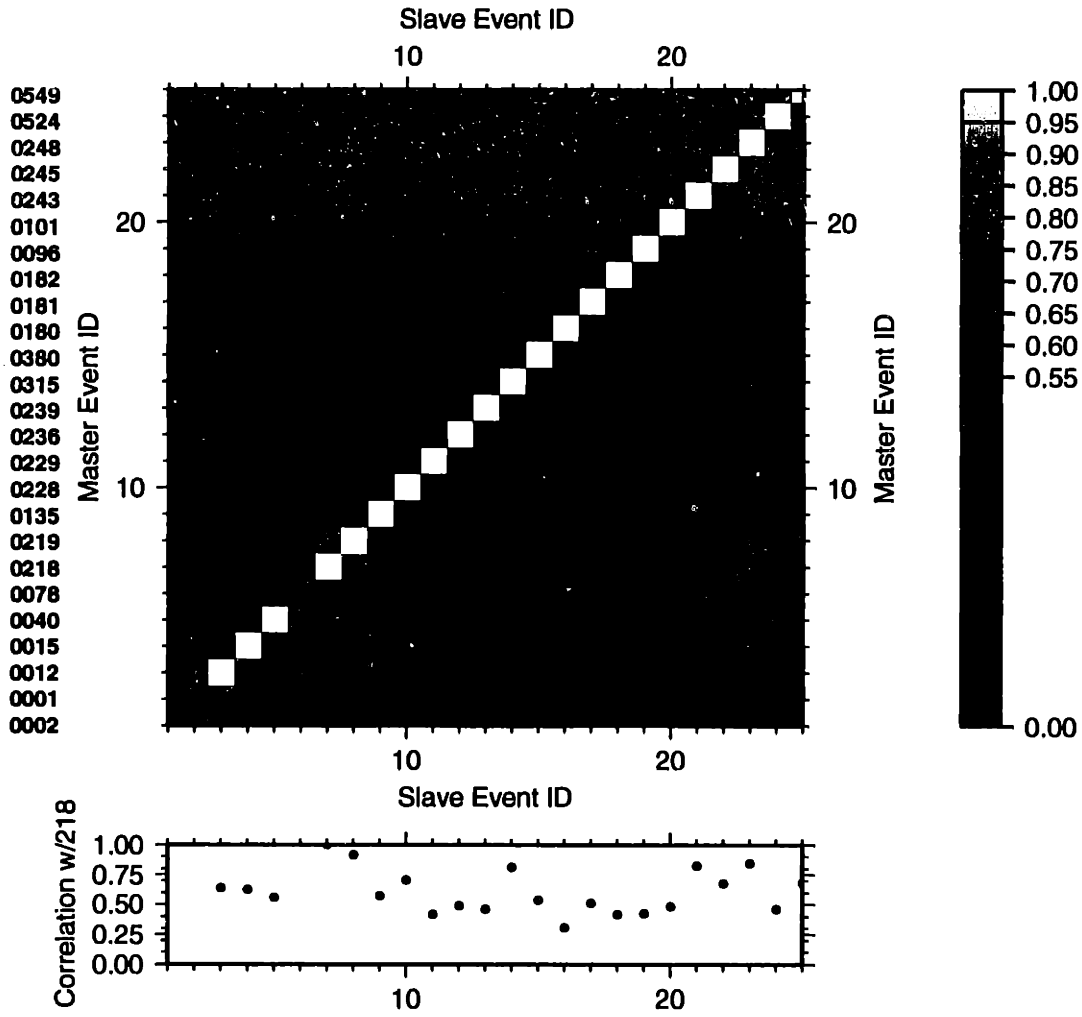

Figure 3-38: Cross (X) correlation matrix (normalized) for the window containing P phase arrivals for events in the LAGO microearthquake cluster as recorded at station CORN. Variation off of 1.0 along the diagonal indicates an event that was not recorded at this station.

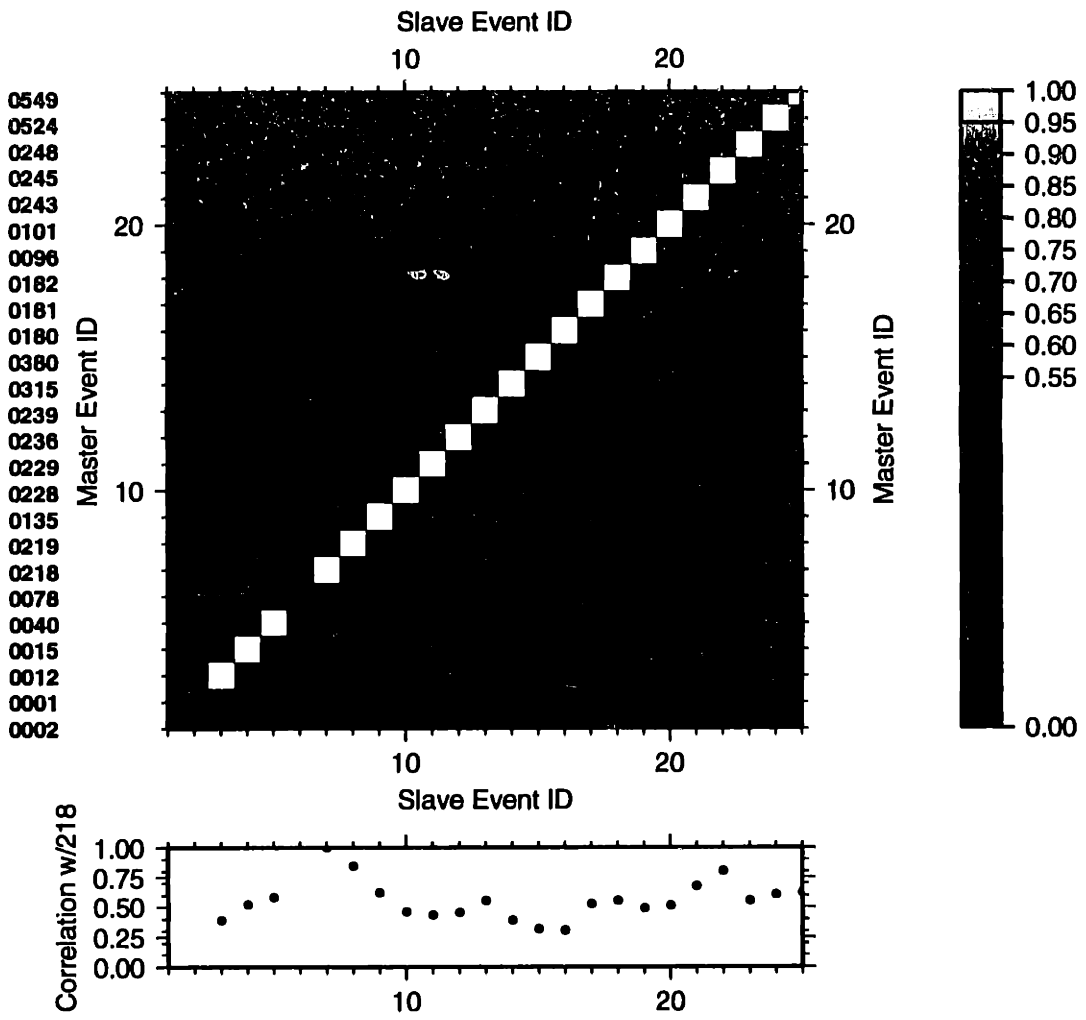

Figure 3-39: Cross (X) correlation matrix (normalized) for a window containing S phase arrivals for events in the LAGO microearthquake cluster as recorded at station CORN. Variation off of 1.0 along the diagonal indicates an event that was not recorded at this station.

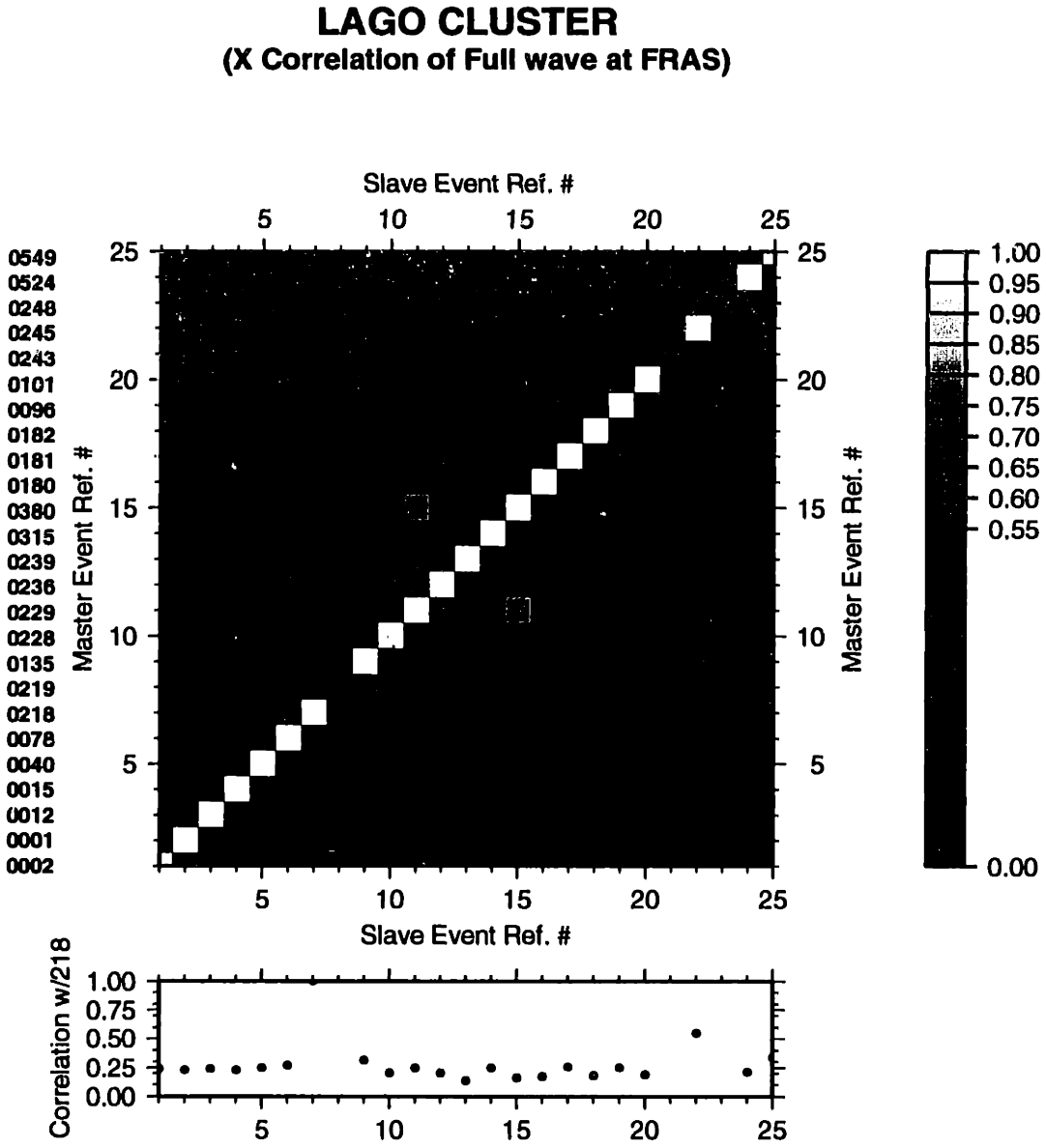

Figure 3-40: Cross (X) correlation matrix (normalized) for a window containing both P and S phase arrivals for events in the LAGO microearthquake cluster as recorded at station FRAS. Variation off of 1.0 along the diagonal indicates an event that was not recorded at this station.

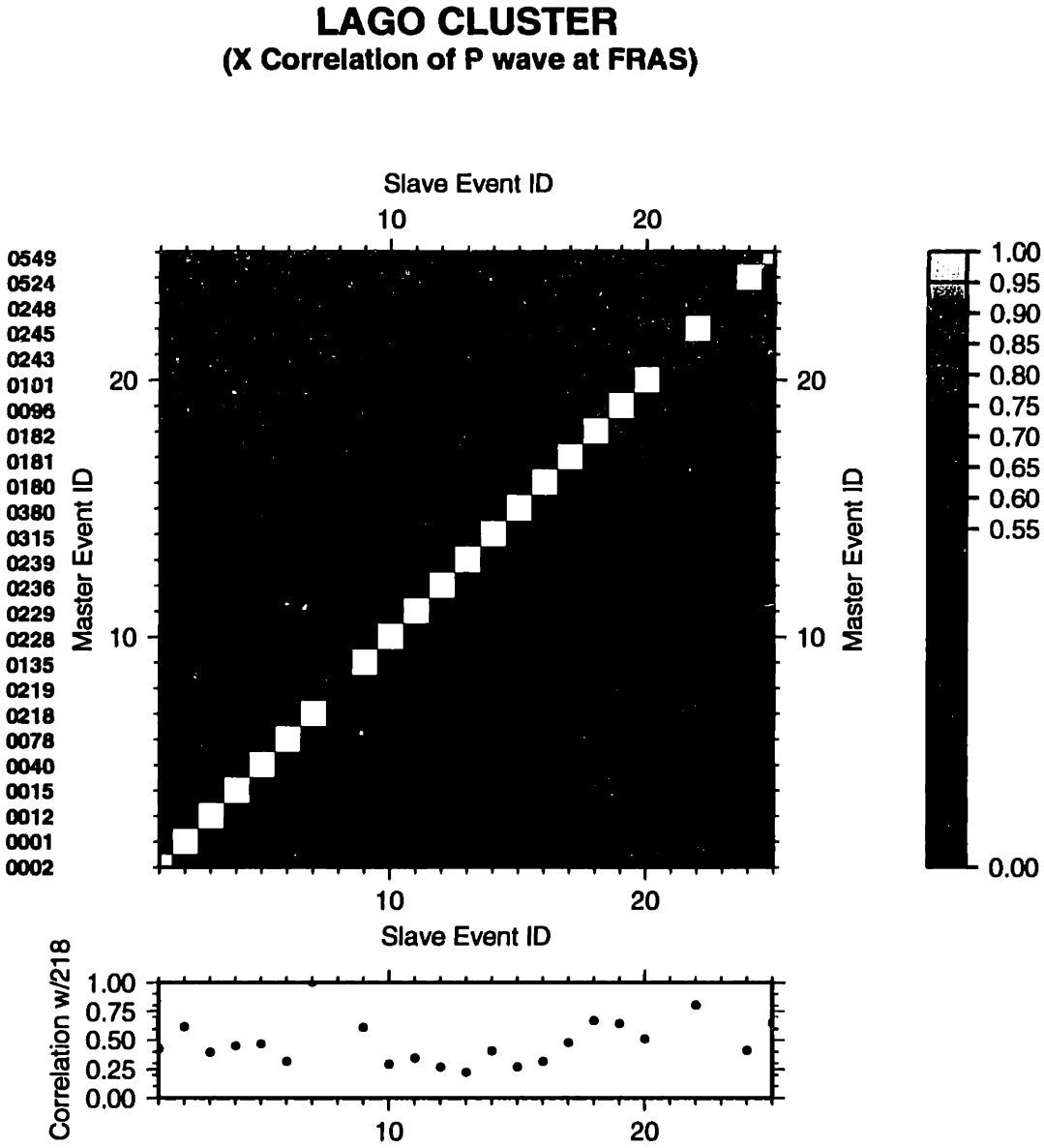

Figure 3-41: Cross (X) correlation matrix (normalized) for a window containing P phase arrivals for events in the LAGO microearthquake cluster as recorded at station FRAS. Variation off of 1.0 along the diagonal indicates an event that was not recorded at this station.

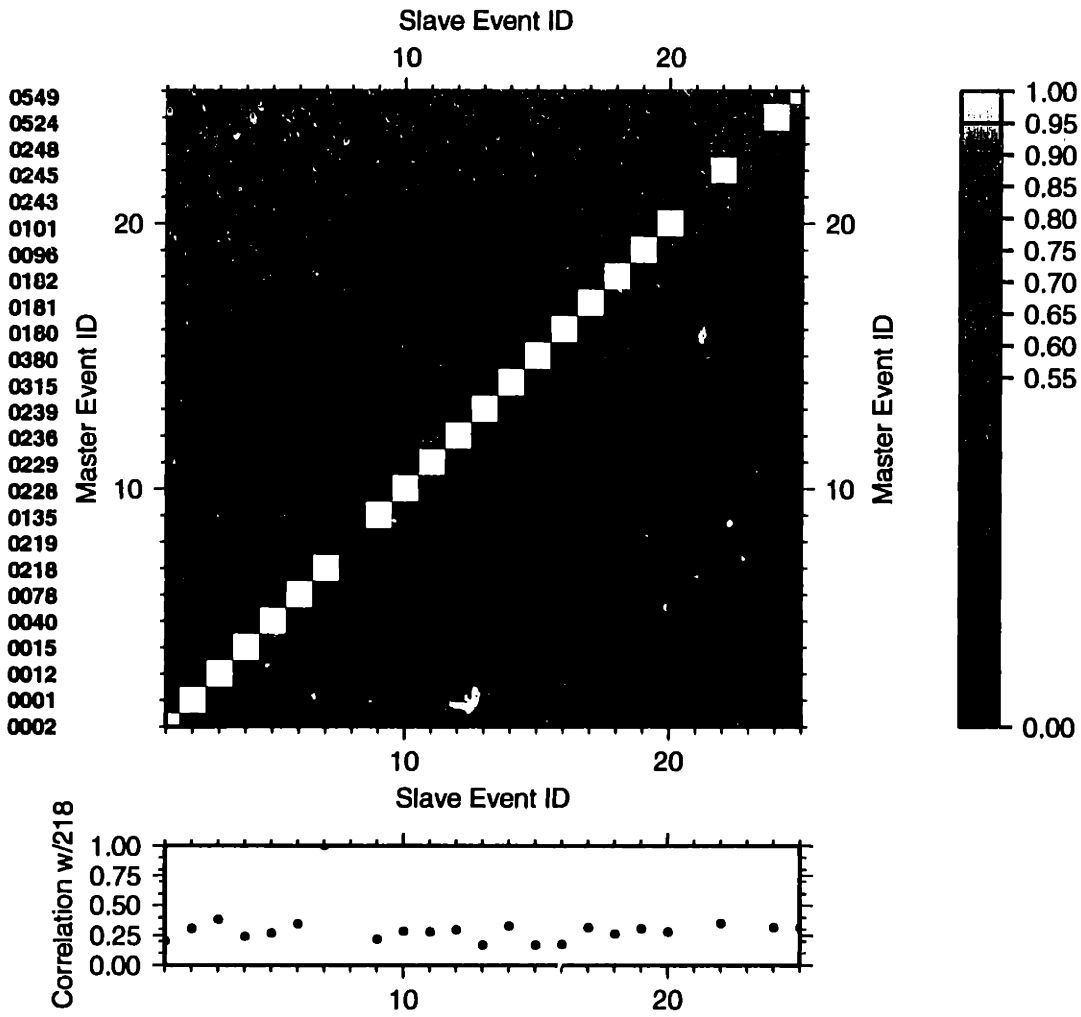

Figure 3-42: Cross (X) correlation matrix (normalized) for a window containing S phase arrivals for events in the LAGO microearthquake cluster as recorded at station FRAS. Variation off of 1.0 along the diagonal indicates an event that was not recorded at this station.

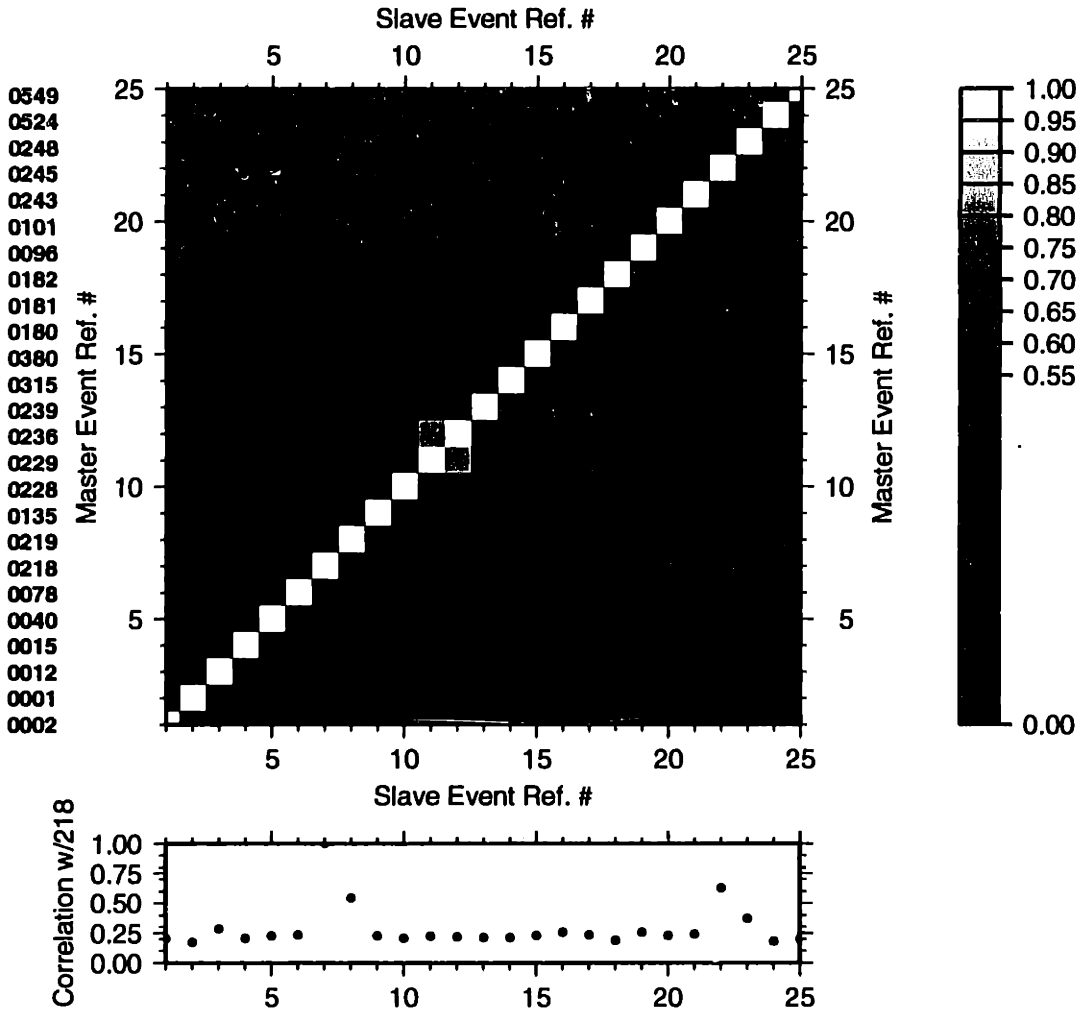

Figure 3-43: Cross (X) correlation matrix (normalized) for a window containing both P and S phase arrivals for events in the LAGO microearthquake cluster as recorded at station VALE. Variation off of 1.0 along the diagonal indicates an event that was not recorded at this station.

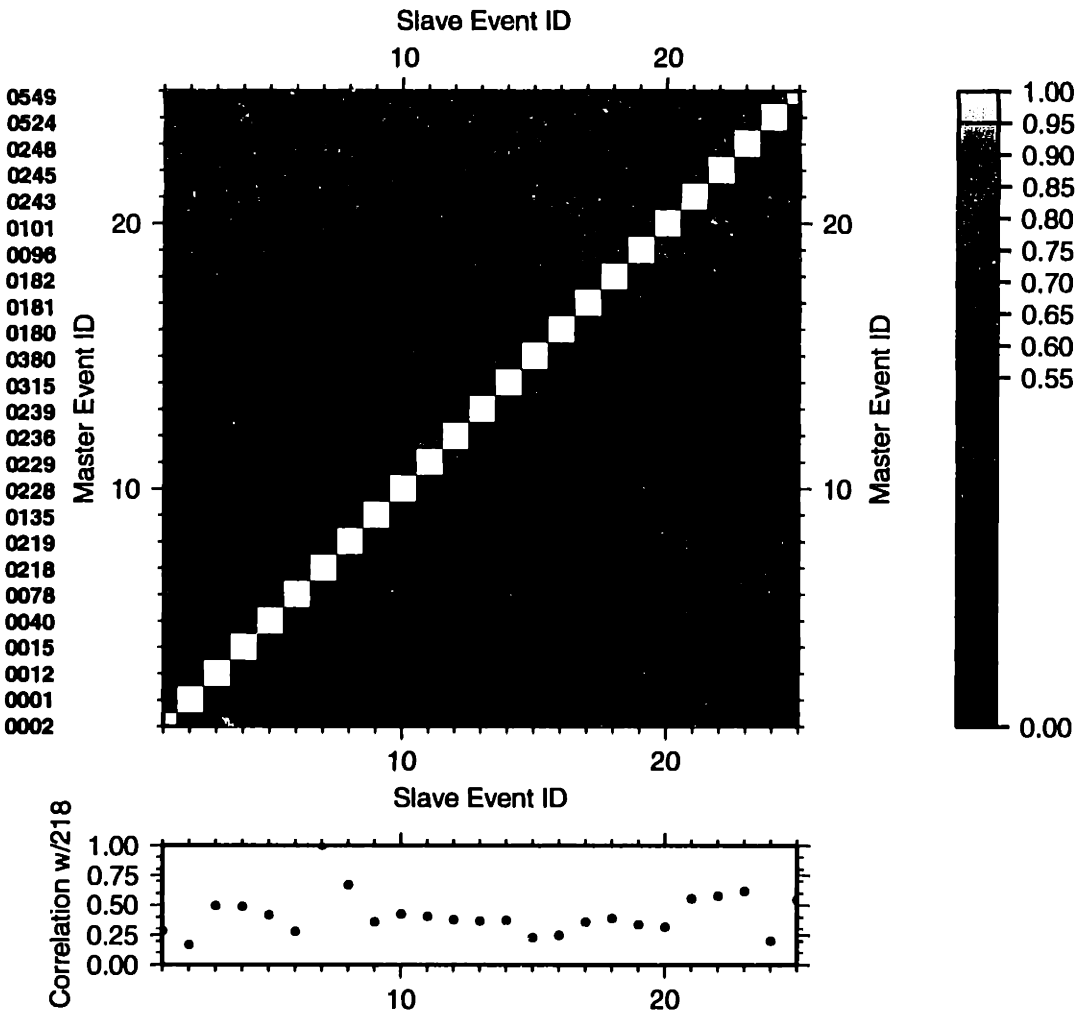

Figure 3-44: Cross (X) correlation matrix (normalized) for a window containing P phase arrivals for events in the LAGO microearthquake cluster as recorded at station VALE. Variation off of 1.0 along the diagonal indicates an event that was not recorded at this station.

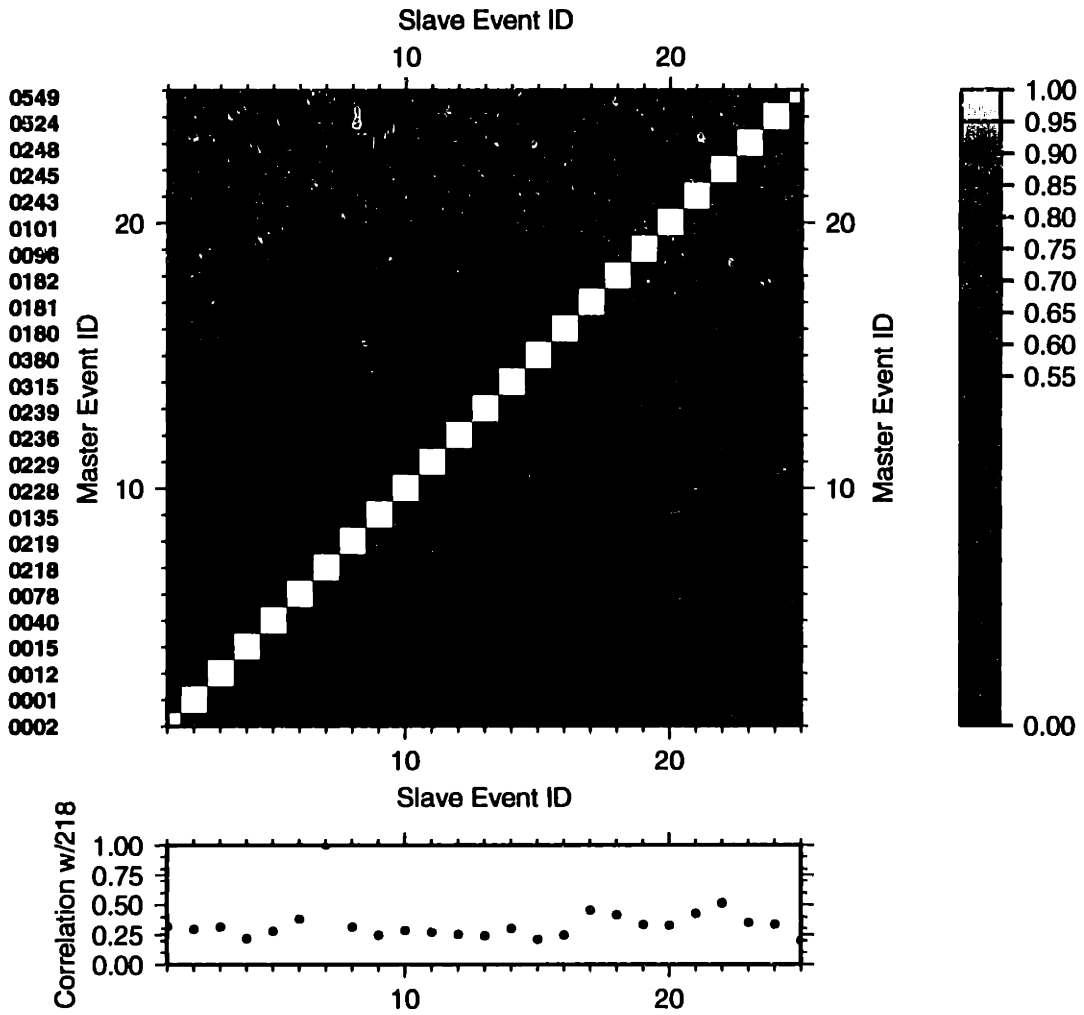

Figure 3-45: Cross (X) correlation matrix (normalized) for a window containing S phase arrivals for events in the LAGO microearthquake cluster as recorded at station VALE. Variation off of 1.0 along the diagonal indicates an event that was not recorded at this station.

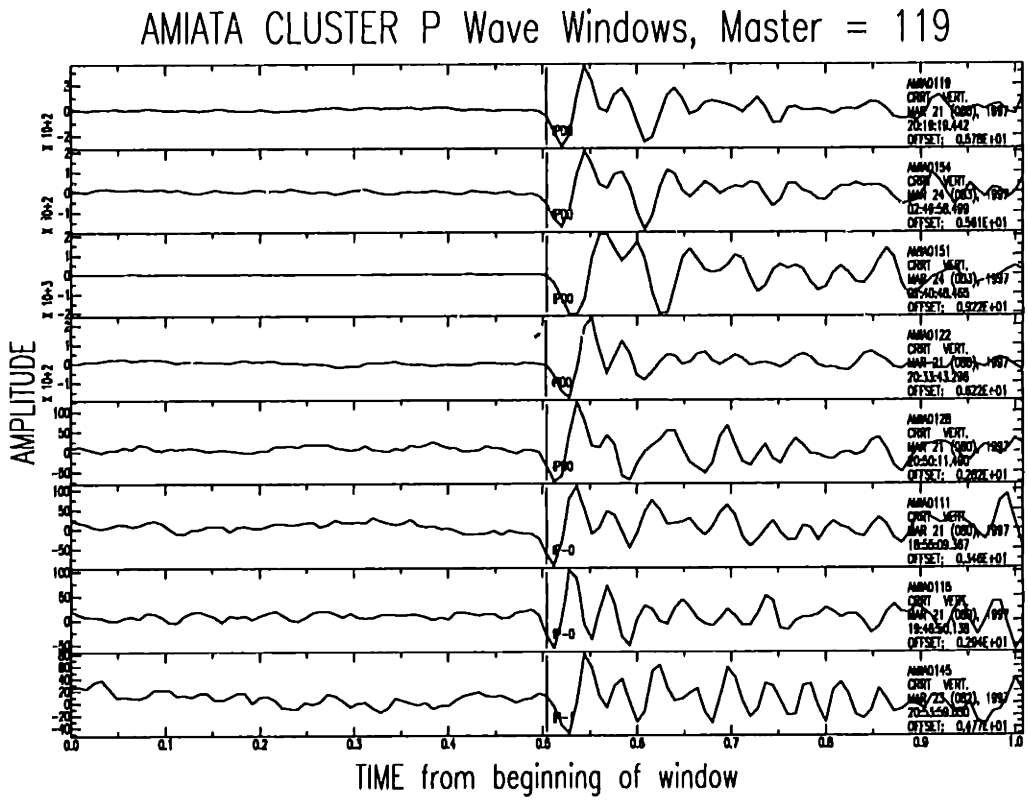

Figure 3-46: Example P arrival windows from station CRRT for eight events in the Monte Amiata microearthquake swarm. Event 0119 was chosen as a master based upon the results of the cross correlation multiplet analysis and is shown here with the P arrival indicated. Seven slave events are additionally presented with various quality P wave arrival estimates.

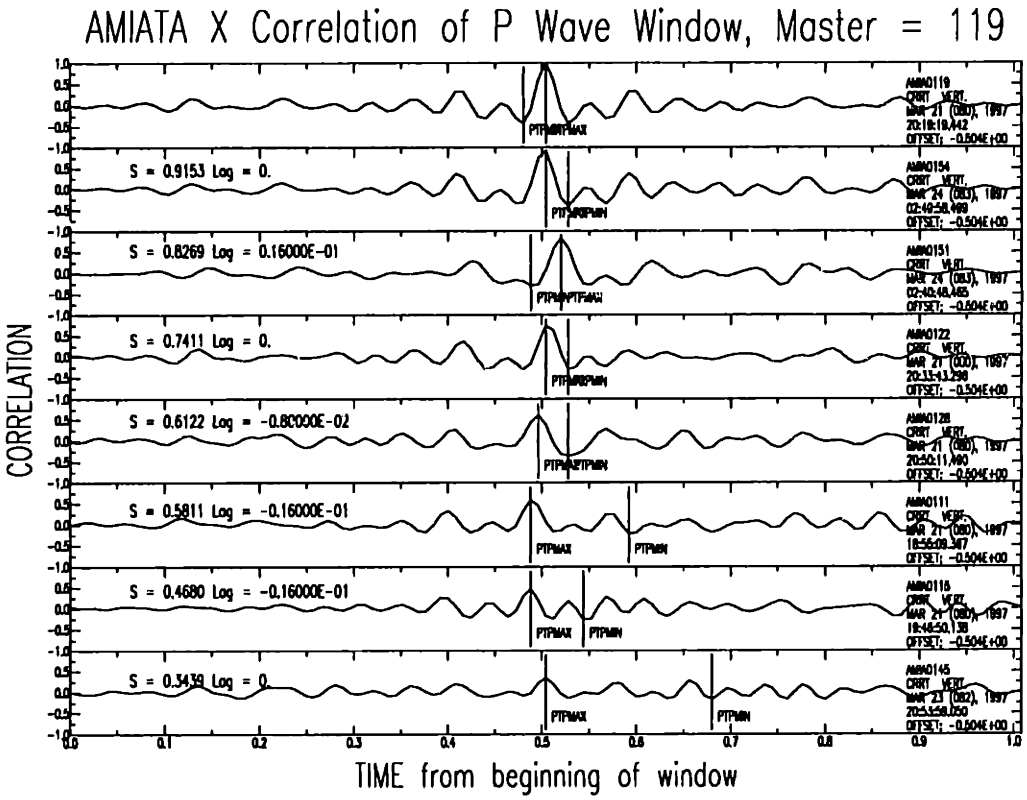

Figure 3-47: Example cross (X) correlation for P arrival windows from station CRRT for eight events in the Monte Amiata microearthquake swarm. Event 0119 was chosen as a master based upon the results of the cross correlation multiplet analysis and the auto-correlation is shown here. Seven slave events are additionally presented with various degrees of cross correlation peak values (S indicated on left in figure) and correlation lags (Lag indicated at left in figure).

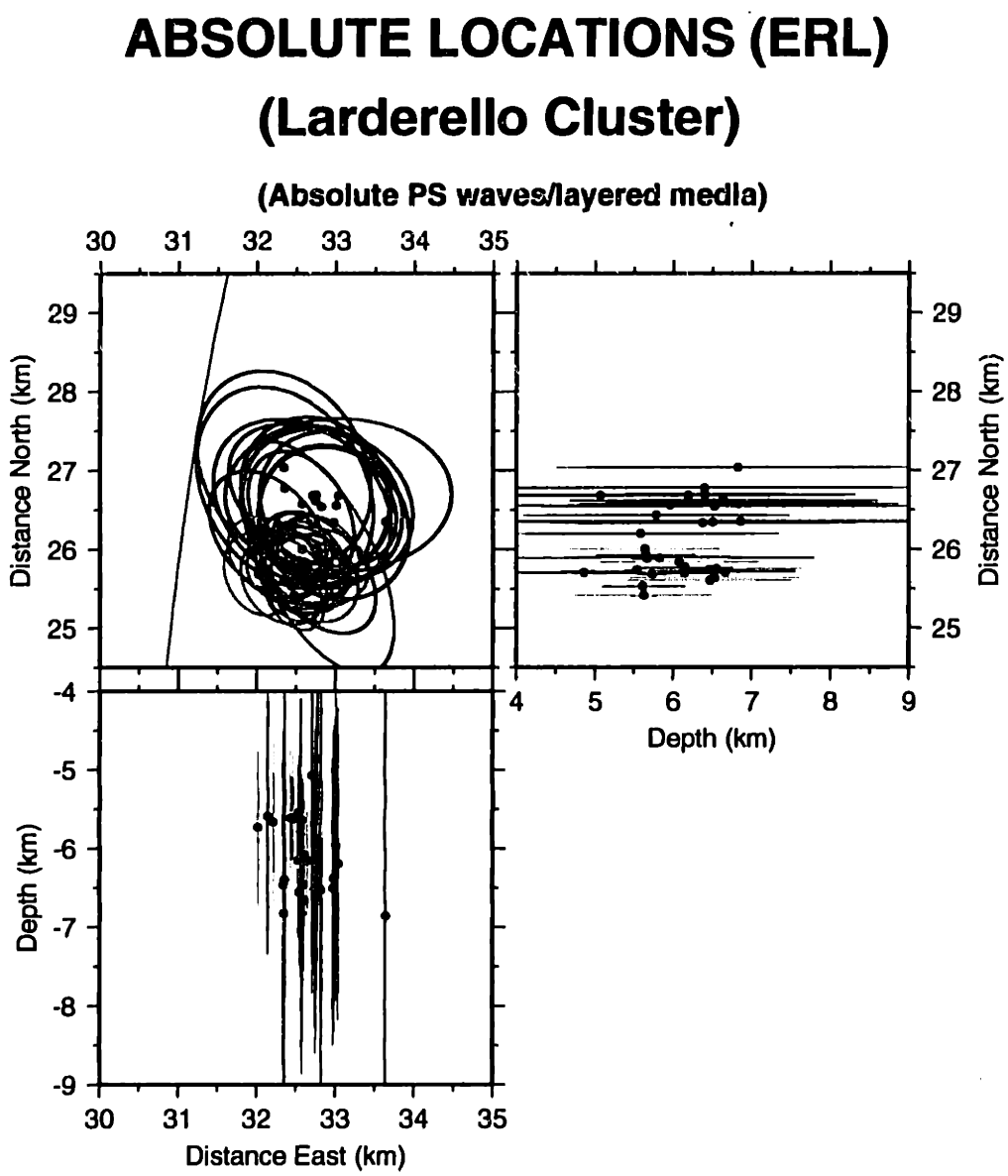

Figure 3-48: Hypocenter location estimates (absolute type) and their 90 percent confidence regions for events of multiplets 0157 and 0174 in the Larderello 1993 microearthquake swarm. These estimates were produced using P and S wave arrivals and station dependent layered velocity models.

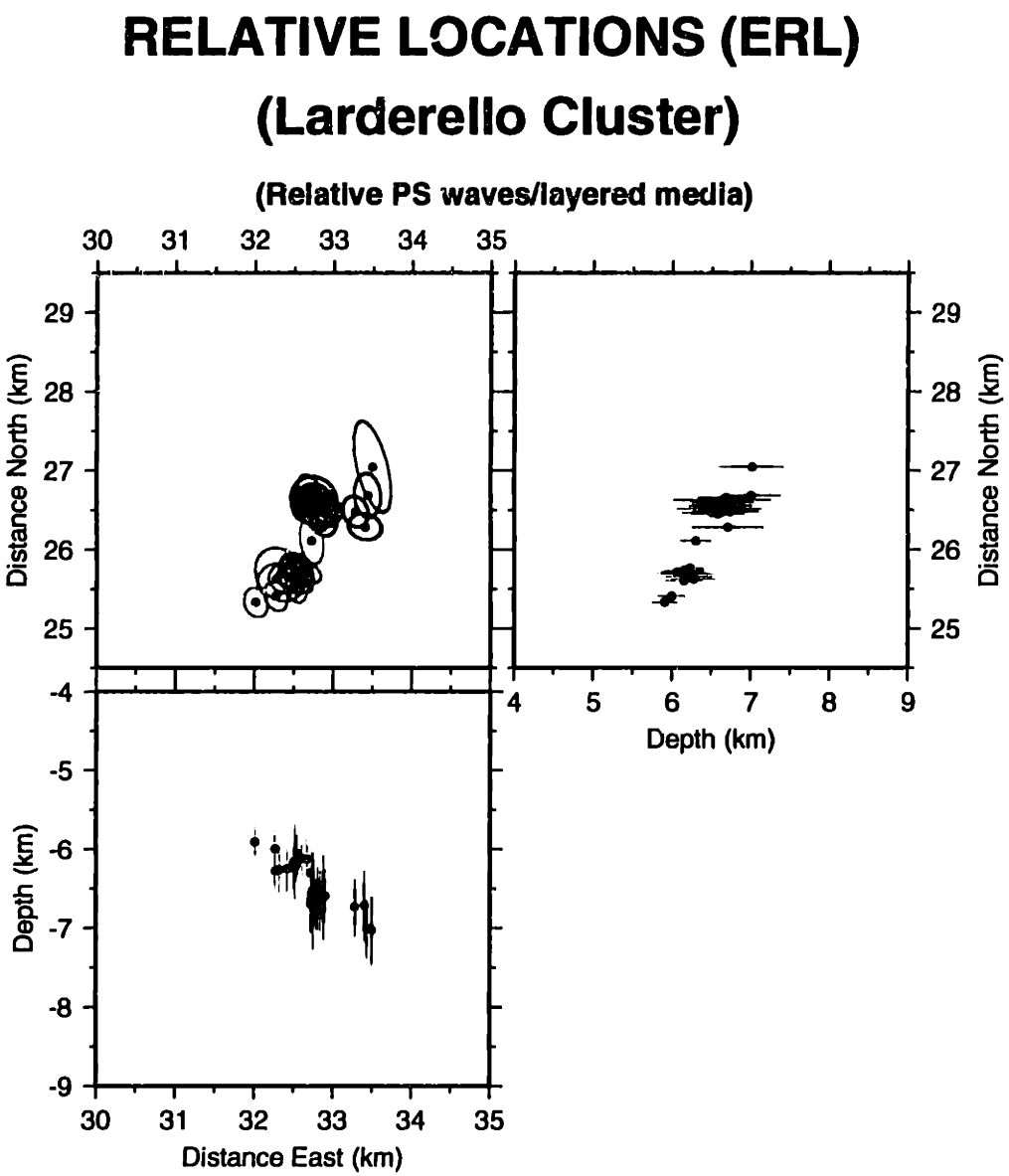

Figure 3-49: Hypocenter location estimates (relative type) and their 90 percent confidence regions for events of multiplets 0157 and 0174 in the Larderello 1993 microearthquake swarm. These estimates were produced using P and S wave arrivals and station dependent layered velocity models. Mean peak cross-correlation = 0.77 for relative P and S arrivals.

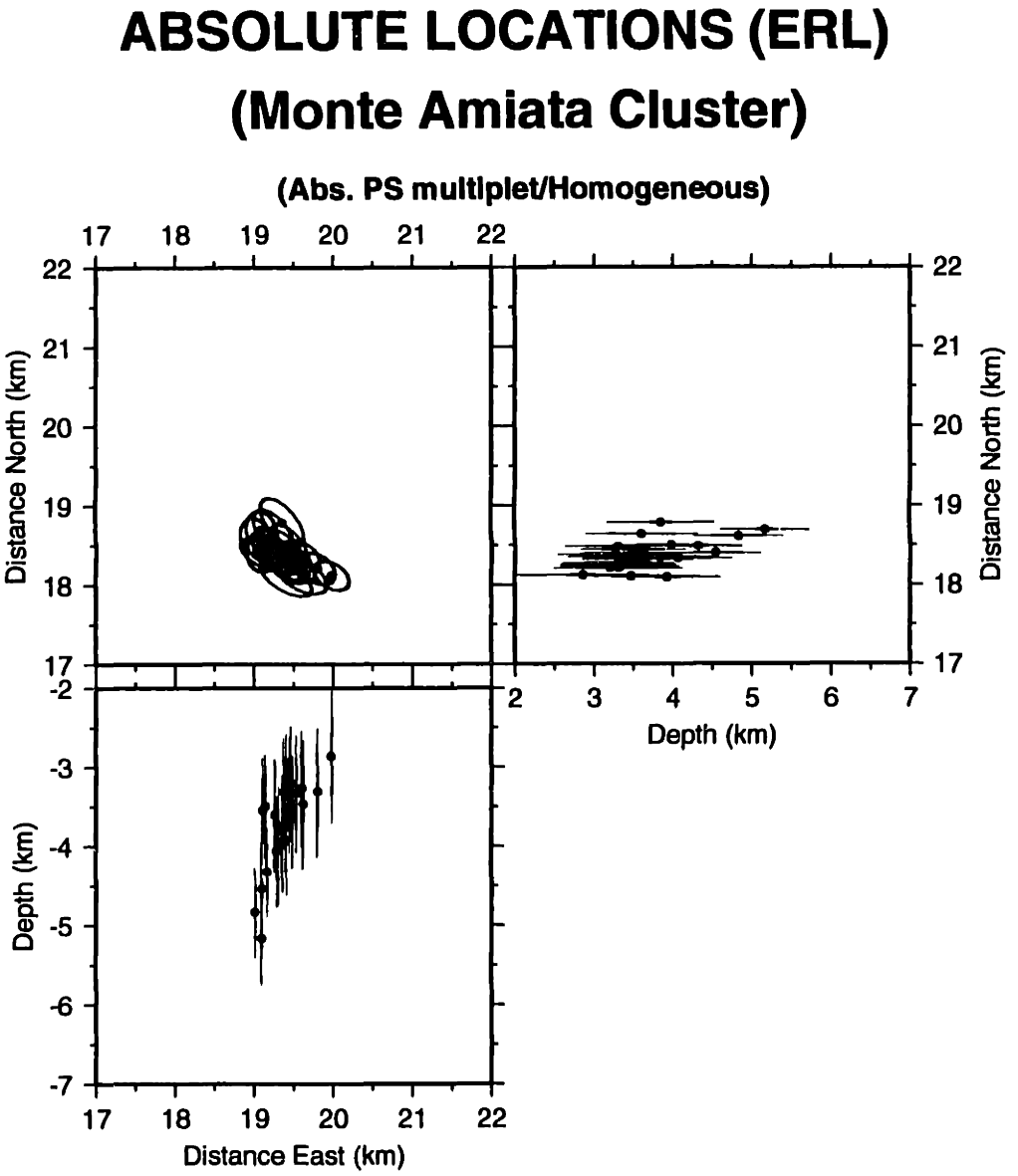

Figure 3-50: Hypocenter estimates (absolute) and their 90 percent confidence regions for events of the 0119 multiplet in the Monte Amiata microearthquake swarm. These estimates were produced using P and S phase arrivals and a homogeneous velocity model for all stations.

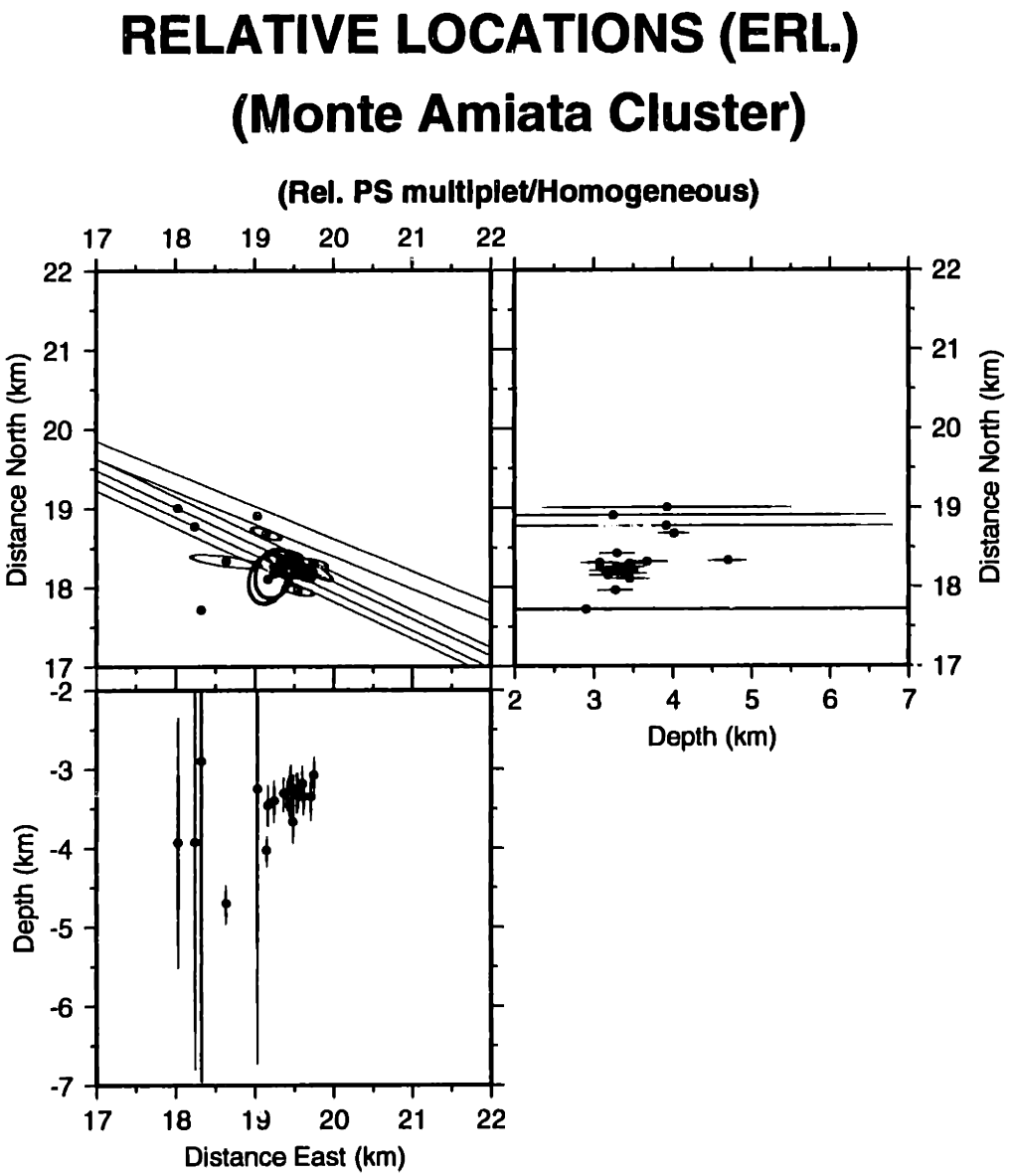

Figure 3-51: Hypocenter estimates (relative) and their 90 percent confidence regions for events of the 0119 multiplet in the Monte Amiata MEQ cluster. These estimates were produced using P and S arrivals and a homogeneous velocity model for all stations. Mean peak cross-correlation = 0.73 for relative P and S arrivals.

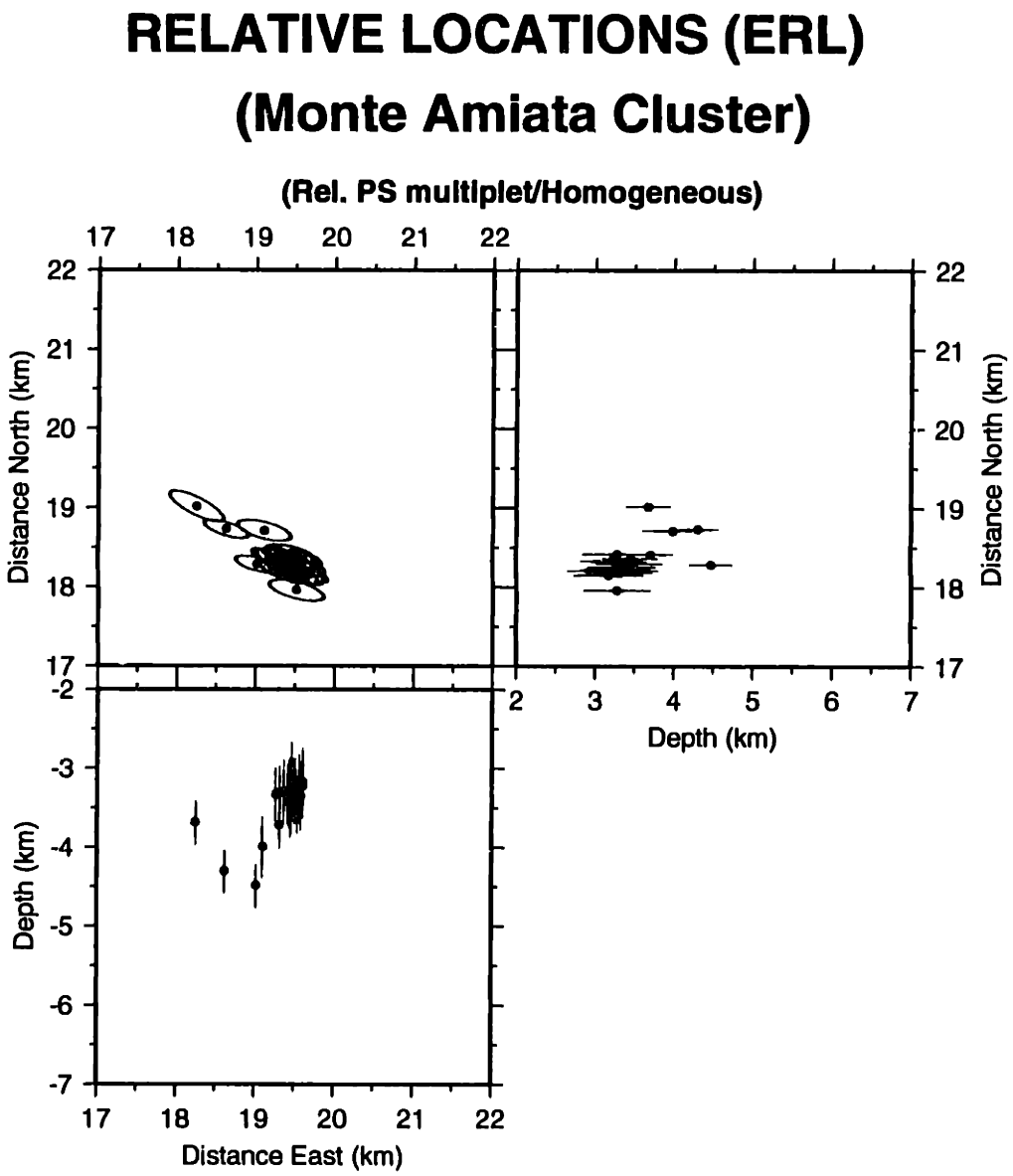

Figure 3-52: Hypocenter estimates (relative type) and their 90 percent confidence regions for events of the 0119 multiplet in the Monte Amiata MEQ cluster. These estimates were produced using P and S arrivals and a homogeneous velocity model for all stations. Mean cross-correlation = 0.68 for relative P and S arrivals.

Chapter 4

Interpretation

4.1 Interpretation Objectives

The objective of interpreting seismological data from production areas is to expand our understanding of how the reservoir responds to natural and production related activities. This objective is reached by collecting data, analyzing them to extract particular information regarding the physical phenomenon of interest and then interpreting the combined information so that the seismicity can be attributed to either natural geodynamic processes (tectonic or volcanic) or to a specific man-made process (fluid extraction or injection). If a likely source process can be identified, then additional objectives may be pursued, particularly in the case of man-made causes. In this case, the MEQ records may be used to further quantify the reservoir response and, in cases of injection, can be used in fracture diagnostic studies.

Many reservoirs, particularly geothermal reservoirs, are associated with areas of active tectonics and therefore the cause of any observed seismicity may be either natural or man-made. A comprehensive approach to observing, interpreting and attributing seismicity includes four principal stages that are generally applicable to most reservoirs, regardless of the site complexity. They are:

1. Identification of anomalous seismicity

    - Detection of anomalous seismicity rates or magnitude scale parameters
    - Preliminary hypocenter parameter estimation
    - Spatial and temporal sort to determine events in cluster or swarm

2. Evaluation and souce type evaluation of anomalous seismicity

    - Establish baseline seismic velocity model
    - Individual Event Analyses
        - Source kinematics (hypocenter location, fault plane solution, slip area, average dislocation, etc.)
        - Source dynamics (source time function analysis, directivity, non-uniform slip, etc.)
    - Clustered Event Analyses
        - Cluster relationship analysis (multiplet analysis, relative event relocation)
        - Cluster scale process kinematics (multiple hypocenter displacement and velocity analyses)
    - Interpretation and source type evaluation (integrates results available from previous studies)

3. Process Diagnostics (if applicable)

    - Cluster scale process dynamics (hypocenter migration relative to known process physics)

4. Follow-on Analysis: Technology evaluation and/or Impact on Production Related Processes(if applicable)

    - Technology evaluation (hydraulic fracture applications)
    - Seismic Hazard Assessment (reinjection processes)

Stage one involves identifying the anomalous seismic activity. This is usually indicated by a change in the normal rate of seismicity or a change in the magnitude scaling relationship normal for the area. Once anomalous seismic activity is identified and specific events recorded, preliminary estimation of the hypocentral parameters allows the event catalog to be sorted to isolate all events associated with the cluster or swarm.

Stage two encompasses all aspects of analysis and interpretation of the anomalous seismicity. Analytical procedures carried out on any one particular set of events are dependent upon various constraints including network capabilities, analysis schedule and available resources. Results contributing to the final interpretation may originate from a single suite of applied methodologies or from various studies conducted by different investigators. Analysis of the events in the four clusters presented in this thesis will incorporate the results described in chapter 3 of this thesis as well as results of additional investigations when they are available.

During the evaluation we seek to find a physical model that explains as much of the available data as we can. For MEQ cluster data, the observables commonly represent information from multiple spatial scales ranging from the size of a single event's slip area (investigated using traditional source kinematic and dynamic methodologies) to a scale exceeding that of the cluster dimensions (evaluated using spatio-temporal analyses and comparison of the cluster geometry and location to *a priori* geologic or production process data).

Traditionally, the process of synthesizing a causative model for clustered seismicity has been referred to as "seismotectonics" because the underlying mechanical processes were invariably tectonic in origin. Interpretation of anomalous seismicity near petroleum or geothermal production operations requires that we admit non-tectonic (non-geologic) processes as possible causes and develop a vocabulary that can be used throughout the interpretation without this presupposition. I will use the general term "process" throughout the discovery phase of the interpretation until a final hypothesis is made regarding the source of each of the clusters presented.

I will use results of both kinematic and dynamic analyses in developing a list of potential causes of the seismicity. Source kinematic and dynamic analytical methods are well established seismological techniques that focus on processes acting at the very local scale and are typically applied to single event data. In these evaluations, volumes of rock are abstracted as "particles" and classic kinematic or dynamic analyses are applied. A similar abstraction can be used for cluster scale characteristics. Specifically, it is common in MEQ interpretation to abstract a hypocenter as a "particle" and then to apply kinematic analysis to evaluate the hypocenter migration parameters (displacement and velocity). Thus, kinematic analysis of multiple hypocenters provides an image of the underlying mechanical process without direct reference to the forces causing the individual MEQs. Similarly, once a potential source process has been identified, the investigation can be expanded and the dynamics of the process can be considered.

One complication of applying kinematic and dynamic analyses to evaluate hypocenter migration is that the events making up a particular cluster may be caused by more than one mechanical process. Thus, a cluster of hypocenters is, potentially, a superposition of multiple clusters and thus care must be taken to apply kinematic and dynamic analyses to the proper subset of events. If the underlying process produces multiple events with similar source mechanisms and limited volumetric coverage, then the waveforms will exhibit high correlation values. When multiple processes are inducing seismicity (such as failure along multiple conjugate joint surfaces), then distinct multiplet sets will be identifiable and the cluster of hypocenters can be divided and the process "images" decoupled.

Additionally, it is important to consider that the process image is only resolvable in as much as the process induces seismicity. Aseismic creep may contribute significantly to overall reservoir response and poses a considerable challenge in interpreting actual earth behavior from the seismicity distributions.

The third stage of interpretation occurs after a causative process has been proposed. In this case, source process dynamics can be evaluated by comparison of modeled process behavior to the observed hypocenter migration and cluster characteristics. For instance, if the

seismicity is attributed to hydraulic injection, hypocenter migration can be compared to fracture modeling results for reservoir stimulation diagnostic objectives, particularly determination of fracture azimuth and length. This aspect of interpretation is highly dependent upon the amount and availability of data on the attributed source process and may not be possible for many clusters of events.

The last stage of interpretation occurs as a follow-up step and involves evaluation of any technology that may be inducing seismicity. In the case of hydraulic fracture stimulation, this follow-up evaluation may include determining how the injection parameters may be modified in order to maximize the effectiveness of the treatment or detectibility of the induced seismicity. In cases of waterflooding or condensate reinjection for reservoir pressure maintenance, the follow-up may include an evaluation of seismic hazard associated with the reinjection if the observed seismicity can be correlated with the reinjection. The follow-up stage is most appropriate during decision making for reservoir managment and is mentioned here for completeness.

4.2 Interpretation of the DWTI Hydraulic Fracture Induced Microearthquakes

4.2.1 Cluster Identification

In preparation for the DWTI hydraulic fracture experiment, ARCO conducted a 3-component VSP microfrac experiment in the Lower Frio sand and bounding shales to determine whether hydraulic injection would produce detectable seismicity in each of the formations (Keck and Withers, 1994; Truby *et al.*, 1994; Keck *et al.*, 1996; Withers *et al.*, 1996; Atlantic Richfield Corporation, 1994). This test confirmed that the target formations were initially seismically quiet and that any injection related events, in either the sand or shale formations, would be detectable above background noise. Indeed, 2400 events were detected during the completion of the main injections with several hundred exhibiting adequate P and S wave amplitudes for use in hypocenter modeling. Due to the excellent site conditions there was

no need for catalog sorting in order to identify the cluster of events for this monitoring experiment.

4.2.2 Cluster Source Process Evaluation

The onset of the DWTI seismicity occurred shortly after injection began and dropped below detectable levels abruptly after final shut-in at the end of the experiment (Keck and Withers, 1994; Truby *et al.*, 1994; Keck *et al.*, 1996; Withers *et al.*, 1996; Atlantic Richfield Corporation, 1994). Figures 4-1 and 4-2 present the final distributions for the 200 largest amplitude events. The hypocenters define a northeast-southwest trending linear feature extending southwest of the injection well and lying north of the two monitoring wells. Depth distribution of the hypocenters is generally restricted to the Lower Frio sand formation (the target formation of the simulated waste injection) and suggests limited seismicity in either the upper or lower bounding shales. Laterally, the distribution of hypocenters exhibits more variation than the distribution in depth, particularly at the most westerly extent of the seismicity and in the linear subset lying north of the injection well, off-angle of the main body of seismicity. Clearly, the DWTI seismicity is attributable to fracture of the Lower Frio sand formation due to injection of the simulated waste.

4.2.3 Process Diagnostics

The spatial distribution of the hypocenters shown in Figures 4-1 and 4-2 suggests that the fracture produced by the injection process departs from the laterally symmetric, "penny shaped" vertical crack predicted by standard tensile crack propagation models for injection at these depths. Most of the departure occurs during the last two cycles of injection. Figures 4-3, 4-4, 4-5 and 4-6 present the areal distribution of hypocenters for the four injection cycles. The distinct difference in the subcluster spatial characteristics between cycles 0 & 1 and 2 & 3, suggests a change in mechanical processes affecting the formations potentially related to fluctuations in downhole pressures during the injection.

Figure 4-7 presents a kinematic evaluation of the hypocenter migration over the course of the four injection cycles. This plot shows the radial distance between each MEQ and the injection (taken to be occurring at a central depth in the perforated section of the injection well as indicated by the depth coordinates of the early MEQ events). The hypocenter offsets (dots) are supperimposed on two important injection parameters, rate of injection (shaded areas) and bottom-hole pressure (solid line).

The seismicity associated with cycles 0 and 1 migrate away from the injection well with a velocity of approximately 100 feet/hour (0.33 inches/second). The seismicity associated with cycles 2 and 3 exhibit significantly different onset and migration behavior. The seismicity in these two cycles first occurs far from the injection well and migrates back toward the well.

Figure 4-8 presents a comparison of the hypocenter kinematics with an estimate of hydraulic fracture length extension. The curved lines are an average solution based on two fracture model estimates calculated by ARCO Keck and Withers (1994); Keck *et al.* (1996); Withers *et al.* (1996); Atlantic Richfield Corporation (1994). The two models: $Stimplan^{TM}$ (a commercially available multilayer stress, pseudo-3D, PKN-type fracture simulator), and $Wastefrac^{3}$ (ARCO's proprietary multilayer stress, pseudo-3D, PKN-type fracture simulator with thick filter cake effects incorporated) were used by ARCO to anticipate the expected fracture response prior to the experiment (Keck and Withers, 1994; Keck *et al.*, 1996; Withers *et al.*, 1996; Atlantic Richfield Corporation, 1994). The seismicity in cycles 0 and 1 are well predicted by the two simulators as evidenced by the similar slopes of the curves and the hypocenters.

The hydraulic fracture simulators predicted the fracture length for a symmetric, elliptical shaped crack extending away from the injection point. Thus, in Figure 4-8, I have indicated the predictive curves as solid lines extending upward away from the time of pumping startup in each of the four injection cycles because this would be the point of initial cracking or cracking after a significant period of shut-in. Additionally, I have also included similar curves (dashed) beginning at intracycle times where the behavior of the hypocenters indicate

similar rates of crack extension or, where other behavior is exhibited, as a guage for rate of extension comparisons.

The existence of "striping" in the hypocenter offset with time suggests either repeated, slip along the pre-existing crack or propagation of a new crack ("crack branching"). The seismicity in cycle 1 delineates a tight linear distribution (See Figure 4-4) and so, clearly, if new branches are being formed, they must be following roughly parallel tracks that are closely spaced compared to the certainty of the hypocenter location estimates. Hypocenter confidence estimates were calculated for the DWTI MEQs in a follow-up study which is presented in full in Appendix C. For MEQs occurring in cycle 1, estimated 90 percent confidence regions define ellipses with major axes striking approximately perpendicular to the strike of the fracture azimuth (a result of the sensor array geometry) and with roughly equal depth and minor axes dimensions. For events located in the region where the "striping" occurs (approximately 400-600 feet along strike in Figure 4-4), the perpendicular uncertainty is approximately 8 to 16 feet on either side of the crack. Thus, the hypocenters cannot resolve the ambiguity of possible crack branches occurring within a fracture zone narrower than 16 feet laterally. No modeling has been done to compare the rate of fracture extension for a new crack to the rate expected for re-inflation of a pre-existing crack and so there is currently no way to compare the goodness of fit of the hypocenter migration rates to either of these hypotheses. This is one possible follow-up study that would be enlightening.

The seismicity occurring in cycles 2 and 3 exhibit considerably different apparent migration rates than that measured for events in cycle 1. This suggests that significantly different physical mechanisms may govern, or at least impact, the MEQ generation processes in the two cycles. The most obvious difference between the cycle 2 seismicity and the cycle 1 seismicity is the distinct delay after pumping before the first events occur (in cycle 2). These first events are recorded nearly 400 feet beyond the farthest events recorded during cycle 1 or 0. These first MEQs are followed by events that migrate back toward the injection well. To more accurately reflect the behavior of the seismicity during cycles 2 and 3, Appendix D contains frame animations illustrating the temporal characteristics event by event (with uniform inter-event spacing, an accomodation for display purposes only). Figure 4-8 reflects

a more accurate accounting of the true inter-event timing). Figures D-1 through D-67 in Appendix D show the DWTI MEQs in sequential order beginning at the end of cycle 1 (the first frame shows the cycle 0 and 1 seismicity as a reference).

The first thing to examine is the image of a cloud of seismicity at a distance of approximately 1150 feet southwest of the injection well. Appendix C presents estimates for the 90 percent confidence regions for events occurring in this vicinity. The calculations indicate that the hypocenter estimates can only resolve events which are separated by more than 100 feet for events in this vicinity. That is, the confidence regions are ellipses with major axes with lengths of approximately 50 feet on either side of the hypocenter estimate, perpendicular to the strike of the cluster. Events at the very far end of the cluster and off the line of strike have confidence regions with major axes measuring less then 200 feet. These confidence regions show that the image of this portion of the cluster is not as well resolved as the areas nearer the injection well. The realization presented in Figure 4-5 is only one possible valid solution. An image presenting the hypocenters aligned along the strike of the cluster would also be a possible valid solution, although it is no more valid than the one shown. One aspect of this portion of the cluster that is resolved is the separation along strike because the dimension of the confidence region minor axes is on the order of 10 feet (20 feet total region width along strike). Because the distribution of hypocenters shown in Figure 4-8 indicates radial distance, it is apparent that the seismicity does, indeed, migrate backward from the far end of the fracture toward the injection well.

In evaluating the distribution of the seismicity in the first part of cycle 2, we may note that in Figure 4-8 there is a distinct pressure peak just before the onset of seismicity. I interpret this pressure phenomenon to indicate that the fracture created in cycles 0 and 1, had been completely re-inflated and pressure build-up was occurring prior to extension of a new fracture beyond the distance of 700 feet. The maximum pressure reached during this pressure peak was approximately 3300 psi, about 300 psi less than required to initiate the fracture during cycle 0. Similar pressure peaks occurred upon injection start-up in both cycles 2 and 3, both of which followed cycles involving a sand/bentonite laden injection. No similar peak occurred during cycle 1, which followed an injection cycle with no sand. Once

fracture extension had been re-initiated, pressure dropped to levels similar to that seen in the later periods of cycle 1. (For a description of time dependent pressure and fracture penetration response as predicted using common geometric models for hydraulic fractures the interested reader is referred to Nolte (1989)).

Examination of the animations presented in Appendix D suggest that reinflation of the fracture during the initial stages of cycle 2 produced no seismicity with sufficient amplitude to be located during this investigation. The first detected and located events in cycle 2 occurred nearly 400 feet beyond the terminal cycle 1 seismicity. To guage the relative rate of extension of this section of the fracture, I compared it to the modeled rate for cycles 0 and 1 fractures, assuming that the new fracture extended away from the furthest reach in cycle 1. Although the guage uses a model that applies to the case of the initial opening of a symmetric crack, (this author is unaware of any numerical models now in use for modeling the reinflation and extension of a preexisting hydraulic fracture), I use it here only to demonstrate the similar rate of extension for these two portions of the fracture. Figure 4-8 shows the comparison of early cycle 2 seismicity to this guage (dashed line extending upward from 700 feet, just beyond the pressure peak). There is a rough correlation of slope and it is possible that the first few events represent extension of the fracture to approximately 1200 feet. Despite this rough correlation, it is clear that the fracture has extended to this distance and it is also clear that it reached this length without producing large (detectable and locatable) events, a behavior that is significantly different than that displayed during fracture extension during cycle 1. Thus, there are two characteristics of the early cycle 2 seismicity that distinguish it from that seen in cycle 1: an apparent change in the number of high amplitude (detectable and locatable) events occuring between 700 and 1200 feet, and an apparent reverse migration direction after the seismicity resumed. A robust interpretation of the full cluster behavior should provide some measure of accomodation for this distinction, but before developing this interpretation, we must first examine the remainder to the events in cycle 2 and those occurring in cycle 3.

Continuing on with our examination of the temporal evolution of cycle 2 events we can see from Figures D-13 to D-30 in Appendix D that after the development of an apparently

diffuse distribution at the furthest end of the fracture, the seismicity jumps back to fill in two patches just south and northwest of the injection well. The remainder of the cycle 2 seismicity is located either at the far end of the fracture or in the near vicinity of the injector with no events of comparable amplitude in the central segment of the fracture. The dimensions of the 90 percent confidence regions for the events close to the injector are on the order of 8 feet (major semi-axis) and 3.5 feet (minor semi-axis and depth) (See modelled grid point Cbxz in Appendix C for an approximate estimate). The orientation of the confidence regions indicate that hypocenter resolution along the fracture azimuth is on the order of 7 feet which, again, is adequate for resolving events along strike but does not rule out the possibility that the events are in the fracture plane rather than being distributed off plane (although again, both solutions are valid).

Cycle 3 events begin in Figure D-31 of Appendix D . After a period of injector well shut-in, the seismicity for cycle 3 began after an initially quiet lag period (see Figure 4-8) and again we can observe a pressure peak just before the onset of new seismicity. The most significant characteristics of the cycle 3 seismicity is the hypocentral locations which begin approximately 400 feet north of the injection well, delineating a linear feature striking north-northeast. (The hypocenter inversion solutions for these off-plane events were carefully confirmed using P wave particle motion data and various alternate velocity models to assure their proper placement relative to the wells.) Again, we can observe an indication of backward migration of the events toward the central segment of the main fracture where the major portion of late cycle 3 seismicity occurred.

Considering the distribution of the seismicity in cycle 1 and comparing it to the distributions observed in cycles 2 and 3, the observations suggest a change in the mechanical process governing the induced stresses. Good agreement between the predicted fracture length and the occurrence of seismicity in cycle 1 suggests that the hydraulic injection produced stable crack extension in the southwest direction away from the injection well during that cycle. Supporting this conclusion are the results of House *et al.* (1996) who determined focal mechanisms for 47 events from cycles 1 and 2 using first motion data. They concluded that the largest events represent shear dislocation on near-vertical, northeast-southwest

trending planes but noted a wide degree of scatter in the slip types for these 47 events including normal or oblique-normal slip as well as nearly pure reverse slip. The authors indicate that the increased degree of scatter was particularly notable for events at distances greater than 100 m from the injection well. As they noted, the predominant NE-SW fault-plane solution is consistent with the orientation of the "down to the gulf", listric growth faults that are major structural features along the northern Gulf coast (See Appendix A for a review of major structural features of the Texas Gulf Coast area).

One particularly interesting feature of the seismicity is the lack of observed events north-east of the injection well. The lack of observed events with amplitudes sufficient for both detection and location, implies nothing about the existence of lower amplitude (undetected or detected but unlocatable) events. Portions of the fracture image where no located events are indicated represent areas were the currently processed data set has no information to offer. Therefore, a gap in the located seismicity to the northeast of the injection well only suggests, but does not prove, that the fracture was "single-winged". Given that fracture extension for portions of the southwestern wing also produced limited locatable events (in that case, at mid fracture distances) , we can clearly not rule out the possibility that a second, north or northeasterly, wing existed. It is possible that the observed northerly events that occurred in cycle 3 represent either new fracture extention along a new strike or continued extension of a fracture along a previously unobserved wing.

One clue regarding this question may be seen in the behavior of the southwestern wing of the fracture. The cycle 2 gap in the fracture image occurred at mid fracture distances. When locatable seismicity resumed in cycle 2, it occurred at the very furthest extent of the fracture and then appeared to migrate slowly back toward the well. A similar backward migration of locatable hypocenters is also evident in the events from the cycle 3 north-northeast striking branch. The similarity between the seismic image gap placement and the backward migration of hypocenters suggests that the north-northeastern striking branch represents a second wing whose behavior mirrors the initial southwestern wing, but whose azimuth lies askew from the main fracture azimuth.

A hydrofracturing operational phenomenon known as "screenout" is one mechanism that may be capable of inducing variations in the local stress fields such that a change in fracture azimuth might be the result. Screenouts occur when an impediment to fracture extension occurs. One such impediment might be an unexpected blockage of the fracture by proppant (sand) resulting in an increase in pressure behind the blockage and a reduction in pressure ahead of the blockage. Screenouts often occur around the perforation but may also occur in more distant portions of the fracture (Daneshy, 1989).

Regarding the DWTI hydraulic fracture, it is possible that the rapid opening of a large segment of fracture during the beginning of cycle 2 produced a rapid drop in pressure (see Figure 4-8) that may have caused a screenout. The drop in pressure on the far side of the blockage and a subsequent decrease in available proppant may have prevented a sufficient mud cake to accumulate on the cycle 2 fracture. This may have allowed infiltration of fluid into the surrounding formation with subsequent failure of weak planes outside of the expected fracture zone. This would explain the character of the initial cycle 2 seismicity at the far end of the fracture. Similarly, pressure increases on the nearside of a screenout may explain the near-wellbore seismicity during the later stages of cycle 2.

An alternative to tip-screenout for explaining failure on a new azimuth may include variations in formation moduli resulting in lateral changes in formation fracture pressure. This seems unlikely given the well documented homogeneity and large lateral extent of the Lower Frio sand formation which Galloway *et al.* (1982) describe as strike-oriented shoreface and beach sand in thick aggradational sequences associated with the Buna Strandplain/Barrier system (See Appendix A).

In either case, it appear likely that hydraulic fracture could not be made to extend further than 1200 feet southwest of the injection well. Subsequent variations in pressure gradients within the fracture may have caused shear failure in areas other than the southwestern crack tip as an alternative fracture direction. The distribution and temporal evolution of cycle 3 seismicity suggests that extension in a north striking wing may have been the best potential fluid flow conduit available if the southwest direction was unobtainable. The

apparent northern azimuth of the cycle 3 events departs significantly from what would be the symmetric second wing aziumth. But, the presence of the wellbore at the eastern end of the fracture may have itself posed an impediment to northeasterly extension of the crack. The effect would be analogous to the technique of drilling a small hole at the end of a fracture in an engineering material to arrest the extension of an unwanted crack. Heterogeneities in the northern borehole wall (or potentially, in some section of the fracture itself) may have represented a more favorable weak point.

This proposal would require some additional support for the apparent angle of failure for the north-striking secondary wing. ARCO conducted a variety of studies in order to anticipate the in-situ stress conditions in the Lower Frio sand. At the target injection depth, the least principal stress direction is horizontal rather than vertical and so the fracture was expected to be vertical with strike in the direction of maximum principal stress. ARCO's studies were designed to determine these directions by both field scale and core scale stress determination methods which included an evaluation of regional and local fault orientations, three core based methods, including Anelastic Strain Recovery (ASR), Differential Strain Curve Analysis (DSCA), and Velan, and borehole televiewer to examine borehole breakouts. The results of the field scale fault analysis suggested that the fracture would propagate with a N80°E direction plus or minus 20 degrees. The three core based methods and the borehole televiewer produced results that differed significantly from the directions suggested by the geologic analysis. Specifically, ASR produced an average estimate of N8°E plus or minus 10 degrees, DSCA produced an average estimate of N18°E plus or minus 10 degrees, Velan produced an average estimate of N35°E plus or minus 5 degrees, and the borehole breakout produced an estimate of N45°E plus or minus 30 degrees. The results of the three core sample analysis were impacted by the poor consolidation of the sand formation and because of the large uncertainties reported for this suite of stress analyses, ARCO conducted a small fracture test in which 500 barrels of bentonite mud were injected into the formation while tiltmeters measured surface deflection. Oriented gamma ray logs were also used to determine the azimuth of the test frac. The results indicated a fracture azimuth of approximately N40°E plus or minus 10 degrees. Based upon the results of this suite of

tests, ARCO anticipated the direction of fracture extension as N40°E.

The azimuth of the main DWTI fracture, as measured using the distribution of hypocenters from cycle 1 seismicity, was N66°E, a number that falls within the confidence of the field scale fault analysis and the borehole breakout evaluation. The azimuth of the cycle 3 seismicity (with an orientation of approximately N18E) also falls within the expected azimuthal range predicted by the borehole breakout analysis. This azimuth also agrees reasonably well with the reported direction of sedimentary depositional structures in the sand, and with two of the three core based analyses. Galloway *et al.* (1982) reported that deposition of the Lower Frio sands were principally parallel to the strike of the Miocene gulf shelf. The authors stated that regionally this direction was coincident with the contemporary Vicksburg Fault system whose strike roughly parellels the present northern Gulf coast. However, they also note that the easternmost segment of the Frio sands were additionally affected by consistent reworking by wave action and variations in sedimentation due to frequent changes in position of localized shelf-edge deltas and embayments. Deposition orientations of S18W would be consistent with an embayment shelf striking east-northeast or with deltaic formations associated with a regionally eastward striking gulf shelf. It seems reasonable that the principal orientation of hydraulic fracture in the Lower Frio sand formation should reflect the regional stress conditions that have historically produced the growth faults that are characteristics of the northern edge of the Gulf of Mexico. However, it would also be conceivable that, in the event of a near-wellbore screenout and fluctuations in pressure gradients within the fracture, a reorientation of the local insitu stresses might favor core scale depositional orientations when fracture extension in the regional direction is impeded.

In summary, this hypothesis attributes the DWTI seismicity to shear failure on one of two geologically consistent failure planes, the first being the northeasterly striking plane parallel to the regional direction of maximum stress (as demonstrated by the existence of the major growth faults characteristic of the northern Gulf of Mexico coastal margin) and the second being a conjugate plane suggested by the sedimentary depositional structures and borehole breakout analysis.

4.2.4 Follow-on Analysis: Implications and Technology Evaluation

The results of the DWTI MEQ analysis highlight a number of issues regarding the use of microseismic monitoring for hydraulic fracture diagnostics as it applies to waste disposal and also for use in reservoir stimulation and enhanced recovery operations. First, I will discuss the issues as they pertain to waste disposal technology applications, followed by a discussion of implications regarding enhanced recovery operations.

The DWTI results show that significant portions of the hydraulic fracture were well imaged by hypocenter location, however, some gaps in the image resulted from the lack of detectable and/or locatable seismicity occurring during the pumping. Image gaps of variable size exist in portions of the fracture between its extension from its cycle 1 half-length of 700 feet to its final half-length of 1200 feet. A follow-up study could be designed to investigate the impact of injection well shut-in on the seismic expression of hydraulic fracturing when bentonite mud and sand proppant are used. Specifically, it would be useful to determine how the pumping parameters affect seismic response, that is, whether fluctuations in pumping rate, volume, or fluid viscosity, mud cake formation or other phenomenon, may increase or reduce the occurance of "usable" (i.e. detectable and locatable) events. Additionally, it would be useful to determine whether an equivalent fracture length of 1200 feet could be reached in one uninterupted injection cycle and whether the entire fracture extension produced continuous seismicity. Similarly, it would also be important to evaluate the effects of screenout on fracture geometry. This could be done by purposefully inducing a screenout while monitoring seismicity. High precision hypocenter location (such as differential travel time techniques) plus fault-plane analysis could be used to carefully map the evolution of the fracture behavior.

On the basis of the high correlation between the cycle 1 MEQ locations and the fracture modeling predictions, I feel that microseismic monitoring for waste disposal can, under carefully controlled circumstances, accurately reflect the location of the induced crack. However, it is important to clarify the impact of intermittent pressure fluctuations on the seismic expression of the induced fracture and incorporate this information into practical

field procedures.

Regarding the implications of the DWTI results on the behavior of hydraulic fractures in non-waste disposal related production activities, it is interesting to consider the impact of fracture asymmetry and/or re-orientations on the eventual resource recovery. For instance, in fields were fracture azimuth must be controlled very finely due to tight interwell spacings, an unidentified reorientation in the fracture may produce unexpected fracture interconnectedness which may ultimately reduce the efficiency of the recovery operations. Further MEQ monitoring studies could help in identifying stimulation design criteria that mitigate undesired fracture geometries and their potential impact on recovery.

4.3 Interpretation of the Tuscany Geothermal Field Microearthquake Clusters

By their very nature, geothermal fields typically experience significant microseismicity. When production related activities are included as potential sources of local seismicity, MEQ interpretation takes on additional complexity. In the following section, I will discuss the results of the three Tuscany geothermal MEQ clusters in light of current geologic and geodynamic models of the region (as described in Appendix B) and in consideration of on-site production activities. The Larderello 1993 MEQ swarm presents an excellent starting point for the discussion.

4.3.1 The Larderello 1993 MEQ Swarm

ENEL established the Larderello seismic network in 1978 in an effort to establish an ongoing monitoring program. The objectives included identifying relationships between natural, seismically active structures and areas of geothermal exploration and production. Of particular interest were locations where condensate was being reinjected as a means of maintaining reservoir pressure. Reinjection had been initiated at the Larderello field in the early 1970s

(Ferrara *et al.*, 1985).

Batini *et al.* (1985c) reported the results of a statistical study of the seismicity recorded during the years 1978 through 1982 and historical seismicity from the years between 1724 and 1978. They state that the Larderello and Travale geothermal areas experienced more than 1000 events with magnitudes between 0 and 3.2 in the five years of the study and that approximately 9 percent of the recorded seismicity occurred in the vicinity of the 1993 swarm evaluated in this thesis. Forty percent of the seismicity occurred in the LAGO area of the Larderello field and 22 percent occurred in the more easterly Travale-Radicondoli field.

The Batini *et al.* (1985c) report also included a review of the b values for seismicity at the Larderello-Travale area (as a whole) during the study period and compared it to local historical values and specific values for each of the three zones (LAGO, Larderello, and Travale-Radicondoli). They report that historically, the regional seismicity could be fit by a line with slope $b = 1.5$, but during the 1978-1982 study period the b value was measured as 1.01. (Batini *et al.*, 1985c). In general, the b value fluctuated from year to year: 0.84 (1978), 1.07 (1979), 0.87 (1980), 1.12 (1981) and 1.22 (1982). The authors note that the b values also varied spatially. In the area of the Larderello 1993 swarm, the measured b value for the five year period was 1.13, while the LAGO area exhibited a b value of 1.04.

The authors state that historical records from 1724 include an earthquake near the Travale field with an estimated Mercali intensity of VII-VIII, but that recent seismicity has exhibited less intense events with maximum magnitudes not exceeding 4.1. The magnitude 4.1 event occurred in 1970 in the town of Monterotondo, east of the LAGO region of the Larderello field (Batini *et al.*, 1985c). Statistical estimates of the maximum expected magnitudes for the three areas predict events with magnitudes not exceeding $M = 3.15$ (based on the 1978 estimate for the entire Larderello-Travale area). Of the three areas studied, the northern seismogenic zone where the 1993 swarm occurred exhibited the lowest magnitude events in general (magnitudes less than 2.25) while the LAGO and Travale-Radicondoli areas exhibited events with magnitudes less than 3.15.

Cluster Identification

The 1993 swarm investigated for this thesis was recorded by the Larderello seismic network and identified by ENEL as being a spatially and temporally isolated series of events with magnitudes consistent with area norms. ENEL's continuing interest in establishing the nature of the Tuscany microseismicity and their concern regarding the effects of fluid reinjection, including all of the Tuscany MEQ study areas investigated in this thesis, prompted the detailed study of this swarm.

Cluster Source Process Evaluation

Batini *et al.* (1985c) report that seismicity in all three seismogenic zones in the Larderello-Travale geothermal areas exhibit a high spatial correlation with the important seismic "K" horizon which was described in section 2. Figure 4-9 presents a western-looking side view of absolute hypocenters for the Larderello 1993 swarm. The hypocenters show the relative position of the swarm with respect to the "K" horizon which is represented in the figure as a dome shaped surface. The surface dips steeply at the outskirts of the geothermal area, a feature that suggests a genetic relationship with the underlying emplaced granitic body thought to be the source of heat for the Larderello field.

Figure 4-10 shows the depth contours for the "K" horizon in the region of the Larderello geothermal field and places the MEQ study areas in their respective positions. Figure 4-11 presents a close-up view of the results of the relative event hypocenter relocations as described in section 3, and their relationship to major faults and the "K" horizon depth contours. The spatial distribution of hypocenters defines a northeast trending linear feature with a plunge that appears to correlate with the dip of the seismic reflector. A northeast-southwest distribution was also noted by Batini *et al.* (1985c) for the 1978-1982 seismicity from this area and they note that those events appeared to be bounded by faults striking in that direction.

To examine the geometry further, I calculated fault plane solutions for 17 events from the 1993 swarm using first motion P wave polarities. The clarity of the P wave arrivals was excellent at most stations and no problems were encountered discerning the sense of the motion. Several stations exhibited variations in the direction of the motion indicating that rays from these stations were emerging near the nodal planes. These stations provided critical information and additional constraint on the final solutions. For the 17 events studied, little variation in the solutions were observed. Figure 4-12 shows examples of the degree of variation. An effort was made to use as many stations as possible and select events with the best coverage available, however, the azimuthal and distance coverage was impacted by a lack of stations in the northwestern quadrant and the location of the swarm near the northern boundary of the network. Events for which focal mechanisms were determined were recorded by between 13 and 16 stations, generally including CLSV, CORN, CRBE, FRAS,FROS, LAGO, LURI, MBAM, MDSV, MGUI, MINI, MONV, POMA, SCAP, TRAV, VALE, and MLUC (see Figure 2-13 to examine the distribution of stations used in determining the fault planes). The number of valid solutions varied according to how many stations were available and the particular set of first motions. However, all events exhibited well defined domains for the three principal axes of the stress tensor. Solutions were calculated using a search increment of 10 degrees, as recommended by Guinn and Long (1977). The number of inconsistent first motions was limited to zero or one. Solutions for all events indicate normal dip slip mechanisms ranging from nearly pure dip slip to predominantly dip slip with some strike-slip component. The two possible fault plane solutions both strike northwest-southeast, but have either northeast or southwest dips with typical angles ranging from 32 to 66 degrees. These results show a remarkable agreement with focal mechanisms reported by Batini *et al.* (1985c) for the 1978-1982 seismicity from this area. This agreement corroborates their observation that the fault plane solutions from this seismogenic zone are notably stable.

Three major structural features in the area show some degree of correlation with the spatial characteristics of this cluster. First, as we have seen, the "K" horizon is correlated strongly in depth as well as in the dip of the surface. Secondly, the Tortonian age extensional faults

strike northwest-southeast, dip steeply in either the northeast or southwest direction and are known to cross-cut the "K" horizon. Thirdly, the metamorphic core complex exhibits evidence of Hercynian age (300ma) compression in the form of northeast-southwest trending fractures (Carmignani and Kligfield, 1990; Batini *et al.*, 1985a; Cameli *et al.*, 1993). These correlations must be considered during the development of an interpretive model for this swarm.

The "K" horizon is a regionally extensive structure that has been shown to correlate well with much of the seismicity in the Larderello and Travale fields, yet the seismicity is clearly not evenly distributed on that surface. It occurs in spatially distinct zones. In the LAGO zone, the "K" horizon reaches its shallowest depth and approximately 40 percent of the observed seismicity occurs there (Batini *et al.*, 1985c). Near the Larderello 1993 swarm, the surface dips steeply giving it the appearance of a halo or drape, and at least some of the seismicity occurs near that depth and tracks that dip. Together, these correlations suggest that the "K" horizon itself may be the plane of slip and this would corroborate theories that the "K" represents a detachment surface. However, in all three seismogenic areas (and others), the "K" is cross-cut from above by extensional normal faults whose strikes and dips correlate well with the strikes and dips of the fault plane solutions, and the spatial distribution of the hypocenters exhibits strong correlations with the Hercynian compressional fractures in the metamorphic basement. These additional correlations suggest a more complex nature for the seismicity than simply slip on the "K" horizon itself.

The fault plane solutions for the events in the 1993 swarm (as well as nearby events from the 1978-1982 study period) are stable and unambiguously define the strike of the failure plane as northwest-southeast. This strike is consistent with either the Tortonian age extensional faults as well as the "K" horizon and therefore this particular piece of data cannot resolve the ambiguity. Similarly, one of the fault plane solutions dips northeast at an angle of approximately 60 degrees, which would also be consistent with either the extensional faults (at the depth of the swarm) or the "K" horizon. Again, the ambiguity cannot be resolved using the fault plane solutions.

The northeast-southwest plunging lineation defined by the spatial distribution of the hypocenters implicates the "K" horizon, but also highlights the question of why events with northwest-southeast fault plane solutions would occur with a linear spatial distribution on a two-dimensional surface such as the "K". Alternatively, the lineation implicates the northeast-southwest Hercynian age fractures, but again, does not clarify the relationship between the hypocenter lineation and the strike and dip of either of the fault plane solutions. Clearly, additional data must be used to supplement the hypocenter distributions and the fault plane solutions if a reasonable model is to be found.

All three seismogenic zones are near areas of active production, high reservoir temperatures, and surface heat flow (Batini *et al.*, 1985b,c). Drilling of the San Pompeo 2 well penetrated the upper portions of the "K" horizon at a depth of 2,930 meters (below sea level) and encountered a zone of highly fractured rock with hydrothermal and contact metamorphism mineral assemblages, fluid pressures in excess of 240 bars (24 MPa) and temperatures in excess of 400C (Cappetti *et al.*, 1985). Recall from chapter 2 that Cappetti *et al.* (1985) reported that drilling penetrated a cap of impermeable phyllites and micashists before encountering the fracture zone, where explosions caused caving of the borehole and backfilling. A zone with these characteristics would clearly be weak, compared to more competent blocks above or below. Alternatively, it could act as a source of pressurized fluids that may weaken local patches of adjacent faults, especially where offsets along the faults favor the formation of structural traps. An illustration of this second alternative is shown in Figure 4-13 where the elements are arranged in such a way as to approximate the major structures in the vicinity of the Larderello 1993 swarm. Displacement on weak portions of the NW-SE striking extensional faults would be consistent with the MEQ fault plane solutions, hypocenter distributions, fault orientations, "K" horizon characteristics, and a back-arc basin extensional stress regime. In addition, this model would also be consistent with small rupture areas and low magnitude events typical of the seismicity in this area.

Temporal migration of the hypocenters is shown in frame animation in Figures D-92 through D-127. The figures show contemporaneous failure along the lineation beginning predominantly with the shallowest events in the cluster. This suggests a down-dip slump type of faulting process which, again, would be consistent with the model illustrated in Figure 4-13.

4.3.2 Follow-on Analysis: Implications and Impact on Production Related Processes

Batini *et al.* (1985c) state that at least 15 injection wells were active in the northern area of the Larderello field during the period 1978-1982 , although most are located west of the town of Larderello in the Valle Secolo area (generally between seismic stations MINI and CLSV). They indicate that an increase in *b* values observed for that period's seismicity (as compared to historical values) suggest that reinjection of condensate may be responsible for an increase in the number of small events. They additionally note that no increase in event magnitudes appeared to be correlated with the beginning of injection however. The authors point out that few records were kept regarding the specifics of the reinjection and so were unable to specifically correlate the effects of the reinjection on the rate of seismicity in the affected areas excepting the observation of a generalized increase in the rate of small events.

The MEQs of the Larderello 1993 swarm exhibit characteristics that are consistent with the geodynamics of western Tuscany and Tyrrhenian Back-arc basin, and although the reinjection of condensate may contribute to changes in reservoir pressure, quantification of the overall contribution to changes in localized stress conditions would not be possible without extensive reservoir modeling and cross-reference to detailed injection parameter data, which is apparently unavailable. Additionally, the depths of the 1993 events, together with their relative distance from the majority of injection wells suggests that showing conclusive

evidence of a hydrologic connection between these two locations would be an extremely complex undertaking even if detailed pumping information were available. I feel that there is a lack of compelling evidence indicating anomalous behavior for the 1993 events and that this suggests that the swarm was a manifestation of geodynamic processes natural for this area rather than a direct result of fluid reinjection.

4.3.3 The LAGO MEQ Cluster

The LAGO area is the most prolific seismogenic zone in the Larderello Geothermal field, contributing nearly 44 percent of the events in the entire region (Batini *et al.*, 1985c). Studies regarding the seismicity there include the Batini *et al.* (1985c) report and two additional items, specifically Console and Rosini (1998) and Berti (1996). Both present the results of studies of fault plane solutions for events in this area. Some of the events represented in those studies were relocated as part of the work completed for this thesis.

Cluster Identification

The set of LAGO area events were identified by ENEL on the basis of the study of focal mechanisms completed by Berti (1996). Berti reported that although most events exhibited P wave first arrival polarities and amplitudes consistent with normal faulting, some of the events appeared to have non-double-couple mechanisms which ENEL attributed to high temperature and high pressure fluids circulating just below the seismic "K" horizon (Batini, 1997). Twelve of the 22 events relocated (as described in chapter 3) were also analyzed for focal mechanisms in the Berti (1996) report. Console and Rosini (1998) reported on focal mechanisms for 4 more of the 22 events, one of which showed a statistically significant non-double-couple component.

Additionally, Batini (1997) indicated that in 1985 (one year before the occurrence of the earliest event reported in this thesis) there were at least 6 condensate reinjection wells operating in the LAGO area although most are further away than 2 km. Clearly, there is

great interest in determining whether these events can be attributed to injection near this site.

Cluster Source Process Evaluation

Figure 4-14 shows the hypocenter locations described in section 3, the seismic "K" horizon depth contours, and some of the known faults and fractures in the immediate vicinity and at comparable depths. Figure 4-10 shows the location of the LAGO study area in relation to the regional view of the "K" horizon surface contours.

The hypocenters shown in Figure 4-14 are absolute locations rather than relative event relocations. The small set of events studied for this thesis did not exhibit a strong degree of waveform similarity in the correlation tests as described in section 3 and while the potential exists that the multiplet test produced a false negative (i.e. that the events are indeed similar, but that some unaccounted for interference masked the effects in the waveform correlation test), I feel that the added value for a more detailed differential time relocation is marginal for this limited set of events. This conclusion is made based upon the following observations.

First, visual inspection of the station records for events in this "cluster" indicate significant variation in waveform with the exception of a few small subsets of events. In a general sense, the waveforms show a minimum of two distinct gross patterns and each of these shows significant variation within the subset. One of the gross patterns exhibits significant P wave energy (especially for close stations), whereas the other pattern shows significantly less P wave energy and more shear energy. Among the events with high P wave energy, there are a few distinct subsets of events that are visually similar, however, these subsets are quite small containing usually no more than 3 or 4 events in each. Aside from the few similar events, consistency of the visual waveform correlation from one station to the next is extremely difficult to visually identify.

The inconsistency of the waveform correlation is represented well by the cross-correlation

matrices presented in Figures 3-37 through 3-45 of chapter 3. Here we can see some correlation manifested in the waveforms from station CORN, particularly in the shear wave arrivals, however, this similarity is not consistent and is barely seen for stations VALE and FRAS. The records evaluated were virtually noise free prior to the onset of the P waves and so the possibility of a false negative being due to uncorrelated noise is highly unlikely. This leaves the possibility of waveform variation being due to either scattered energy represented by variations in coda waveform, or by variations in source mechanisms or a combination of both. Visual inspection confirms waveform variation in coda but also in the first few cycles of the P arrivals. This suggests variation in focal mechanism as well as in source location. Indeed, the focal mechanisms reported by Console and Rosini (1998) and Berti (1996) indicate events with components of normal faulting, strike-slip faulting, and for 9 events, significant contributions from non-double-couple processes. Additionally, the lack of temporal correlation together with possible variations in reservoir pressure over the 10 years of the cluster duration supports the likelihood that many of these events are different enough to affect the waveform correlations. Relocation by the method of differential travel times requires that the events be related in source process so that variations in relative hypocenter location can be determined by the observation of slight variations in P - S times. Poor correlation of focal mechanisms violates the criteria for application of the differential traveltime methodology. This fact, however, does not impact the quality of the absolute locations.

The absolute hypocenter locations were carefully computed using four velocity models of varying complexity including a homogeneous model, a layered model, a model with velocity increasing with depth, and a piecewise vertical gradient model that reflected the known lithology of the area. The results of these models indicated very similar final hypocenter distributions that show several scattered subclusters of 3 or 4 events in each. This result also supports the conclusion that the events may have distinct source processes.

Interpeting the focal mechanisms as presented by Console and Rosini (1998) and Berti (1996) and hypocenter locations as described in chapter 3 suggests four important characteristics of this set of LAGO events. First, the minimum depths of the hypocenters suggest a

rough correlation with the minimum depth estimates for the seismic "K" horizon. Secondly, the fault plane solutions indicate a variety of focal mechanisms including normal faulting, strike-slip and non-double-couple processes, although many appear to have at least some component of normal faulting with planes oriented in the northwest-southeast direction. Thirdly, the absolute locations indicate that the hypocenters are distributed on a roughly northwest-southeast striking plane with a vertical distribution of approximately 1.5-2 km and with some indication of the cluster being composed of a set of spatially distinct subclusters, each being composed of a few events. Lastly, again there appears to be some degree of bounding of the seismicity to blocks between the northeast-southwest basement fractures and the northwest-southeast trending extensional normal faults.

These four characteristics are not inconsistent with the model described for the Larderello 1993 cluster which was illustrated in Figure 4-13 if the geometry of the component structures is reconfigured to reflect the conditions in the LAGO area. Here, the "K" horizon reaches its shallowest point and is configured as a gently curved dome (compared to the sharp drop near the location of the 1993 swarm). A relatively horizontal, high temprature, high pressure fluid filled fracture zone, cross-cut from above by the Tortonian age extensional faults, and cross-cutting the basement Hercynian age fractures can still account for much of the observed behavior of the LAGO seismicity without the addition of reinjected fluids (although it does not rule out this additional process either).

The distribution of hypocenters appears bounded by the two major lineations and although the focal mechanisms show some variety, this may indicate that the cluster of seismicity reflects failure on several of the represented planes, rather than on only one as was suggested for the Larderello 1993 swarm. Although the origins of the "K" horizon are still actively being researched, the results of drilling the San Pompeo 2 well has shown that the resulting fractures do contain highly pressurized, high temperature fluids (Cappetti *et al.*, 1985). Unfortunately, the degree and orientation of fracturating within the zone has not been established and so it is not possible to say how slip on planes within the zone may contribute to the complexity of the source mechanisms for the observed events. However, we can speculate that if the "K" horizon represents a detachment horizon re-

lated to the initial compression of the Appenines, then one would expect some correlation with a northeast-southwest axis of compression and the majority of fault plane solutions would reflect this dominant fracture orientation with relatively low dip angles. If the "K" represents an older detachment related to the earlier Hercynian orogenesis, then we would expect fractures reflecting a northwest-southeast axes of compression. If the "K" horizon represents a fractured zone reconfigured by an upward flexure of the crust due to vertical migration of an underlying hot magma body, then we would expect fractures arranged appropriately for the orientation and degree of flexure, which would likely include a variety of azimuths and dips. Similarly, failure due to flexure induced by cooling of the underlying magma body may also produce complex focal mechanisms reflecting failure on both new and pre-existing planes. In any of these cases, the movement of high pressure, high temperature fluids between hydrologically connected fractures with multiple orientations could (under varying fluid pressures) produce a complex variety of fault plane solutions, potentially including some component of non-double-couple processes, regardless of whether the fluids were naturally occurring or re-injected condensate (which, due to its shallower depth has more potential influence in the LAGO area than was proposed for the Larderello 1993 swarm).

In summary, I feel that the LAGO area seismicity examined here exhibits characteristics that are consistent with the geodynamic models of western Tuscany, and that the observation that the fault plane solutions include some non-double-couple components is not clearly inconsistent with naturally occurring processes of this complex geothermal region. The data does not support, nor does it refute, the possible contribution of condensate reinjection to the seismicity of the LAGO area. Additionally, it is not clear whether seismological data alone can provide an adequate discrimination for this problem given the apparent nature of the "K" horizon and the existence of interacting fault and fracture zones in an area of active extension.

Figures D-69 through D-90 presents one realization of the temporal evolution of the LAGO cluster of events (as represented by the absolute P wave, layered media solutions). This solution set is less well constrained in depth than the P and S solutions, but clearly shows the lateral location of the multiple subclusters. This lateral, subclustering was robust for all inversion trials. Four small patches of events occur but not in a spatially linear progression. In fact, it appears that the evolution occurs as an "X" pattern beginning in the eastern portion of the cluster, progressing the far western edge, moving to the southern edge and then crossing over to the northern edge. This pattern supports the conclusion of a complex underlying source process (or processes).

4.3.4 Follow-on Analysis: Implications and Impact on Production Related Processes

Batini *et al.* (1985c) concluded that an increase in *b* value over the 1978-1982 study period indicated that reinjection of fluids was influencing the seismicity in the local vicinity by increasing the number of small events, thereby preventing the accumulation of stess and reducing the occurrence of larger magnitude events. Console and Rosini (1998) concluded that events exhibiting focal mechanisms with significant dipolar components is suggestive of the influence of reinjected fluids, but proposed that a larger data set be evaluated to examine this problem further. Clearly, this is warranted. However, if it is possible to couple this seismological evaluation with hydrological modeling of the effects of variations in injection parameters, or with thermal or reservoir engineering modeling efforts, the combined results are more likely to illuminate this highly complex problem.

4.3.5 The Monte Amiata MEQ Swarm

Cluster Identification

The 1997 swarm of events occurred near the northern boundary of the Piancastagnaio production area of the Monte Amiata geothermal field. ENEL identified the swarm and noted that it occurred during a period of active deep condensate reinjection but added that nearby geologic structures have been seismically active in the past. The area exhibits a medium-high degree of natural seismicity with several notable historical events occurring in the last 80 years, including a Mercali intensity IX event in 1919 and several VII-VIII events in the last fifty years (Batini, 1997). Figure 4-15 recalls the MEQ study area for this swarm and places it in its geologic context near the western edge of the Radicondoli Graben, just east of the Monte Amiata Volcano.

Cluster Source Process Evaluation

Figure 4-16 shows the relative event relocation hypocenter estimates for the Monte Amiata swarm compared to some important local geologic structures. The spatial distribution of hypocenters shows a strong correlation with the inferred location of a northwest-southeast striking, northeast dipping fault. Placement and orientation of this fault is approximate and was inferred from Gianelli *et al.* (1988) and Calamai *et al.* (1970).

The depth distribution of the hypocenters suggests a spatial correlation with the deeper of two productive fractured horizons in this vicinity. This deep fractured horizon is reportedly located within the Tuscan basement formations, unlike the shallow reservoir which is located in anhydrites and dolostones of the Triassic Burano Formation Gianelli *et al.* (1988). The authors additionally point out that this fracture zone is distinct from the seismic "K" horizon which is identifiable at a depth of approximately 5 - 6 km (as inferred from reflection seismic two-way traveltimes). Batini (1997) stated that the 1997 swarm occurred during a period of active condensate reinjection. The exact location and depth of these wells, along with

rates of injection or injection pressure are not currently available in literature on the area, however, some wells with depths reaching or exceeding the depths of the hypocenters are confirmed in Gianelli *et al.* (1988). This report does not indicate whether these wells are production or injection wells.

The location of the hypocenters and their spatial distribution suggest that this cluster is related to slip on the indicated northwest-southeast striking fault at depths near the deep reservoir, however, it is not yet clear how production related activities may have contributed to the onset of seismicity. Montone *et al.* (1995) reported that focal mechanisms for 67 events from the local MEQ catalog and borehole breakouts from two wells near the Piancastagnaio area confirm a northeast-southwest direction of active extension for this area. Although fault plane solutions have not been generated for the events in this cluster to date, we can anticipate that events attributable to the NE-SW extension would produce events with some component of dip-slip in their focal mechanisms. Anomalous focal mechanisms may indicate reactivation of the fault by either increases or decreases in reservoir pressure which could be due to either natural circulation of fluids or condensate reinjection. If anomalous focal mechanisms were to be observed for these events, additional information would be required to discriminate between natural and injection related fluid circulation.

Process Diagnostics

Figures D-128 through D-150 present the temporal evolution of the Monte Amiata swarm. The migration of the hypocenters indicates that failure first occurred either below or near the bottom of the fractured zone and proceeded upward toward the top of the zone. The spatial subclustering of the later events suggests the presence of a barrier to rupture extension. This barrier may indicate the upper boundary of fluid induced weakening of the NW-SE normal fault. Alternatively, failure may be occurring on planes within the fracture zone which are localy weakened by infiltration of precipitation along the high angle faults. Completion of fault plane solutions for these events may help to distinguish these two possible alternatives if the fractures within the deep reservoir are oriented significantly differently than the large

NW-SE normal fault.

4.3.6 Follow-on Analysis: Implications and Impact on Production Related Processes

The problem of differentiating injection induced events from natural events in geothermal fields is clearly a non-unique one. Combining evidence of non-double-couple focal mechanisms with correlations between onset of seismicity and pumping initiation dates, pumping volume and injection rates is more likely to resolve the non-uniqueness than focal mechanisms and hypocenter locations alone. This author has reviewed no reports to date where focal mechanism solutions for events attributed to high pressure fluid injection have exhibited unambiguously tensile crack source mechanisms. Even in cases where injection pressures have been high and focal mechanisms have been computed, they often reflect significant components directly associated with regional stress conditions. If an MEQ were clearly and unambiguously shown to be due to non-double-couple sources, the problem would still exist that natural processes in volcanic and geothermal systems are also capable of producing similar moment tensor solutions, most notably thermoelastic expansion or contraction caused failure and naturally anomalous stress conditions caused by circulating geothermal fluids. Correlating seismically active geologic structures with hypocenter locations, carefully computed focal mechanisms, seismicity rates and onsets and reinjection parameters are all clearly needed to resolve this ambiguity.

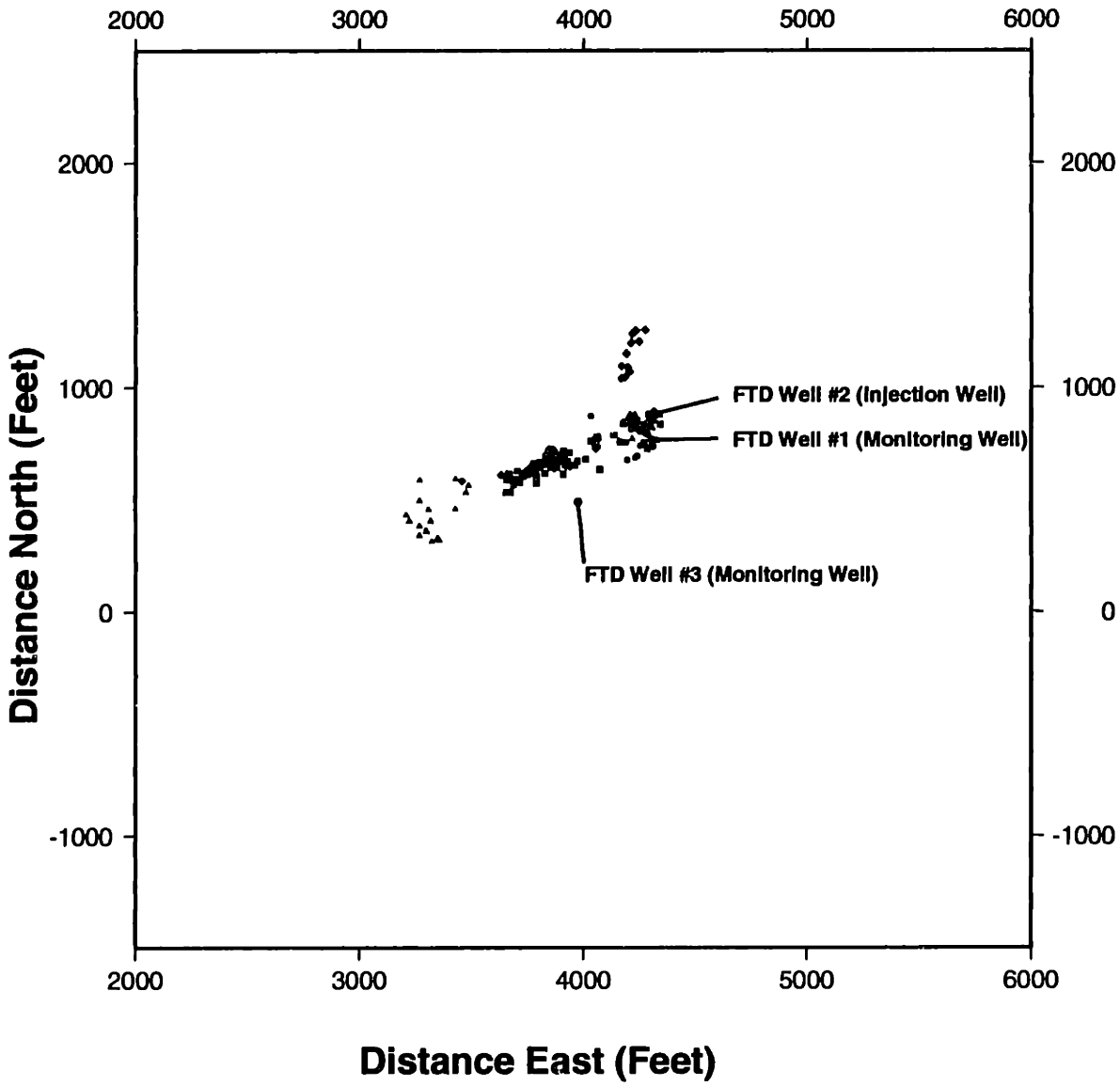

Figure 4-1: Areal view of hypocenter distribution for the DWTI hydraulic injection experiment calculated using least squares inversion with depths free to vary. Symbols indicate injection cycle in which the event occurred: Circles = Cycle 0, Squares = Cycle 1, Triangles = Cycle 2, Diamonds = Cycle 3.

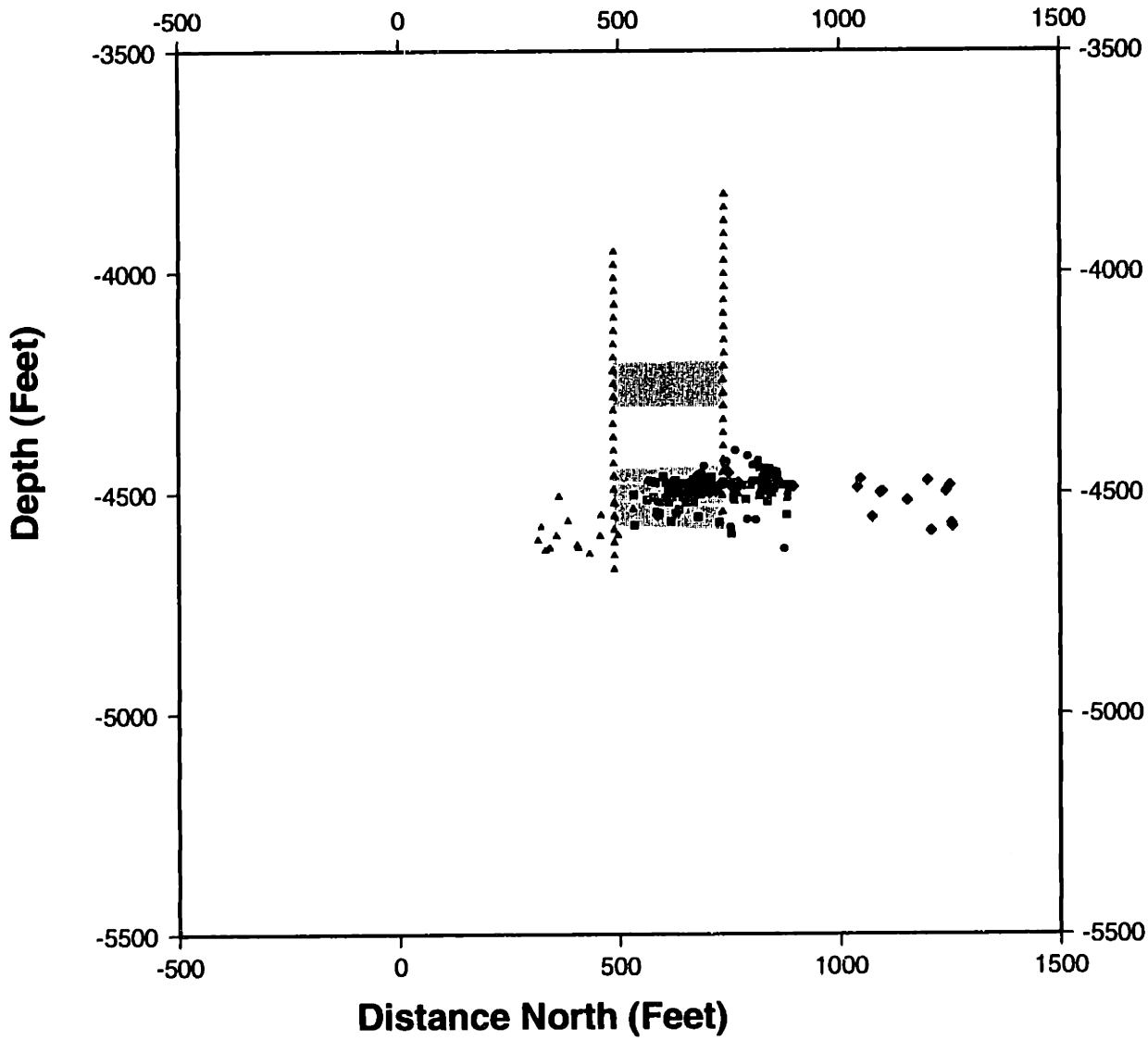

Figure 4-2: Side view (looking west) of hypocenters distribution for the DWTI hydraulic injection experiment calculated using least squares inversion with depths free to vary. Symbols indicate injection cycle in which the event occurred: Circles = Cycle 0, Squares = Cycle 1, Triangles = Cycle 2, Diamonds = Cycle 3.

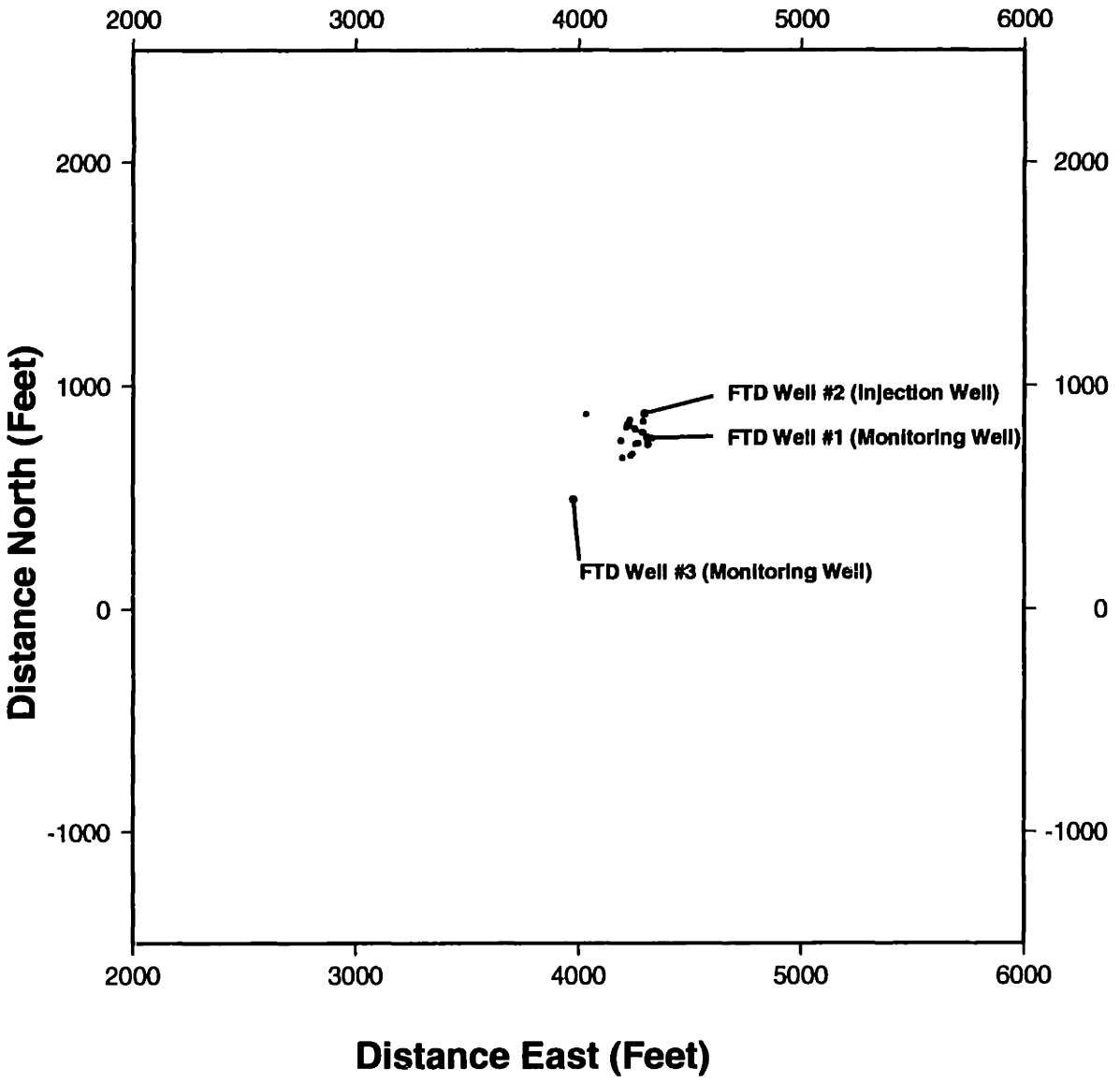

Figure 4-3: Areal view of cycle 0 hypocenter distribution for the DWTI hydraulic injection experiment calculated using least squares inversion with depths free to vary. Symbols indicate injection cycle in which the event occurred.

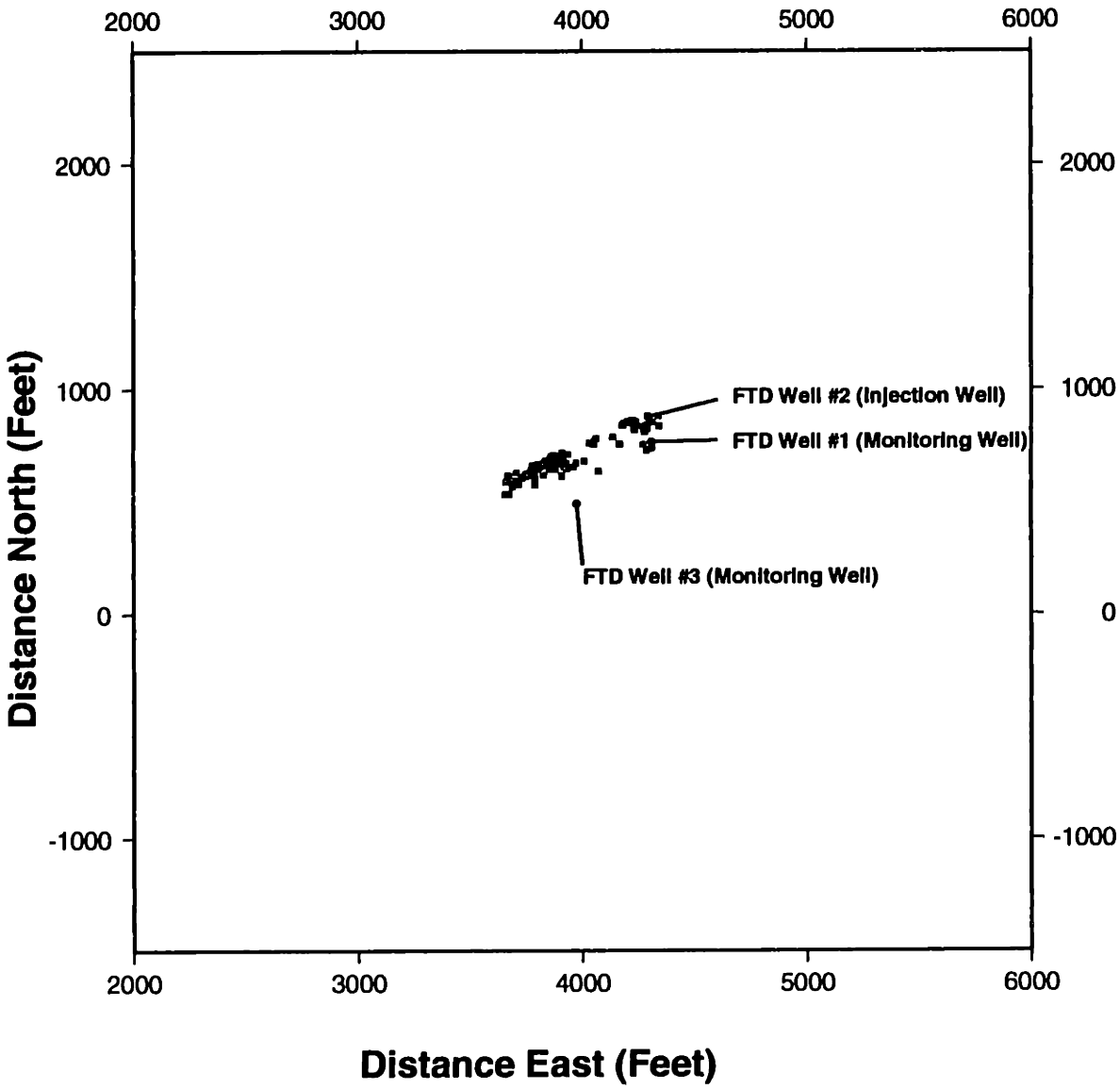

Figure 4-4: Areal view of cycle 1 hypocenter distribution for the DWTI hydraulic injection experiment calculated using least squares inversion with depths free to vary. Symbols indicate injection cycle in which the event occurred.

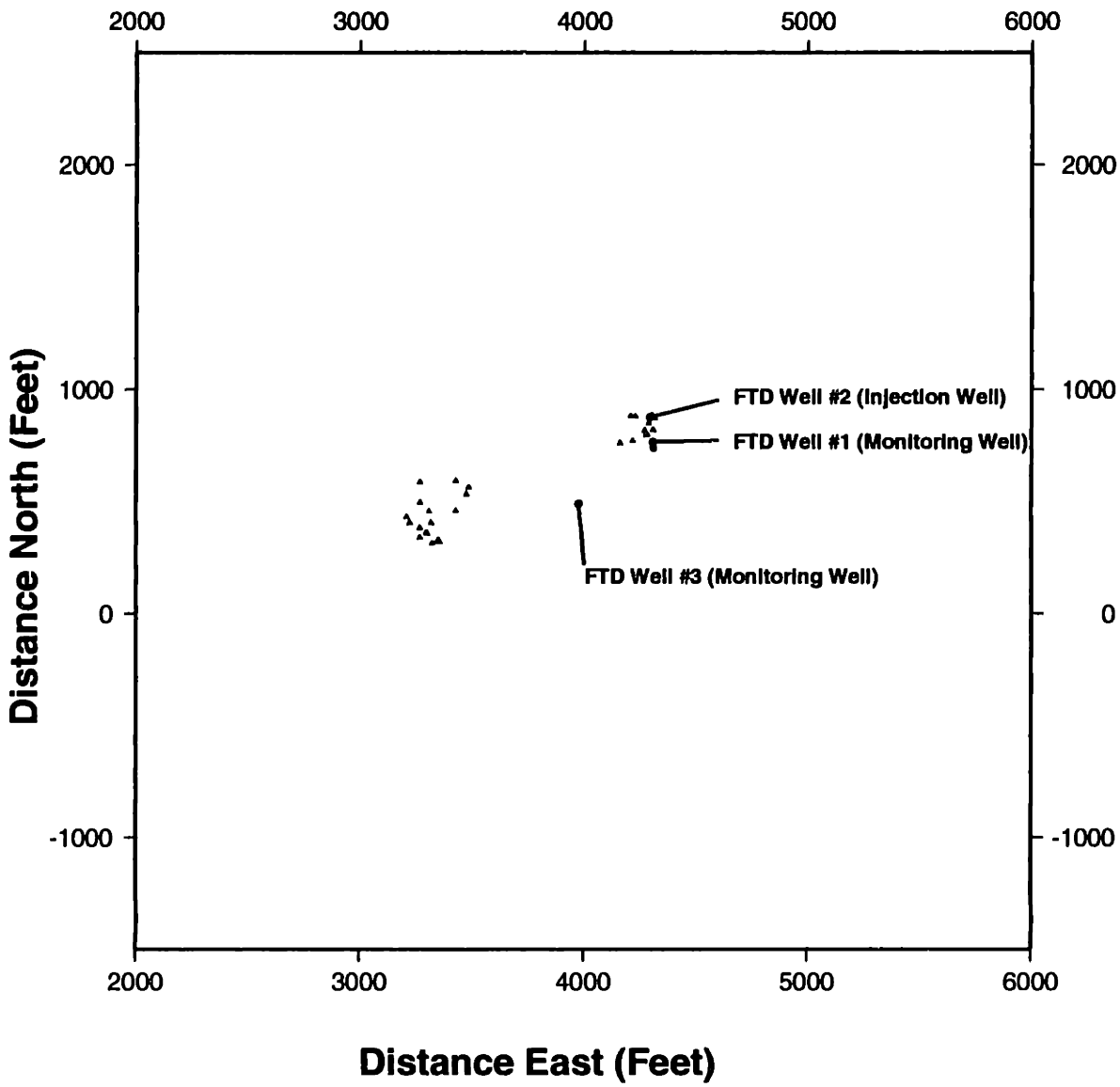

Figure 4-5: Areal view of cycle 2 hypocenters distribution for the DWTI hydraulic injection experiment calculated using least squares inversion with depths free to vary. Symbols indicate injection cycle in which the event occurred.

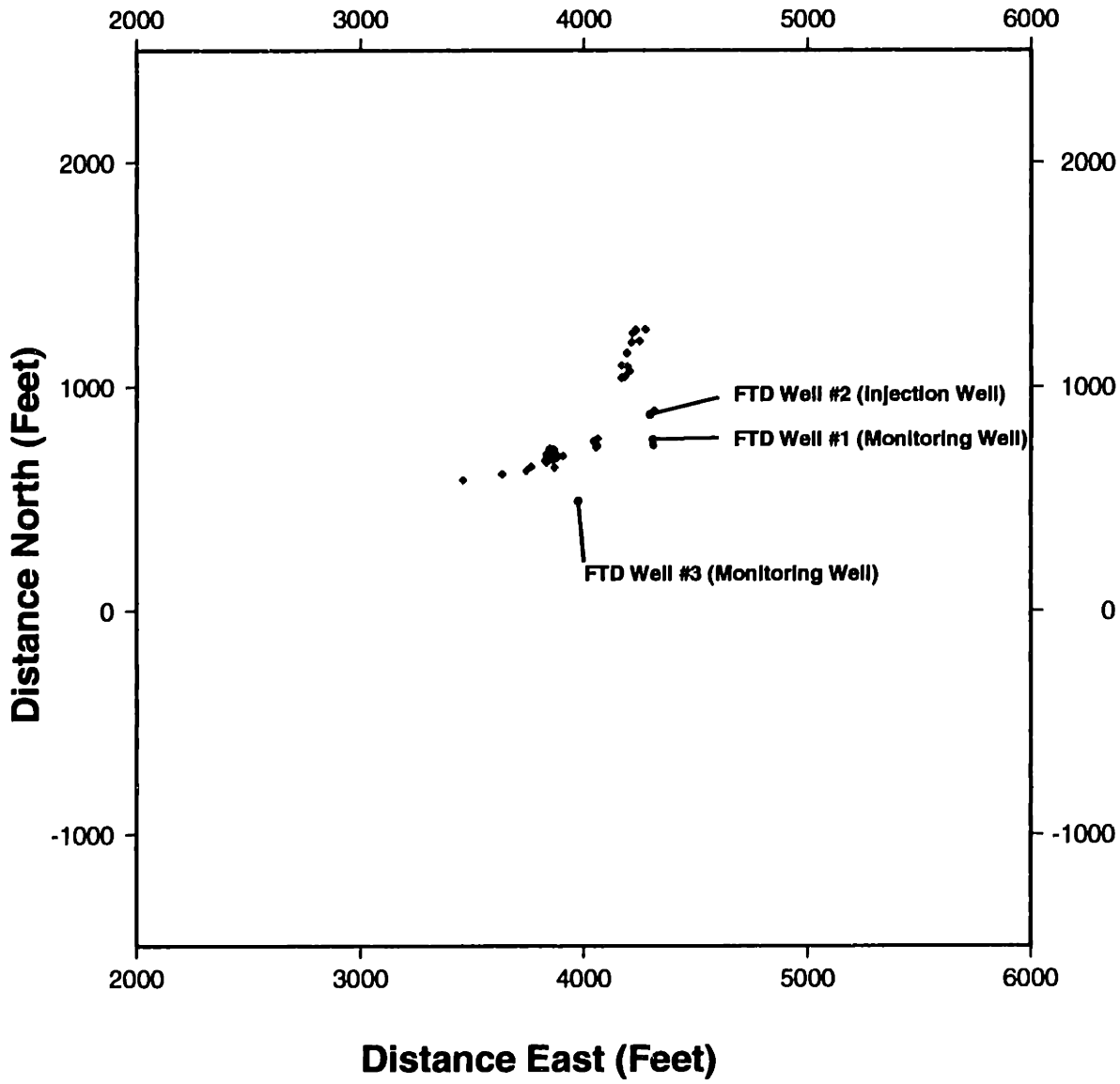

Figure 4-6: Areal view of cycle 3 hypocenters distribution for the DWTI hydraulic injection experiment calculated using least squares inversion with depths free to vary. Symbols indicate injection cycle in which the event occurred.

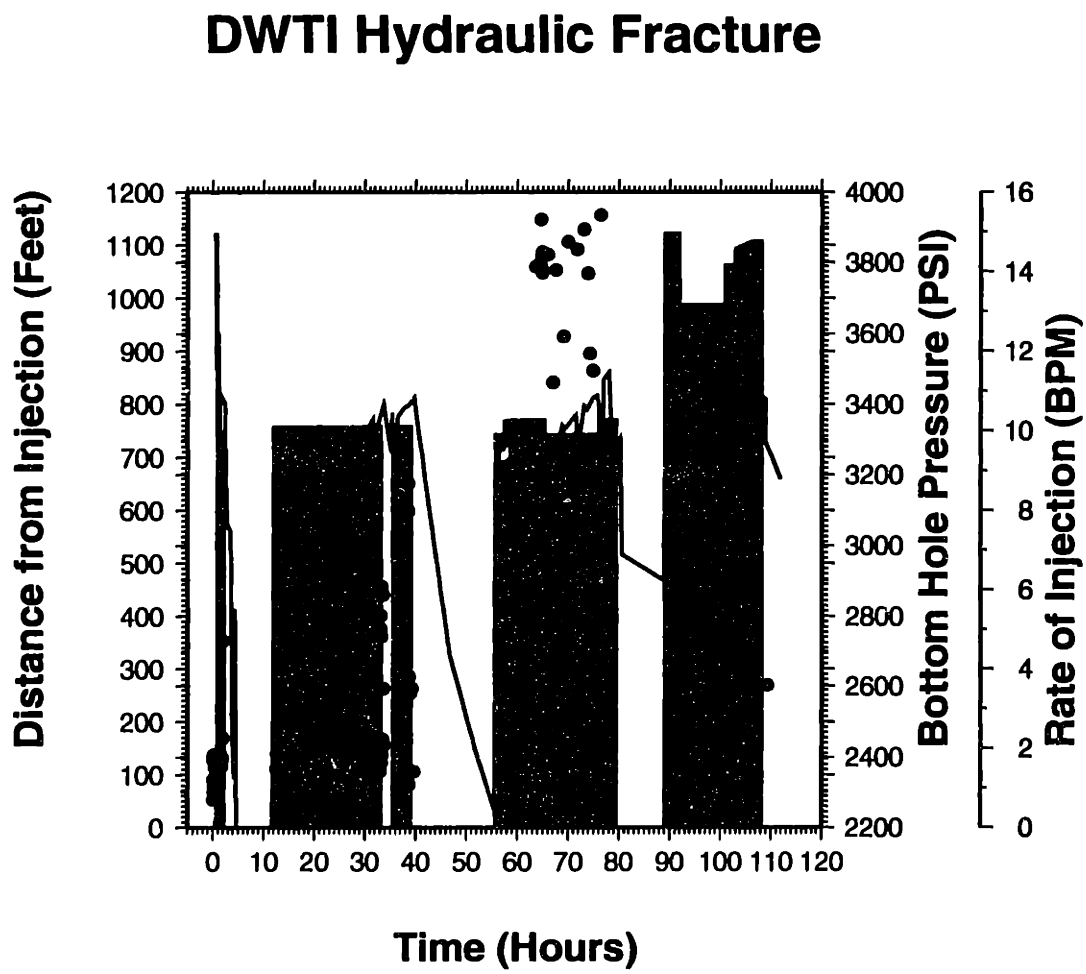

Figure 4-7: Event offset (from injector) versus time as compared to the injection parameters of bottom-hole pressure (heavy line) and injection rate (shaded areas)

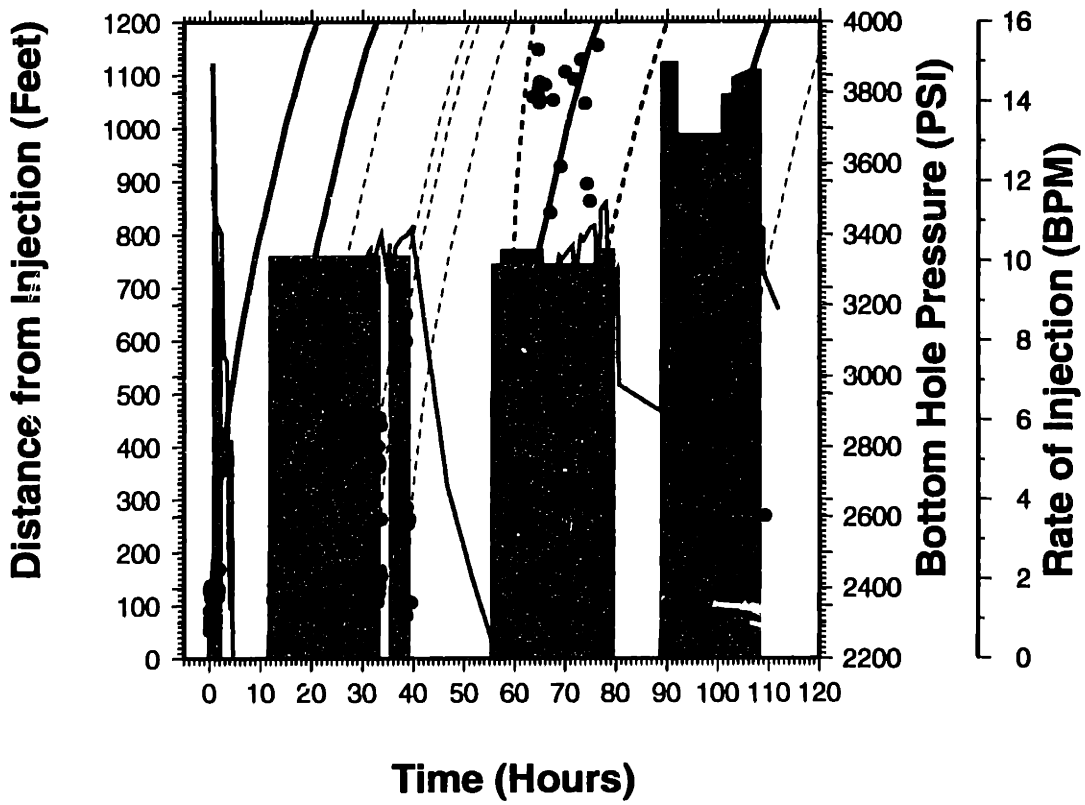

Figure 4-8: Event offset (from injector) versus time as compared to predicted fracture length as modeled by ARCO (curved solid and dashed lines). Solid lines represent predicted values from beginning of injection cycle. Dashed lines represent projected predictions for intercycle fracture extension.

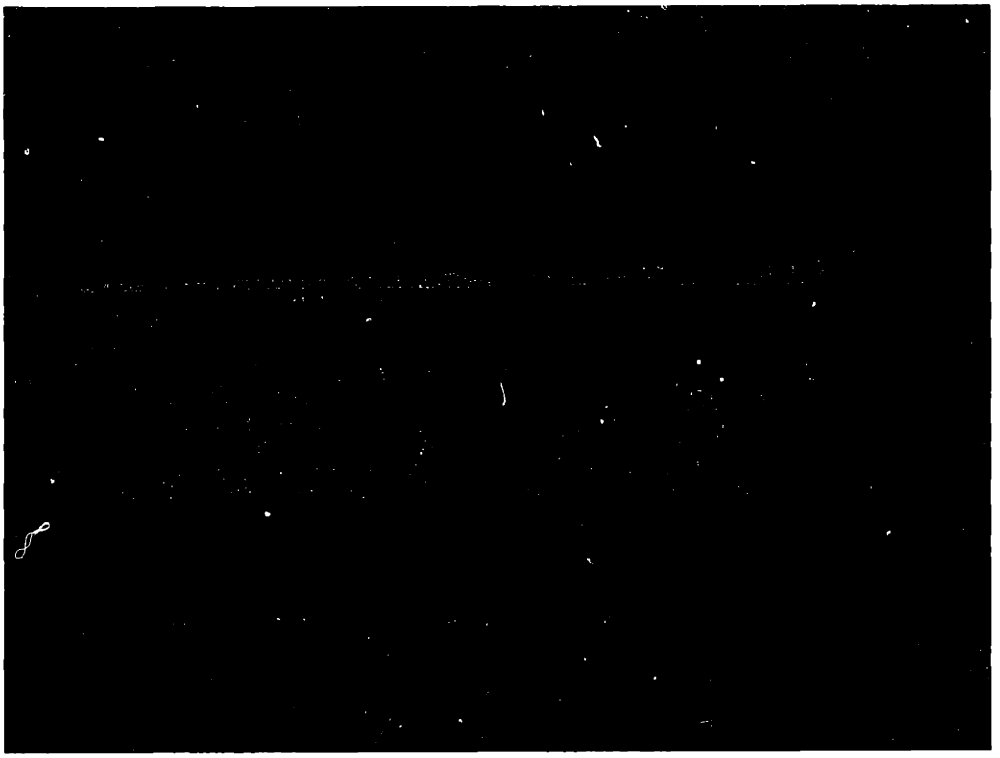

Figure 4-9: Cross-section looking due west showing location of the Larderello 1993 MEQ swarm with respect to the seismic reflector known as the "K" horizon. (Full cluster set of absolute locations.)

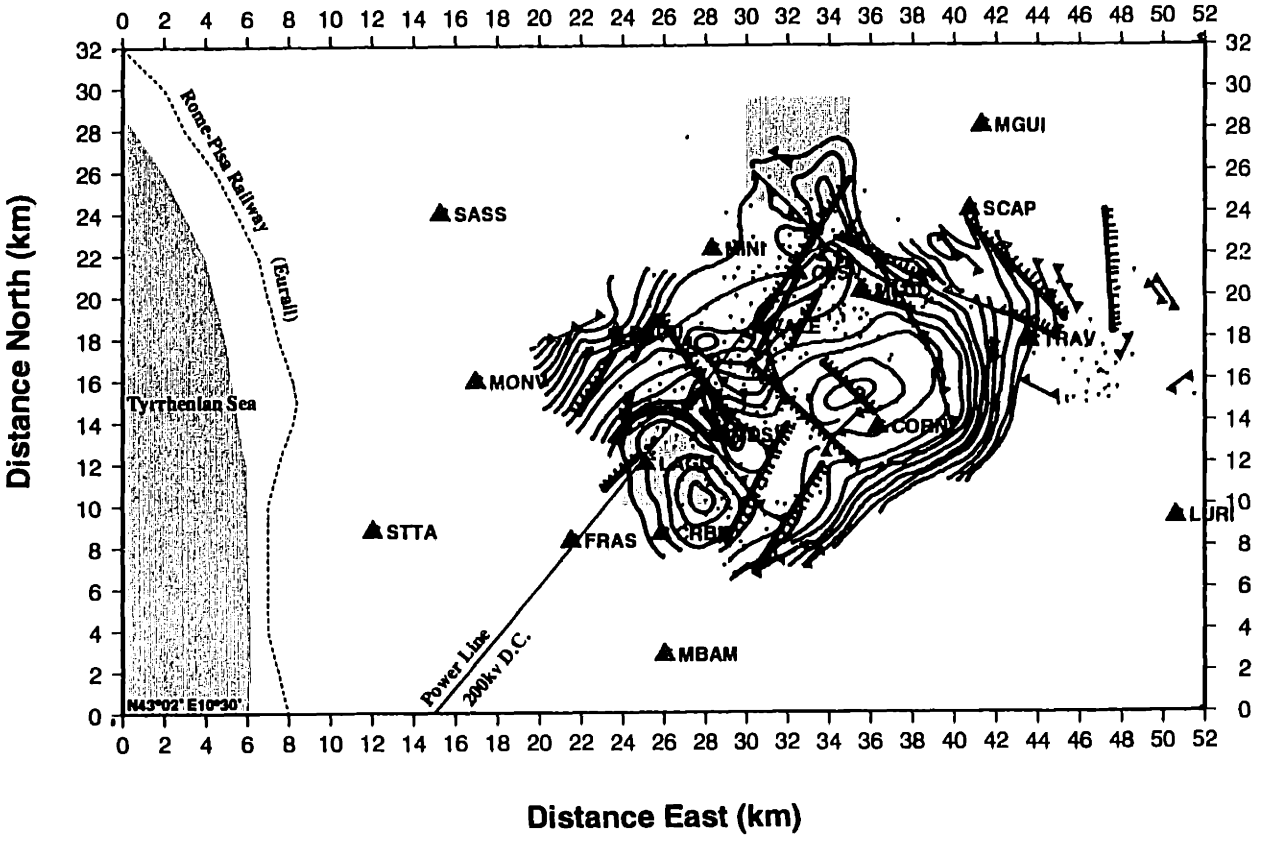

Figure 4-10: Local map of the Larderello Geothermal Field. Dots indicate geothermal wells. Hatchured lines indicate fault traces at depths intersecting the seismic "K" horizon. Shaded blocks indicate the two LGF MEQ study areas, the Larderello 1993 MEQ swarm area (north) and the LAGO MEQ study area (south). Triangles indicate the locations of seismographic stations (excluding the most northerly station, POMA, which is located just off the map north of the MINI and CLSV stations). Sources: (ENEL-Unita Nazionale Geotermica, 1988; Batini *et al.*, 1985c)

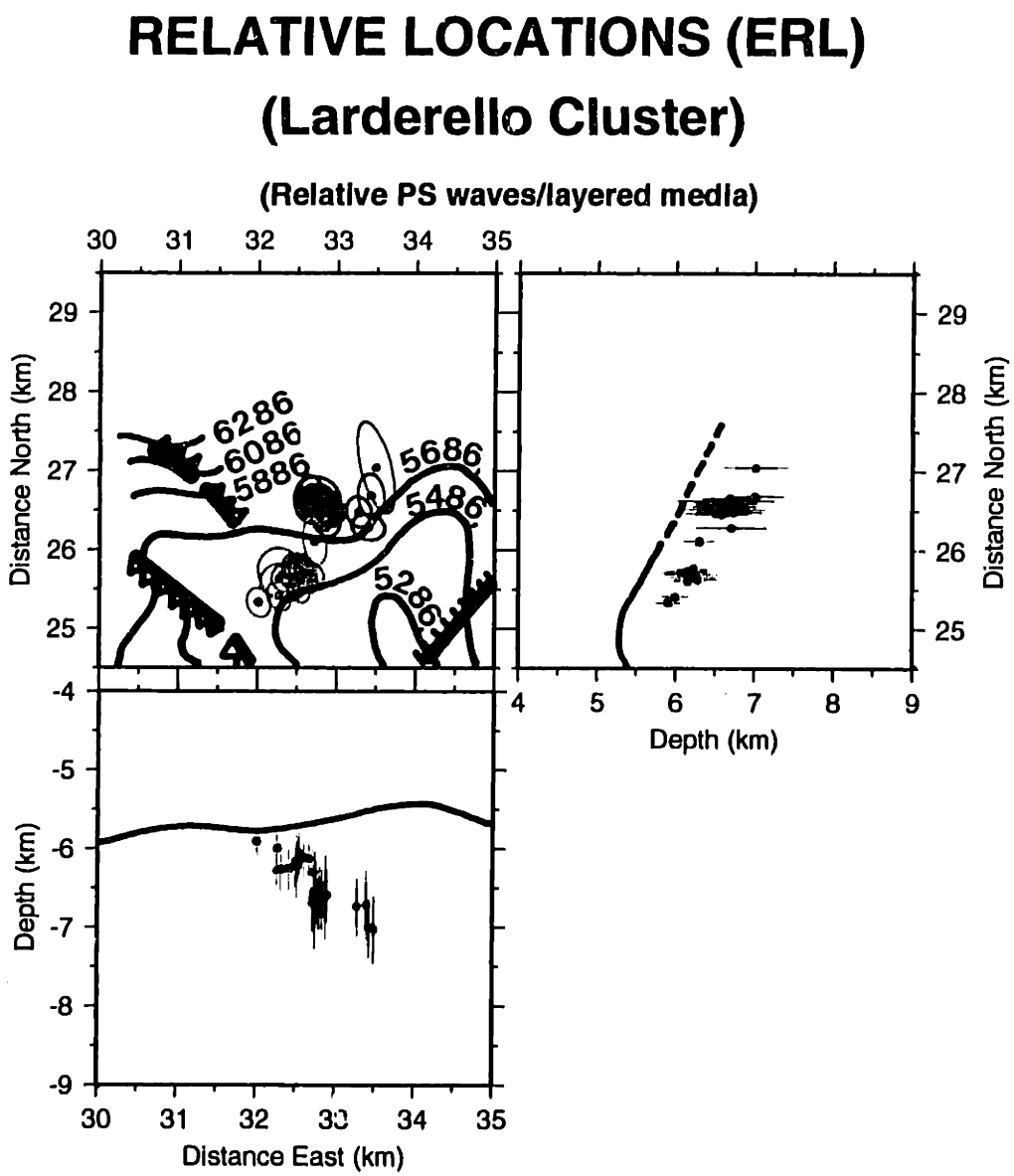

Figure 4-11: Hypocenter estimates (relative) and their 90 percent confidence regions for events of multiplets 0157 and 0174 in the Larderello 1993 MEQ swarm with "K" horizon and faults. Sources: (Batini *et al.*, 1985c; ENEL-Unita Nazionale Geotermica, 1988)

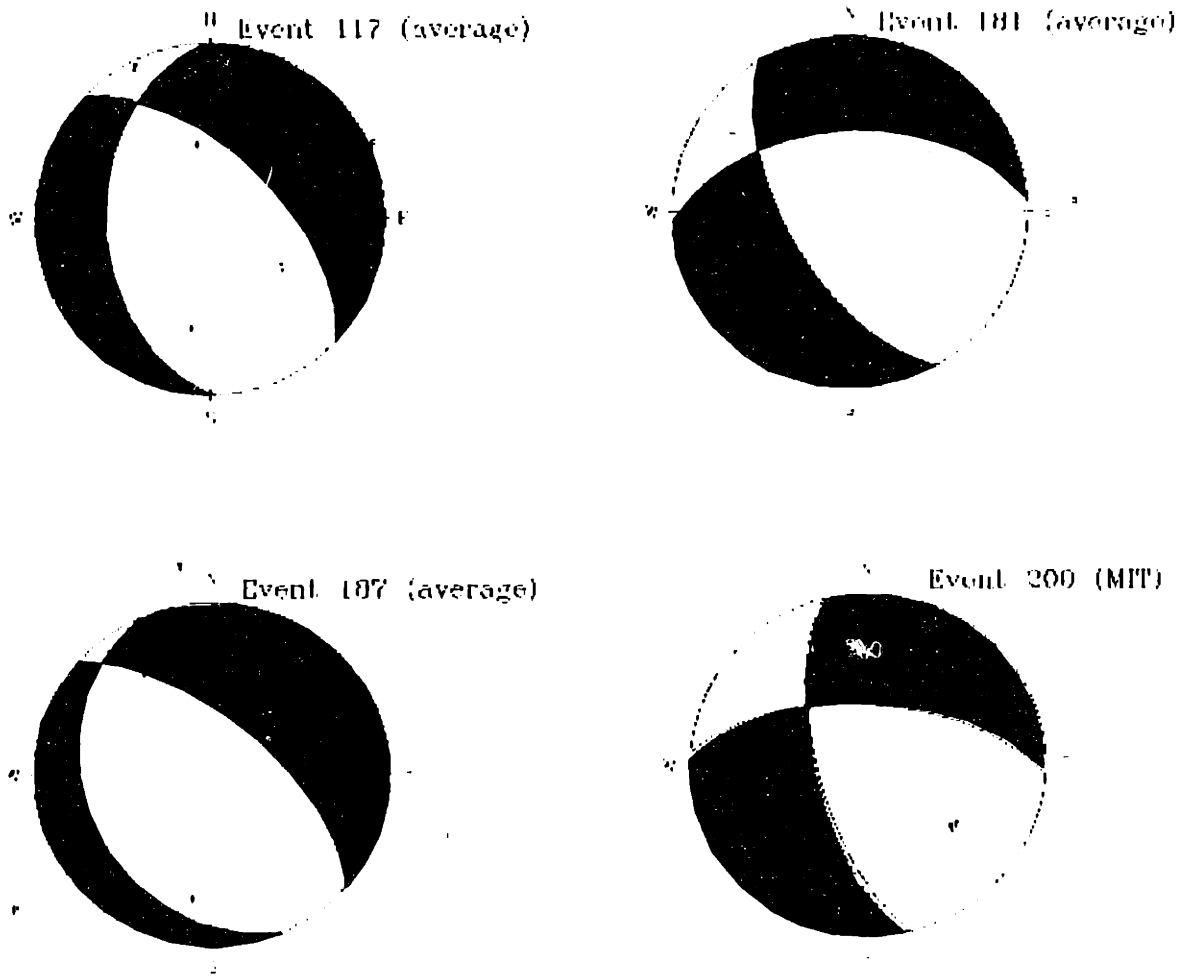

Figure 4-12: Focal mechanisms for four events. These examples are representative of the range of solutions found for 17 events from the Larderello 1993 swarm.

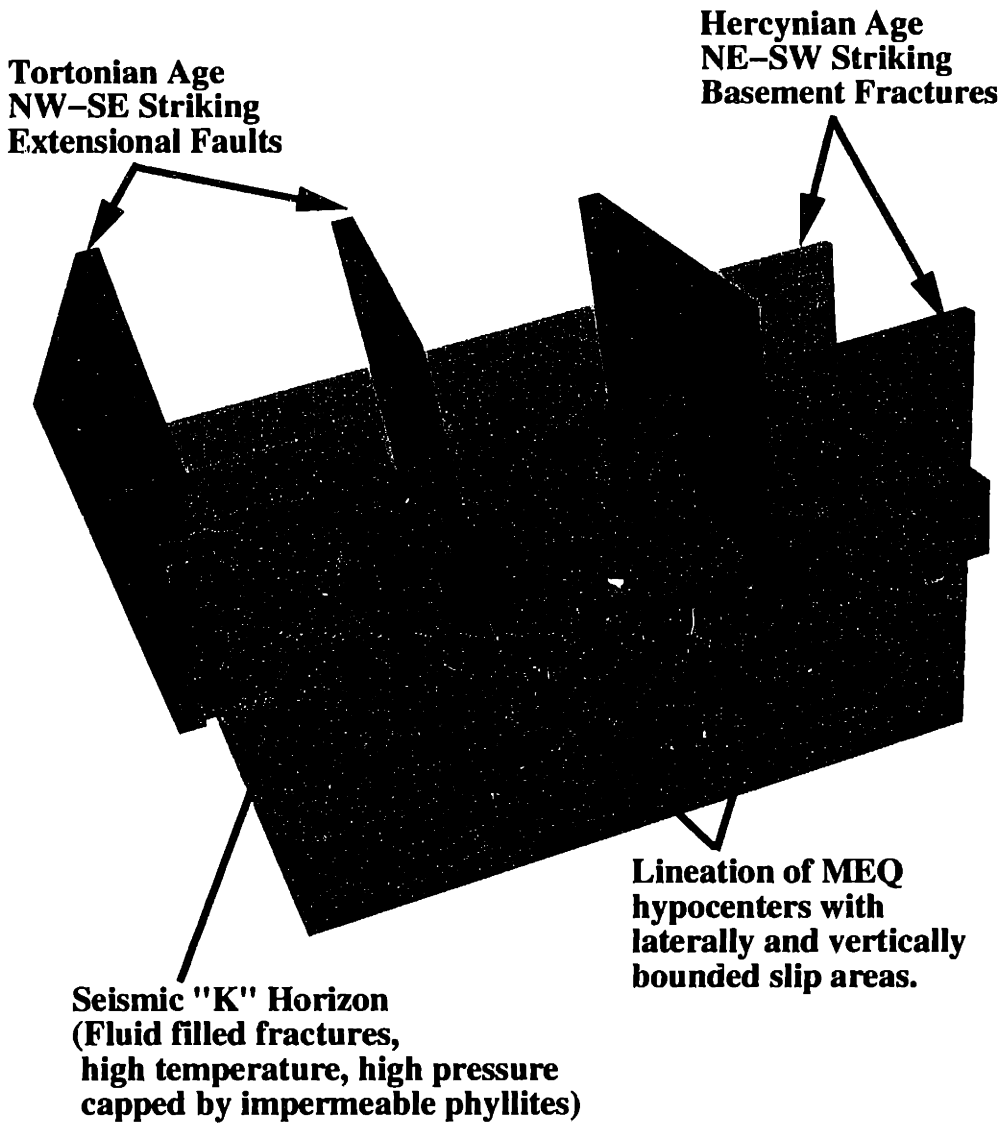

Figure 4-13: Schematic model illustrating the spatial relationships between the seismic "K" horizon, the Tortonian age extensional faults, the Hercynian age fractures and the MEQ hypocenters from the Larderello 1993 swarm.

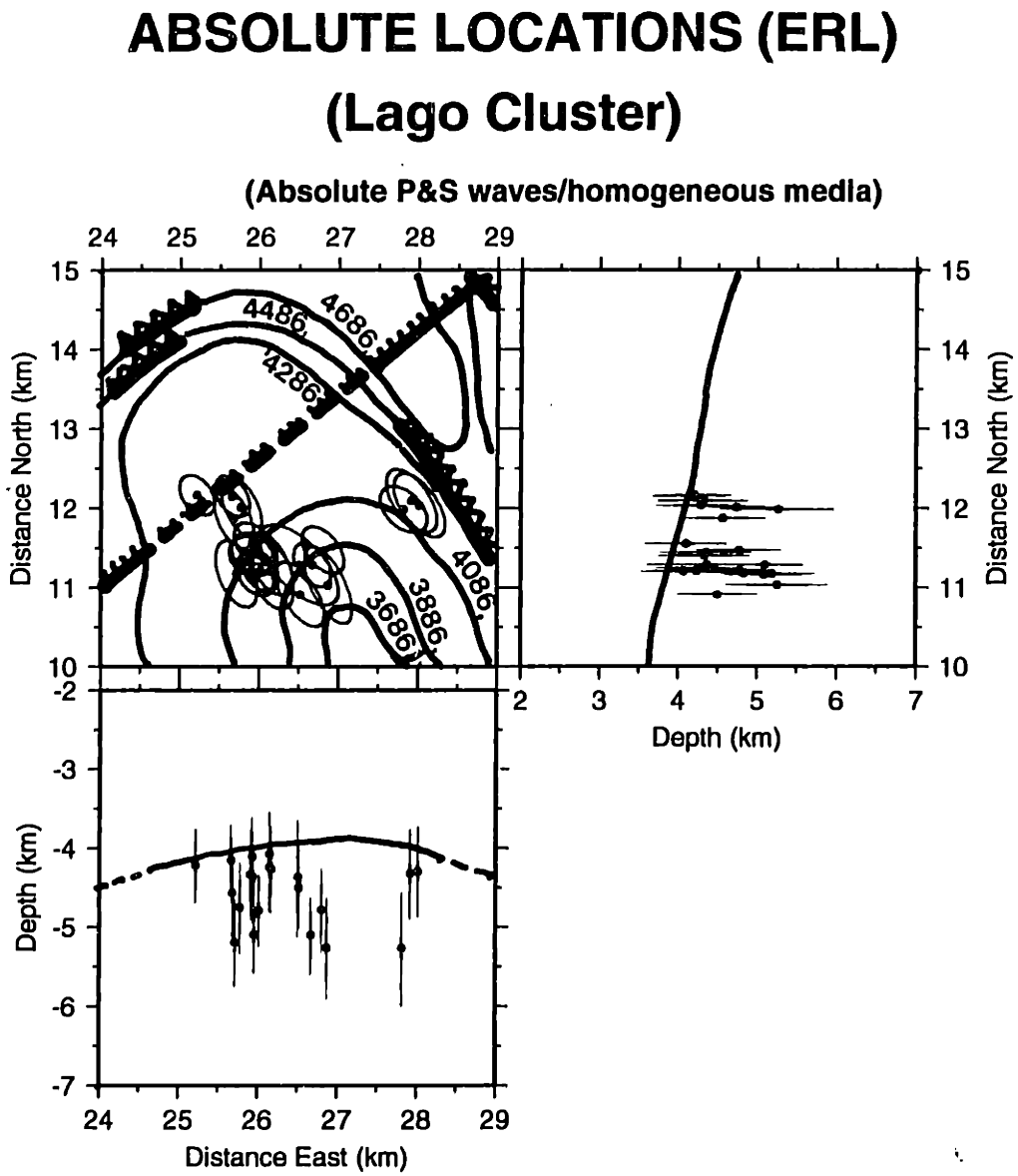

Figure 4-14: Hypocenter estimates (absolute) and their 90 percent confidence regions for events of the LAGO MEQ cluster compared to depth contours of the seismic "K" horizon, faults and fractures. "K" horizon sources: (ENEL-Unita Nazionale Geotermica, 1988)

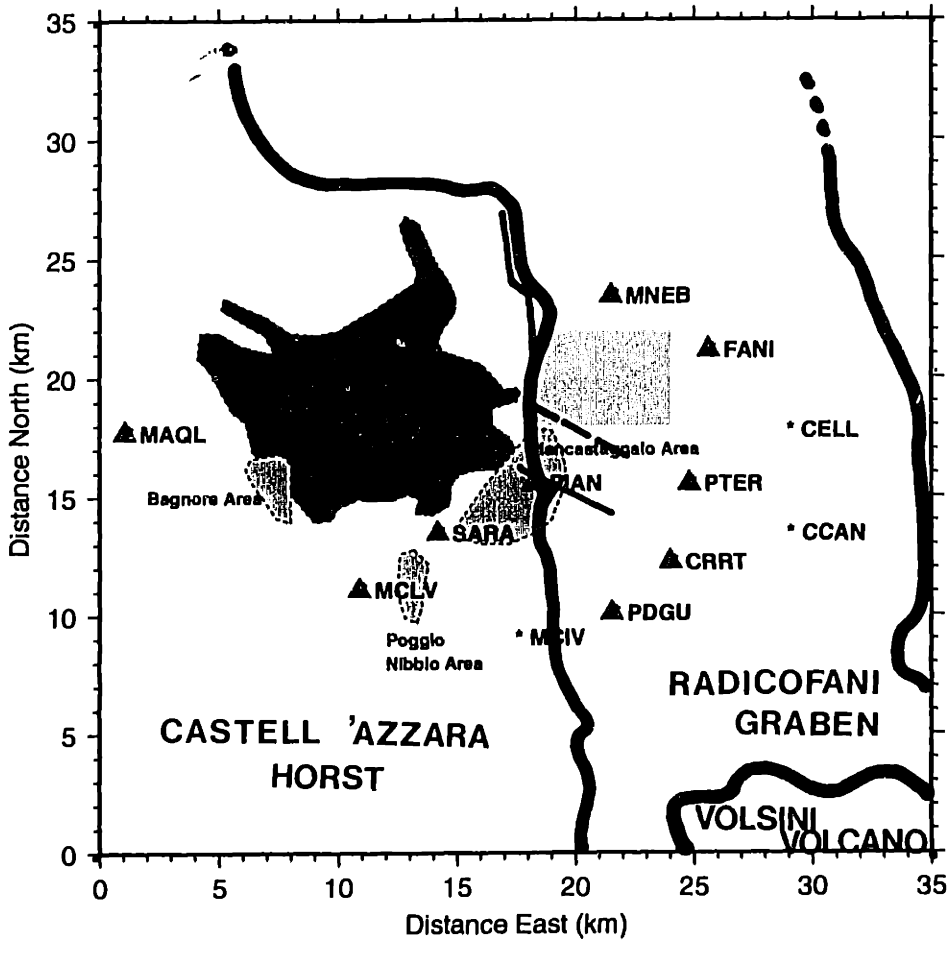

Figure 4-15: Map of the Monte Amiata geothermal field showing the Monte Amiata volcano, seismographic stations(triangles) and the three geothermal production areas. Sources for geology and fault placement, etc: (Gianelli *et al.*, 1996; Calamai *et al.*, 1970; Bertini *et al.*, 1985)

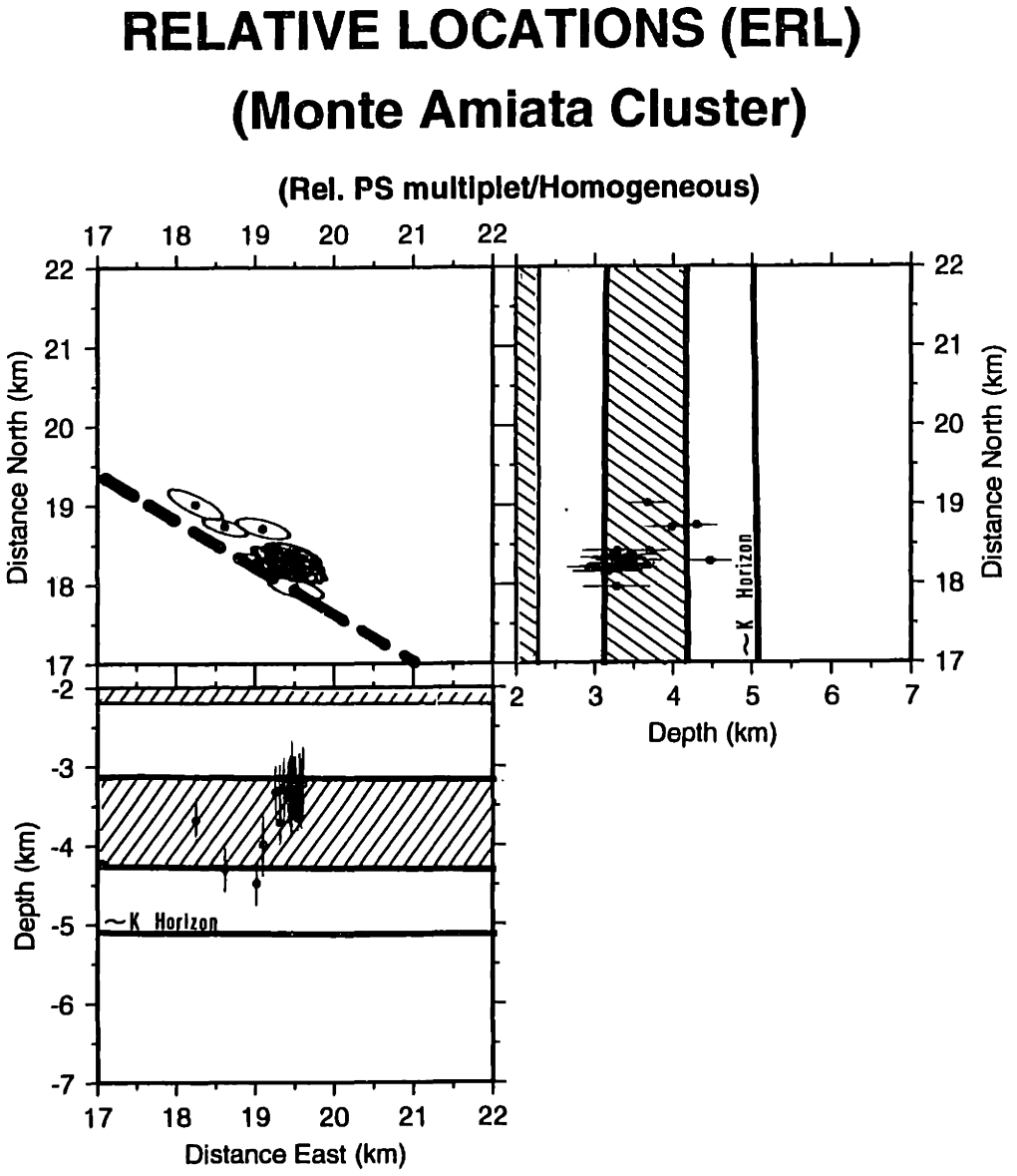

Figure 4-16: Hypocenter estimates (relative) and their 90 percent confidence regions for events of the 0119 multiplet in the Monte Amiata MEQ cluster compared with fault traces and depths of known fluid filled fracture zones. Sources: (Gianelli *et al.*, 1996; Calamai *et al.*, 1970; Bertini *et al.*, 1985)

Chapter 5

Discussion and Conclusions

5.1 Discussion

The results presented in this thesis suggest a number of future research directions. First, I feel that careful hypocenter estimation and focal mechanism studies for hydraulic fracture experiments like ARCO's DWTI demonstration project present unique opportunities to study the effects of fluid flow on fracture geometry under controlled conditions. Advances in our understanding of fracture asymmetry, fracture branching, fracture initiation offset from the wellbore, and multiple failure plane orientations may be obtainable through the careful design of MEQ monitoring experiments. These potential directions are also suggested in the results of many of the hypocenter distributions from Hot Dry Rock and petroleum application experiments identified in Chapter 1. Taken together, the results of these various hydraulic injection experiments represent a database of how reservoirs respond to high pressure fluids and, due to the diversity of conditions underwhich they were carried out, present an additional opportunity to compare the effects of variations in fracture geometry in different lithologies and tectonic environments.

In the realm of advancing real-time hypocenter modeling technologies, I feel that integration of focal mechanism analysis and spectrographic analysis would greatly expand the diagnostic

capabilities of the method. The results of these analyses could be compared to the expected results of fracture parameter simulators. This in-field comparision would give the fracture engineers quantitative information regarding the effectiveness of the stimulation process. Likewise, these results could be compared to other fracture diagnostic methods such as tilt-meter and radioactive tracer analysis.

The development of smaller and more environmentally tolerant sensors, together with a real-time hypocenter location code, would make a powerful and versatile diagnostic tool that could be applied in a wide variety of applications. Reservoirs with complex tectonic conditions and active onsite production operations would particularly benefit because on-going monitoring of fluid injection could provide active and continuous reservoir response information. The additional incorporation of high resolution relocation methods to the MEQ monitoring system would provide a necessary reduction in hypocenter uncertainties which may make analysis of fracture branching a realistic research goal.

5.2 Conclusions

In this thesis, I have demonstrated the application of "Real-time" hypocenter modeling for hydraulic fracture diagnostics and shown how high resolution hypocenter relocation can be used to improve our understanding of complex geothermal reservoir behaviors.

Analysis of ARCO's Deep Well Treatment and Injection waste simulation data indicated that the pumping of a viscous mixture of bentonite, water, and sand into the Lower Frio sand formation of east Texas produced a hydraulic fracture that exhibited strong spatial asymmetry. I showed that the clustered seismicity changed character over the course of the four injection cycles, which I proposed suggested a change in the mechanical processes inducing the seismicity. For the first two injection cycles, I showed that the spatial and temporal distribution of seismicity was well predicted by ARCO's hydraulic fracture simulators, but that the seismicity for the final two injections exhibited anomalous characteristics not well predicted by the simulators. I suggested that the phenomenon of "screenout", a

situation where the hydraulic fracture can be extended no further resulting in anomalous pressure behavior in different portions of the fracture, may be sufficient to cause failure on off-angle pre-existing cracks. I further suggested that, in the case of the Lower Frio sand, the direction of this secondary failure may have been predicted by core scale stress analyses.

Analysis of the three data sets from the geothermal fields of western Tuscany were completed using high resolution, relative event relocation methods. I showed that a swarm of events in 1993 near the northern boundary of the Larderello Geothermal field occurred just below an important regional seismic reflector known as the "'K" horizon and that the events were spatially distributed in a tight line plunging northeastward along the reflecting surface. I proposed that seismic slip on steeply dipping, northwest-southeast striking Tortonian age normal faults could account for the observed spatial distribution of hypocenters. I suggested that high pressure fluids circulating in the fracture zone of the "K" horizon may weaken localized patches of the faults, thereby facilitating slip commensurate with the regional NE-SW extensional stress regime. I further suggested that the seismicity may be laterally constrained to failure of limited areal extent on blocks delineated by the Tortonian age faults and NE-SW striking Hercynian age basement fractures. Due to the relative depth of this swarm, compared to reservoir depths, this cluster was attributed to the natural geodynamics of this complex area.

Analysis of a set of non-temporally correlated events from the LAGO seismogenic zone in the southern portion of the Larderello Geothermal field again showed a spatial association with the seismic "K" horizon. However, for this cluster, I showed that the events exhibited inconsistent waveform similarity. This dissimilarity, coupled with the non-temporal distribution of events over a ten year period and variation in focal mechanisms, suggested that the events in this cluster were not similar enough to qualify for relative event relocation by differential travel time analysis. However, I concluded that the results of the absolute hypocenter modeling showed some degree of spatial correlation with the "K" horizon and a lateral NW-SE linear distribution that correlated well with extensional faults associated with regional extension. Due to the correlation with known active structures capable of producing complex seismicity distributions and source mechanisms, I concluded that this

set of seismic events could not be unambiguously attributed to reinjection of condensate from the geothermal power plants. I further suggested that the addition of detailed pumping information paired with an analysis of localized seismicity onsets would complement the hypocenter location and fault plane solution results, thereby improving the likelihood that the seismicity can be attributed to an appropriate source process.

Finally, I reported the results of the relative event relocation for a 1997 swarm of events from the Monte Amiata geothermal field. I showed that the hypocenters are located very near a northwest-southeast striking fault at depths within the deeper of two actively producing fracture zones the Piancastagnaio field. As with the seismicity analyzed from the LAGO area of the Larderello field, I concluded that the proximity of the cluster to geologic structures capable of producing the observed event characteristics prevented attributing the events to reinjection of condensate, but noted that additional work regarding individual event focal mechanisms, paired with detailed reinjection data may help to differentiate induced events from tectonic events.

The results reported in this thesis support the conclusion that microseismicity monitoring is an effective active production technology. The additional capability of real-time hydraulic fracture diagnostics expands the method's applicability from its traditional role as a regional geodynamic indicator to a field operations tool for enhancing resource recovery. High resolution relative event relocation reduces the uncertainty in designating a probable cause to natural tectonic and volcanic source processes, thereby reducing the number of anomalous events potentially attributable to man-made causes. Combining relative event relocation with real-time computing, operational pumping data and, eventually, high temprature and microelectronic sensor technology would greatly enhance our understanding of how fluid flow affects fracturing in reservoirs and naturally active seismogenic zones.

Appendix A

Review of the Natural Resources and Geology of Texas and the Gulf of Mexico Basin

A.1 Introduction

The Gulf of Mexico (including its adjacent basin margins) is rich in natural resources. Most noted for its oil and natural gas, it also contains economically significant non-hydrocarbon resources such as lignite, coal, deposits of phosphor-bearing marine sediments, sulfer, uranium, geopressured-geothermal energy and groundwater (Nehring, 1991; Riggs *et al.*, 1991; Sharp Jr. *et al.*, 1991). The richness of these resources and the complexity of the geologic environment that developed and controls them is attested to by the volumes of research published on the subject, both in book form and as peer reviewed journal articles. Much of the work completed thus far reflects the work of geologists and geophysicists representing the exploration interests of the petroleum industry, either directly, or indirectly through the Bureau of Economic Geology at the University of Texas at Austin, the Geological Society of America, and/or the Gulf Coast Association of Geological Societies.

This appendix is provided as a supplement to the main text for those readers unfamiliar with the structure and evolution of the Texas gulf coast and the associated sedmentary formations penetrated during ARCO's DWTI experiment. I will motivate the review with a brief introduction to the hydrocarbon resources for the basin, in known ultimate recovery (KUR), which will lead us to a generalized overview of the geologic history of the basin as a whole. The review will continue with a brief look at the structure of the sedimentary systems, which include the Lower Frio Sands and Shales, and conclude with a recap of the energy resources which may, ultimately, be recovered more completely with the aid of production enhancement technologies such as hydraulic fracturing.

A.2 Introduction to the Natural Resources of the Texas Gulf Coast

Oil and natural gas, the two most abundant natural resources produced out of the Gulf of Mexico, have defined a century of Texas history beginning before the turn of the century when oil seeps provided a small (but alluring) supply of oil which was principally used in the production of kerosene. Exploration and production of Gulf hydrocarbons was to grow at a staggering rate during the twentieth century, eventually revealing the Gulf of Mexico as one of the world's largest (in KUR) petroleum provinces rivaling even the superprovinces of the Middle-east and Western Siberia (Nehring, 1991). As the volume of oil and gas in the gulf became known, the approach to recovering those resources evolved to make maximum use of all available knowledge and technology. Nehring (1991) divides the exploration history of the gulf into four periods. From 1901 to 1922, discoveries were made predominantly on the drilling of direct evidence such as oil seeps and shortly thereafter, on drilling the crests of small "knobs", and the surface expression of the towering salt dome upon which the oil would pool (Crutchfield, 1996; Salvador, 1991a; Nehring, 1991). This period was epitomized by the dramatic events near Beaumont in the South Eastern Texas Gulf Coast when the drilling of one such "knob" (named "Spindletop ") produced the first "gusher" well and, with a 70,000-100,000 barrel per day (bpd) production rate. This event nearly instantaneously doubled the entire US oil production and increased the world's oil production by 20 percent

(Crutchfield, 1996).

The second period of Texas oil production (1928-1941), according to Nehring (1991), produced discoveries of 21 giant fields of the Gulf Coast margins, primarily by drilling the major salt structures, salt-core anticlines, and in the Texas coastal areas by drilling the fault-controlled structures that characterize this subprovince. These discoveries were made possible by the advent of geophysical techniques such as gravimetry and seismic refraction.

As the onshore fields became known and discoveries began to dwindle, exploration moved to the shallow offshore environments during the period from 1948 to 1958. Again, discoveries increased delineating 10 giant fields. The most recent change in exploration in the Gulf is described by Nehring as beginning in 1970 when technological advances in deepwater drilling allowed movement toward deep-offshore frontiers. This phase of exploration is ongoing (Nehring, 1991).

The Gulf Coast, as a whole, produces 9 percent of the world's hydrocarbon liquids and 11 percent of the natural gas. In 1987, that percentage equalled approximately 222.5 billion barrels of oil equivalents (BOE). This does not include the oil discovered and produced since 1987, particularly in the deep offshore fields. New technologies of horizontal drilling and enhanced oil recovery techniques also adds to the production. Much of this oil is produced from three of the 13 super provinces (known ultimate recoveries between 25 and 100 billion BOE), and four major provinces (including the SuperGiant Field in the East Texas Province). The super provinces, the Gulf Coast Onshore, the Gulf Coast Offshore, and Campeche, are three of the 15 known super provinces in the world (Nehring, 1991).

The Frio Formation, the target for ARCO's Deep Well Treatment and Injection (DWTI) demonstration project, is one of the most important petroleum producing intervals in the Paleogene sedimentary sequences in the Texas Onshore Gulf Coast Province, producing approximately 15 percent of the Gulf's total recovery. The Frio formation, as it is represented in the northeastern portion of the coastal region, is characterized by petroleum reservoirs associated with salt structures and fault controlled traps (Nehring, 1991; Galloway *et al.*,

1982).

The petroleum resources in the Gulf provinces differ in character from many of the other world's sources. The total volume is disseminated among a very large number of stratigraphic traps and individual fields, rather than being located in a few giant or supergiant fields. This characteristic of the Gulf's fields increases the degree of complexity involved in maintaining and sustaining adequate exploration and recovery rates. Additionally, the geologic (particularly sedimentary) characteristics in the Onshore Gulf Coast producing strata adds complexity to the interpretation of the local stress field. This subsequently, impacts the interpretation of hydraulic fracture diagnostic methods such as microseismic monitoring. The remainder of this appendix focuses on describing the general development and evolution of the Gulf of Mexico Basin as a whole and an overview of the sedimentary formations and related faulting of the Lower Frio sand and shale sequences.

A.3 Review of the Geology and Geodynamics of the Gulf of Mexico Basin

The descriptions that follow are derived from a number of excellent summaries of the development and evolution of Texas, Florida, Mexico, and the Gulf of Mexico, specifically, the detailed collection of articles in Volume J of "The Gulf of Mexico Basin: The Geology of North America", published by The Geological Society of America, edited by Amos Salvador (1991) and the Report of Investigations No.122 of the Bureau of Economic Geology entitled "Frio Formation of the Texas Gulf Coast Basin-Depositional Systems, Structural Framework, and Hydrocarbon Origin, Migration, Distribution, and Exploration Potential", by William E. Galloway, David K Hobday and Kinji Magara (1982). Because this thesis focuses on the geophysical details of microseismic monitoring which, in turn (for interpretational purposes), relies on a strong understanding of the present and historical stress conditions in the vicinity of the fracture, I have depended on the information available in these and various other geological references. The information presented here is my own encapsulation of their fine work and is offered only as a general informational overview.

Although care has been taken in the development of this summary, any omissions or misinterpretations of the original works are my own. For more information, the interested reader is encouraged to refer directly to the original cited works for specific and particular details.

Reconstruction of the Pre-Triassic Plate Configurations and Mesozoic Evolution of the Crustual Structure of the Gulf

The Gulf of Mexico Basin (See Figure A-1) had its beginnings during the Late Triassic time (208-230 ma) when the supercontinent of Pangea was still intact. Late Paleozoic tectonic elements surrounded the future Gulf and played a role in defining the character of the forming basin. Suture zones and associated mountain ranges (remnant structures of a previous opening and closing of the proto-Atlantic ocean) delineate the future northern boundary of the Gulf and are represented in Figure A-1 by the Ouachita Orogenic Belt. Portions of this paleozoic deformed belt are visible in a limited number of outcrops in the central portion of Texas westward from the escarpments that divide the coastal region from the central hill country (including various uplifts, such as the Llano (shown) and the Marathon (not shown)) (Spearing, 1991; Salvador, 1991b).

During Late Triassic-Early Jurassic time rifting of the continental crust began again south of the Ouachita Mountains, although Sawyer, Buffler and Pilger (1991) suggest that it was not until middle Jurassic time (150-170 ma) that significant crustal thinning began. Crustal extension separated the North American from the African plates along a divergent boundary with a roughly east-northeast/west-southwest strike (Salvador, 1991b). As the African Plate (which included present South America at this time) moved away from the North American Plate, an embayment formed that eventually opened to the proto-Pacific Ocean. This opening allowed the influx of sea water into the proto-gulf basin, where it experienced a series of evaporative episodes forming the very thick "Louann Salt" at the base of the Gulf coast sedimentary succession (Spearing, 1991; Salvador, 1991b).

According to Salvador (1991), the period of crustal thinning extended over a period of

50 million years from Late Triassic and Early-Middle Jurassic times. However, the final extension and subsidence occurred quickly ($\sim$ 5 million years) during Late Jurassic time. During this time the Yucatan Platform, originally connected to the North American Plate, moved south and rotated counter-clockwise toward its current position east of Mexico. Similarly, the Florida Platform (whose rock types suggest an African origin) was sutured to the North American Plate where it now delineates the eastern boundary of the present Gulf Basin (Salvador, 1991b).

Sometime between Late Jurassic and Early Cretaceous times, the spreading slowed in the vicinity of the Gulf and relocated eastward to its present location in the mid-Atlantic. The total crustal extension has been estimated at 500-520 km and led to formation of oceanic crust along the axis of the Gulf (Salvador, 1991b).

The western edge of the Basin is defined by the Sierra Madre Oriental orogenic belt and the associated compressional features in easterm Mexico generated during Late Cretaceous and Early Tertiary time (80-55 ma) (Ewing, 1991). During the same time period, compression formed the Laramide orogeny and raised the Rocky Mountains in the western United States. This event set the stage for the next phase of development of the Gulf of Mexico, specifically, the subsidence of the basin due to the tremendous weight of sediments being shed from the Rocky Mountains into the Gulf during Cenozoic time (Spearing, 1991; Salvador, 1991b).

A.3.1 Sedimentary Structures of the Texas Gulf Coast

The Cenozoic deposition of material from the Rocky mountains into the Gulf from the north and northwest produced a prograding coastline (Gulfward moving) which caused subsidence of the crust. The compaction of prograded terrigenous clastic sediments (particle size fining gulfward) created a density inversion with the Louann Salt and evaporite deposits, causing them to migrate upward and laterally to interfinger with the Cenozoic sedimentary layers forming the famous Gulf Coast salt diapirs, salt-core anticlines, salt dome controlled structural hydrocarbon traps (Salvador, 1991b), and allochthonous salt sheets.

Deposition of material eroded from the Rocky Mountains into the Gulf from Early Cenozoic time to the present has produced sediment thicknesses exceeding 15,000 feet (Galloway *et al.*, 1982). Rapid variations in sea level and constant shifting of river beds, led to complex lateral changes in the sedimentary facies. This complexity impacts the interpretation of hydrocarbon and geopressured geothermal reservoir potential due to the heterogeneity of porosity, permeability, hydraulic conductivity, transmisivity and other critical reservoir controlling parameters. Indeed, a large volume of the literature available on geologic structures in the Gulf Coast is dedicated to describing the depositional environments controlling these factors and delineating the major stratigraphic units (MSUs) in the area.

For instance, Salvador (1991) describes the depositional environment of the northern and northwestern province (Texas Gulf Coast, onshore and offshore) as beginning in the Early Cretaceous (and continuing into the Late Cretaceous) with the deposition of the Del Rio and Grayson shale layer which, due to its laterally homogeneity and consistency of thickness, is interpreted to have formed on a fairly shallow marine shelf during a reasonably stable period. Various periods of coastal transgression followed affecting the already present Mississippi embayment, producing changes in the depositional patterns and at times reconnecting the Gulf to the Pacific via the Western Mexico embayment (Salvador, 1991b).

Variations in sea level and uplifting in parts of the Basin margins eventually produced a gulf coastal province that Galloway, Hobday and Magara (1982) describe as being defined by an undulating series of arches and embayments. Three important embayments (and/or basins), specifically, the Mississippi Embayment, the East Texas Basin, and the Rio Grande Embayment are indicated in Figure A-1. These depressions are separated by structural highs, however, we shall focus primarily on the sedimentary features associated with the embayments and sub-basins.

Galloway, Hobday and Margara (1982) divide the Texas portion of the Gulf Coast succession into seven principal depositional systems (See Figure A-2). They suggest that the deposition of sediments into the Gulf was accomplished much as it is today, via numerous rivers and streams that cross the coastal plains. They show two deltaic systems, the

Houston Delta System in the north and the Norias Delta System in the South, located near the present-day Rio Grande Embayment. The deltas were separated by one inter-deltaic embayment.

Inland of the deltaic environments are two Fluvial depositional systems (the Chita-Corrigan Fluvial system northwest of the Houston Delta, and the Gueydon Fluvial System west of the Norias Delta). Whereas the character of the sedimentation in the fluvial systems varies from a mixed-load system (Chita-Corrigan) in the north to a bed-load system (Gueydon) in the south, both the deltaic systems are characterized by indications of several smaller, repetitive and laterally overlapping deltas comprising the larger deltaic environments (Galloway *et al.*, 1982). The depositional environments between the two fluvial/deltaic regions are assigned to streamplain systems and Barrier/streamplain systems. In addition to the Greta/Carancahua Barrier/Streamplain system to the Southwest of the Houston Delta another Streamplain/Barrier System, referred to as the "Buna" system, is located to the north-northeast of the Houston delta (Galloway *et al.*, 1982).

The Frio Formation, of Oligocene-Miocene age, consistes of a wedge of the prograding clastic sediments. The term "wedge" refers to the shape taken by the sedimentary deposits that thicken gulfward along the steepest part of the basin margin and thins farther south along the deepest part of the horizontal gulf bottom. Sediments deposited in this way often develop high-angle, listric "Growth" faults (faults that are concave upward and flatten to horizontal downward). These faults are formed when the saturated sediment settling out on the steeply dipping edge of the prograded sub-marine shelf become unstable and "slump" down the slope to a more stable position (Bates and Jackson, 1984; Ewing, 1991). Growth faults, like the sedimentary formations that they crosscut, exhibit a gulfward younging direction and often are reduced in numbers and abundance farther offshore. This feature limits the gulfward extent of shallow, growth fault controlled hydrocarbon traps and possible petroleum exploration targets.

The Lower Frio Sand, which served as the target formation for the DWTI injection experiment, is one member of the Frio Formation (Galloway *et al.*, 1982). The Frio Formation, as

a whole, is a major stratigraphic unit (MSU) that is identifiable along the entire length of the Texas Gulf Coast and is crosscut by numerous growth faults and salt diapirs, particularly in the area of the North Texas gulf coast and East Texas Embayment (Galloway *et al.*, 1982). The Lower Frio Sand, as represented in Jasper County at the DWTI site, has been described as a laterally continous, high porosity (30-35 percent), high permeability (1-3 darcy) stratigraphic unit that is bounded above and below by shale layers of considerable thickness (Atlantic Richfield Corporation, 1994).

A.4 Hydrocarbon and Geopressured Geothermal Resources

Although the Frio Sand is one of the major hydrocarbon producing formations in the Texas Gulf coast, there is evidence to suggest that pressure and temperature conditions within the Frio may also meet the requirements for production of geopressured-geothermal energy (Riggs *et al.*, 1991). Specifically, pore fluids trapped within a formation during rapid subsidence and compaction (as described above) partially support the weight of the sedimentary column above, causing overpressuring of the formation. The pressurized fluids are prevented from escaping by offset and sealed growth faults and/or impermeable sedimentary stratigraphic confining layers. Several of the Texas Gulf Coast Sand/Shale formations appear to meet the temperature and pressure gradient criteria for future use as a low-temperature geothermal resource (Riggs *et al.*, 1991).

The interpretation of the spatial and temporal distribution of microseismic events produced during hydraulic fracturing of the Frio sand has implications beyond waste solid injection, which was the intended purpose of the DWTI demonstration. Understanding the fracture behavior of this formation has the potential of not only providing a viable disposal technology but also of improving hydrocarbon and geopressured-geothermal reservoir production.

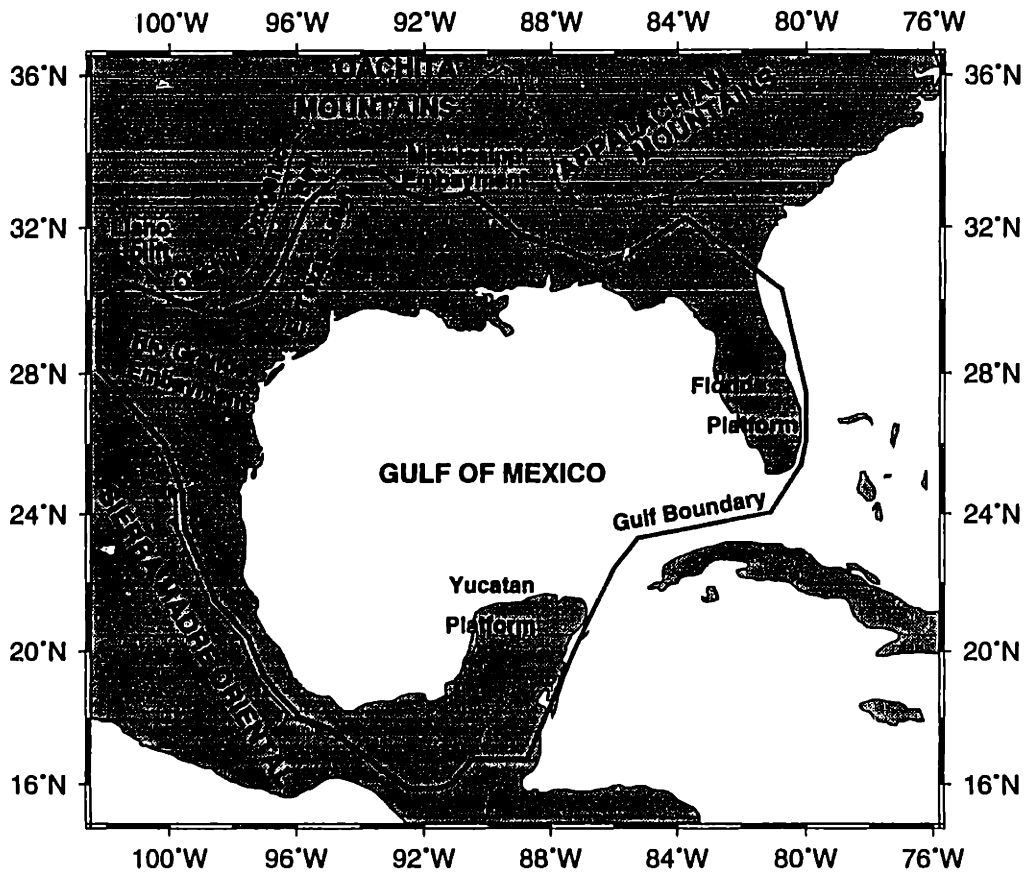

Figure A-1: Regional map of the Gulf of Mexico Basin and its boundaries. This figure was adapted from: (Salvador, 1991a; Spearing, 1991).

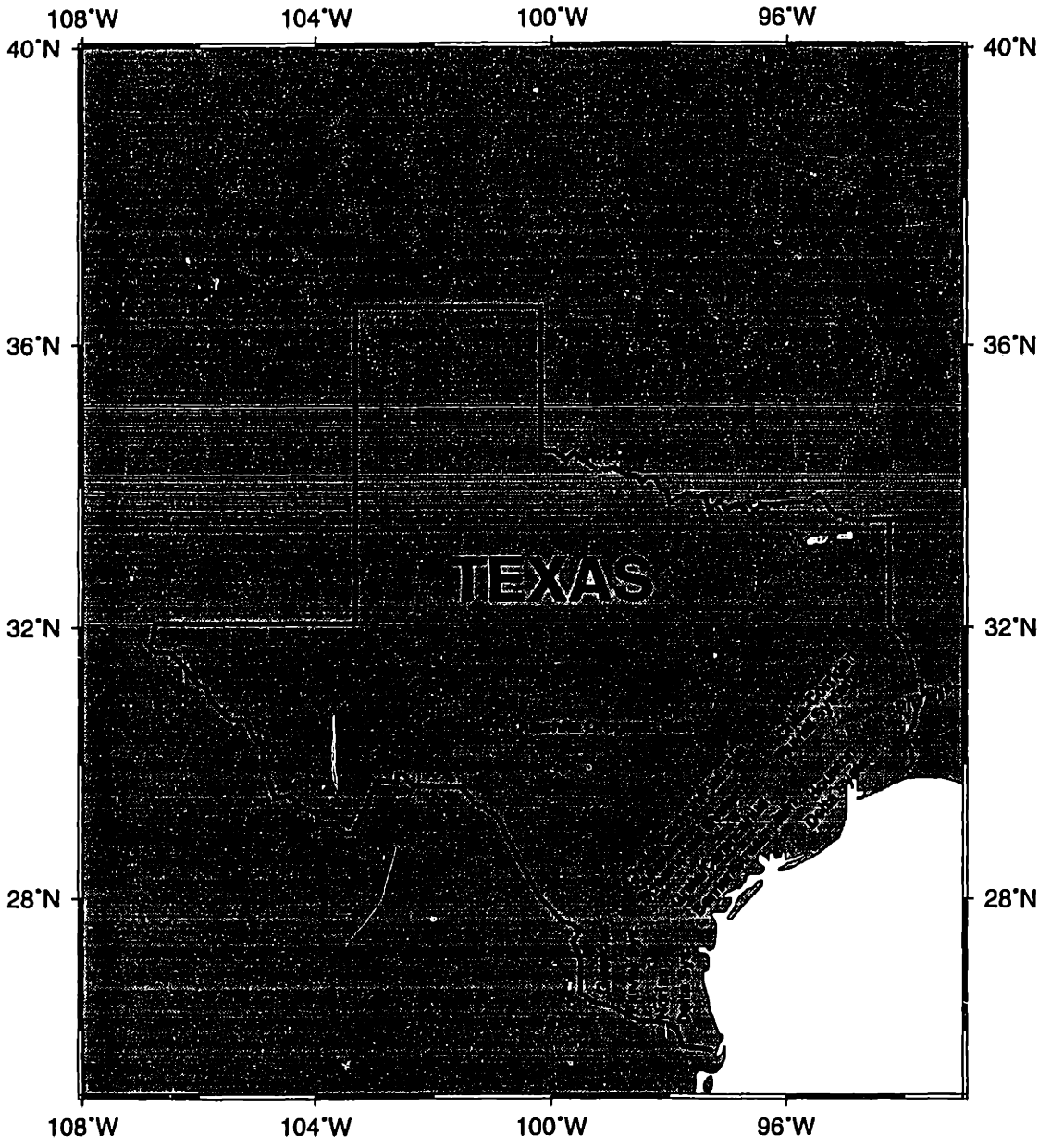

Figure A-2: Generalized map of major sedimentary formations of the Texas Gulf coast. This figure was adapted from: (Galloway *et al.*, 1982, 1991)

Appendix B

Review of the Energy Resources and Geology of Tuscany and the Tyrrhenian Back-Arc Basin

B.1 Introduction to Energy Production in the Geothermal Fields of Tuscany

Industrial use of geothermal resources in Italy began more than 100 years ago when superheated fluids were used to provide heat and chemicals. The extraction of chemical products from the geothermal fluids expanded to include the first production of electricity in 1913, and by the mid 1960s the commercial production of electricity had superceded chemical production as the primary industrial use (Ferrara *et al.*, 1985; Duprat and Ungemach, 1985). The installed capacity of the Italian geothermal electrical production plants reached 545 Megawatts (MW) in December, 1989 with a production of 3,150 Gigawatt hours per year (GWh/y) (1.5 percent of total electrical generation for 1989) (Cataldi *et al.*, 1990). Continued development and expansion of the facilities is ongoing including expanding the installed capacity to reach or exceed 900 MW (Cataldi *et al.*, 1990; DiPippo, 1985).

Geothermal resources in Italy are excellent because of the geodynamic conditions in the Alpine-Mediteranean region. In Italy, tectonically active areas along the Tyrrhenian Sea, and in the southernmost portion of the penninsula, provide the most favorable conditions for the commercial production of electricity and other geothermal uses. Additional resources have been explored and utilized in the more northerly sections of the country near the southern margin of the Italian Alps (Cataldi *et al.*, 1990; Allegrini *et al.*, 1981). Geothermal resources are utilized according to site specific reservoir characteristics and these, in turn, are dependent upon the local geology, hydrogeology, and geothermal conditions. In Italy, maximum reservoir temperatures are associated with Quaternary age calderas and a belt of vapor dominated fields in Tuscany (near Larderello) (Carella, 1985).

Exploration and development of the Italian geothermal resources are primarily conducted by two public agencies; the Ente Nazionale per L'Energia Elettrica of Italy (ENEL) (the governmental utility), and AGIP (the national oil company) (Cataldi *et al.*, 1990; Carella, 1985). Mining rights to the most important geothermal areas (the Tuscany vapor dominated fields) are held exclusively by ENEL. Outside of this area (in the areas of the Quaternary calderas or in areas with significantly lower reservoir temperatures), rights are held by either AGIP (in joint venture with ENEL), or other smaller independent entities (Carella, 1985).

Uses of geothermal resources in Italy are determined primarily by the capabilities of the individual reservoir. Electric power generation is limited to fields where fluids can be extracted at temperatures in excess of 130°C, however, non-power generating uses can utilize fluids extracted at much lower temperatures (Allegrini *et al.*, 1981; Cataldi *et al.*, 1990). Near the vapor dominated reservoirs in Tuscany and the fields associated with the calderas, the uses include electric power generation, industrial uses (such as chemical production, drying, and laundry), and lower temperature uses (such as space heating, greenhouse heating and fish cultivation). Fields with lower ambient temperatures (generally outside of the ENEL exclusive zone) are used primarily for space and greenhouse heating (Cataldi *et al.*, 1990). Commercial production of electric power is limited to plants operating from the vapor dominated reservoirs of southern Tuscany and those associated with the calderas (Ferrara *et al.*, 1985).

Geothermal reservoirs can be classified according to how energy is stored in the reservoir or transferred from the reservoir to the earth's surface. The three main types of reservoirs are: 1) hydrothermal (vapor or liquid dominated), 2) geopressured, and 3) hot dry rock. Usually, the hydrothermal classifications are referred to separately as steam or vapor dominated hydrothermal or liquid hydrothermal. The hydrothermal fields may also be referred to as either 'wet' or 'dry steam' dominated. Geopressured reservoirs make use of water trapped in overpressured geologic structures. Hot, dry rock reservoirs require the addition of transfer fluid (cold water) to extract the heat stored in the rock matrix (Edwards *et al.*, 1982).

Electric power from geothermal energy is produced in a variety of ways according to the characteristics of the particular reservoir. For instance, in vapor dominated systems, a Rankine cycle is used for dry or saturated steam expansion in a low-pressure condensing turbine. For liquid dominated systems, the incoming fluid is flashed to steam prior to entering the turbines. Any residual unflashed fluids may be diverted for a secondary flashing. Systems using this design are referred to as dual stage flashed steam processes. Particulate matter and contaminants must be removed from the steam prior to entering the turbines to avoid damage. (Edwards *et al.*, 1982; Look and Sauer, 1986). Systems for liquid dominated reservoirs may utilize a closed-loop Rankine cycle called binary-fluid processes. In binary processes, heat is transferred from the geothermal fluid to a secondary fluid whose boiling temperature is lower. One advantage of using a closed-loop binary system is that the transfer of heat to the secondary fluid prior to condensing bypasses the concern of non-condensable gases in the primary fluids (Edwards *et al.*, 1982). Dry steam reservoirs are the 'cleanest' type of geothermal energy sources as they require the fewest modifications from standard turbine generator designs and materials (Look and Sauer, 1986).

Electric power from geothermal resources is produced at four major facilities: Larderello, Travale-Radicondoli, Monte Amiata, and Latera. The reservoirs are all located along the western coast, northwest of the Quaternary calderas and recently active volcanic areas (Carella, 1985). The reservoirs are primarily associated with triassic anhydrites and limestones, overlying carbonate complex formations, or the underlying metamorphic basement rocks (phyllites and quartzites) (Allegrini *et al.*, 1981). The Larderello field is a dry-steam

reservoir (Look and Sauer, 1986). The Travale field and Monte Amiata field are steam, and the Latera field is a water-steam mixed, liquid dominated reservoir (Allegrini *et al.*, 1981). The average depths of the reservoir rocks are (approximately): 800m (Larderello), 1200m (Travale), 1600m (Monte Amiata), and 2200m (Latera) (Cataldi *et al.*, 1990). The number of wells drilled at each field as of 1989 were: 503 (Larderello), 61 (Travale), 95 (Monte Amiata), and 21 (Latera) (Cataldi *et al.*, 1990). The temperatures for these fields are: 120-400C (Larderello), 120-250C (Travale), 150-300C (Monte Amiata), and 210C (Latera). In 1989, the installed capacity of these fields were: 408.2 MW (Larderello), 90 MW (Travale), 42 MW (Monte Amiata), and 21 MW (Latera) (Cataldi *et al.*, 1990).

Managing geothermal resources involves estimating and tracking the expected productivity and lifetime of the specific reservoir. In steam producing areas such as at Larderello, the deficit in mass balance within the reservoir and frictional losses in pressure from steam moving through fractures and discontinuities are of the utmost concern. These concerns are being addressed for the steam dominated sites by implimenting field maintenance programs such as: 1) reducing the pressure losses due to steam migration through a combination of deeper drilling, directional drilling and stimulating increased local permeability, 2) increasing the level of microseismic monitoring, and 3) upgrading the older generating plants. At Larderello, specific plans are underway to deepen existing wells, drill new, 'deep' wells near the center of the reservoir (to depths of 3-5 km), explore drilling at or near the boundaries of the reservoir, inject steam to encourage recharge of the reservoir, and upgrade the older units to 20 and 60 MW (Cataldi *et al.*, 1990).

B.2 Review of the geology and geodynamics of Italy and the Alpine-Mediterranean Region

To facilitate an understanding of the local geologic conditions in southwestern Tuscany, it is advantageous to establish a working hypothesis describing regional geologic and geodynamic conditions. Fortunately, the Alpine-Mediteranean region is an area subjected to intensive study, particularly since 1970.

This section of the work will focus on describing proposed models of the structure and dynamics of the Alpine-Mediteranean region. The literature on this subject is extensive and an effort has been made to limit the investigation and discussion of regional characteristics to major theories where they apply directly to explaining the local structures pertinent to Geothermal production.

B.2.1 Geodynamics of the Alpine-Mediteranean Region

Rigid Body Synthesis and Reconstruction of Post-Tethys Plate Configurations

Synthesis of Alpine-Mediteranean geodynamic evolution in the context of plate tectonics began with a plate model proposed by McKenzie (in 1970) and a least-squares fit of the continental edges by Alan Smith (in 1971). Since the publication of these works, rigid body synthesis of the regional geodynamics has provided considerable insights regarding local and regional geomorphology, mineralization, neo-geodynamics, and seismicity. The model proposed by Smith was supported by independent studies of seafloor spreading rates and paleomagnetic reconstructions (Hsu, 1982; Smith and Woodcock, 1982). An excellent, brief summary of Smith's model is given by Hsu (1982):

> *"The development of the Alpine 'Geosyncline' (the Tethys) and of the Mediterranean through the Mesozoic and Cenozoic was a consequence of relative movements among North America, Eurasia and Africa.....*
>
> *During the 'Geosynclinal' (or Tethyan) phase of the Alpine evolution, Africa moved sinistrally away from North America and Eurasia, which continued to be bound together. The seafloor-spreading during the Jurassic and early Cretaceous created the Atlantic between Africa and North America, and the Tethys, or the ancestral Mediterranean, between Africa and Eurasia. When Eurasia started to move away from North America in the late Cretaceous (81 m.y.), the movement between Europe and Africa became dextral and compressional. The coming together of the two plates gave rise to the Alpine orogenesis and the gradual*

elimination of the Tethys Ocean, of which the Eastern Mediterranean is its last remnant."

The development of this model spurred much work on the subject of Alpine geodynamics in general and on local manifestations of plate tectonics and its implications. The complexity of the region's evolution is attested to by the numberous models which were proposed during the mid-1970s by Hsu, Smith, and others. By the early 1980s the number of variations and studies supporting them had grown significantly. Smith and Woodcock provide a list of major points which were generally accepted and provide a framework for further, detailed evaluations of specific works (paraphrased):

- At the end of the Triassic, Eurasia and Gondwanaland were separated by a major ocean area (the Tethys Sea).
- The present Mediterranean basins are not relics of the Paleozoic Tethys, but are youngerMesozoic or Cenozoic basins (Neotethys).
- Continental margin sequences and 'Tethyan' oceanic basins are found deformed within several Alpine orogens. They show that some 'Tethyan' ocean basins have been partly or wholly destroyed.
- Alpine tectonic history spans Mesozoic and Cenozoic time.
- The Mesozoic and Cenozoic tectonics of the Mediterranean region have been constrained and largely controlled by the relative displacements between Eurasia and Gondwanaland.
- Some continental fragments between Africa and 'stable' Europe have moved independently of both bounding continents for at least part of post-paleozoic time.
- There is no simple Tethyan tectonic solution (Smith and Woodcock, 1982).

The basic ideas establish by McKenzie provide the core elements of the geodynamic model of the Alpine-Mediterranean as it existed at the beginning of the 1980s. A detailed description

of the development of this model up until 1982 may be found in Alpine-Mediterranean Geodynamics edited by H. Berkhemer and K. Hsu, 1982.

Microplate Reconstructions

One aspect of Alpine-Mediterranean geodynamics that created much discussion and disagreement was data suggesting the existence of a number of continental fragments located between Europe and Africa. Paleomagnetic data suggested that these fragments moved independently from Europe and Africa, and extensive research was conducted in an effort to determine the character of these fragments. Model variations were proposed suggesting a different number of microplates. Estimates ranged from three (proposed by Hsu) to as many as 20 (proposed by Dewey and others). The three microplates proposed by Hsu are the Iberian plate, the Corso-Sardinia plate, and the Adriatic Plate (Hsu, 1982; Smith and Woodcock, 1982). Paleomagnetic data suggests that most of the microplates have rotated in a counter-clockwise direction with respect to stable Europe (with a few exceptions) and one later model describing the Tuscan anatectic magmatism relies on anticlockwise rotation for its basic premise (Civetta *et al.*, 1978).

The delineation of the boundaries and relative motion of the Mediterranean microplates is a critical element in describing Alpine-Mediteranean geomorphology, including the origin and development of orogenic zones and backarc basins. Recent research on the complex interactions of these microplates establishes the processes by which plate boundaries transition from a compessional environment to an extensional environment.

The Alpine-Mediterranean Orogenic Zones

Two mechanisms for the development of mediterranean orogenic belts are described by Royden and Burchfiel (1989). They suggest that differences in the ratios of plate convergence rates to plate subduction rates at convergent boundaries will determine the structural and morphologic character that distinguishes the orogenesis type (Royden, 1993a). More

specifically, where the rate of subduction exceeds the rate of convergence of the two plates, an orogenic belt will form which is typically characterized by *"low topographic elevations, regional extension in the upper plate, little erosion or denudation, low-grade or no metamorphism, little or no involvement of crystalline basement in shortening, and a protracted history of flysch deposition in front of the advancing orogenic belt"*. These types of thrust belts are thus formed by what Royden and Burchfiel(1989) term retreating plate boundaries.

If the rate of subduction is exceeded by the rate of convergence, the orogenic belt will develop *"antithetic thrust belts, large amounts of erosion and denudation, exposure of high-grade metamorphic rocks at the surface, extensive deformation of crystalline basement to midcrustal depths and a protracted history of molasse deposition in front of the advancing orogenic belt"* (Royden, 1993b). They subsequently term this type of convergence an advancing plate boundary.

Royden has also provided a summary of the geological and tectonic characteristics of five Alpine-Mediterranean orogenic belts in the work "The Tectonic Expression of Slab Pull at Continental Convergent Boundaries" (Royden, 1993b). The five orogenic belts are; the Apennines of central and eastern Italy, the Carpathian System, the Hellenic System, the Himalayan System, and the Western, Eastern and Southern Alps. Each of these orogenic belts reflect the characteristics of the associated convergent plate processes. Later in this section a more detailed description of the Apennines will be presented in light of that system's association with geologic processes at the Larderello geothermal field.

Post-Collision Extensional Regimes - Backarc Basins

The orogenic belts which developed during the evolution of the Alpine-Mediterranean region are defined by major tectonic processes within the region. One other important feature of the Alpine-Mediterranean region which cannot be overlooked is the development of characteristic Mediterranean type backarc basins.

Horvath and Berckhemer describe four backarc basins in their work Mediterranean Backarc Basins

(in Alpine-Mediterranean Geodynamics, 1982). These backarc basins are: the Pannonian Basin which lies south and west of the Carpathian orogenic belt, the Aegean Basin (underlying the Aegean Sea), the Alboran-South Balearic Basin (located south of Spain just east of the straits of Gibralter), and the Tyrrhenian Basin (located between the Italian penninsula and the islands of Corsica and Sardinia). From their study, Horvath and Berckhemer describe fifteen general features of Mediterranean backarc basins. They conclude, in part, that

- *"all young mediterranean backarc basins are secondary result of collisions that occurred between the converging African and European plates"*
- *"backarc basin extension is, at least in part, contemporaneous with phases of compression in the arc"*
- *"Nappes are thrusted unidirectionally onto the external foreland, at least in part, by gravitational sliding"*
- *"the outer (generally non-volcanic) arc consists of metamorphic sialic basement of Mesozoic or Paleozoic age, sometimes with a carbonate cover (Hellenic arc, Apennine, Sicily), sedimentary thrust sheets (nappes), flysch, olistostromes, Tertiary marine and continental sediments"*
- *"The inner, young volcanic 'arc' of calc-alkaline character is much less pronounced than the outer sedimentary arc"*
- *"Shallow and intermediate deep seismicity occurs. Benioff zones are only occasionally fairly well developed (western and eastern Hellenic arc). Discontinuous clusters of intermediately deep shocks (Tyrrhenian Sea, Carpathian arc-Vrancea zone) or even isolated deep shocks are observed"*
- *"Approximately isostatic equilibrium exists in the basin, but positive free air anomalies at the inner-, and negative free air anomalies outside the outer arc" (Horvath and Berckhemer, 1982).*

For more specific details of backarc basin evolution, the reader is referred to the extensive bibliography presented in that work.

B.2.2 The Geology and Geodynamics of Italy - The Apennine Orogeny

Since 1990, a number of works have been published examining the major geologic and tectonic structures of Italy and its near vicinity in light of plate tectonic concepts (Carmignani and Kligfield, 1990; Royden, 1993b,a). The conclusions drawn in these works elaborate on earlier studies of specific areas (Malinverno and Ryan, 1986; Royden *et al.*, 1987; Kastens *et al.*, 1988; Della Vedova *et al.*, 1984; Barberi *et al.*, 1973). These works are part of an extensive, multidisciplinary effort to define the geodynamic processes that control and constrain phenomena at convergent plate boundaries.

The Alpine-Mediterranean region presents an extraordinary opportunity to study collisional processes, and particular attention has been given to examining convergent boundaries of the Corsica-Sardinia microplate. Three popular models have been proposed to explain observed phenomena along this plate margin, however, one model deserves particular attention. The outward arc migration with post collision extension model shows fewer inconsistencies with the observed data than the other models and provides an excellent framework for understanding the local geology of the Tuscan geothermal region (Carmignani and Kligfield, 1990; Malinverno and Ryan, 1986; Royden, 1993b,a; Royden *et al.*, 1987).

Carmignani and Kligfield (1990) provide an excellent starting point for our discussion:

> *"The Northern Apennines have been regarded as a compressional fold-thrust belt whose innermost (western) portion formed during the collision of the Corsica-Sardinia microplate against the Italian peninsula in the Oligocene [Boccaletti et al., 1971; Alvarez et al., 1974; Kligfield, 1979]. From the Miocene to the present, this thin-skin, accretionary fold-thrust belt propagated from west to east across the Italian peninsula [Merla, 1952; Bally et al., 1988]. Today, gravity, structural and magnetic data have been interpreted to suggest that continental crust of the Adriatic plate is underthrusting the central Apennines with a trench located beneath the Po Basin-Adriatic Sea Boundary [Royden et al., 1987]."*

Within the context of the arc-migration model (with post collisional extension) we can go on to describe briefly some of the characteristics of the major associated freatures: the Apennine orogenic zone, the Tyrrhenian Sea backarc basin, and the Po Plain foredeep basin (See Figure B-1).

The Apennine Orogenic Belt

The Apennine Orogenic belt trends northwest through the Italian peninsula and marks the location of a sharply curved thrust belt that extends south and then west through Calabria and Sicily (Figure B-1) (Royden *et al.*, 1987). The structure of the Apennines reflect at least three separate phases of tectonic disturbances, which are recognized by remnant features in both the sedimentary formations as well as some of the basement formations. The primary structure of the mountains formed during the Apennine Orogeny (a sub-classification within the middle Alpine Orogeny, approximately middle Eocene to Oligocene, 30-50 Ma) (Cameli *et al.*, 1993).

The first disturbance, the Eocene-Oligocene phase of deformations, is referred to by Carmignani and Kligfield as the D1 phase and represents structural features created by northeast-southwest oriented compression caused by the initial collision of the Corsica-Sardinia microplate with the Adriatic microplate (Carmignani and Kligfield, 1990). The D1 phase created nappe structures by displacing preexisting sedimentary formations along detachment horizons (Cameli *et al.*, 1993; Carmignani and Kligfield, 1990). The sedimentary formations involved in the nappe building are identified as the Ligurid complex which tectonically overlies the Tuscan Nappe. These two sequences are composed of the following:

- Ligurid Complex (Jurrassic to Paleogene Sediments)
  - Flysch (Cretaceous-Paleogene)
  - Pelagic Sediments (Early Cretaceous)
  - Radiolarites (Jurassic)

- Ophiolites (Jurassic)

- Tuscan Nappe (Triassic to Paleogene Sediments)
  - Flysch (Late Paleogene)
  - Radiolarites (Jurassic)
  - Marls (Jurassic)
  - Cherty Limestones (Jurassic)
  - Limestones (Jurassic)
  - Anhydrites (and in some locations, dolomites) (Triassic)

- (Cameli *et al.*, 1993; Block, 1991; Batini *et al.*, 1985b).

The Tuscan formation is discontinuous due to extensional thinnning. In some locations, the Tuscan Nappe formations (when present) are underlain, or replaced by what are referred to as "Tectonic Slices". These slices, or overthrust wedges, are tectonically displaced portions of the Tuscan series and underlying core complex metamorphic formations. The sedimentary formations have been referred to in the liturature as "upper plate" formations (See Figure B-2) (Carmignani and Kligfield, 1990).

Underlying the Tectonic slices is the main body of the metamorphic complex. It is called the Monteciano-Roccastrada Unit (or Tuscan Metamorphic sequence) and includes three distinct metamorphic units:

- Monteciano-Roccastrada Unit (Mesozoic-Paleozoic)
  - quartz metaconglomerates
  - quartzites and phyllites
  - phyllites and quartzites
  - micashists

Underlying the Monteciano-Roccastrada Unit lies a pre-Alpine gneiss complex (Ordovician-Silurian age). Cameli, Dini, and Liotta (1993) note that the gneissic unit shows no evidence of the Apennine deformational phases, therefore suggesting that it may have been part of the Apennine foreland. The metamorphism affecting these strata originated in the Hercynian Orogeny (approximately 300 Ma) and structures of this event include the NE-SW trending fractures (Batini *et al.*, 1985b; Block, 1991; Cameli *et al.*, 1993; Carmignani and Kligfield, 1990).

The Monteciano-Roccastrada unit overlies:

- Gneiss Unit (Ordovician-Silurian)
  - gneisses interbedded with amphibolites (Batini *et al.*, 1985b)

The Gneiss and Monteciano-Roccastrada Units are often referred to as being representative of the lower plate. In addition, the term "basement" has been found to refer either to the Tuscan Nappe, or alternatively, to the Monteciano-Roccastrada Unit.

The compressional stresses that lead to the displacement of the Ligurid and Tuscan sedimentary sequences onto the core complex was followed by a period of post collisional extension, referred to by Carmignani and Kligfield as the D2 deformation. The late Tortonian (Miocene) D2 tensional stresses created boudinage structures within the cherty limestones of the metamorphic complex (Carmignani and Kligfield, 1990)attesting to the extensional affects at mid-crustal depths (below 3 km). Effects of the D2 deformation on the upper crust can be seen in northwesterly trending extensional normal faults. Vertical displacement along these faults created Horst-Graben structures into which sediments were deposited during the Miocene and Pliocene (Cameli *et al.*, 1993; Carmignani and Kligfield, 1990). These sediments are composed of clays, sands and conglomerates and are referred to by various names including, "Neogene sediments" and as a "neoautochthonous complex".

The third episode of tectonic disturbances includes Pliocene and younger magmatism. The D2 extensional deformation creating the NW-SE faults and associated fractures migrated

eastward across the Italian peninsula during Pliocene and Quaternary time. The Existence of the faulting provided flow pathways for younger magmatism (Puxeddu, 1984). This magmatism is thought to be responsible for the formation of the Quaternary volcanics located in Tuscany, Italy, as well as numerous granitic intrusions emplaced throughout the geothermal region. It has been suggested that most of Tuscany is underlain by granitic intrusions. Petrologic data suggest the age of these rocks are 2.5-3.7 Ma. The temporal and spatial relations of extension and magmatism is in agreement with the eastward arc migration model of Adriatic subduction (Carmignani and Kligfield, 1990).

The Tyrrhenian Backarc Basin

The Tyrrhenian Sea is located between the Italian peninsula to the east and the islands of Corsica and Sardinia to the west. Data collected regarding the structure of the Tyrrhenian Sea support the hypothesis that its origins are related to post collisional backarc basin extension (Horvath and Berckhemer, 1982; Malinverno and Ryan, 1986; Kastens *et al.*, 1988; Carmignani and Kligfield, 1990; Royden, 1993b). Lithologic, paleoentologic, and paleomagnetism data collected during Leg 107 of the Ocean Drilling Project (ODP) provide information regarding the age of rock samples from various locations from the Tyrrhenian sea floor. The data indicates that there are two areas of basaltic crust within the basin, one in the northwestern one in the south-central part of the Tyrrhenian sea, and that they formed during the lower Pliocene and early Pleistocene time (during the Gilbert and Olduvai Magnetic events) (Kastens *et al.*, 1988). Malinverno and Ryan place the beginning of the opening of the basin at 17 Ma (early Miocene) (Malinverno and Ryan, 1986). Both these estimates agree well with the period of extension observed for normal faulting along the western part of the Apennines, suggesting that indeed the two phenomenon are temporally related.

Royden (1993a) concludes from analysis of gravity data collected across the Apennines and other areas in the Alpine-Mediterranean region, that "regional extension within the overriding plate (e.g. backarc extension) behind these orogenic belts appears to be a passive

phenomenon driven by the poor transmission of horizontal compressional stress across the adjacent subduction boundary" and subsequently that the Apennines appear to have formed above a retreating plate boundary (Royden, 1993a). Further works by Royden, Patacca, and Scandone indicate segmentation of the subducting Adriatic microplate, and relate the segment locations to the geomorphology of the Po Plain and structural configuration in the central and southern Apennines (Royden *et al.*, 1987).

The southeastern boundary of the Tyrrhenian Sea is marked by the Calabrian Arc, a currently active convergent boundary where oceanic crust from the Ionian Sea is being subducted under the Corsica-Sardinia microplate. Evidence of this subduction includes the existence of a Benioff zone extending northwesterly away from the arc into the interior of the basin, active volcanos on the southeastern edge of the Tyrrhenian basin, tholeiitic magmatism active within the basin, high heatflow of 200 mW/m2 , and high amplitude magnetic anomalies (Kastens *et al.*, 1988). In addition, it has been observed that heatflow increases toward the western edge of Italy near the Tuscany geothermal region (Della Vedova *et al.*, 1984). The thickness of the crust under the Tyrrhenian Sea varies; depths to the "Moho" range from 8 km in the central portion of the Bathyal plain to 25 km at the basin margins, and these depths are based upon seismic refraction studies and supported by interpretations of gravity data. Associated with the thinnest sections of crust is high heatflow in excess of 150 mW/m2. These values are thought to be associated with recent magmatism (ages less than 2 million years) (Della Vedova *et al.*, 1984).

The Po Plain Fore-deep Basin

Another tectonic feature related to the collision between the Corsica-Sardinia plate and the Adriatic plate is the foredeep basin located beneath the Po Plain. The geomorphology of the Plain has been related to the formation of the foredeep basin and to flexural loading of the Adriatic downgoing slab. Analysis of gravity data collected across the plain suggests that the slab has segmented into at least four pieces which are related to four distinct outer-rise segments observed in the basal Pliocene surface (Royden *et al.*, 1987). The foredeep basin

is filled with approximately 8-9 km of sediments and it has been estimated that the depth to the "Moho" is approximately 25-35 km (Royden *et al.*, 1987).

B.3 The Tuscan Geothermal Fields

B.3.1 Local Geology

The geology in the vicinity of the Larderello geothermal field consists of all of the major units described above (See Figure B-2). The upper 2 km of the crust have been shown from well samples to consist of a complex combination of the neogene sediments, Ligurid units, and Tuscan formations. Locally, the Tuscan series may, however, be thinned or missing altogether. This complexity of rock units can be attributed, at least in part, to vertical displacements along NW-SE trending, high-angle faults. The top of the gneiss unit has been identified from samples collected at a depth of approximately 0.8 km from the S. Pompeo 2 and VC11 wells (Block, 1991). Depth to the "Moho" has been estimated for Southern Tuscany to vary significantly from approximately 20-25 (in the southeast) to as much as 30-35 km (in the northwest) (Foley, 1990). Some evidence exists suggesting that there may be remnants of subducted crust at depths as great as 60 km, however, controversy on this point is reported and little discussion of the idea has been included in recent liturature (Foley, 1990).

B.3.2 The Larderello Hydrothermal Reservoir

The geothermal source at Larderello is thought to be related to a granitic intrusion (Batini *et al.*, 1985b; Block, 1991). In support of this theory is the identification of aplitic veinlets in samples from deep wells (Minissale, 1991). The Larderello geothermal field, as was described earlier, is of the vapor-dominated, hydrothermal type, producing steam primarily from a "shallow reservoir" of highly fractured Tuscan Anhydrites at depths from 100-3000m (Batini *et al.*, 1985b; Ferrara *et al.*, 1985; Block, 1991). The Neogene and Ligurid sediments

act as cap rock at the reservoir (Minissale, 1991).

With production of electricity, the pressure at the well head has declined over time and major exploration projects have been initiated to better characterize the geology and identify new productive horizons within the reservoir (Batini *et al.*, 1985b; Puxeddu *et al.*, 1977; Cappetti *et al.*, 1985; Foley, 1990; Block, 1991).

Location and Characterization of the Geothermal Heat Source

Various methods have been used to better characterize the heat source at the Larderello geothermal field. The general objectives include delineating the 3-dimensional shape and location of the igneous intrusion.

The results of a 1985 gravity survey of the Larderello geothermal field indicated the existence of an anomaly of approximately 25 mgals in the vicinity of the center of the field in the active geothermal zone where temperatures from 150C to 300C have been recorded. Subsequent modeling suggested the presence of a roughly elliptical object with a density of 2.58 g/cm3 embedded in a media of 2.7 g/cm3 (Dini, 1989). These results are consistent with the hypothesis that the body is a granitic intrusion.

Extensive seismic reflection studies completed by ENEL included profiles over the Tuscan Geothermal fields (Batini *et al.*, 1985a,b). 340 km of seismic lines were run in the Larderello, Travale, and Monte Amiata areas with the objective to investigate structure and macrofracture trends. Data were collected and compared to lithologic logs and Vertical Seismic Profiling data from wells at the sites. Interpretation of the data indicate the existence of seismic amplitude anomalies in metamorphic and crystalline rock units. An effort has been made to correlate the location of important seismic reflectors to known geologic features such as lithologic changes or an increase in fracture density. According to Cameli *et al.* (1993), the most important reflectors are;

- The "L" horizon- tentatively attributed to the interface between the Neogene sedi-

ments and the top of the Ligurian formation.

- The "T" horizon- tentatively attributed to the top of the Tuscan Sequence.
- The "B" horizon- identified as the top of "Basement" formations
- The "K" horizon- this horizon has not been conclusively explained

The "K" horizon, the most important horizon for exploration, has subsequently been identified in other parts of Southern Tuscany. Depths to the "K" horizon vary from 3 km at the center of the Larderello area to as much as 9 km in other areas of Tuscany including under the Monte Amiata field (Cameli *et al.*, 1993). Interest is based upon several suggestions regarding the origins of this seismic anomaly. One suggestion proposes that the "K" horizon is a zone of increased fracturing of the metamorphic units (possibly fluid bearing), and thus it may prove to be a potential production horizon (Batini *et al.*, 1985a,b). Other proposed origins suggest that the "K" horizon represents: a rheological boundary, a petrological boundary related to contact metamorphism, or perhaps a mylonite band marking the location of a detachment horizon formed during the nappe building phase of compression (Batini *et al.*, 1985a,b; Cameli *et al.*, 1993). The suggestion that the "K" horizon represents a mylonite band is supported by work on the relationship between core complex geometries and regional flow in the lower crust (Block and Royden, 1990).

Block (1991) conducted inversion of teleseismic travel time residuals to delineate crust and upper mantle velocity structure in the Larderello geothermal area. Inversion was carried out using data from ENEL's local seismic network. Interpretation of the inversion results indicated the presence of a roughly cylindrical low velocity zone with a diameter of approximately 15-20 km near the center of the Larderello field. The data suggests the depth to the top of the body is approximately 6 km and that it extends to more than 20 km, perhaps even 40 km (Block, 1991). The results agree very well with those from the gravity survey, studies of the local heat flow, and the elevations of the "K" horizon as indicated from seismic reflection data. Block (1991) interpreted the shallow portions of the low velocity zone to represent hot geothermal fluids trapped in fractured zones beneath an impermeable cap

and the deeper portions to represent the granitic intrusion thought to be the source of heat for the field.

Identification and Delineation of Fractured Horizons

Fractured zones are of primary interest because of their potential as future production horizons. Characterizing the fracture zones includes determining bulk properties of the fractured media, and when possible, imaging the zone with increasing resolution until adequate information has been obtained to determine whether exploratory drilling is advisable. ENEL initiated geophysical characterization of macrofracture trends using seismic reflection in a study published in 1985 (Batini *et al.*, 1985a,b).

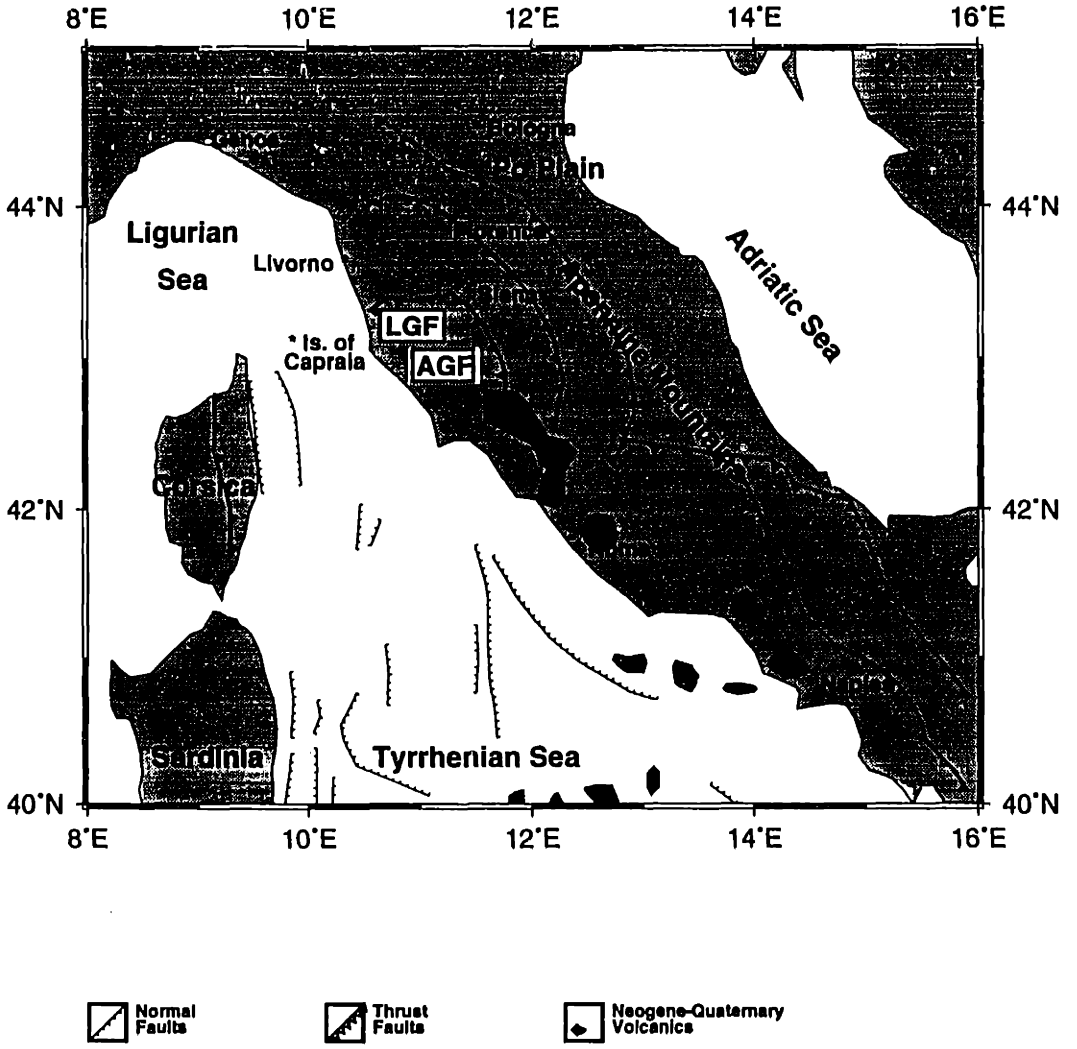

Figure B-1: Map of Italy and the Tyrrhenian Basin indicating the relative locations of major geodynamic structures including the Apennine Mountains, thrust faults associated with nappe building, some of the back-arc basin thrust faults and the location of major Quaternary age volcanics.

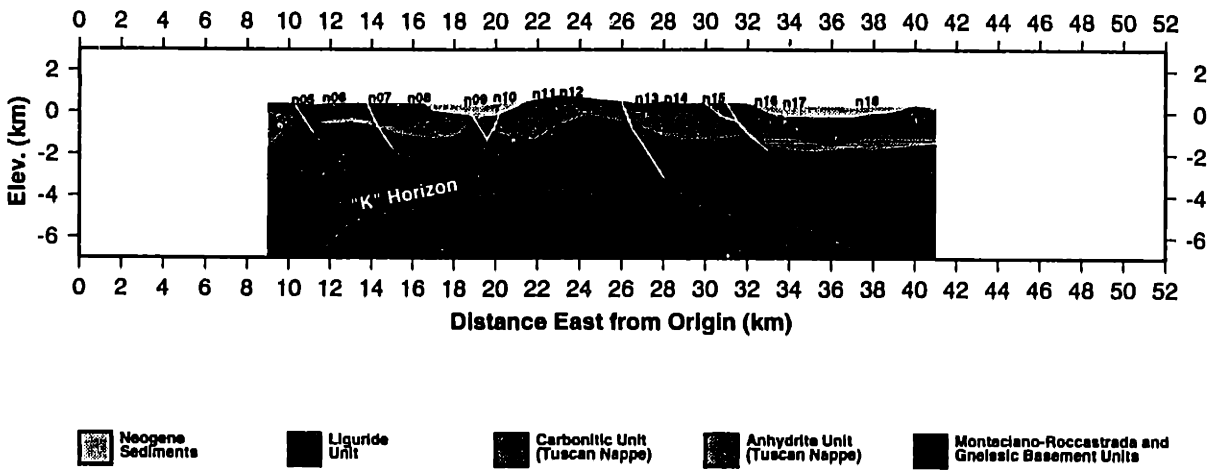

Figure B-2: Generalized geologic cross-section of the Larderello Geothermal field indicating the relative locations of the major stratigraphic units, the Tortonian age extentional faults and the Seismic "K" horizon. This figure was adapted from (Fiordelisi *et al.*, 1995; Batini *et al.*, 1985b; ENEL-Unita Nazionale Geotermica, 1988)

Appendix C

Confidence region estimation for ARCO's DWTI Demonstration Project Induced MEQs

The objective of this study was to assess the lateral variation of the 90 percent confidence regions for the hypocenters of hypothetical (synthetic) microearthquake clusters located along the azimuth of the DWTI hydraulic fracture. Figures C-1 and C-2 present six synthetic event clusters with two different inter-event spacingsf (50 feet and 100 feet) upon which I conducted my numerical experiments.

I calculated the P and S wave arrival times for the synthetic hypocenters shown in figures C-1 and C-2 at a depth of 4500 feet using a horizontally layered velocity structure model with sand and shale velocities as described in chapter 2. In calculating the arrival times, I specified picking error uncertainties derived from a linear dependence on horizontal distance between the hypocenter and the monitoring well. These errors were approximated by adding pseudo-random noise with a gaussian distribution. Ispecified the standard deviations based upon and estimate of the picking error for the primacord shots (1 ms) and on RMS errors for previously located events in cycle 2 (located near the farthest extent of fracture propagation)

of 6 ms. Figure C-3 presents the results of a test conducted to confirm the accuracy of the 90 percent confidence regions for one of the synthetic hypocenters from Grid Ab (event Abyy). This figure shows the predicted hypocenters determined using 60 independent sets of noise. 54 of the 60 hypocenter estimates (93 percent) fall within the 90 percent confidence region, demonstrating that the regions calculated for this study are correct. (The confidence region presented for comparison is taken from the most accurate relocated event of the 60 studied).

I tested the accuracy of the hypocenter location algorithm by comparing the location of the 90 percent confidence regions with the true location of the hypocenters. The results of this study are presented beginning with the grid furthest southwest (Grid A) and progressing toward the northeast. With this ordering, the confidence ellipses begin large, pass through the expected minimum size, and then increase again as we exit the area best covered by the receiver geometry. The ellipses determined for grids A through E (at 50 foot spacing) are presented in Figures C-4, C-5, C-6, C-7, C-8 and C-9. The circles plotted represent the true locations of the hypocenters where as the estimated hypocenters are at the center of the 90 percent confidence regions as estimated by the inversion algorithm. Additionally, I included the location of real hypocenters from the DWTI (as originally located by ARCO) to indicate the relative spacing between actual events. The confidence regions for grids D, E and F (Figures C-7, C-8 and C-9) illustrate the poor confidences possible for areas northeast of the wells. No further consideration of events in grids D, E or F will be given based upon these results.

The results from the forward modeling for grids Aa-Ea quantify the spatial variation in confidence regions over the length of the southwestern wing of the fracture (Figures C-4, C-5 and C-6). The average maximum semi-axis for the events in this wing varies from a maximum of 55 feet (center of grid Aa) to 12 feet (center of grid Ca). The average minimum semi-axis for the events varies from a maximum of 11 feet (center of grid Aa) to 4 feet (center of grid Ca). The 90 percent confidence region for the depth axis varies from a maximum of 12 feet (center of grid Aa) to a minimum of 3 feet (center of grid Ca). All range values are rounded to the nearest foot. It is also apparent that the geometry of the wells contributes to

the characteristics of the confidence regions. The average azimuthal direction of the major axis varies spatially from N21.3W (grid A) to N8.5E (grid B), a clockwise rotation around the wells. For grids A and B, the wells are both located on the eastern side. The azimuth changes to N37.8W for grid C, located longitudinally between the two wells.

I also calculated the regions for grids with 100 foot spacing to evaluate the lateral variation in region size and orientation (Figures C-10, C-11 and C-12). The results of the inversions for the 100 foot grids are quantitatively presented in table 1. Convergence was commonly attained within 11 iterations of the conjugate gradient algorithm with final RMS misfits and average posteriori standard deviations of approximately 1.00. These results show the variation in the major semi-axis of the confidence regions as a function of distance away from the line connecting the two monitoring wells. Li and Thurber (1991) demonstrated that for receiver arrays with only two laterally separated monitoring locations, the spatial resolution is poor for events along the plane separating the observation points (Li and Thurber, 1991). We observe this effect for the DWTI data by comparing the semi-major axes diagonally across the grids. This axis dimension increases by a factor of 1.88 for grid A, far from the intersecting plane, but by a factor of 3.47 for grid C, nearest the intersecting plane. We also observe the effect of distance from the plane by inspecting the change in ellipse azimuth across the grid. Grid A shows a variation of approximately 12.3 degrees (clockwise rotation) between event Abzz and Abxx. Variations of 36.9 degrees and 4.9 degrees (counter-clockwise), are observed for grids B and C, respectively.

I used the 90 percent confidence regions predicted for grids A through C to qualitatively determine the resolvability of events within the actual DWTI fracture zone, as determined from the events located by ARCO. It is clear from inspection of the semi-major axis dimensions for all three grids that the resolution in the northeast-southwest direction is good, especially for events located within the region covered by grid C. However, resolution of the hypocenter coordinates in the northwest-southeast direction varies considerably over the length of the extent of the fracture wing. Actual events from the early phases of the DWTI injection (cycle 1) were determined to be located within grid C (Figures C-6 and C-12). These events are closely spaced but resolvable in many instances. The events induced dur-

ing cycle 2 are less well resolved, particularly in the northwest-southeast direction (Figure C-10).

These results compare favorably with those found for other experiments of this type. For example, House (1987) located the hypocenters of 805 microseismic events at the Fenton Hill Geothermal Field using similar techiques. These events were located with an accuracy of 25 to 30 meters. Vinegar et al. estimated the accuracy of relative event location of events in a downhole experiment similar to the DWTI demonstration as being 1.5 foot radially and 1 foot vertically, but noted that absolute locations would be much greater (Vinegar *et al.*, 1992).

C.0.3 Conclusions

The results indicate that microseismic events induced by hydraulic fracturing during the Atlantic Richfield Corporation Field Demonstration Project can be confidently located for areas near the monitoring wells but away from the plane intersecting the two observation points. I determined that the minimum dimensions of the 90 percent confidence regions for events within our study area are approximately 8 feet in the northwest-southeast direction, 3 feet in the northeast-southwest direction, and 3 feet in depth.

This study suggests that the resolution provided by the technique of absolute hypocenter location as it applies specifically to the the Field Demonstration Experiment, are comparable to that found in other similar studies. However, we show that the area of good resolution excludes the extreme lateral extent of the fracture thus limiting the detail with which we can examine the fracture process. The location errors can be interpreted as the minimum distance between fractures that is resolvable using this technique.

Event	Iterations	RMS Misfit	σ posteriori	Ellipse Strike	Major axis (ft)	Minor axis (ft)	Depth (ft)
Abxx	10	1.053	1.05	-14.8	45.93	11.59	13.37
Abxy	9	1.050	1.05	-14.2	39.99	11.50	12.00
Abxz	7	0.959	0.97	-17.4	37.87	10.52	9.92
Abyx	8	0.976	0.98	-20.2	58.26	10.71	12.75
Abyy	11	0.968	0.98	-21.3	55.90	10.61	11.48
Abyz	21	0.986	0.98	-25.1	66.87	10.75	10.50
Abzx	21	1.019	1.02	-26.3	98.25	11.20	13.73
Abzy	16	0.998	1.00	-26.8	92.37	10.91	12.27
Abzz	8	1.012	1.02	-27.1	86.50	11.04	11.27
Bbxx	6	1.051	1.05	5.0	12.43	7.06	5.53
Bbxy	5	1.050	1.05	7.1	10.20	7.16	4.79
Bbxz	5	0.961	0.97	2.6	7.82	6.77	3.84
Bbyx	6	0.975	0.98	-6.7	15.39	6.51	5.09
Bbyy	5	0.968	0.98	-8.5	13.58	6.51	4.36
Bbyz	6	0.986	0.99	-13.0	12.60	6.65	3.80
Bbzx	6	1.019	1.02	-18.4	26.10	6.72	5.40
Bbzy	8	0.996	1.00	-21.0	25.40	6.59	4.58
Bbzz	11	1.011	1.02	-25.2	28.11	6.65	4.01
Cbxx	6	1.053	1.05	-41.9	8.05	4.01	3.88
Cbxy	5	1.051	1.05	-33.2	8.94	3.73	3.75
Cbxz	6	0.955	0.97	-25.1	8.33	3.57	3.37
Cbyx	5	0.974	0.98	-46.3	8.57	3.38	3.25
Cbyy	5	0.970	0.98	-37.8	11.88	2.99	3.23
Cbyz	10	0.994	1.00	-32.3	17.27	3.02	3.33
Cbzx	5	1.019	1.02	-49.6	10.97	3.44	2.98
Cbzy	10	0.953	1.00	-39.6	25.35	2.86	3.04
Cbzz	16	1.011	1.02	-37.0	27.92	2.90	3.29
Dbxx	6	1.057	1.06	-54.9	24.65	8.09	6.51
Dbxy	10	1.050	1.05	-46.6	50.01	8.02	6.87
Dbxz	27	0.957	0.97	-45.3	59.59	7.41	6.89
Dbyx	11	0.974	0.98	-50.3	25.77	7.40	5.44
Dbyy	10	0.971	0.98	-43.3	61.80	7.40	5.87
Dbyz	17	0.992	1.00	-27.7	55.25	7.62	6.78
Dbzx	14	1.019	1.02	-44.0	41.17	7.56	5.28
Dbzy	12	0.996	1.00	-27.5	41.37	7.52	5.72
Dbzz	11	1.001	1.01	-25.1	39.48	7.71	6.46

Table C.1: Inversion output parameters for Grids Aa-Da

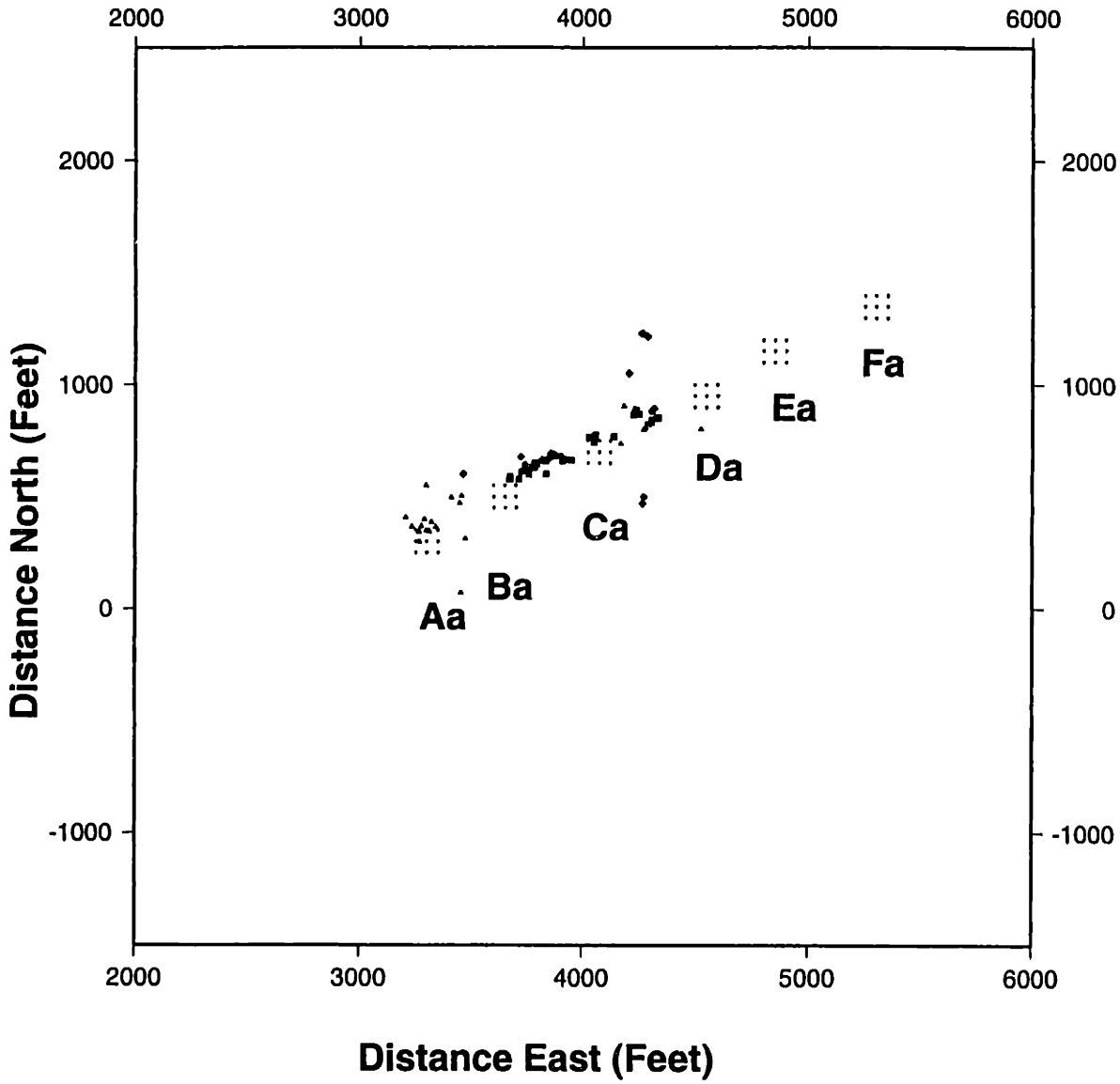

Figure C-1: Synthetic microseismic event hypocenter grids Aa through Fa.

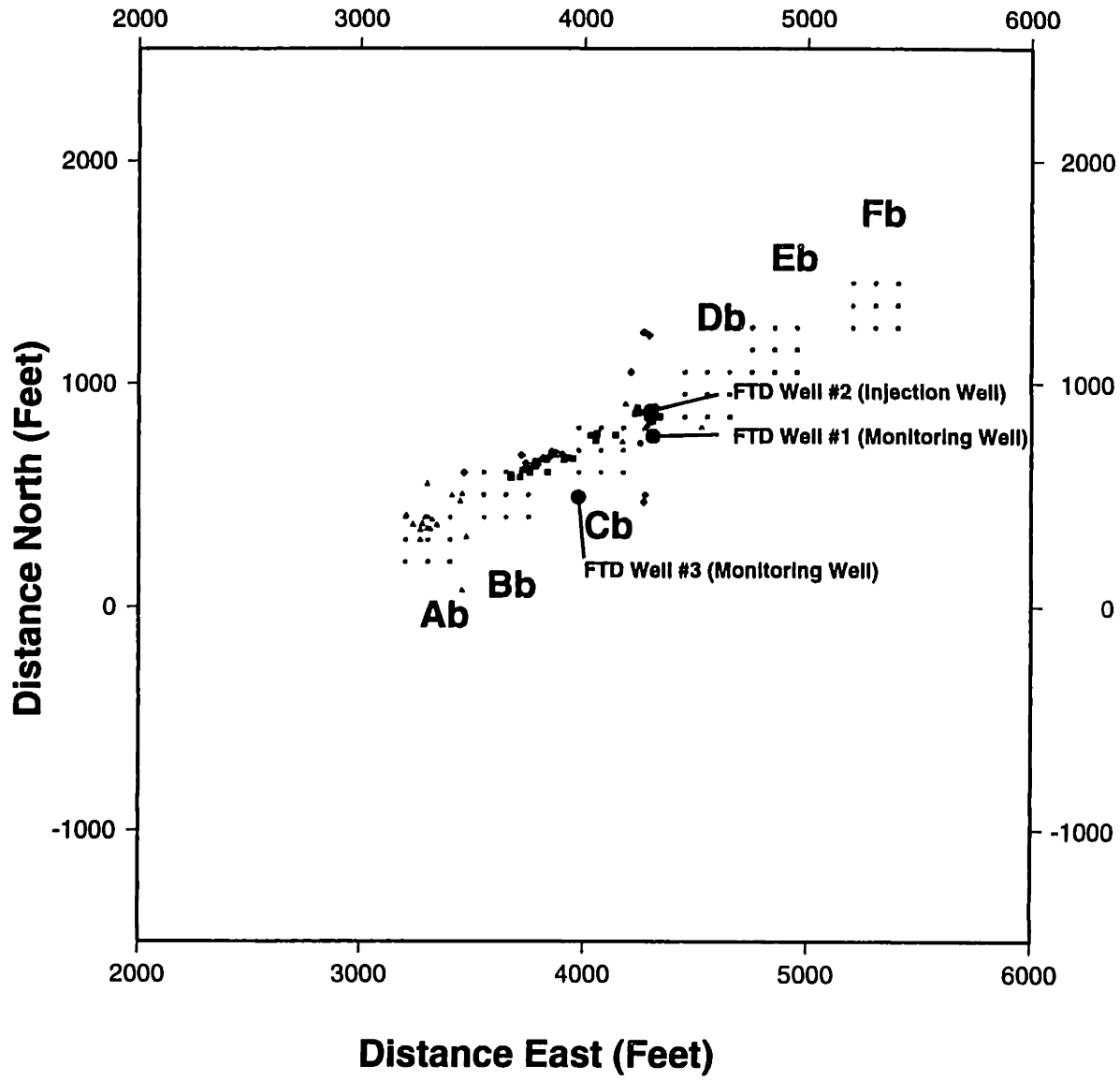

Figure C-2: Synthetic microseismic event hypocenter grids Ab through Fb.

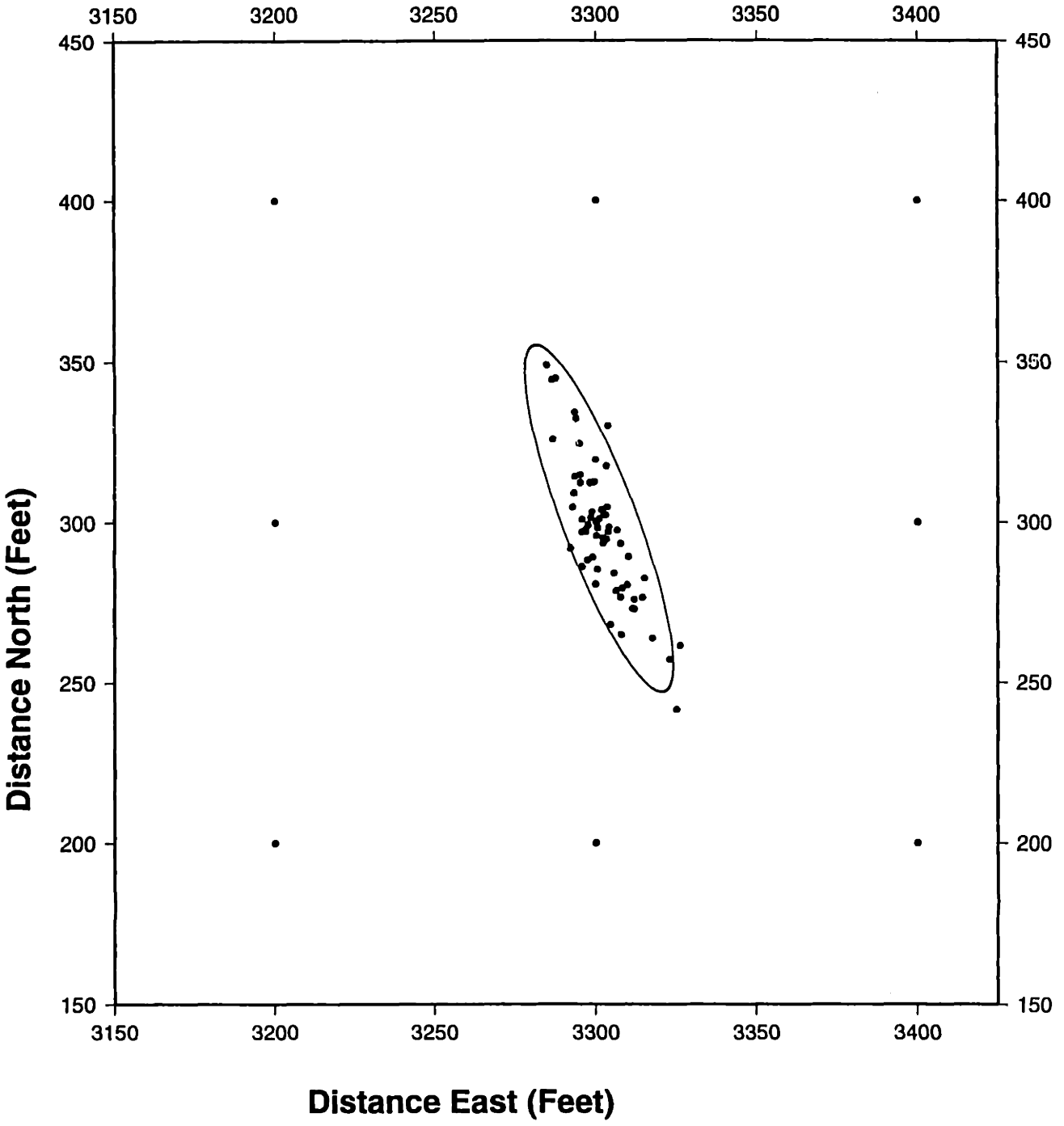

Figure C-3: Predicted epicenters for event Abyy recalculated 60 times. (Triangles=real events from cycle 2).

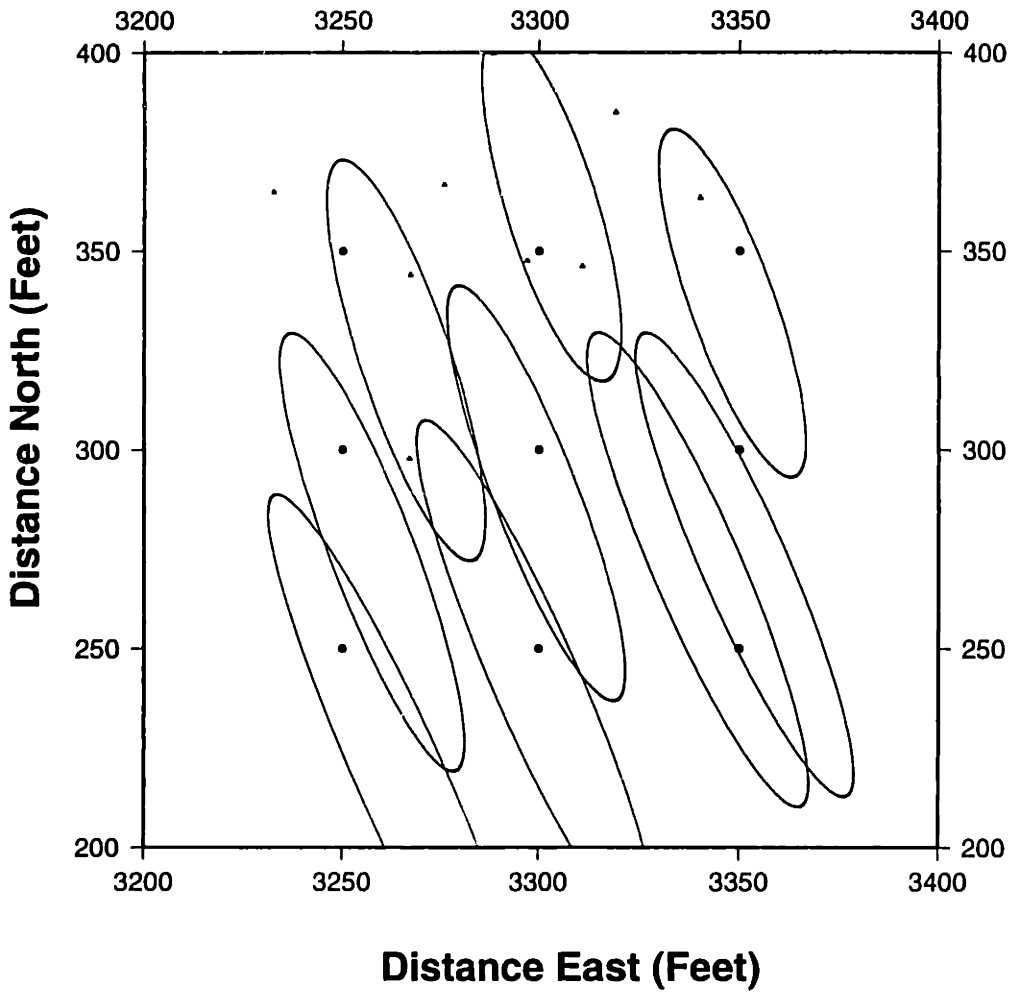

Figure C-4: Projections of the absolute location 90 percent confidence regions for 9 events from grid Aa. (Triangles=real events from cycle 2)

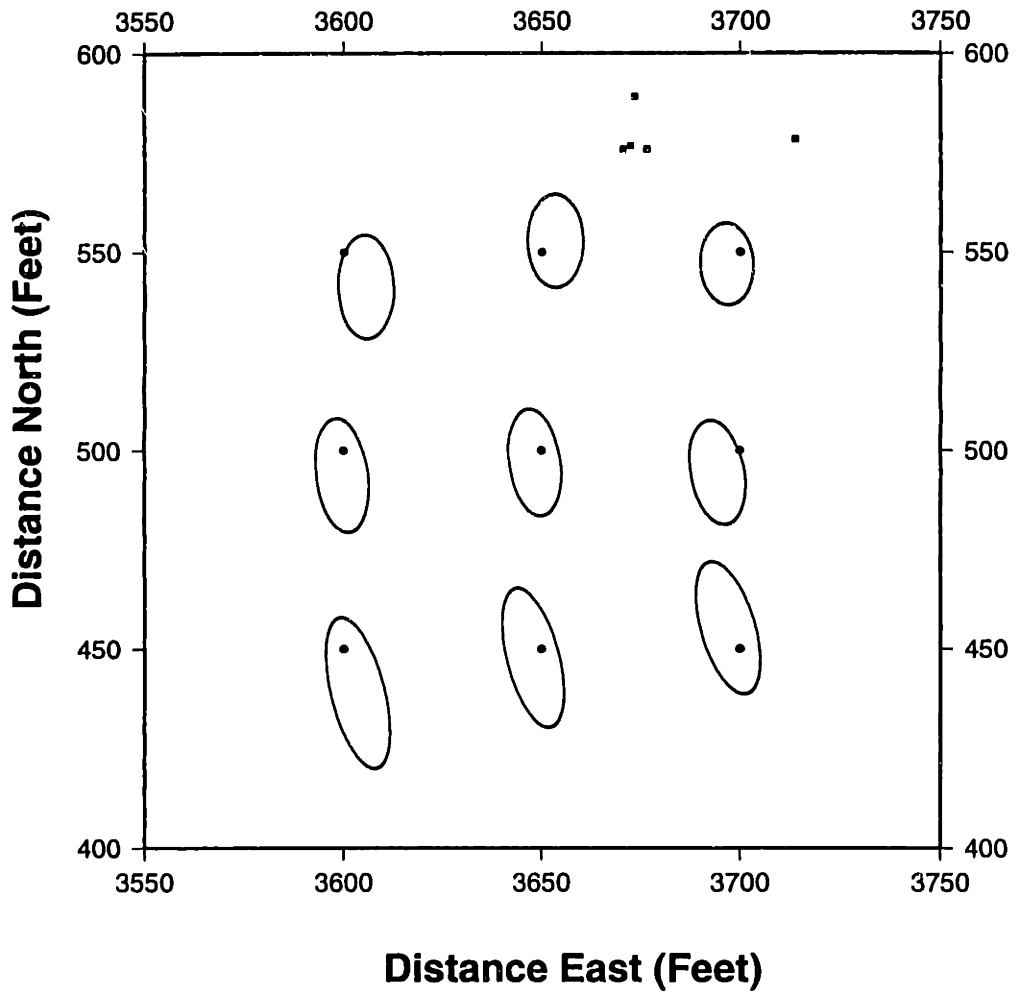

Figure C-5: Projections of the absolute location 90 percent confidence regions for 9 events from grid Ba. (Squares=real events from cycle 1)

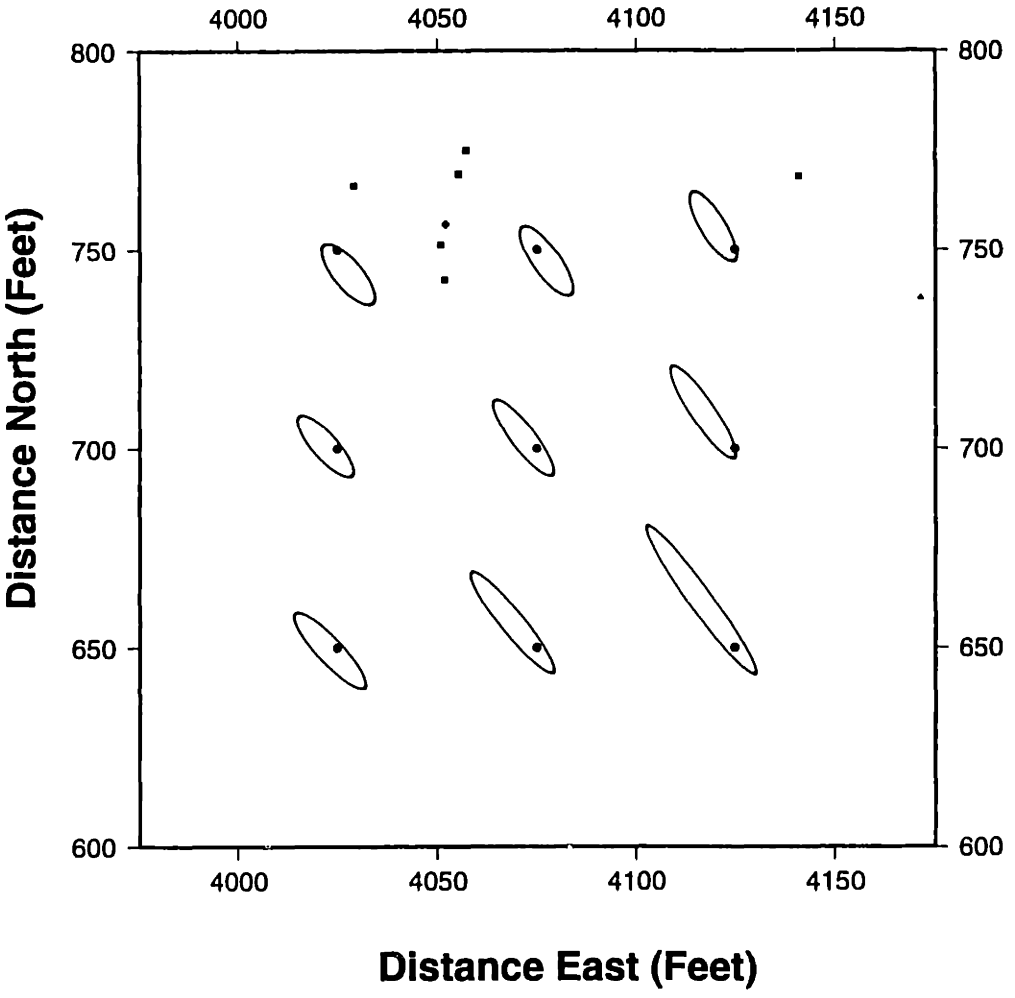

Figure C-6: Projections of the absolute location 90 percent confidence regions for 9 events from grid Ca. (Squares=real events from cycle 1, diamonds=real events from cycle 3)

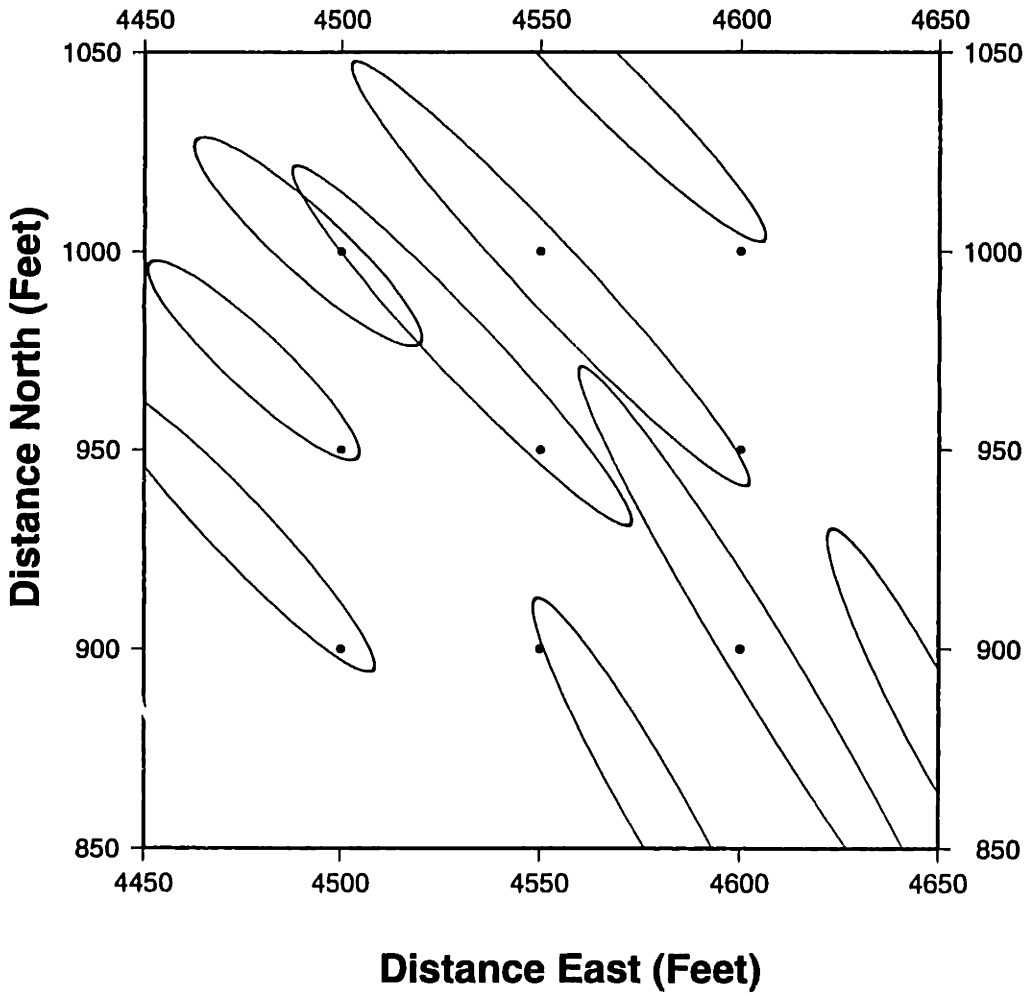

Figure C-7: Projections of the absolute location 90 percent confidence regions for 9 events from grid Da.

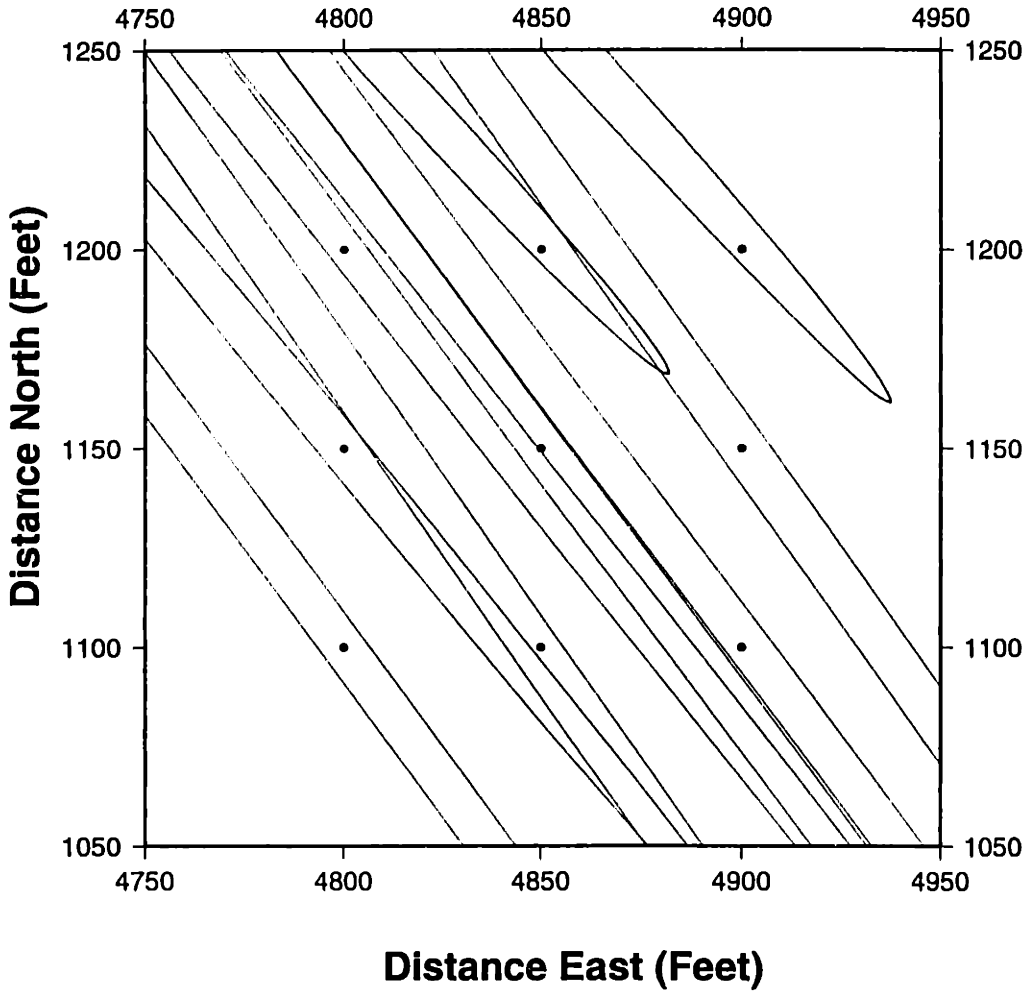

Figure C-8: Projections of the absolute location 90 percent confidence regions for 9 events from grid Ea. (Triangles=real events from cycle 2)

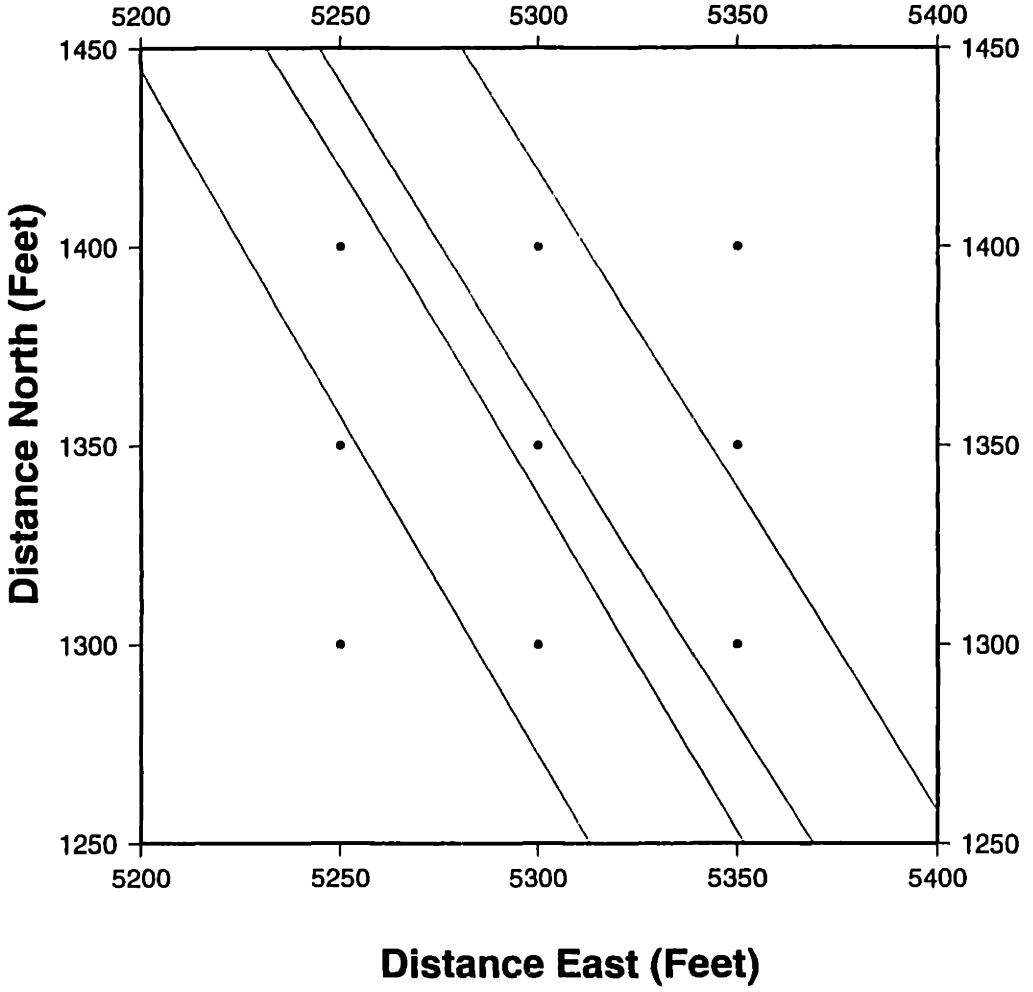

Figure C-9: Projections of the absolute location 90 percent confidence regions for 9 events from grid Fa. (Triangles=real events from cycle 2)

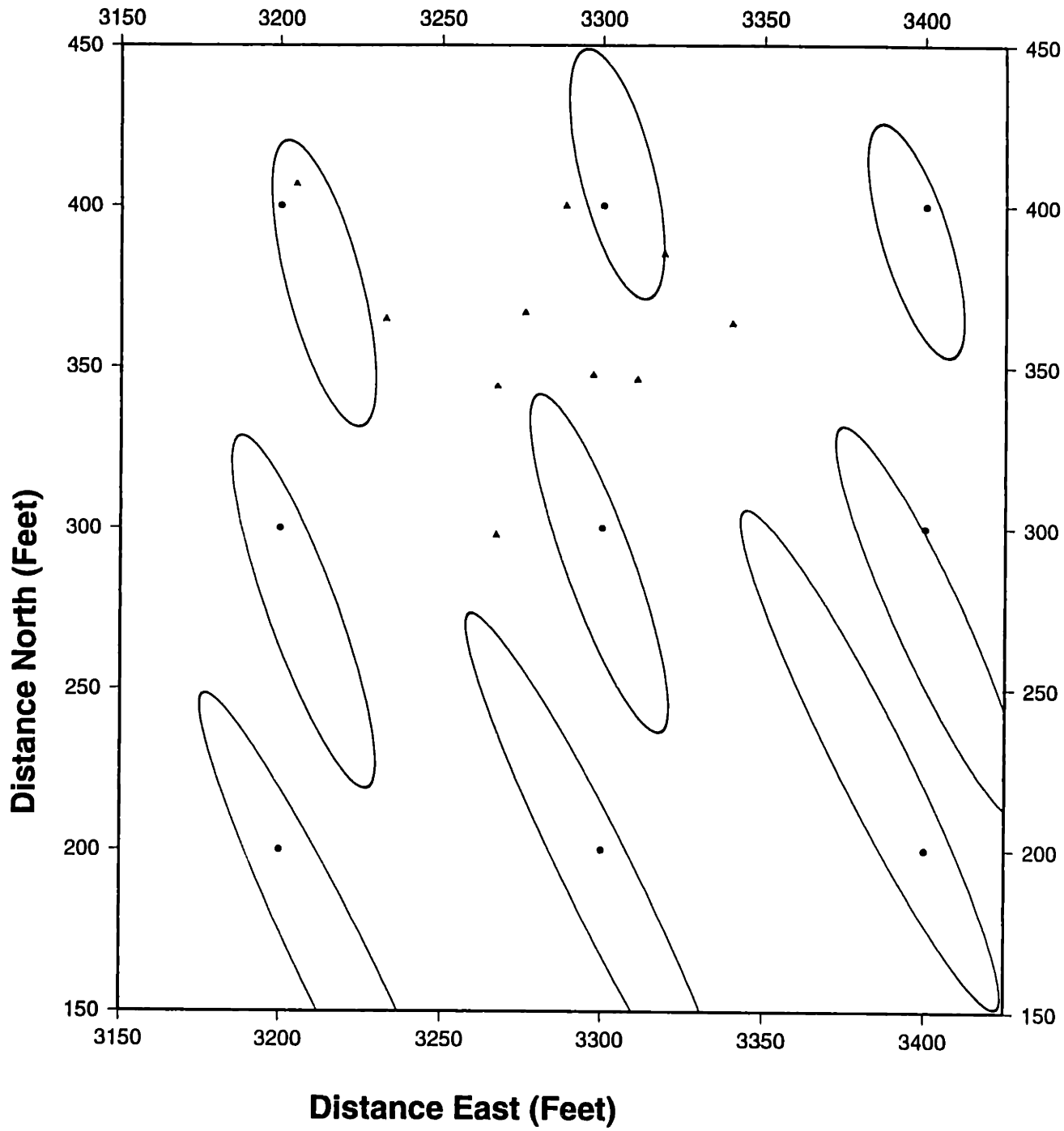

Figure C-10: Projections of the absolute location 90 percent confidence regions for 9 events from grid Ab. (Triangles=real events from cycle 2)

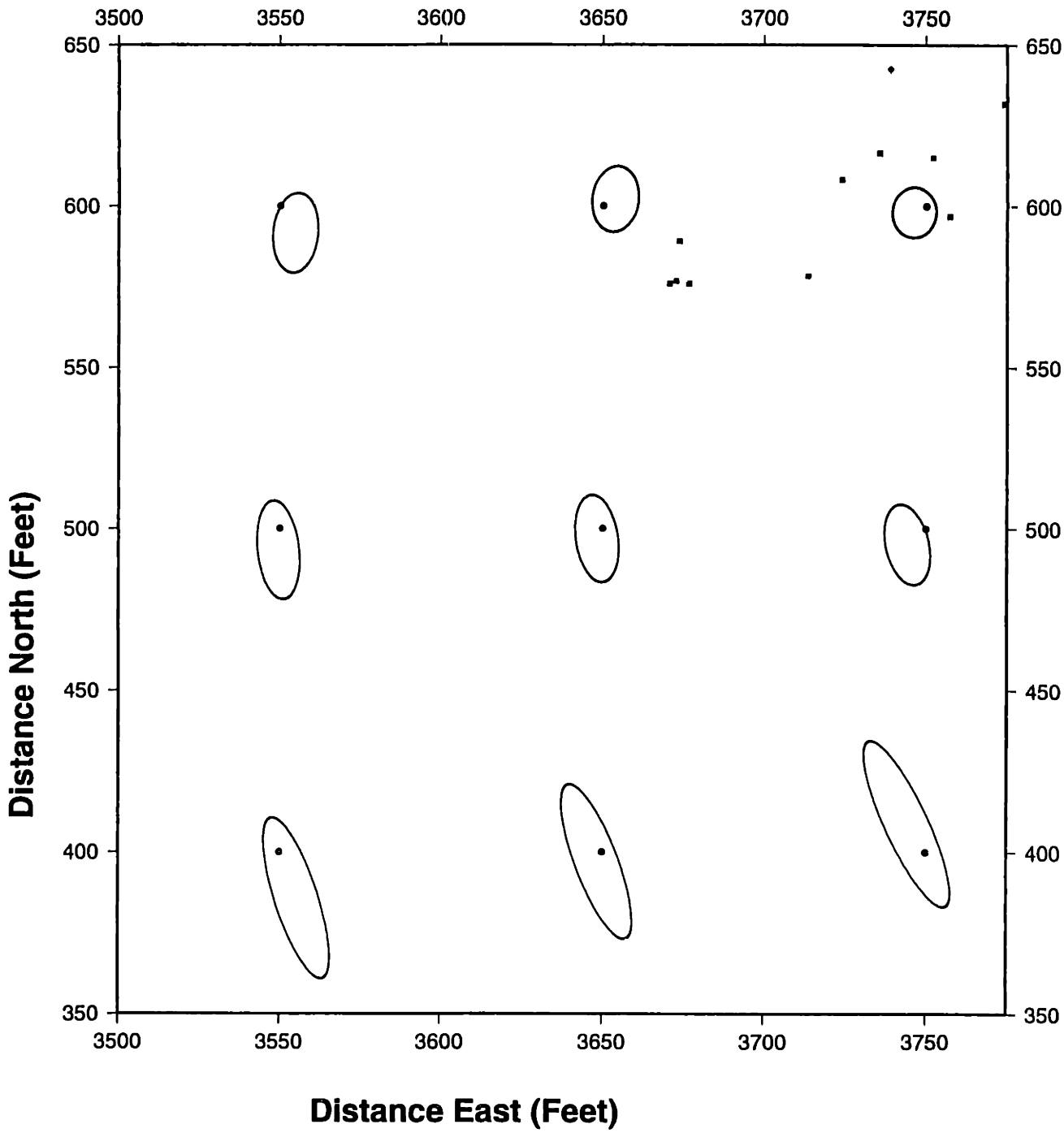

Figure C-11: Projections of the absolute location 90 percent confidence regions for 9 events from grid Bb. (Squares=real events from cycle 1)

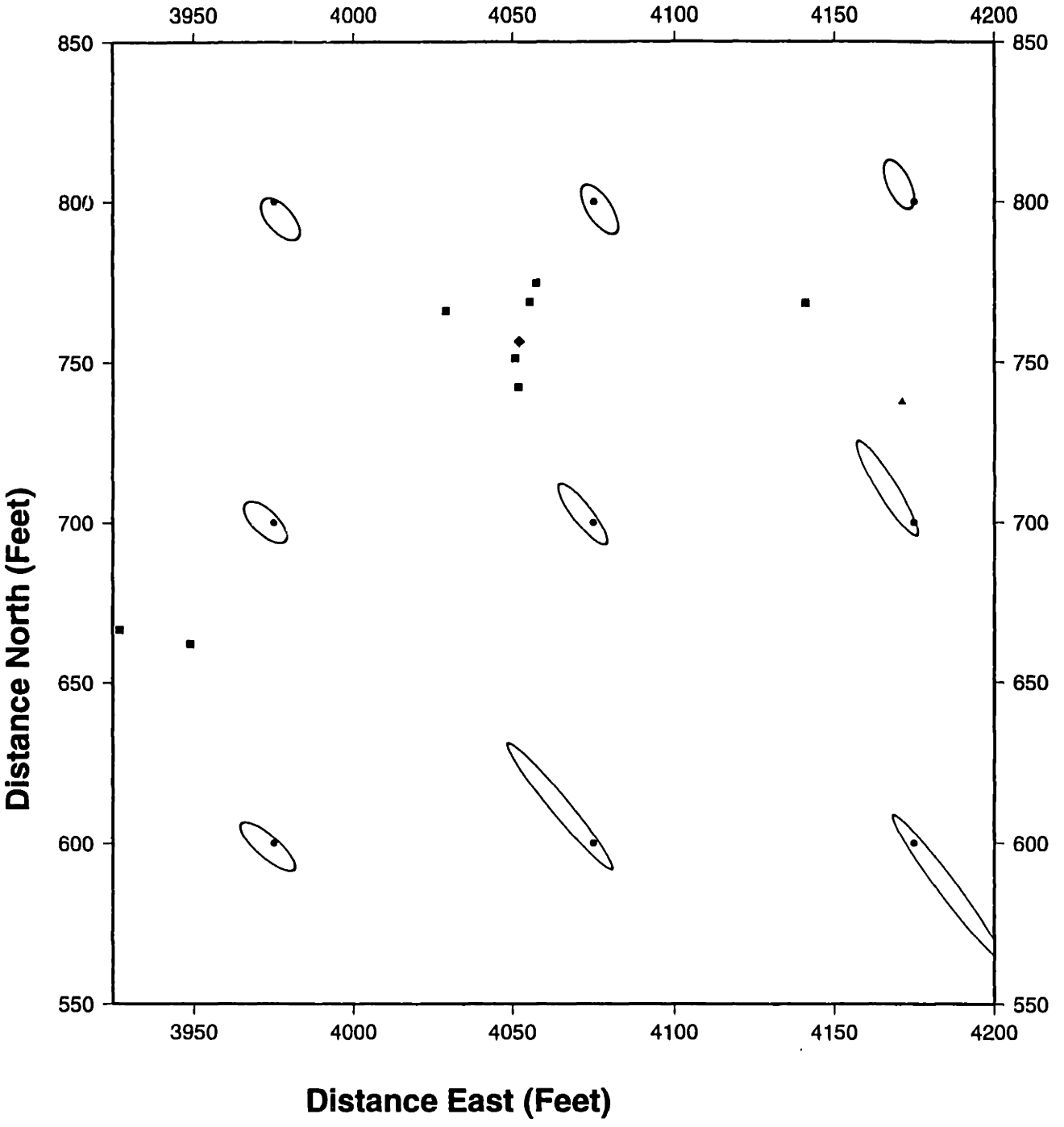

Figure C-12: Projections of the absolute location 90 percent confidence regions for 9 events from grid Cb.

Appendix D

Animations

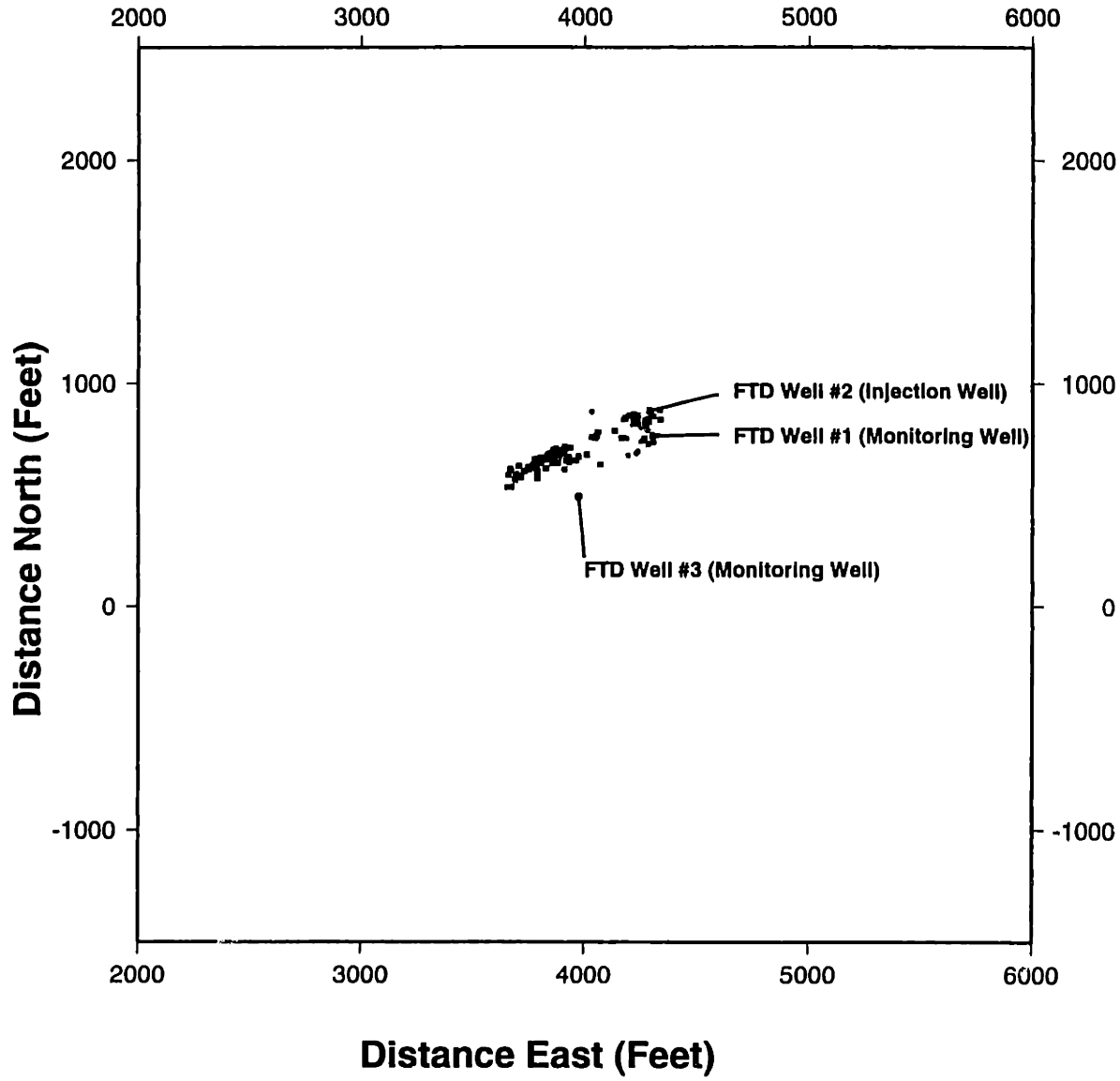

Figure D-1: DWTI Cluster at end of cycle 1

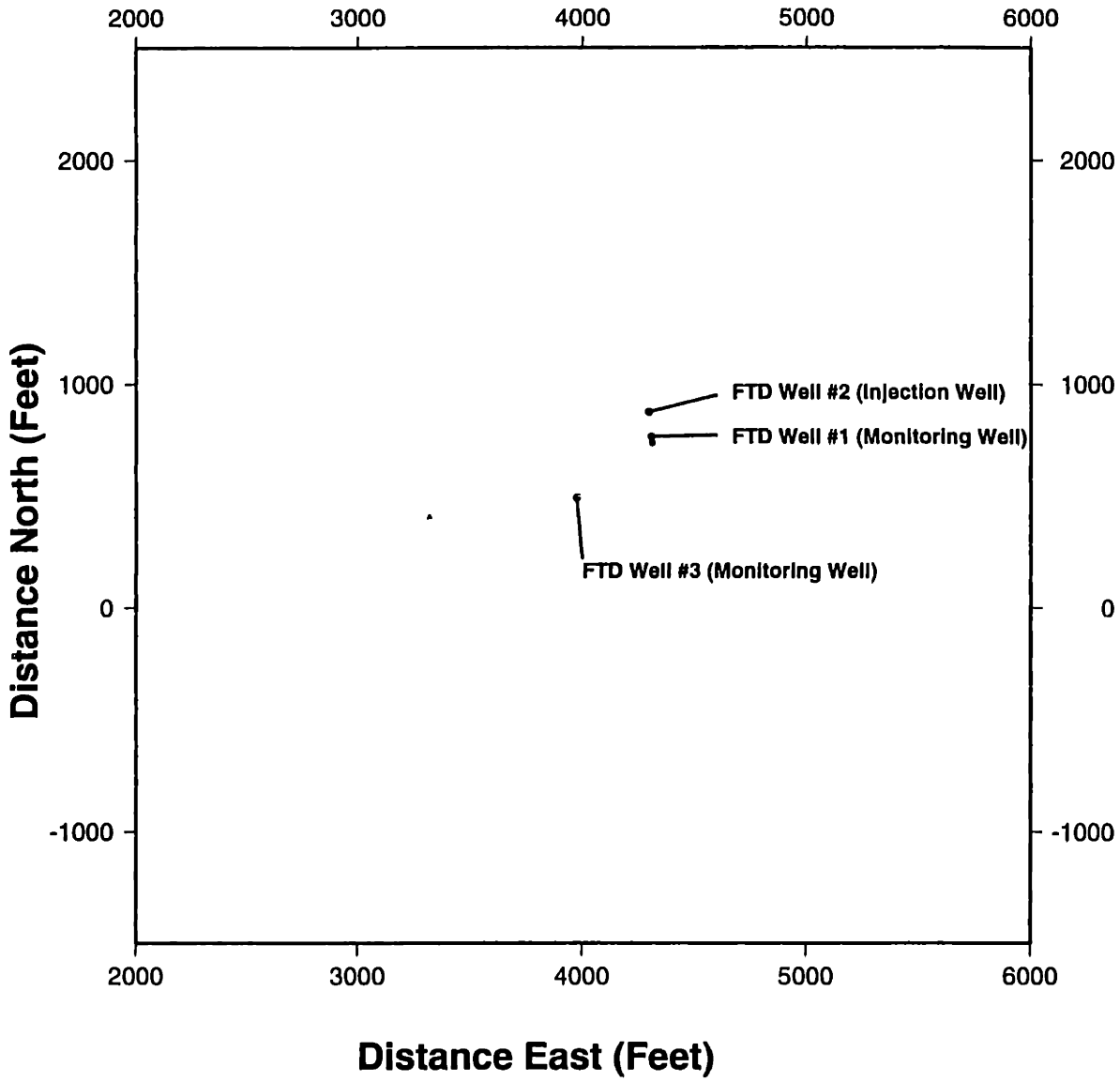

Figure D-2: DWTI Cluster Frame 00

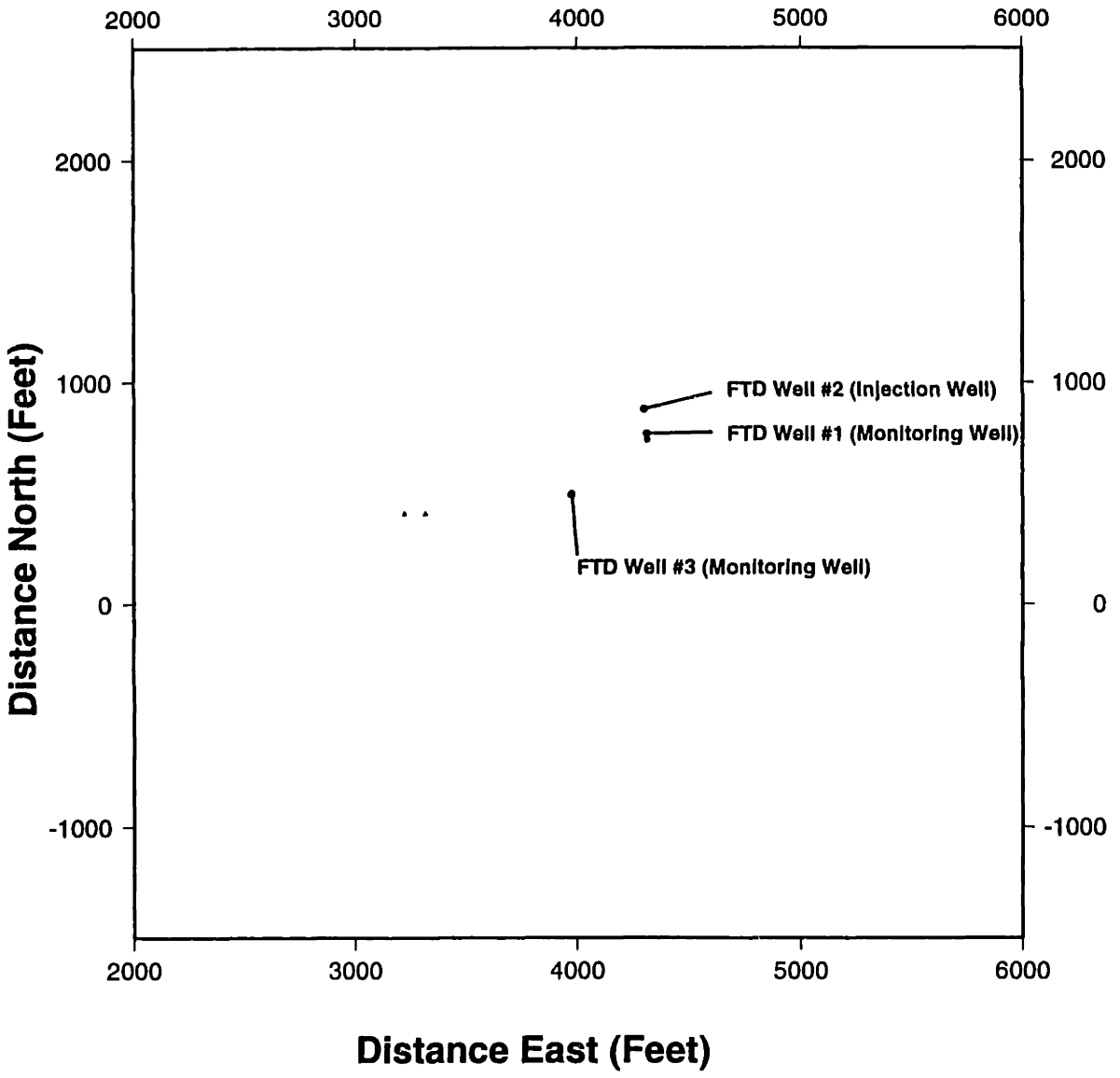

Figure D-3: DWTI Cluster Frame 01

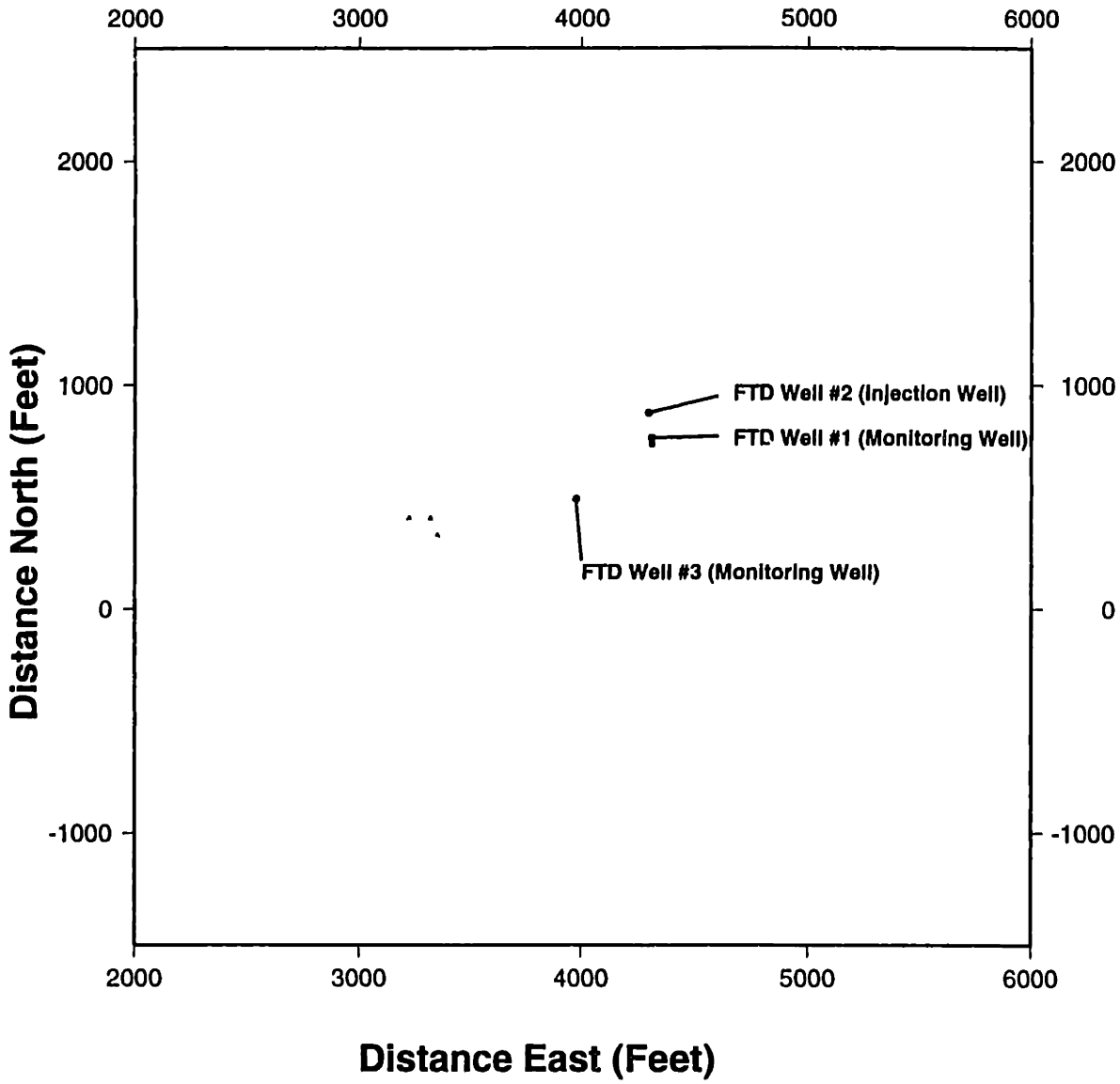

Figure D-4: DWTI Cluster Frame 02

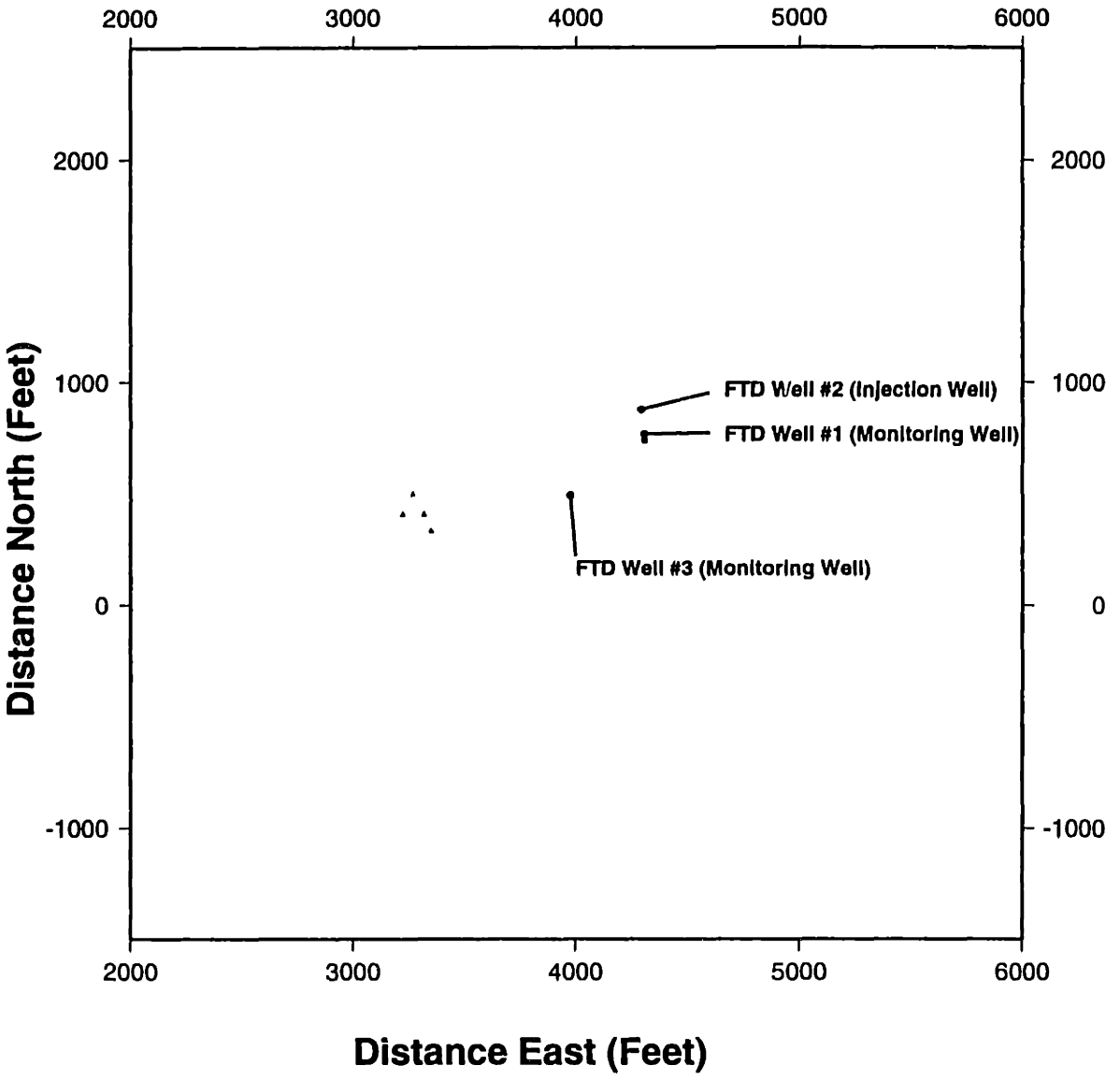

Figure D-5: DWTI Cluster Frame 03

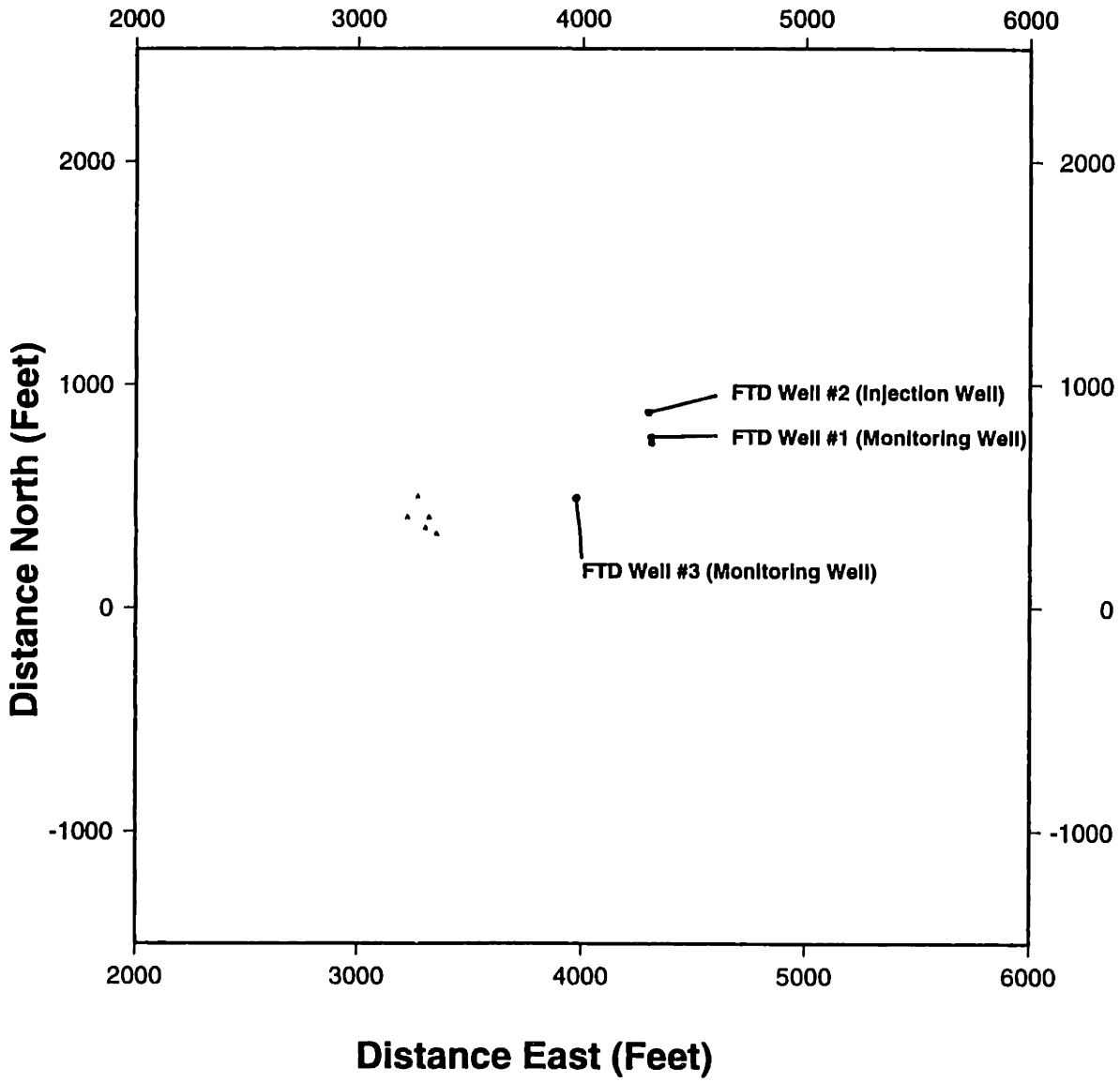

Figure D-6: DWTI Cluster Frame 04

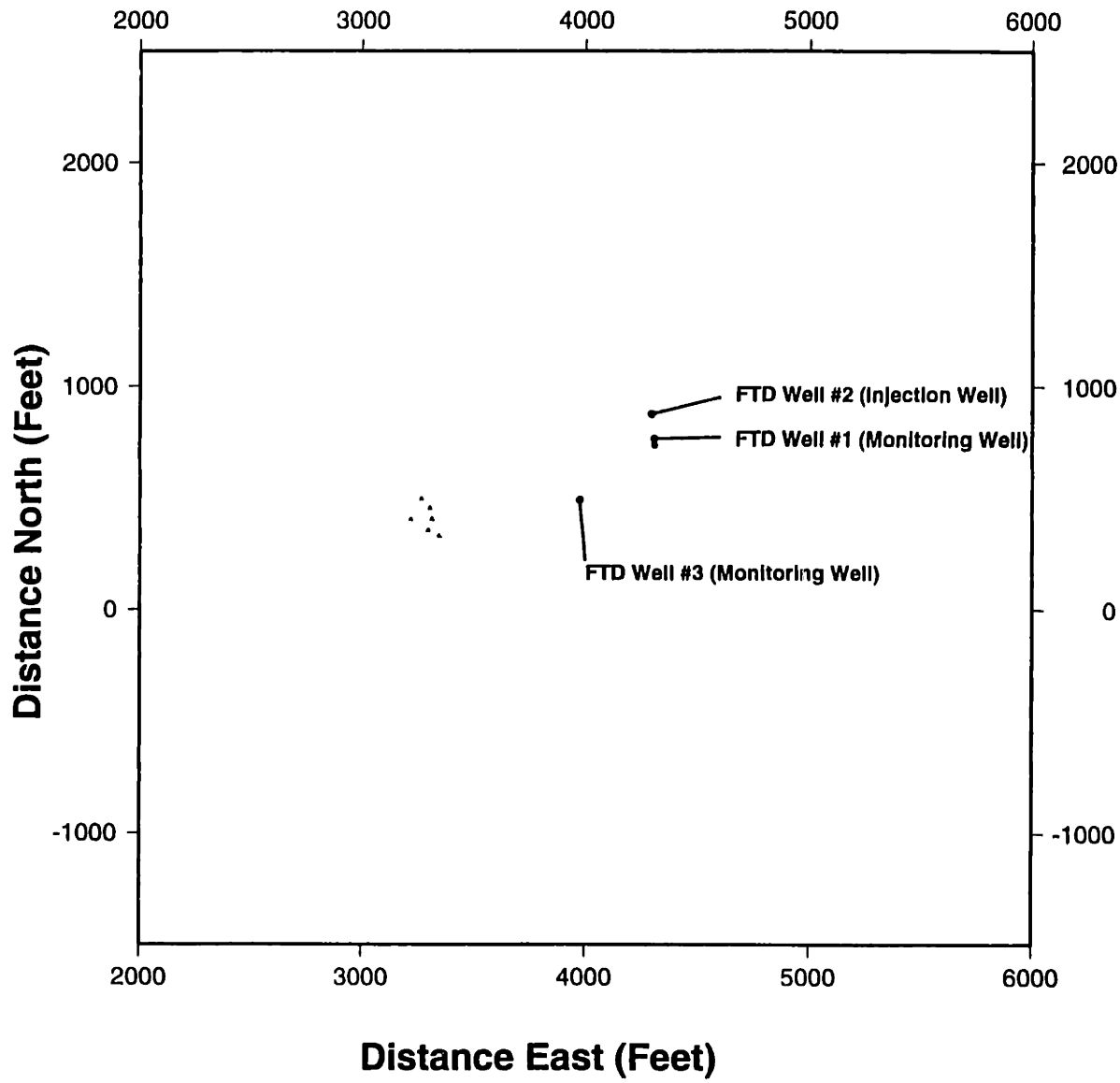

Figure D-7: DWTI Cluster Frame 05

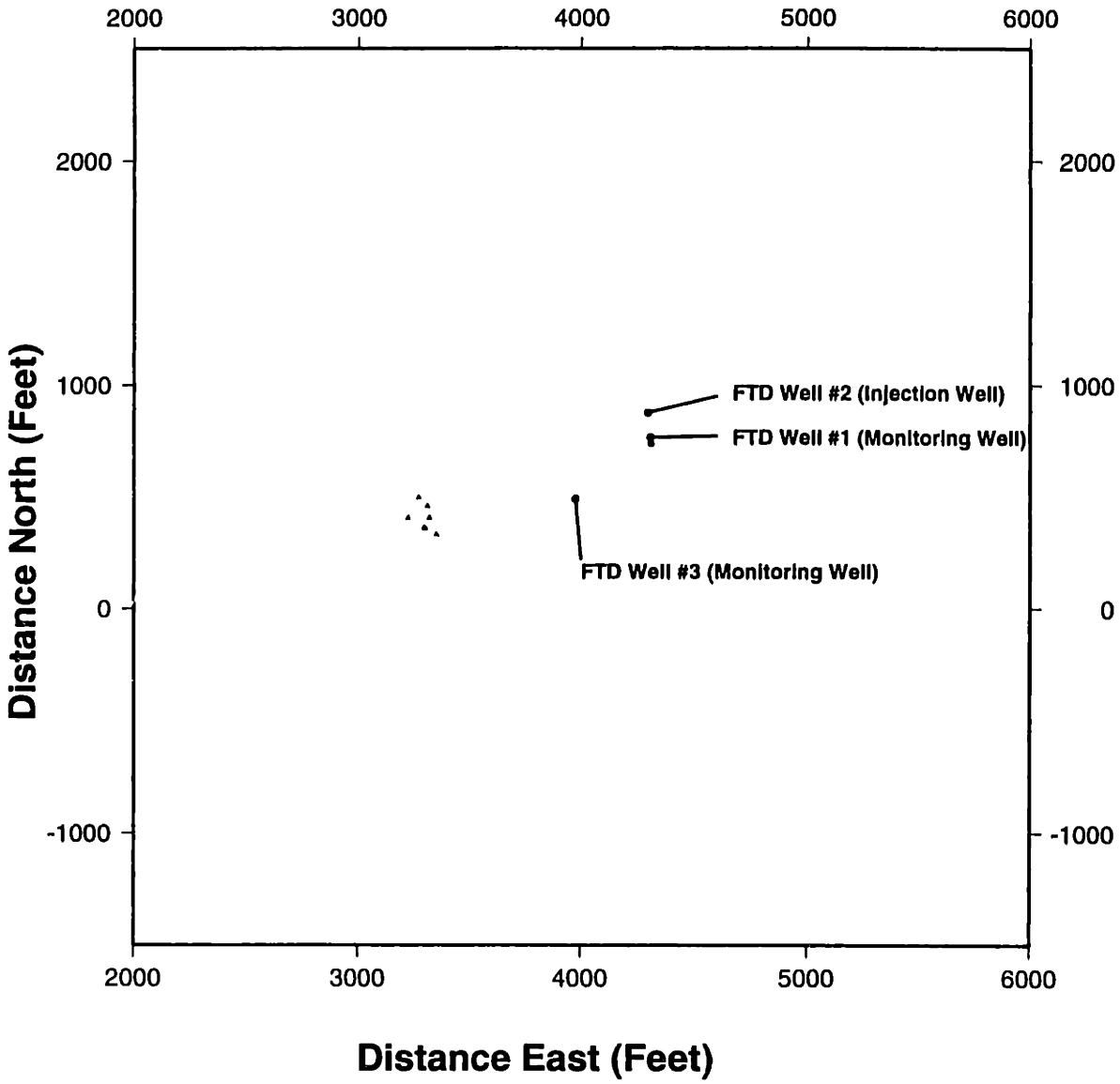

Figure D-8: DWTI Cluster Frame 06

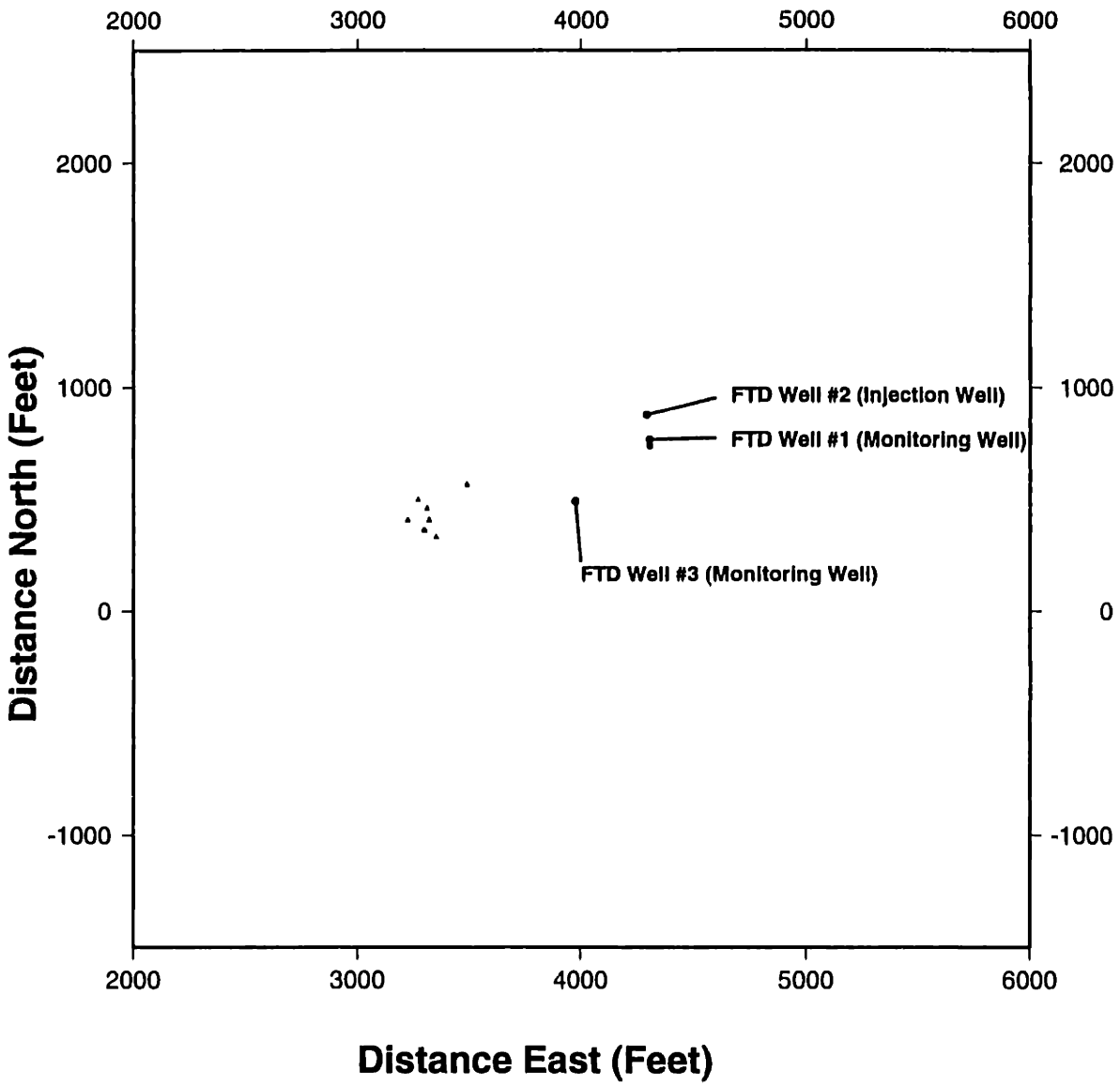

Figure D-9: DWTI Cluster Frame 07

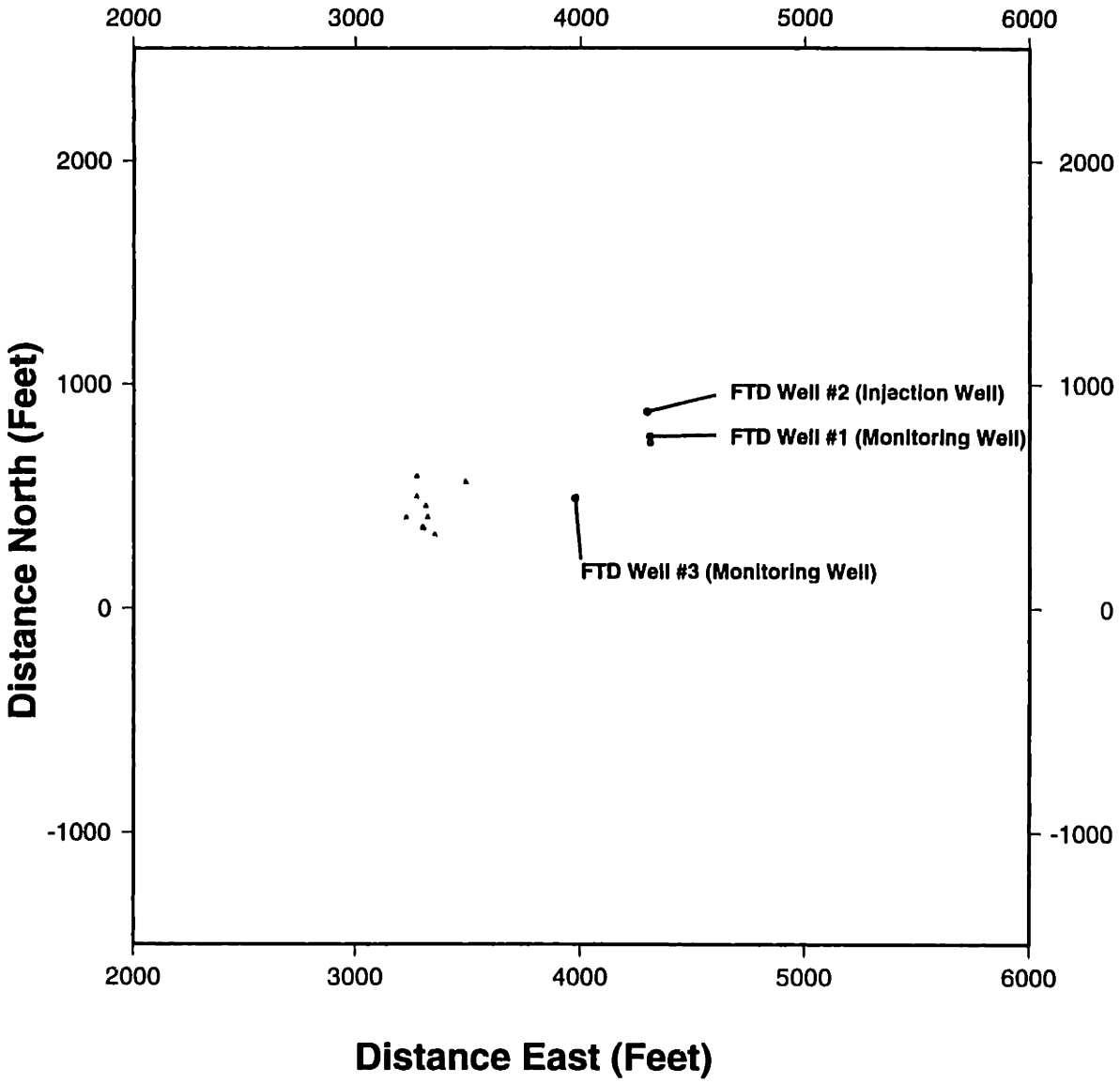

Figure D-10: DWTI Cluster Frame 08

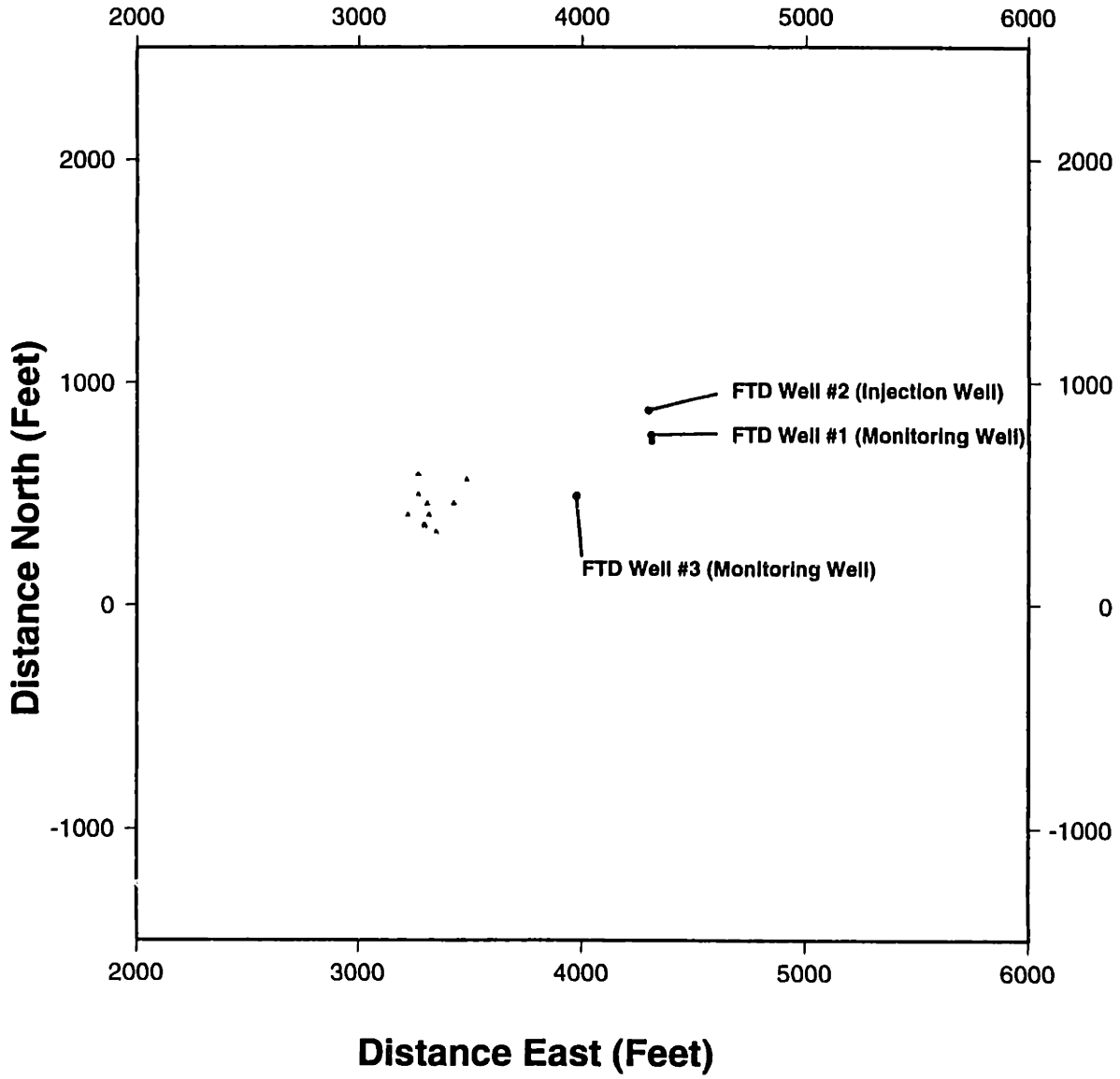

Figure D-11: DWTI Cluster Frame 09

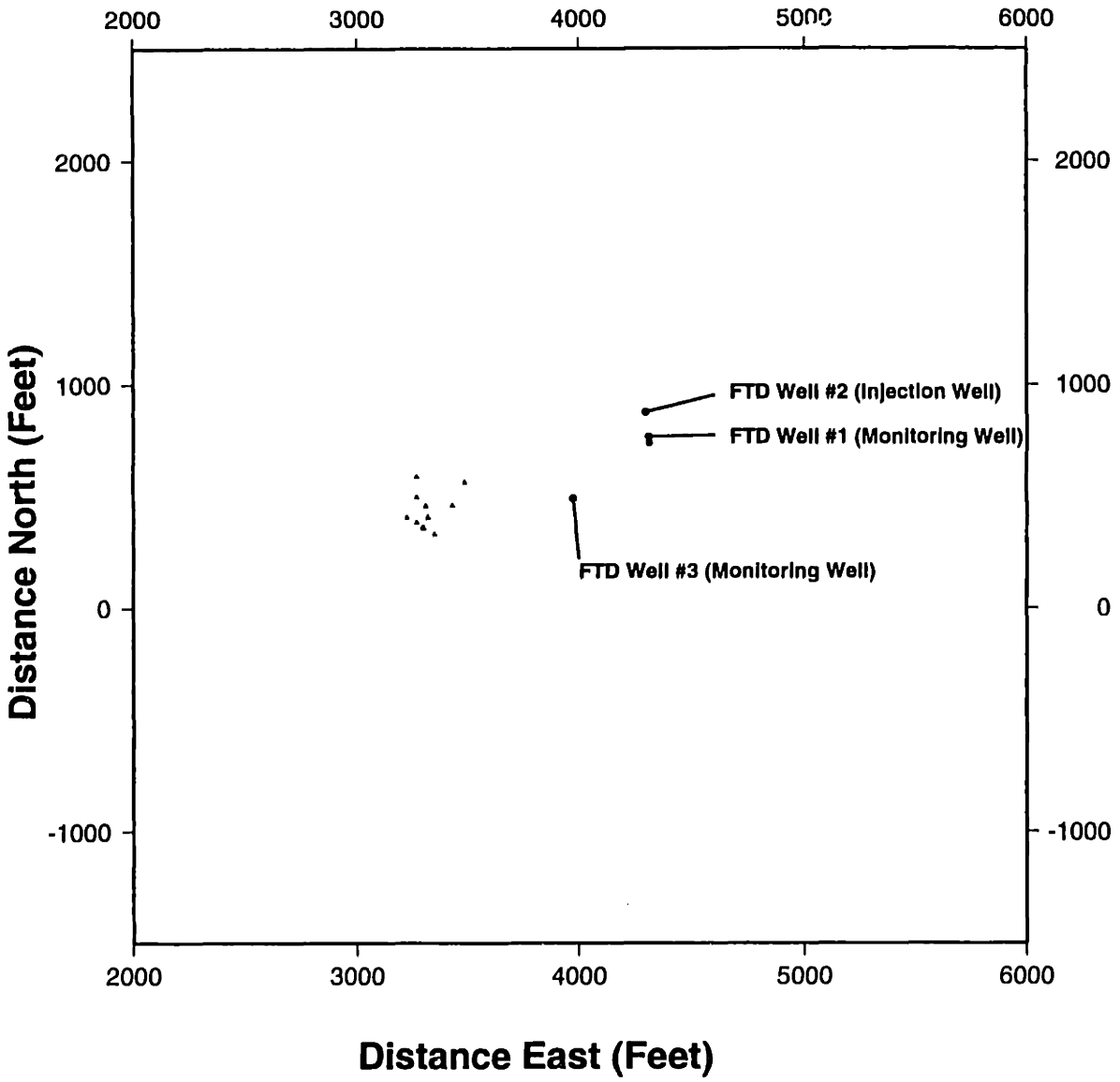

Figure D-12: DWTI Cluster Frame 10

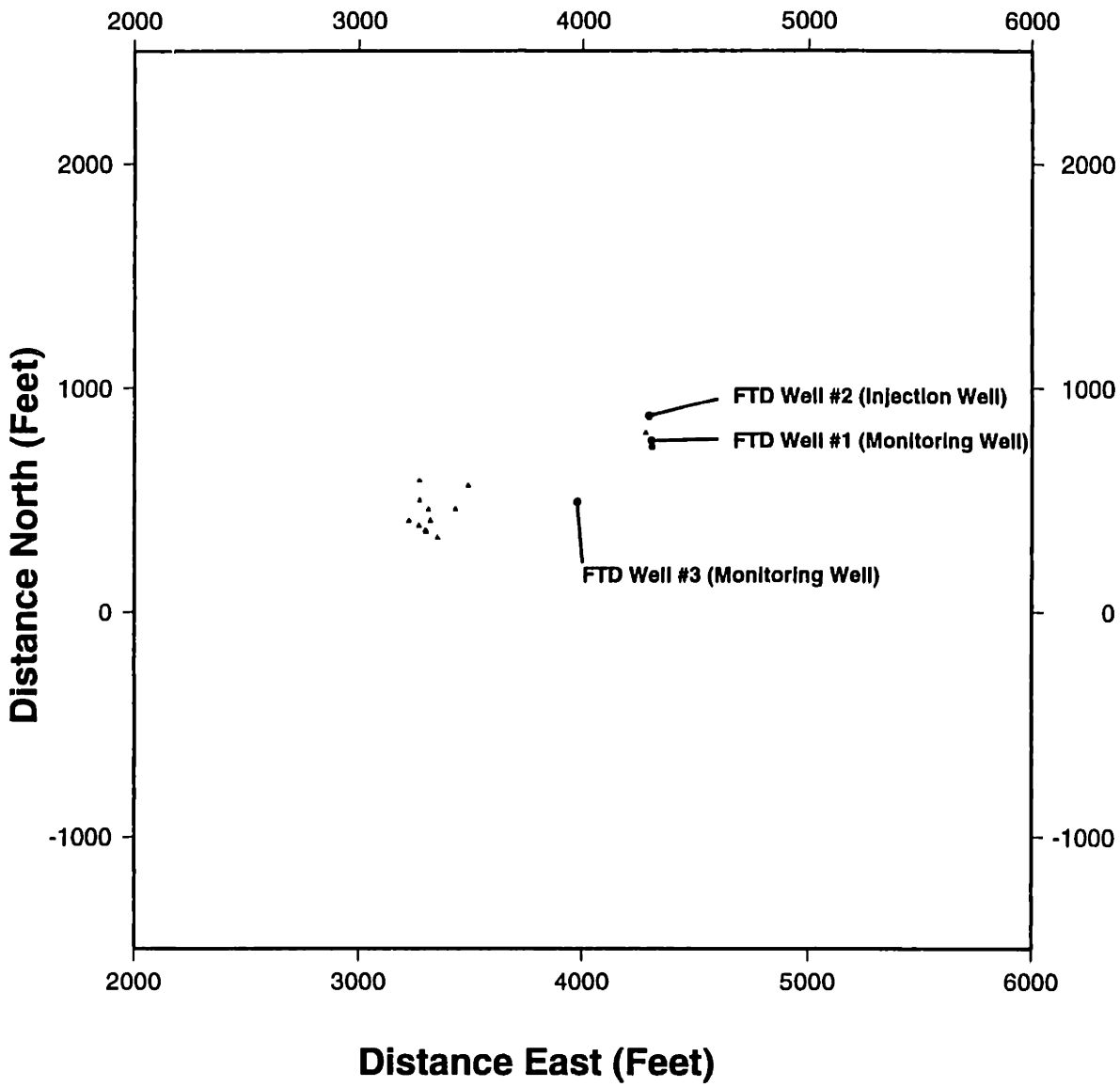

Figure D-13: DWTI Cluster Frame 11

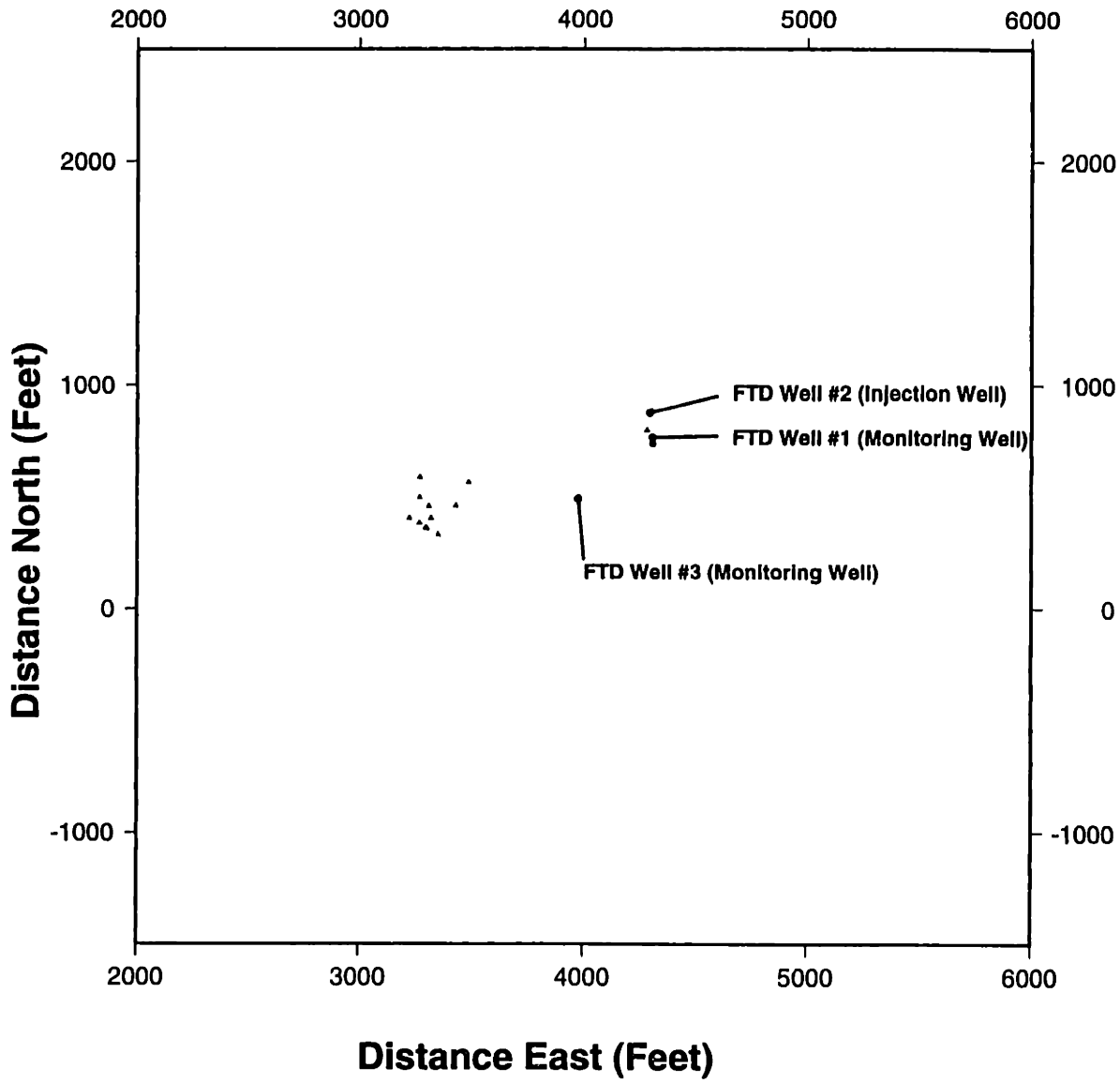

Figure D-14: DWTI Cluster Frame 12

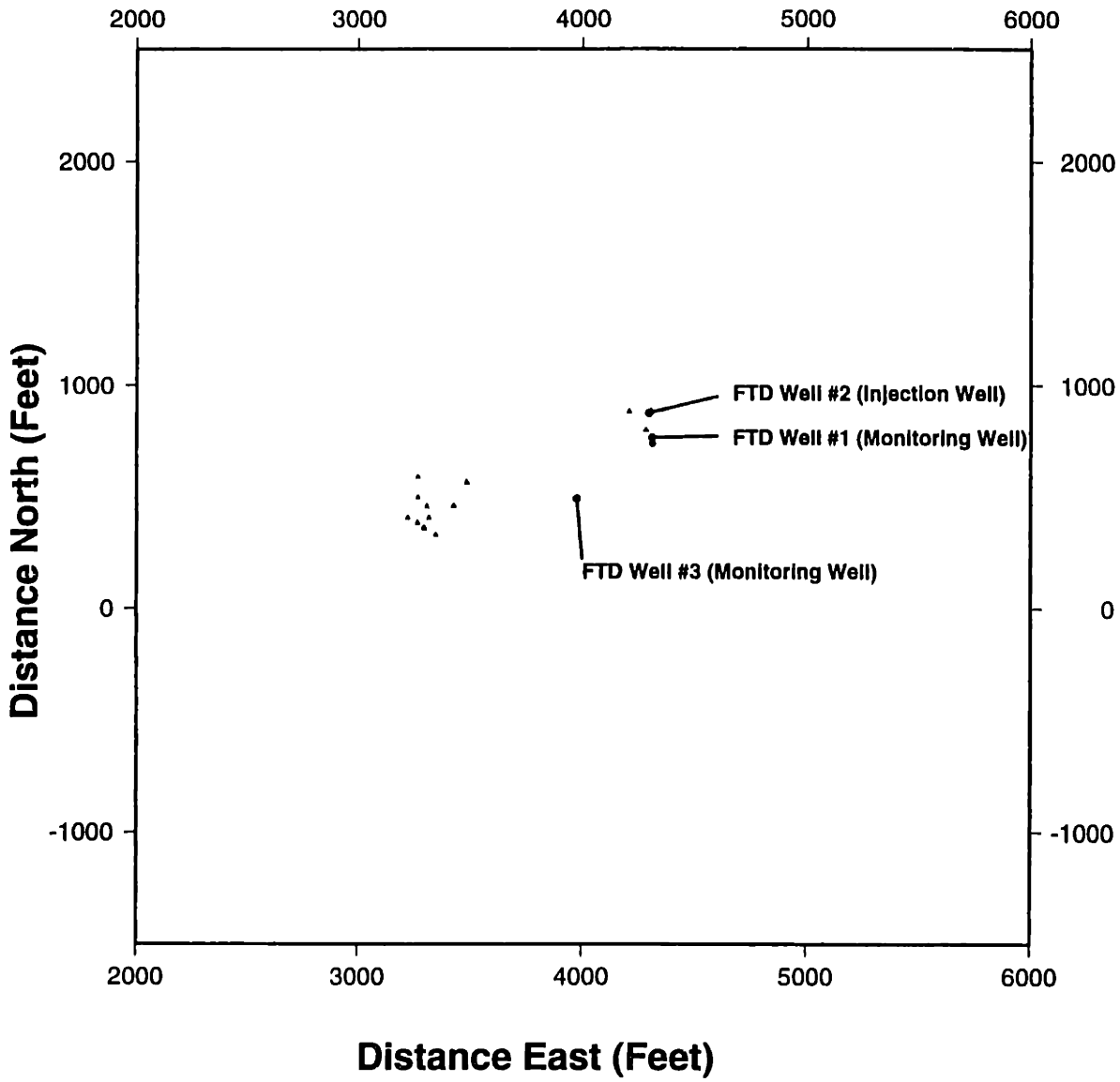

Figure D-15: DWTI Cluster Frame 13

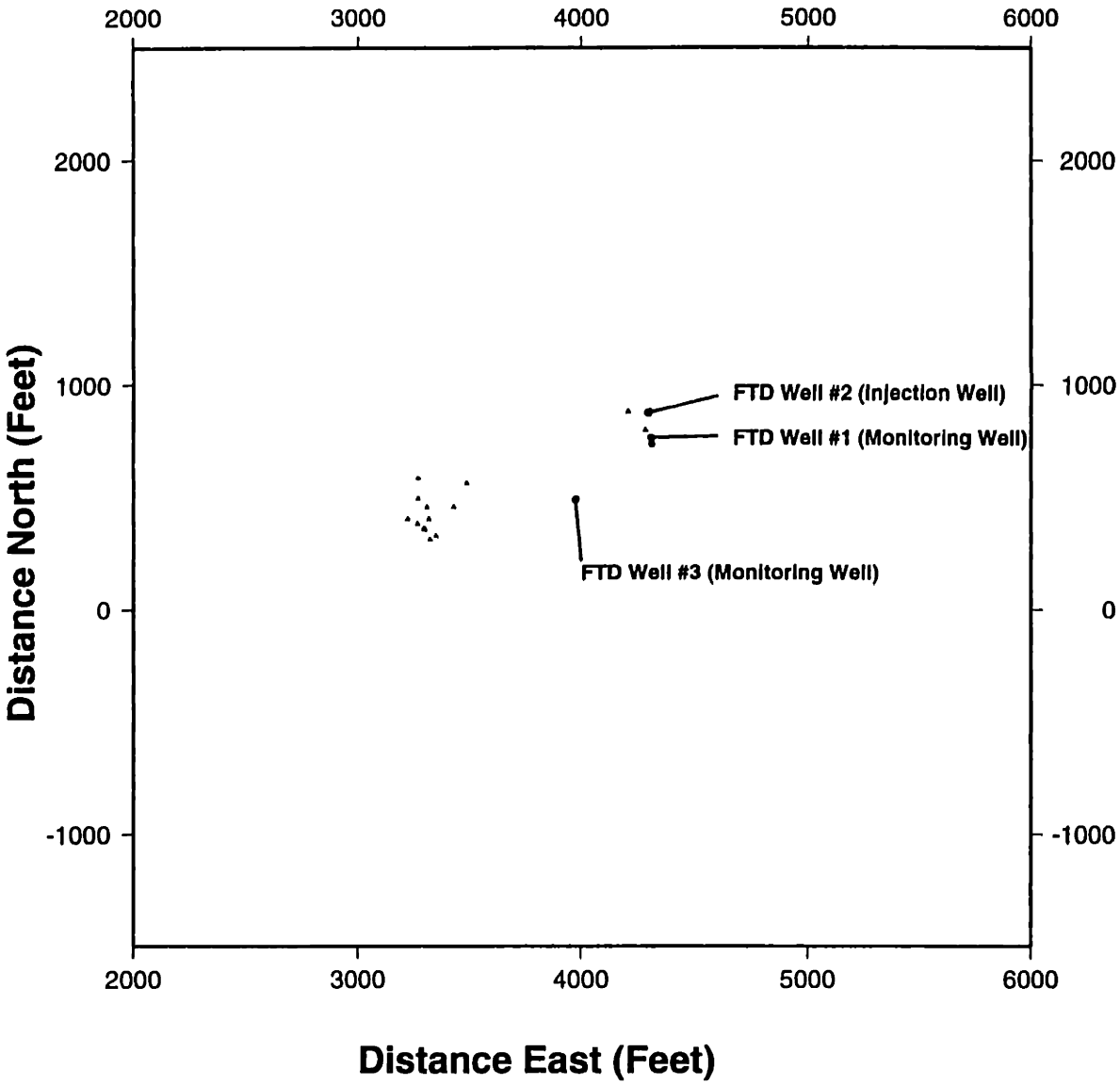

Figure D-16: DWTI Cluster Frame 14

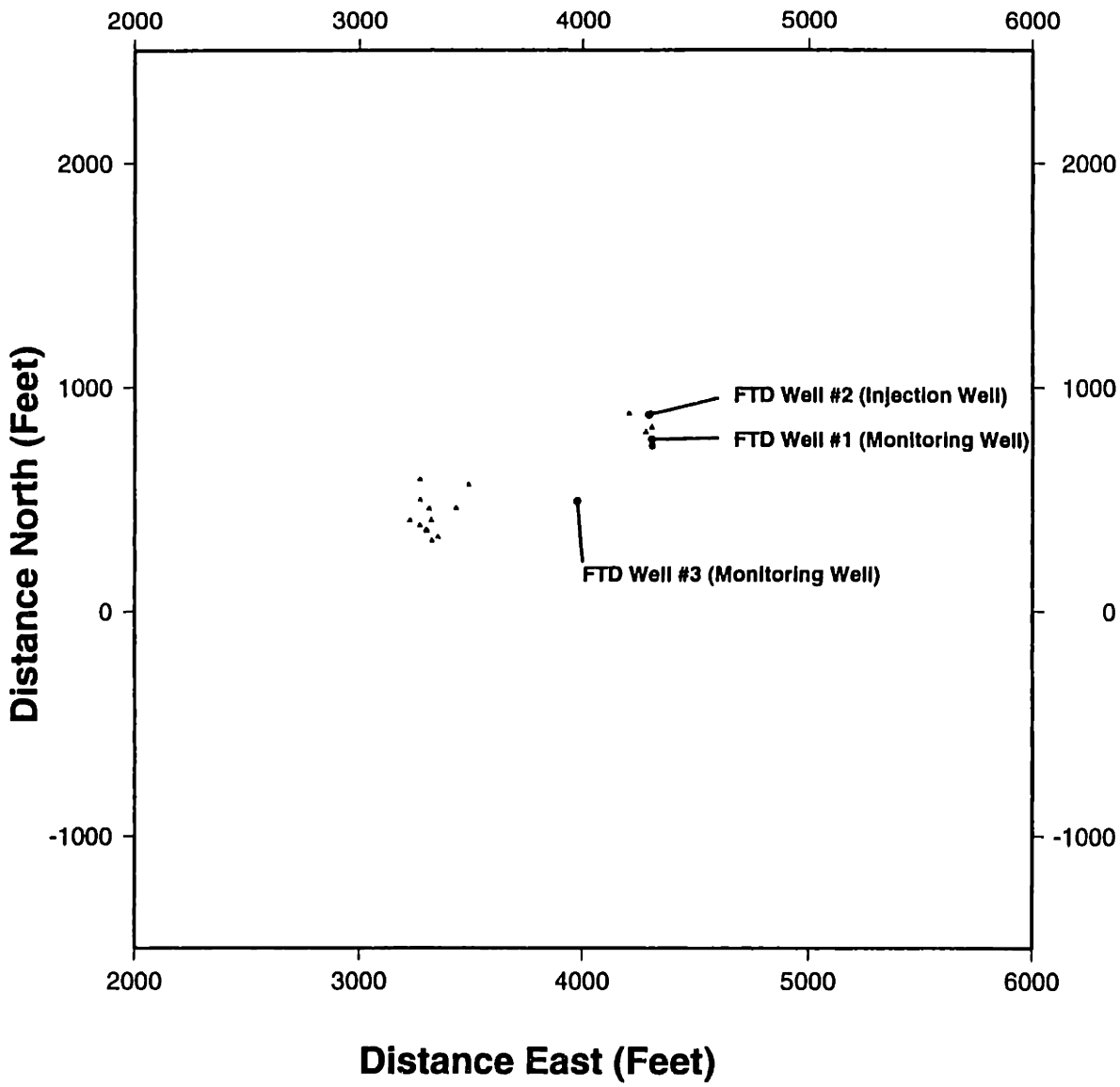

Figure D-17: DWTI Cluster Frame 15

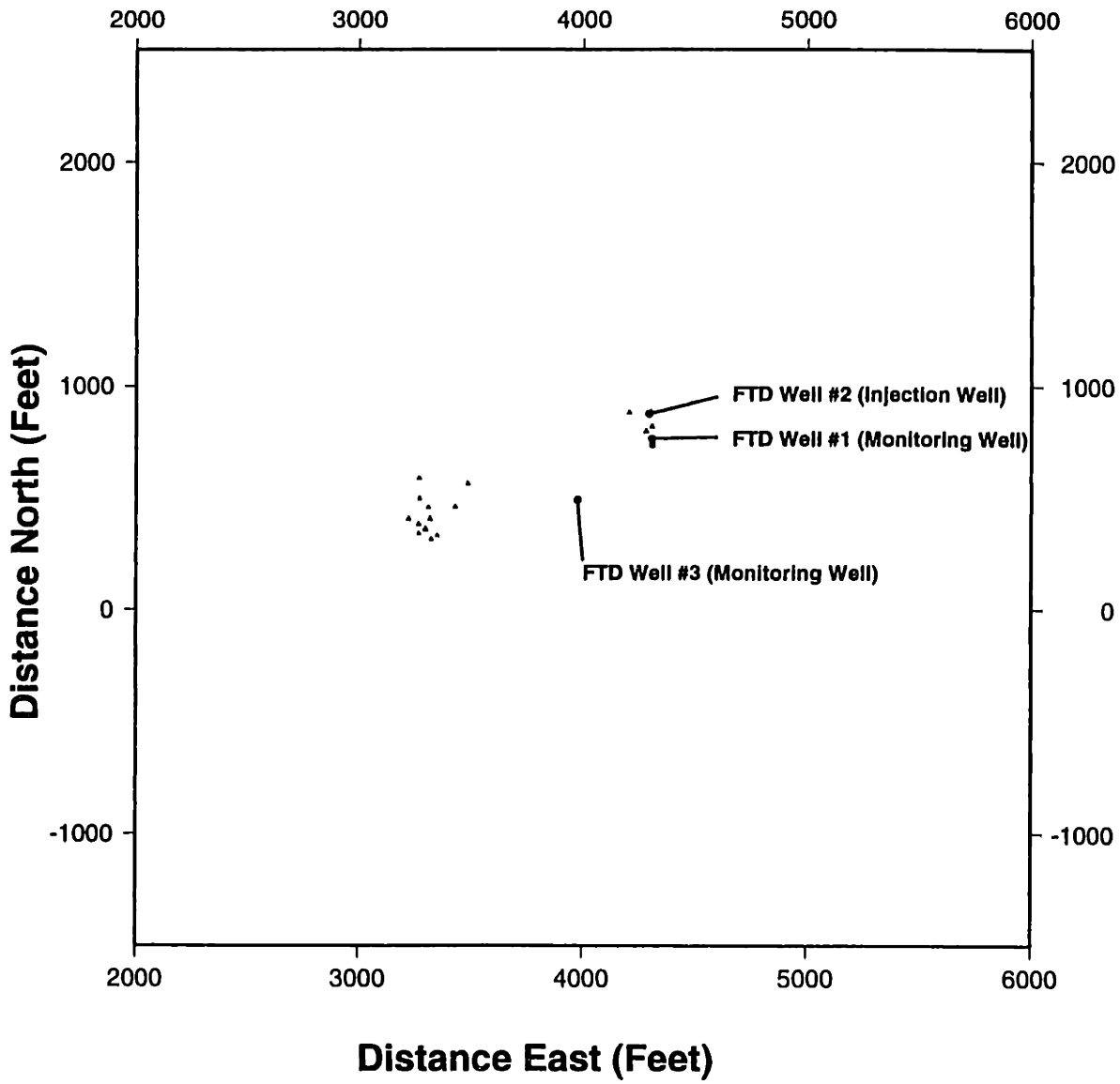

Figure D-18: DWTI Cluster Frame 16

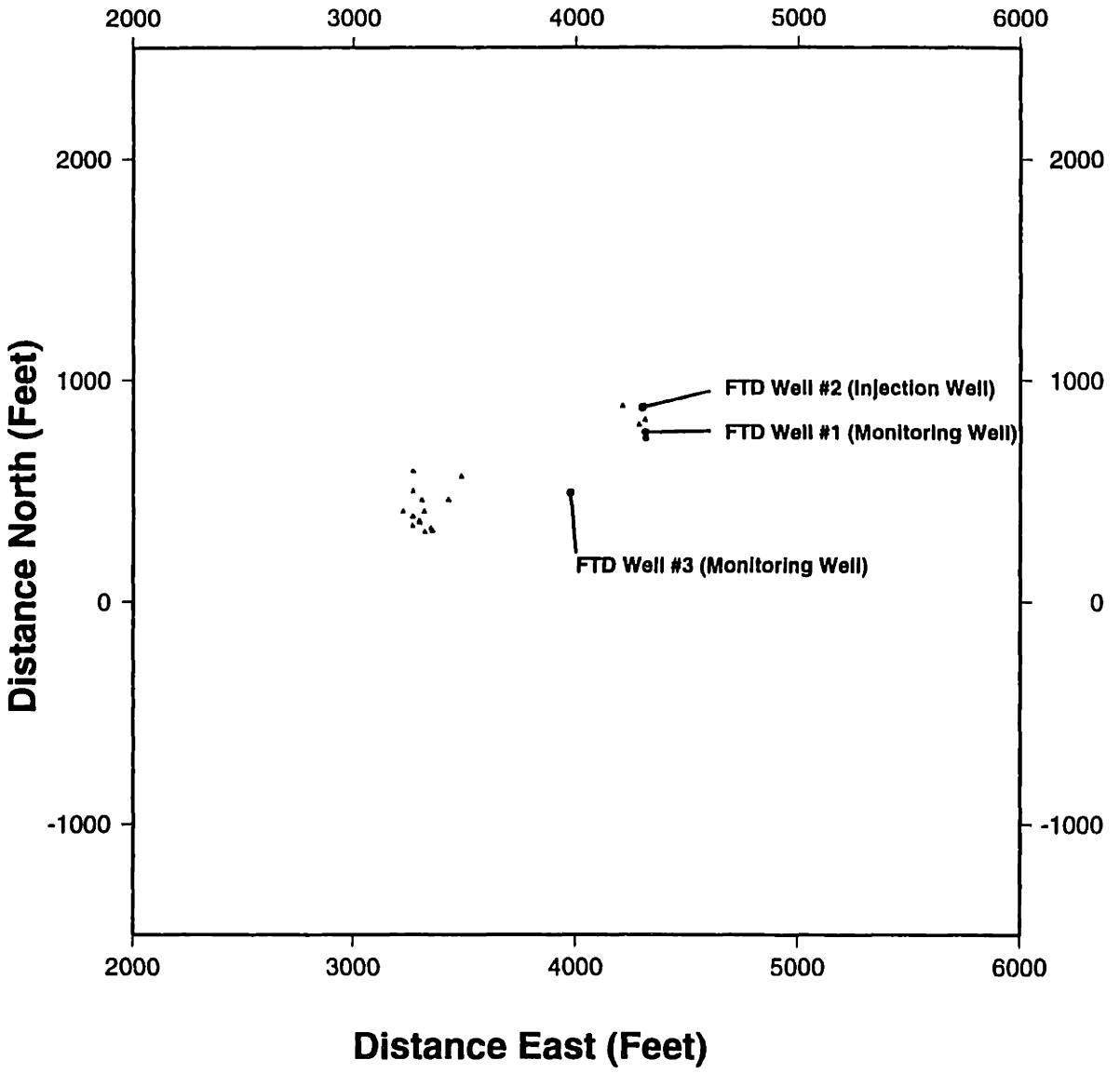

Figure D-19: DWTI Cluster Frame 17

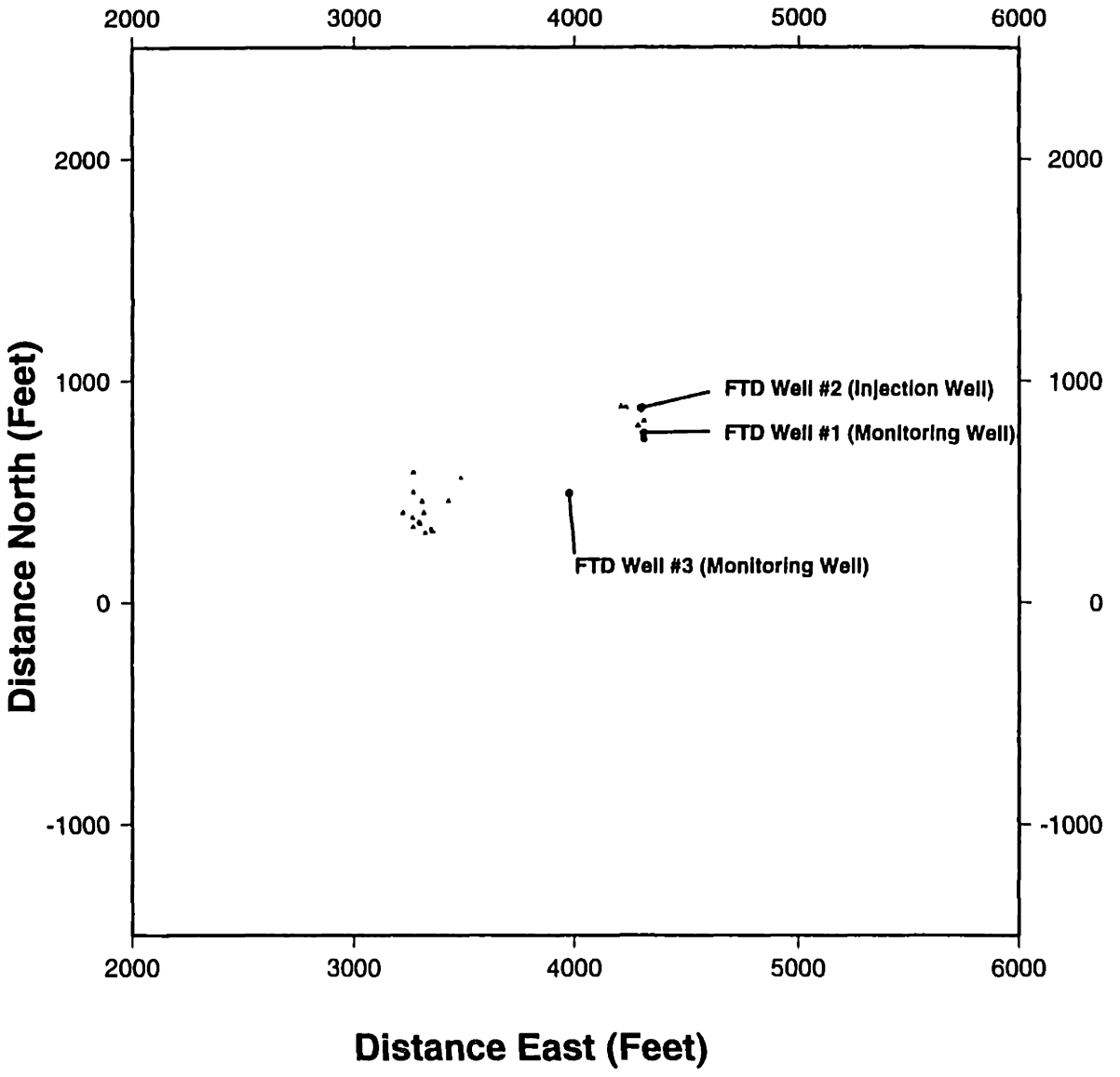

Figure D-20: DWTI Cluster Frame 18

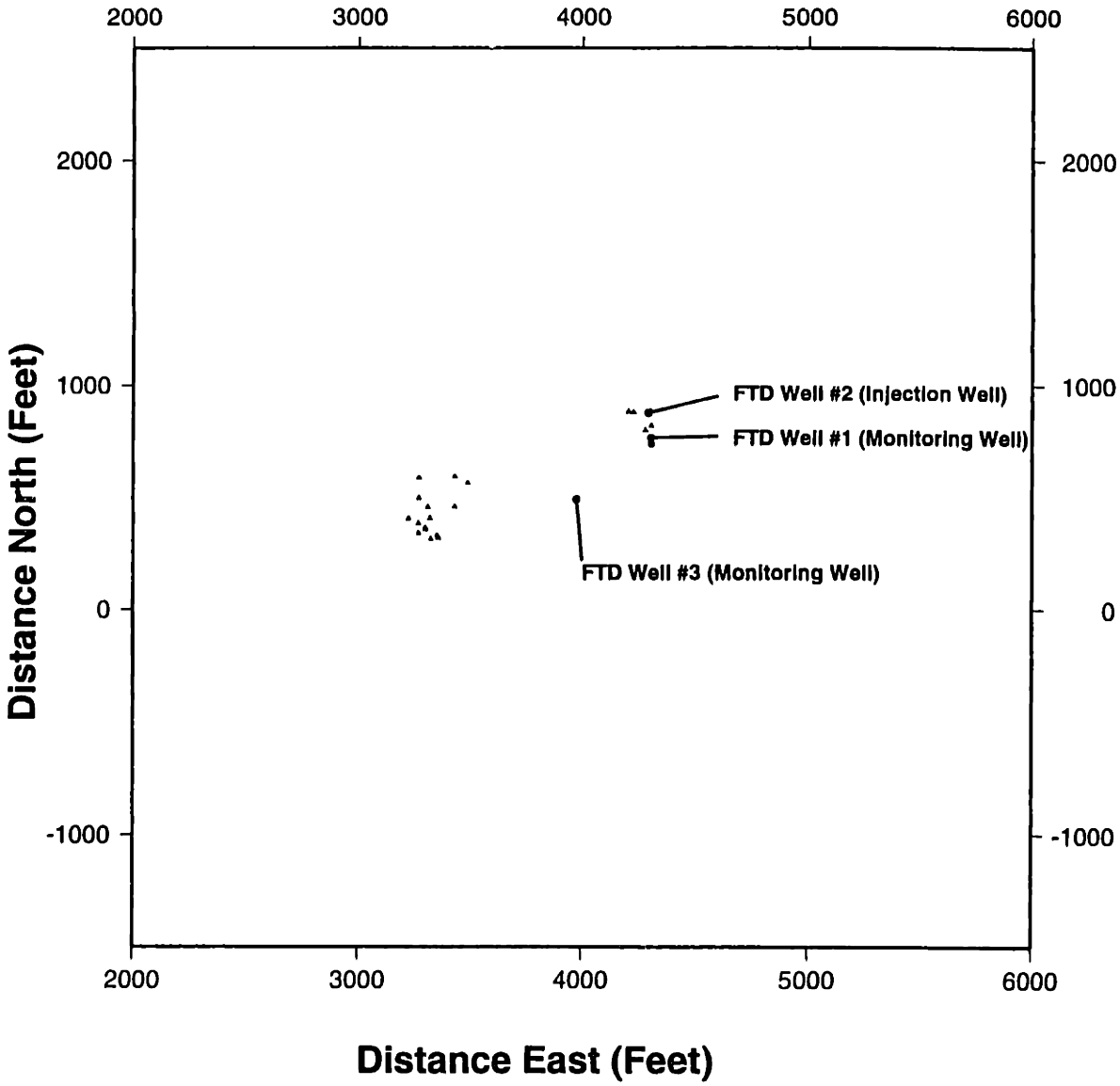

Figure D-21: DWTI Cluster Frame 19

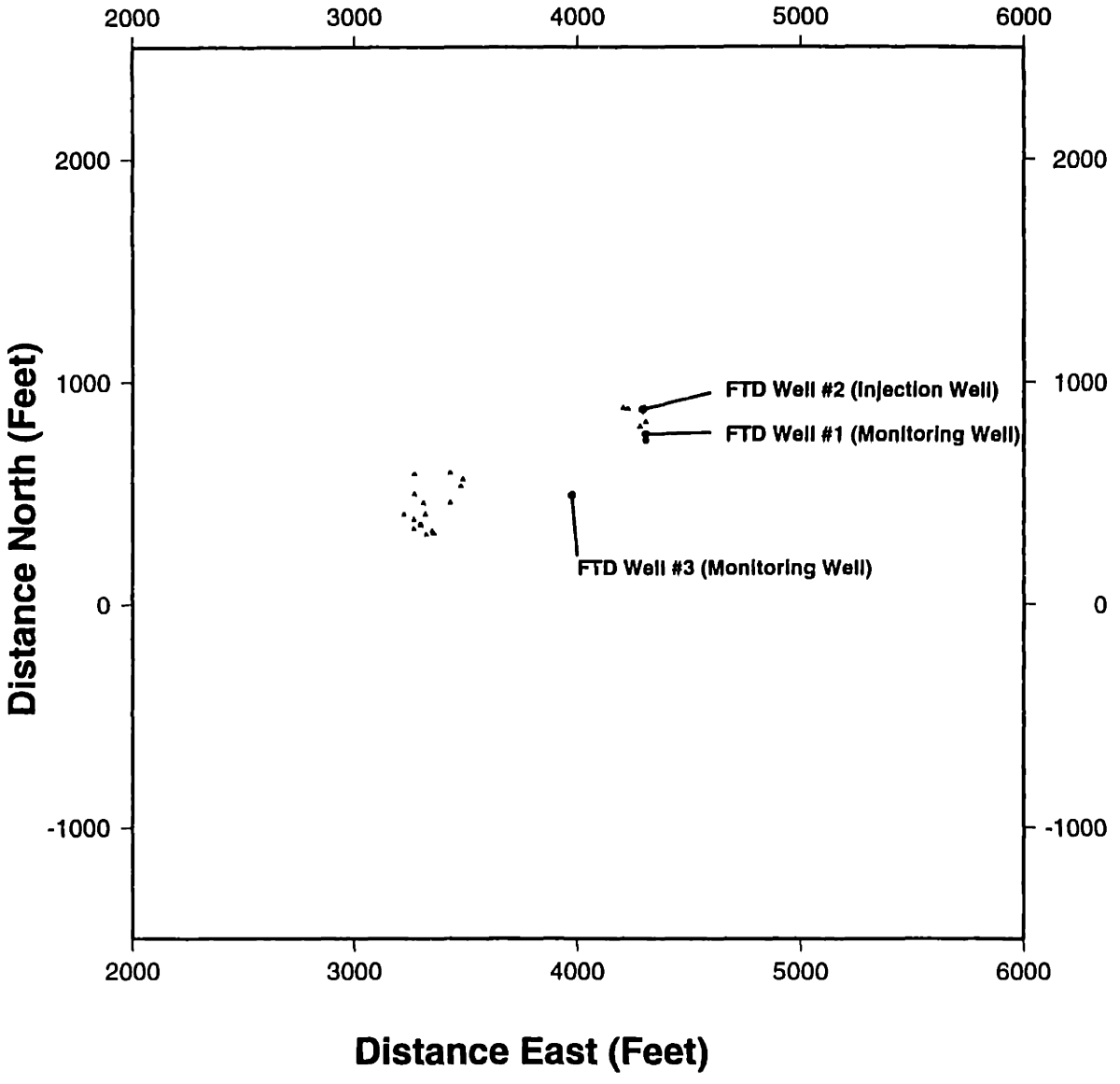

Figure D-22: DWTI Cluster Frame 20

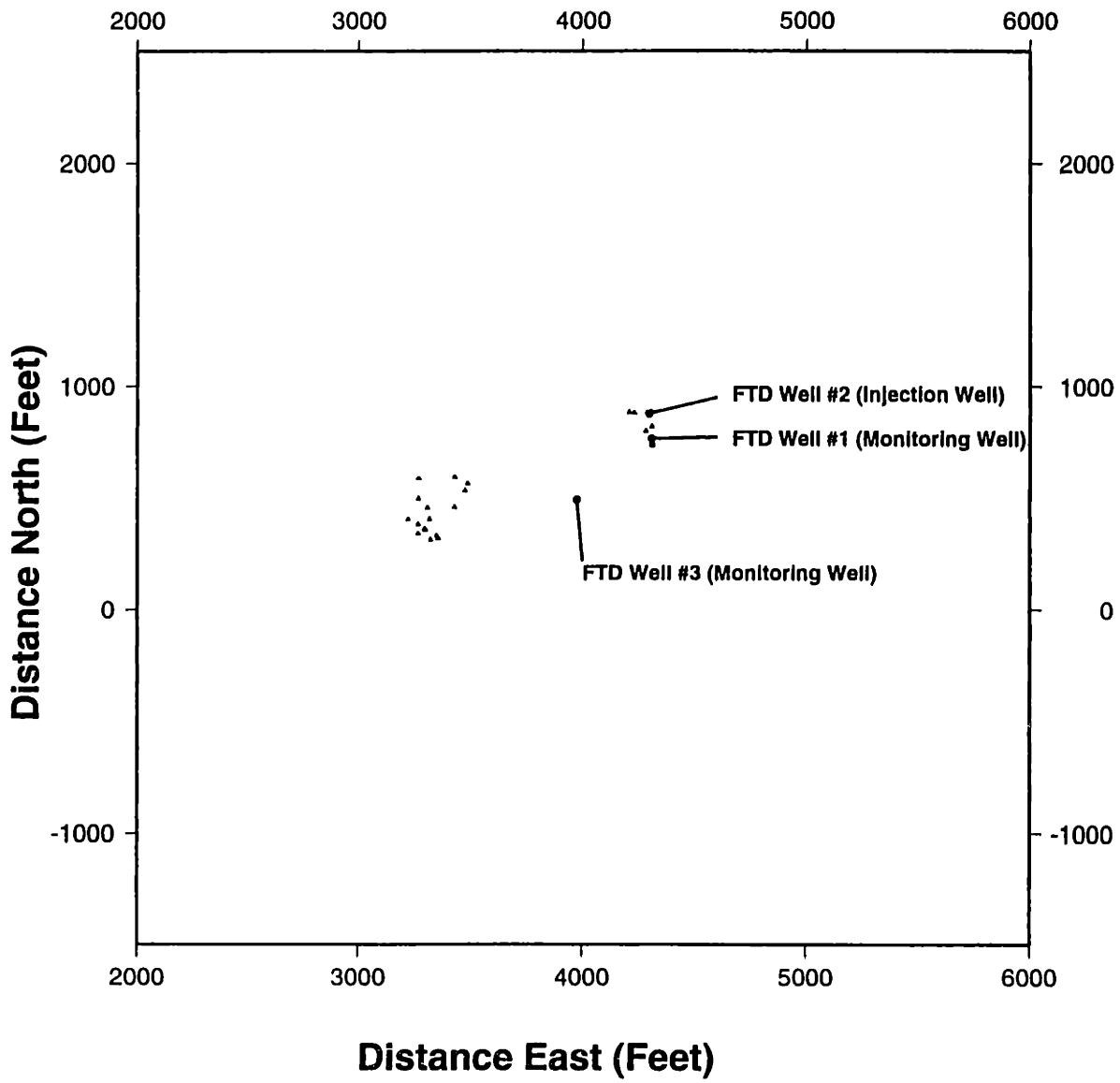

Figure D-23: DWTI Cluster Frame 21

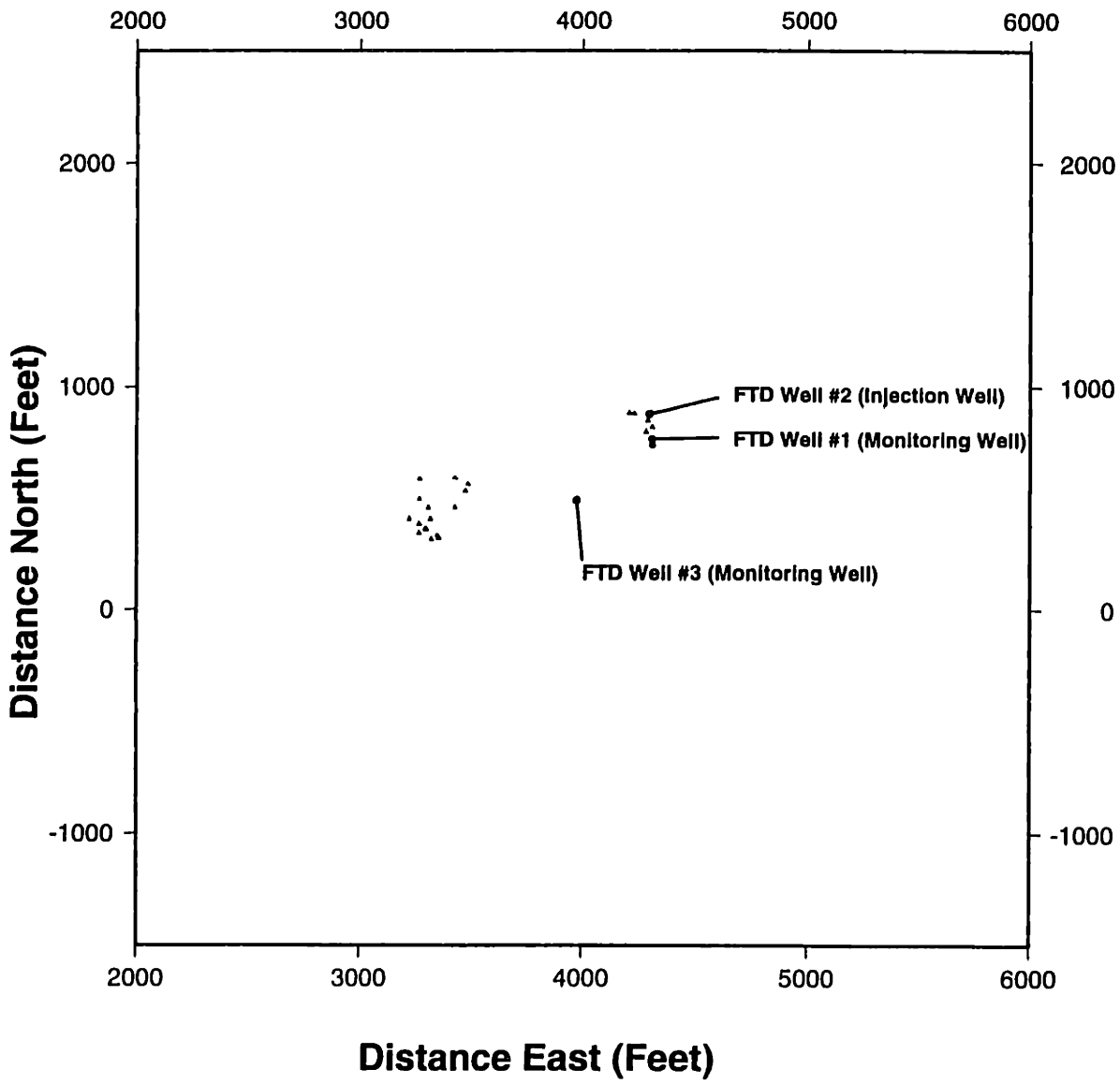

Figure D-24: DWTI Cluster Frame 22

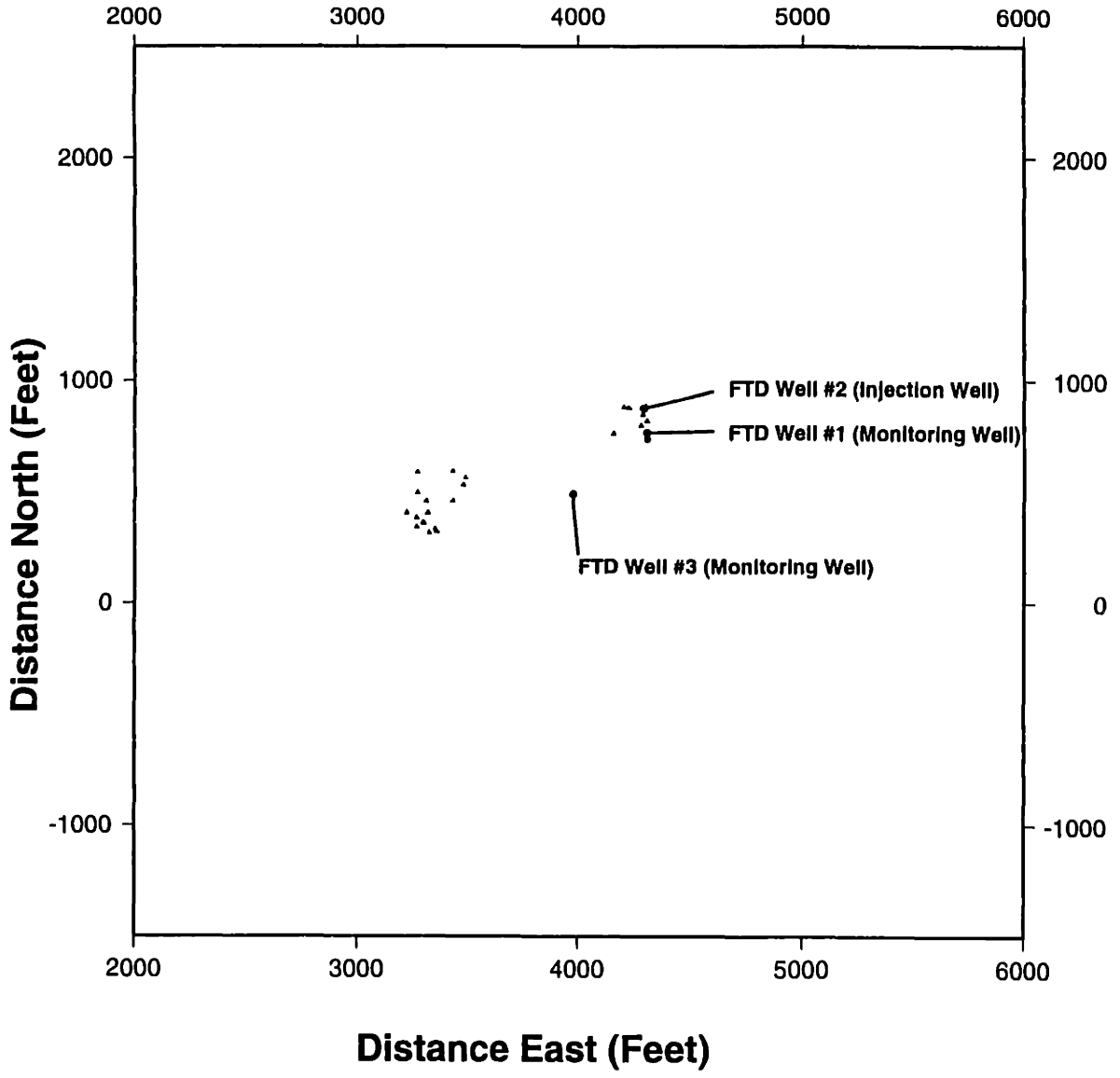

Figure D-25: DWTI Cluster Frame 23

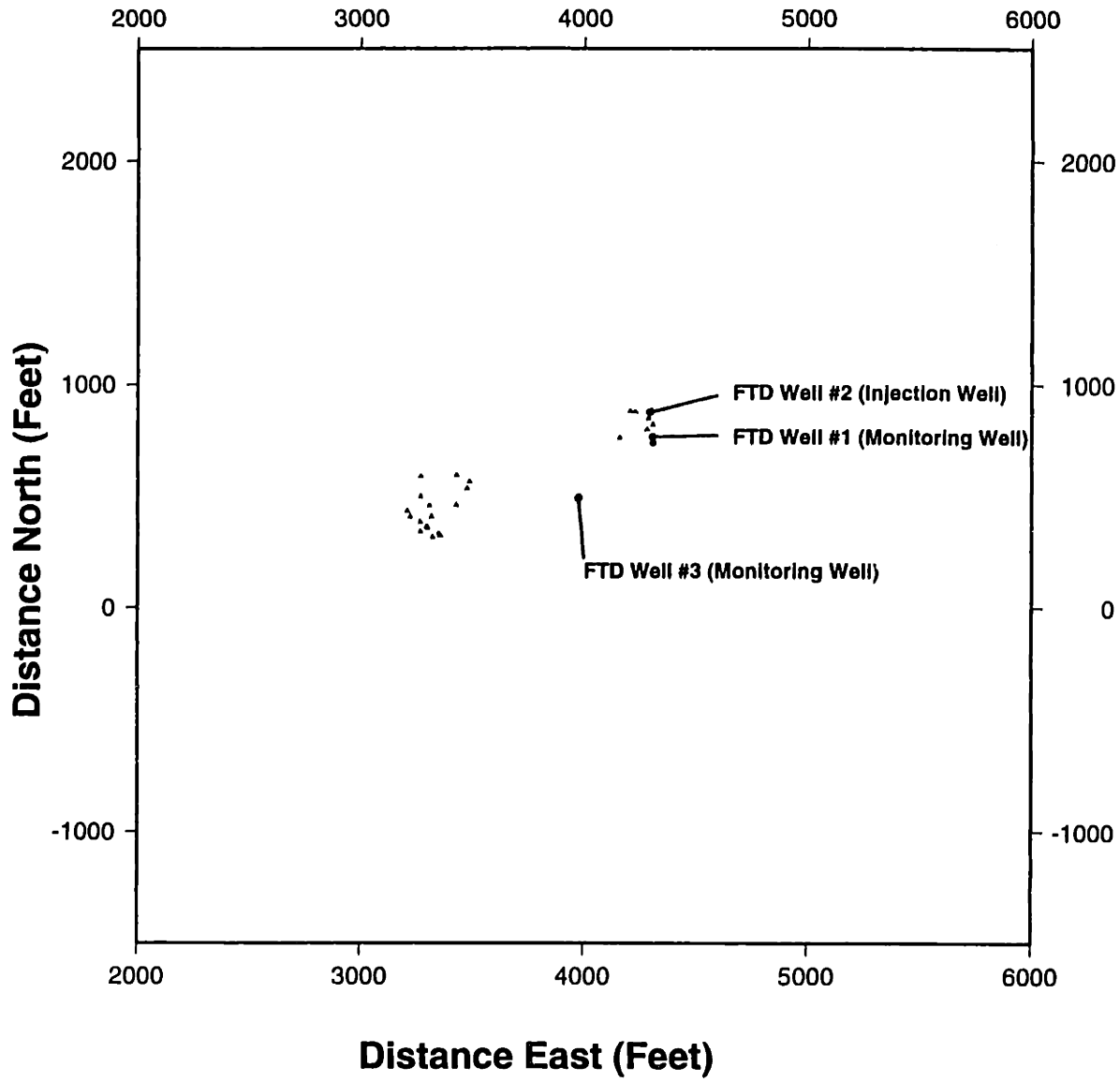

Figure D-26: DWTI Cluster Frame 24

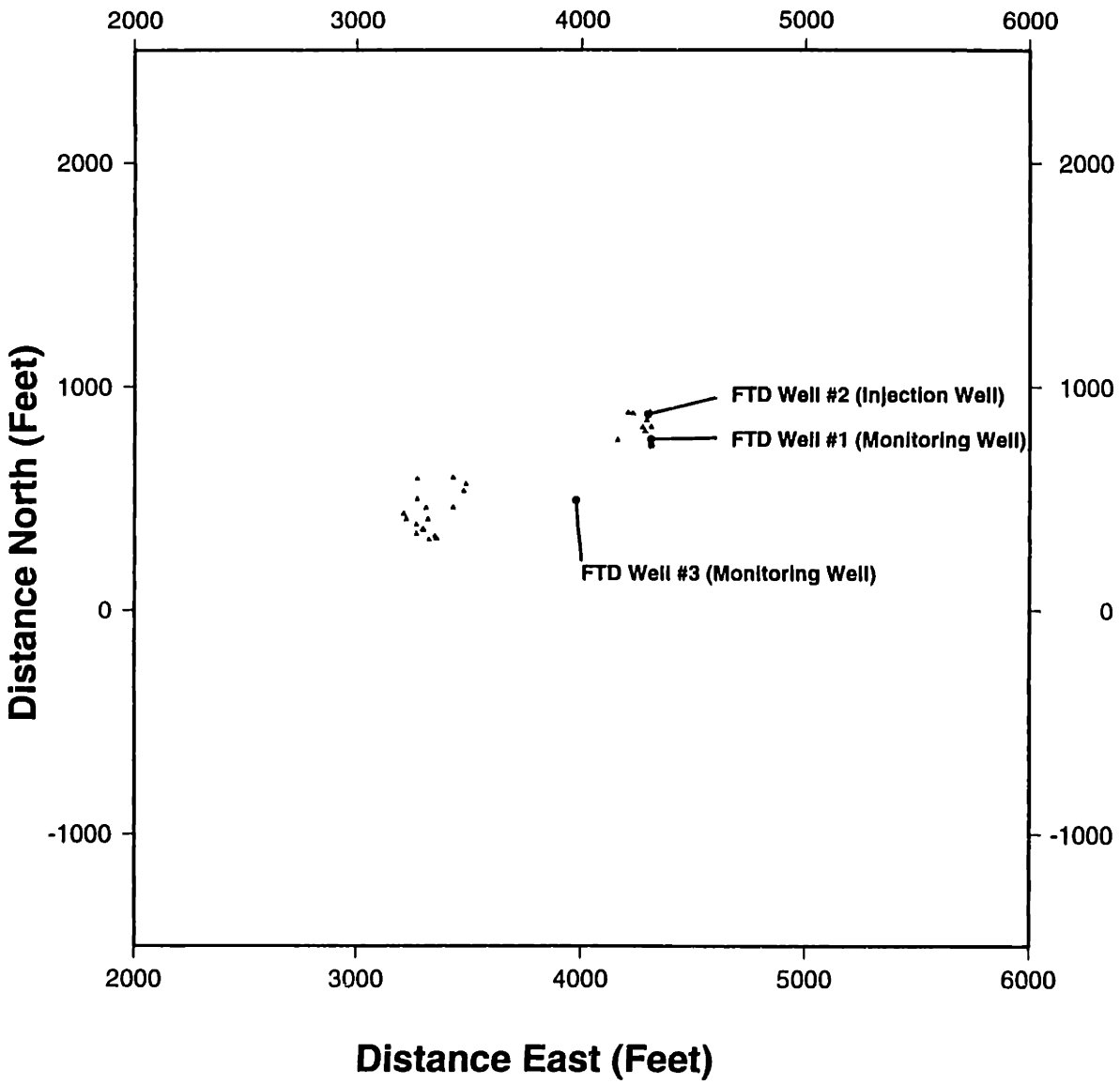

Figure D-27: DWTI Cluster Frame 25

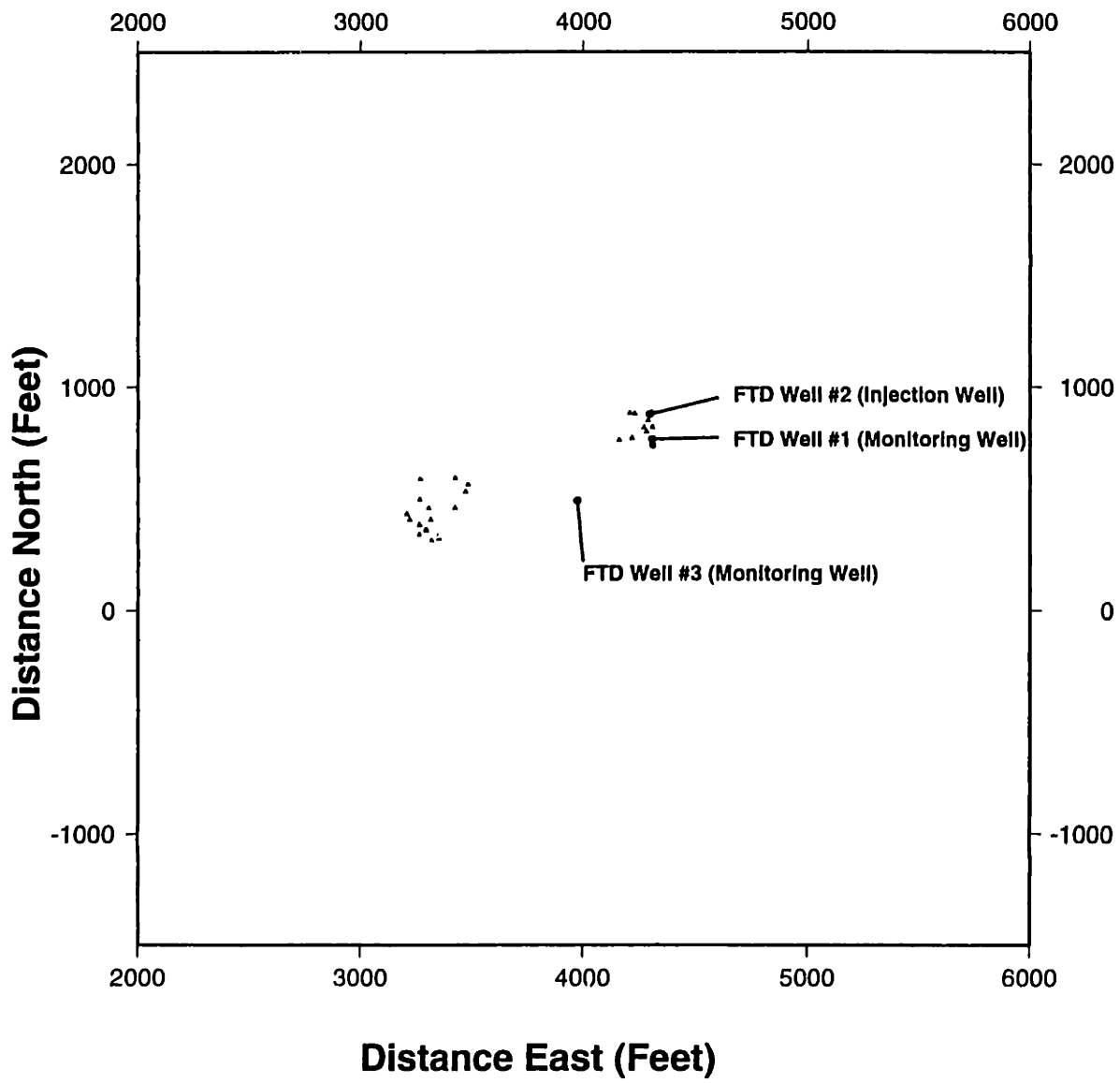

Figure D-28: DWTI Cluster Frame 26

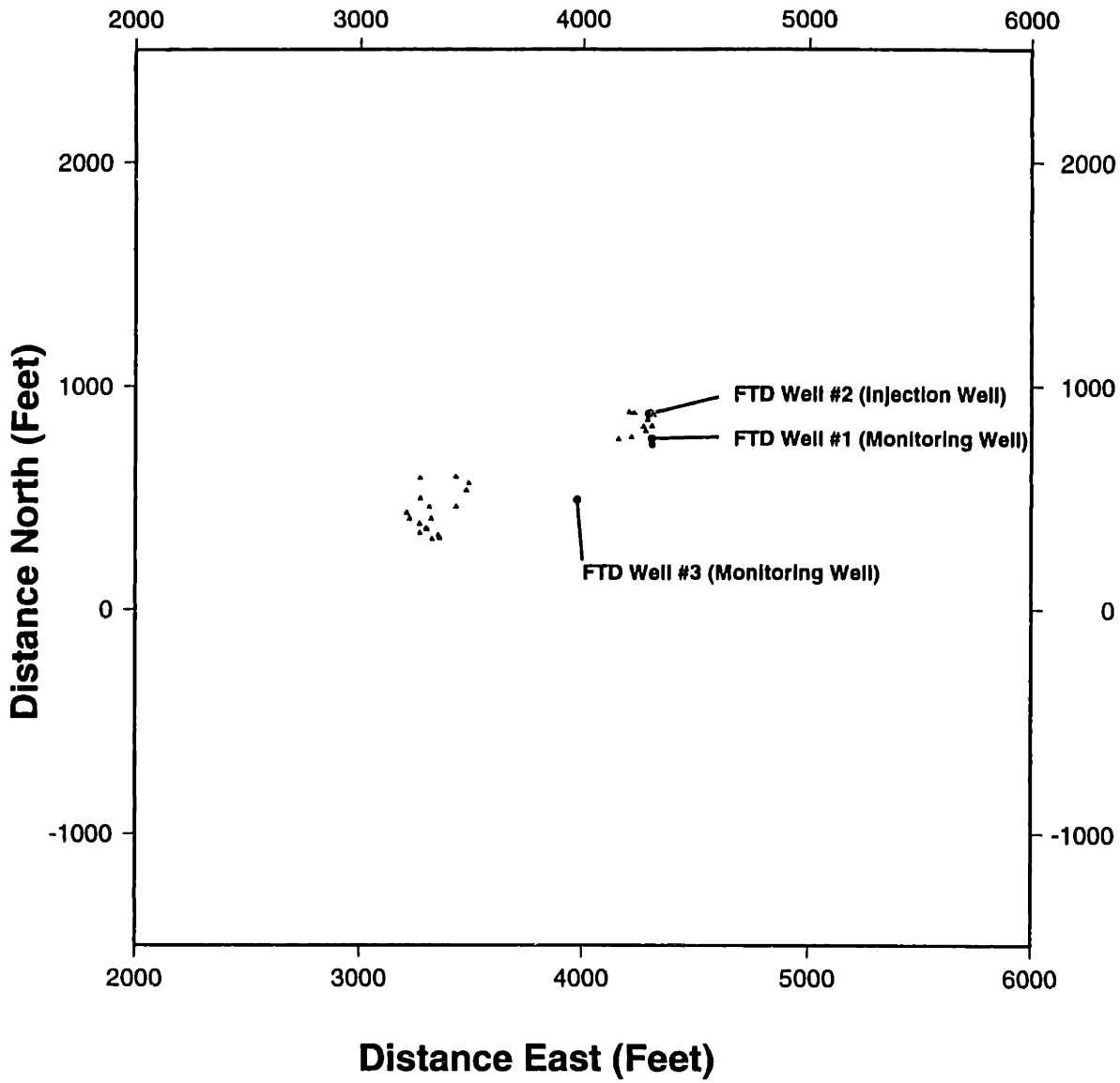

Figure D-29: DWTI Cluster Frame 27

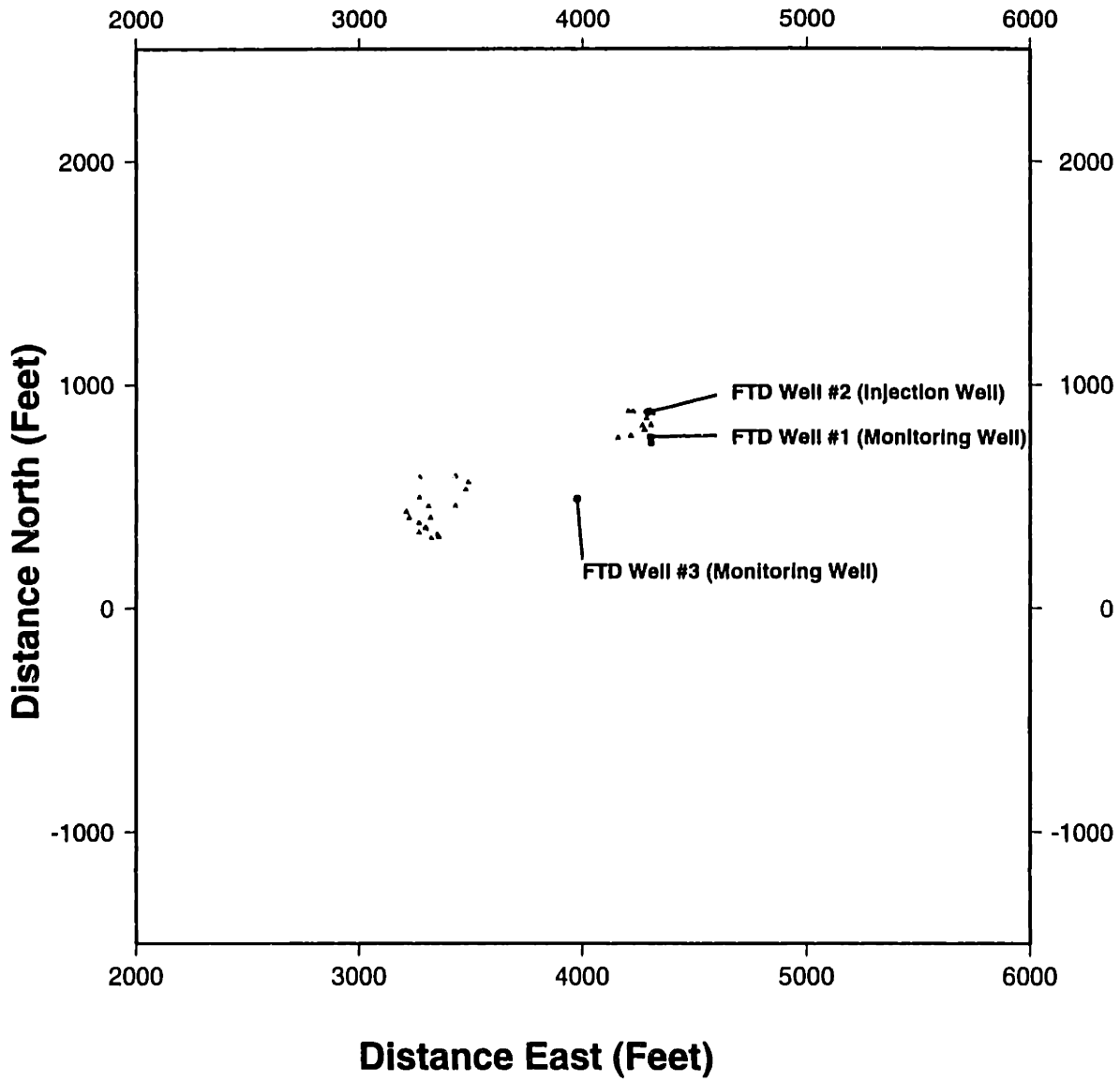

Figure D-30: DWTI Cluster Frame 28

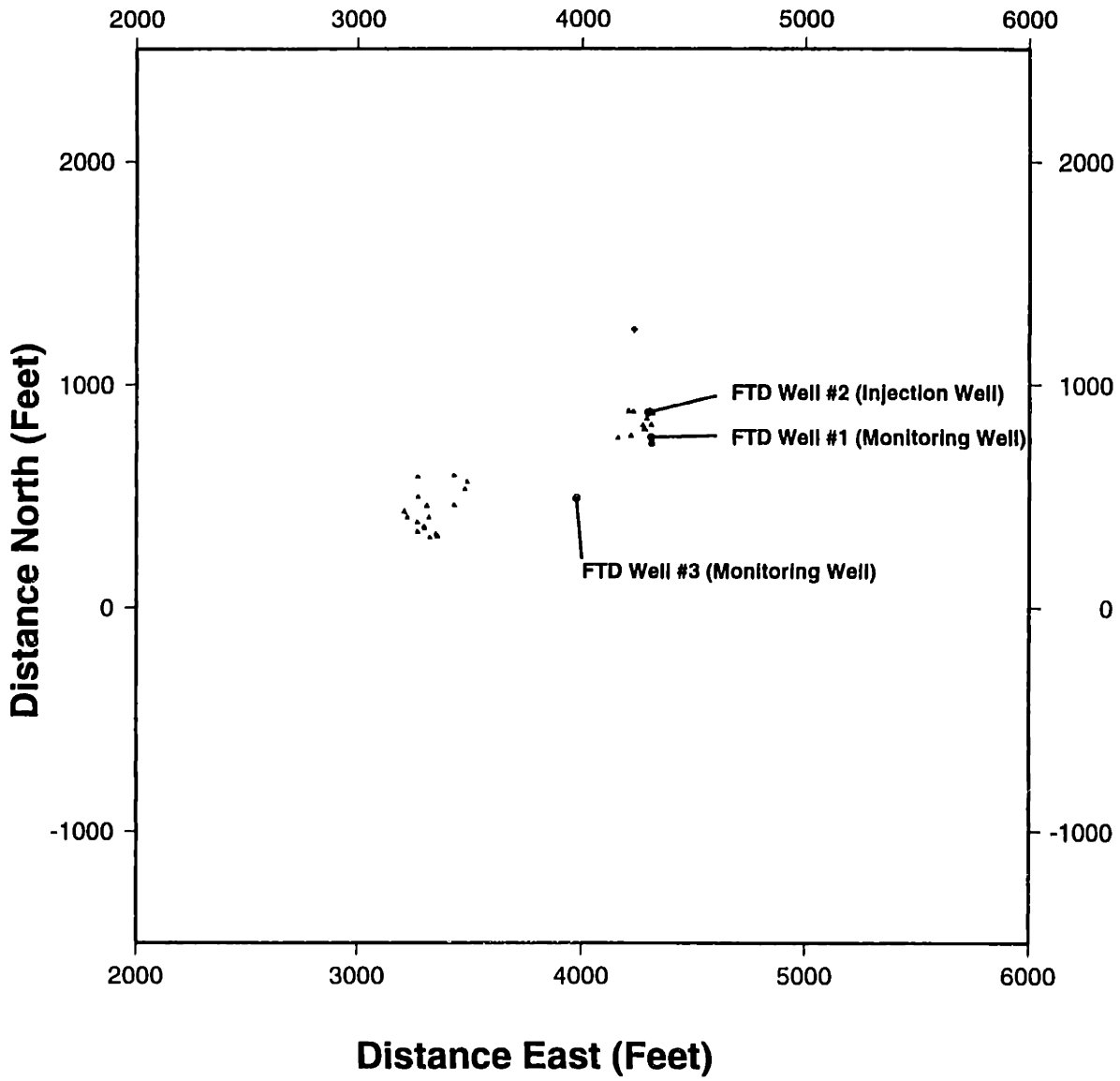

Figure D-31: DWTI Cluster Frame 29

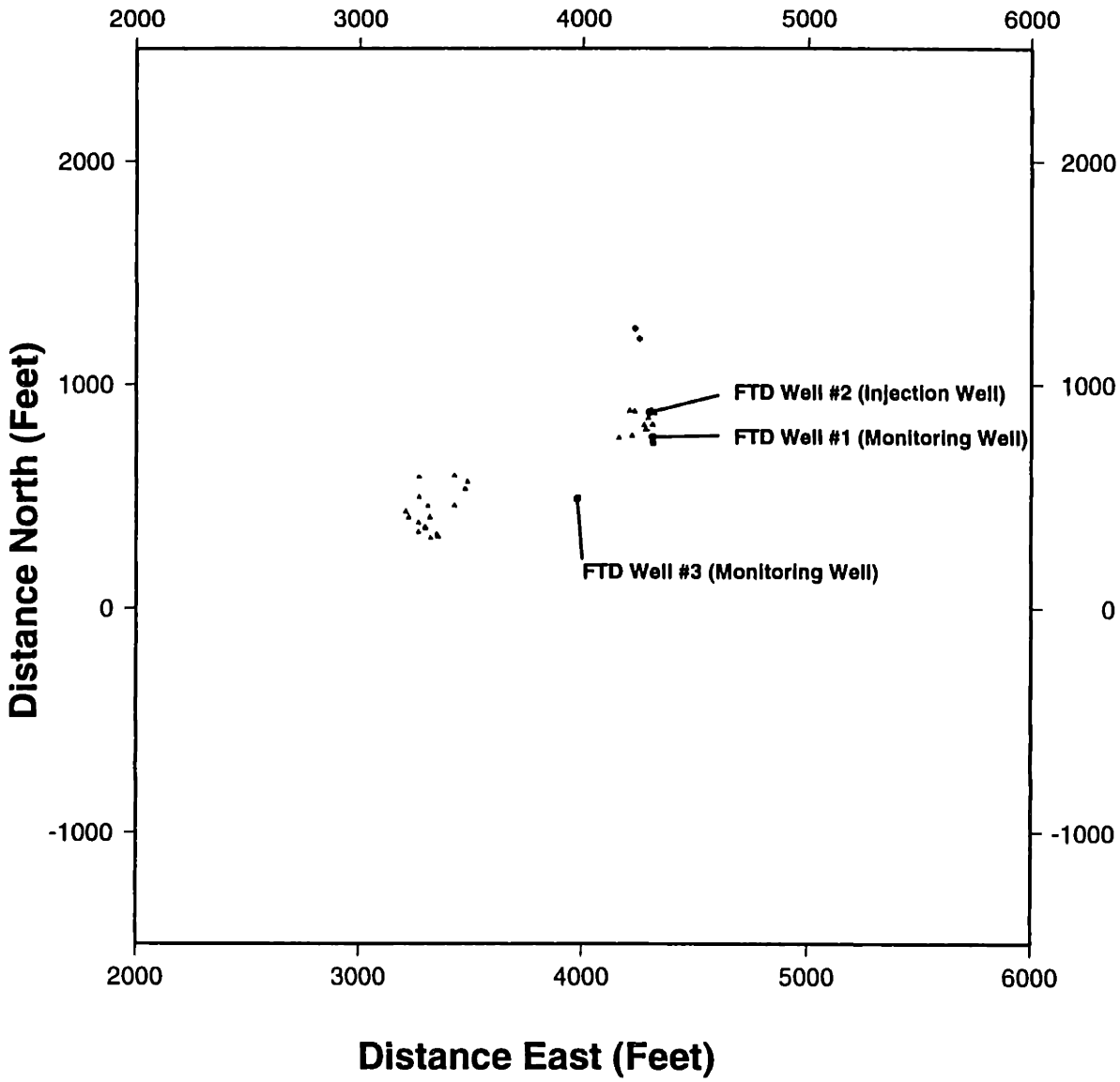

Figure D-32: DWTI Cluster Frame 30

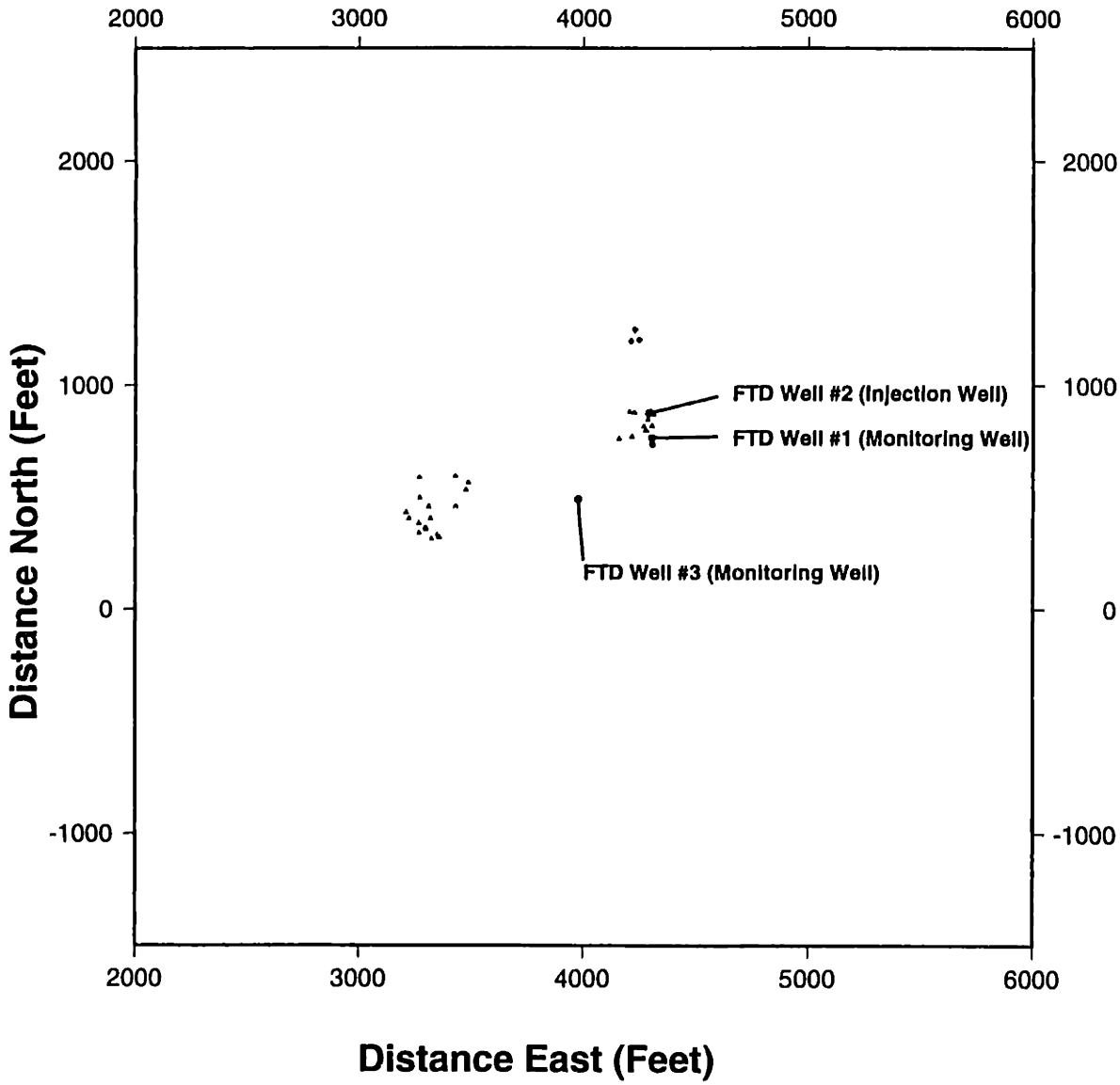

Figure D-33: DWTI Cluster Frame 31

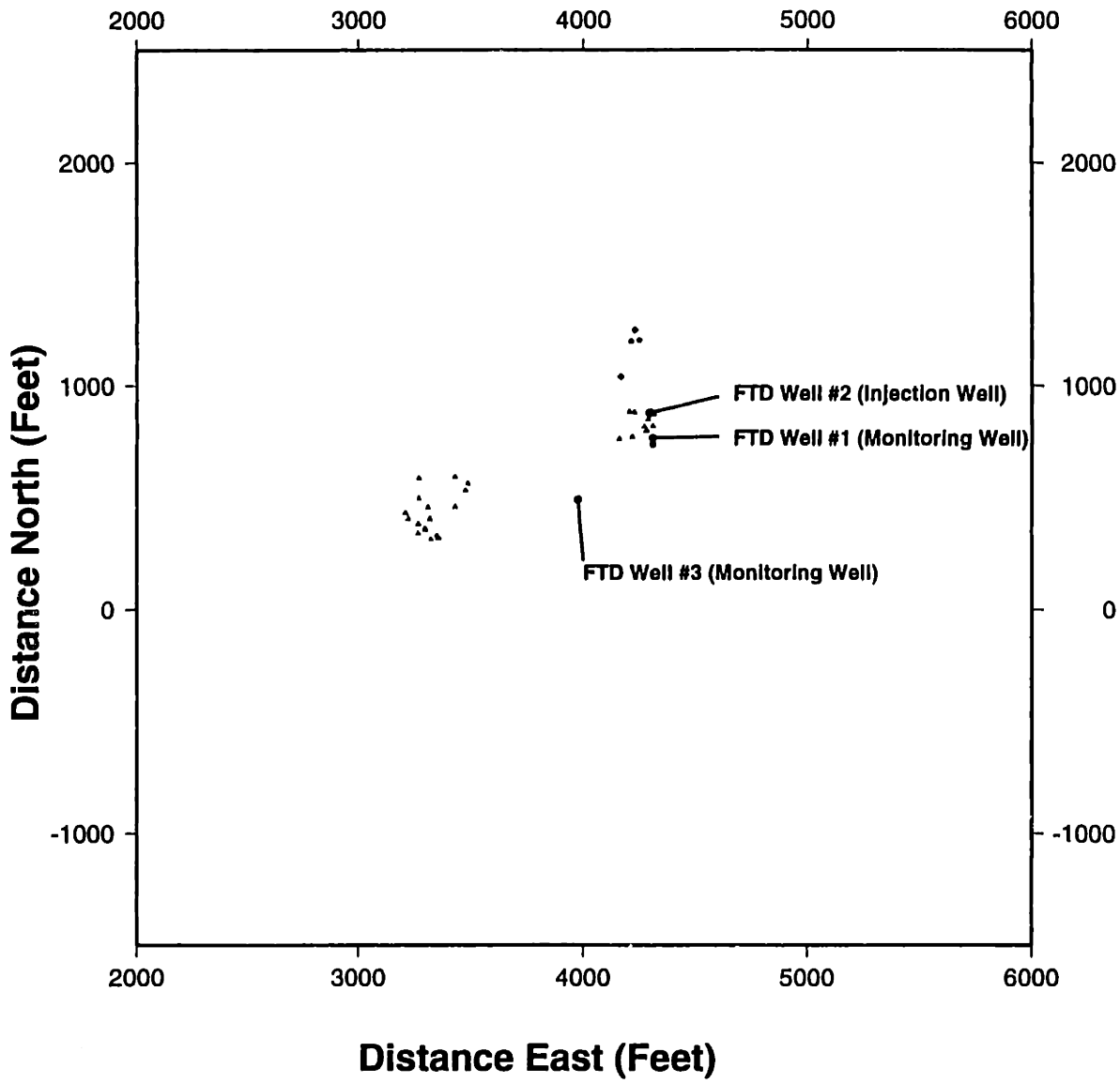

Figure D-34: DWTI Cluster Frame 32

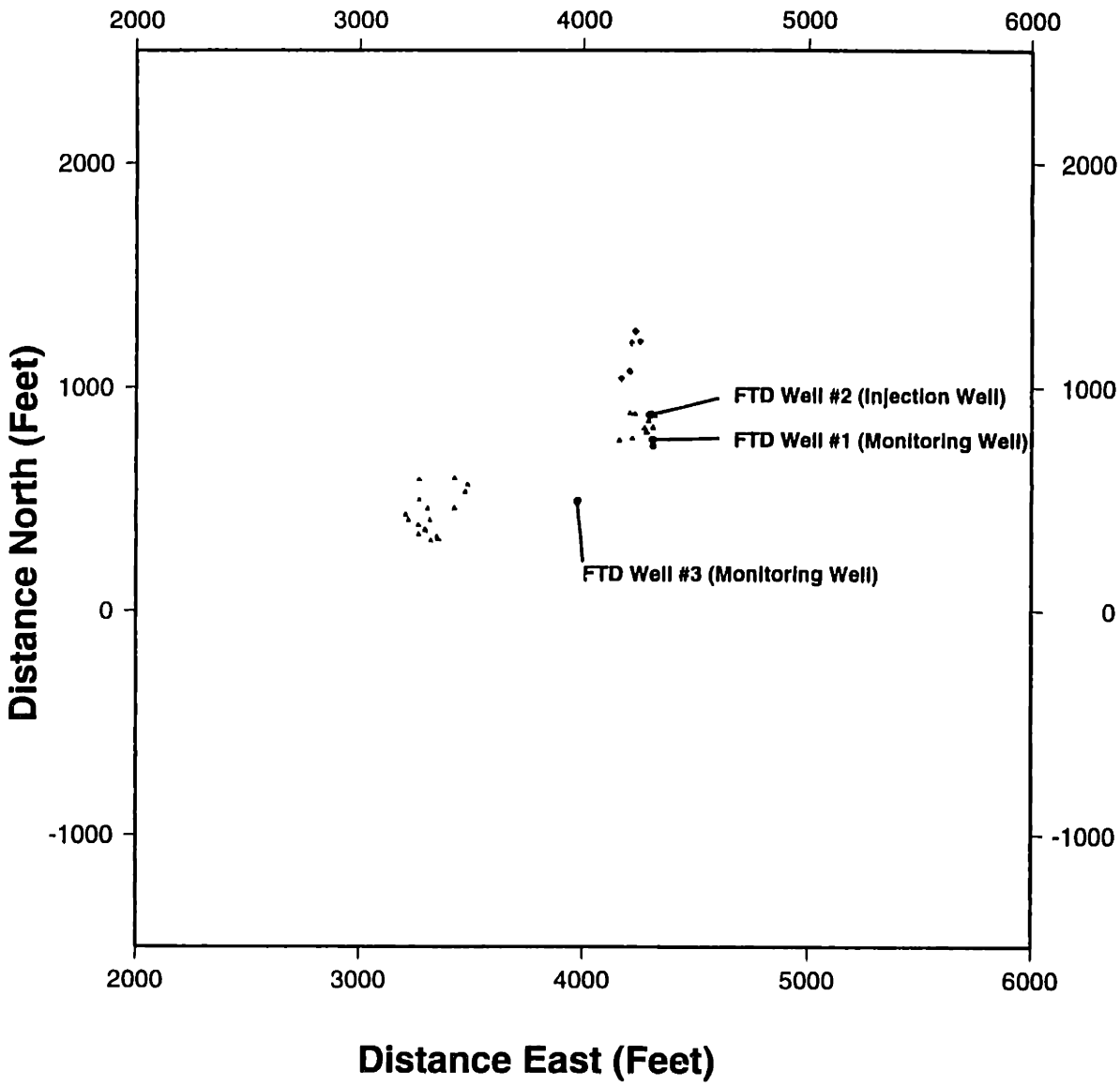

Figure D-35: DWTI Cluster Frame 33

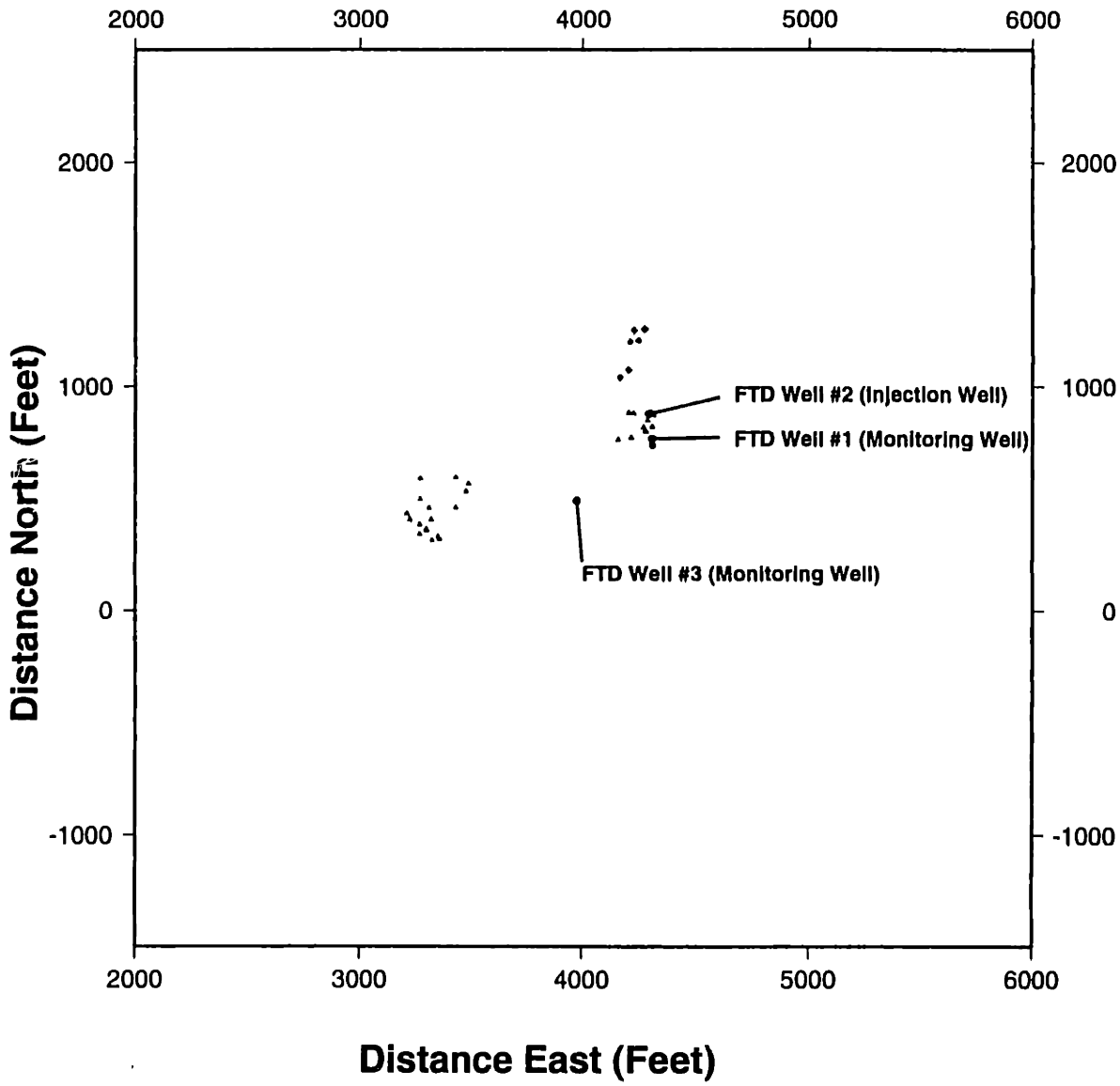

Figure D-36: DWTI Cluster Frame 34

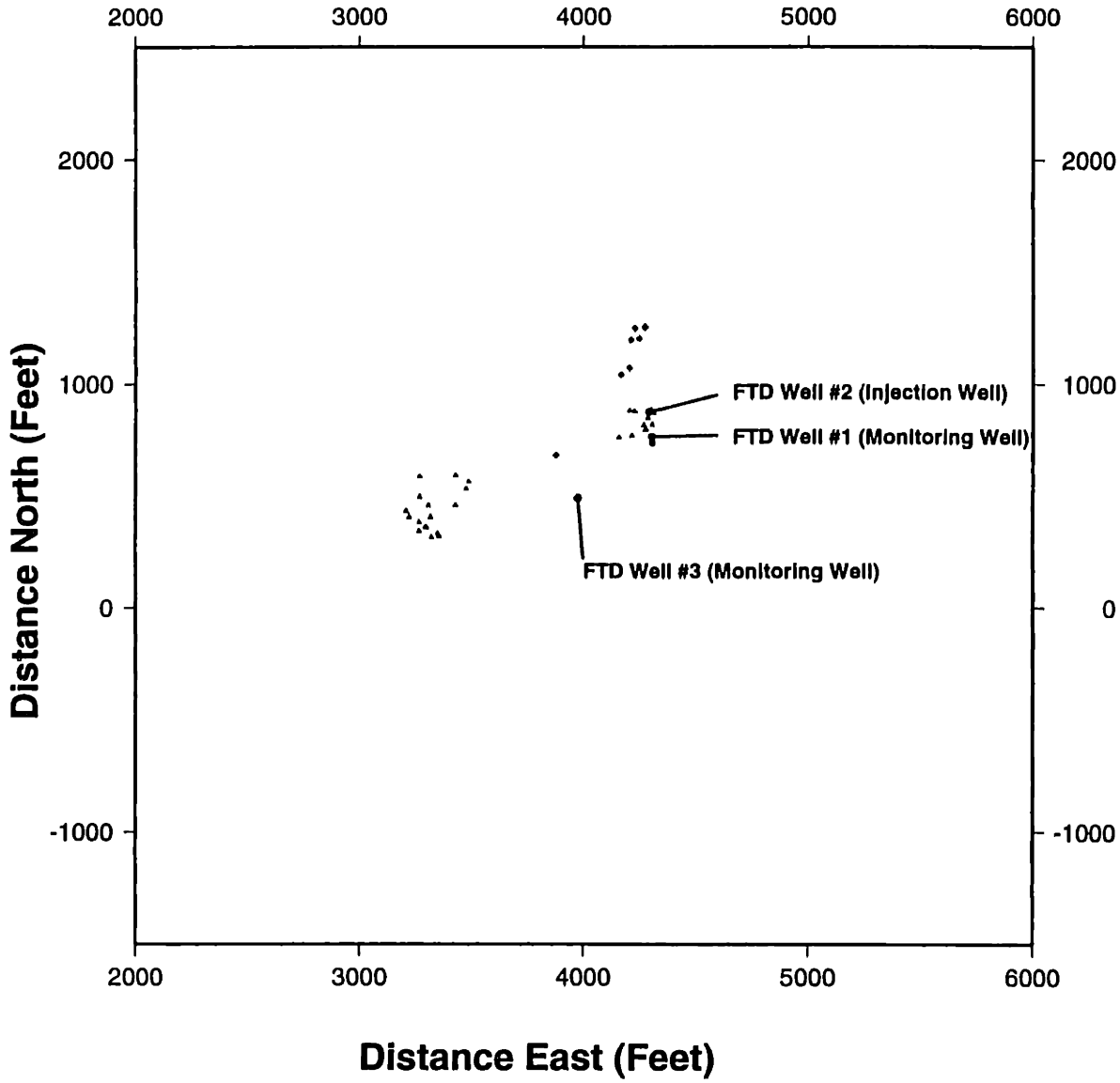

Figure D-37: DWTI Cluster Frame 35

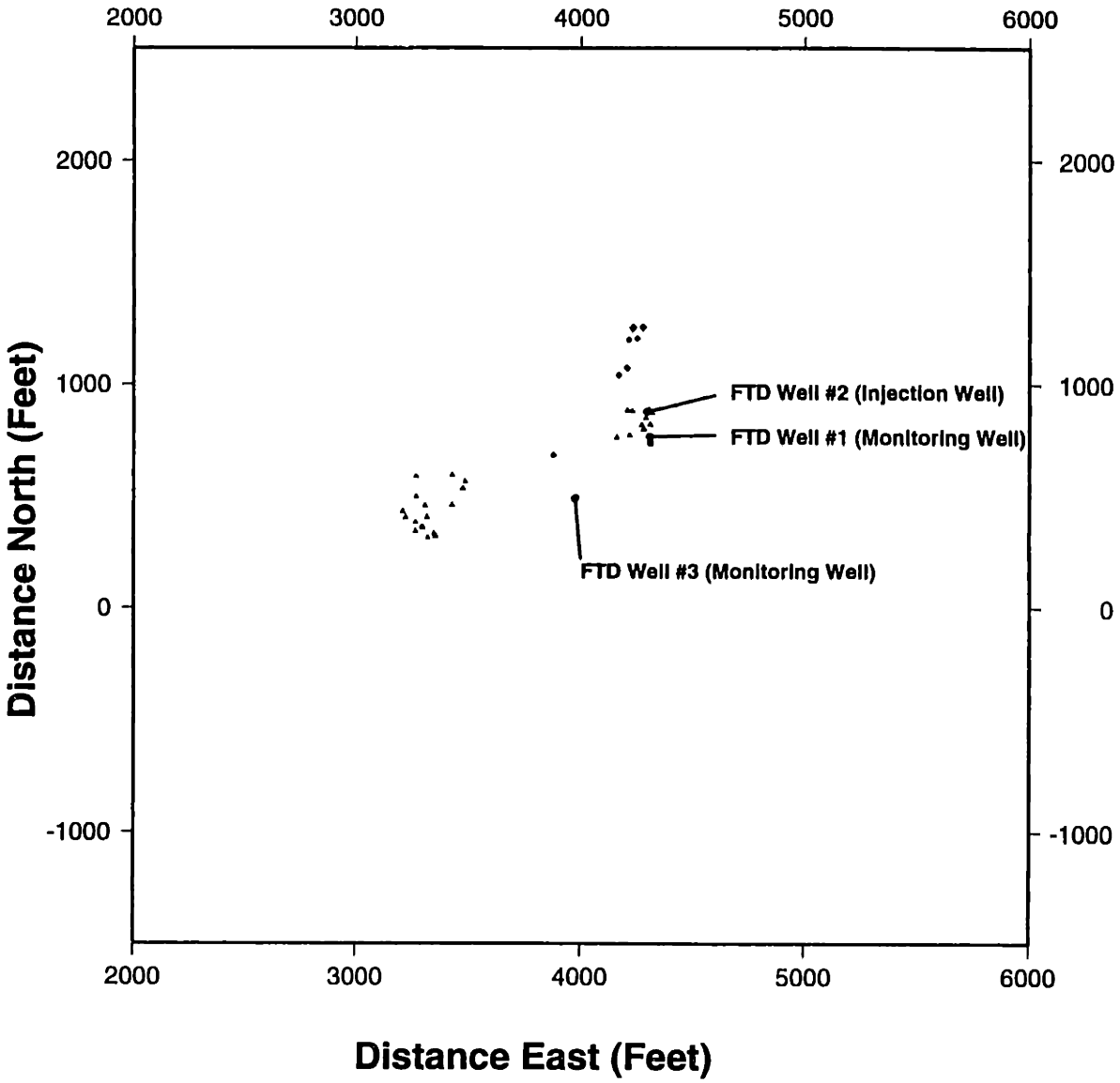

Figure D-38: DWTI Cluster Frame 36

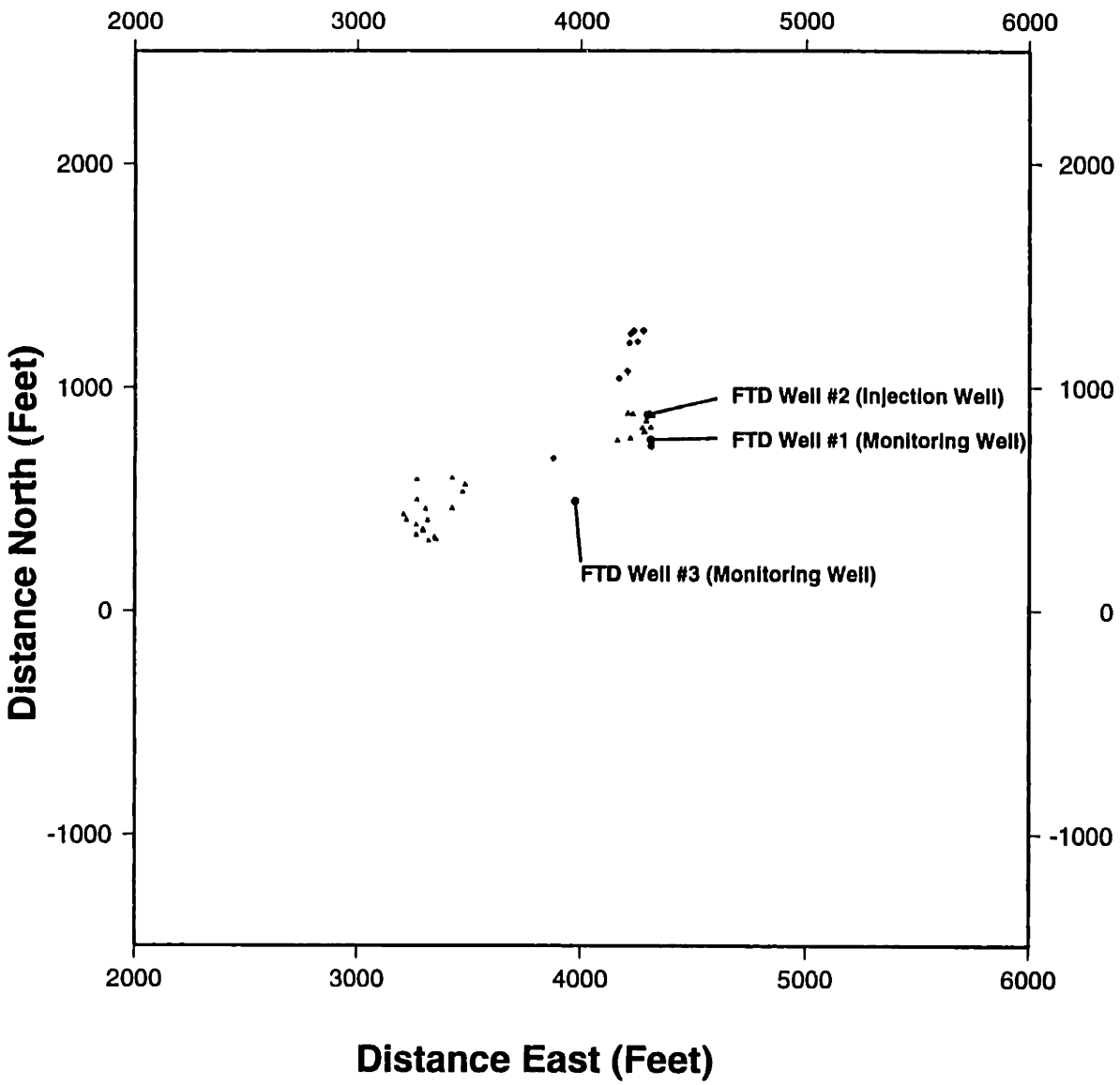

Figure D-39: DWTI Cluster Frame 37

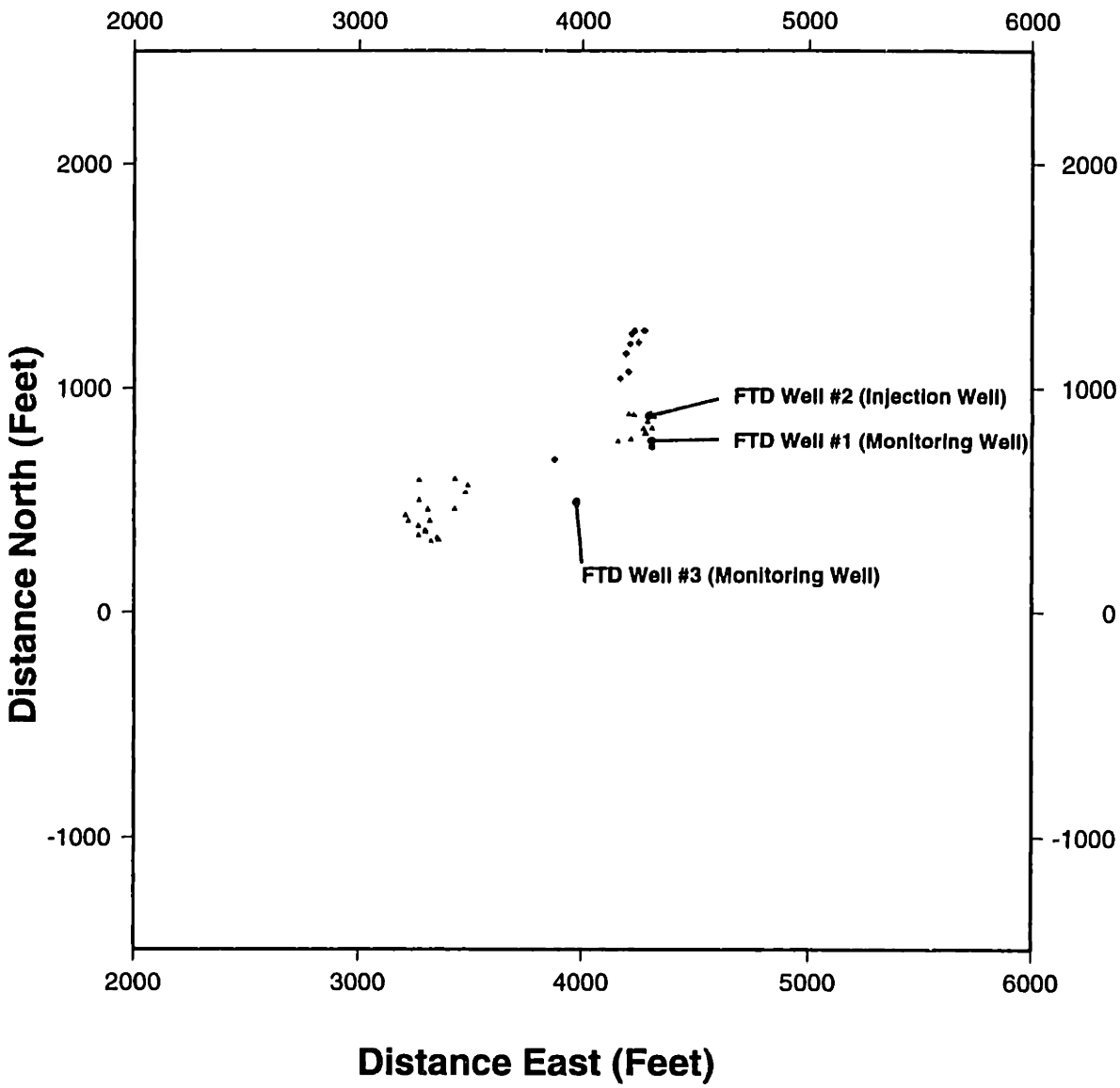

Figure D-40: DWTI Cluster Frame 38

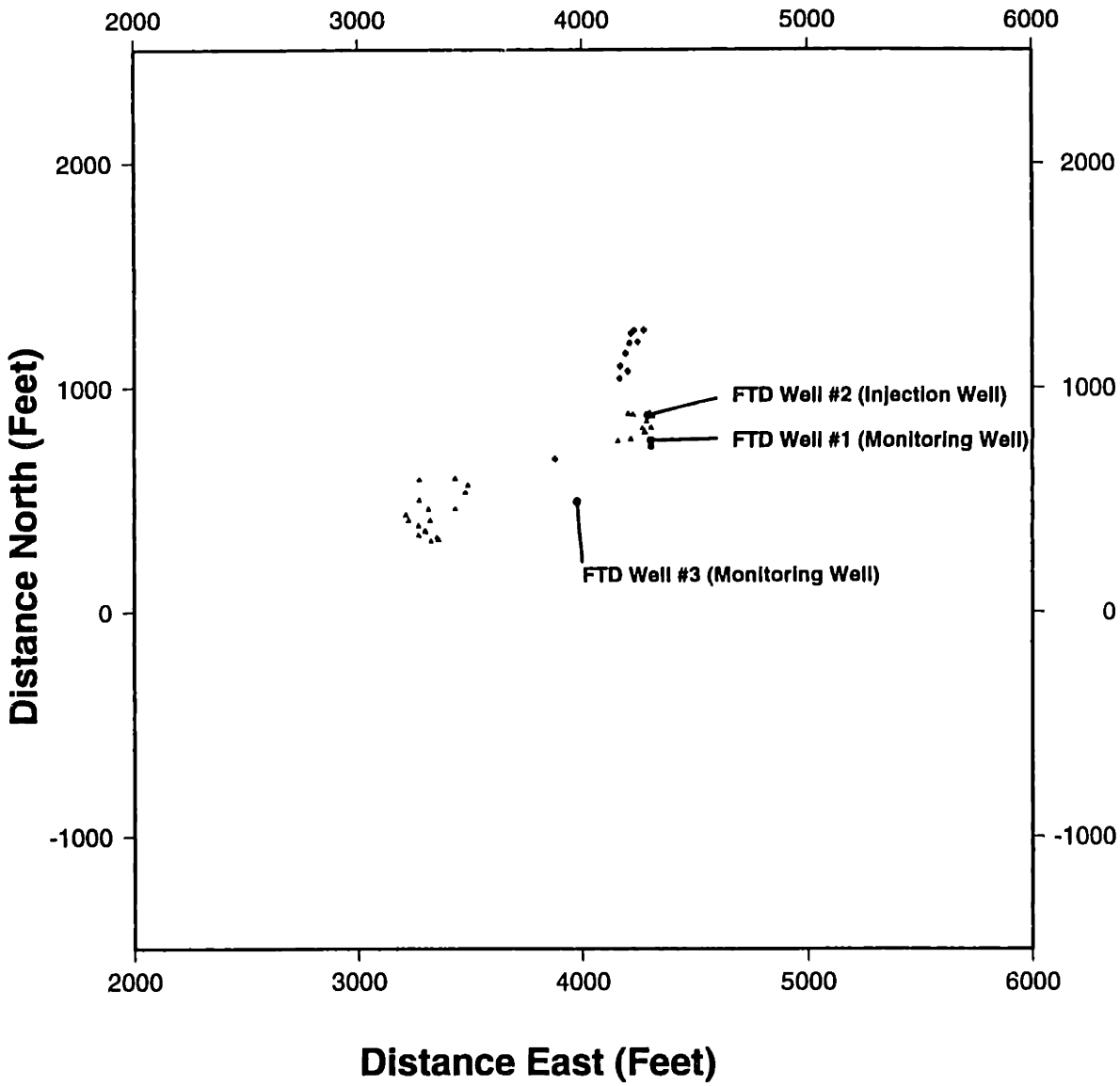

Figure D-41: DWTI Cluster Frame 39

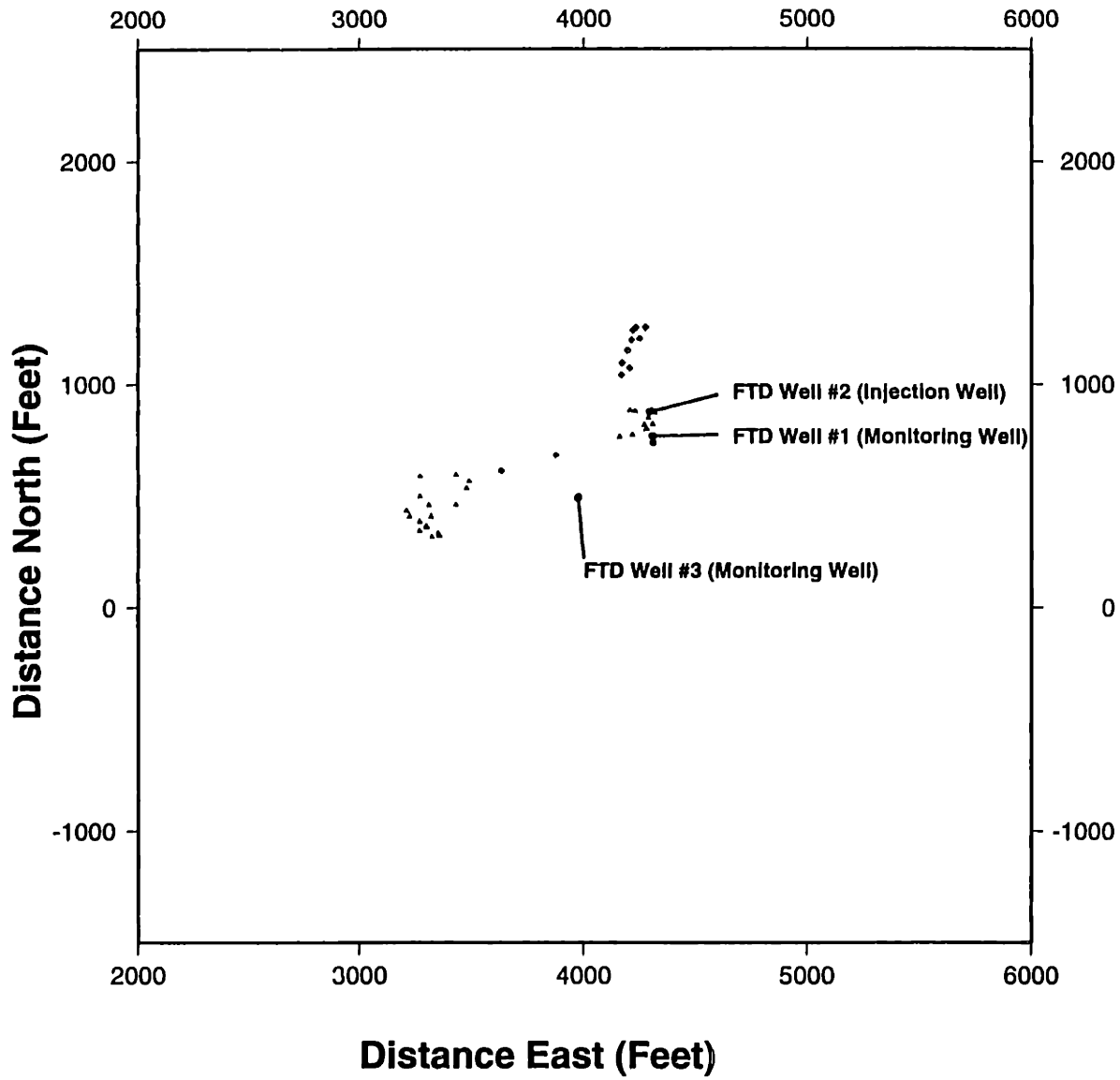

Figure D-42: DWTI Cluster Frame 40

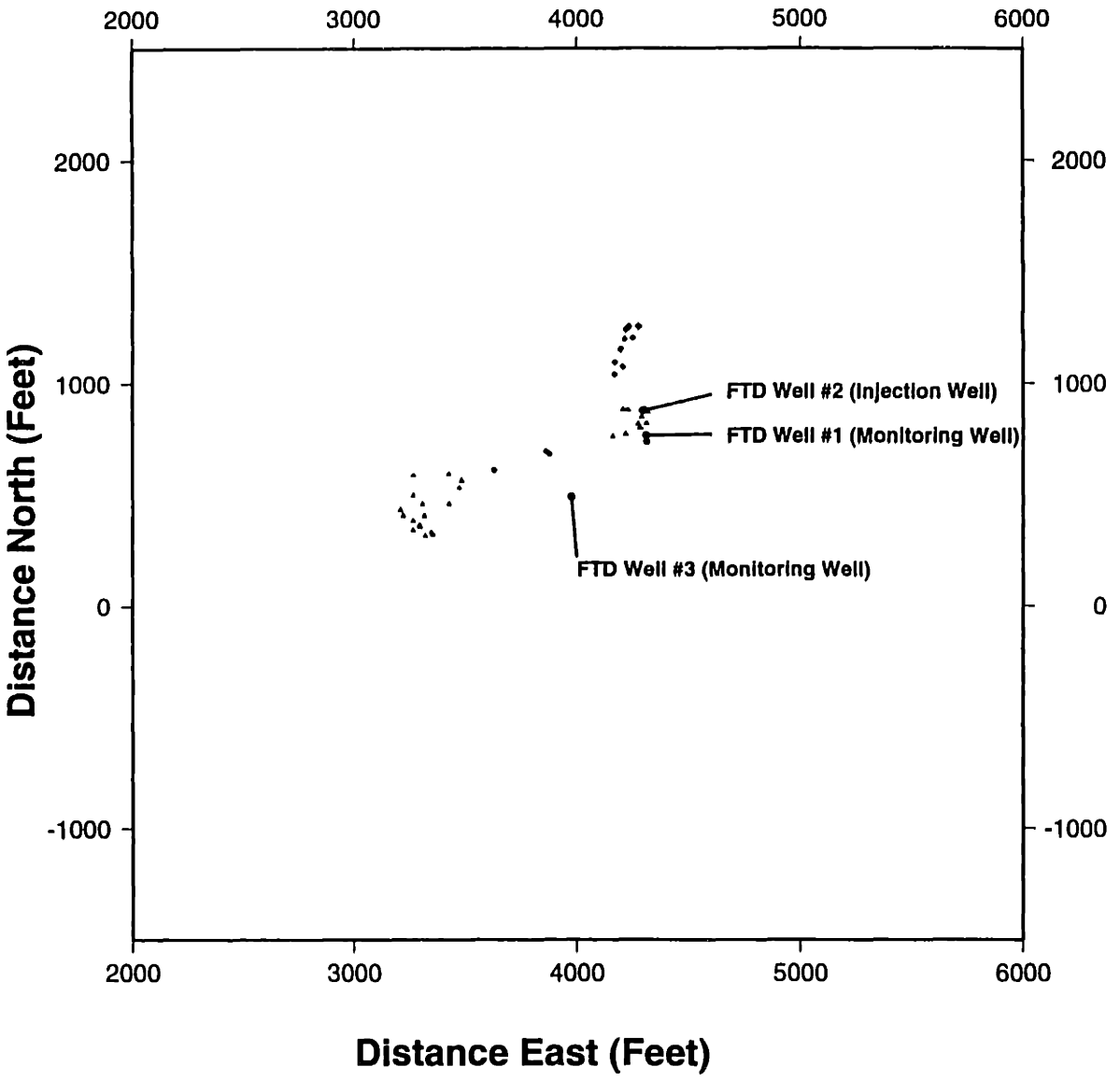

Figure D-43: DWTI Cluster Frame 41

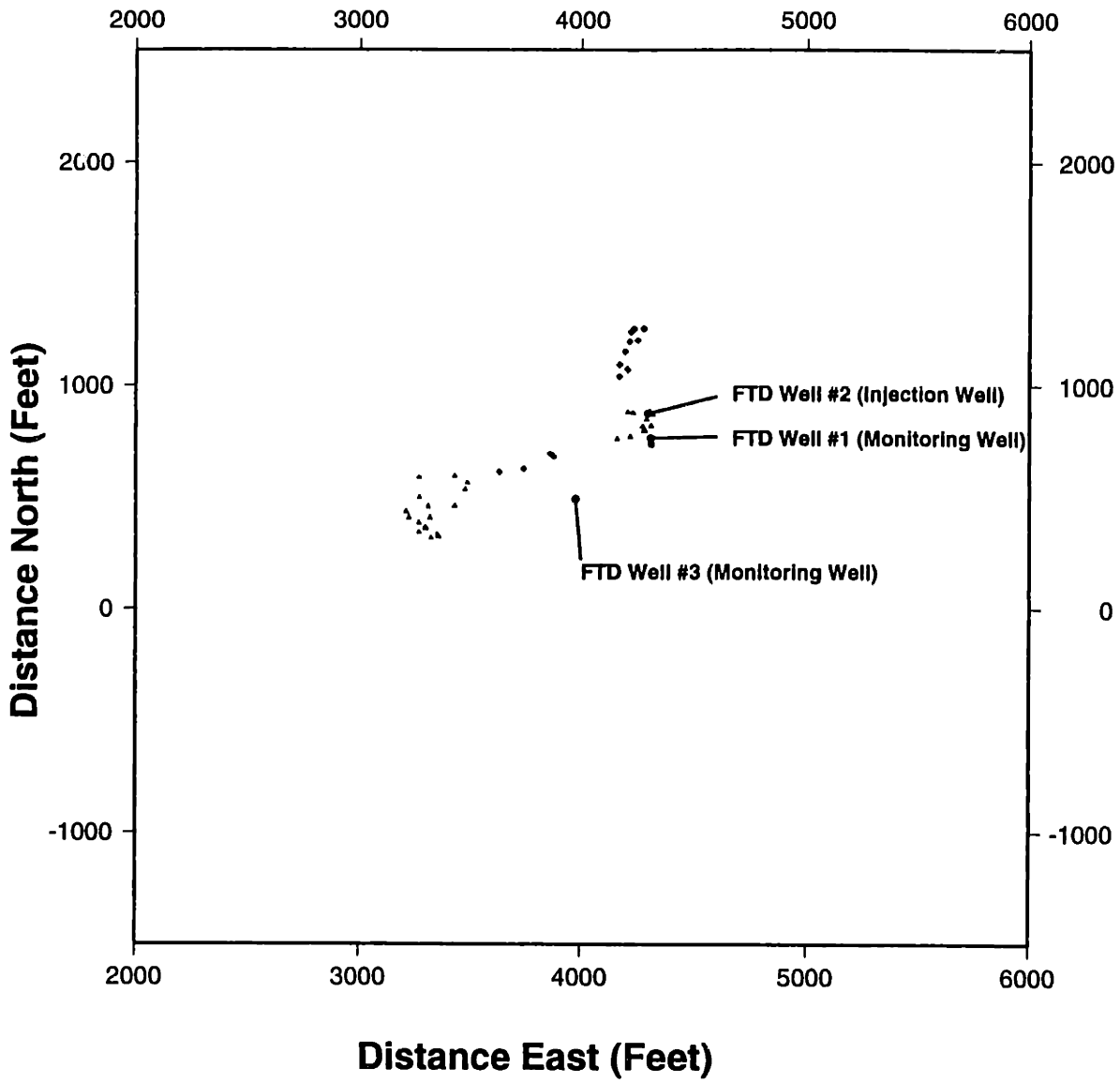

Figure D-44: DWTI Cluster Frame 42

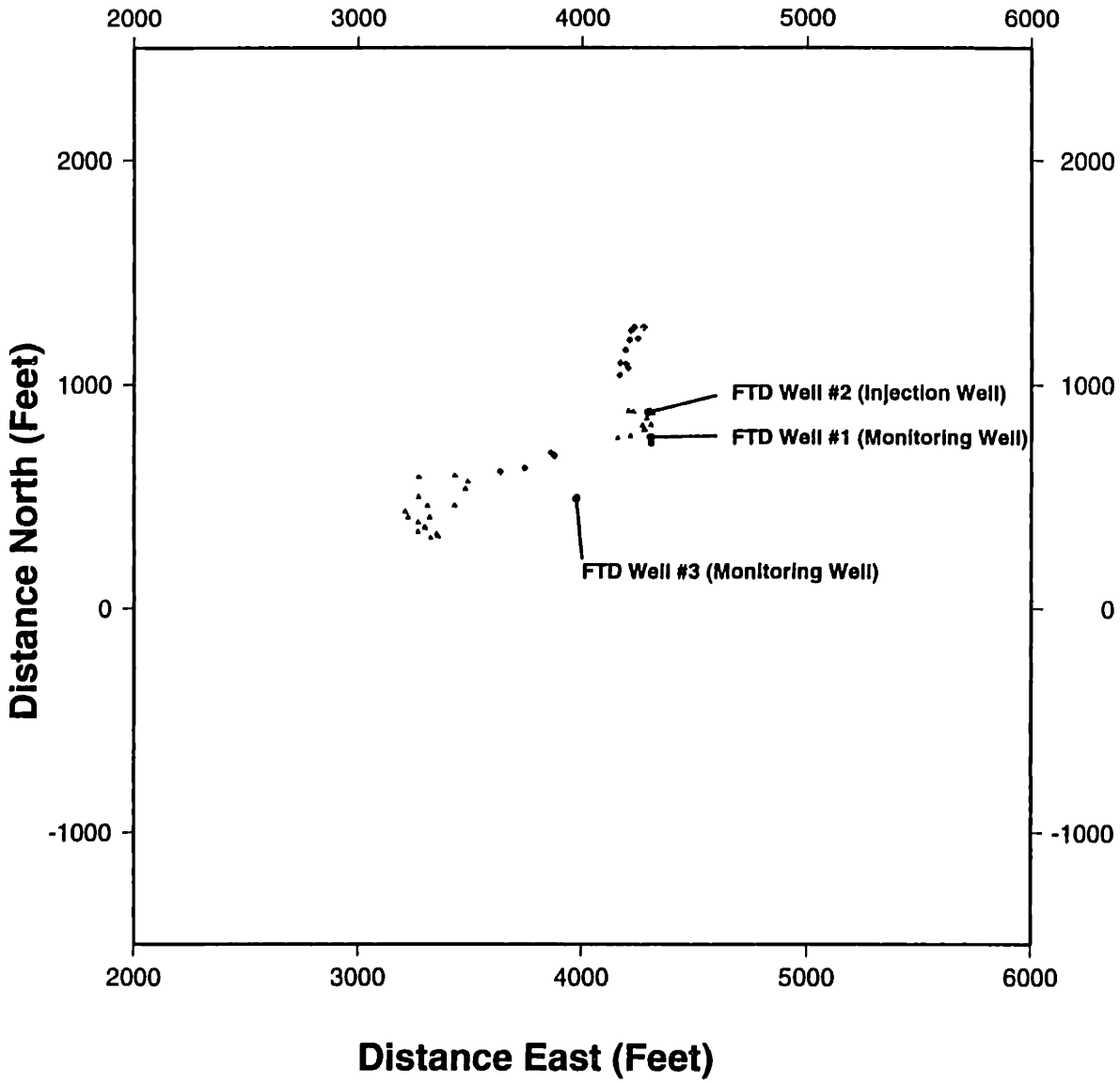

Figure D-45: DWTI Cluster Frame 43

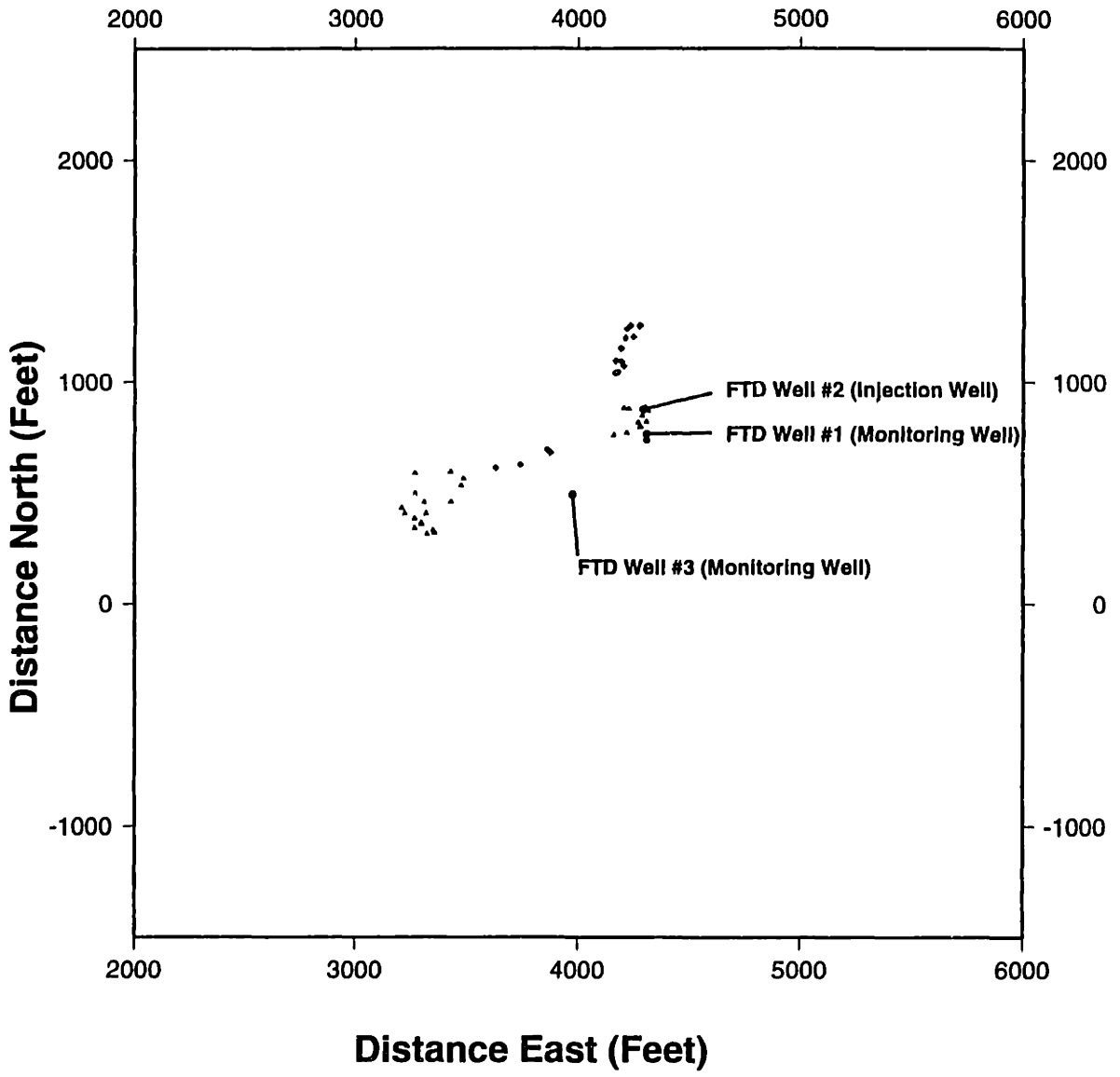

Figure D-46: DWTI Cluster Frame 44

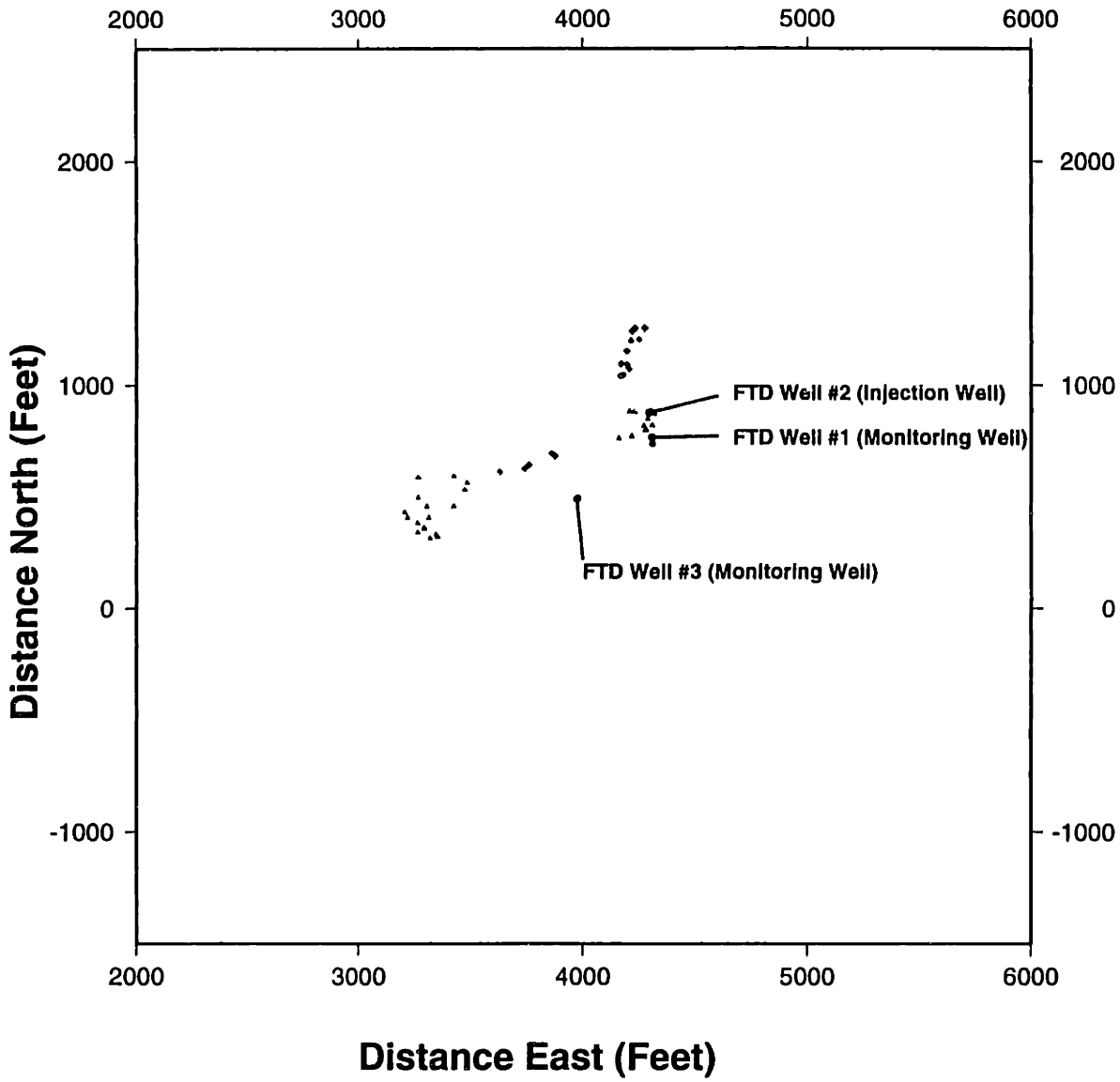

Figure D-47: DWTI Cluster Frame 45

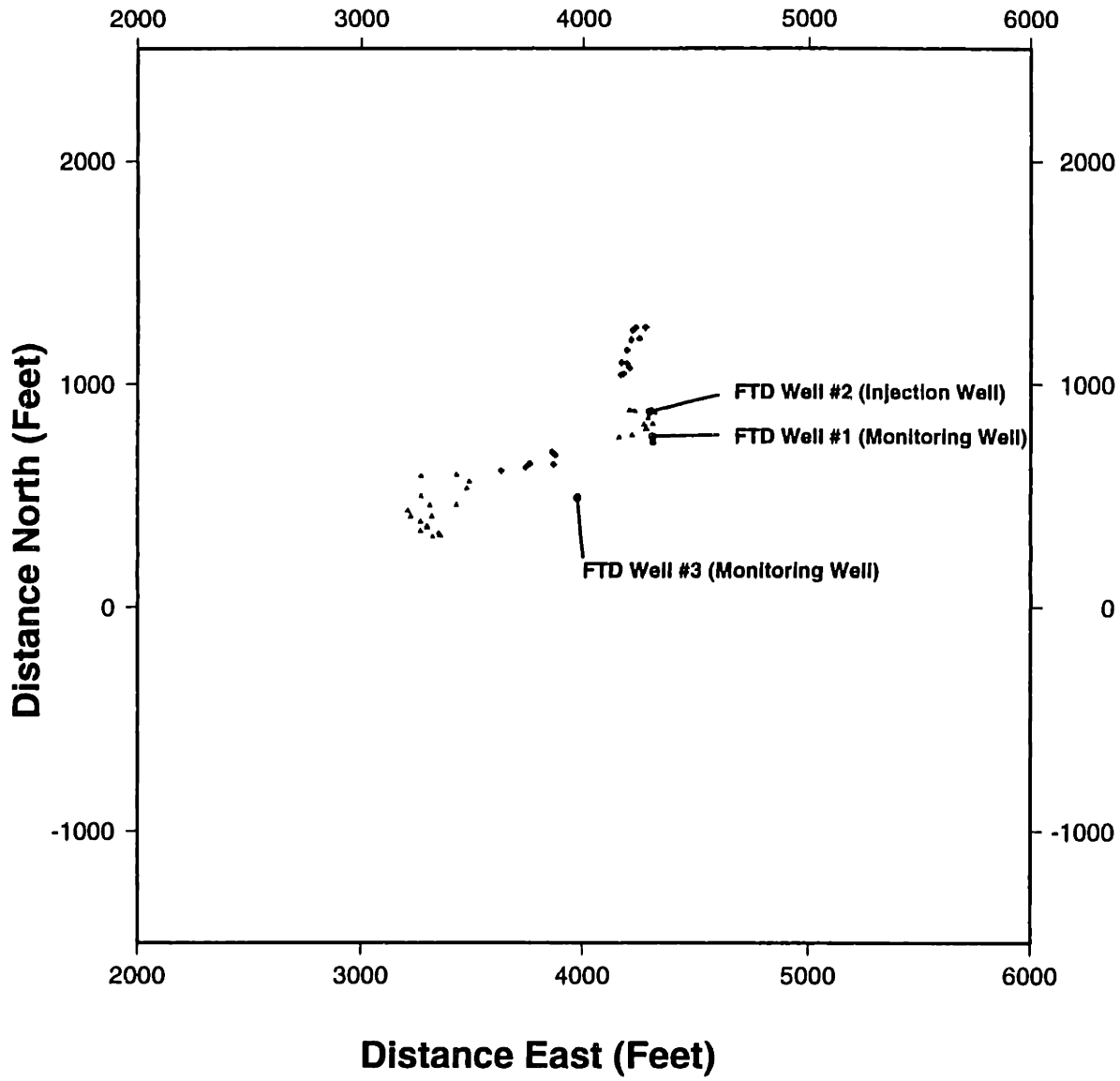

Figure D-48: DWTI Cluster Frame 46

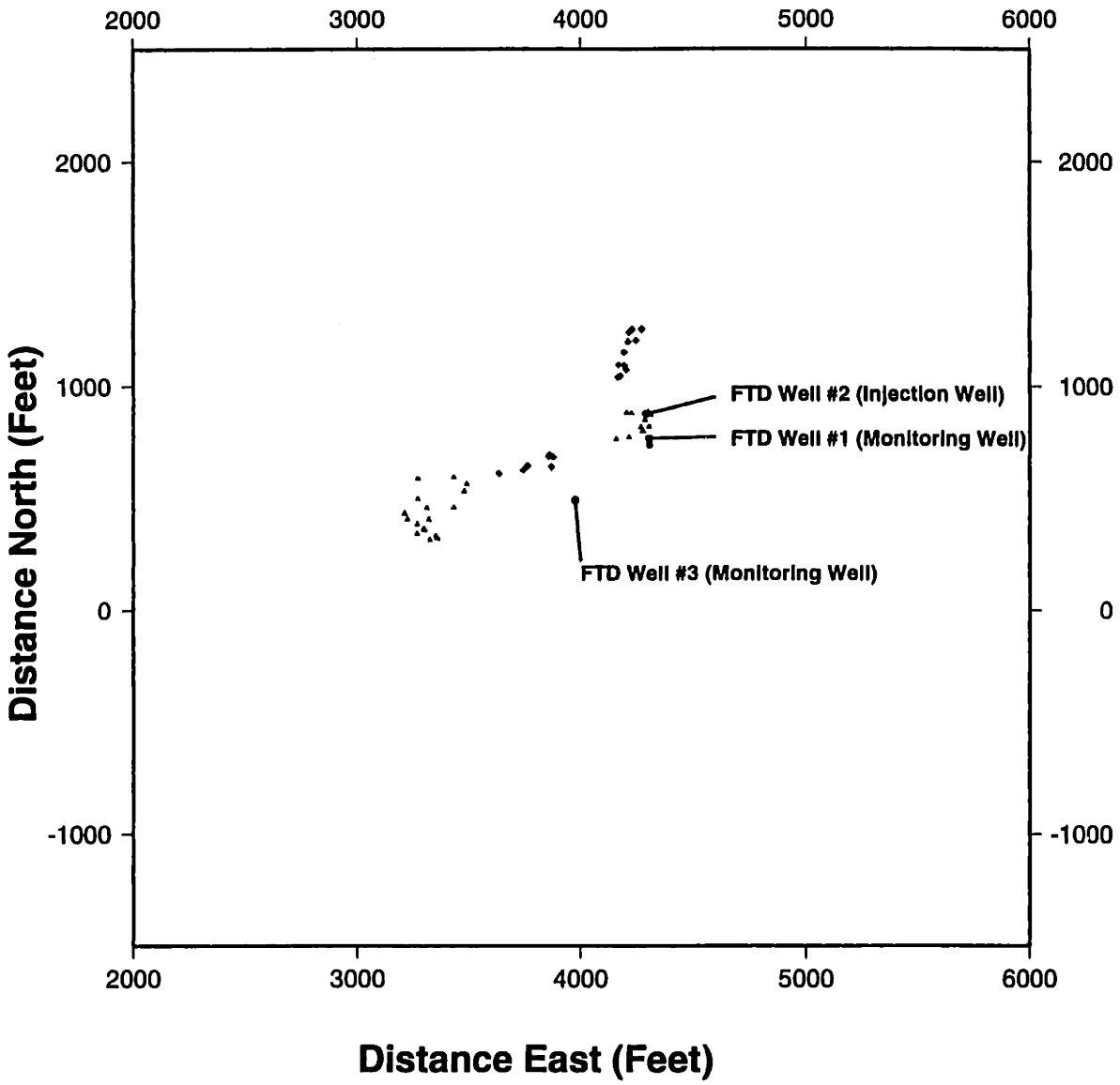

Figure D-49: DWTI Cluster Frame 47

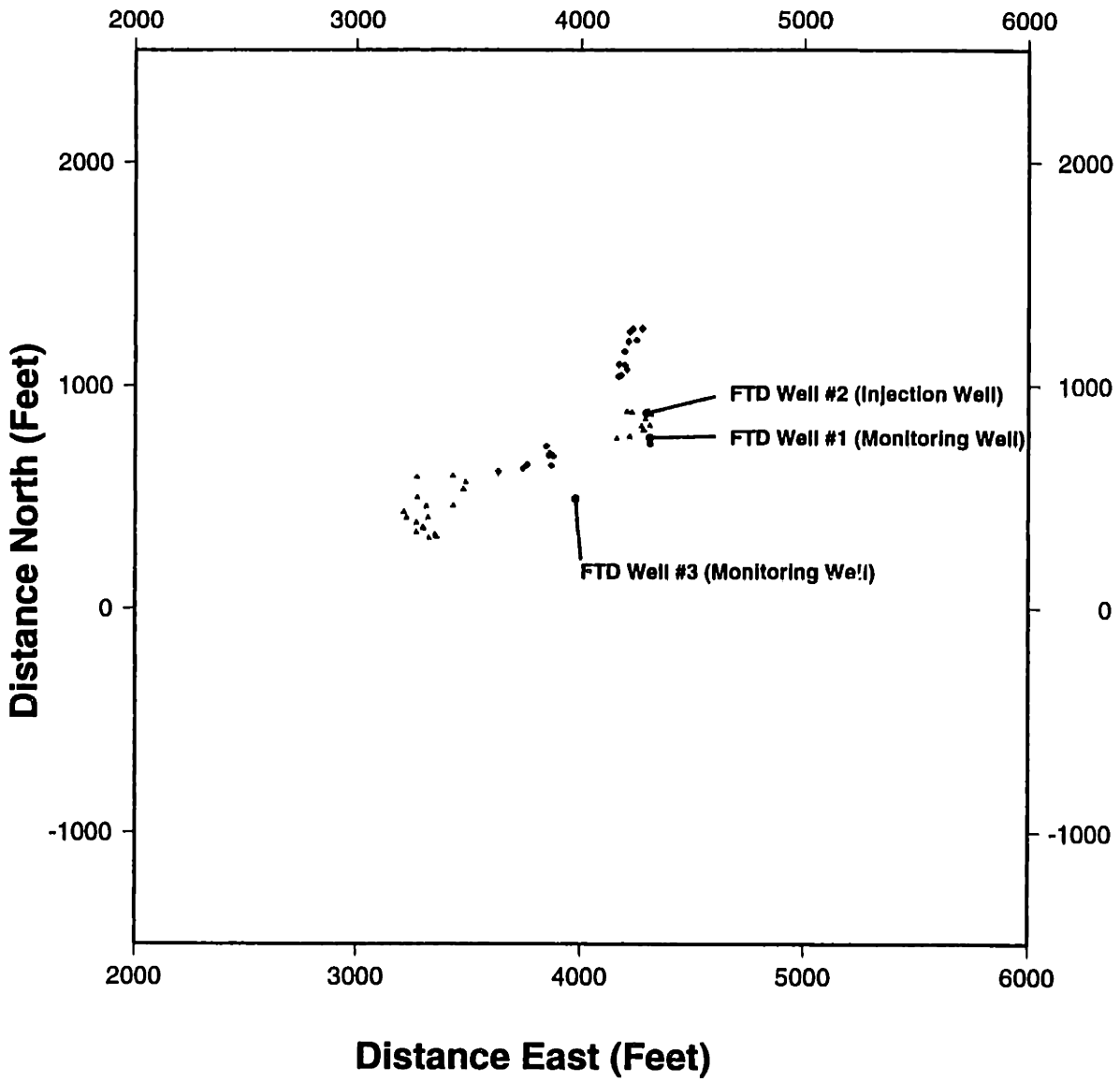

Figure D-50: DWTI Cluster Frame 48

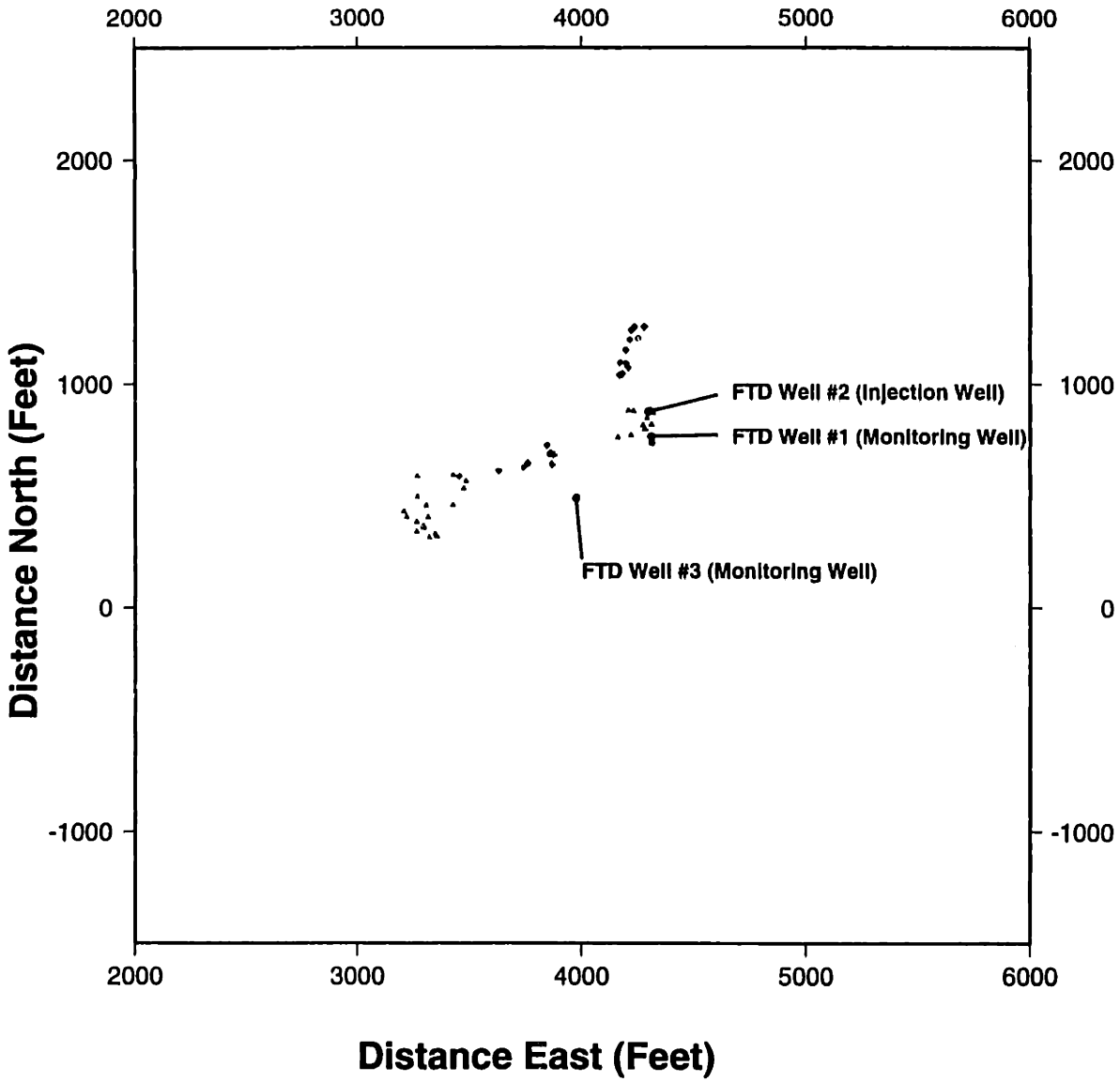

Figure D-51: DWTI Cluster Frame 49

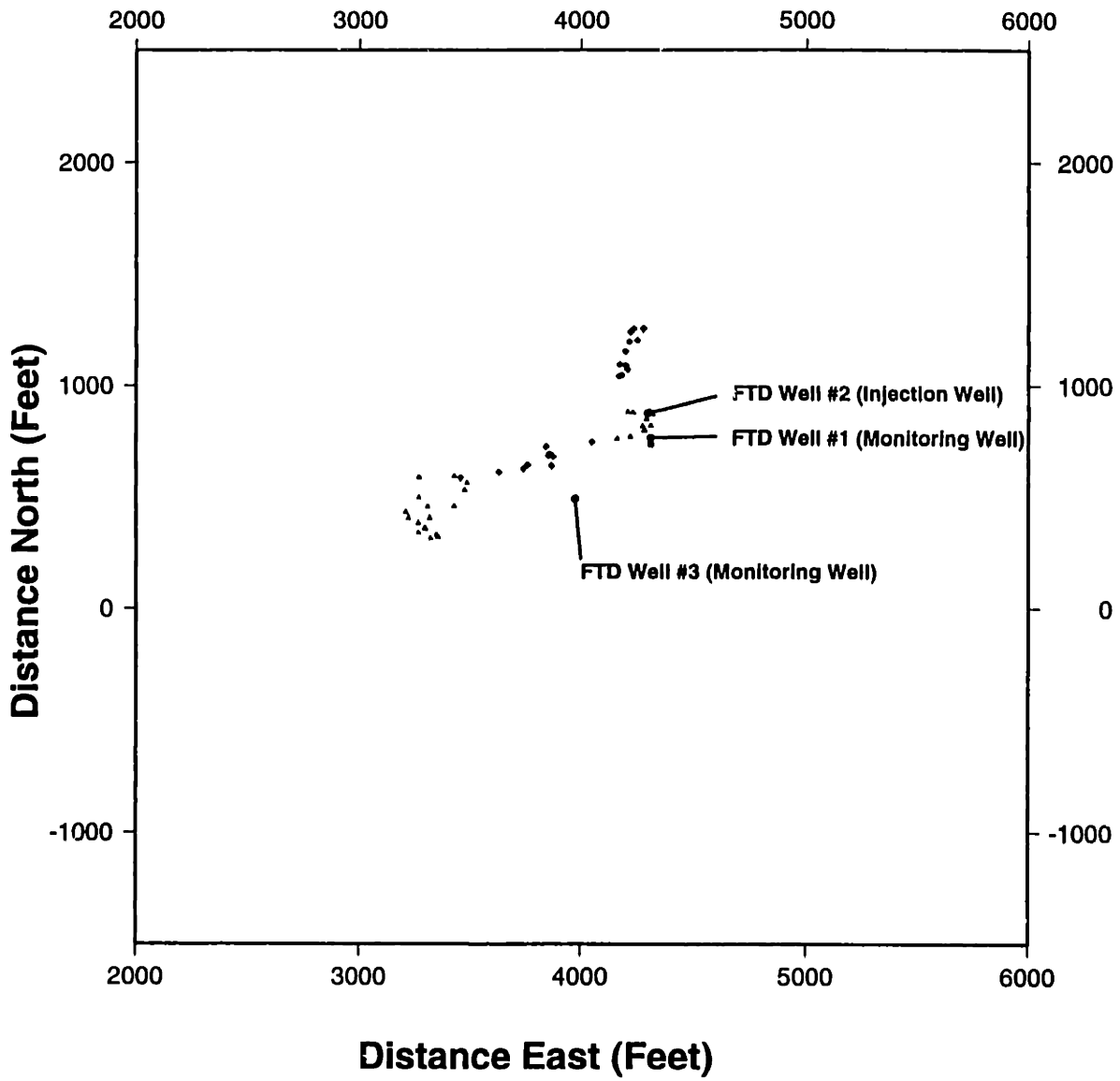

Figure D-52: DWTI Cluster Frame 50

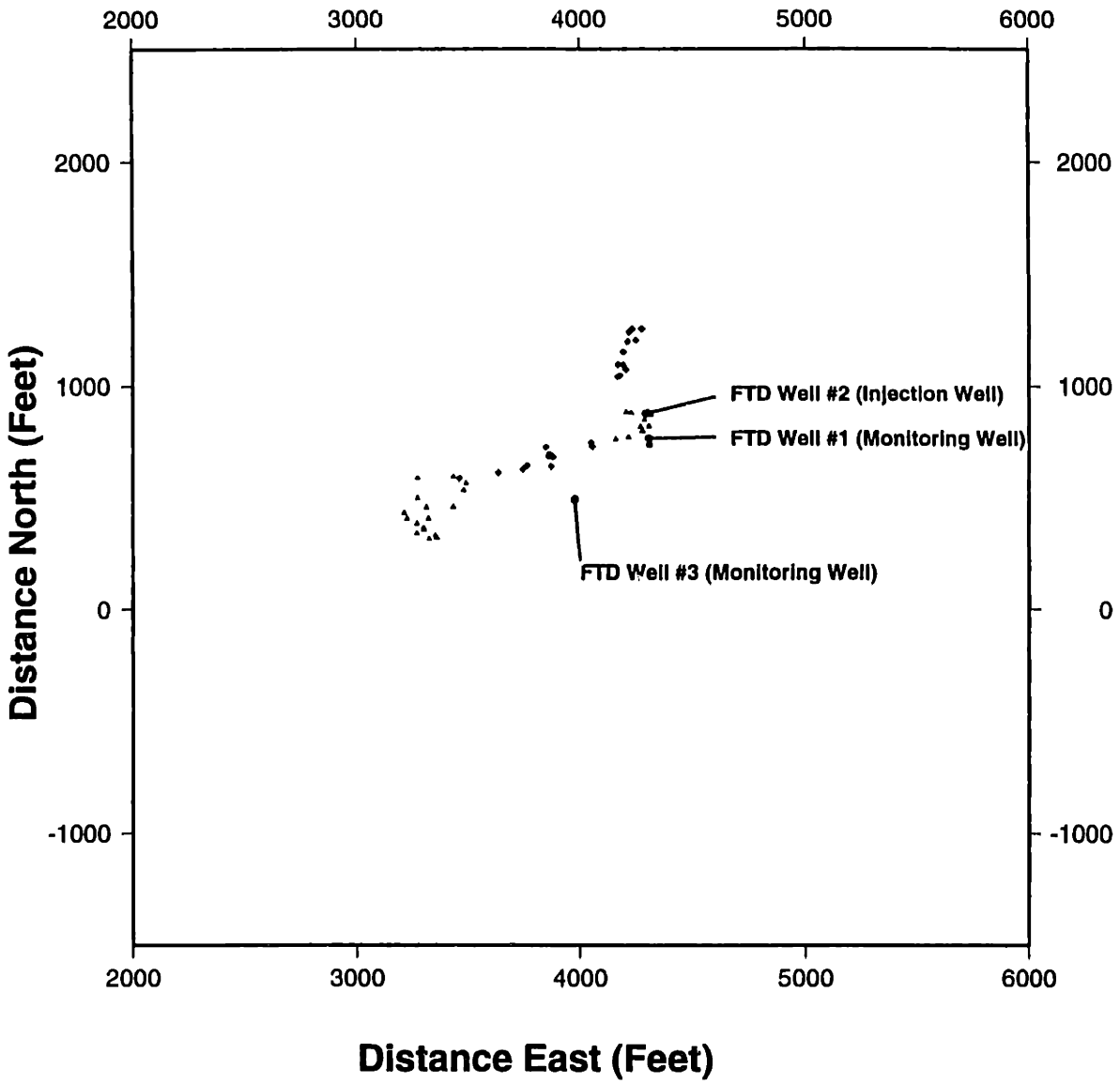

Figure D-53: DWTI Cluster Frame 51

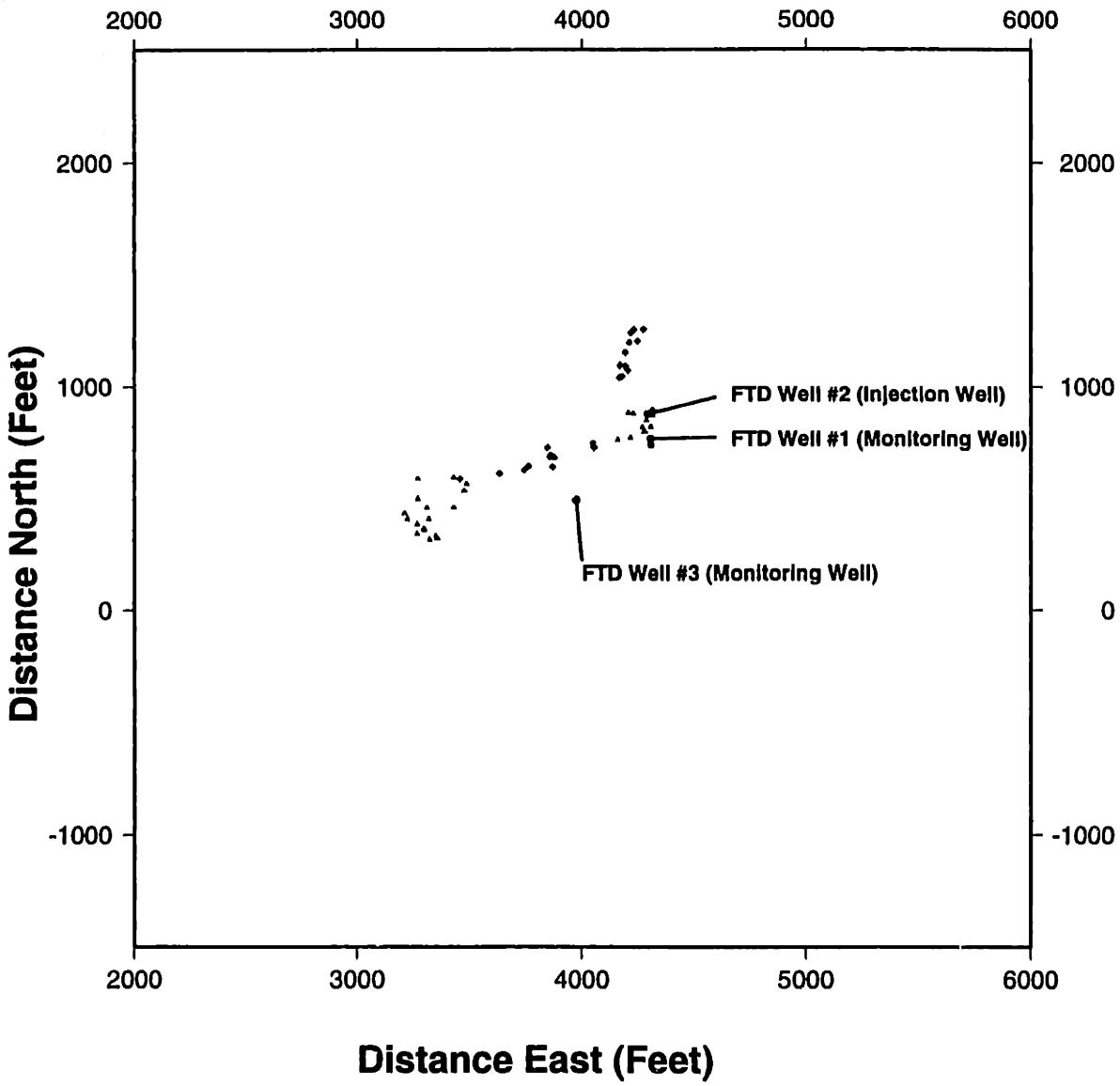

Figure D-54: DWTI Cluster Frame 52

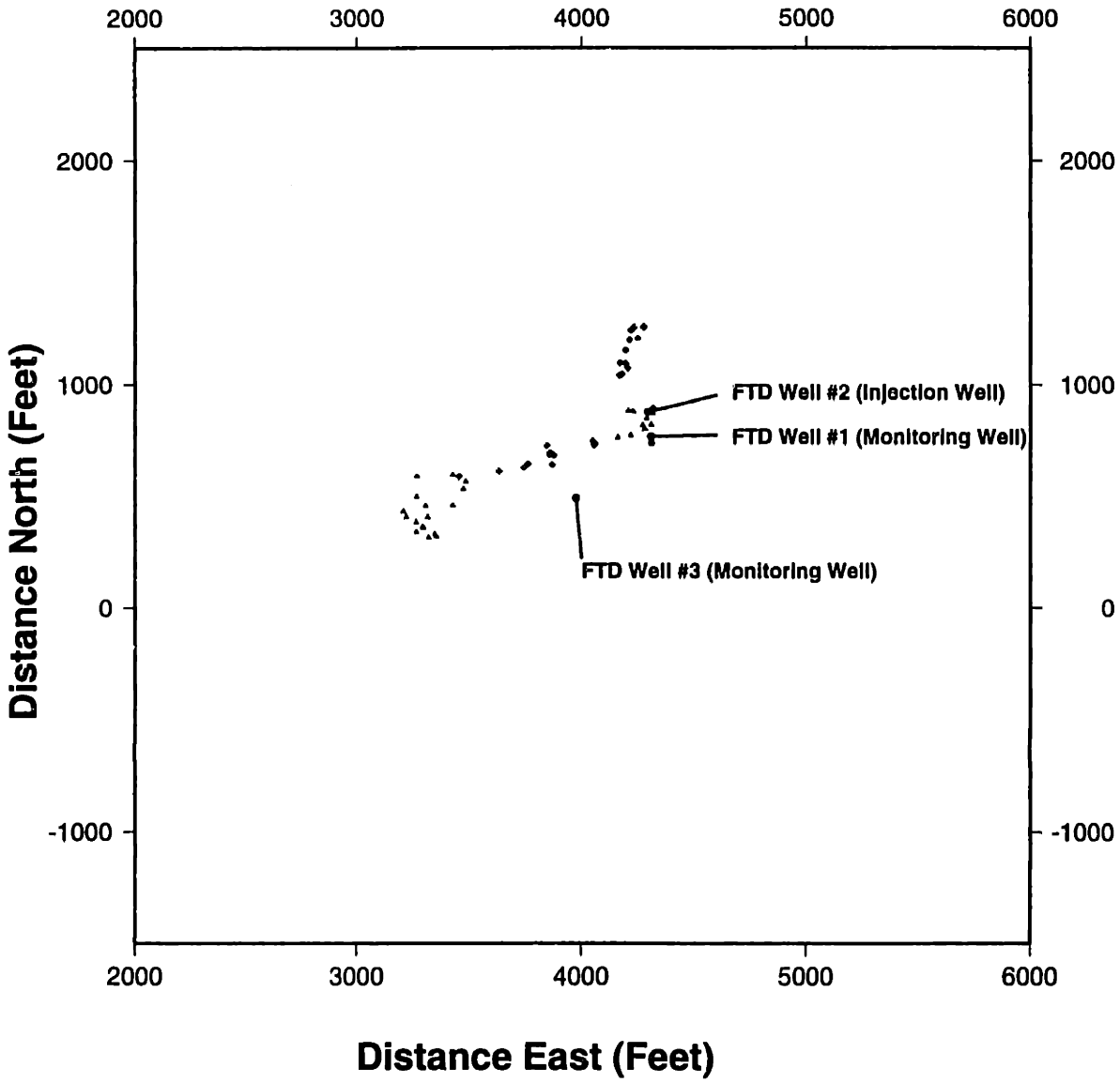

Figure D-55: DWTI Cluster Frame 53

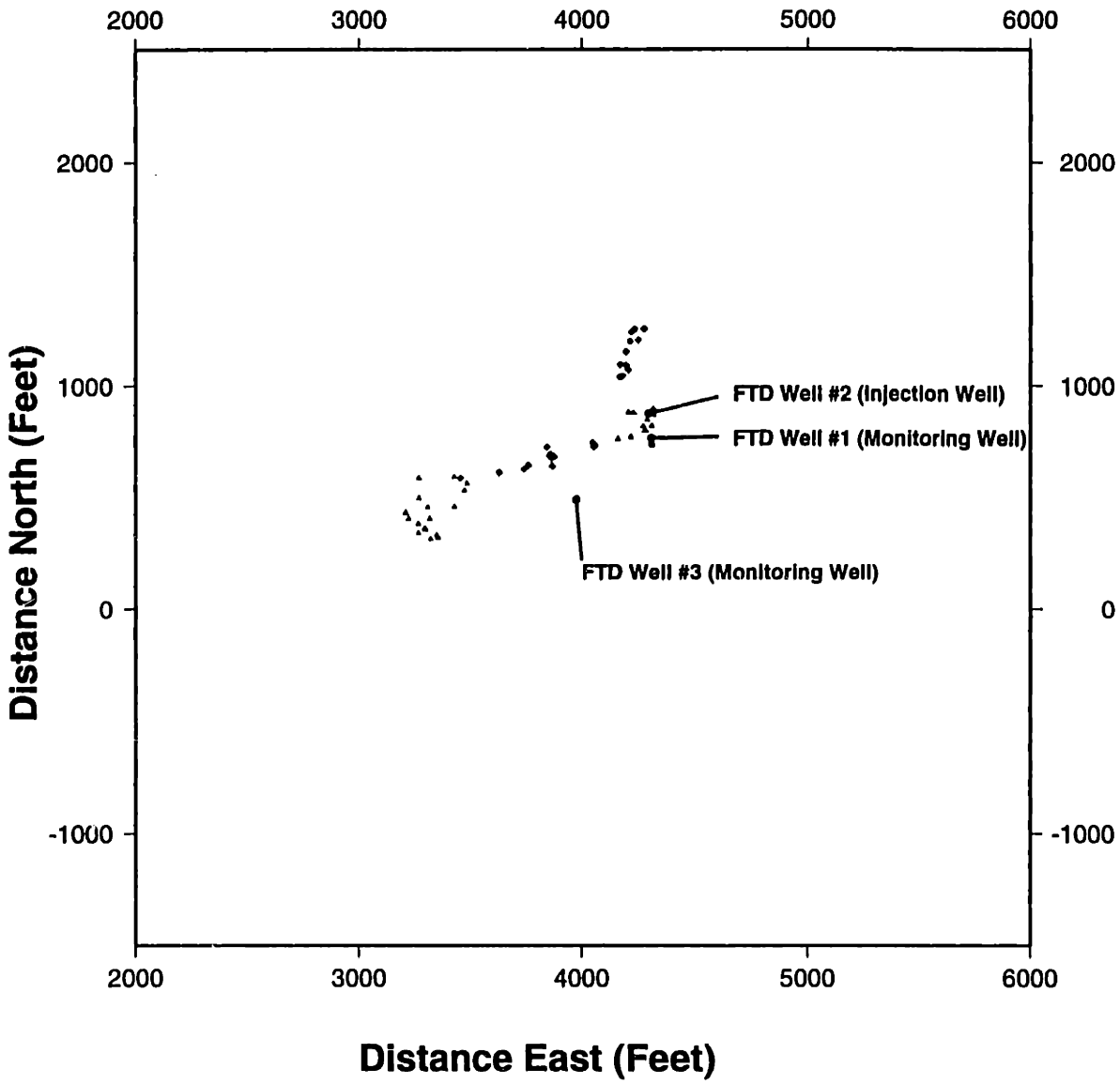

Figure D-56: DWTI Cluster Frame 54

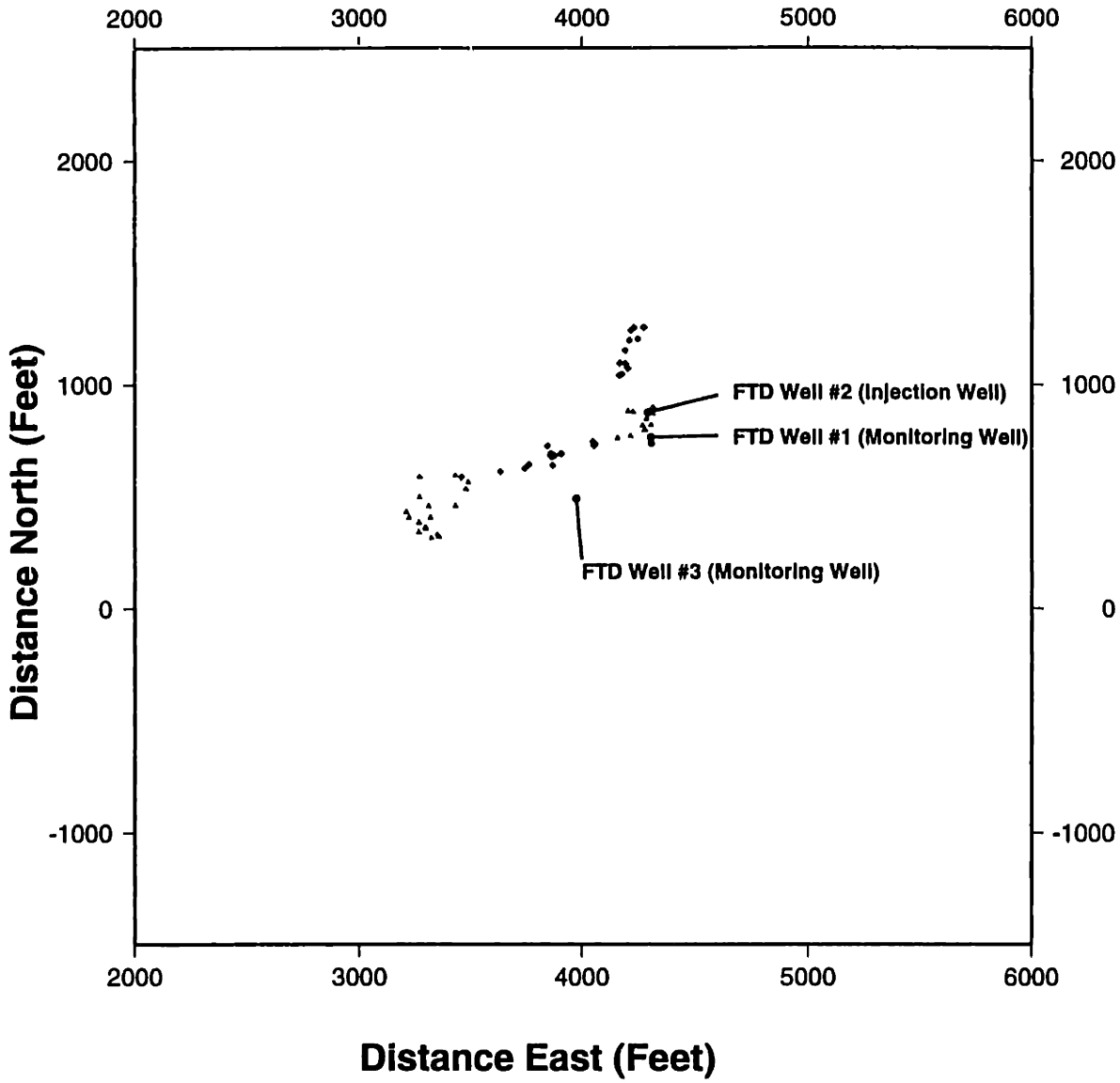

Figure D-57: DWTI Cluster Frame 55

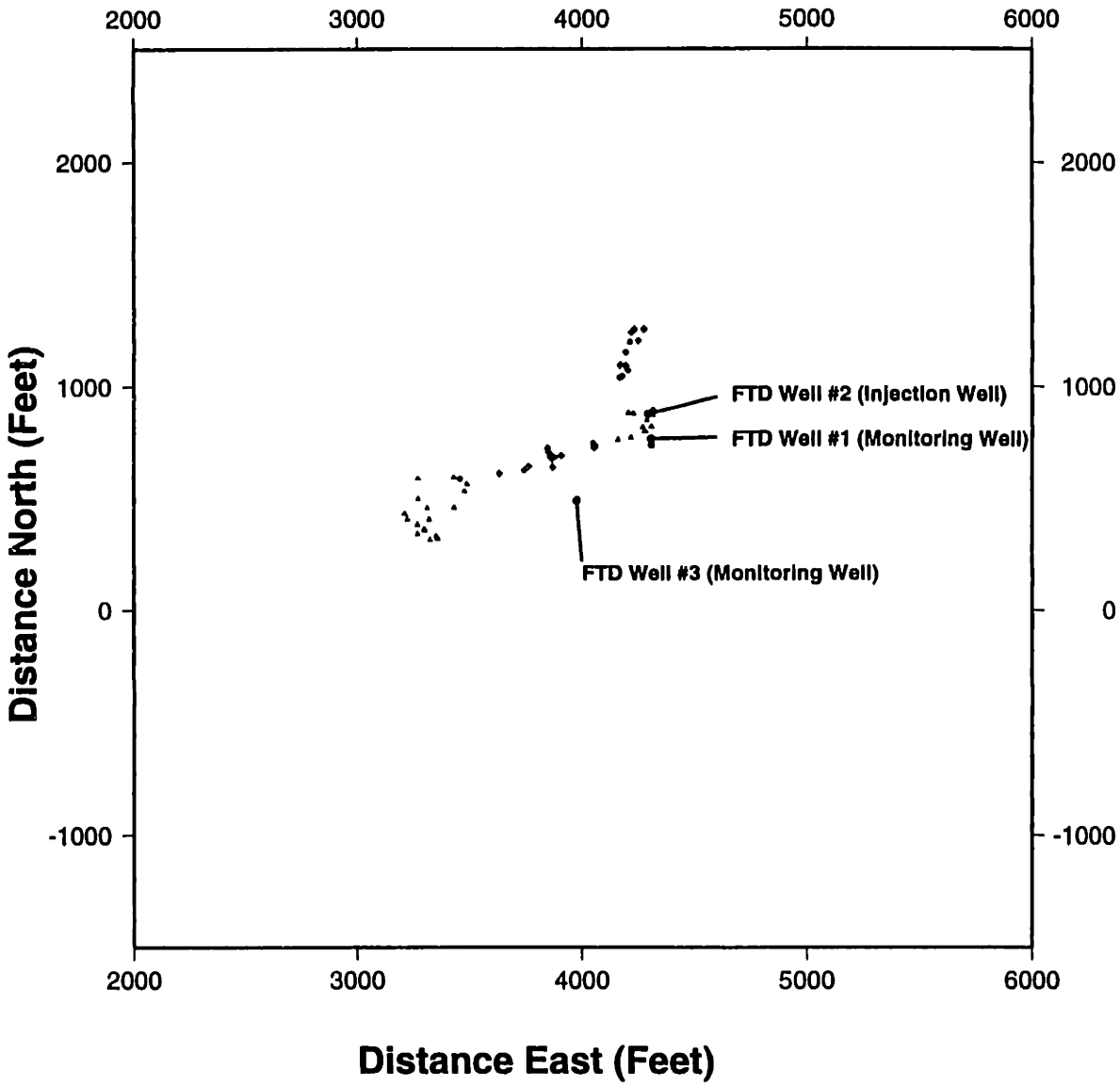

Figure D-58: DWTI Cluster Frame 56

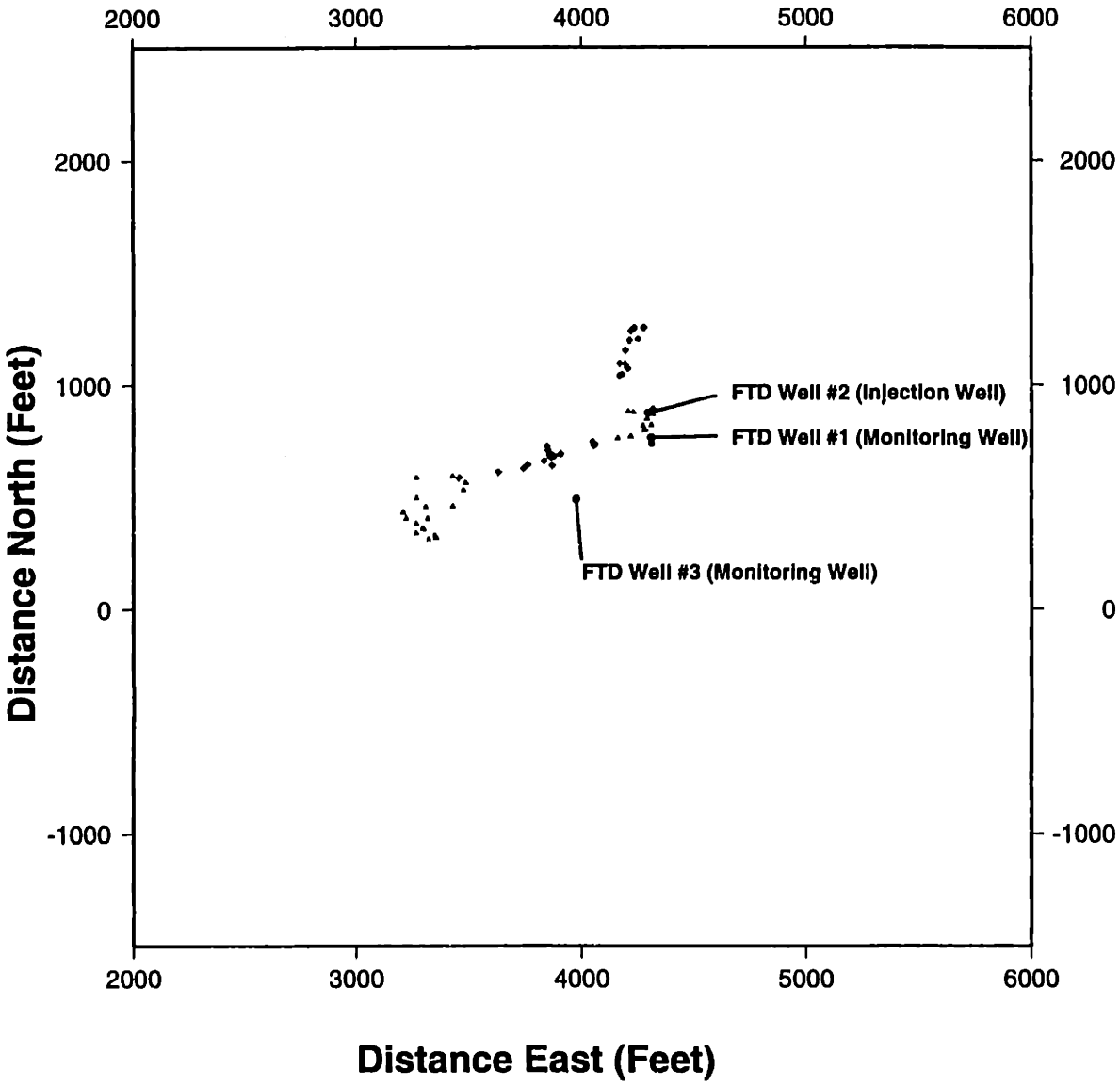

Figure D-59: DWTI Cluster Frame 57

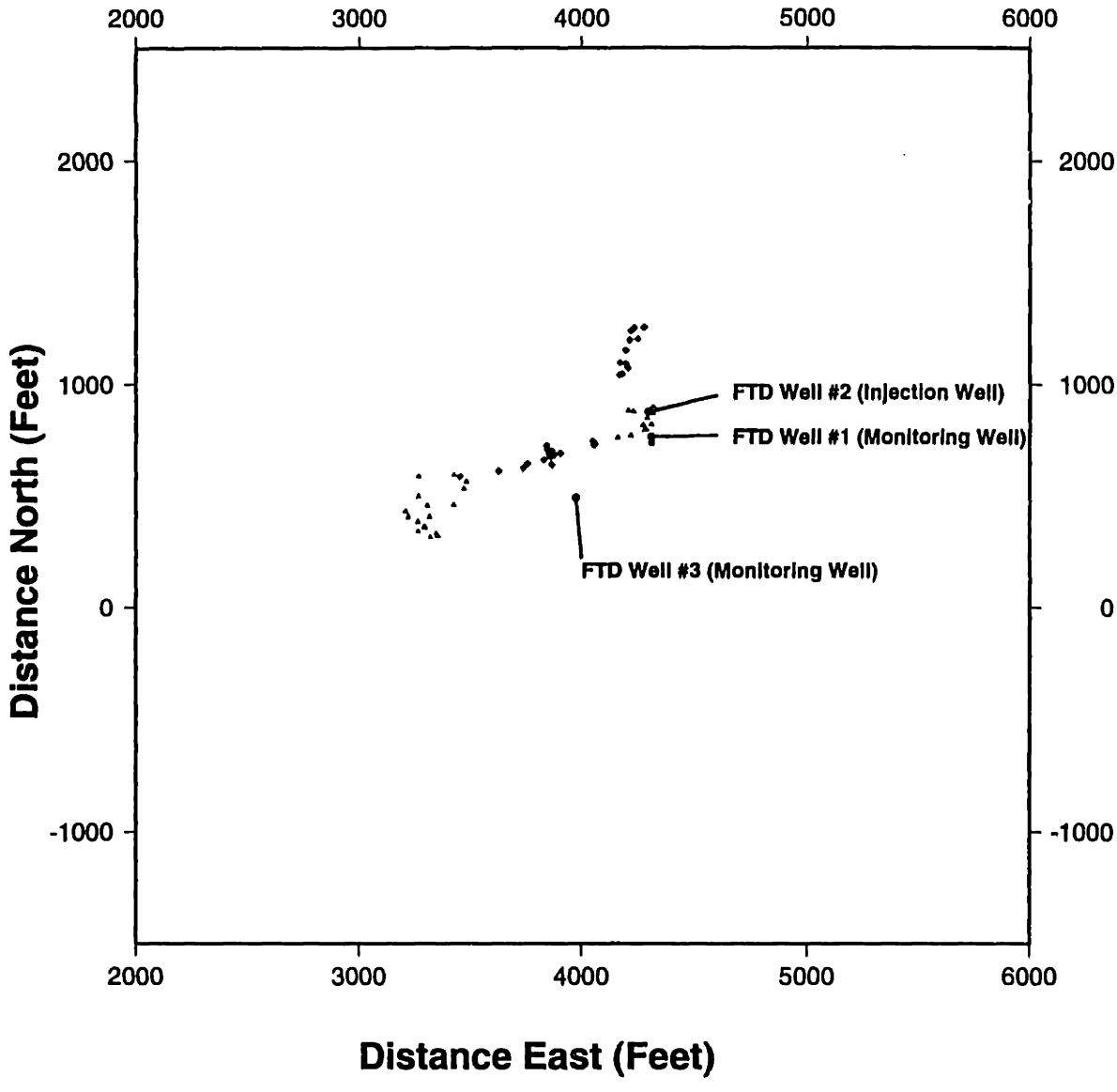

Figure D-60: DWTI Cluster Frame 59

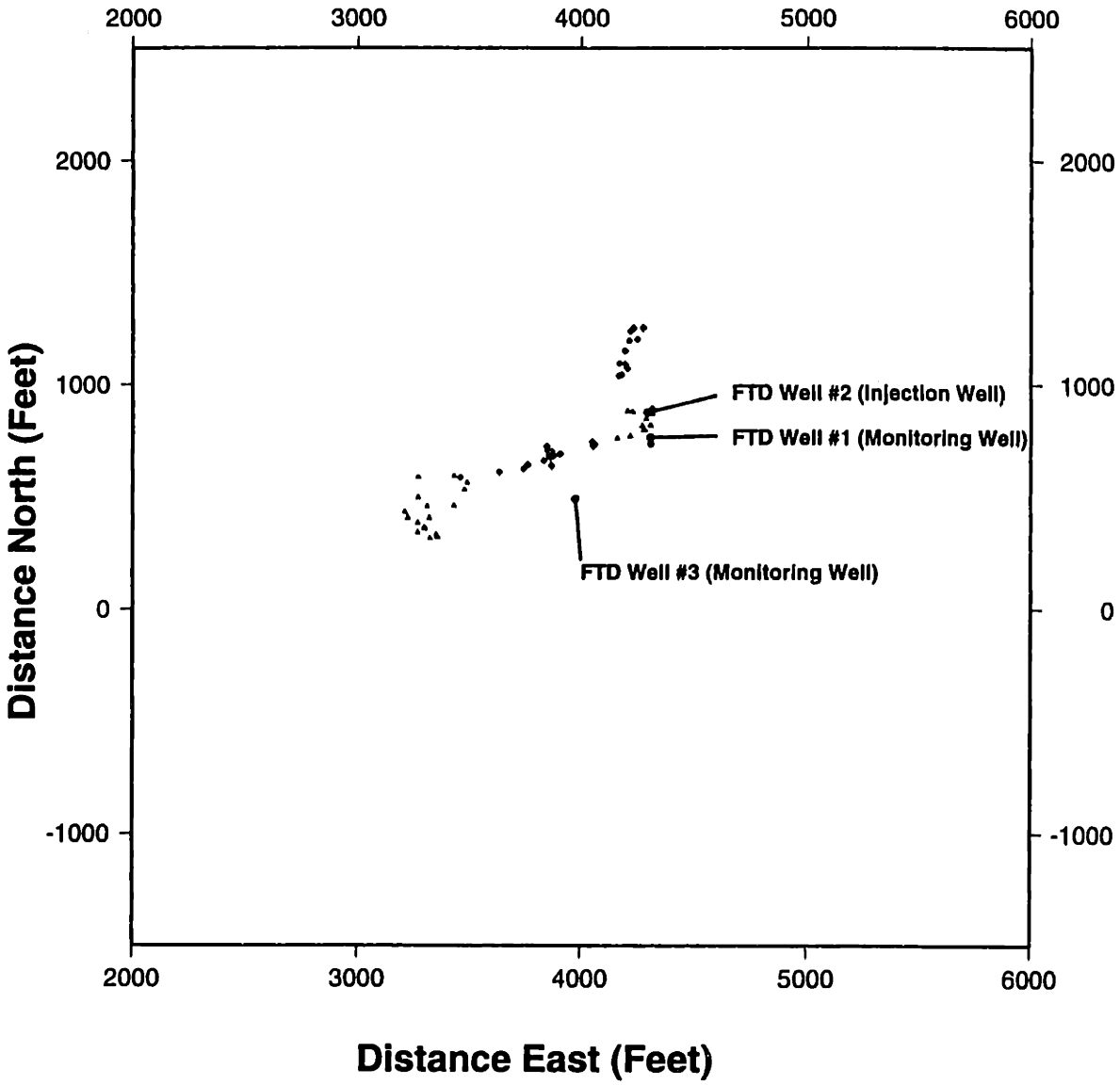

Figure D-61: DWTI Cluster Frame 60

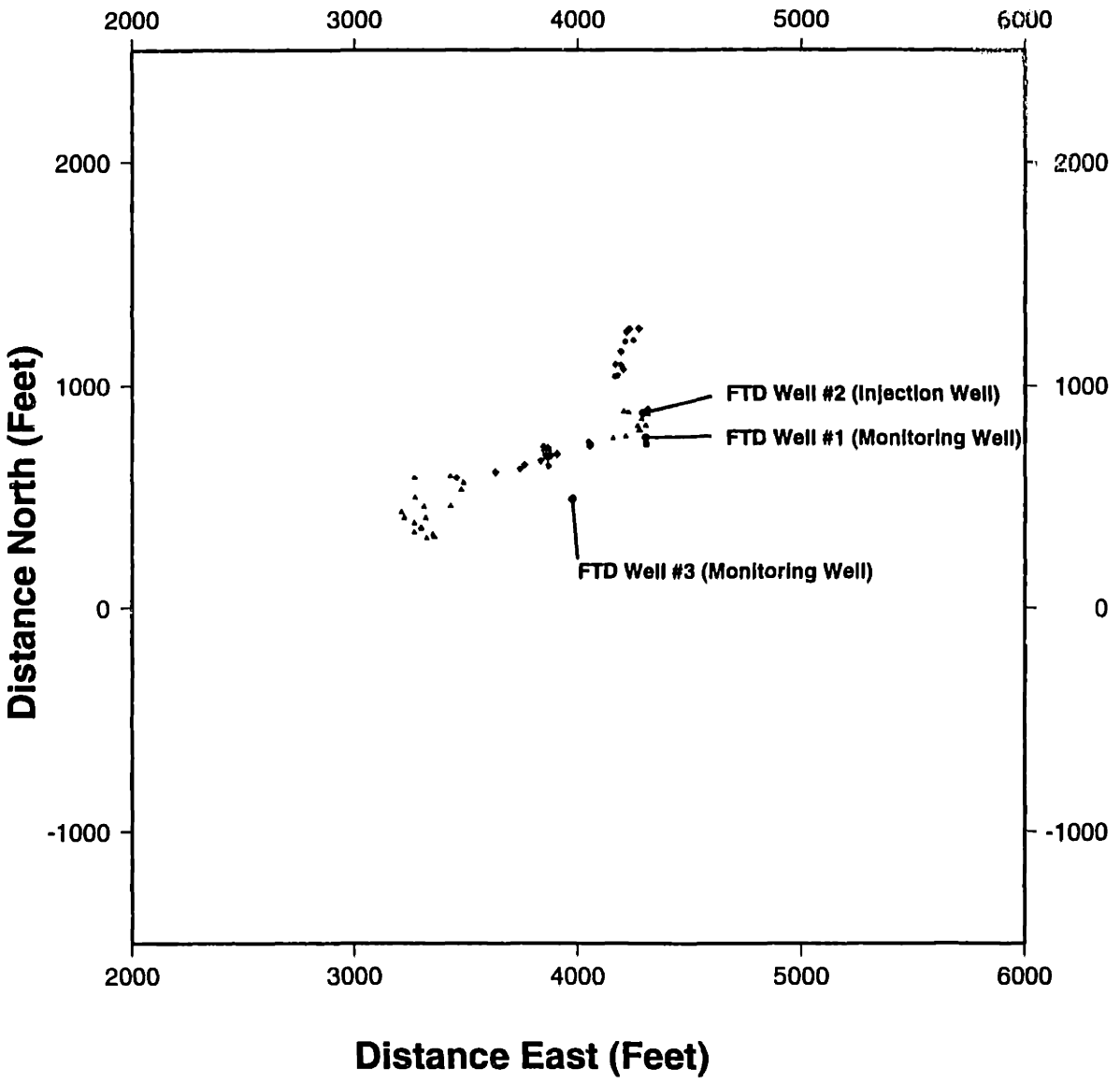

Figure D-62: DWTI Cluster Frame 61

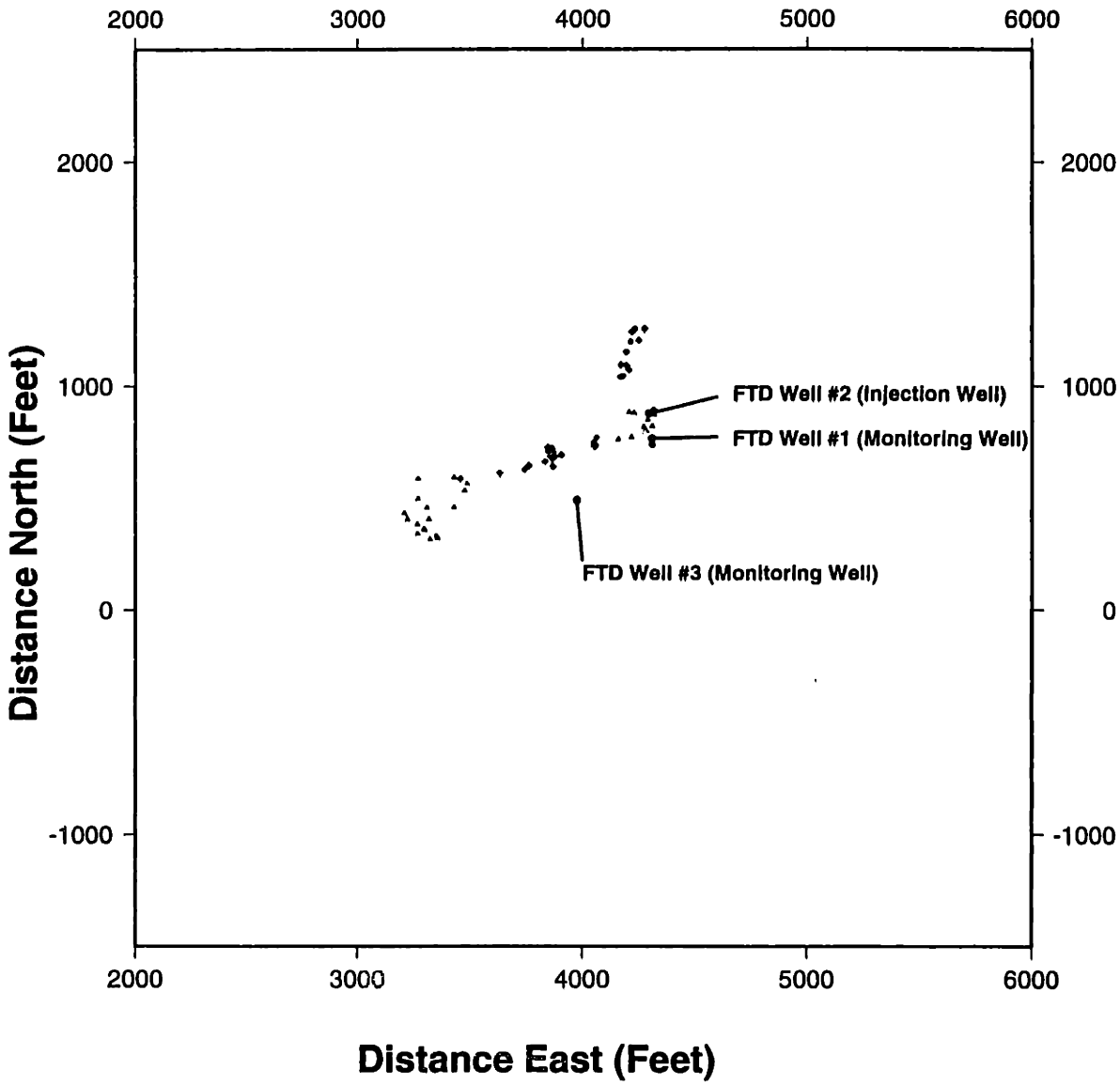

Figure D-63: DWTI Cluster Frame 62

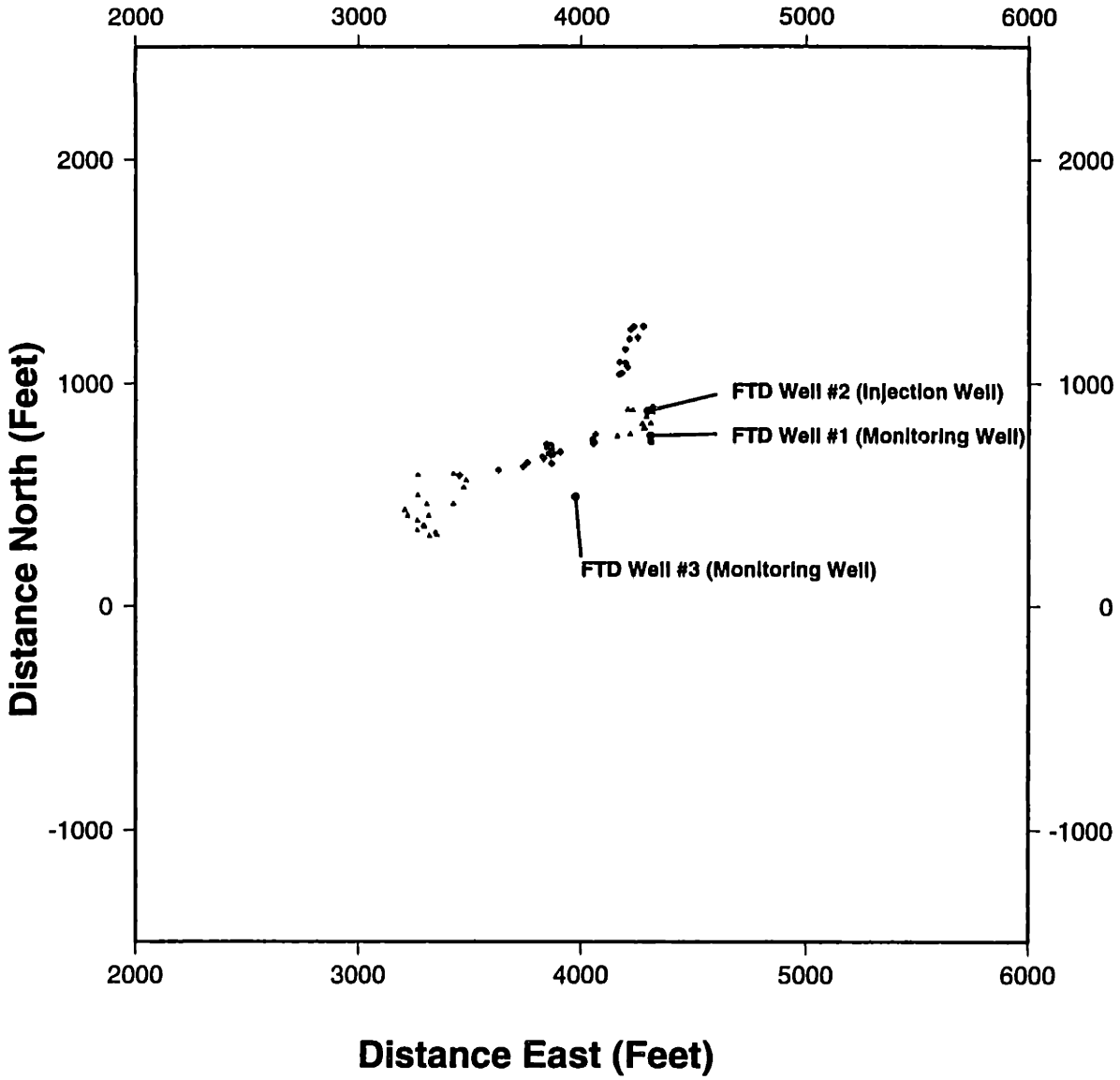

Figure D-64: DWTI Cluster Frame 63

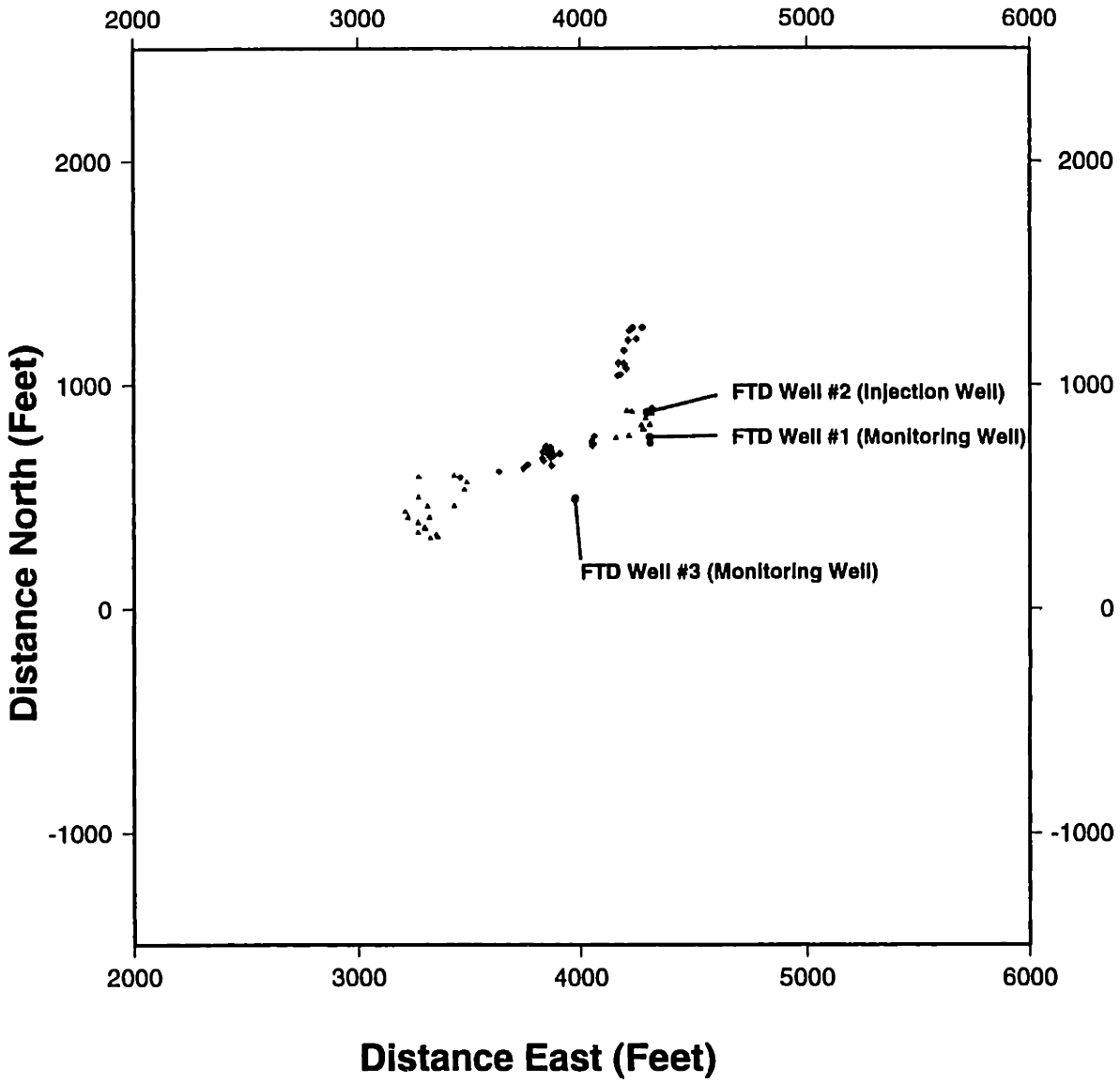

Figure D-65: DWTI Cluster Frame 64

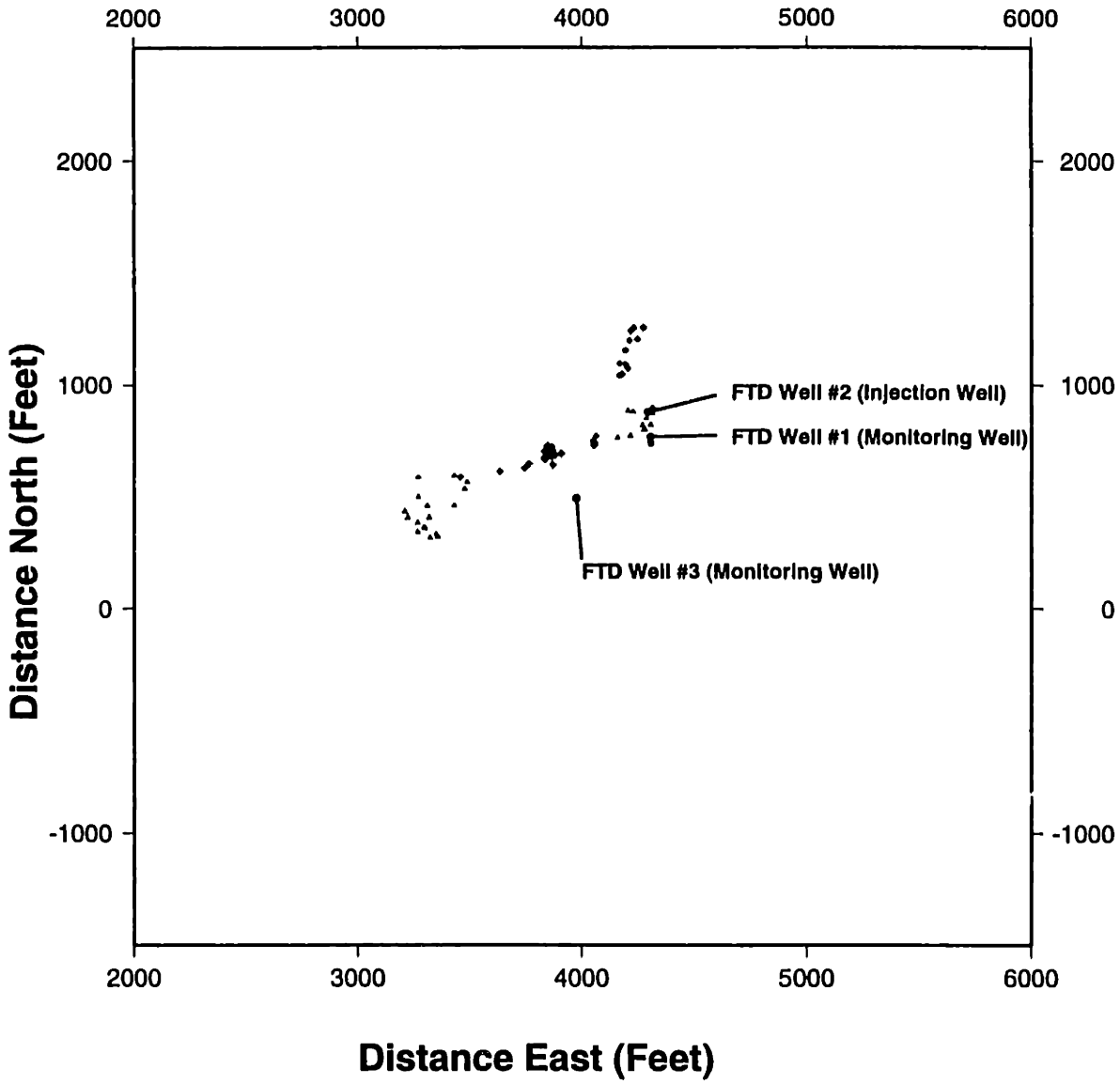

Figure D-66: DWTI Cluster Frame 65

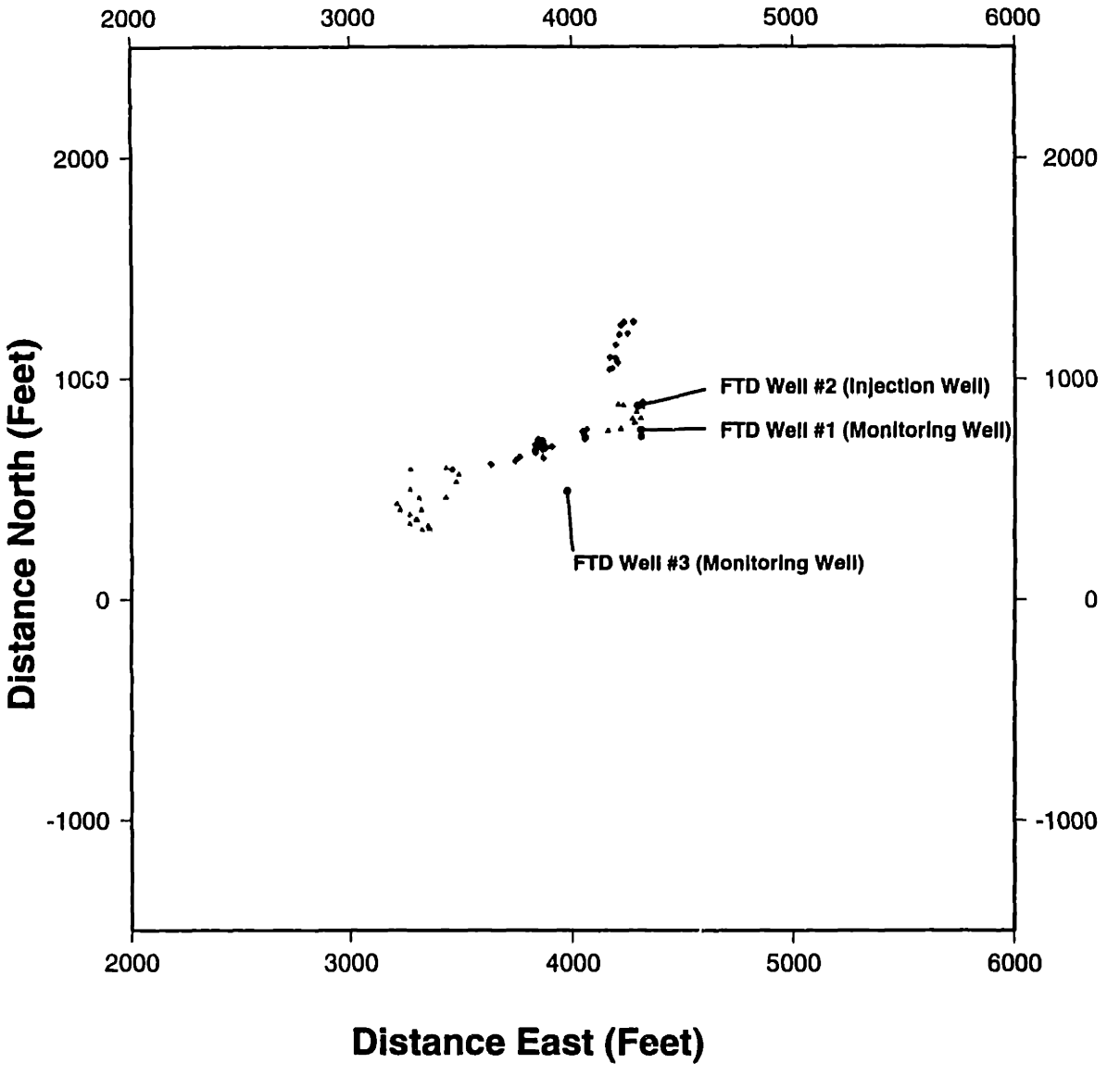

Figure D-67: DWTI Cluster Frame 66

(This page intentionally left blank.)

Figure D-68:

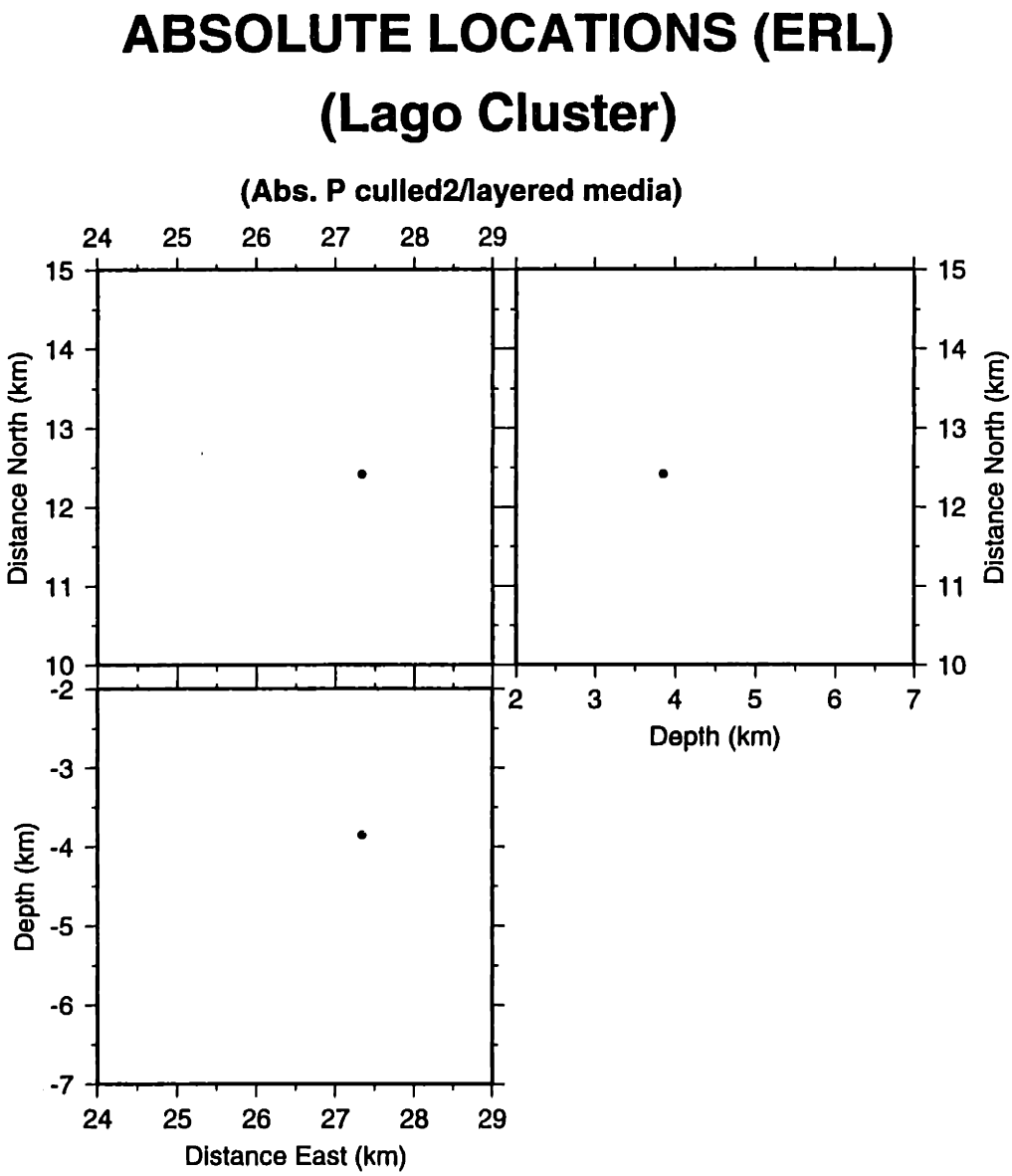

Figure D-69: LAGO Cluster Frame 1

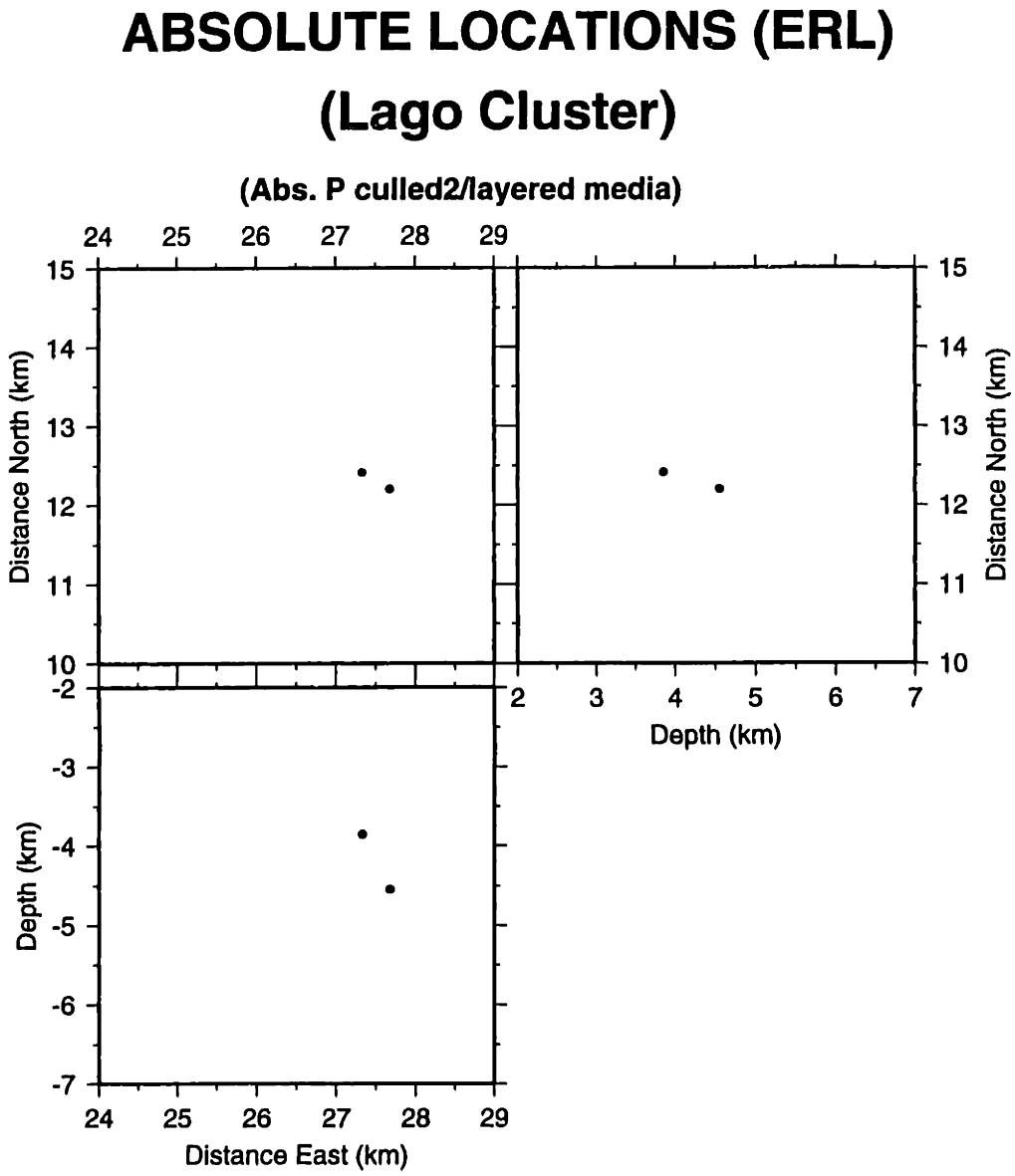

Figure D-70: LAGO Cluster Frame 2

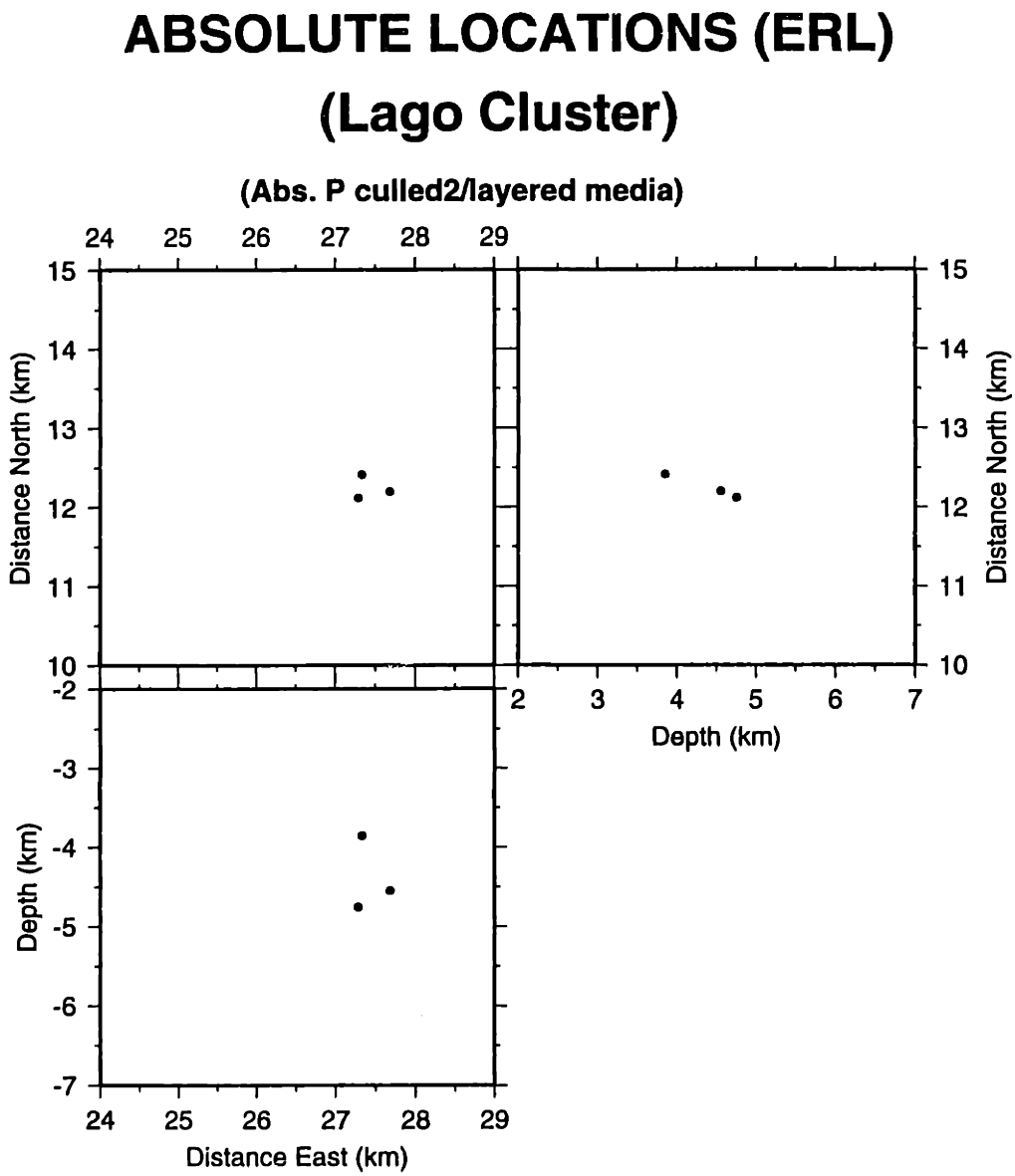

Figure D-71: LAGO Cluster Frame 3

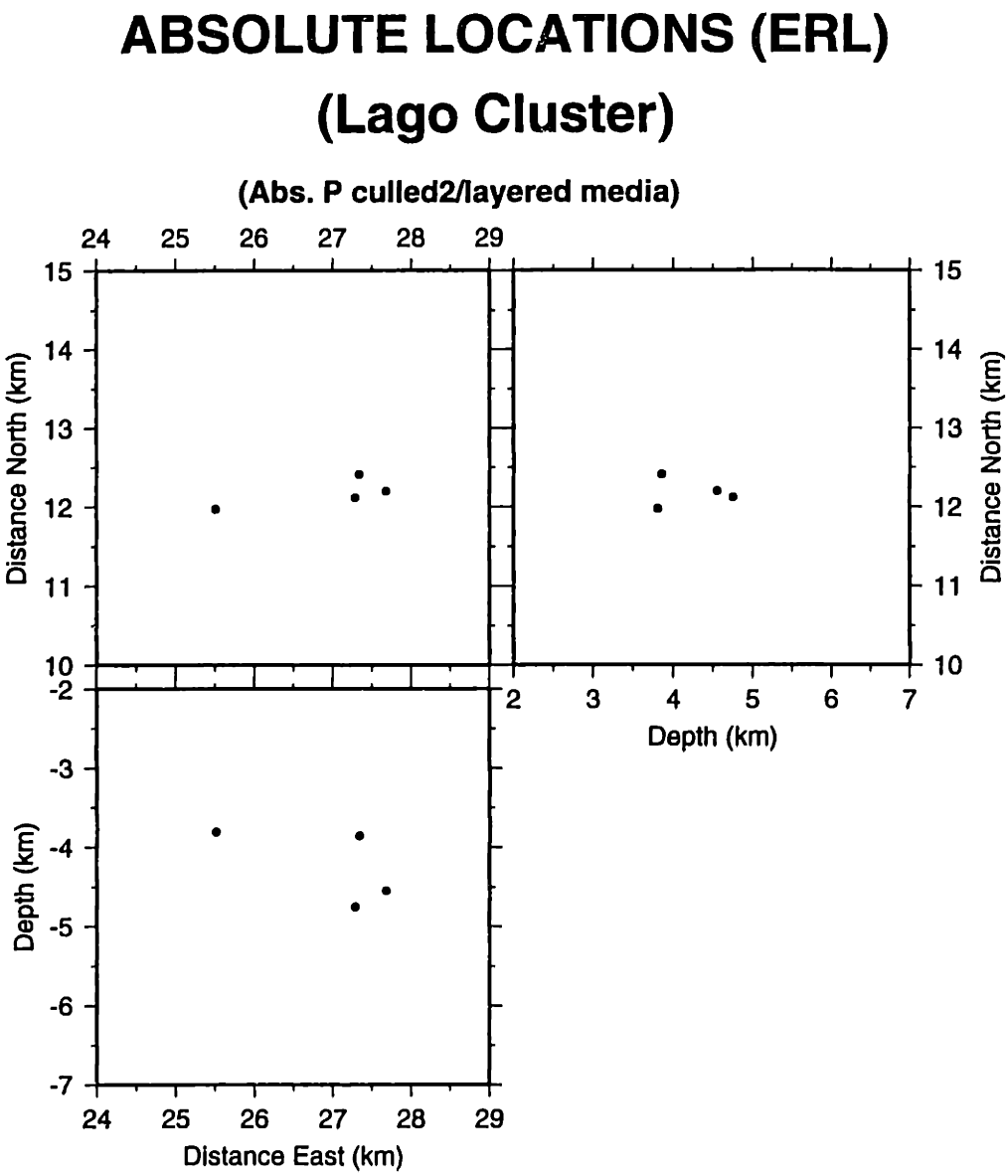

Figure D-72: LAGO Cluster Frame 4

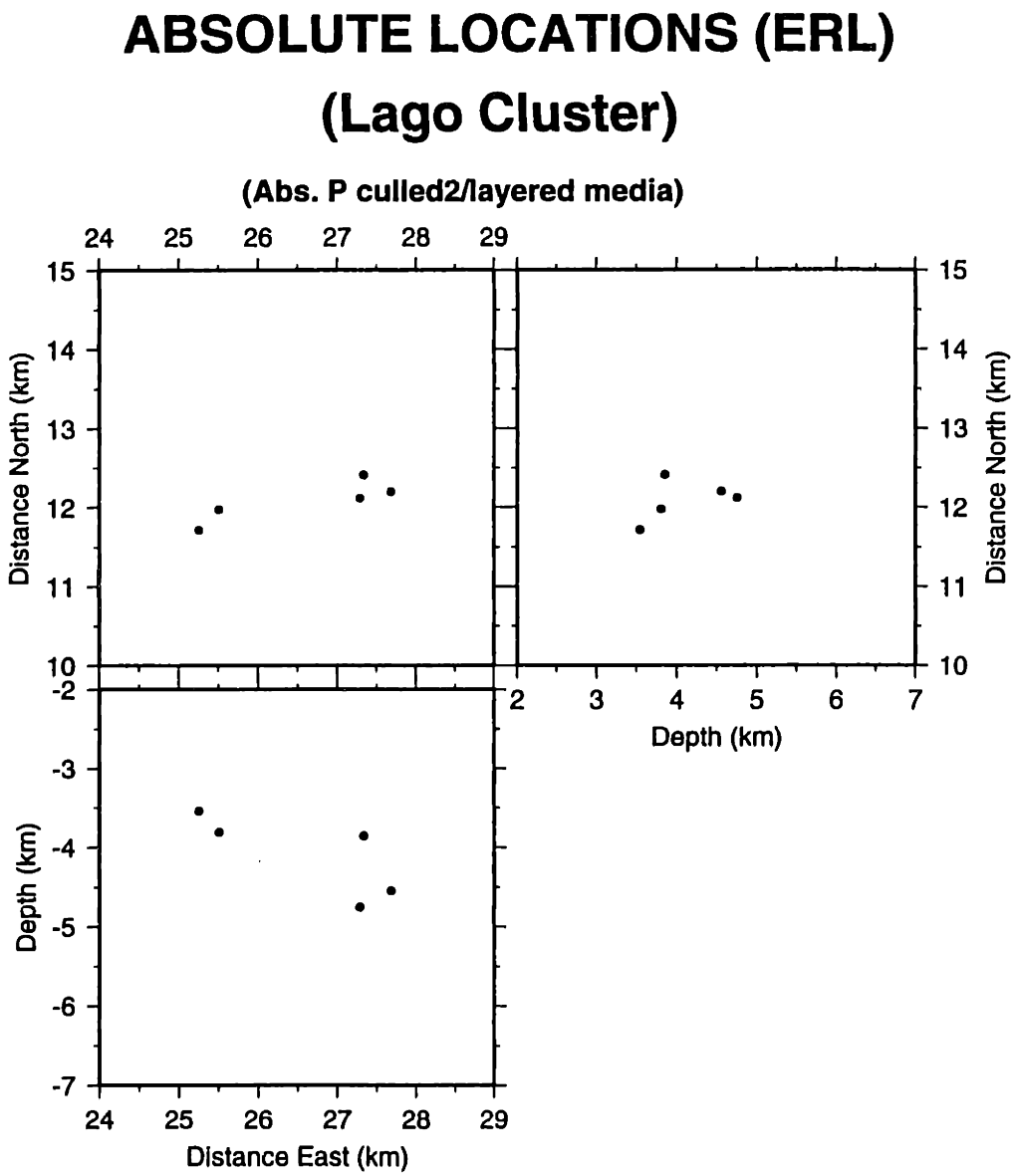

Figure D-73: LAGO Cluster Frame 5

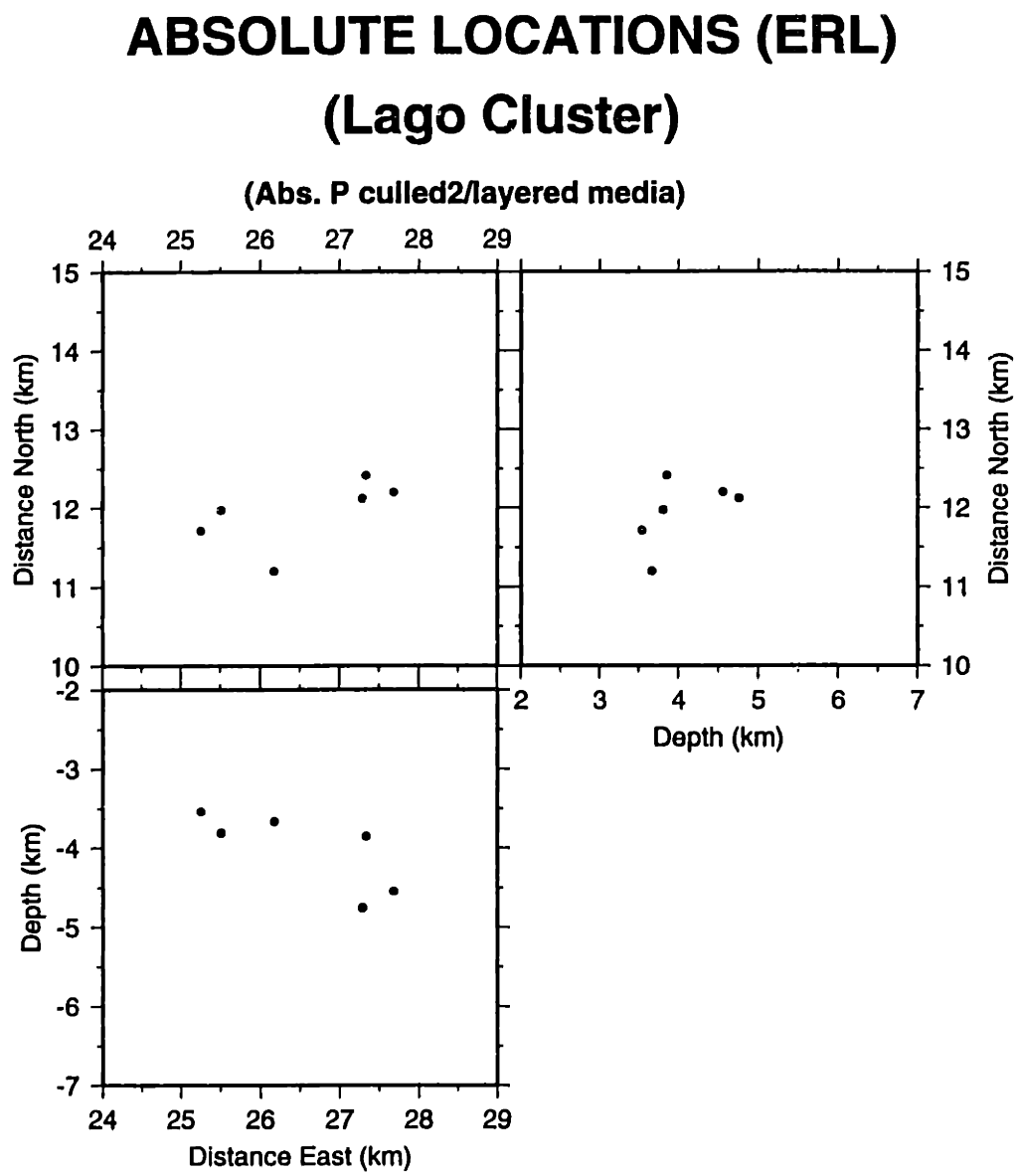

Figure D-74: LAGO Cluster Frame 6

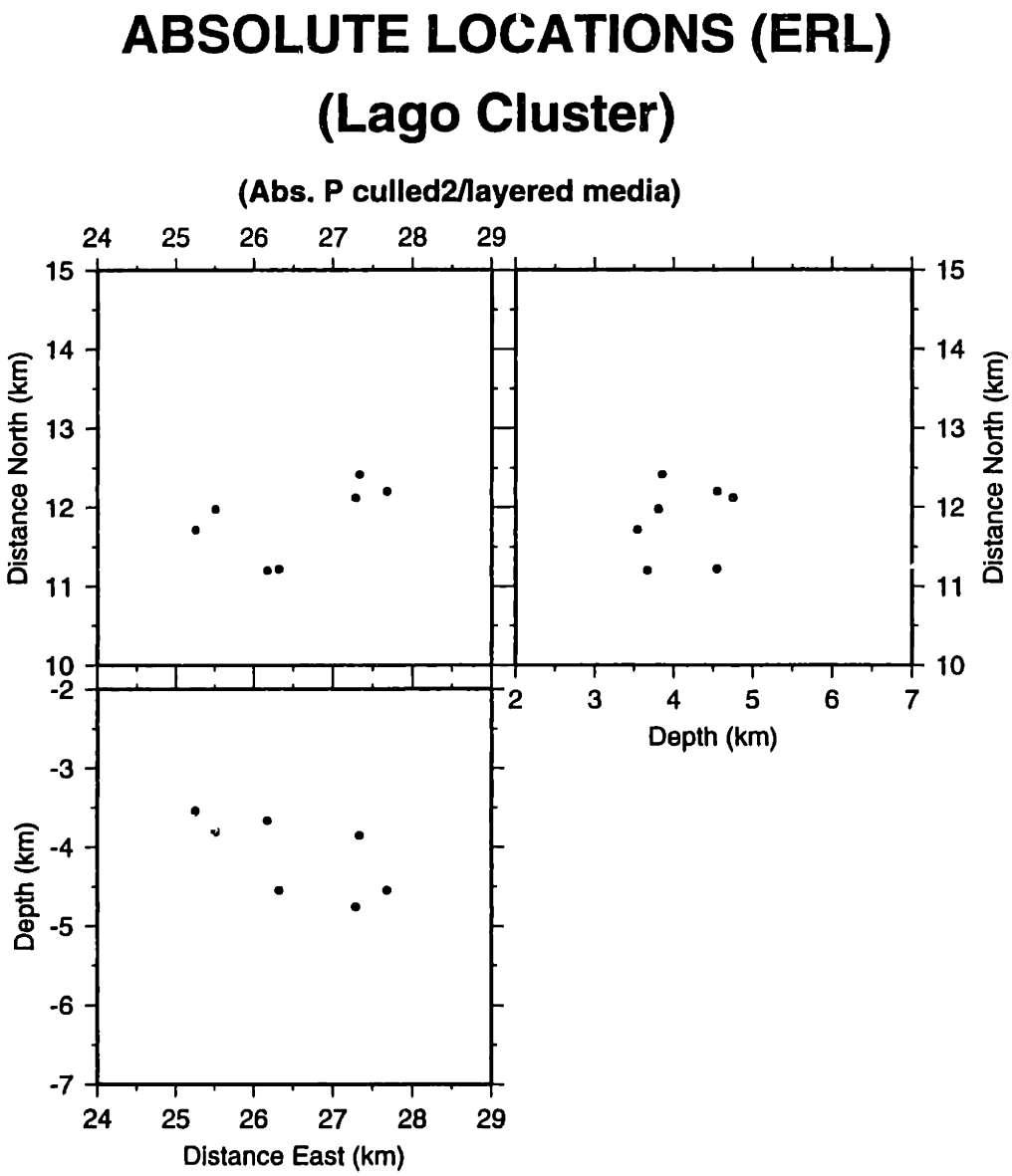

Figure D-75: LAGO Cluster Frame 7

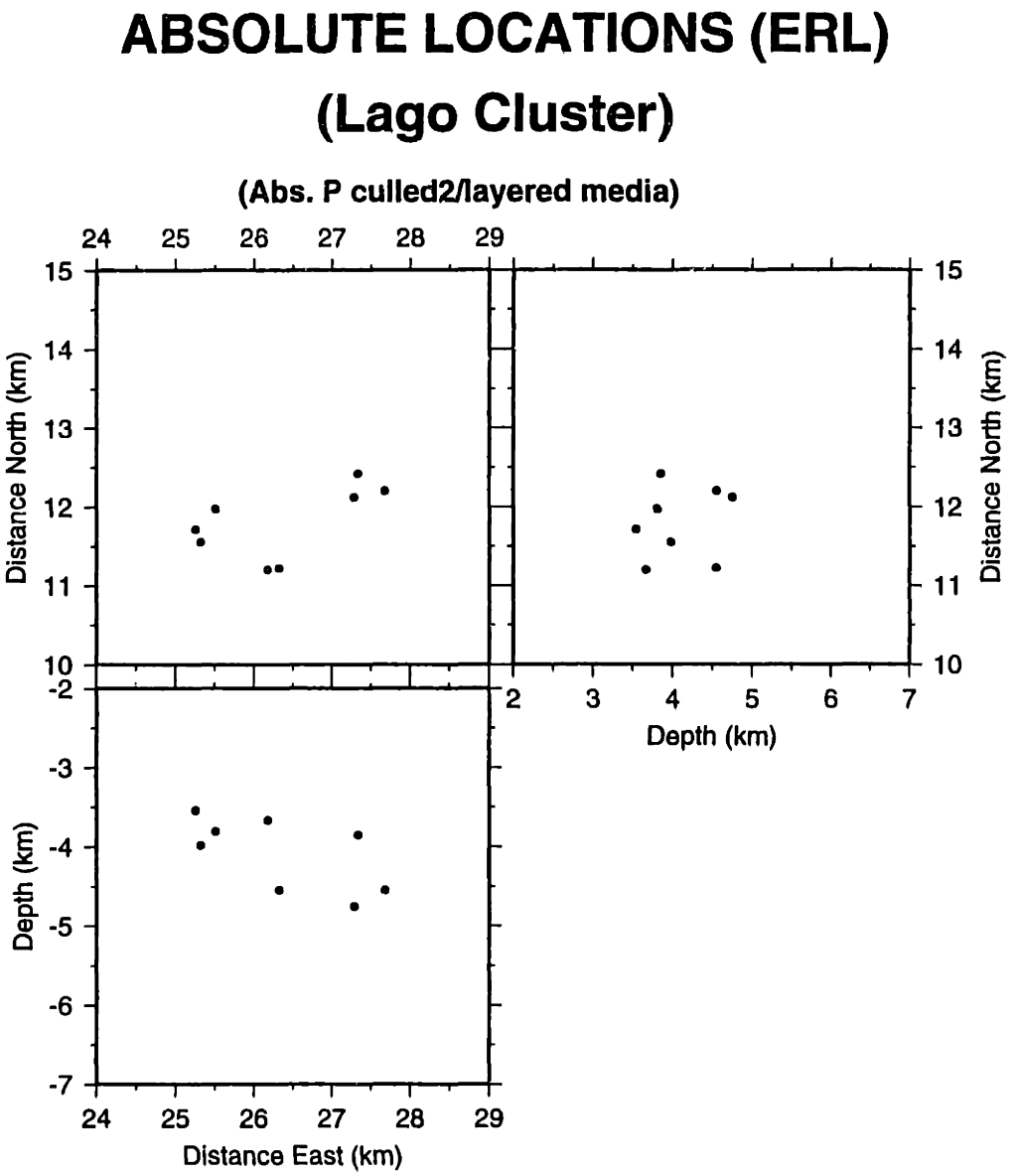

Figure D-76: LAGO Cluster Frame 8

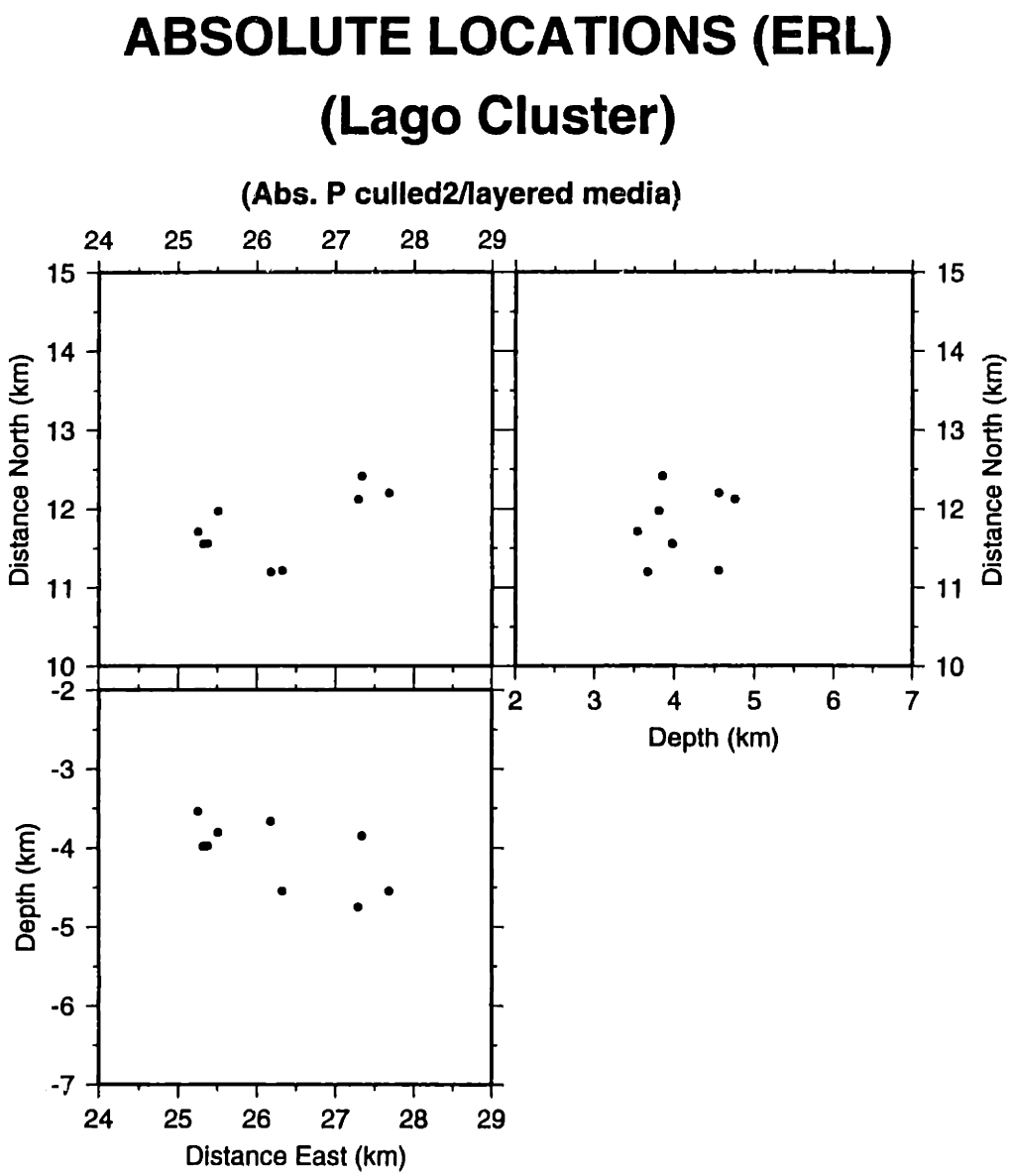

Figure D-77: LAGO Cluster Frame 9

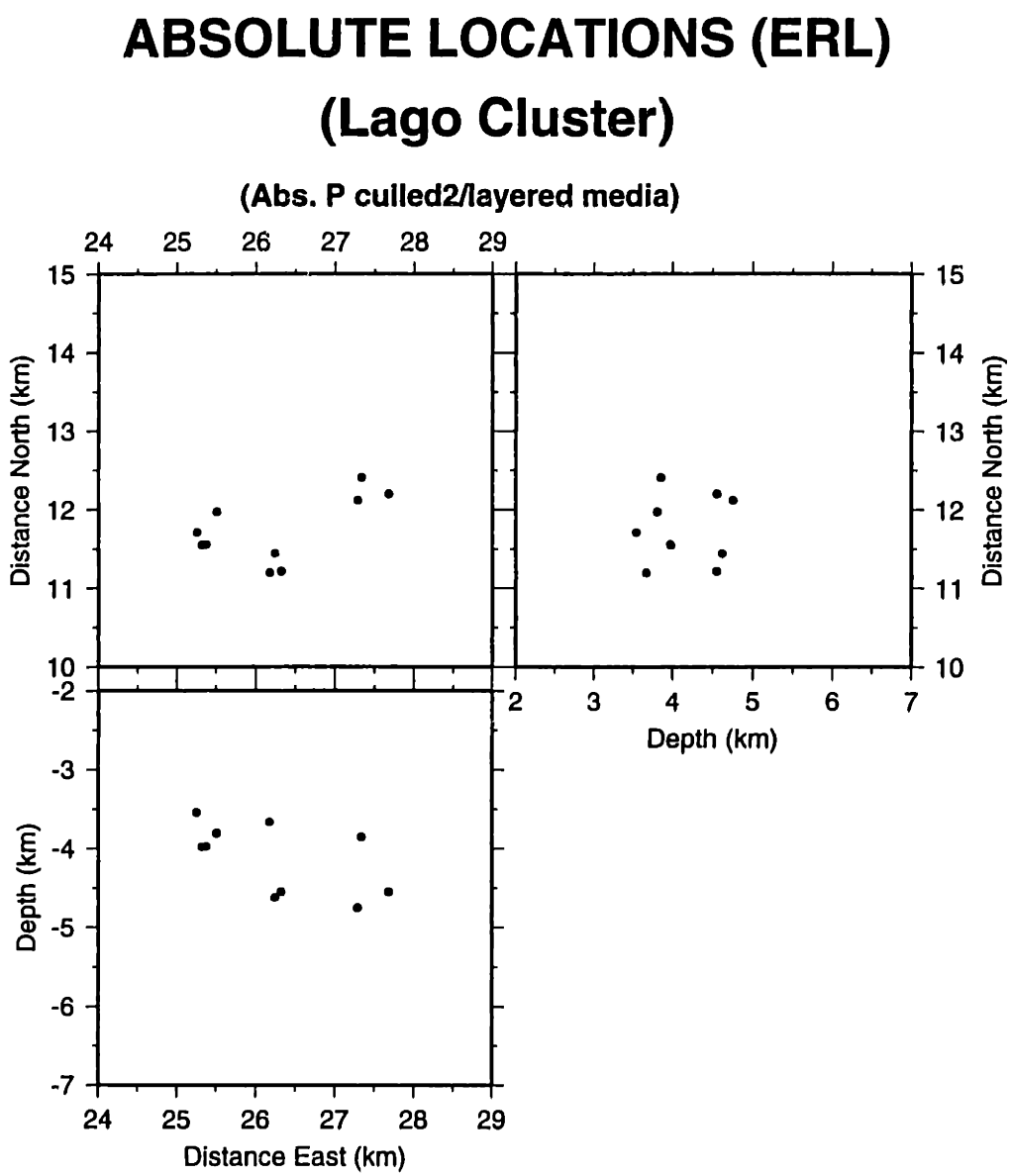

Figure D-78: LAGO Cluster Frame 10

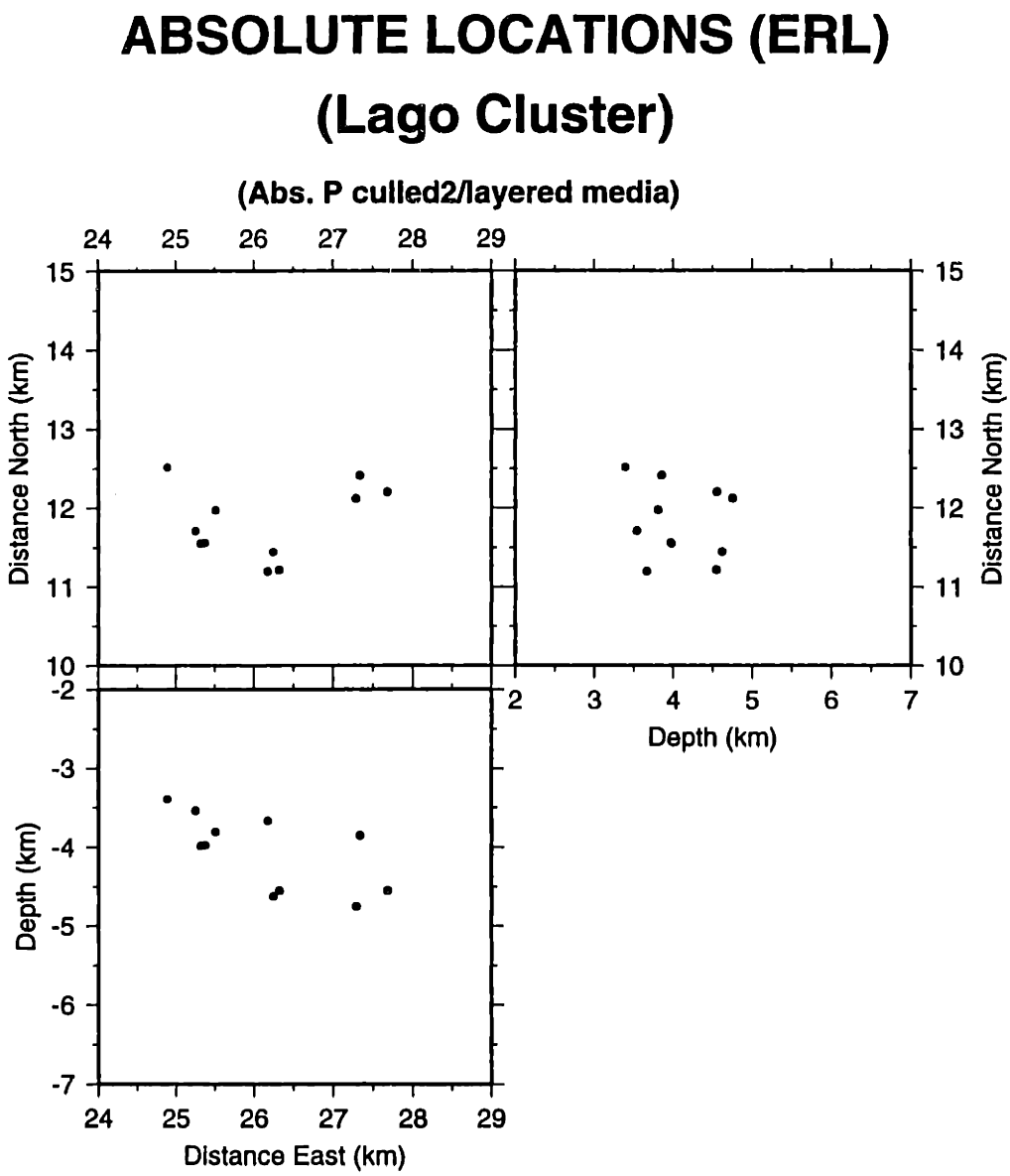

Figure D-79: LAGO Cluster Frame 11

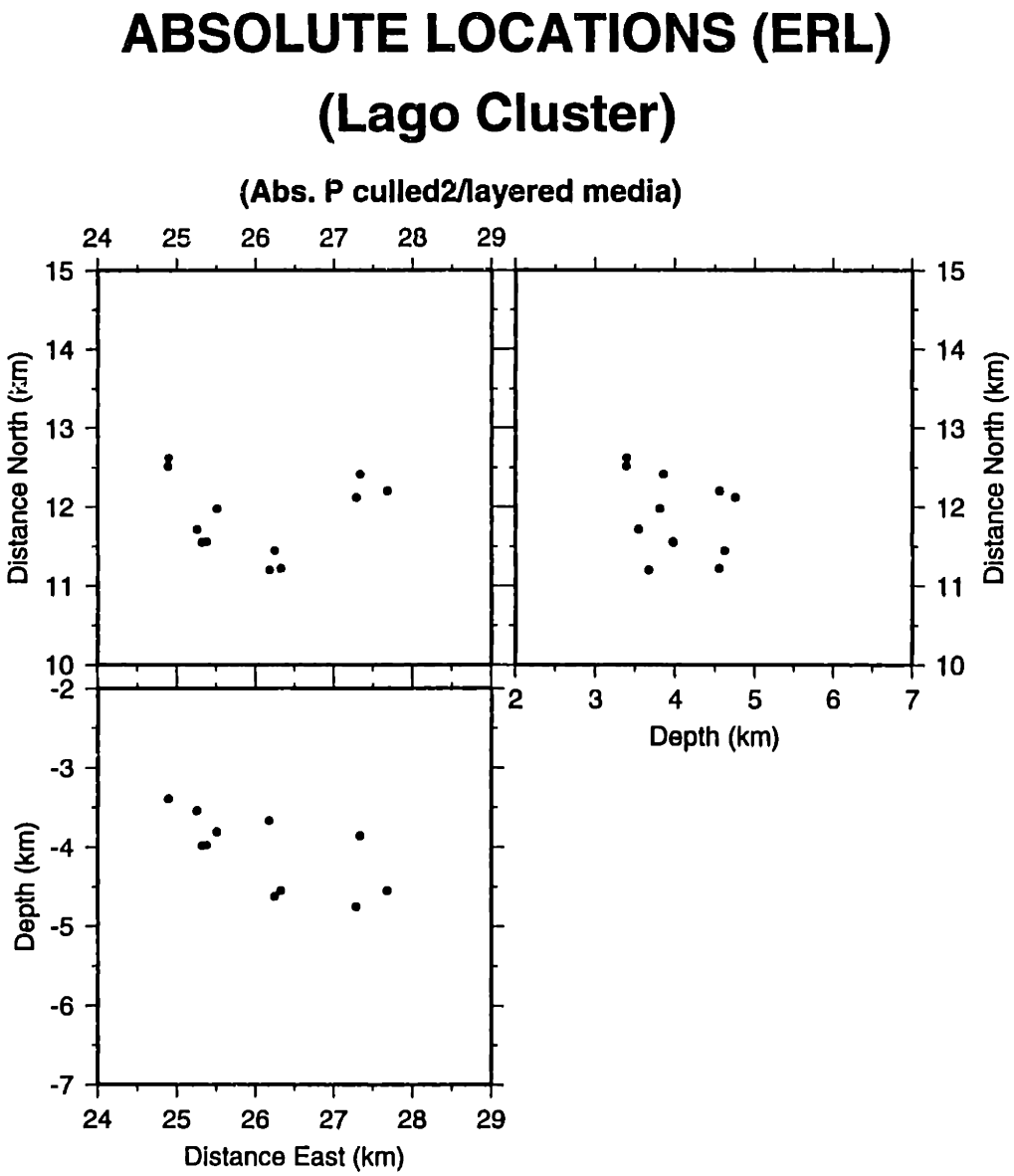

Figure D-80: LAGO Cluster Frame 12

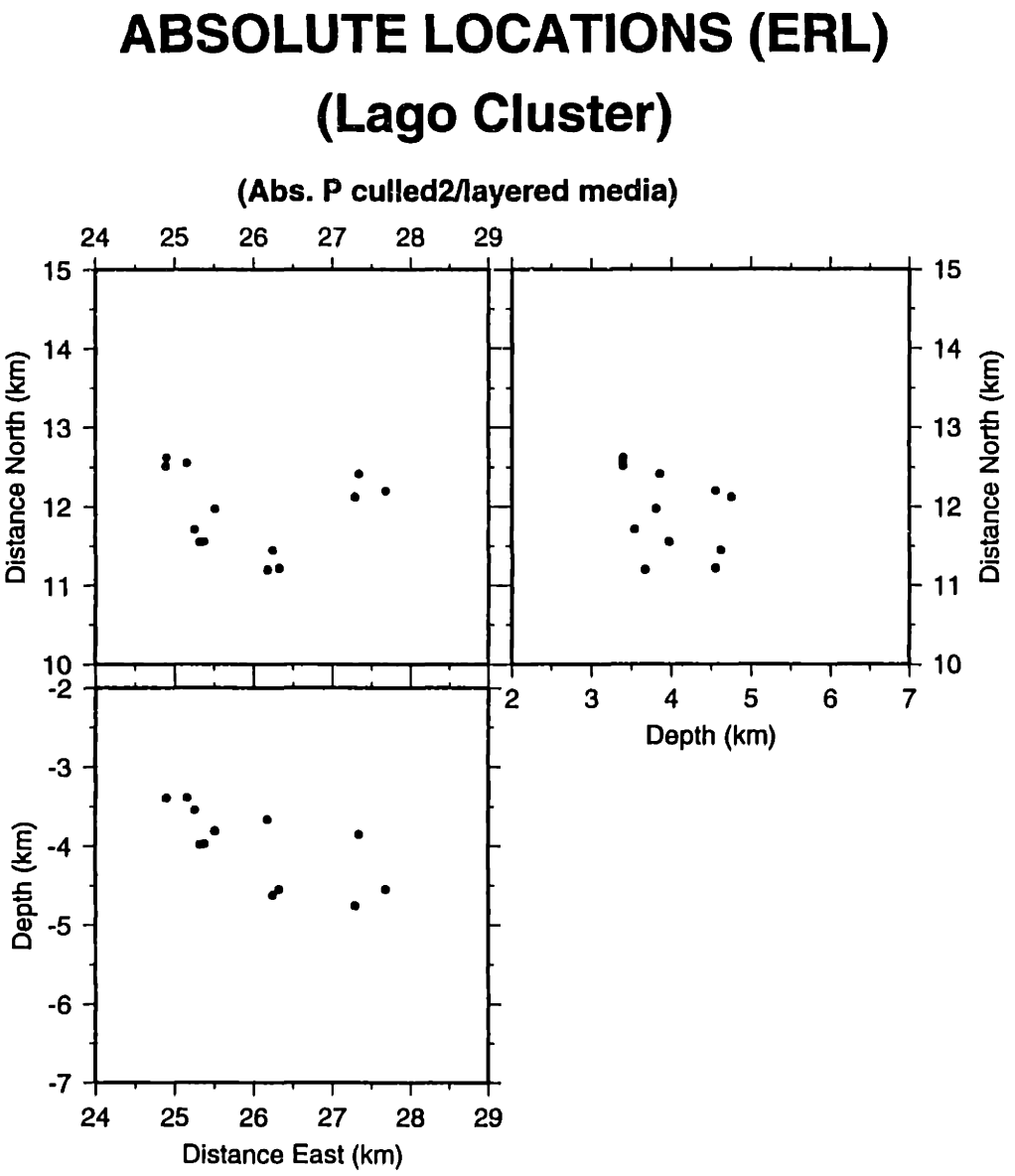

Figure D-81: LAGO Cluster Frame 13

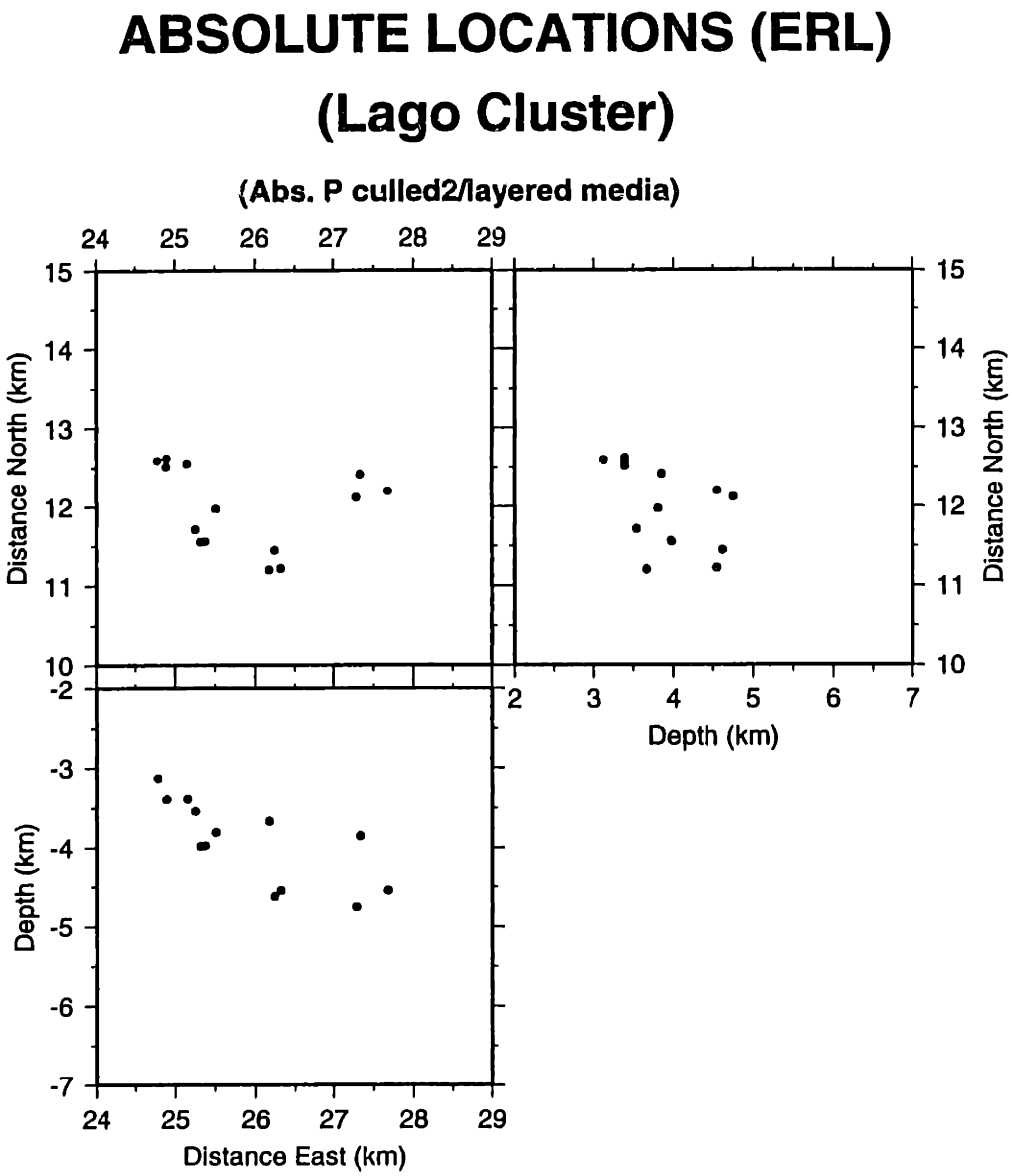

Figure D-82: LAGO Cluster Frame 14

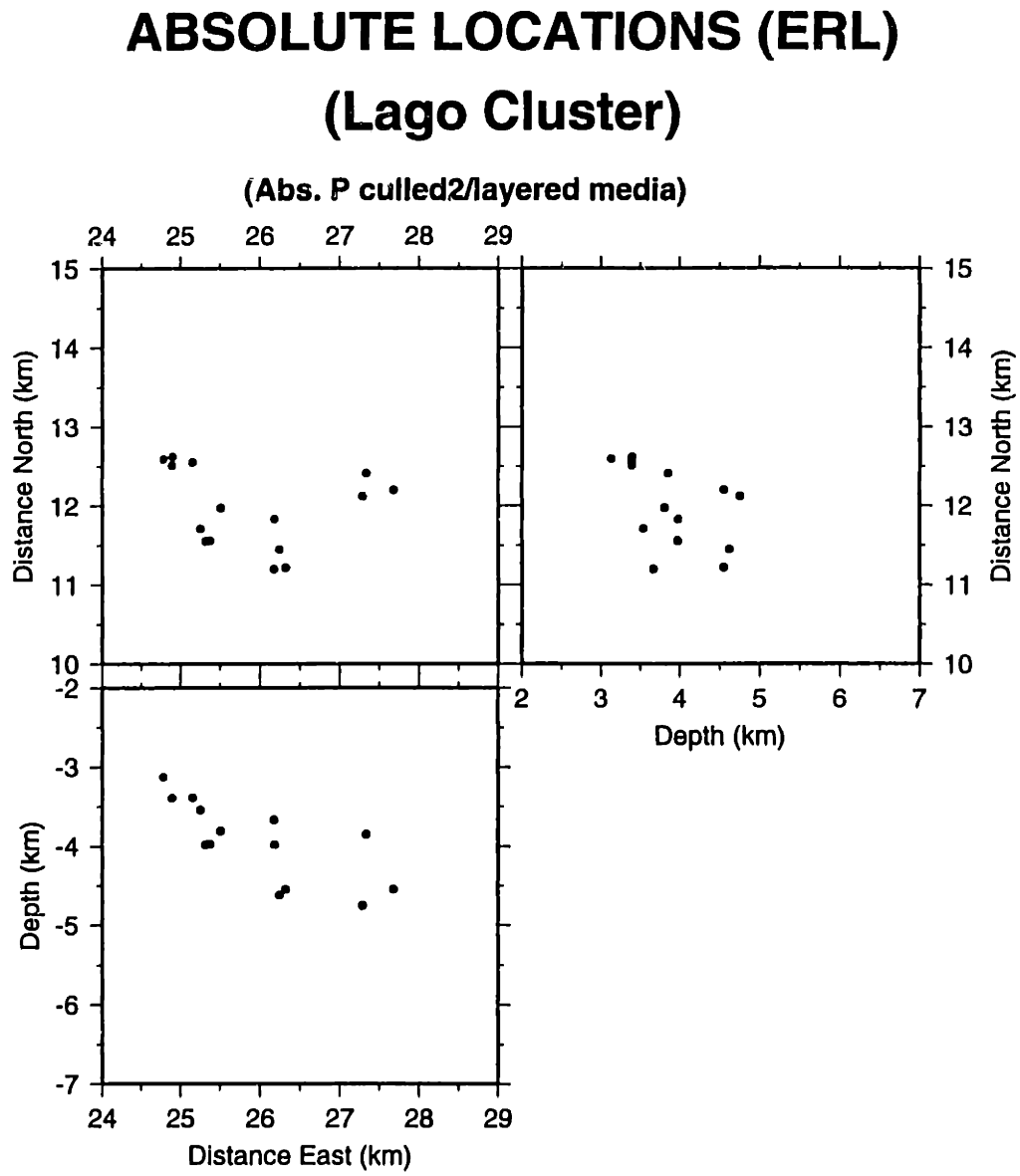

Figure D-83: LAGO Cluster Frame 15

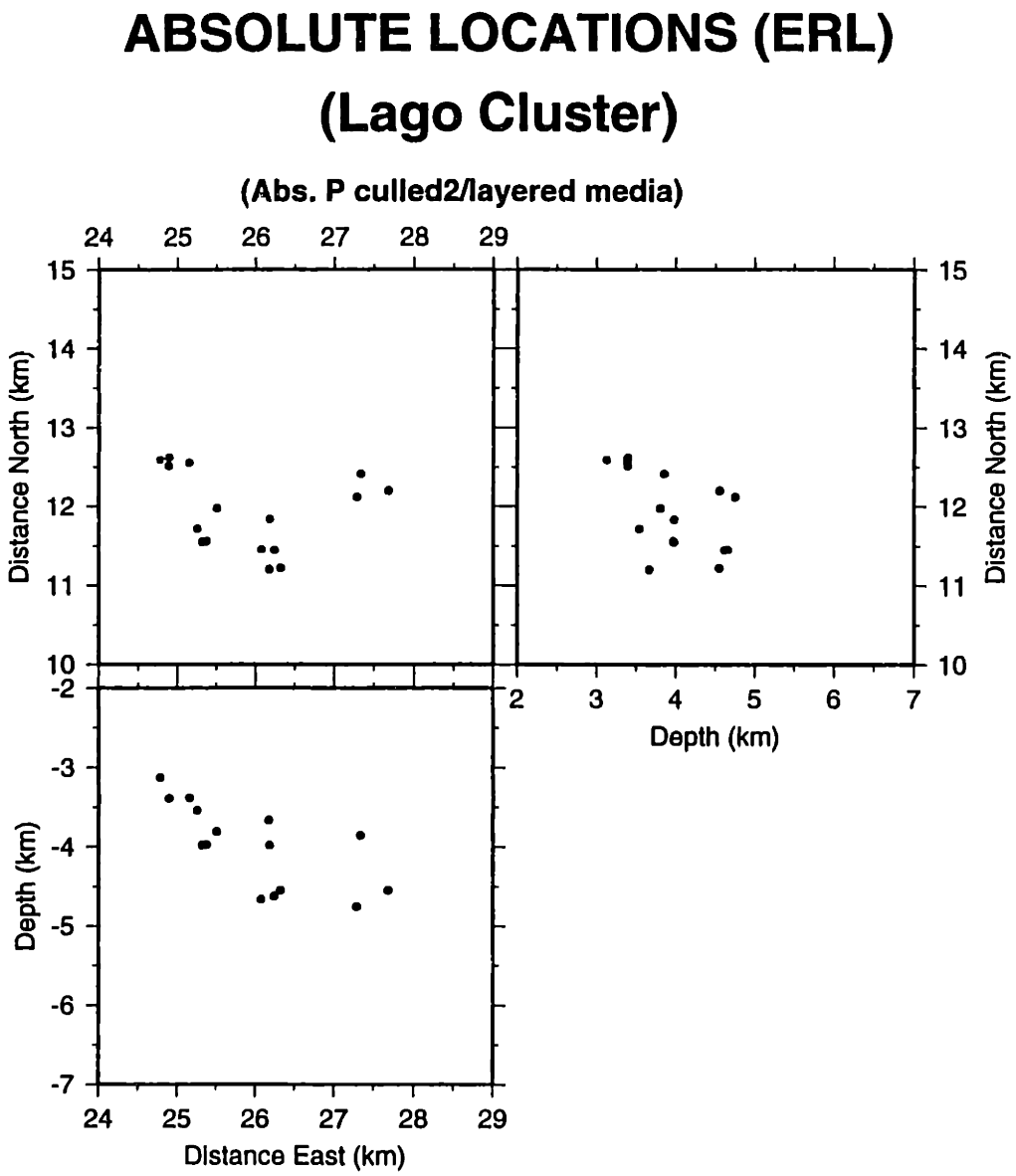

Figure D-84: LAGO Cluster Frame 16

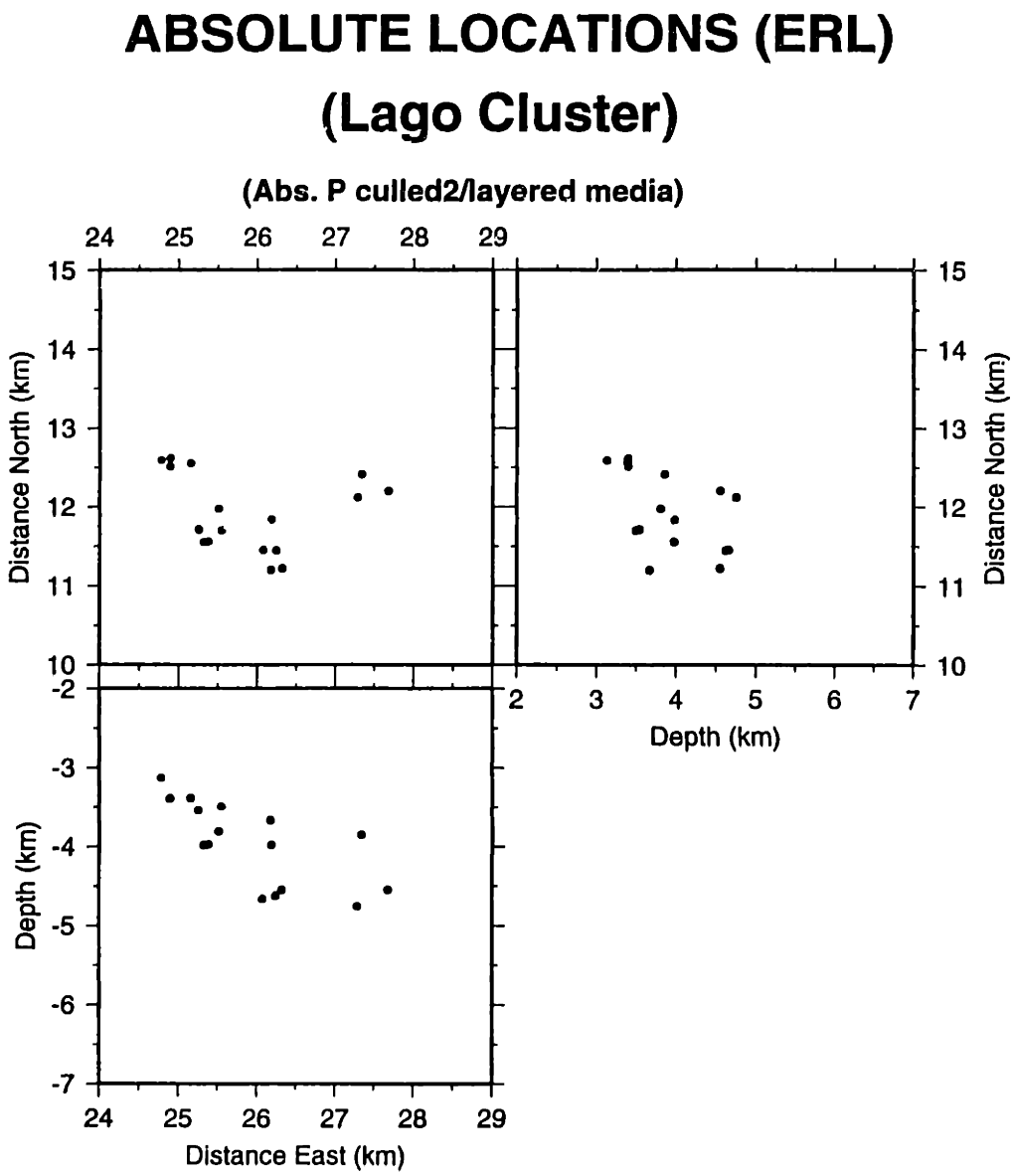

Figure D-85: LAGO Cluster Frame 17

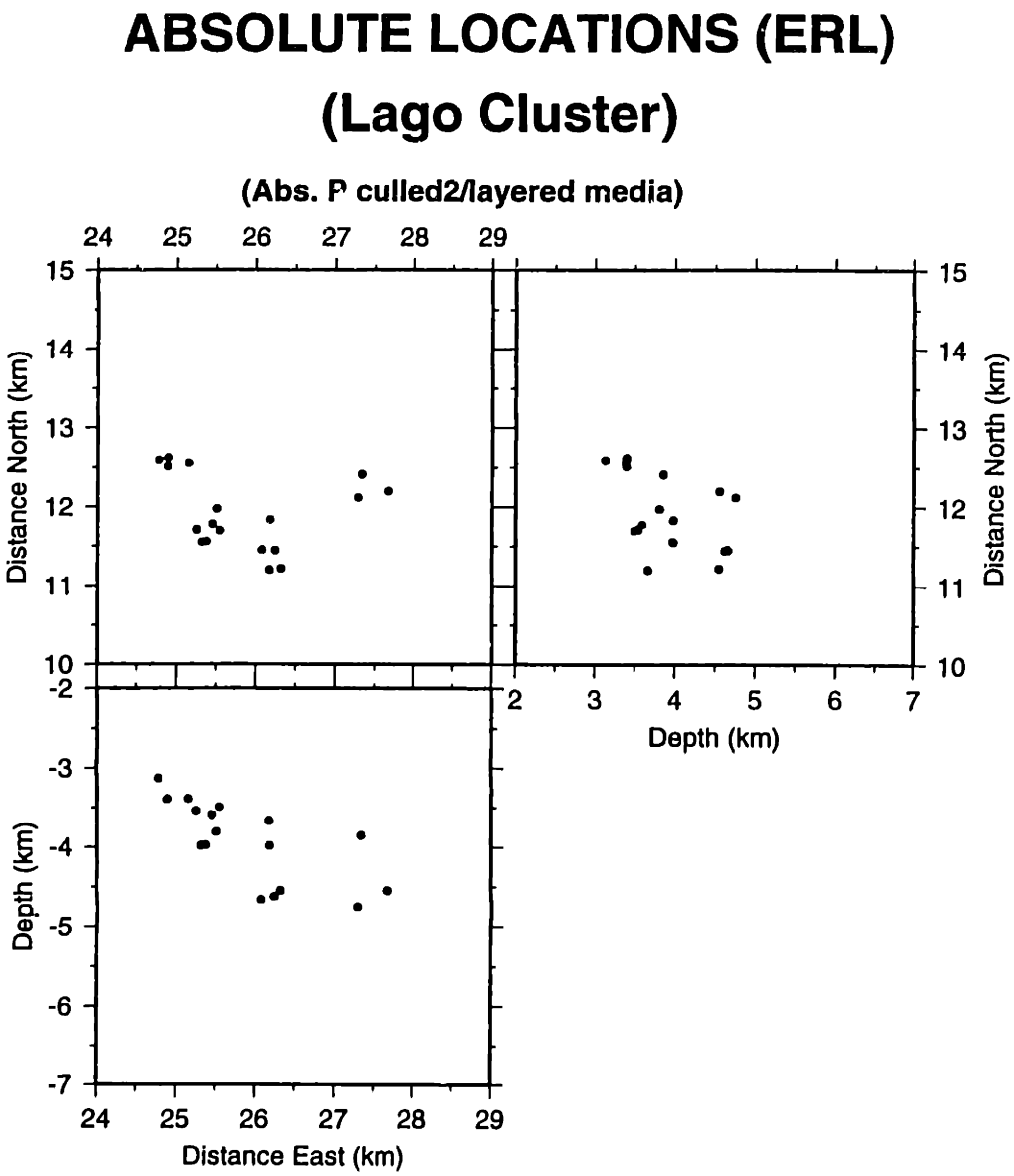

Figure D-86: LAGO Cluster Frame 18

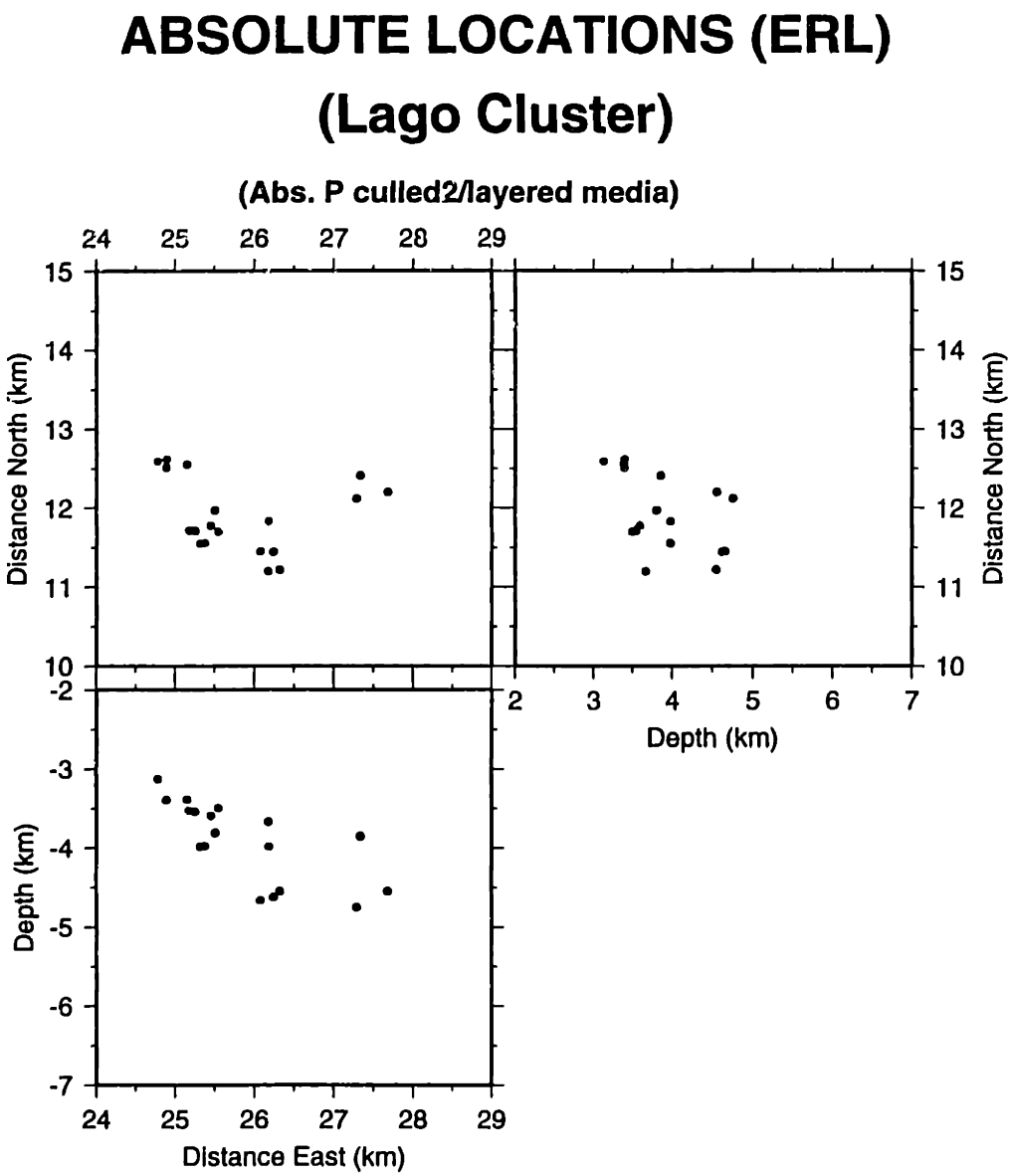

Figure D-87: LAGO Cluster Frame 19

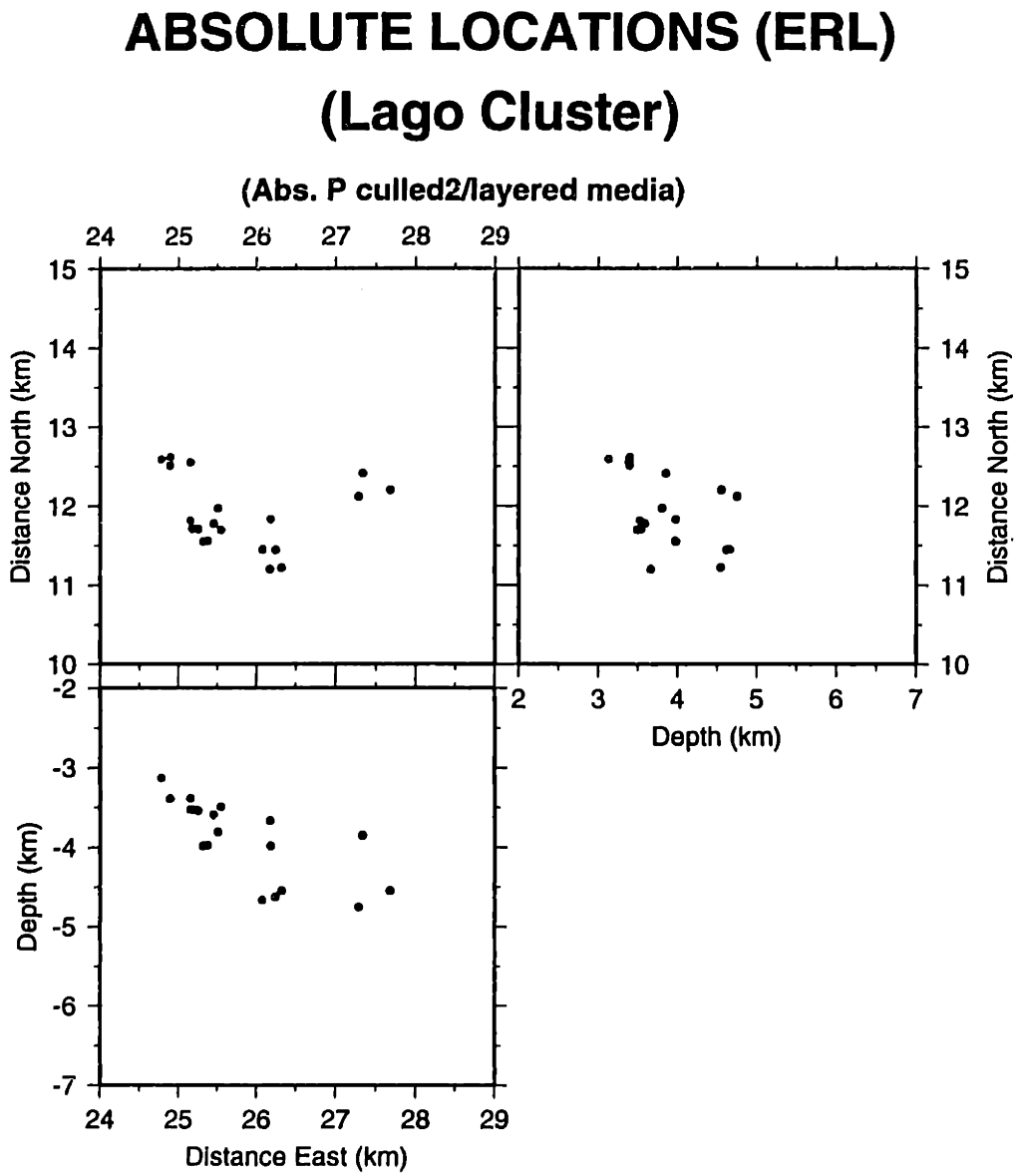

Figure D-88: LAGO Cluster Frame 20

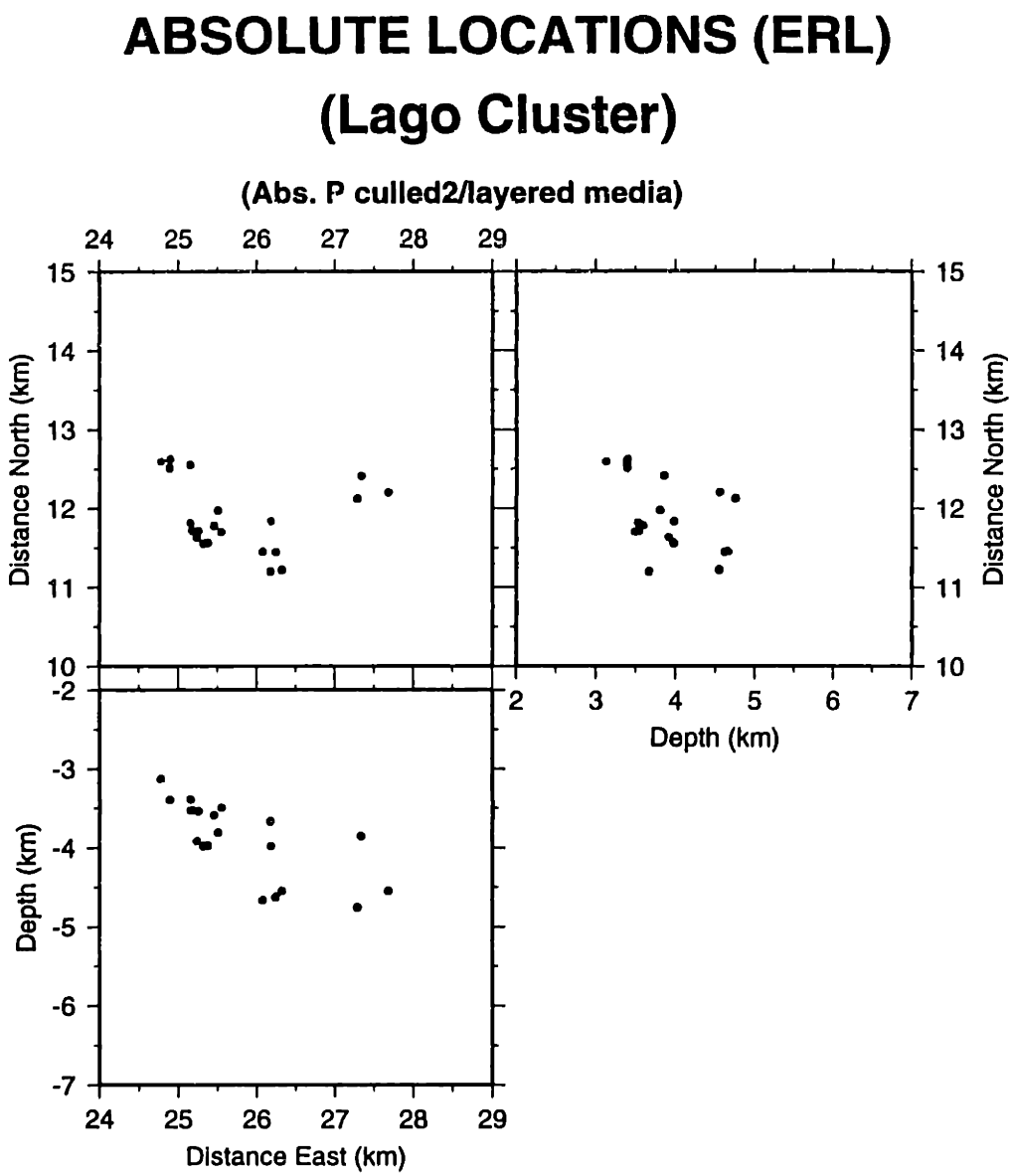

Figure D-89: LAGO Cluster Frame 21

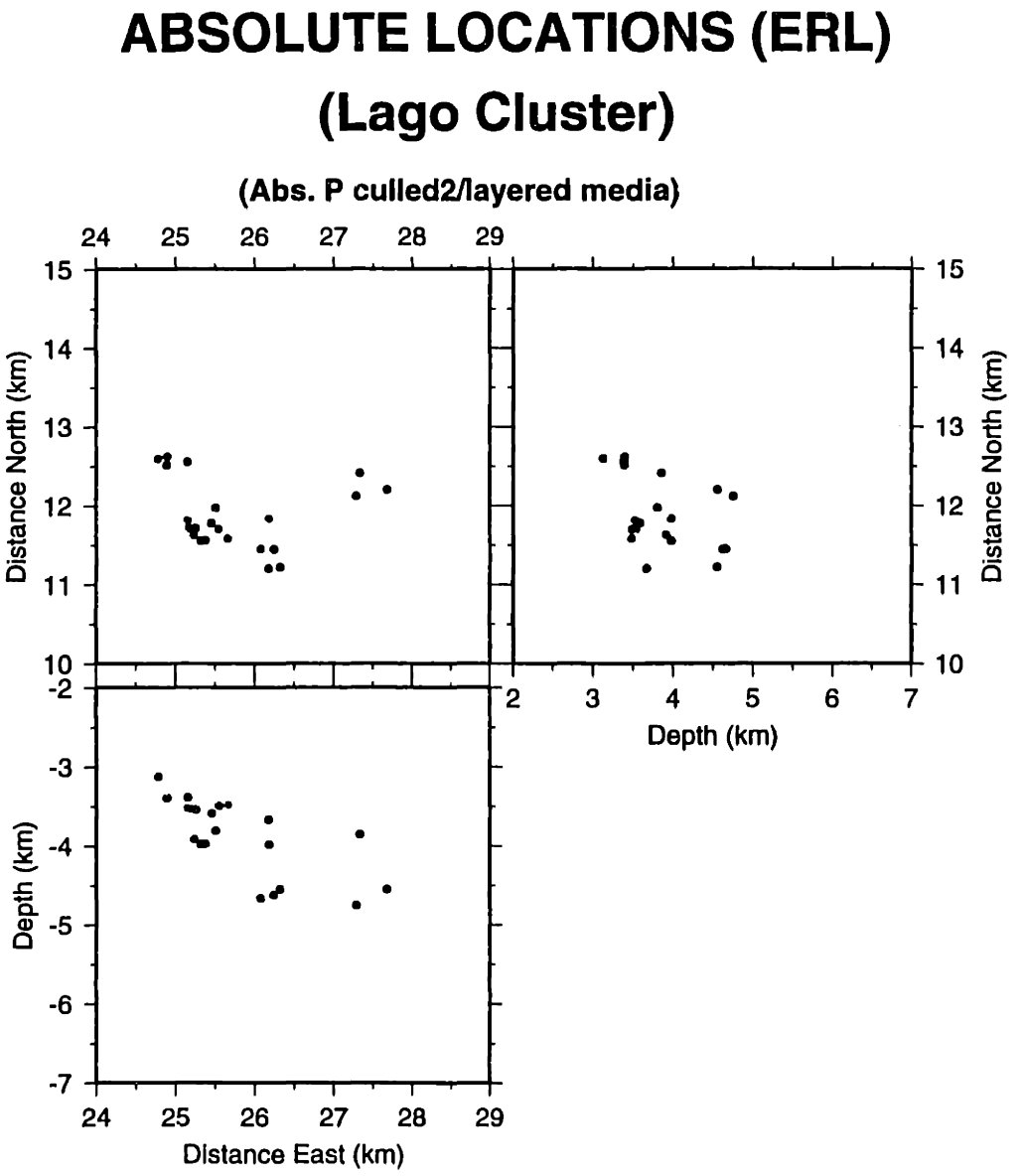

Figure D-90: LAGO Cluster Frame22

(This page intentionally left blank.)

Figure D-91:

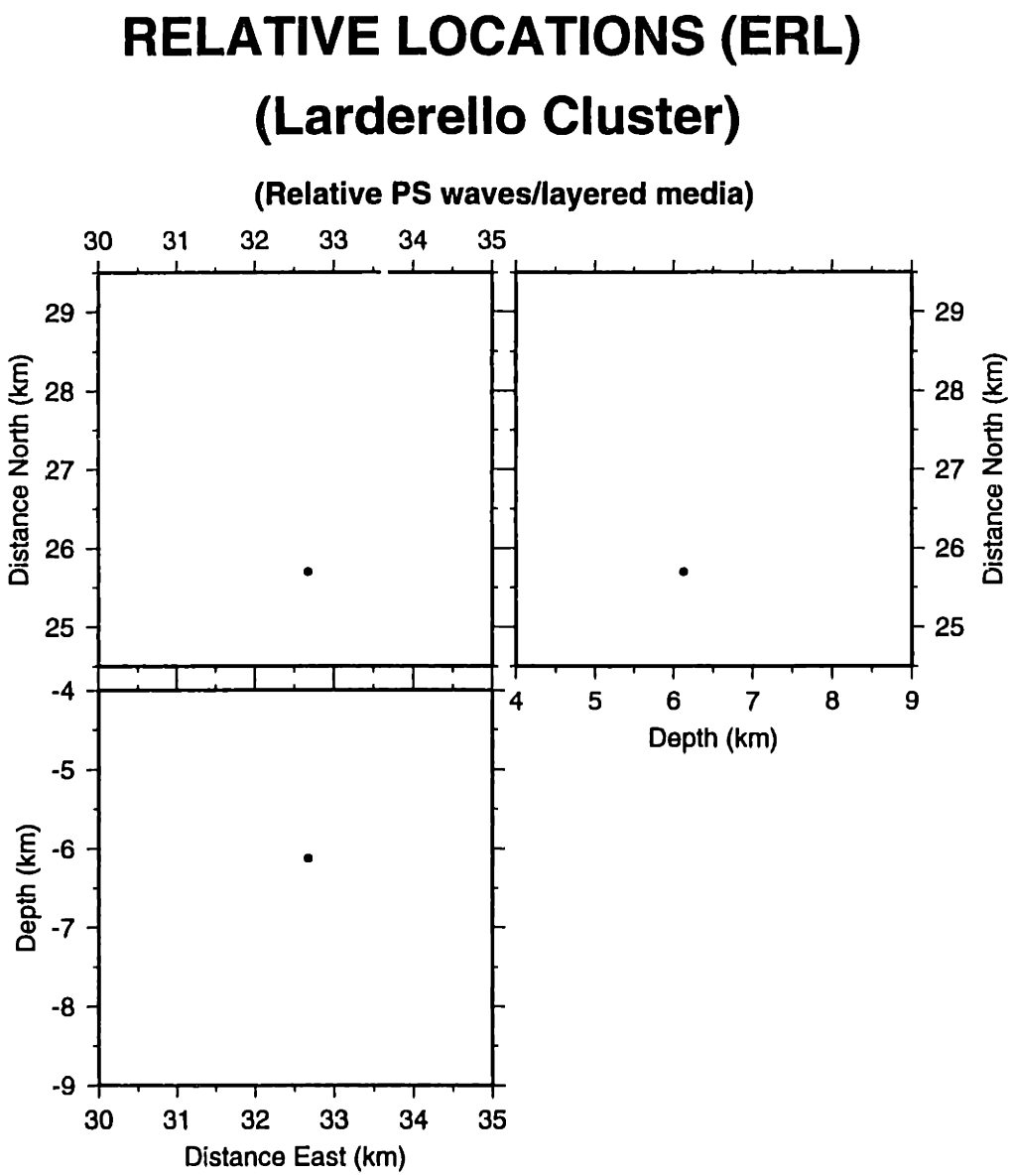

Figure D-92: Larderello 1993 Cluster Frame 00

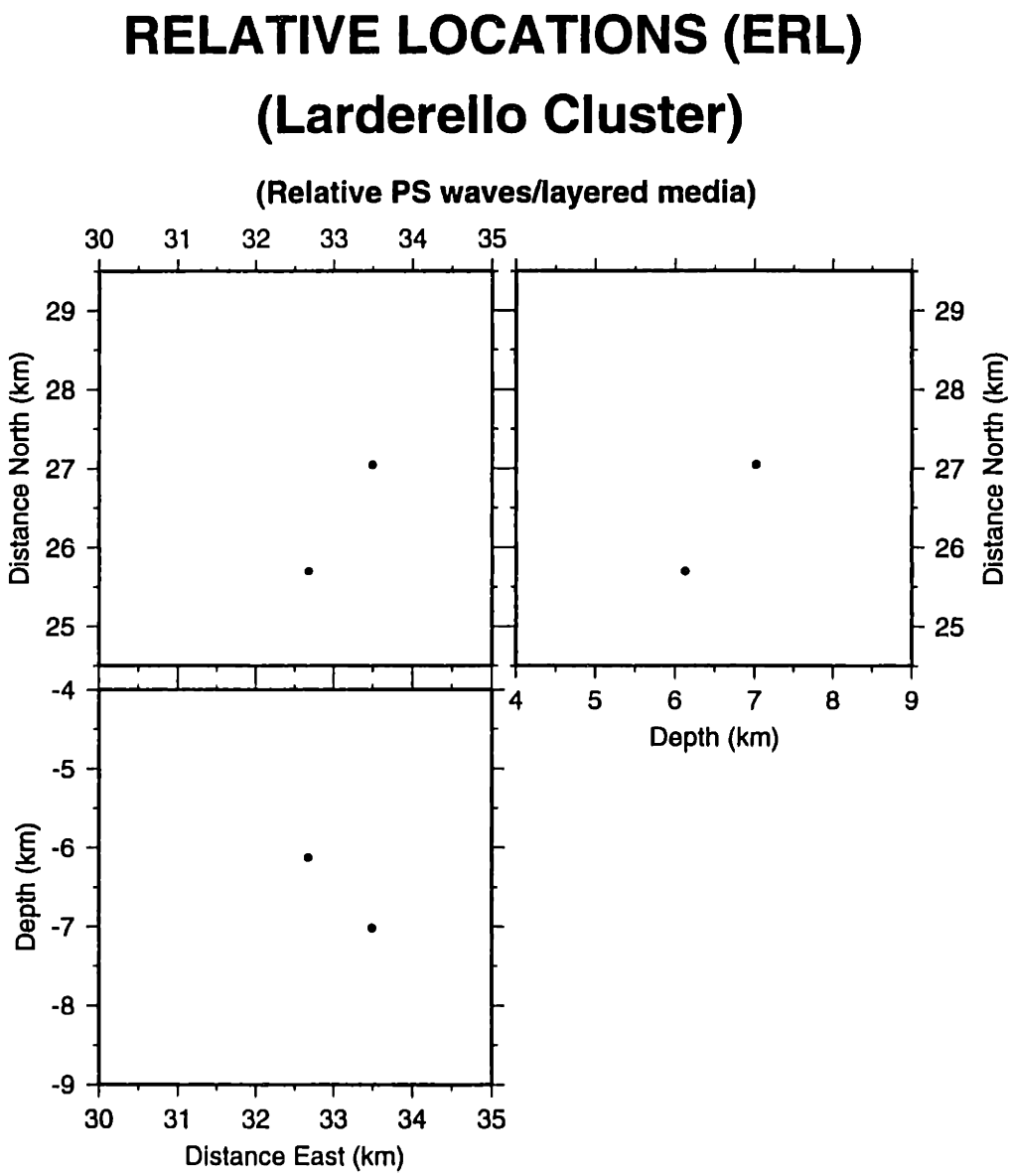

Figure D-93: Larderello 1993 Cluster Frame 01

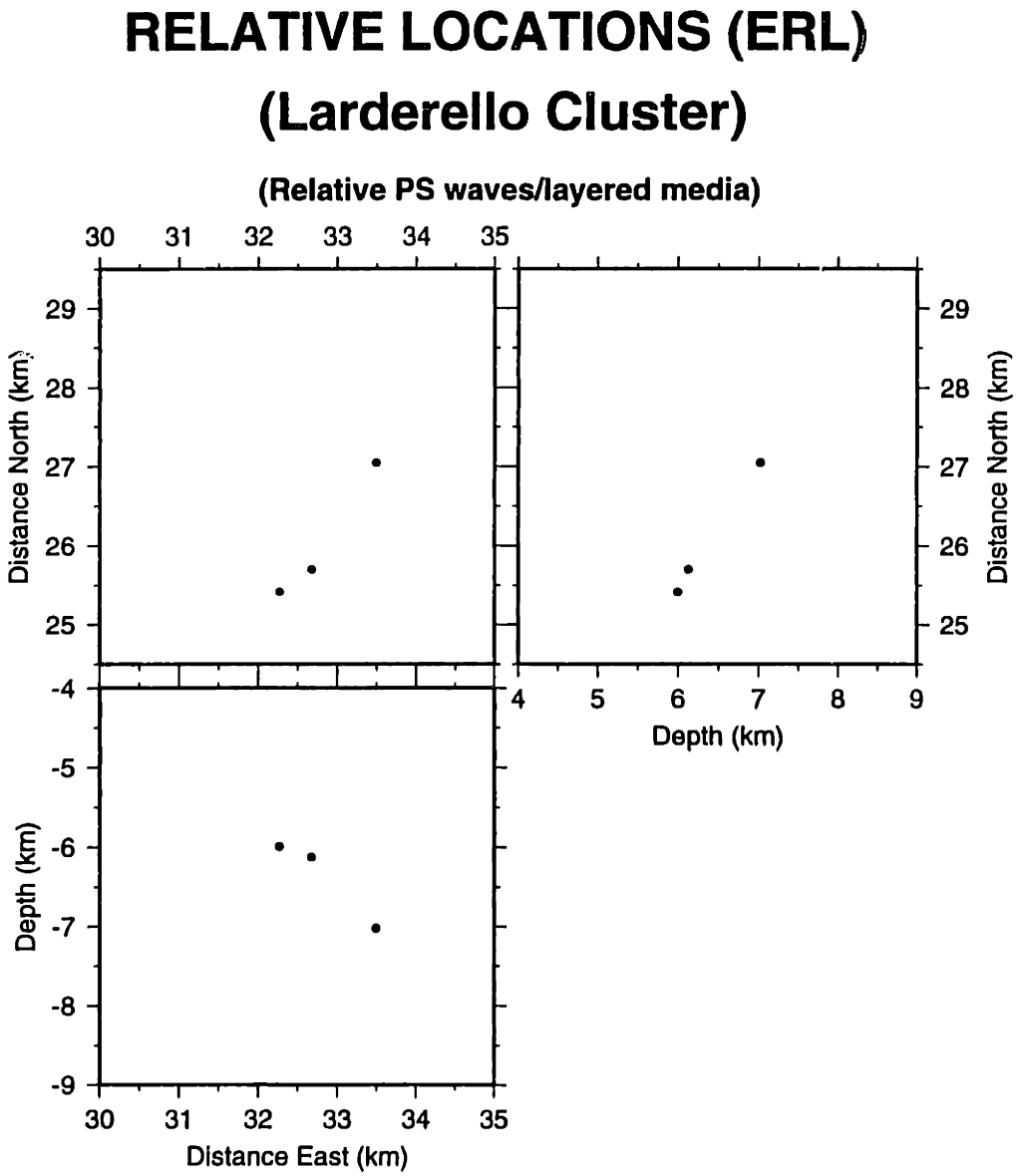

Figure D-94: Larderello 1993 Cluster Frame 02

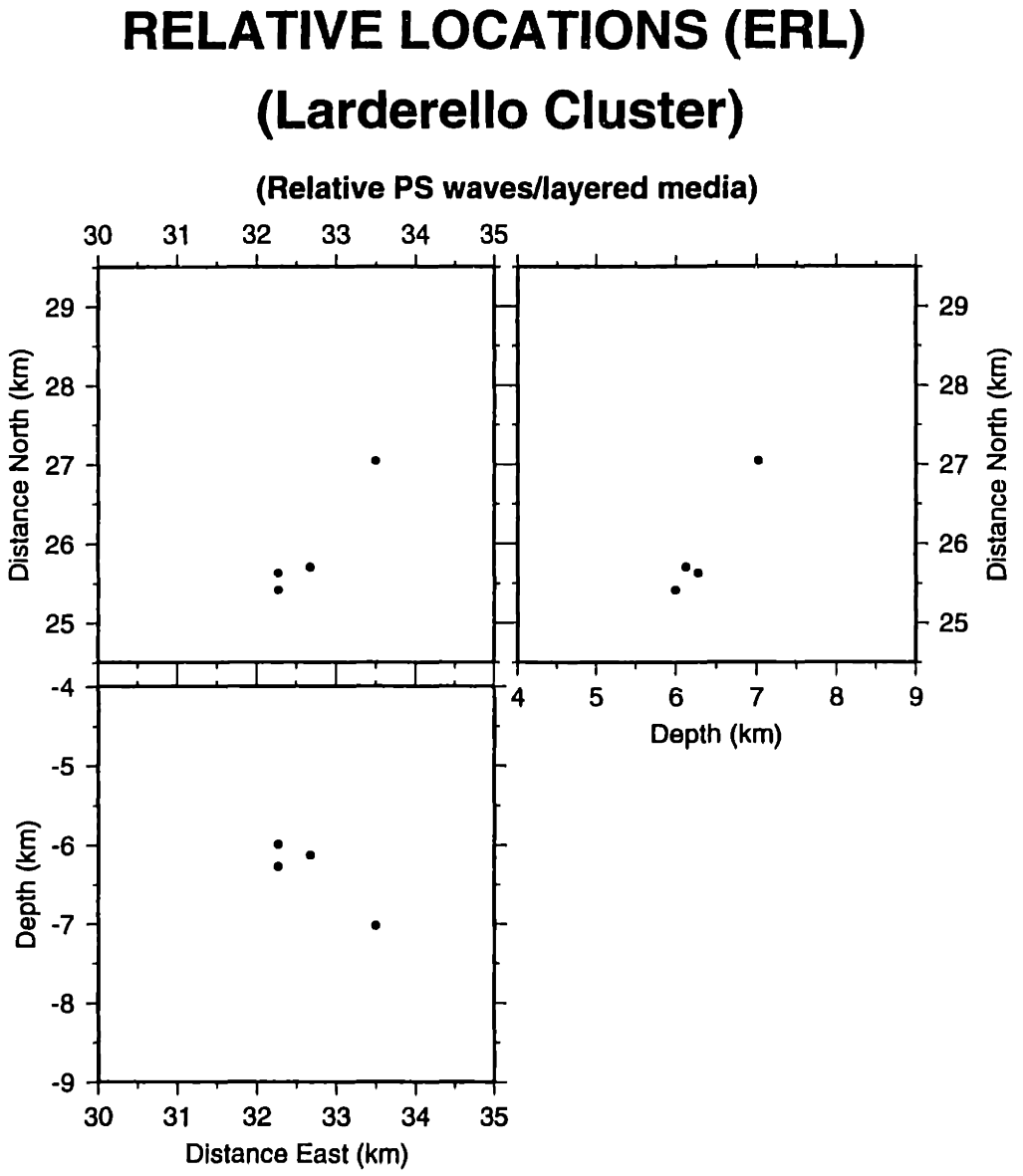

Figure D-95: Larderello 1993 Cluster Frame 03

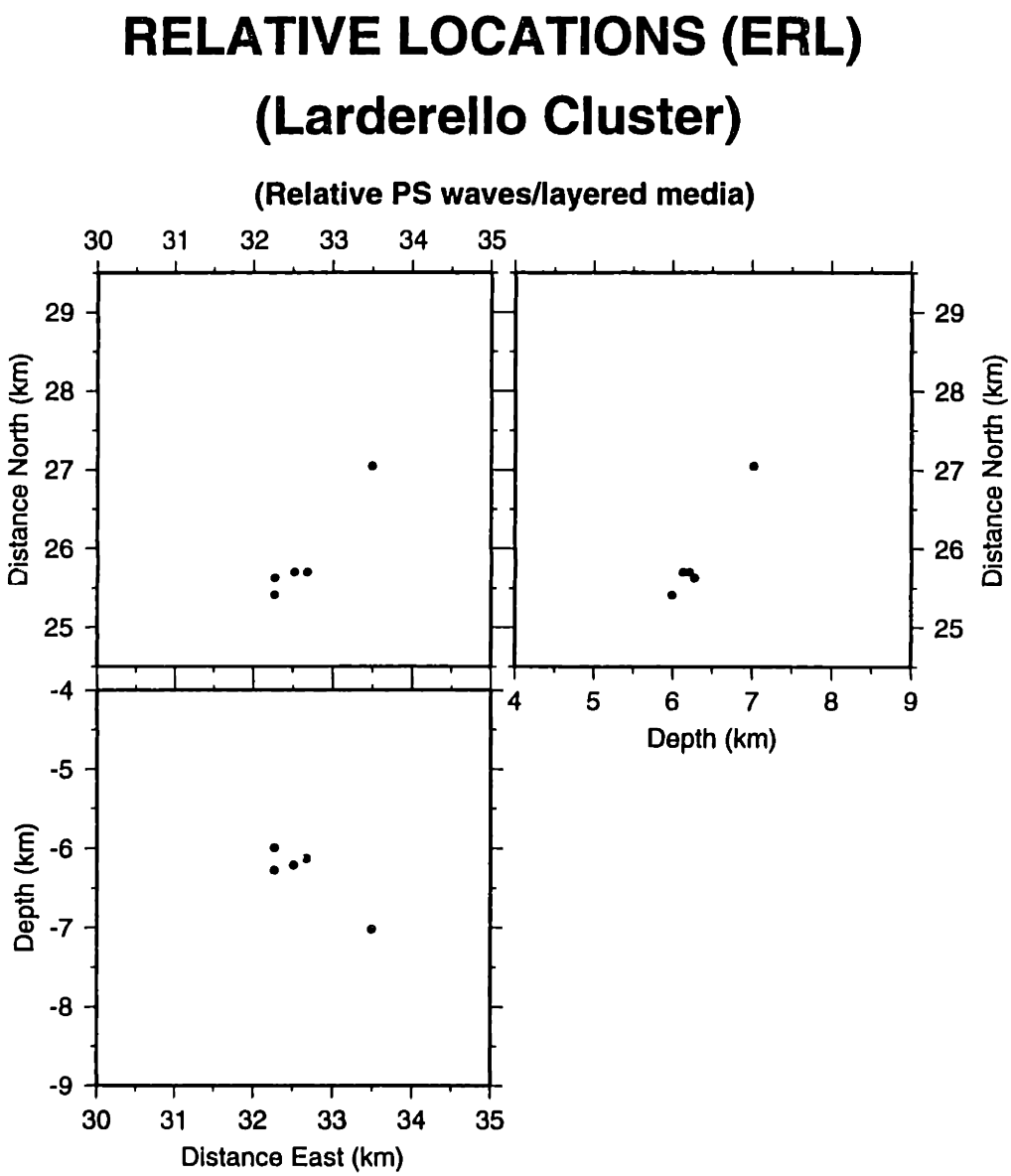

Figure D-96: Larderello 1993 Cluster Frame 04

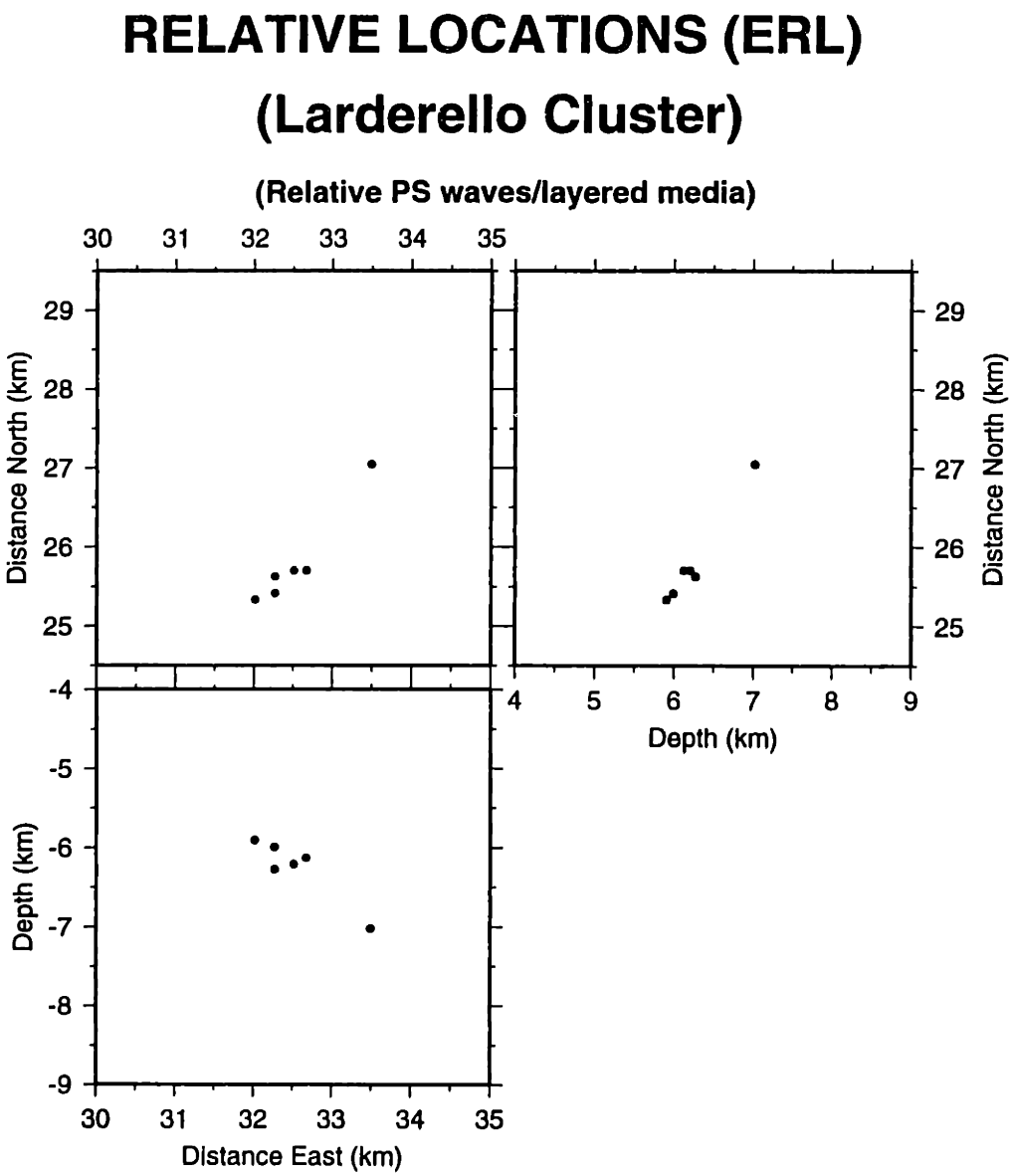

Figure D-97: Larderello 1993 Cluster Frame 05

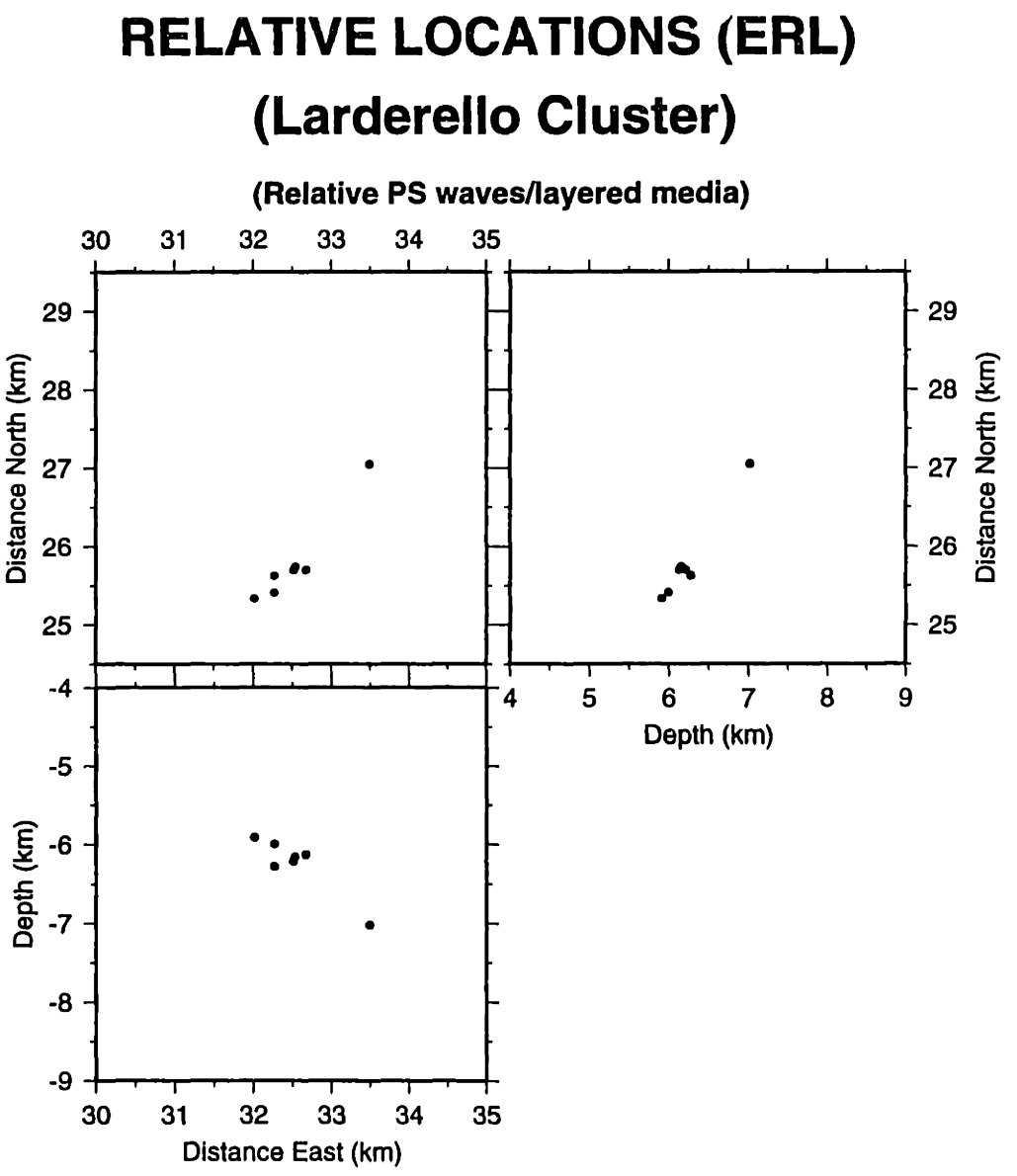

Figure D-98: Larderello 1993 Cluster Frame 06

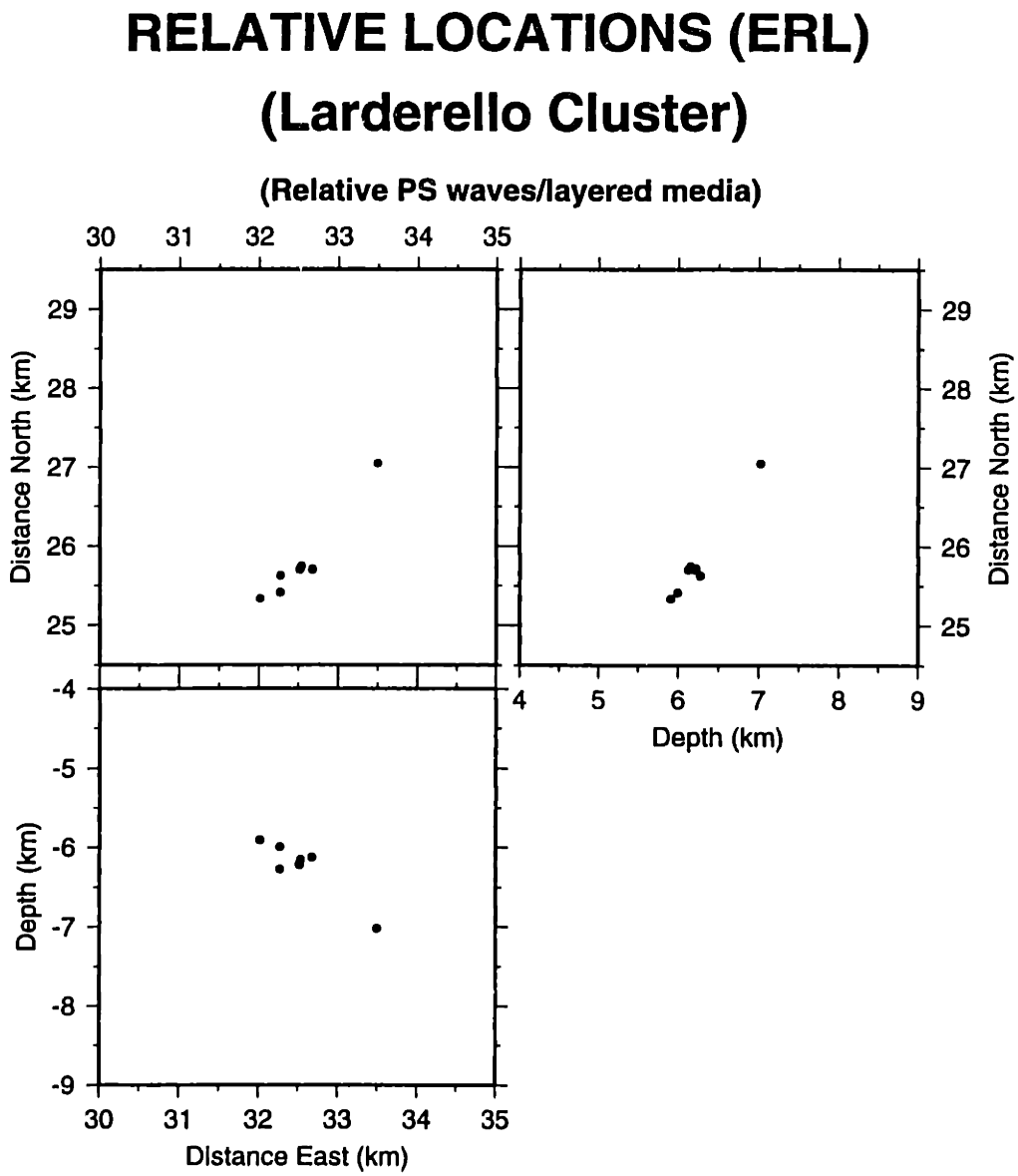

Figure D-99: Larderello 1993 Cluster Frame 07

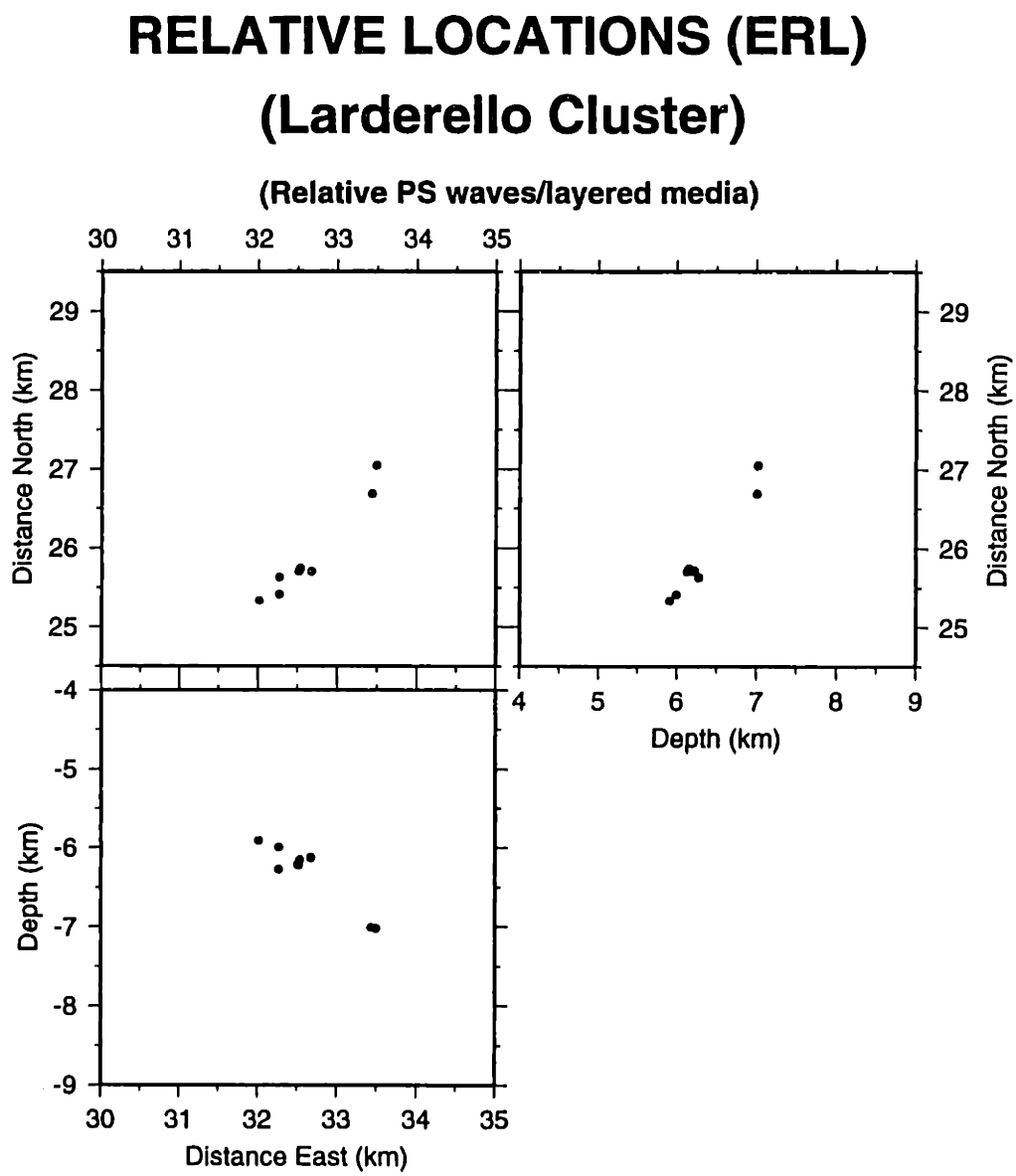

Figure D-100: Larderello 1993 Cluster Frame 08

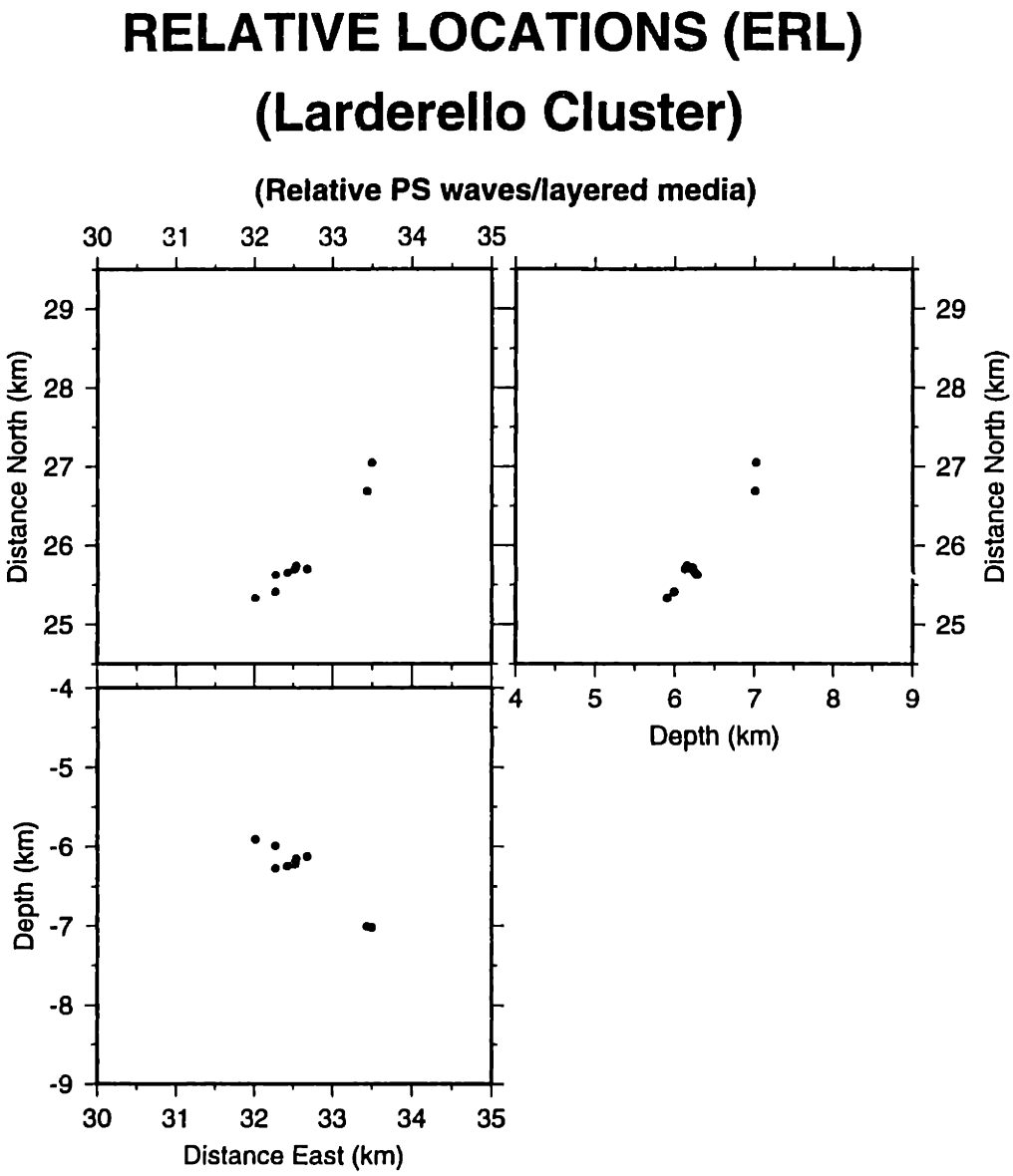

Figure D-101: Larderello 1993 Cluster Frame 09

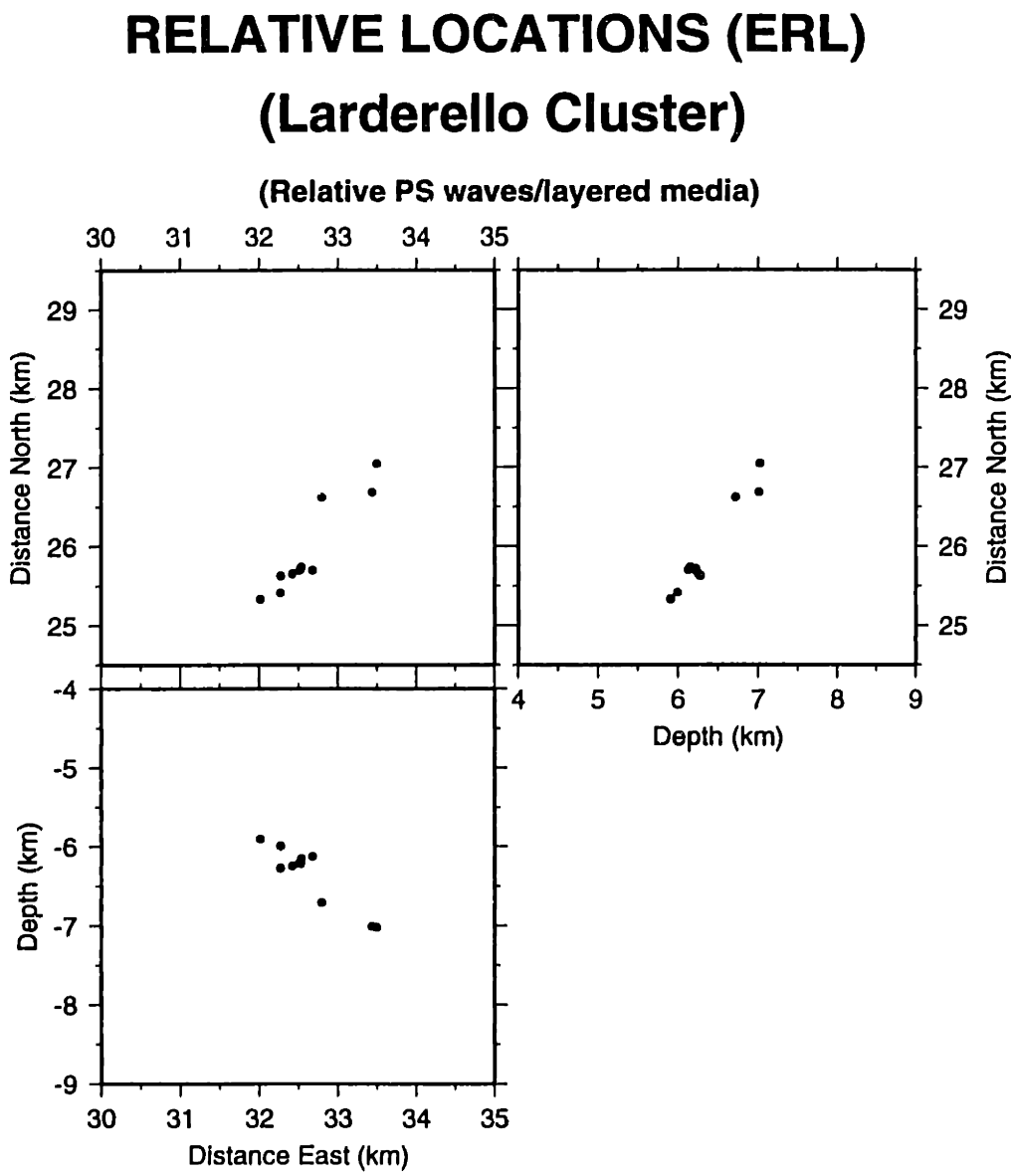

Figure D-102: Larderello 1993 Cluster Frame 10

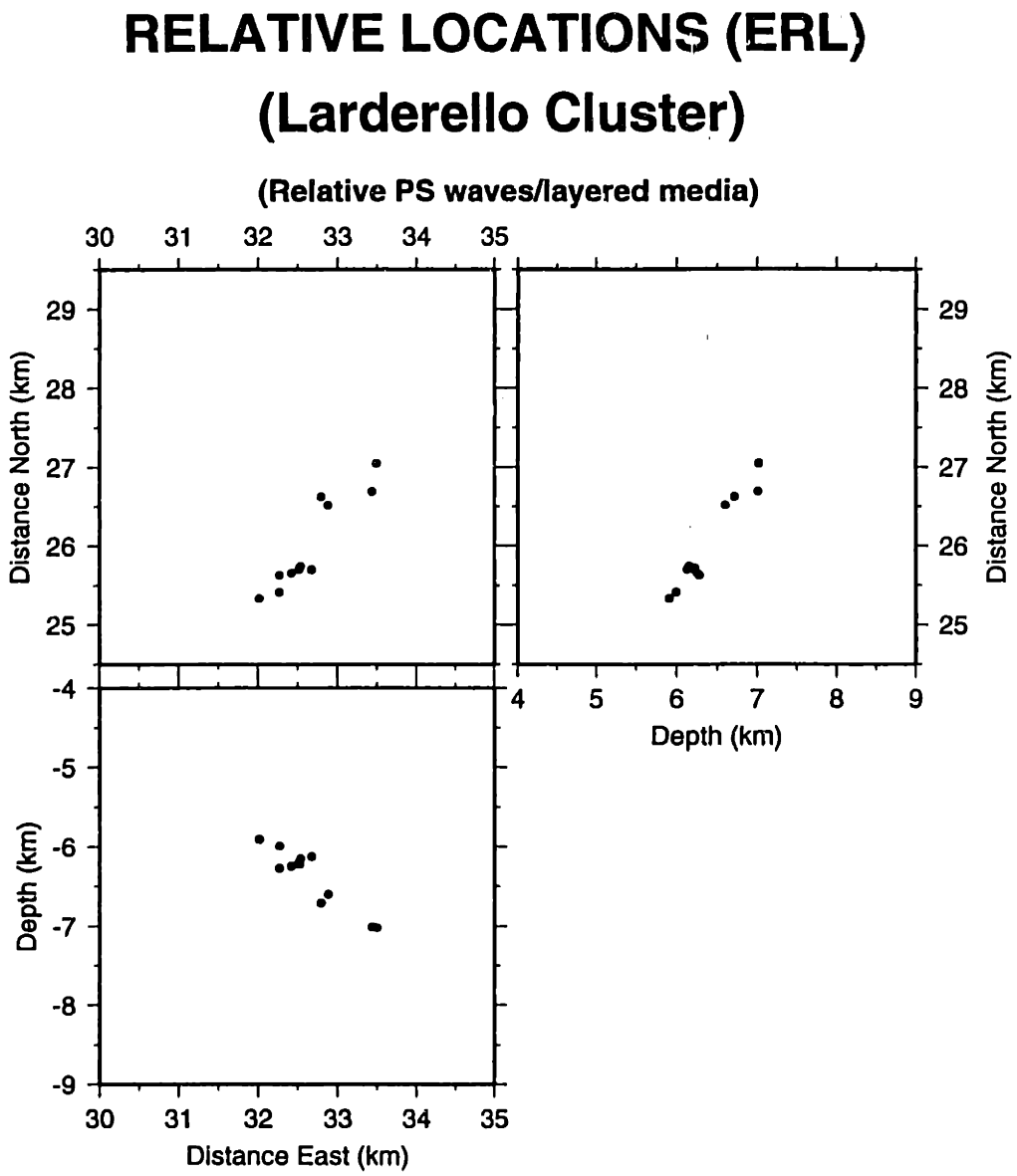

Figure D-103: Larderello 1993 Cluster Frame 11

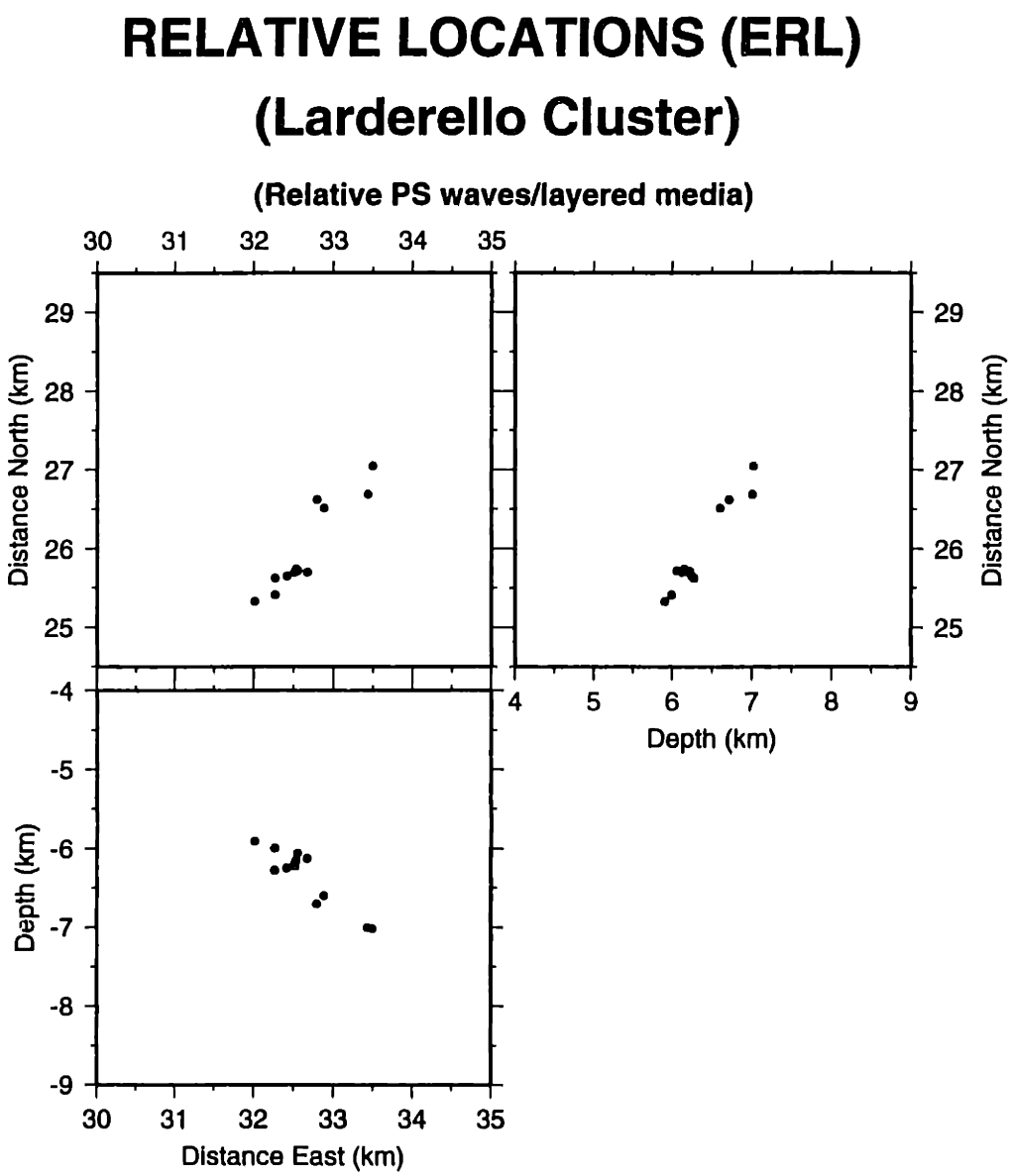

Figure D-104: Larderello 1993 Cluster Frame 12

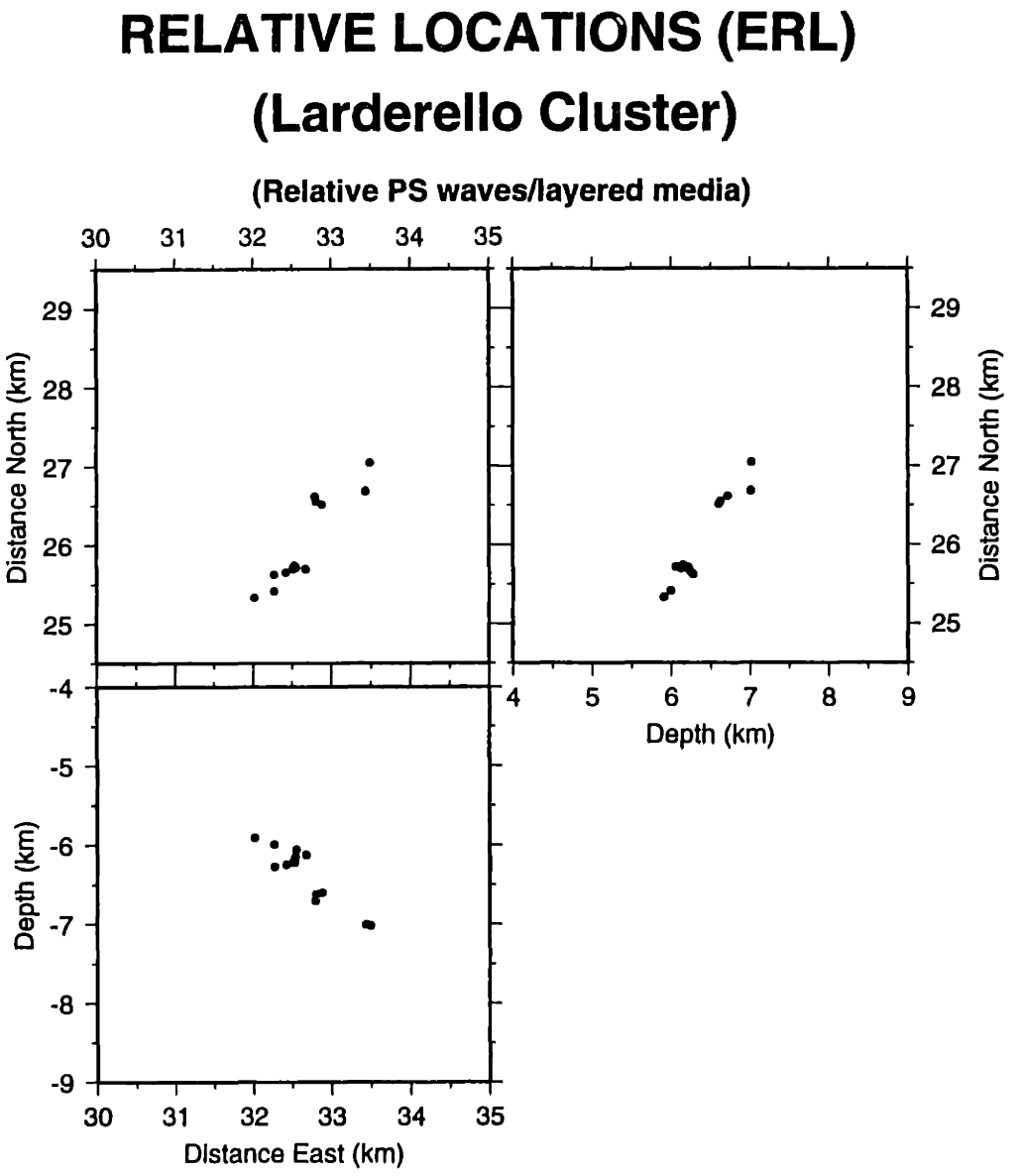

Figure D-105: Larderello 1993 Cluster Frame 13

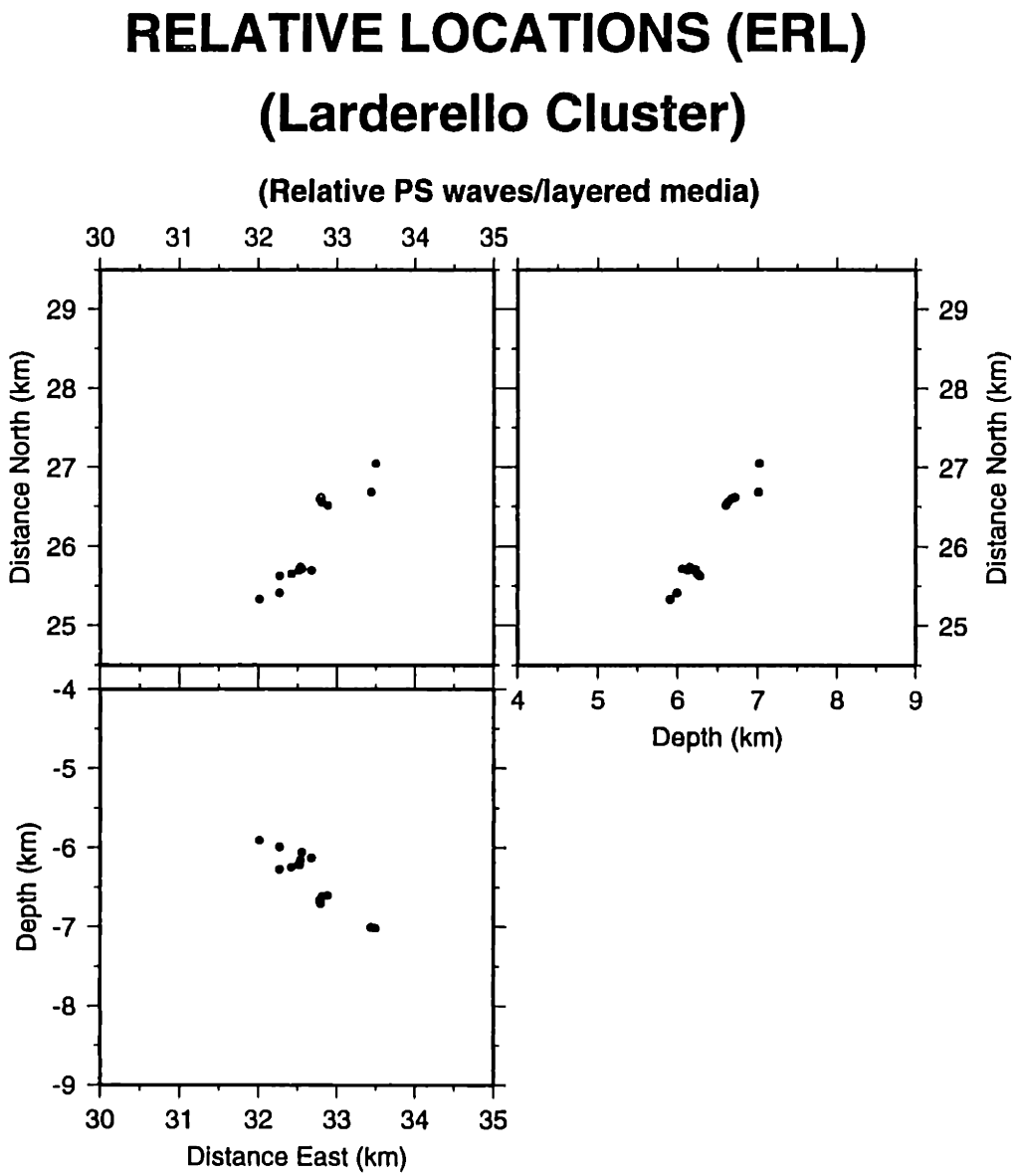

Figure D-106: Larderello 1993 Cluster Frame 14

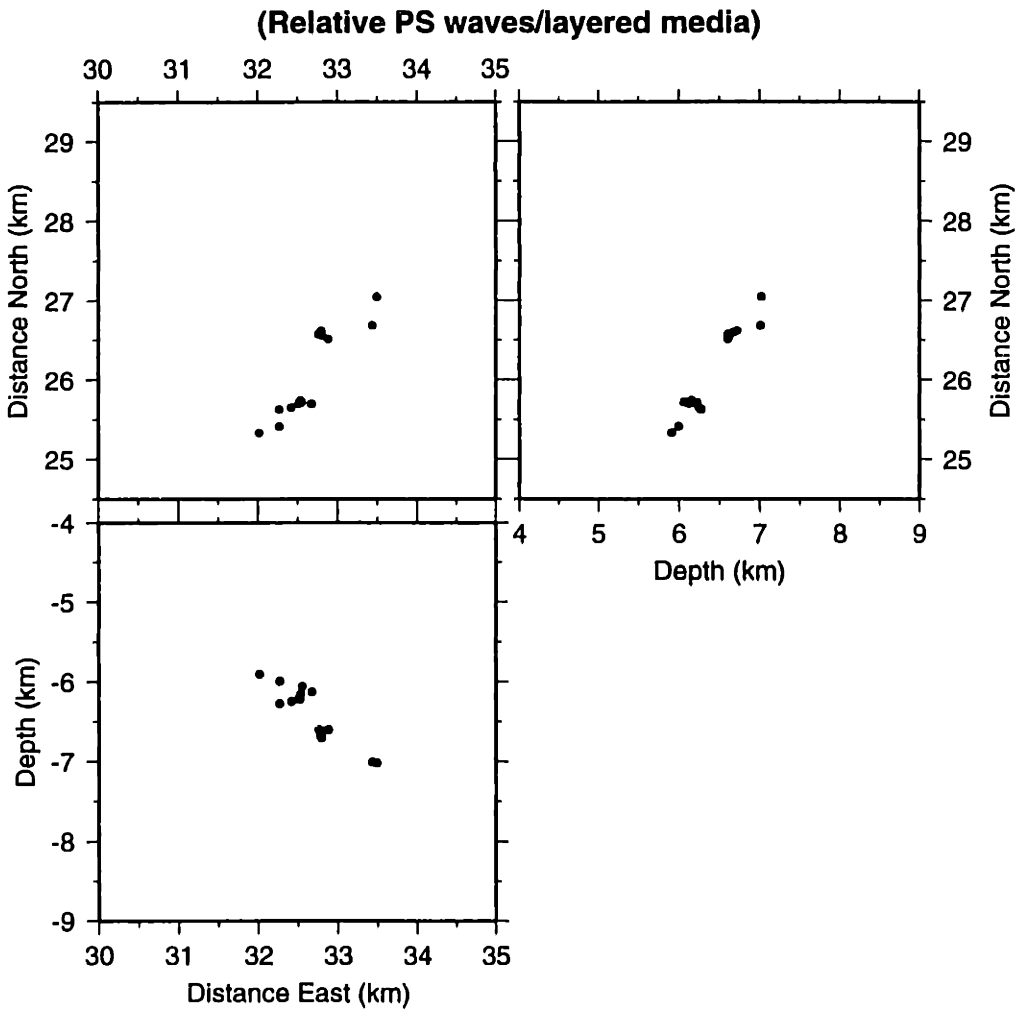

Figure D-107: Larderello 1993 Cluster Frame 15

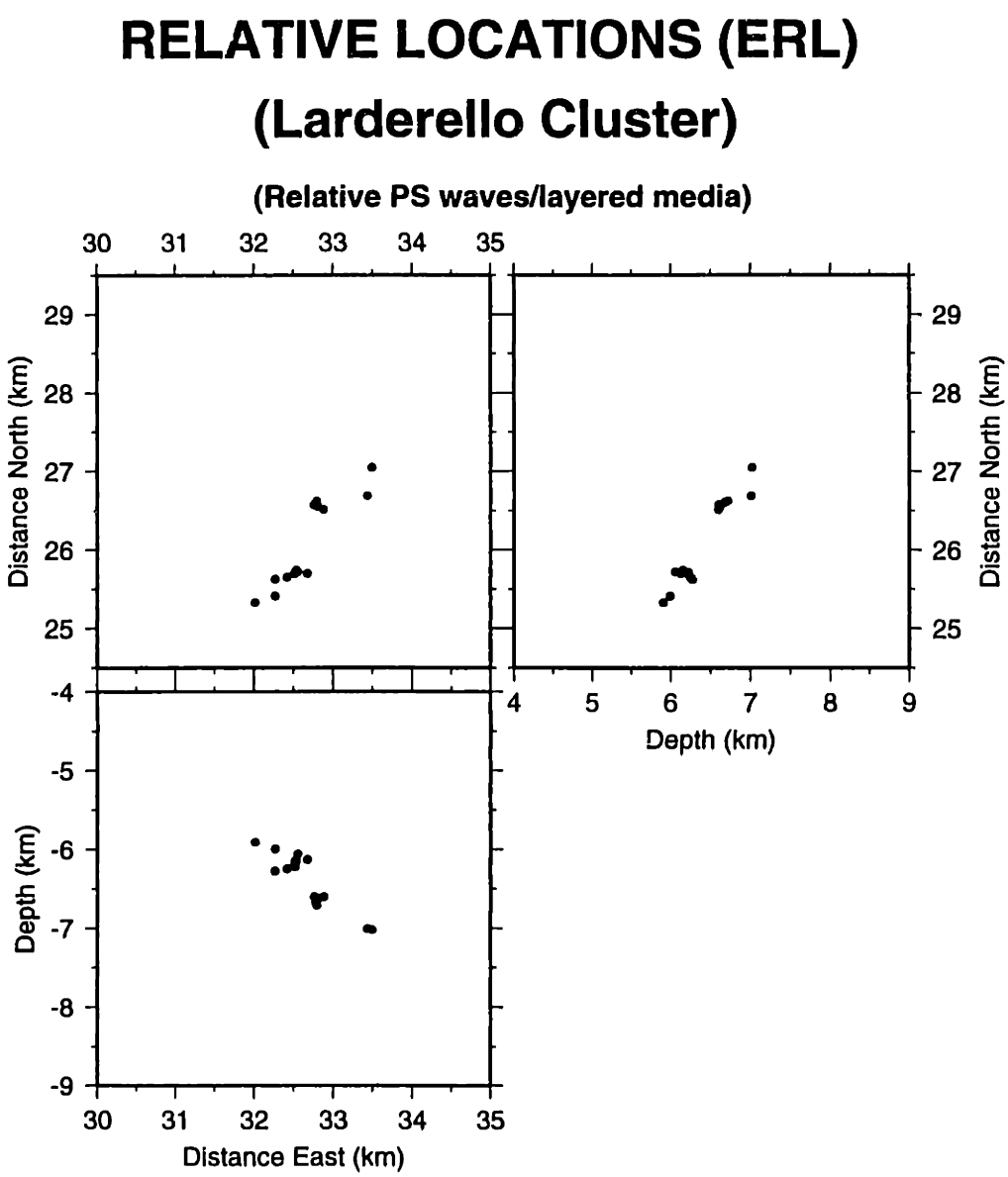

Figure D-108: Larderello 1993 Cluster Frame 16

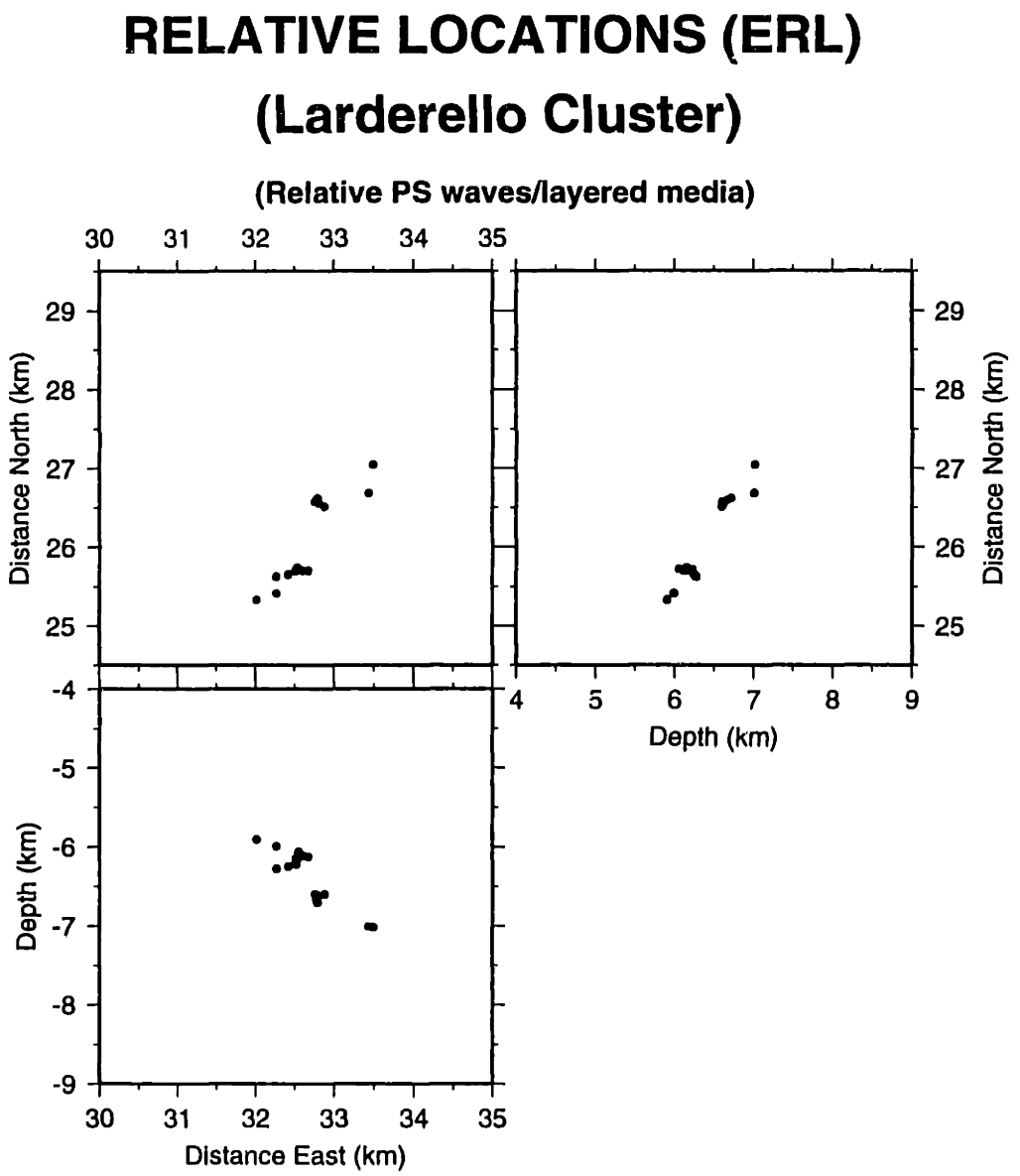

Figure D-109: Larderello 1993 Cluster Frame 17

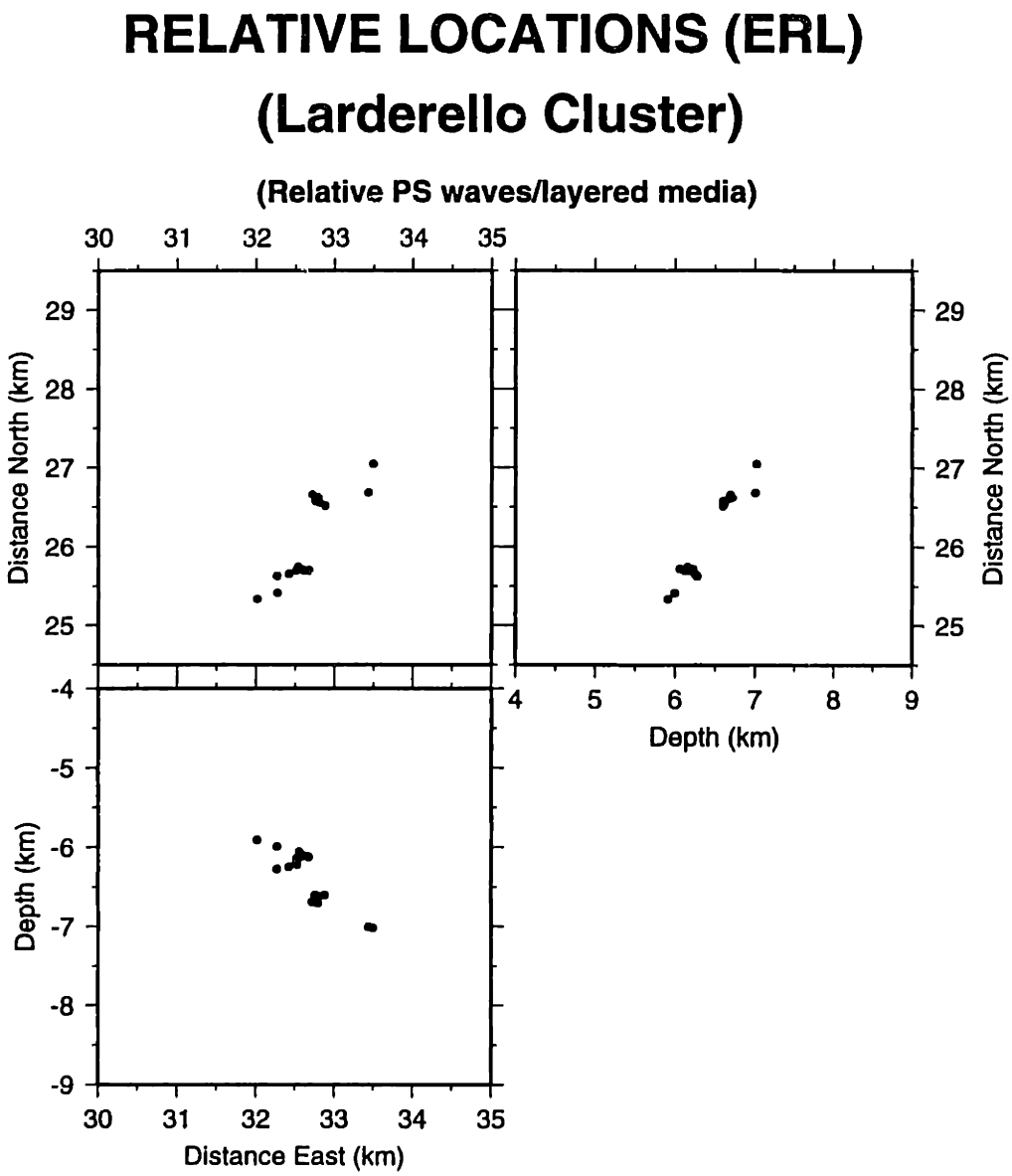

Figure D-110: Larderello 1993 Cluster Frame 18

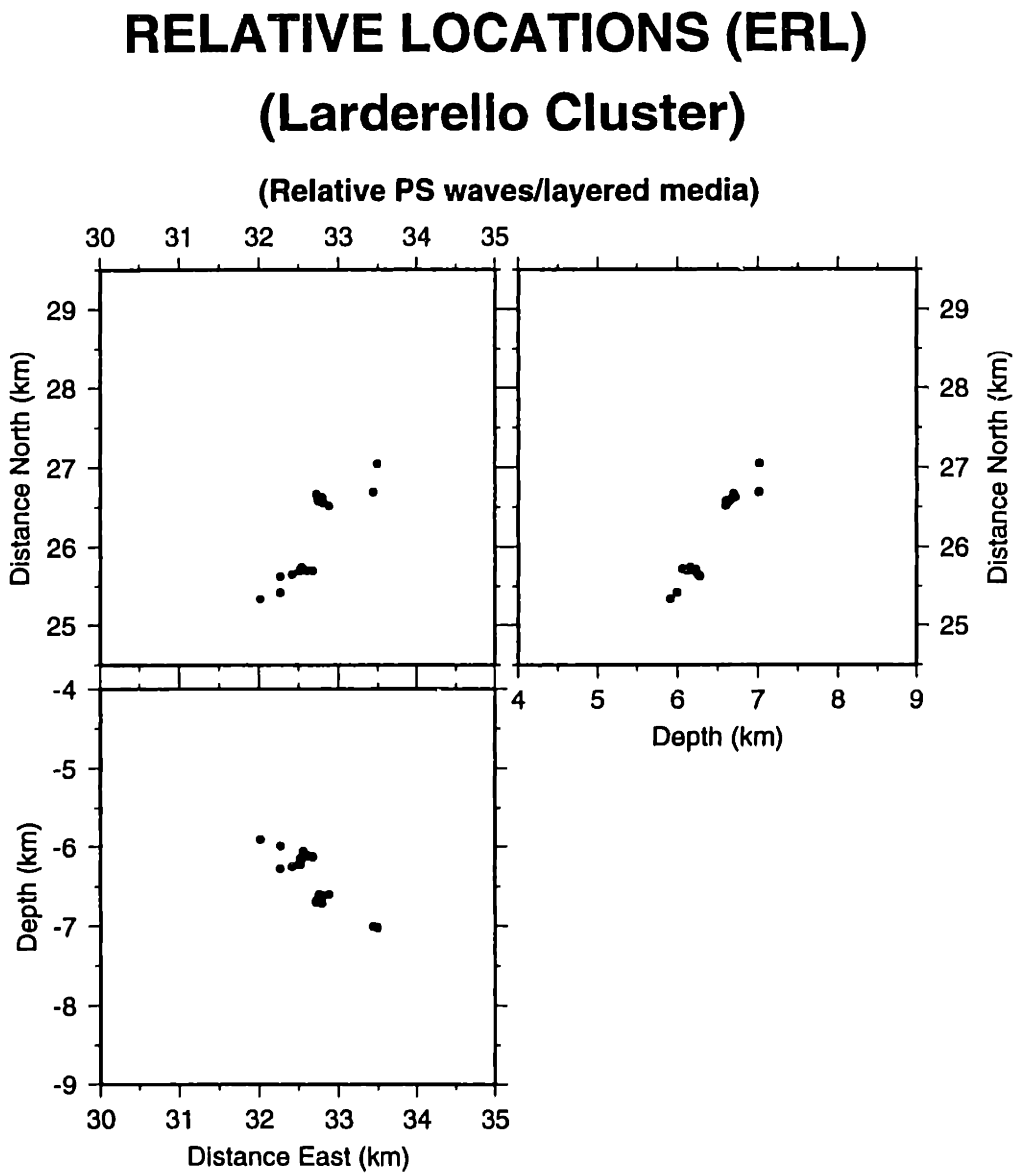

Figure D-111: Larderello 1993 Cluster Frame 19

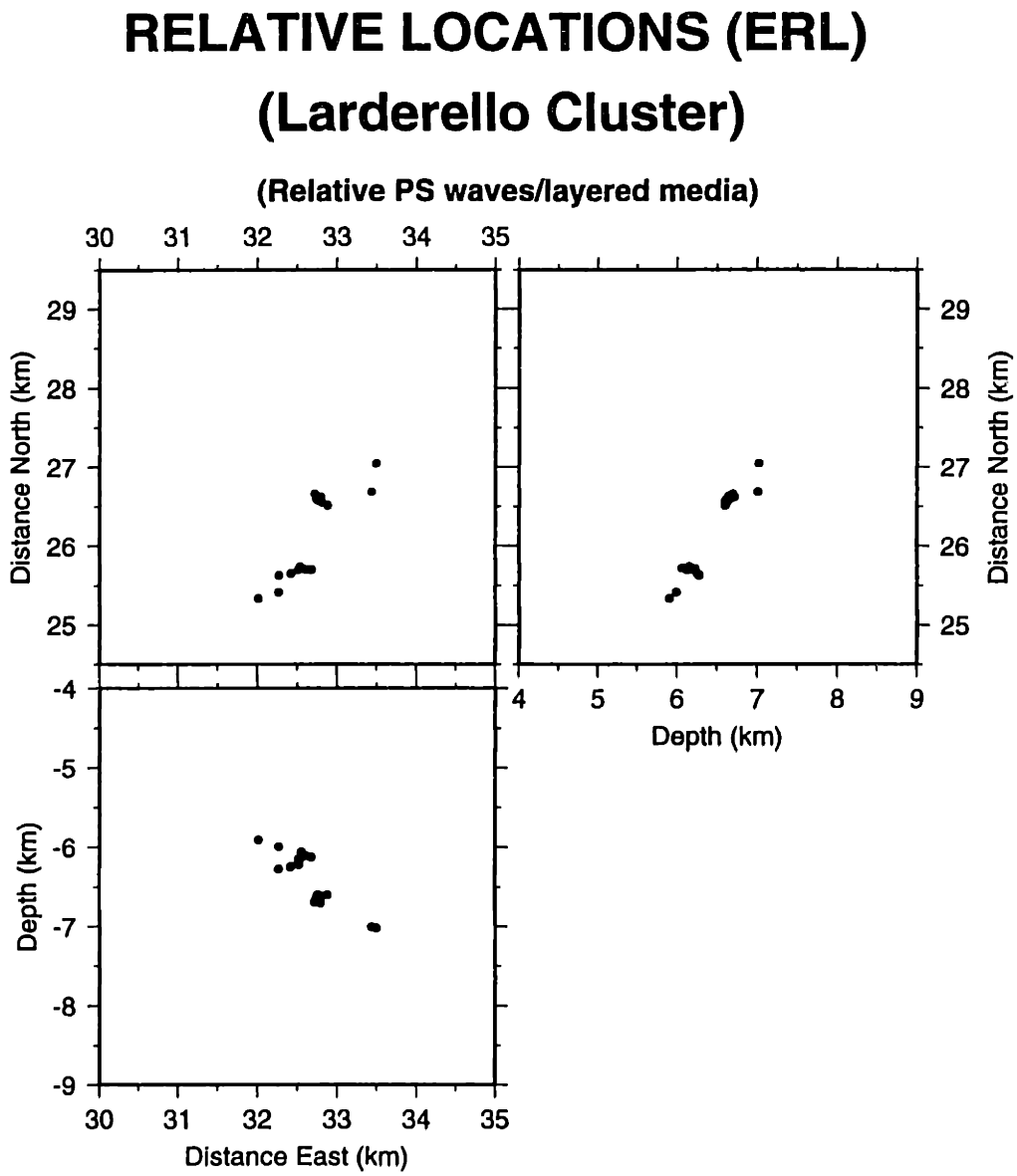

Figure D-112: Larderello 1993 Cluster Frame 20

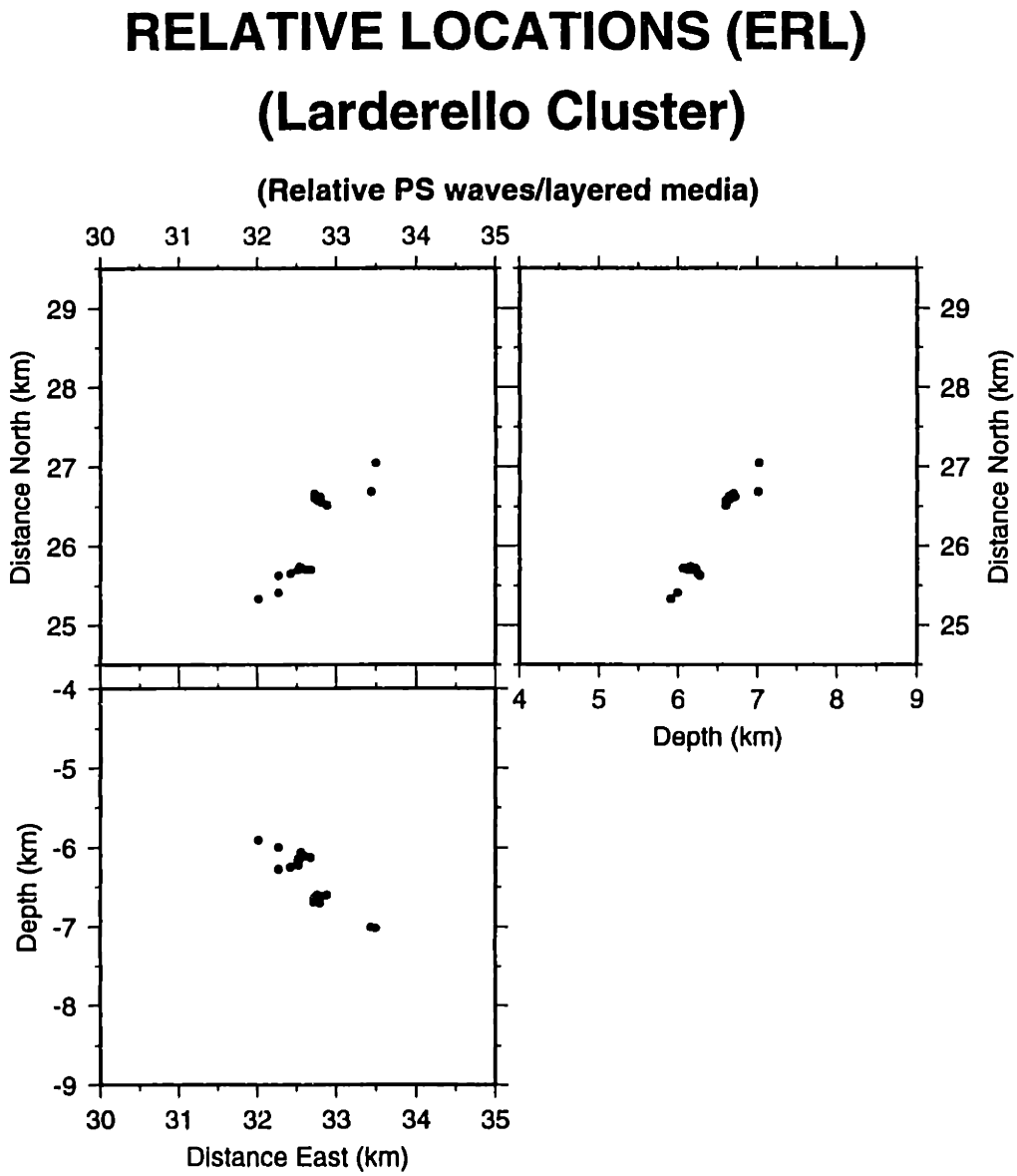

Figure D-113: Larderello 1993 Cluster Frame 21

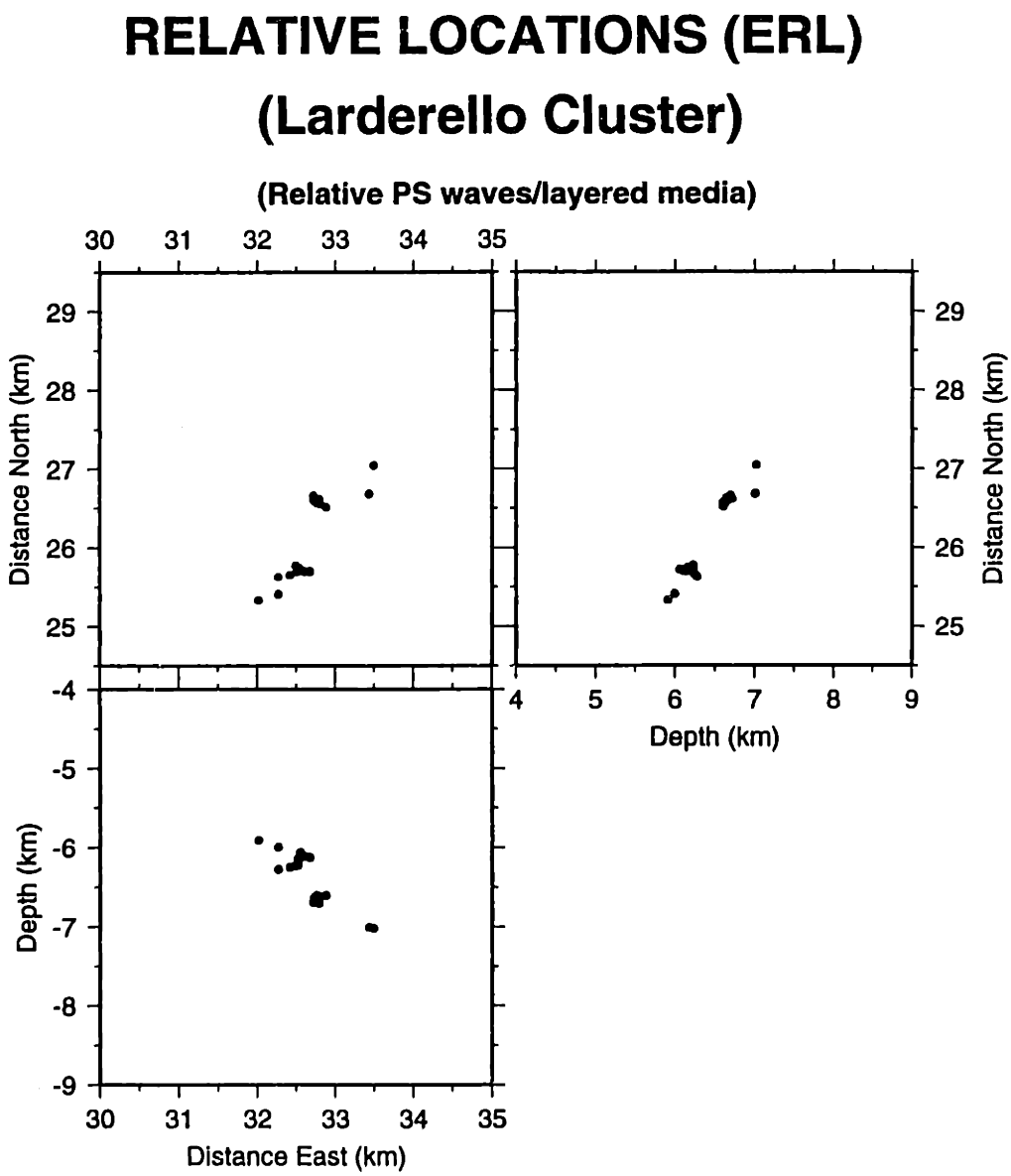

Figure D-114: Larderello 1993 Cluster Frame 22

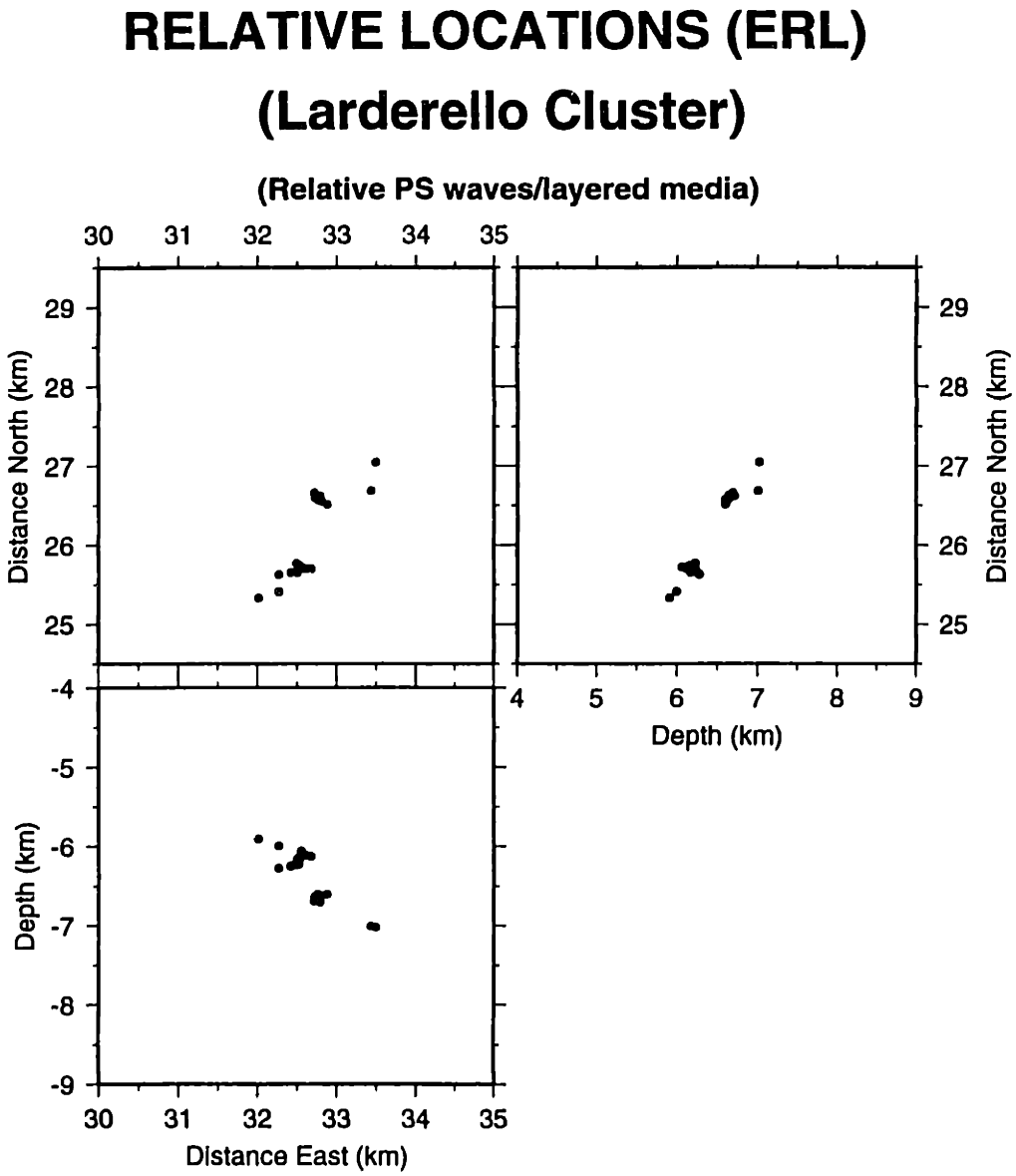

Figure D-115: Larderello 1993 Cluster Frame 23

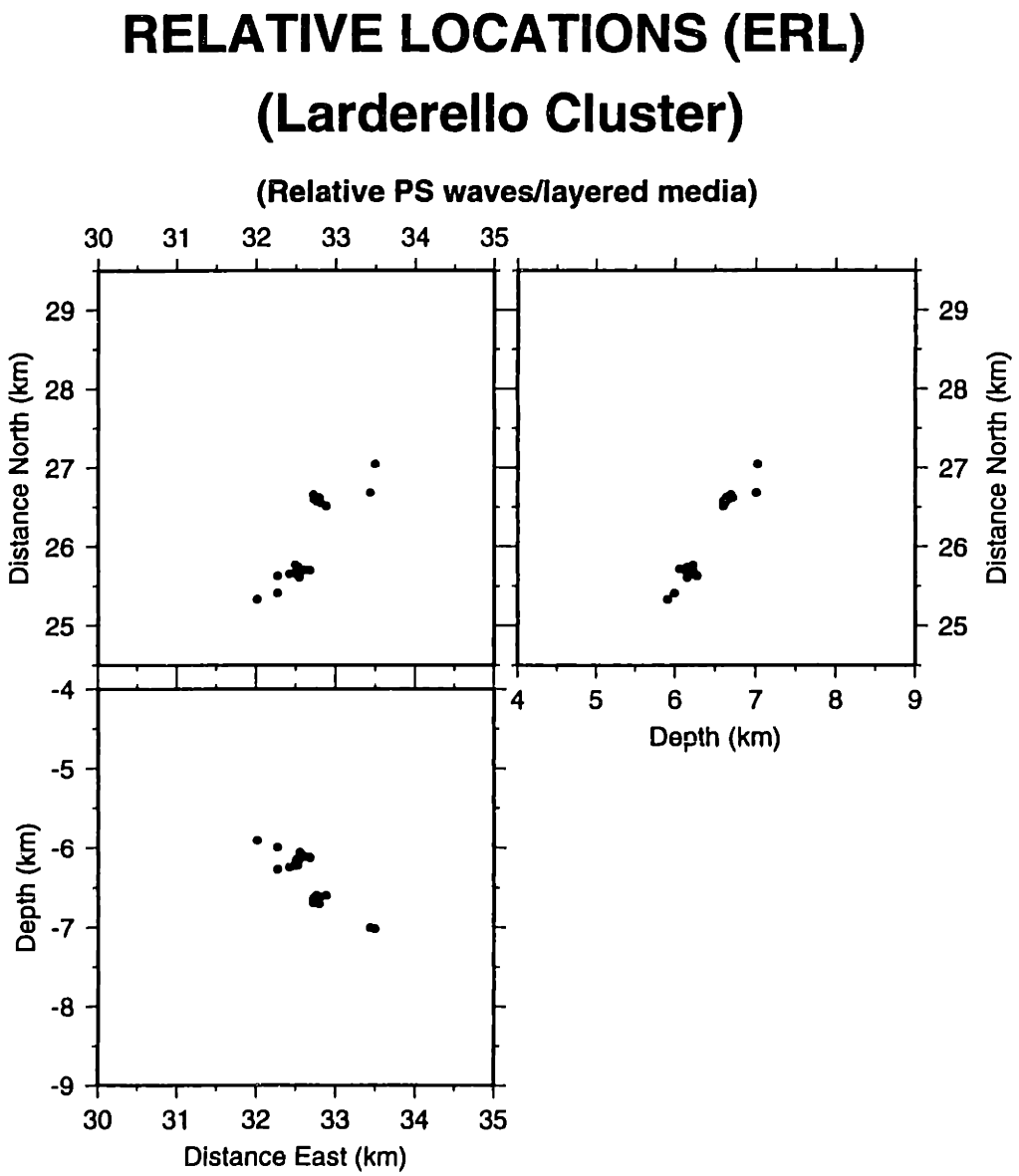

Figure D-116: Larderello 1993 Cluster Frame 24

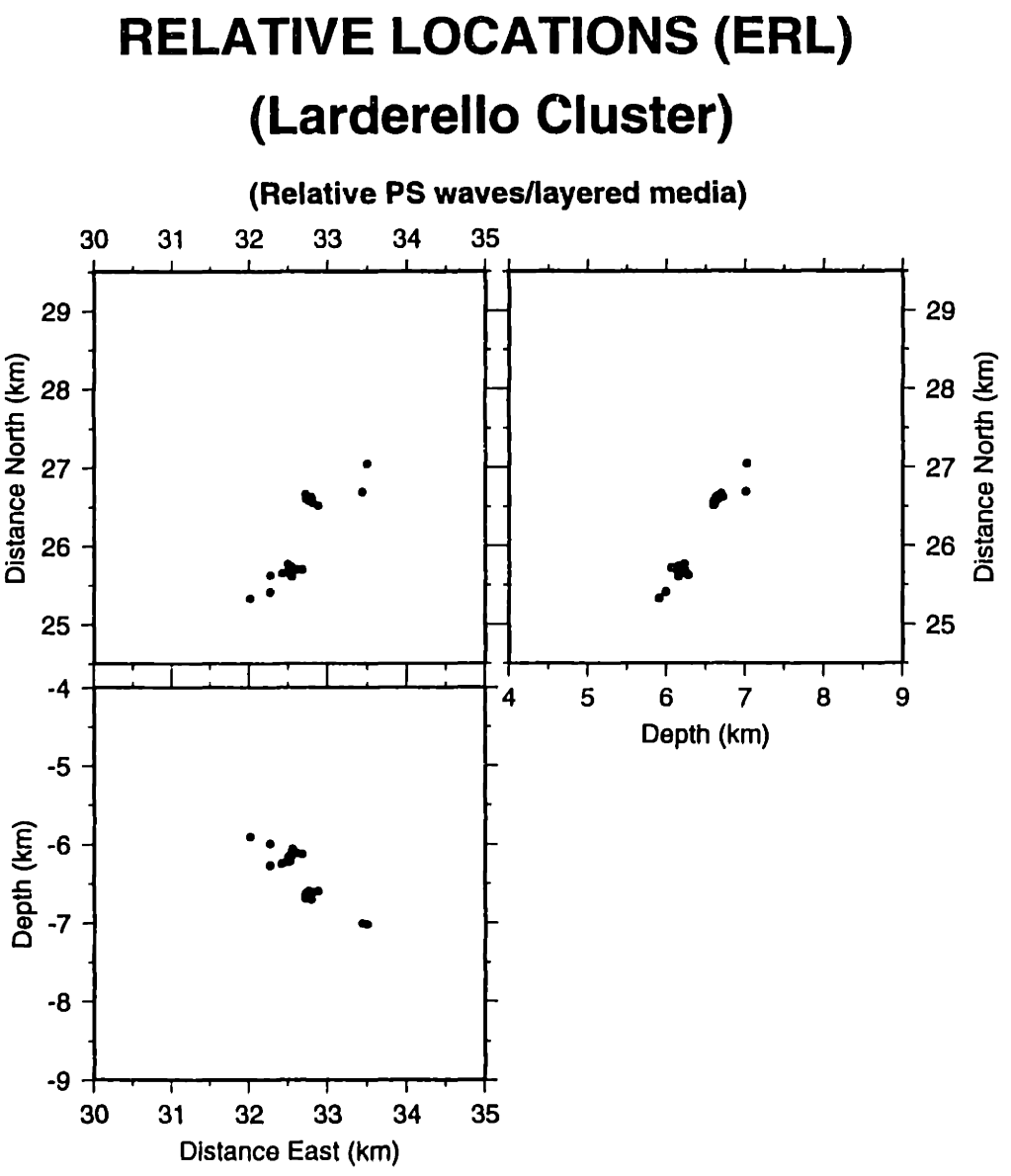

Figure D-117: Larderello 1993 Cluster Frame 25

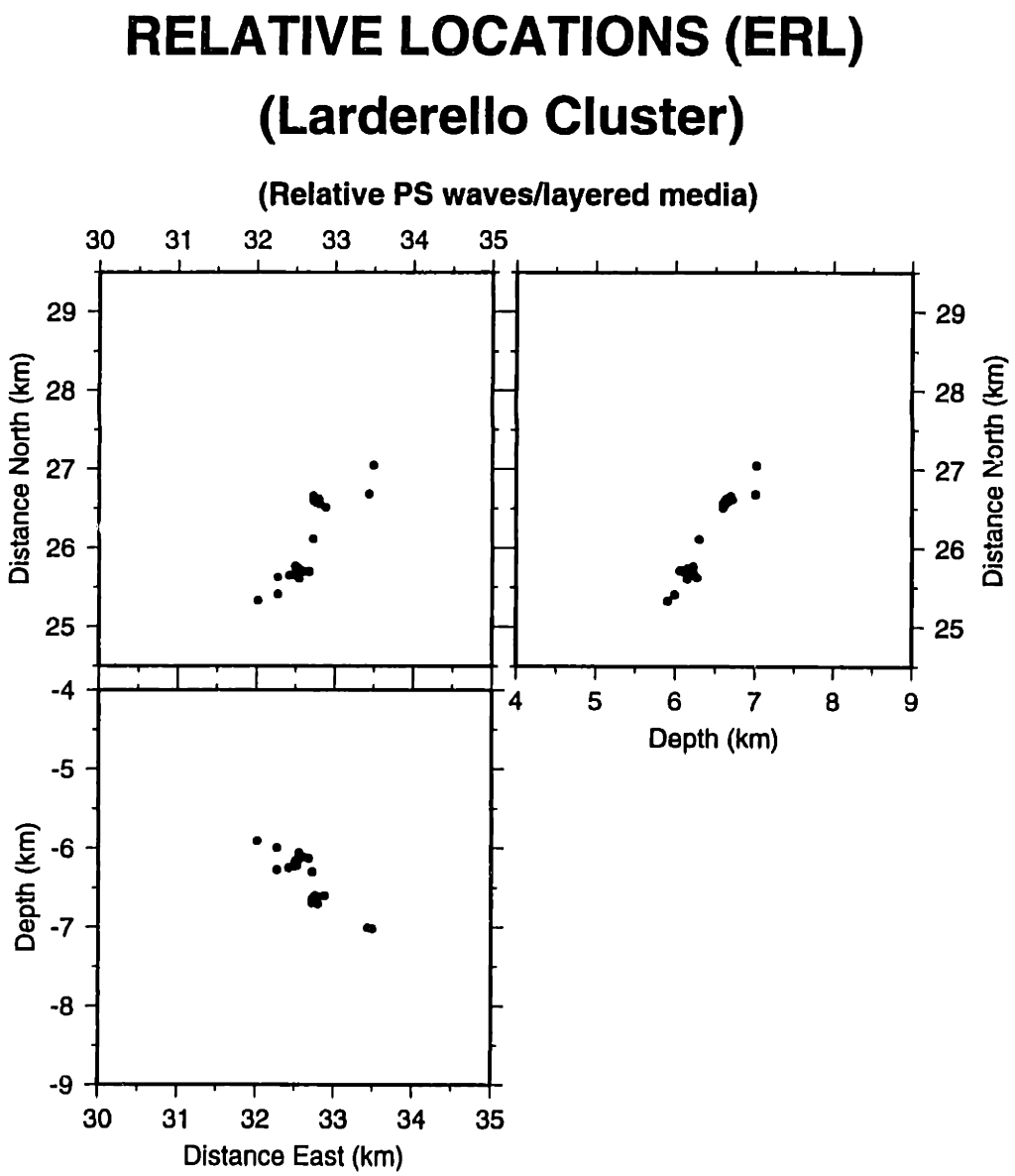

Figure D-118: Larderello 1993 Cluster Frame 26

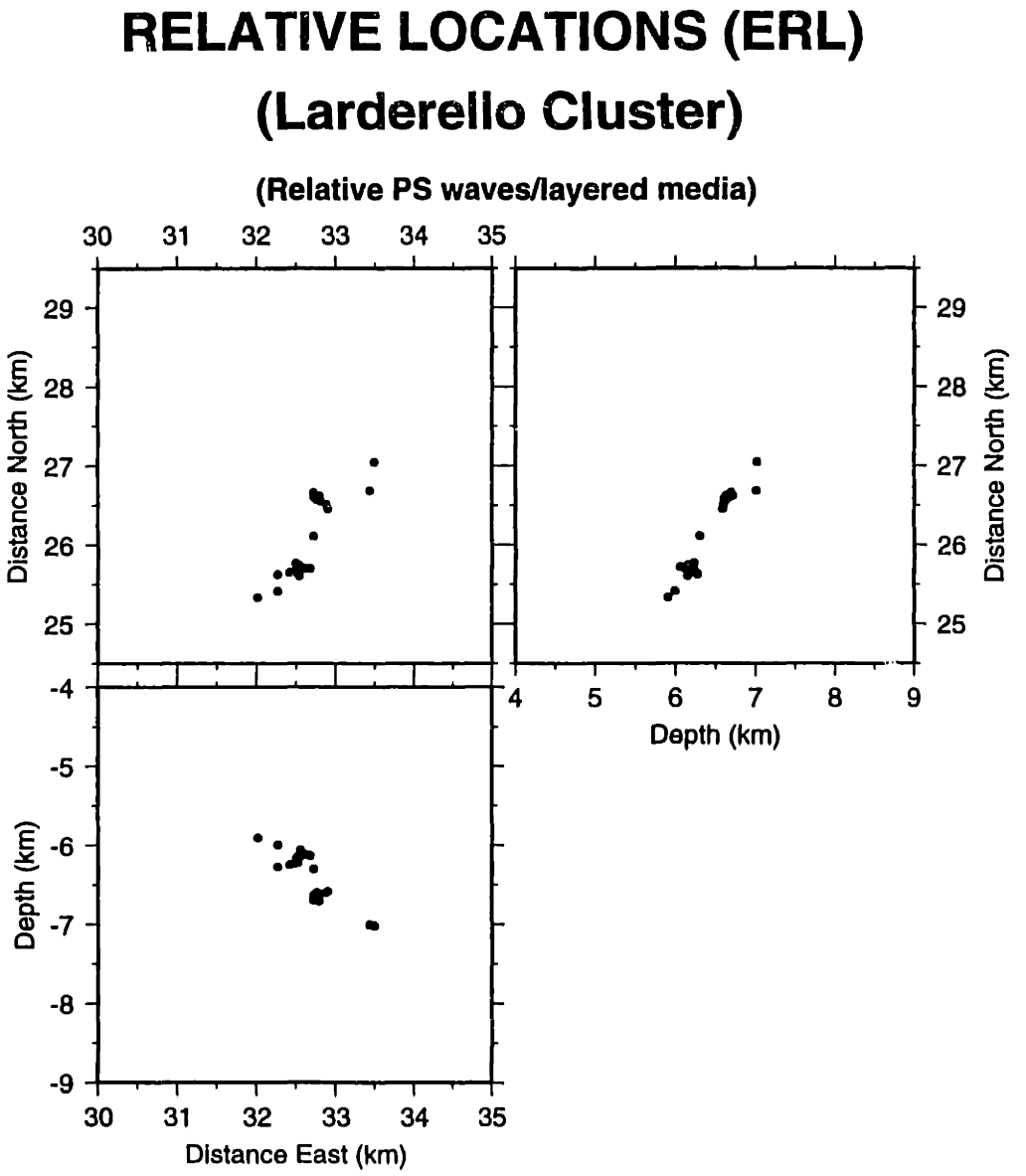

Figure D-119: Larderello 1993 Cluster Frame 27

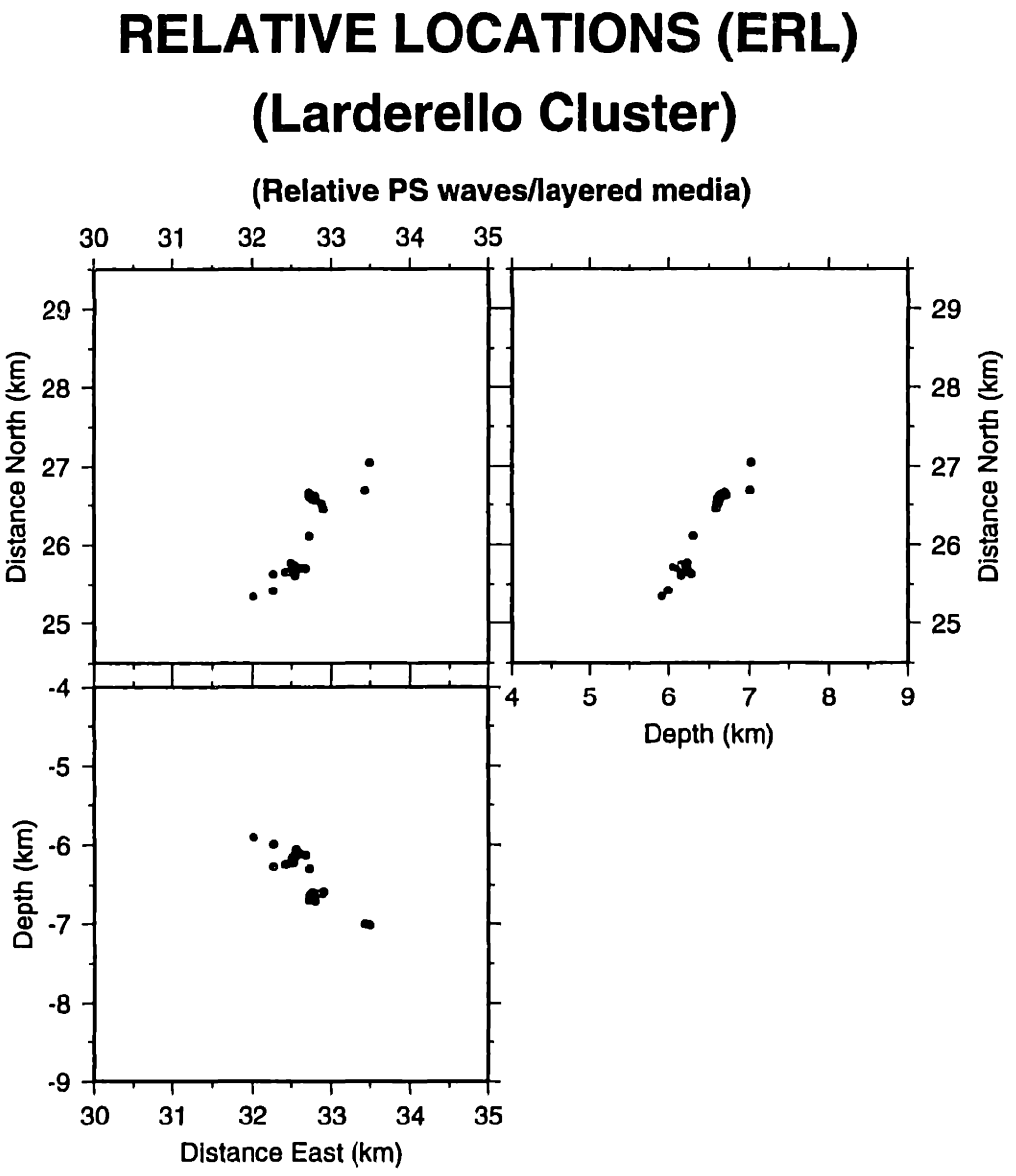

Figure D-120: Larderello 1993 Cluster Frame 28

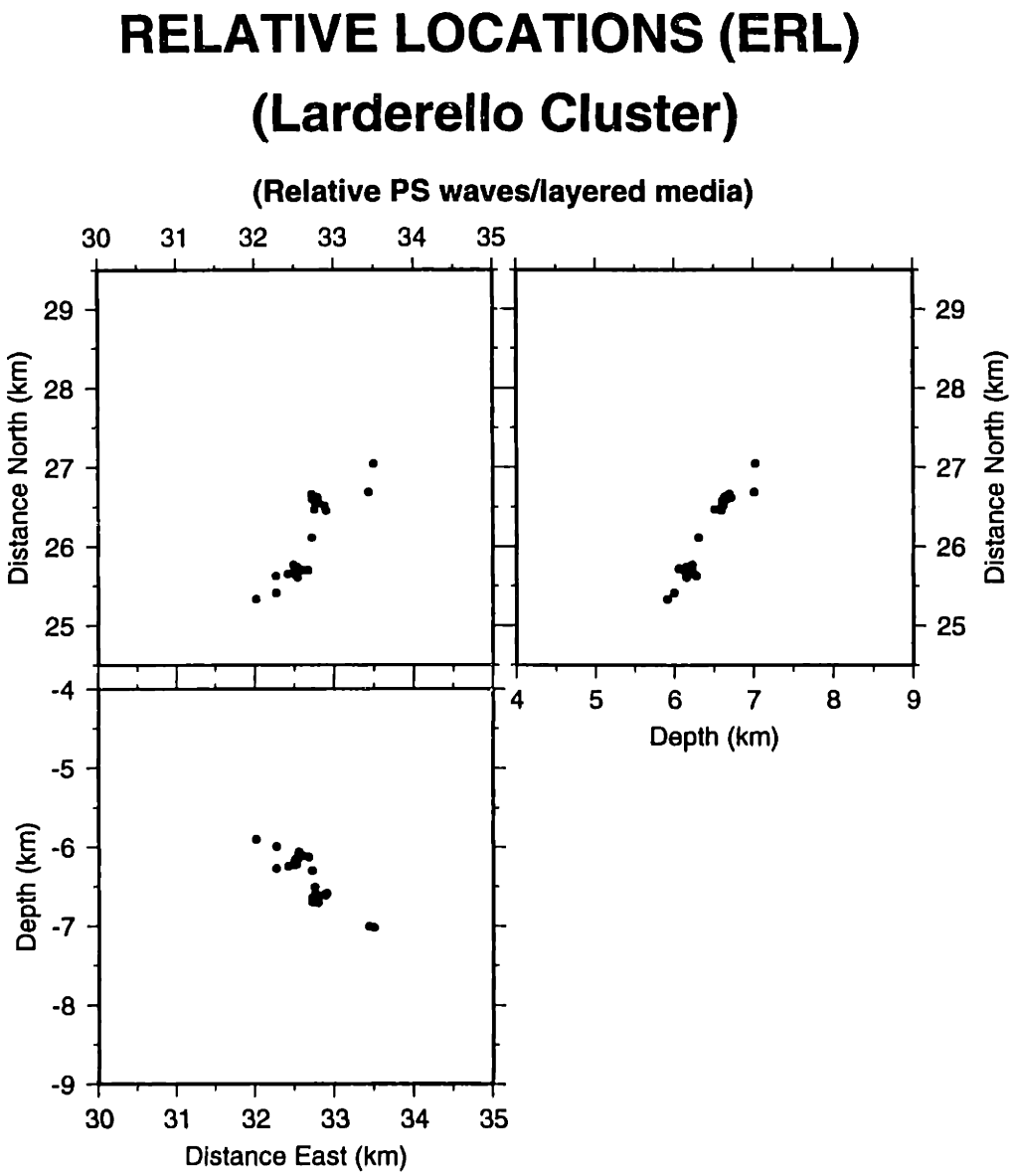

Figure D-121: Larderello 1993 Cluster Frame 29

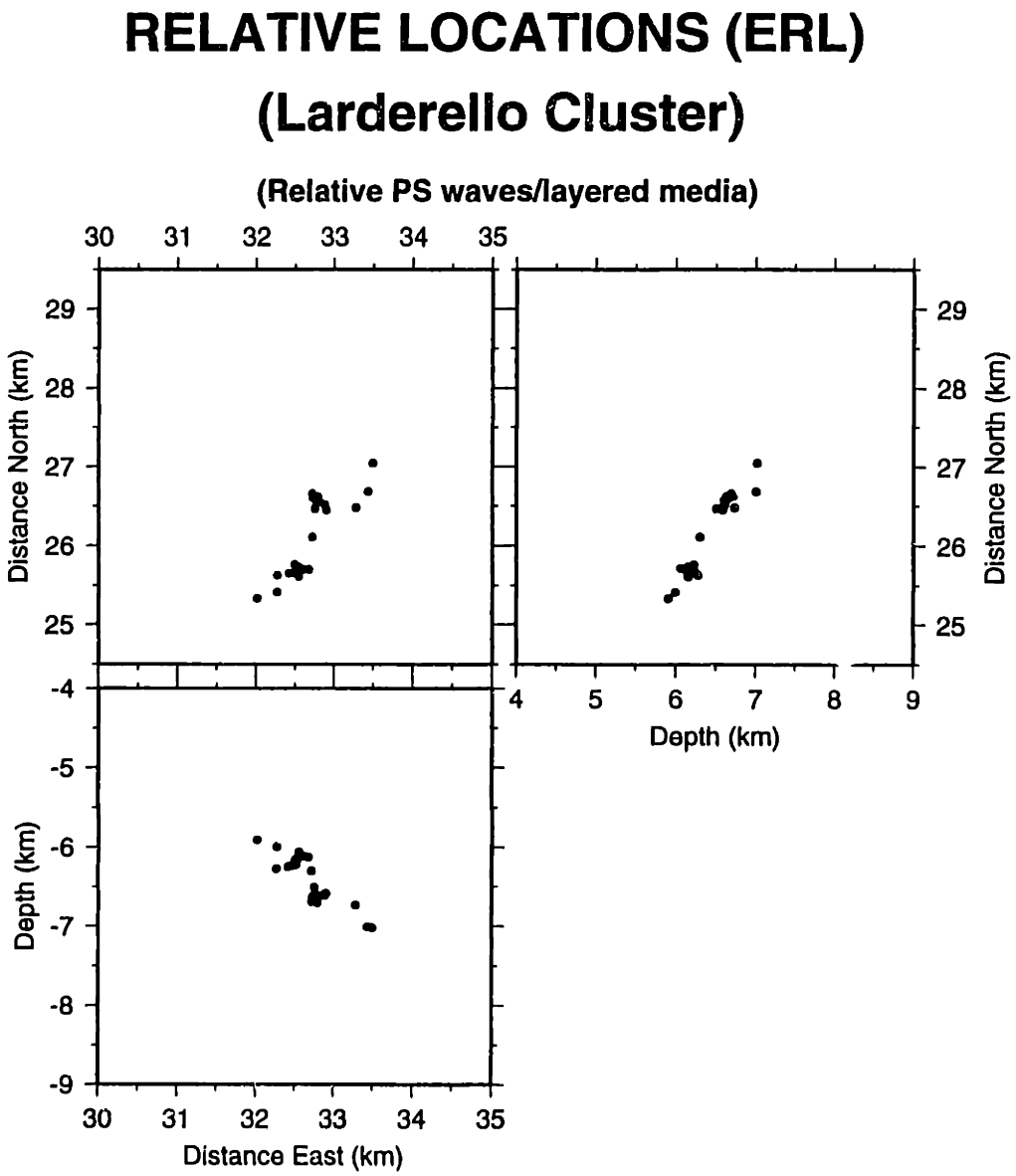

Figure D-122: Larderello 1993 Cluster Frame 30

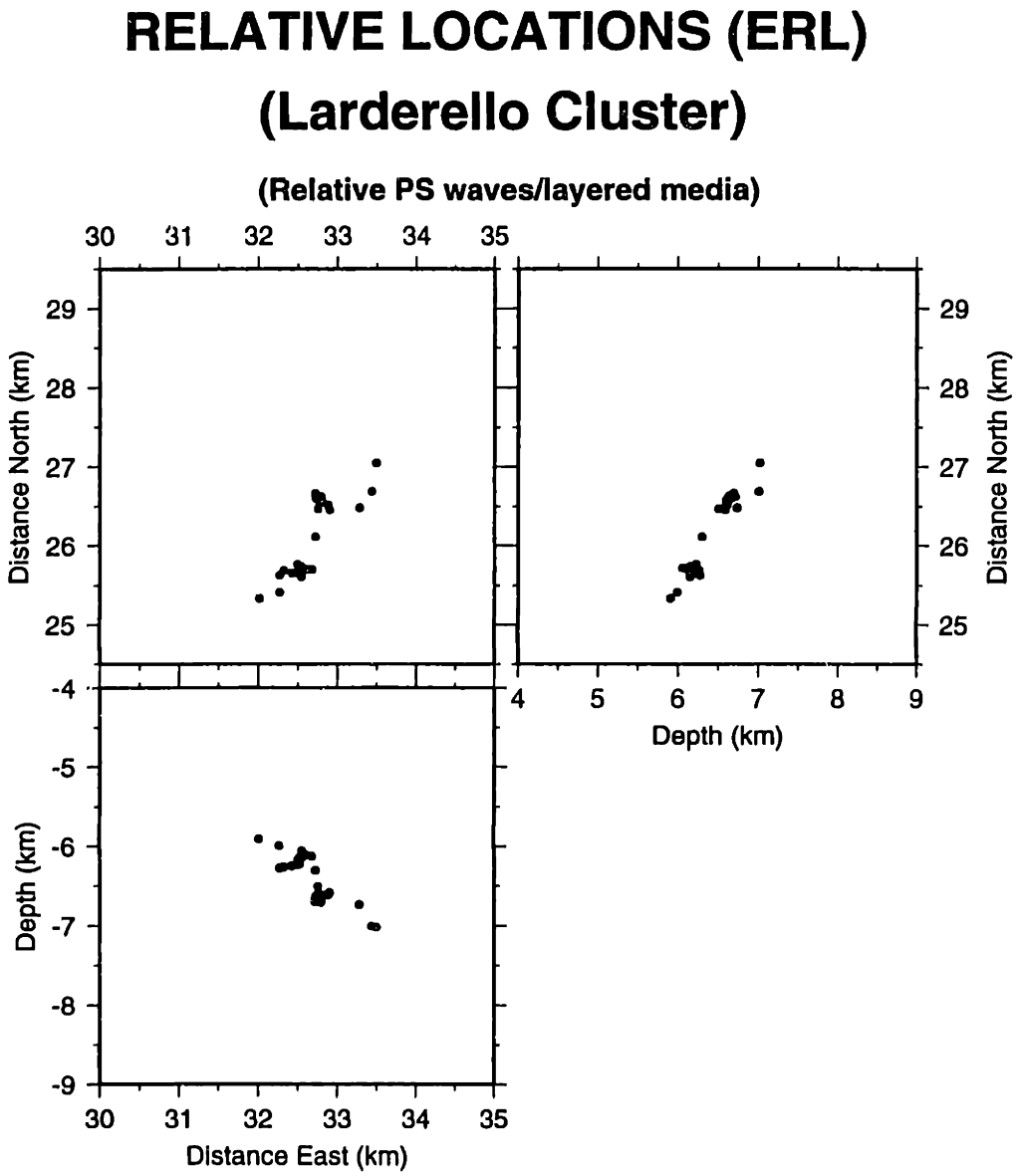

Figure D-123: Larderello 1993 Cluster Frame 31

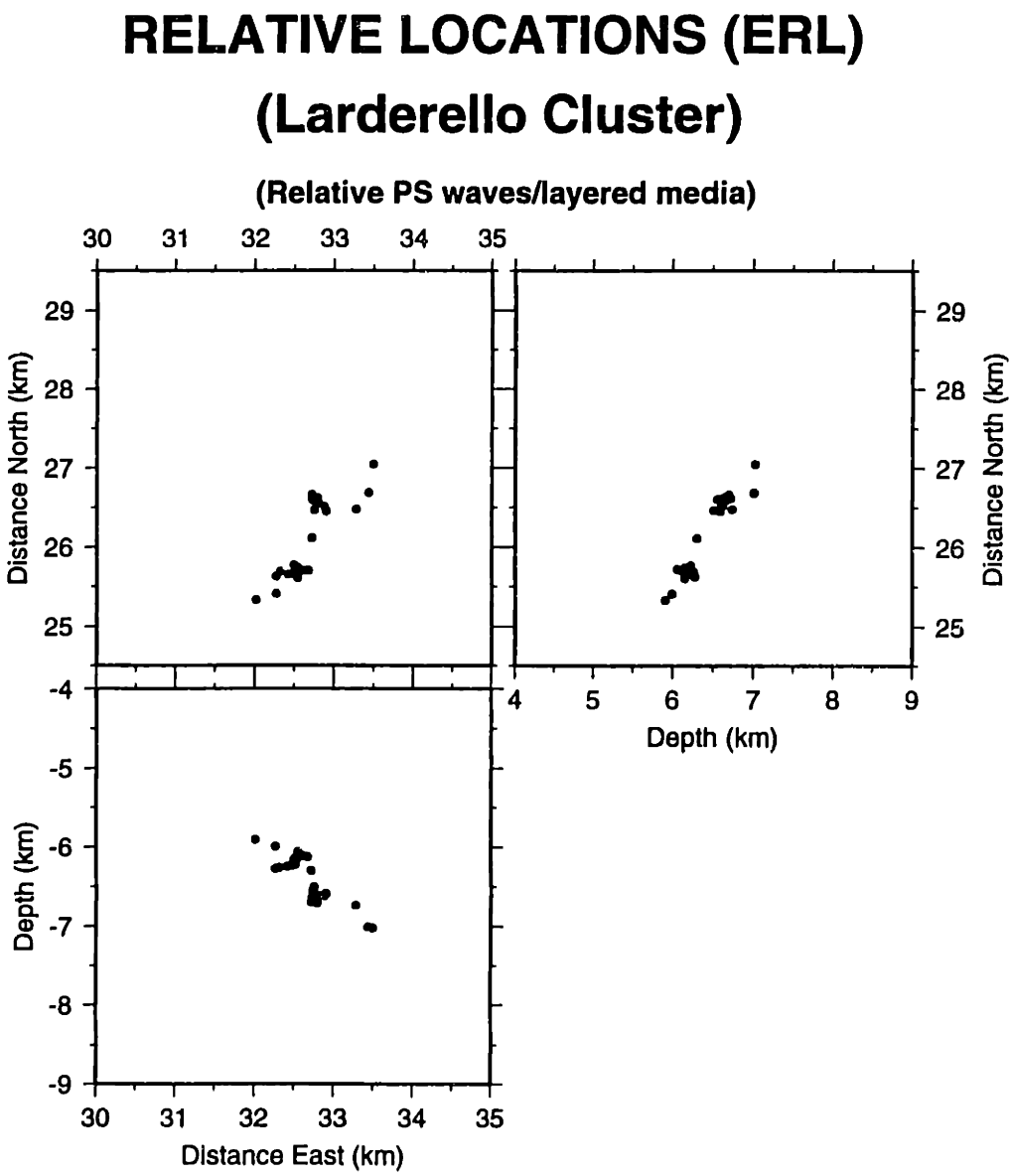

Figure D-124: Larderello 1993 Cluster Frame 32

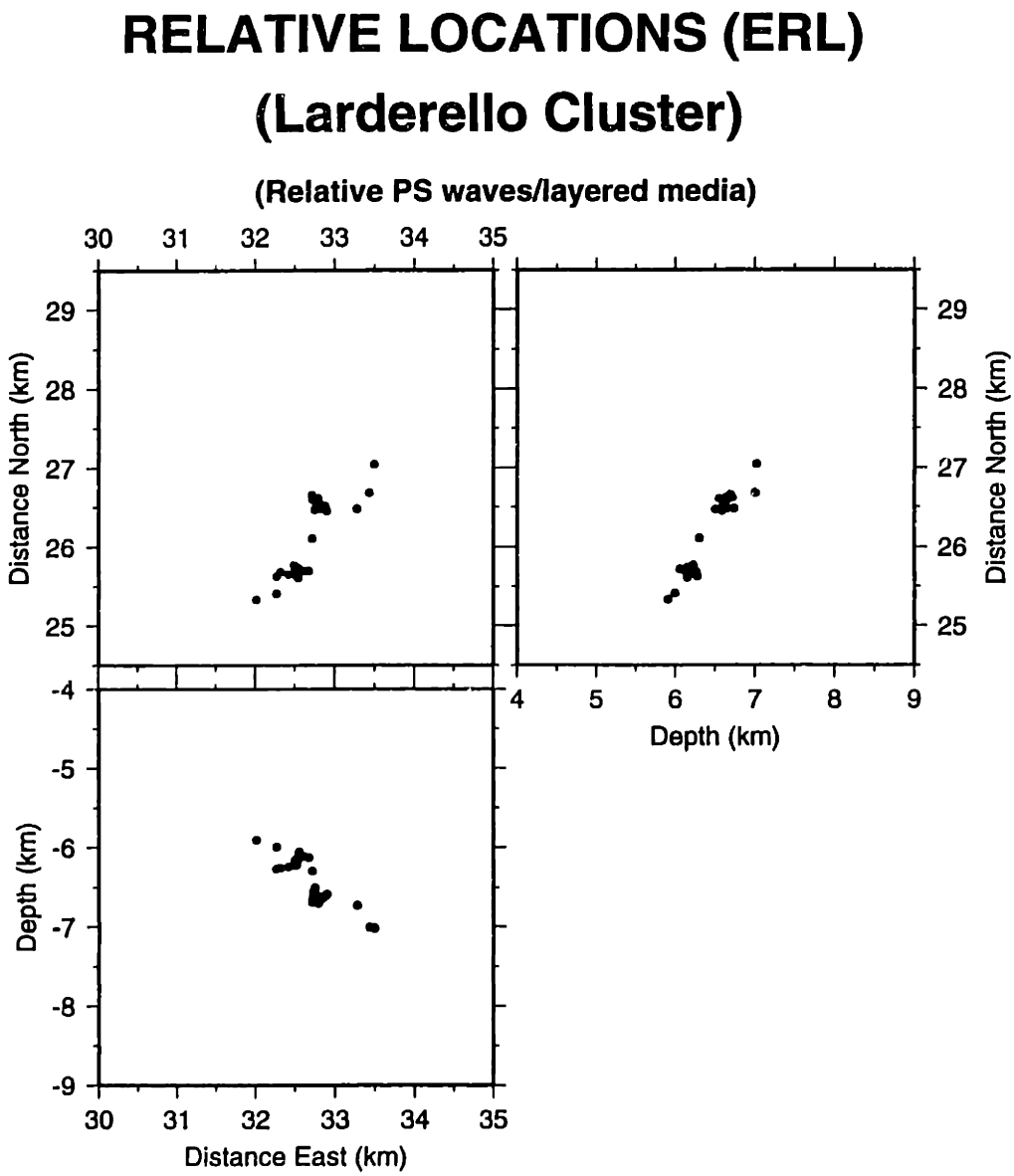

Figure D-125: Larderello 1993 Cluster Frame 33

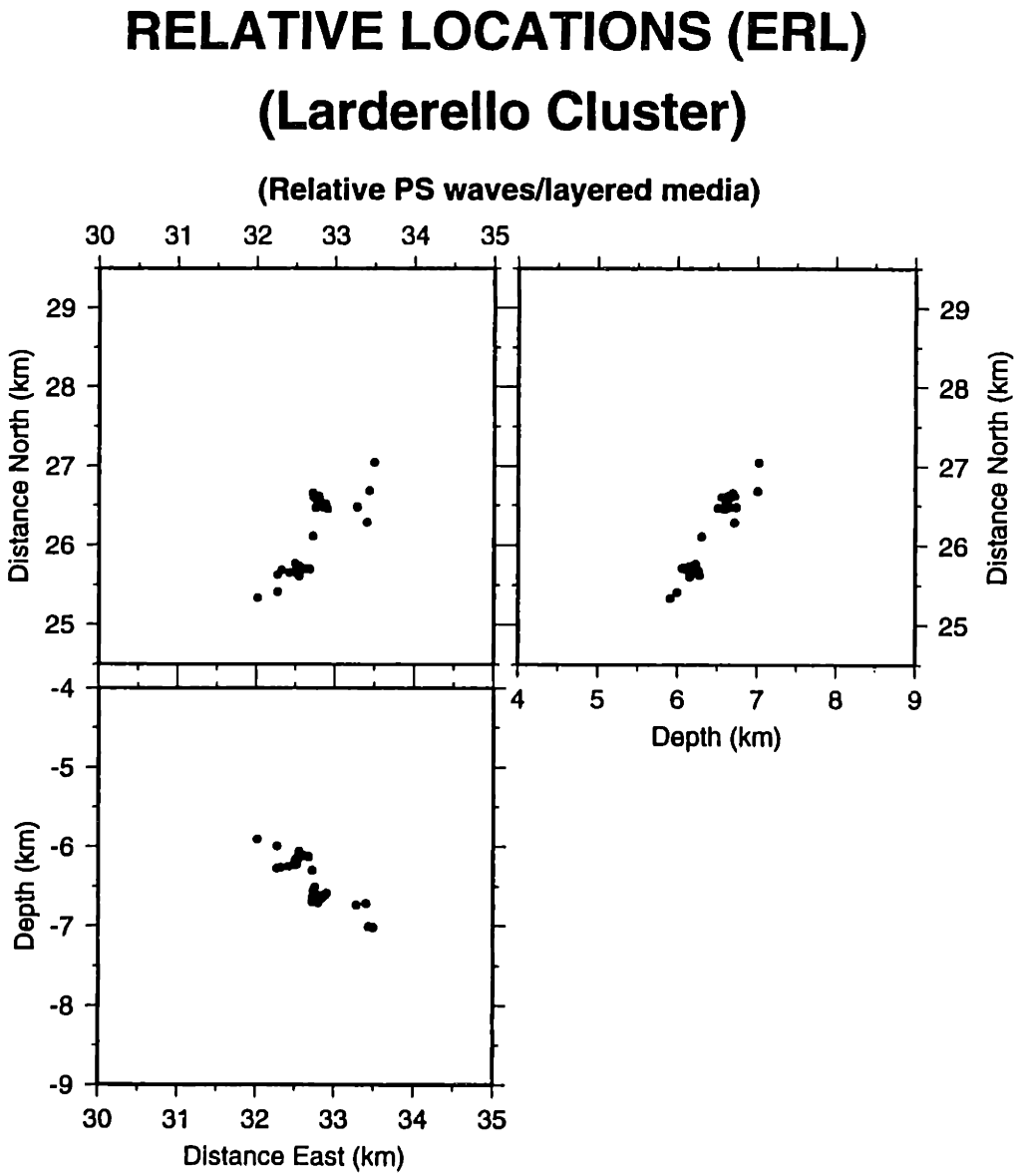

Figure D-126: Larderello 1993 Cluster Frame 34

(This page intentionally left blank.)

Figure D-127:

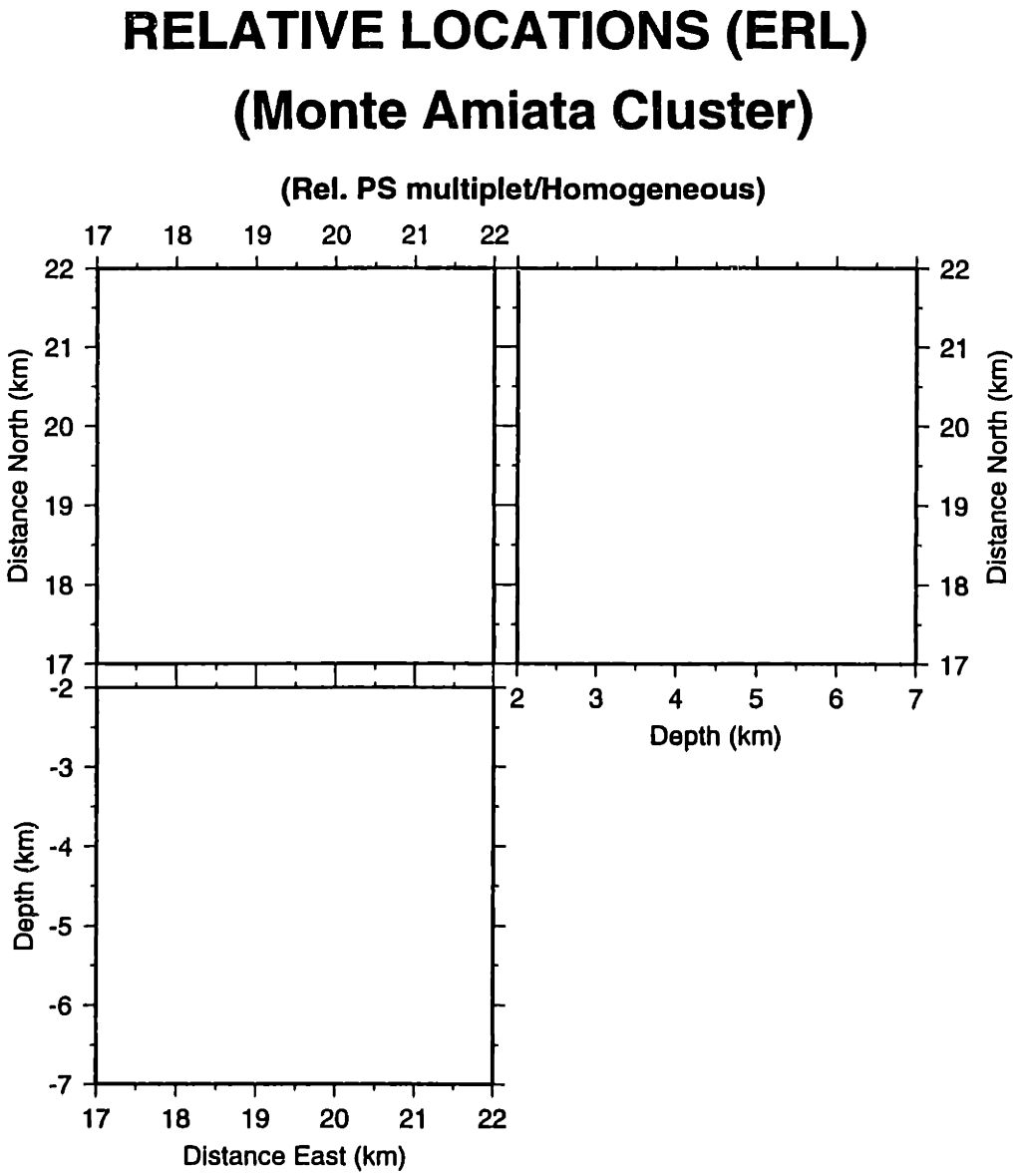

Figure D-128: Monte Amiata Cluster Frame 00

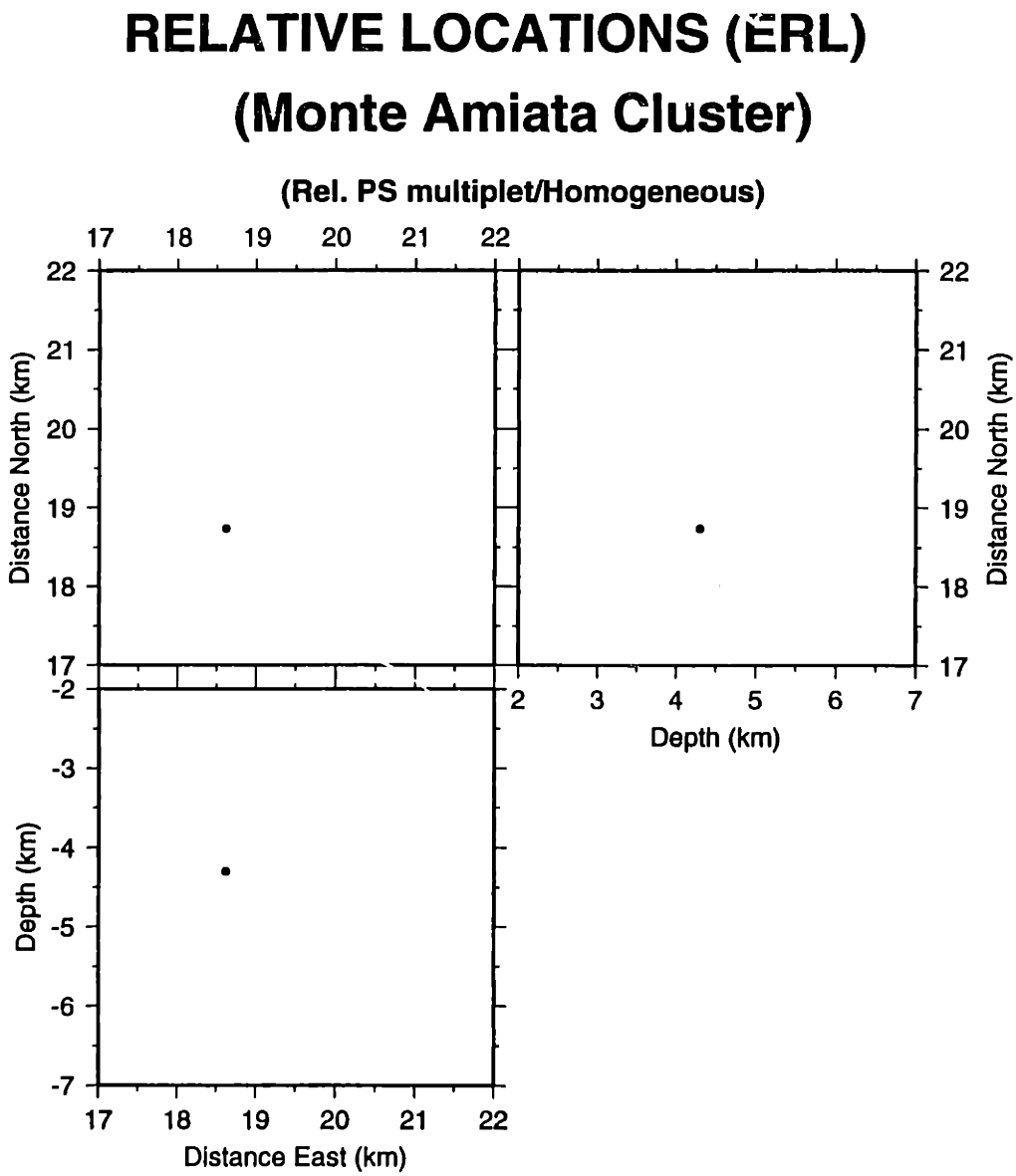

Figure D-129: Monte Amiata Cluster Frame 01

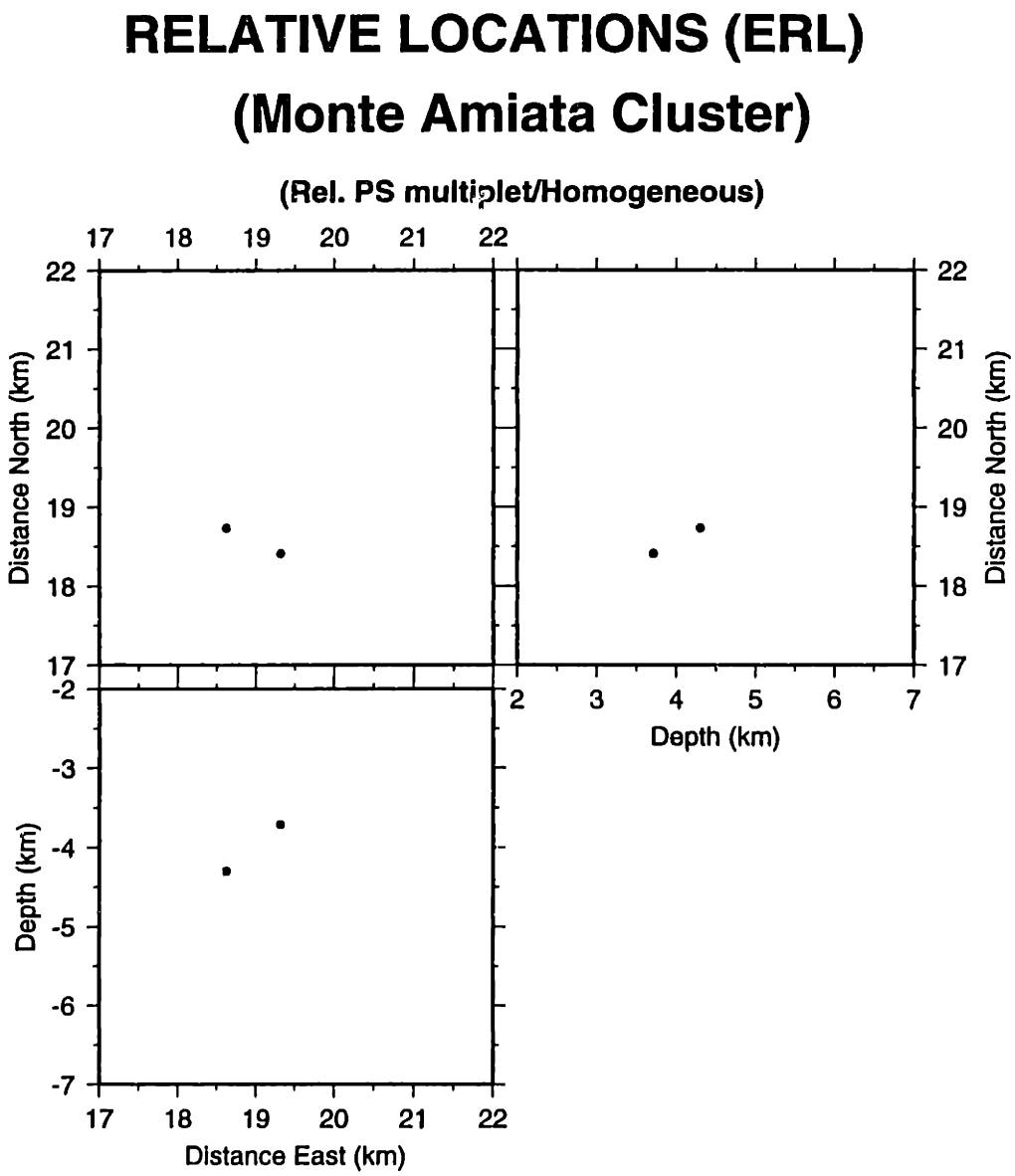

Figure D-130: Monte Amiata Cluster Frame 02

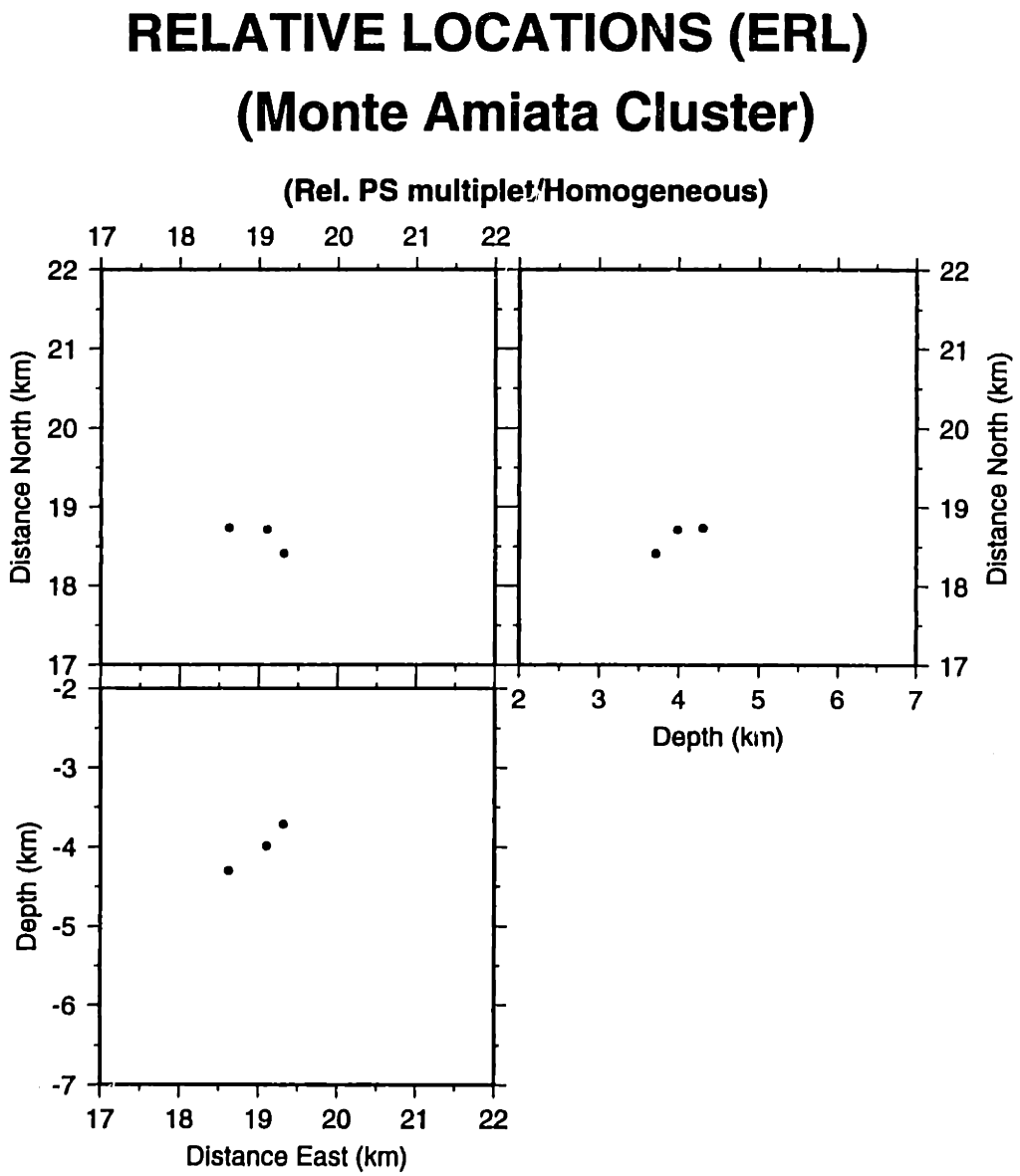

Figure D-131: Monte Amiata Cluster Frame 03

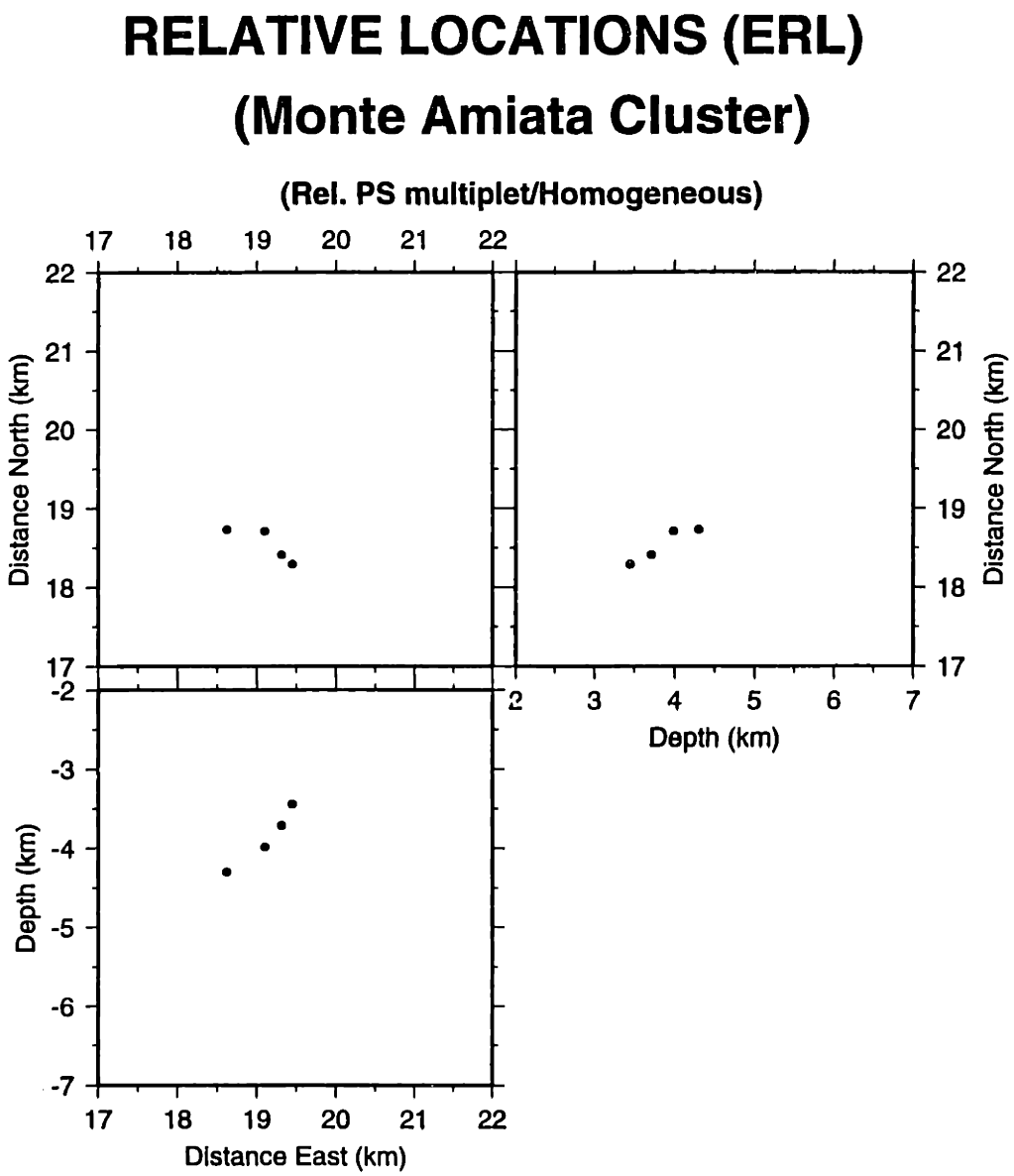

Figure D-132: Monte Amiata Cluster Frame 04

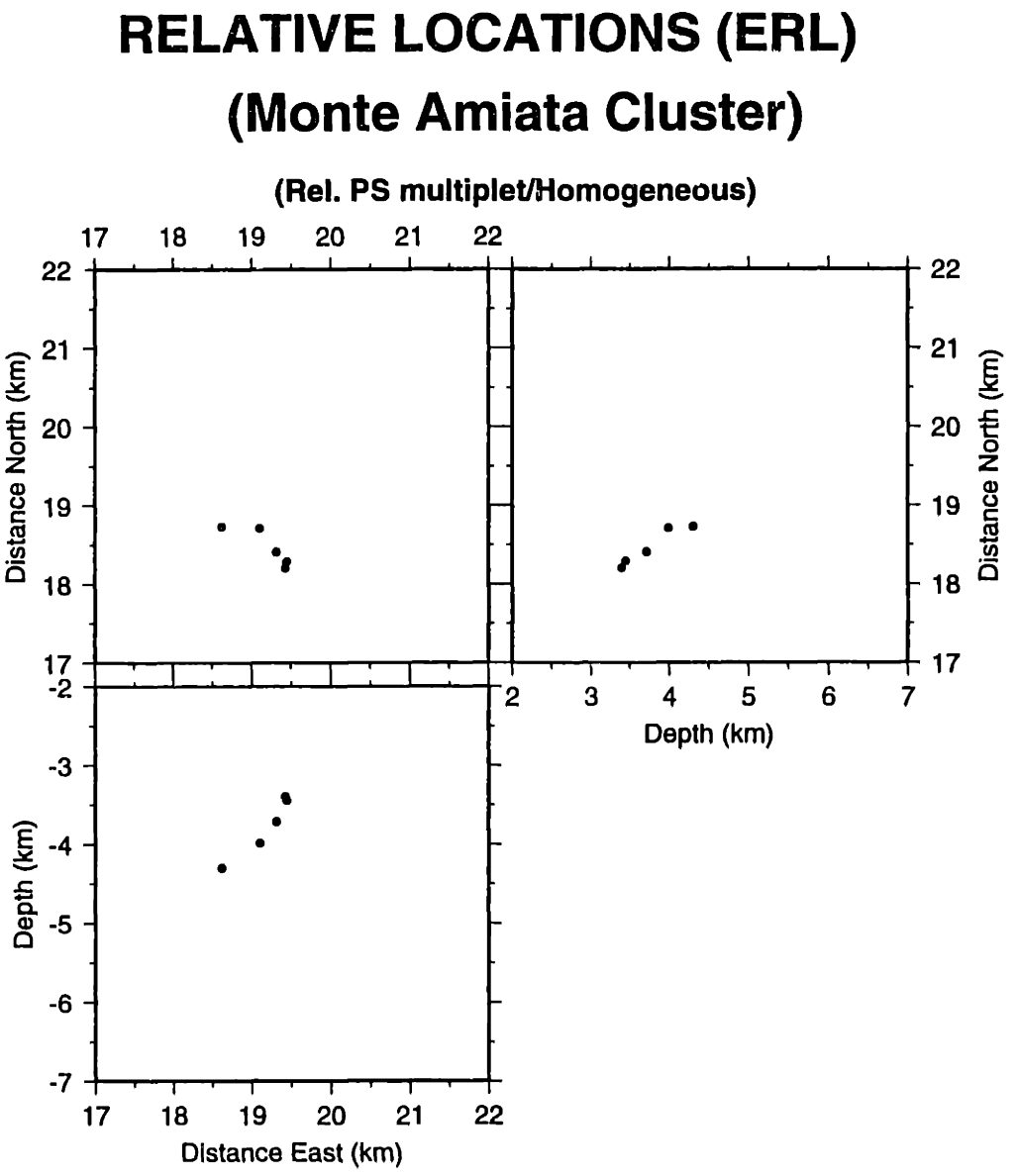

Figure D-133: Monte Amiata Cluster Frame 05

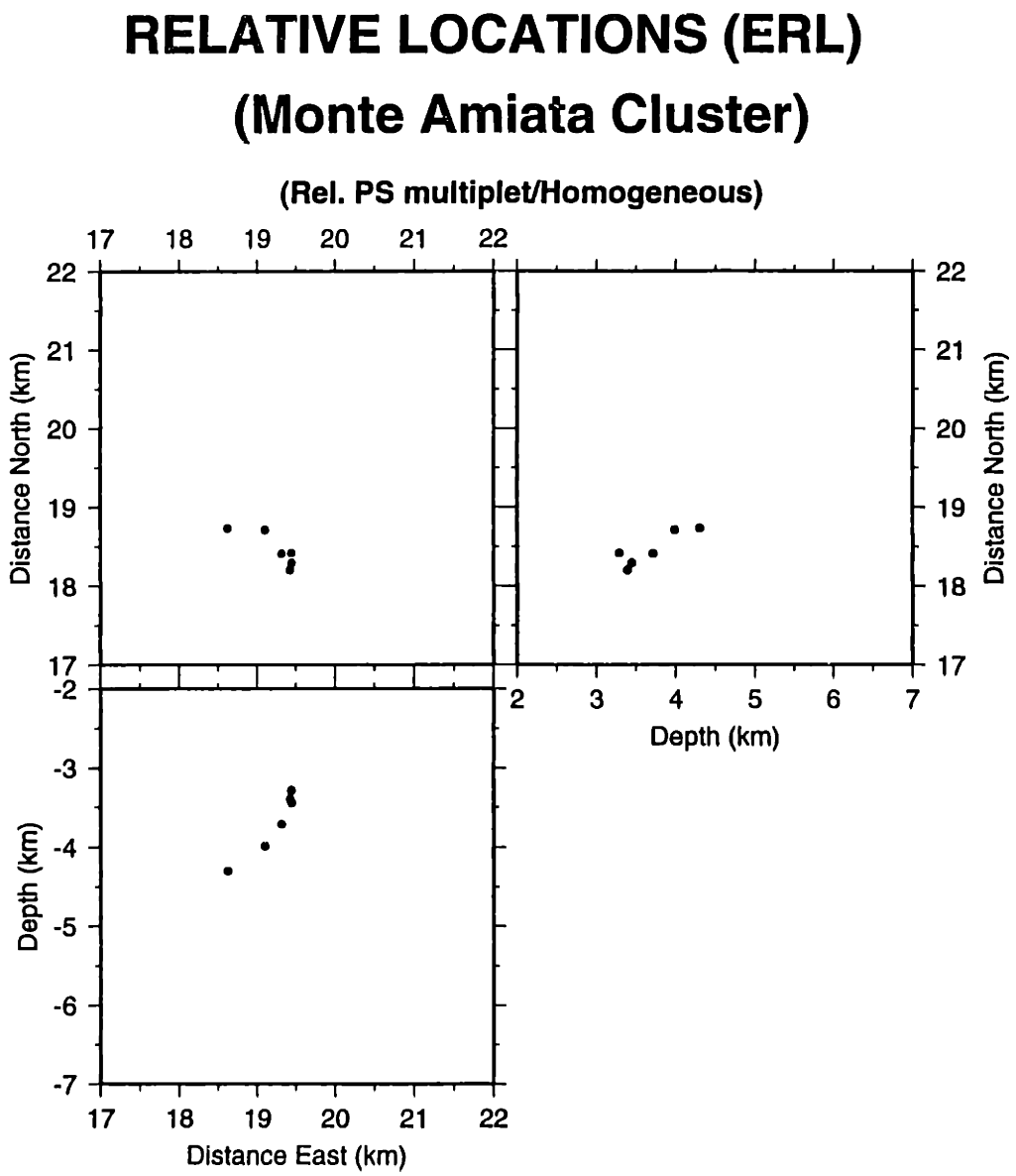

Figure D-134: Monte Amiata Cluster Frame 06

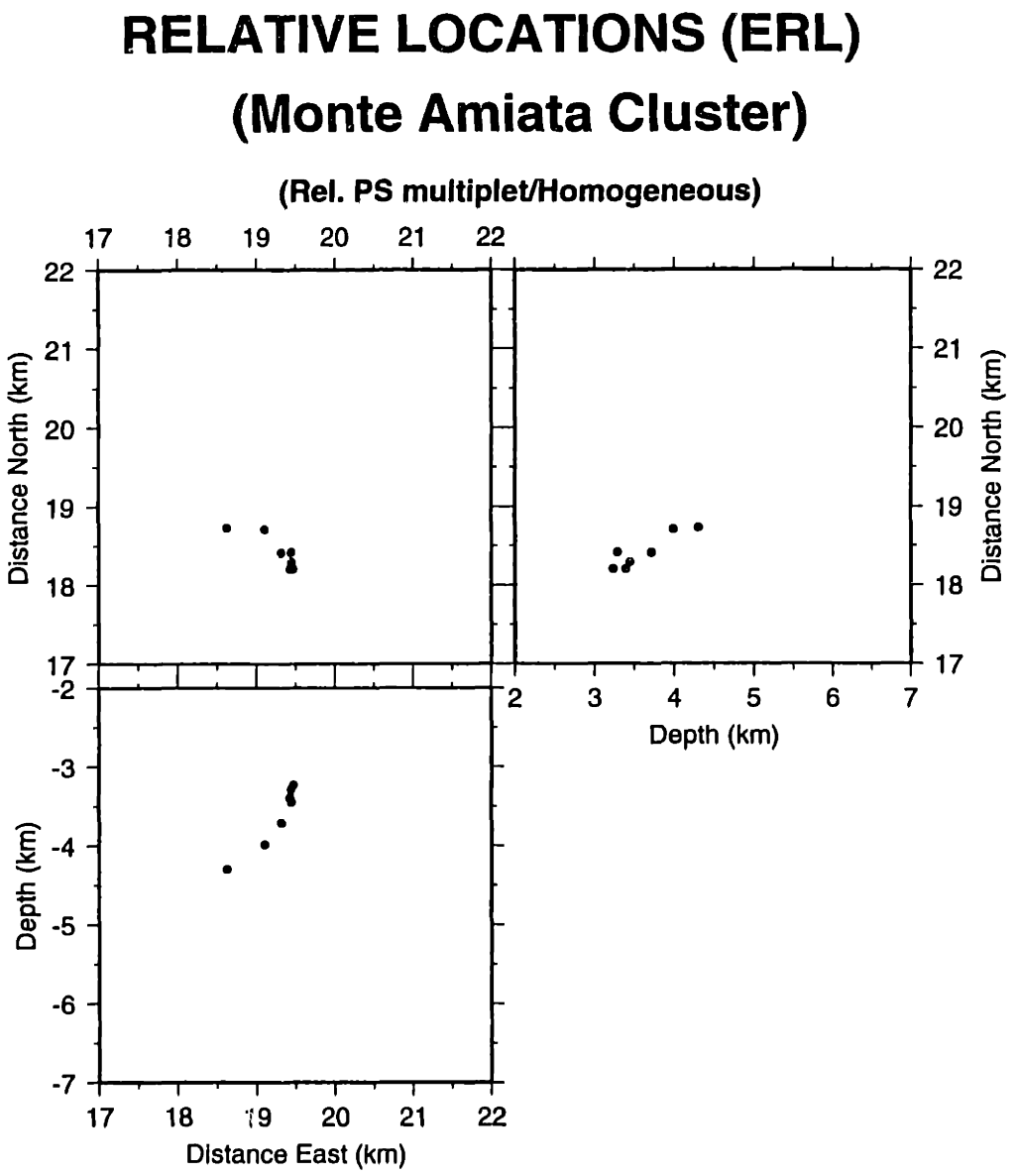

Figure D-135: Monte Amiata Cluster Frame 07

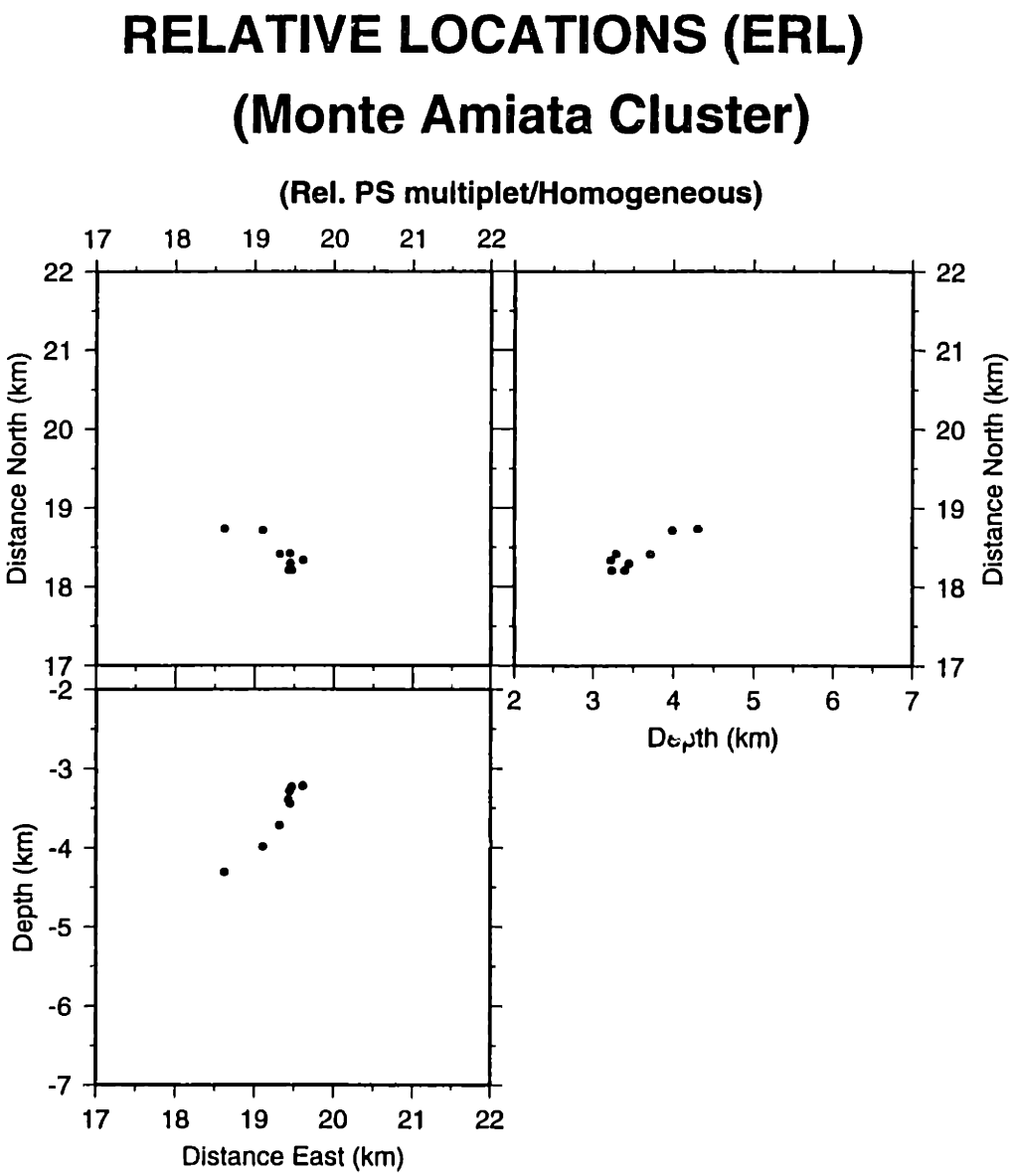

Figure D-136: Monte Amiata Cluster Frame 08

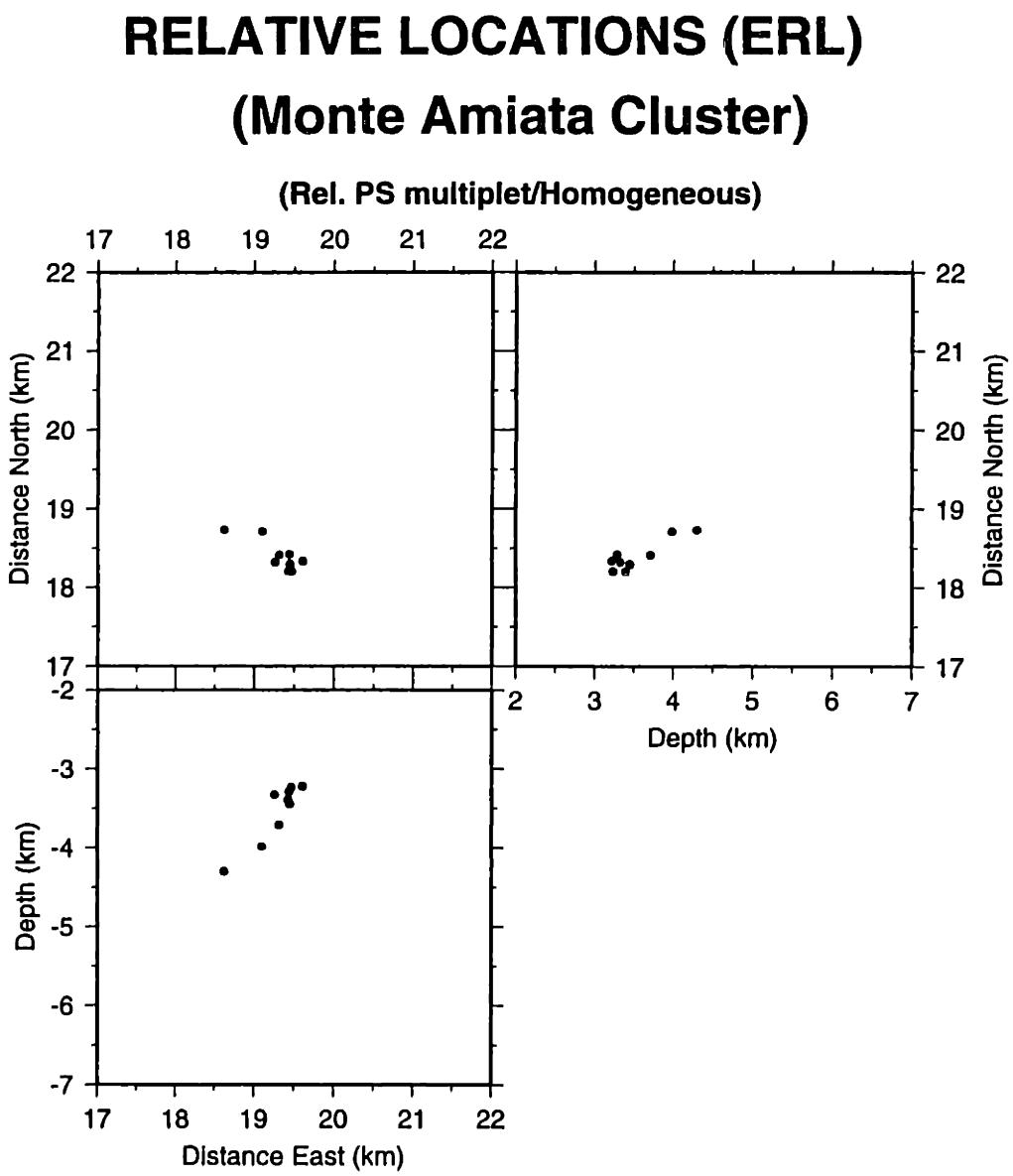

Figure D-137: Monte Amiata Cluster Frame 09

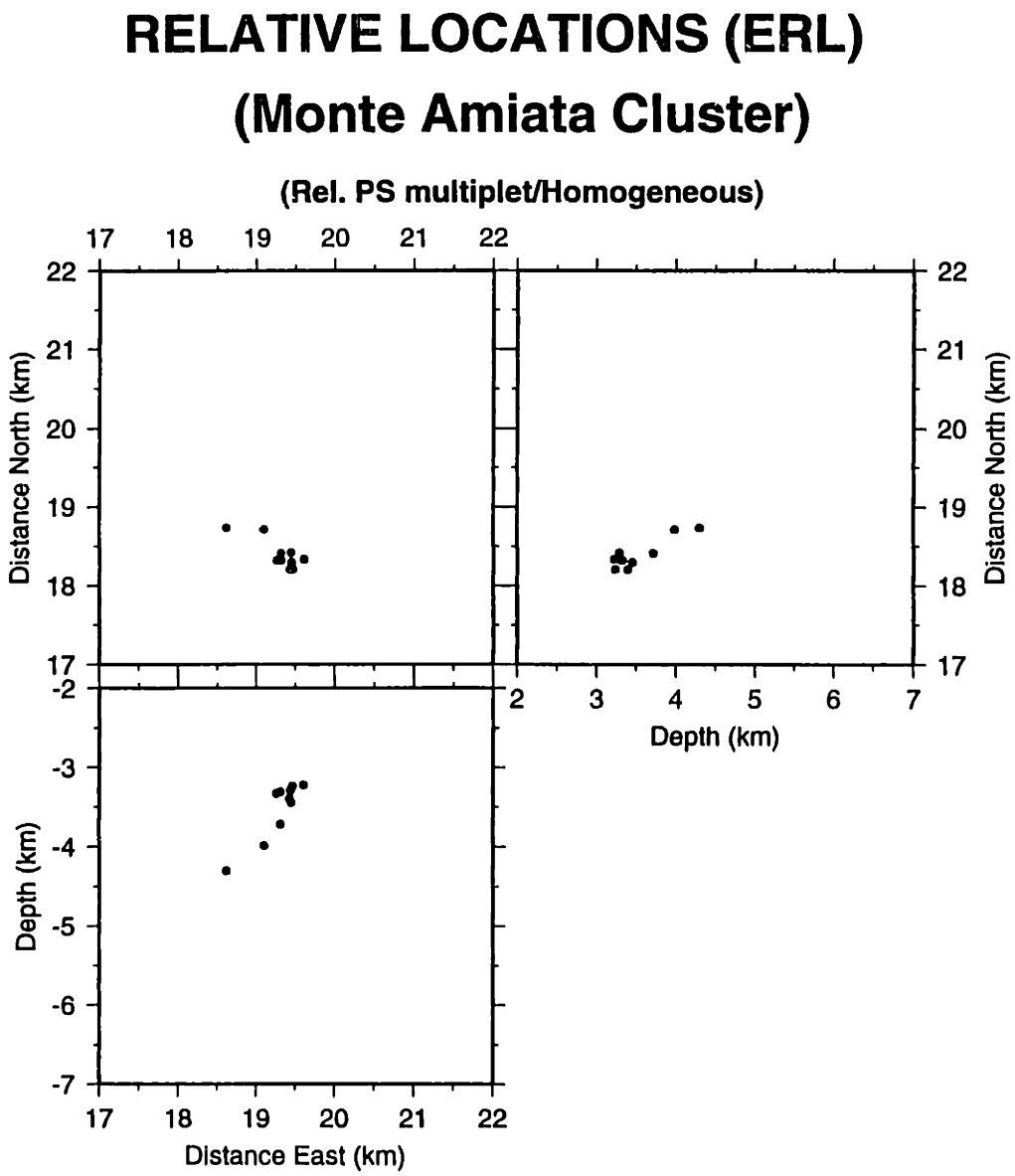

Figure D-138: Monte Amiata Cluster Frame 10

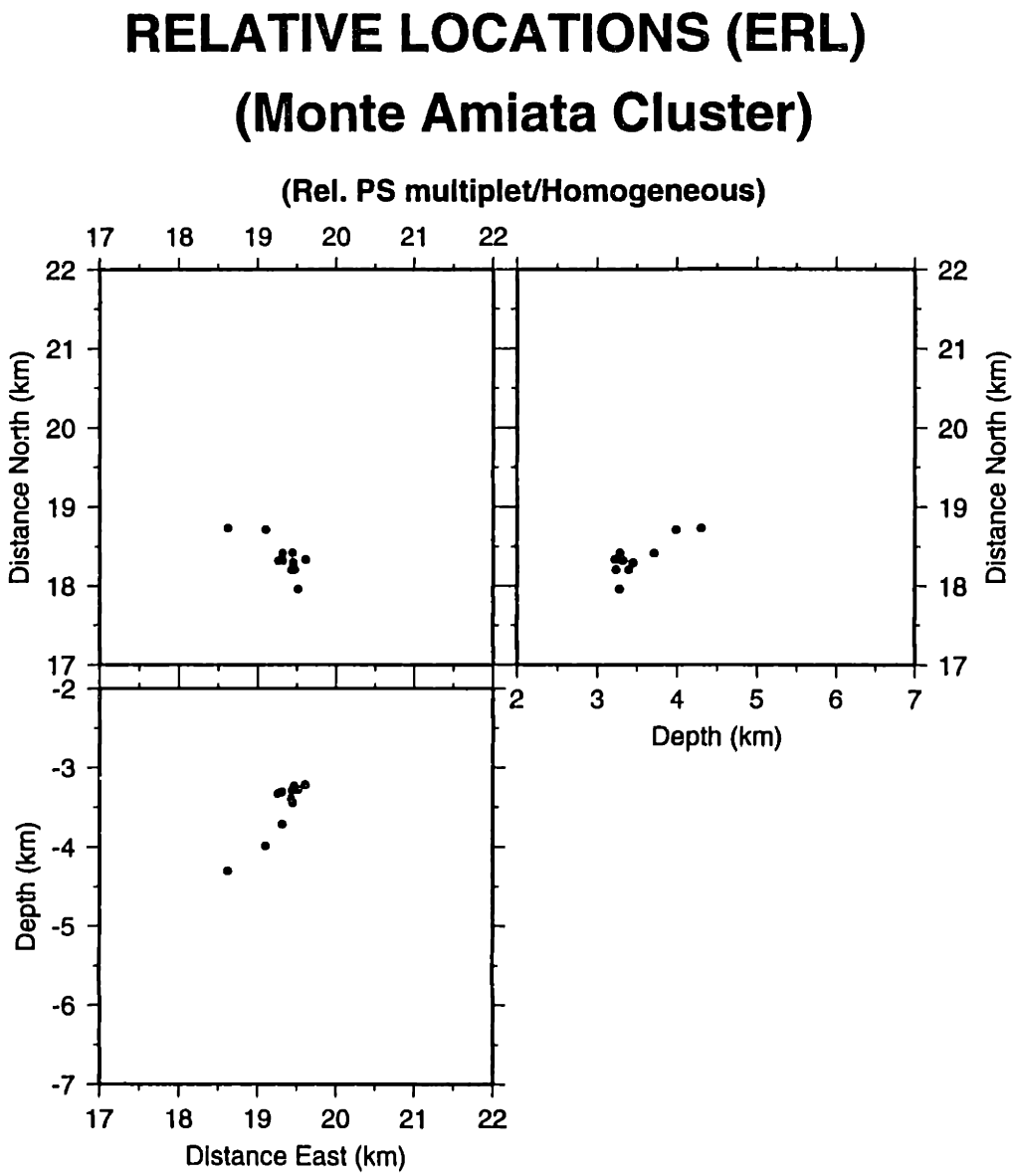

Figure D-139: Monte Amiata Cluster Frame 11

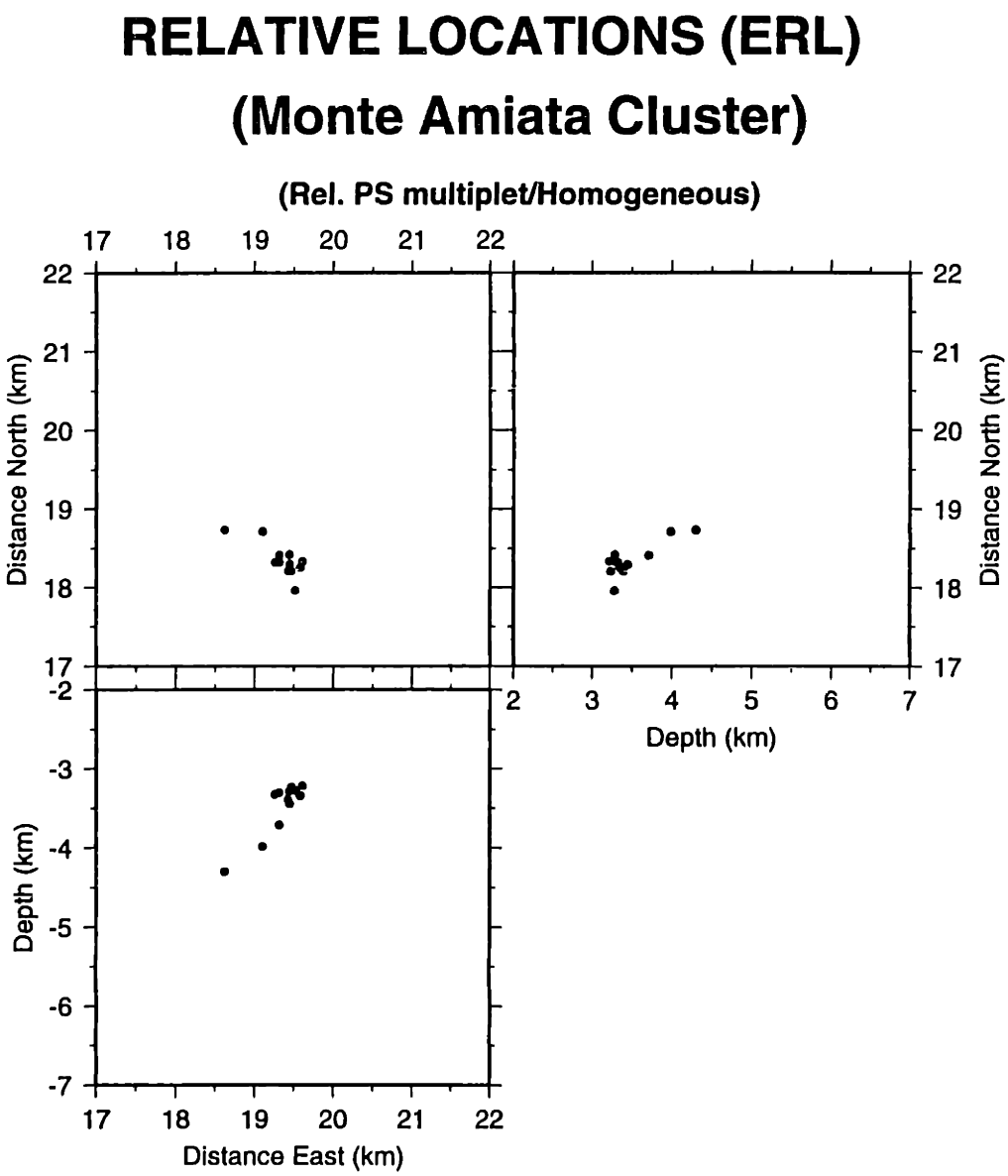

Figure D-140: Monte Amiata Cluster Frame 12

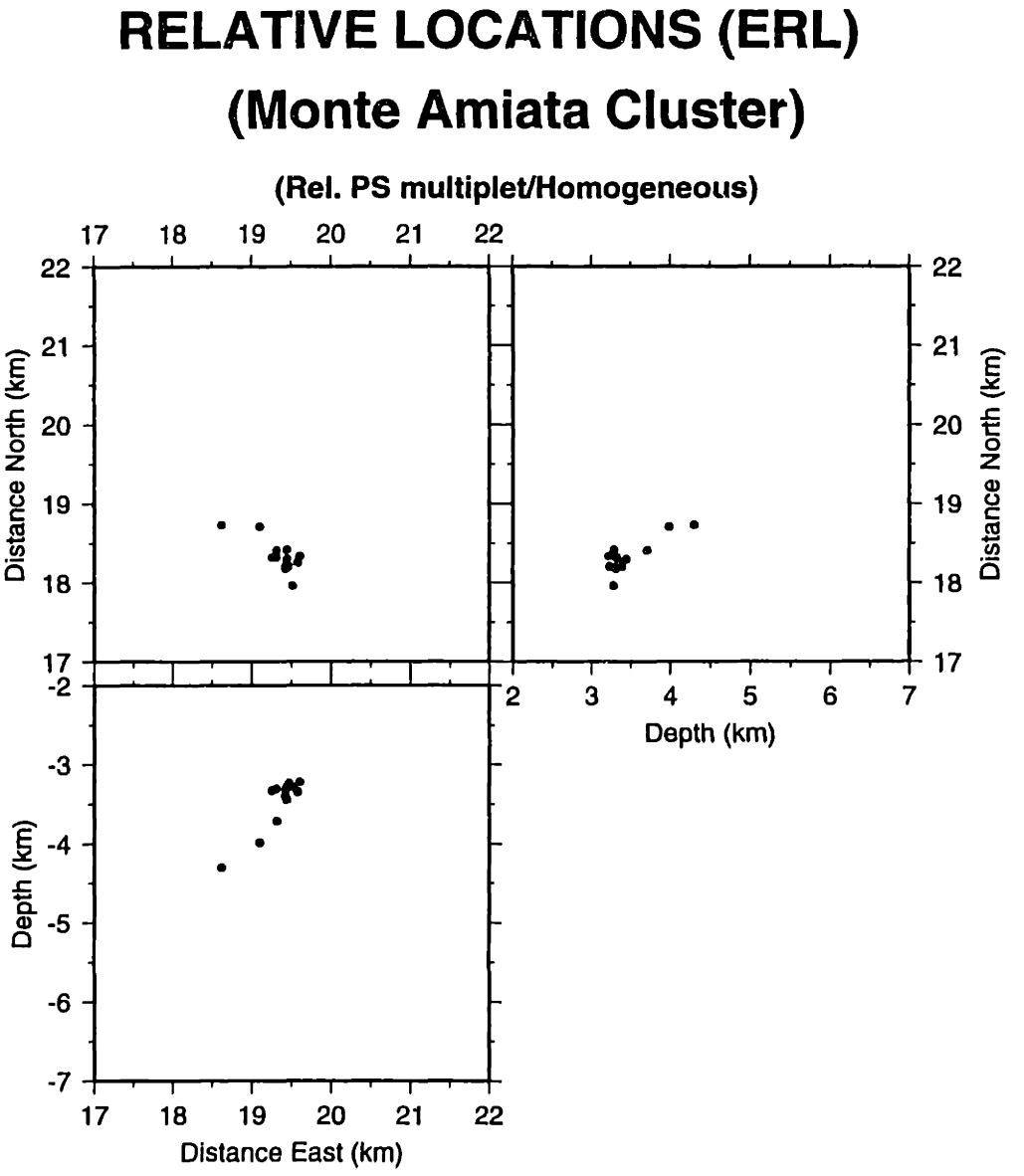

Figure D-141: Monte Amiata Cluster Frame 13

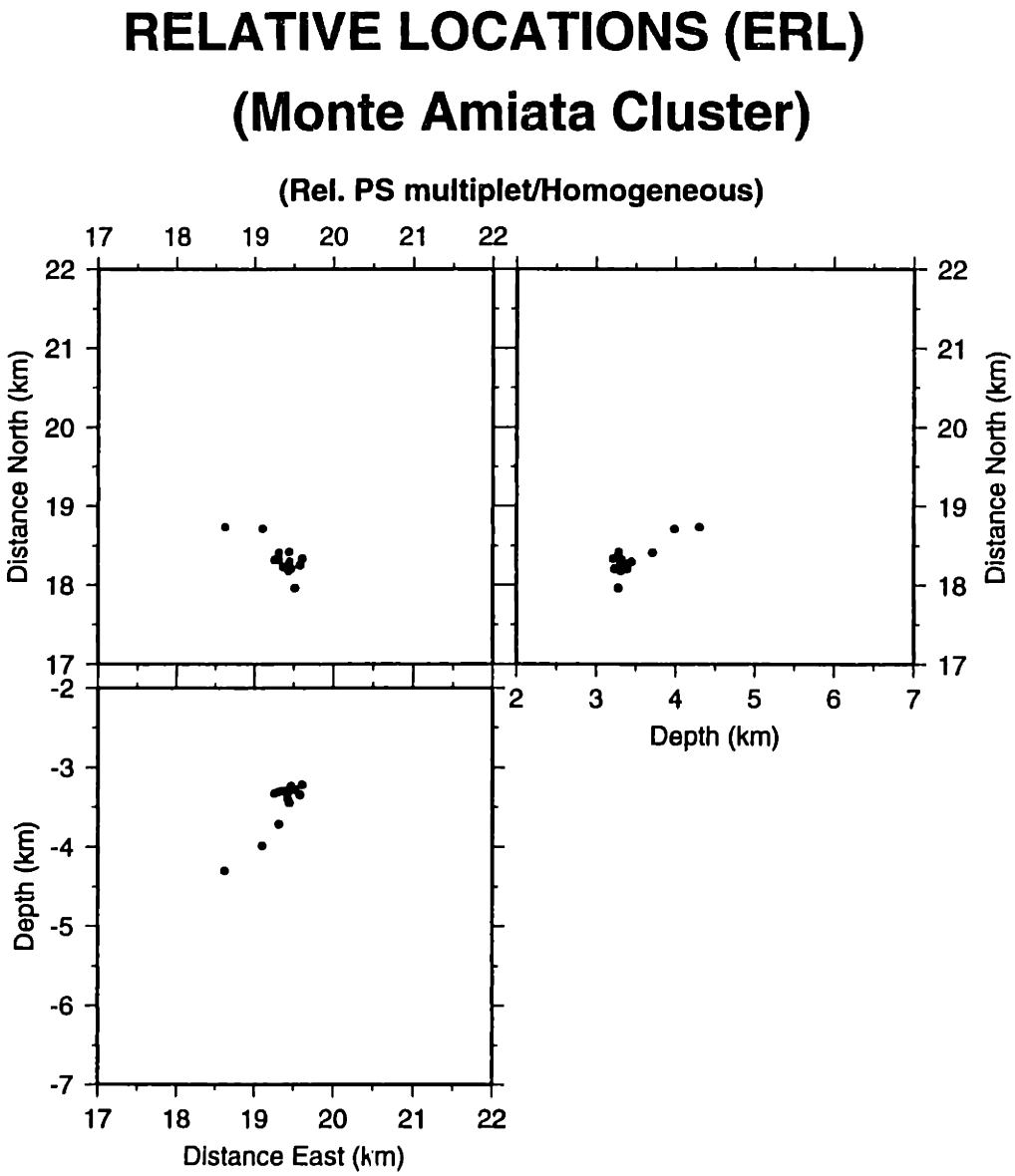

Figure D-142: Monte Amiata Cluster Frame 14

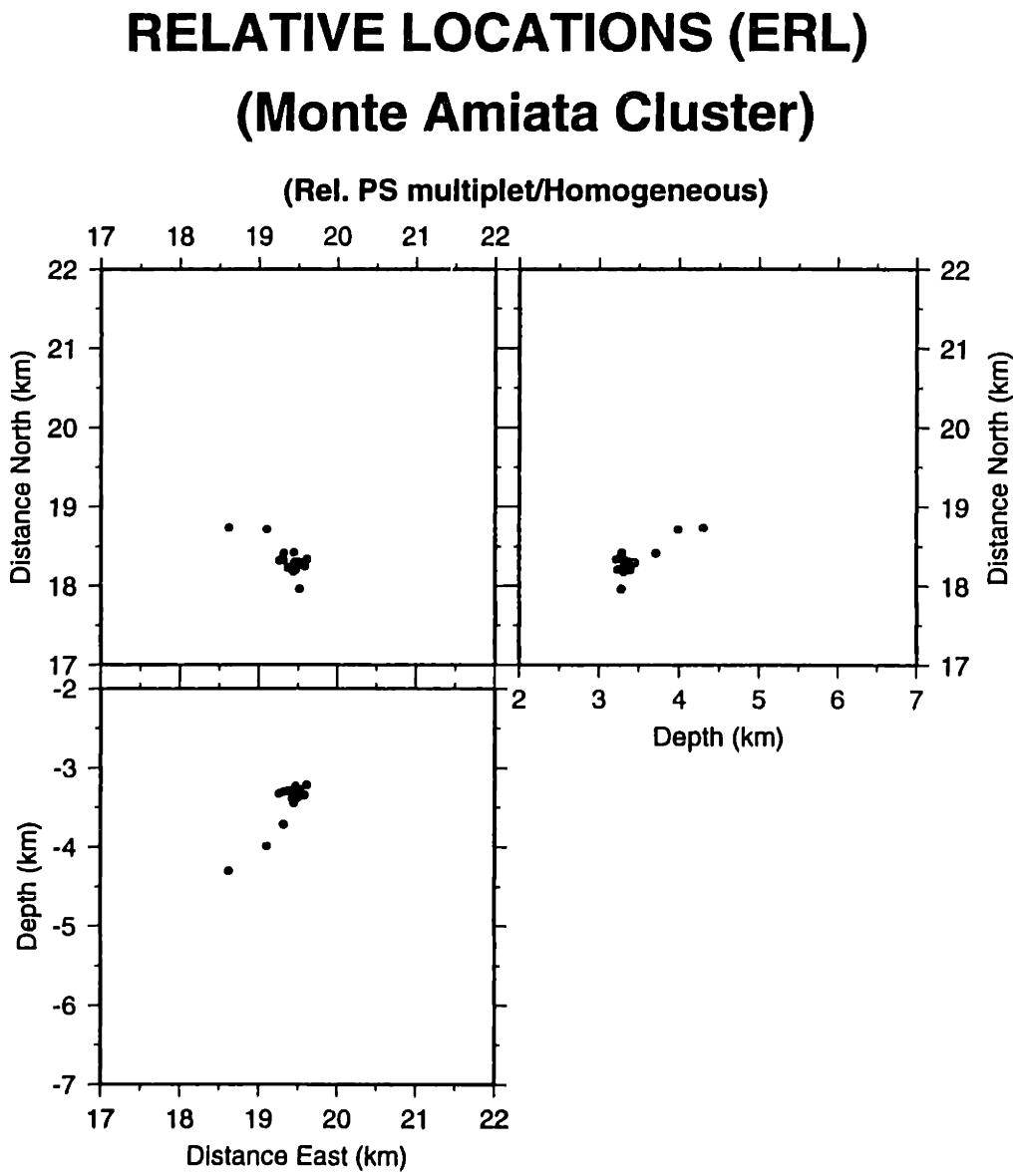

Figure D-143: Monte Amiata Cluster Frame 15

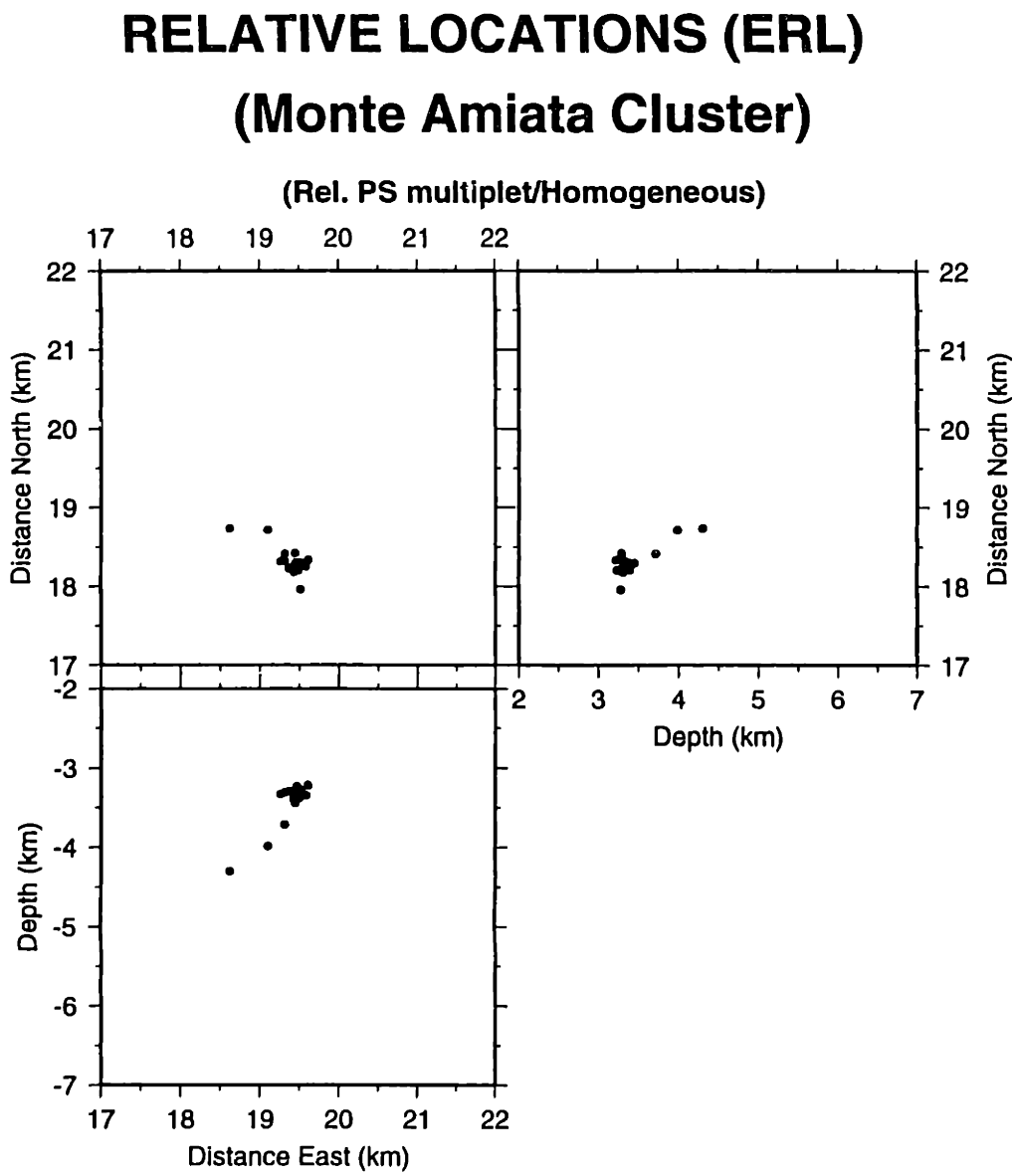

Figure D-144: Monte Amiata Cluster Frame 16

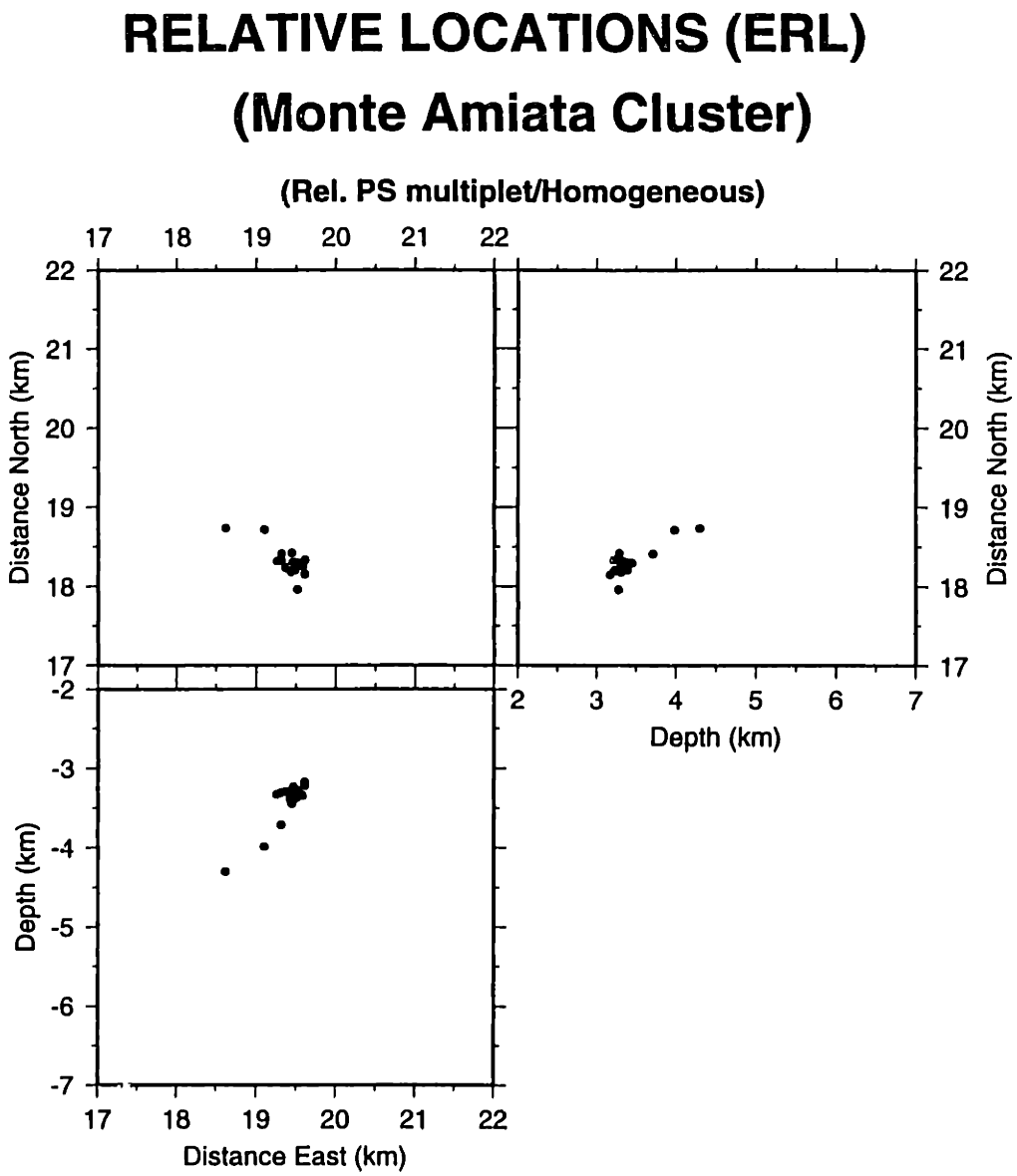

Figure D-145: Monte Amiata Cluster Frame 17

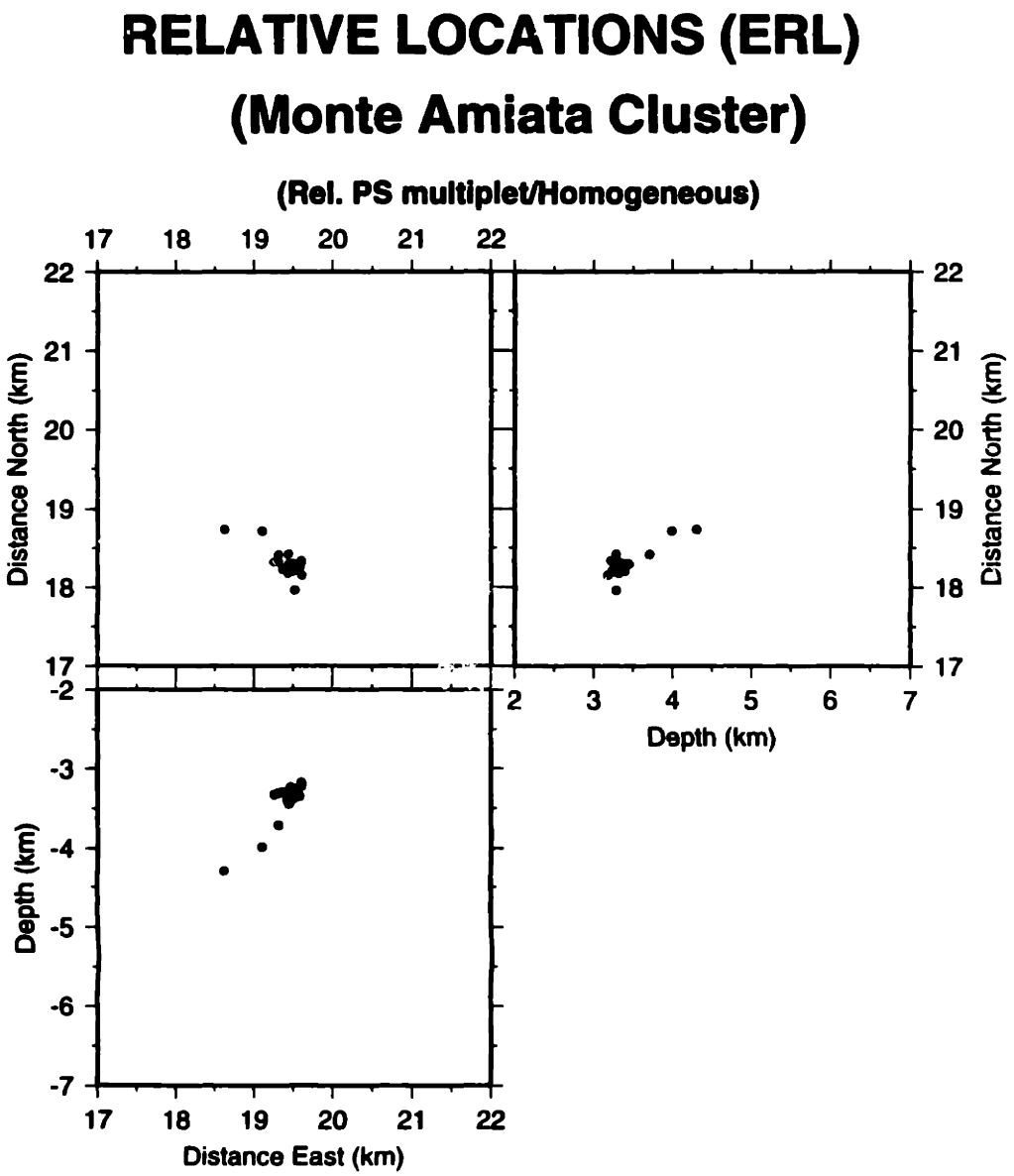

Figure D-146: Monte Amiata Cluster Frame 18

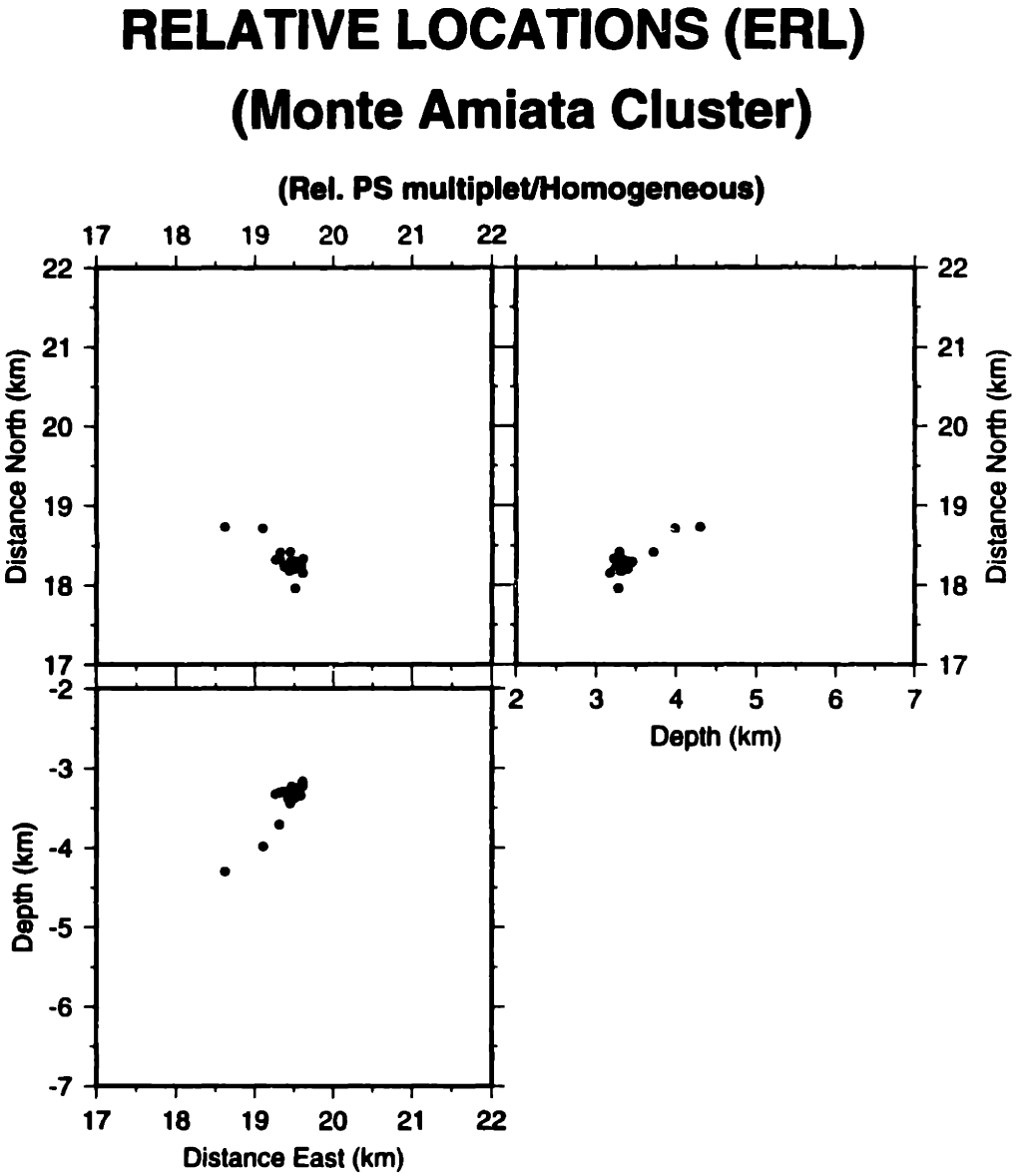

Figure D-147: Monte Amiata Cluster Frame 19

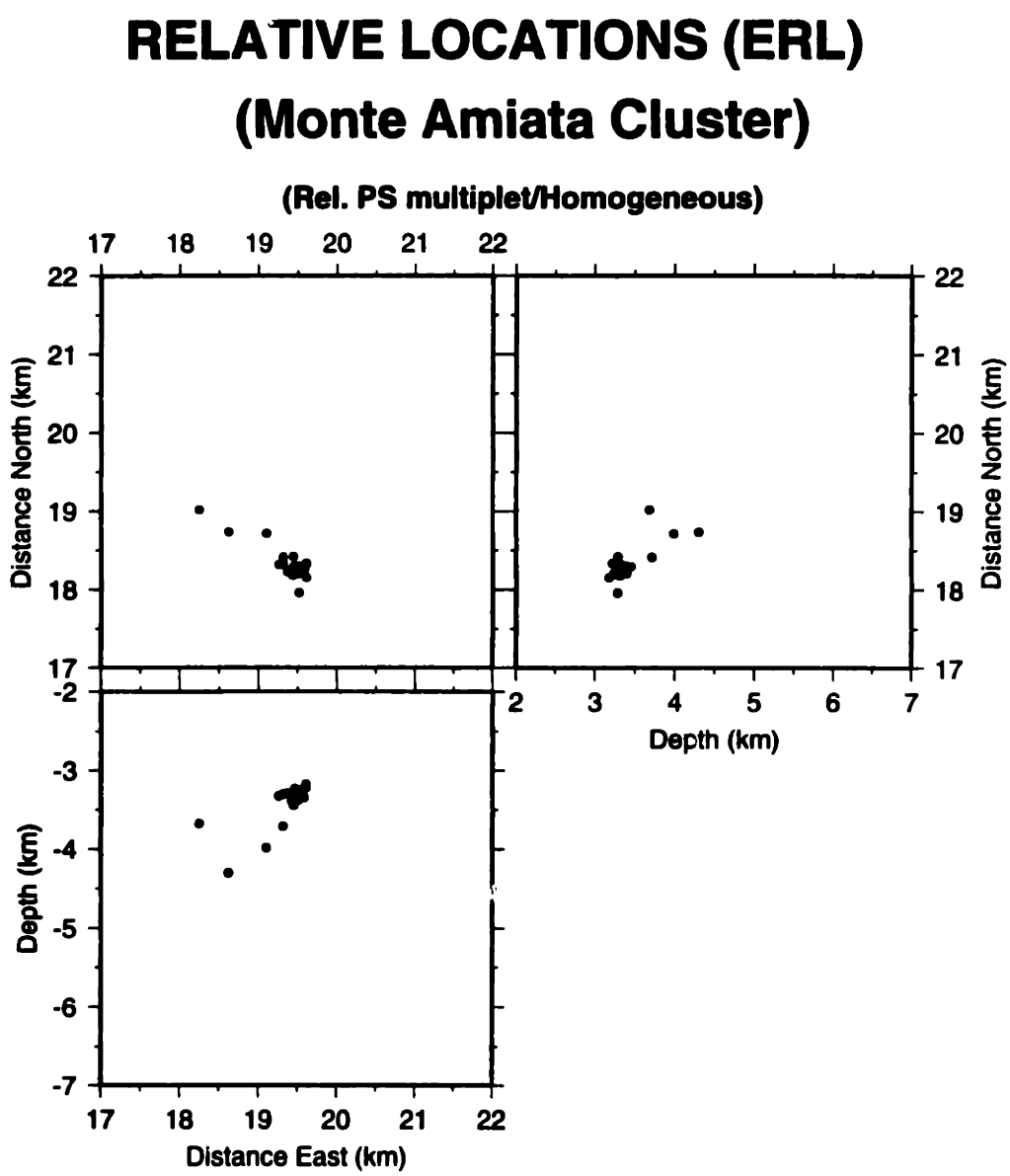

Figure D-148: Monte Amiata Cluster Frame 20

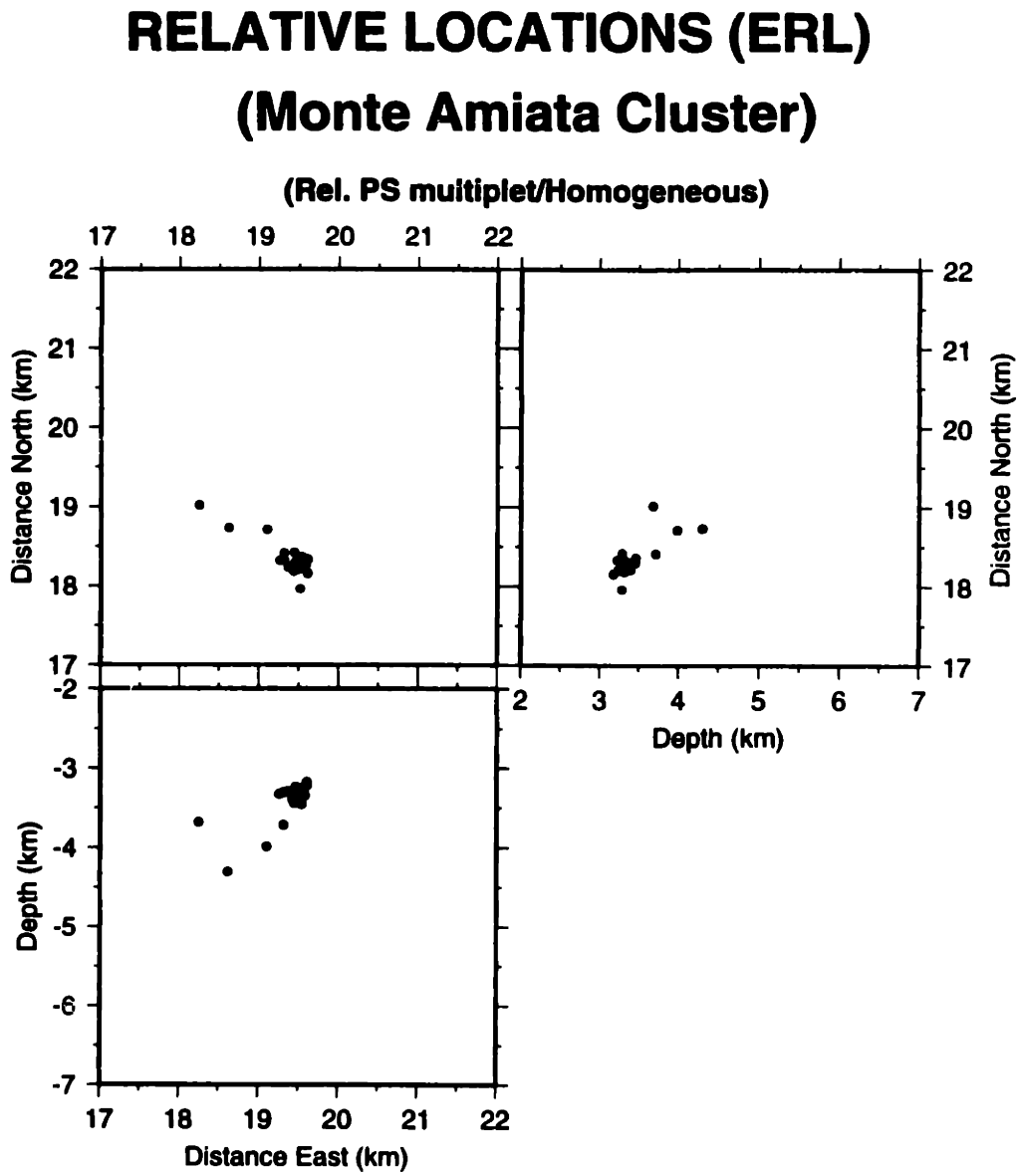

Figure D-149: Monte Amiata Cluster Frame 21

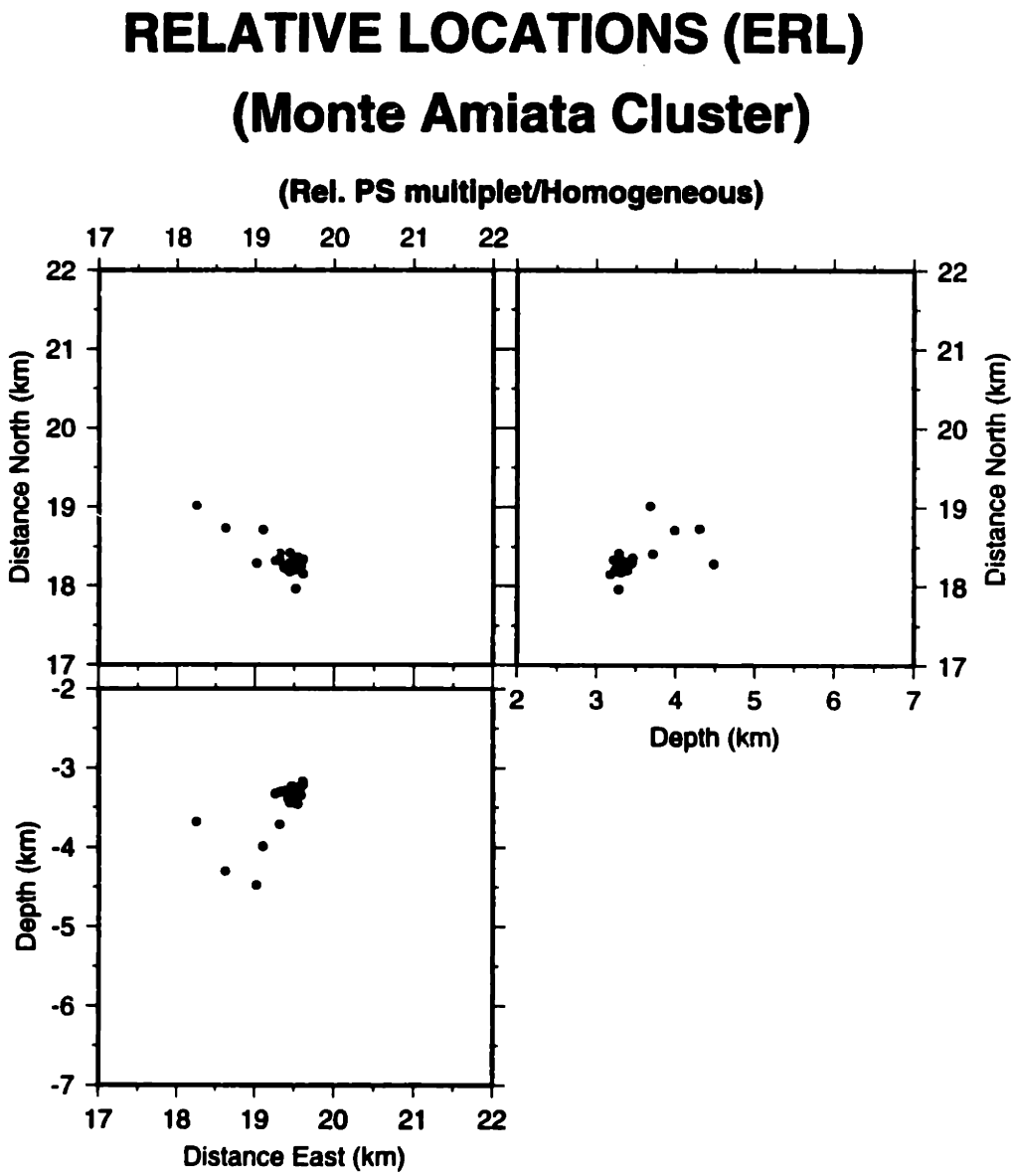

Figure D-150: Monte Amiata Cluster Frame 22

Bibliography

Albores, A., Reyes, A., Brune, J., Day, S., Gonzalez, J., Nava, A., Garcilazo, L., and Vaillard, I. (1977). Microearthquake study at the Cerro Prieto, Mexico, geothermal field. *EOS-Transactions of the American Geophysical Union*, **58**(12).

Albright, J. (1976). Preliminary seismic mapping of the main fracture in GT-2. *EOS-Transactions of the American Geophysical Union*, **57**(4), 349.

Allegrini, G., Burgassi, P., and Sartini, E. (1981). Present status and new prospects of geothermal energy in italy. In *Transactions of the Geothermal Resources Council*, volume 5. Geothermal Resources Council.

Atlantic Richfield Corporation (1994). The deep well treatment and injection program. Fracture Technology Field Demonstration Project.

Bachelor, T. (1996). A European view of the development of Hot Dry Rock Geothermal Fields. In *Proceedings of the 3rd International HDR Forum*, Santa Fe, New Mexico.

Barberi, F., Innocenti, F., Ferrara, G., Keller, J., and Villari, L. (1973). Evolution of eolian arc volcanism (southern tyrrhenian sea). *Earth and Planetary Letters*, **21**, 269–276.

Bard, P., Grasso, J., Fourmaintraux, D., and Koller, M. (1995). A methodology for induced seismic risk evaluation around hydrocarbon recovery sites: validation on the Lacq gas field, France. In *IUGG XXI General Assembly Abstracts (Week A)*. International Union of Geodesy and Geophysics. Abstract number SA21D-7.

Baria, R., Gérard, A., Baumgärtner, J., and Garnish, J. (1996). Progress at the European HDR site, Soultz, France. In *Proceedings of the 3rd International HDR Forum*, Santa Fe, New Mexico.

Bates, R. L. and Jackson, J. A., editors (1984). *Dictionary of Geological Terms*. Doubleday, third edition.

Batini, F. (1997). Personal correspondence to professor m. nafi toksöz, Earth Resources Laboratory, MIT.

Batini, F., Duprat, A., and Nicolich, R. (1985a). Contribution of seismic reflection to the study of geothermal reservoirs in tuscany (italy). In *Transactions of the Geothermal Resources Council*, volume 9-Part I. Geothermal Resources Council.

Batini, F., Bertini, G., Gianelli, G., Pandeli, E., Puxeddu, M., and Villa, I. (1985b). Deep structure, age and evolution of the lardarello-travale geothermal field. In *Transactions of the Geothermal Resources Council*, volume 9-Part I. Geothermal Resources Council.

Batini, F., Console, R., and Luongo, G. (1985c). Seismological study of the Larderello-Travale geothermal area. *Geothermics*, **14**(2/3), 255–272.

Berti, M. (1996). *Individuanzione di strutture sismicamente attive nell'area geotermica di Larderello*. Master's thesis, Universita' Degli Studi Di Pisa.

Bertini, G., Gianelli, G., Pandeli, E., and Puxeddu, M. (1985). Distribution of hydrothermal minerals in Larderello-Travale and Mt. Amiata geothermal fields (Italy). In *Transactions of the Geothermal Resources Council*, pages 261–266. Geothermal Resources Council.

Block, L. (1991). *Joint hypocenter-velocity inversion of local earthquake arrival time data in geothermal regions*. Ph.D. thesis, Massachusetts Institute of Technology.

Block, L. and Royden, L. (1990). Core complex geometries and regional scale flow in the lower crust. *Tectonics*, **9**(4), 557–567.

Bredehoeft, J., Raleigh, C., and Healy, U. (1974). Control of earthquakes at Rangely, Colorado. In *Circum-Pacific Energy and Mineral Resources Conference, AAPG Bulletin*, volume 58, page 1432. American Association of Petroleum Geologists.

Calamai, A., Cataldi, R., Squarci, P., and Taffi, L. (1970). Geology, geophysics and hydrogeology of the Monte Amiata Geothermal fields. *Geothermics*, **Special Issue 1**.

Cameli, G., Dini, I., and Liotta, D. (1993). Upper crustal structure of the lardarello geothermal field as a feature of post-collisional extensional tectonics (southern tuscany, italy). *Tectonics*, **24**, 413–423.

Cappetti, G., Celati, R., Cigni, U., Squarci, P., Stefani, G., and Taffi, L. (1985). Developments of deep exploration in the geothermal areas of tuscany, italy. In *International Symposium on Geothermal Energy, International Volume*, volume 9-Part I. Geothermal Resources Council.

Carella, R. (1985). Status of geothermal activities by agip in italy. In *Transactions of the Geothermal Resources Council*, volume 9-Part I. Geothermal Resources Council.

Carmignani, L. and Kligfield, R. (1990). Crustal extension in the northern appennine: The transition from compression to extension in the alpi apuane core complex. *Tectonics*, **9**(6), 1275–1303.

Cataldi, R., Ferrara, G., Palmerini, C., and Sabatelli, F. (1990). Comparative progress report 1985-1989 and projections on future development of geothermal energy in italy. In *Transactions of the Geothermal Resources Council*, volume 14-Part I. Geothermal Resources Council.

Ceccarelli, A., Celati, R., Grassi, S., Minissale, A., and Ridolfi, A. (1987). The southern boundary of the Larderello geothermal field. *Geothermics*, **16**(5/6), 505–515.

Civetta, L., Orsi, G., Scandone, P., and Pece, R. (1978). Eastwards migration of the tuscan anatectic magmatism due to anticlockwise rotation of the apennines. *Nature*, **276**, 604–605.

Console, R. and Rosini, R. (1995). Non-double-couple microearthquakes in the Geothermal Field of Larderello, Central Italy. In *IUGG XXI General Assembly Abstracts (Week A)*. International Union of Geodesy and Geophysics. Abstract number SA21E-20.

Console, R. and Rosini, R. (1998). Non-double-couple microearthquakes in the geothermal field of Larderello, central Italy. *Tectonophysics*, **289**(1-3), 203–220.

Crutchfield, J. A. (1996). *It happened in Texas*. Falcon Press Publishing.

Cypser, D. and Davis, S. (1995). Induced seismicity and the potential for liability under American law. In *IUGG XXI General Assembly Abstracts (Week A)*. International Union of Geodesy and Geophysics. Abstract number SA21E-2.

Daneshy, A. (1989). Proppant transport. In J. L. Gidley, S. A. Holditch, D. E. Nierode, and R. W. J. Veatch, editors, *Recent Advances in Hydraulic Fracturing*, volume Monograph 12 of *Henry L. Doherty Series*, chapter 1, pages 210–222. Society of Petroleum Engineers.

Deichmann, N. and Garcia-Fernandez, M. (1992). Rupture geometry from high-precision relative hypocentre locations of microearthquake clusters. *Geophys. J. Int.*, pages 501–517.

Della Vedova, B., Pellis, G., Foucher, J., and Rehault, J. (1984). Geothermal structure of the tyrrhenian sea. *Marine Geology*, **55**, 271–289.

Dini, L. (1989). Structural model of the lardarello geothermal field; main geophysical lineaments of the metamorphic basement. Technical report, U.N.G. Geominerario Uff. Explorzione, ENEL, Posa, Italy.

DiPippo, R. (1985). Geothermal electric power, the state of the world-1985. In *International Symposium on Geothermal Energy, International Volume*. Geothermal Resources Council.

Draper, N. R. and Smith Jr., H. (1981). *Applied Regression Analysis*. John Wiley and Sons, second edition.

Dreesen, D. S., Malzahn, M. V., Fehler, M. C., and Dash, Z. V. (1987). Identification of MHF fracture planes and flow paths: A correlation of well log data with patterns of induced seismicity. In *Geothermal Resources Council Transactions*, volume 11, pages 339–348.

Duchane, D. and Albright, J. N. (1996). Review of teh Fenton Hill HDR Project. In *Proceedings of the 3rd International HDR Forum*, Santa Fe, New Mexico.

Duprat, A. and Ungemach, P. (1985). An updated conceptual model of the travale geothermal field based on recent geophysical and drilling data. *Geothermics*, **14**(5/6), 755–774.

Eberhart-Phillips, D. and Oppenheimer, D. H. (1984). Induced seismicity in the Geysers Geothermal Area, California. *Journal of Geophysical Research*, **89**(B2), 1191–1207.

Edwards, L., Chilingar, G., Rieke III, H., and Fertl, W. (1982). *Handbook of Geothermal Energy*. Gulf Publishing Company, Houston, Texas.

ENEL-Unita Nazionale Geotermica (1988). Isobate dell'orizzonte sismico K.

Evernden, J. F. (1969). Precision of epicenters obtained by small numbers of world-wide stations. *Bulletin of the Seismological Society of America*, **59**(3), 1365–1398.

Ewing, T. E. (1991). Structural framework. In A. Salvador, editor, *The Gulf of Mexico Basin*, volume J of *The Geology of North America*, chapter 1, pages 31–72. The Geological Society of America.

Fabriol, H., Beauce, A., Jacobo, R., and Quijano, J. (1992). Microseismic monitoring during production and reinjection tests in the Chipilapa geothermal field (El Salvador). In *Geothermal Resources Council Transactions*, volume 16, pages 221–226.

Fehler, M. (1989). Sress control os seismicity patterns observed during hydraulic fracturing experiments at the Fenton Hill Hot Dry Rock Geothermal Energy Site, New Mexico. *International Journal of Rock Mechanics and Mining Sciences & Geomechanics Abstracts*, **26**(3–4), 211–219.

Fehler, M. and House, L. (1995). Seismicity accompanying hydraulic fracturing: relation between the larger events and the spatial-temporal development of locations and velocity changes. In *IUGG XXI General Assembly Abstracts (Week A)*. International Union of Geodesy and Geophysics. Abstract number SA22D-8.

Fehler, M., House, L., and Kaieda, H. (1987). Determining planes along which earthquakes occur: Method and application to earthquakes accompanying hydraulic fracturing. *Journal of Geophysical Research*, **92**(B9), 9,407–9,414.

Feignier, B. and Grasso, J.-R. (1990). Seismicity induced by gas production: I. Correlation of focal mechanisms and dome structure. *Pure and Applied Geophysics*, **134**(3), 405–426.

Feng, Q. and Lees, J. (1995). Microseismicity, stress and fracture within the Coso Geothermal Field. In *IUGG XXI General Assembly Abstracts (Week A)*. International Union of Geodesy and Geophysics. Abstract number SA22D-7.

Ferrara, G., Luccioli, F., Palmerini, G., and Scappini, U. (1985). Update report on geothermal development in italy. In *International Symposium on Geothermal Energy, International Volume*. Geothermal Resources Council.

Fiordelisi, A., Mackie, R. L., Madden, T., Manzella, A., and Rieven, S. (1995). Application of the magnetotelluric method using a remote-remote reference system for characterizing deep geothermal system. In *Proceedings of the World Geothermal Congress*, volume 2, pages 893–897, Florence, Italy. International Geothermal Association.

Fletcher, J. and Sykes, L. (1977). Eearthquakes related to hydraulic mining and natural seismic activity in western New York State. *Journal of Geophysical Research*, **82**(26), 3,767–3,780.

Flinn, E. (1965). Confidence regions and error determinations for seismic event location. *Reviews of Geophysics*, **3**(1), 157–185.

Foley, J. (1990). *Crustal Structure from Teleseismic Bodywave Data*. Ph.D. thesis, Massachusetts Institute of Technology.

Frankel, A. (1982). Precursers to a magnitude 4.8 earthquake in the virgin islands: spatial clustering of small earthquakes, anomalous focal mechanisms, and eathquake doublets. *Bulletin of the Seismological Society of America*, **72**, 1277–1294.

Fremont, M. and Malone, S. (1987). High precision relative locations of earthquakes at Mount Saint Helens, Washington. *Journal of Geophysical Research*, **92**, 10,223–10,236.

Galloway, W., Bebout, D., Fisher, W., Dunlap Jr., J., Castro-Cabrera, R., Lugo-Rivera, J., and Scott, T. (1991). Cenozoic. In A. Salvador, editor, *The Gulf of Mexico Basin*, volume J of *The Geology of North America*, chapter 1, pages 245–324. The Geological Society of America.

Galloway, W. E., Hobday, D. K., and Magara, K. (1982). Frio formation of the Texas Gulf Coast - depositional systems, structural framework, and hydrocarbon origin, migration, distribution, and exploration potential. Technical Report 122, University of Texas at Austin.

Garnish, J. (1985). Hot, Dry rock, A European perspective. In *International Symposium on Geothermal Energy, International Volume*. Geothermal Resources Council.

Geller, R. and Mueller, C. (1980). Four similar earthquakes in central California. *Geophysical Research Letters*, **7**, 821–824.

Gianelli, G., Puxeddu, M., Batini, F., Bertini, G., Dini, I., Pandeli, E., and Nicolich, R. (1988). Geological model of a young volcanic-plutonic system: The geothermal region of Monte Amiata (Tuscany, Italy). *Geothermics*, **17**(5/6), 719–734.

Gianelli, G., Manzella, A., and Puxeddu, M. (1996). Crustal models of the geothermal areas of Larderello and Mt. Amiata, Italy. In *Transactions of the Geothermal Resources Council*, volume 20, pages 287–293. Geothermal Resources Council.

Glowacka, E. and Nava, F. A. (1996). Major earthquakes in Mexicali Valley, Mexico, and fluid extraction at Cerro Prieto Geothermal Field. *Bulletin of the Seismological Society of America*, **86**(1A), 93–105.

Gomez, J., Meredith, P., Sammonds, P., Tateno, M., and Takanohashi, M. (1995). Modelling damage evolution using microseismicity induced by fluid extractiona dn injection in the Kakkonda Geothermal Field, Japan. In *IUGG XXI General Assembly Abstracts (Week A)*. International Union of Geodesy and Geophysics. Abstract number SA21E-19.

Grannell, R., Zelwer, R., and Randall, G. (1982). Gravity and surface elevation changes at the Cerro Prieto Geothermal Field. *EOS-Transactions of the American Geophysical Union*, **63**(45).

Grasso, J., Plotnikova, L., Nuaev, B., and Bossu, R. (1995). The three M=7 Gazli earthquakes, Usbekistan, Central Asia: The largest seismic energy release by human activity? In *IUGG XXI General Assembly Abstracts (Week A)*, page pp. A363. International Union of Geodesy and Geophysics. Abstract number SA21D-1.

Grasso, J.-R. and Feignier, B. (1990). Seismicity induced by gas production: II. Lithology correlated events, induced stresses and deformation. *Pure and Applied Geophysics*, **134**(3), 427–449.

Guinn, S. and Long, L. (1977). A computer methods for determination of valid focal mechanisms using p-wave first motions. *Earthquake Notes*, **48**, 21–33.

Heineman-Glutsch, B. and Kappelmayer, O. (1996). Economic analysis of HDR power plants with special reference to the European HDR site. In *Proceedings of the 3rd International HDR Forum*, Santa Fe, New Mexico.

Helm, J. and Hoang-Trong, P. (1996). Natural and induced seismic hazards of the European Hot Dry Rock geothermal energy site of Soultz sous Fôrets. In *Proceedings of the 3rd International HDR Forum*, Santa Fe, New Mexico.

Horvath, F. and Berckhemer, H. (1982). Mediterranean backarc basins. In K. Hsu, editor, *Alpine-Mediterranean Geodynamics*, volume 7 of *Geodynamics Series*, pages 141–173. American Geophysical Union, Washington, D.C.

House, L. (1987). Locating microearthquakes induced by hydraulic fracturing in crystalline rock. *Geophysical Research Letters*, **14**(9), 919–921.

House, L., Flores, R., and Withers, R. (1996). Microearthquakes induced by a hydraulic injection in sedimentary rock, East Texas. In *Technical Program Expanded Abstracts with Authors Bibliographies*, volume I, pages 110–113, Denver. Society of Exploration Geophysicists.

Hsu, K. (1982). Editor's introduction, apline mediterranean geodynamics: Past, present, and future in alpine-mediterranean geodynamics. In K. Hsu, editor, *Alpine-Mediterranean Geodynamics*, volume 7 of *Geodynamics Series*, pages 7–13. American Geophysical Union, Washington, D.C.

Israelsson, I. (1990). Correlation of waveforms from closely spaced regional events. *Bull. Seism. Soc. Am.*, **80**(6), 2177–2193.

Ito, A. (1985). High resolution relative hypocenters of similar earthquakes by cross-spectral analysis method. *J. Phys. Earth*, **33**, 279–294.

Ito, A. (1990). Earthquake swarm activity revealed from high resolution relative hypocenters-clustering of microearthquakes. *Tectonophysics*, **175**, 47–66.

James, D. E. and Savage, M. K. (1990). A search for seismic reflections from the top of the oceanic crust beneath Hawaii. *Bulletin of the Seismological Society of America*, **80**(3), 675–701.

Jarpe, S., Kasameyer, P., and Johnston, C. (1989). Passive seismic monitoring of a flow test in the Salton Sea geothermal field. In *Transactions-Geothermal Resources Council*, volume 13, pages 265–270, Santa Rosa, CA. Geothermal Resources Council.

Johnson, R. A. and Wichern, D. W. (1998). *Applied Multivariate Statistical Analysis*. Prentice Hall, fourth edition.

Jones, R., Beauce, A., Bitri, A., and Wilson, S. (1996). The analysis and interpretation of microseismicity induced during the 1995 stimulation and circulation experiments at the European HDR project at Soultz-Sous-Fôrets, france. In *Proceedings of the 3rd International HDR Forum*, Santa Fe, New Mexico.

Jordan, T. and Sverdrup, K. (1981). Teleseismic location techniques and their application to earthquake clusters in the south-central Pacific. *Bulletin of the Seismological Society of America*, **71**, 1,105–1,130.

Julian, B., Miller, A., and Foulger, G. (1993). Non-shear focal mechanisms of earthquakes at the Geysers, California, and Hengill, Iceland, geothermal areas. In *Transactions of the Geothermal Resources Council*, volume 17, pages 123–128.

Kastens, K., Mascle, J., Auroux, C., Bonatti, E., Broglia, C., Channel, J., Curzi, J., Emeis, K., Glacon, G., Hasegawa, S., Hieke, W., Mascle, G., McCoy, F., McKenzie, J., Mendelson, J., Muller, C., Rehault, J., Robertson, A., Sartori, R., Sprovieri, R., and Torii, M. (1988). Odp leg 107 in the tyrrhenian sea: Insights into passive margin and back-arc basin evolution. *Geological Society of America Bulletin*, pages 1140–1156.

Keck, R. and Withers, R. (1994). A field demonstration of hydraulic fracturing for solid waste injection with real-time passive seismic monitoring. In *SPE 69th Annual Technical Conference and Exhibition*, pages 319–334, New Orleans, LA. Society of Petroleum Engineers.

Keck, R., Fletcher, P., and Withers, R. (1996). *A Field Demonstration of Hydraulic Fracturing for Solids Waste Disposal, Part One: Injection Operations and Engineering Data Analysis*. Academic Press.

Kirkpatrick, A., Peterson Jr., J., and Majer, E. (1995). Occurance and mechanism of microearthquakes at the southeast Geysers Geothermal Field, California. In *IUGG XXI General Assembly Abstracts (Week A)*. International Union of Geodesy and Geophysics. Abstract number SA22D-6.

Kovach, R. L. (1974). Source mechanisms for Wilmington Oil Field, California subsidence earthquakes. *Bulletin of the Seismological Society of America*, **64**(3), 699–711.

Kuriyagawa, M., Yamaguchi, T., Sato, Y., and Takasugi, S. (1996). Evaluation of Hot, Dry Rock Resources in Japan. In *Proceedings of the 3rd International HDR Forum*, Santa Fe, New Mexico.

Lay, T. and Wallace, T. C. (1995). *Modern Global Seismology*. Academic Press.

Lee, T. (1976). Earthquake risk in Geothermal energy extraction from Salton Sea Field, California. *EOS-Transactions of the American Geophysical Union*, **57**.

Li, Y. and Thurber, C. H. (1991). Hypocenter constraint with regional seismic data: a theoretical analysis for the natural resources defense council network in Kazakstan, USSR. *Journal of Geophysical Research*, **96**(B6), 10159–10176.

Li, Y., Cheng, H., and Toksöz, M. (1995). Seismic imaging of hydraulic fracture at Los Alamos HDR experiment site. In *Proceedings of the 3rd SEGJ/SEG International Symposium on Geotomography and Fracture Imaging*. The Society of Exploration Geophysicists of Japan and The Society of Exploration Geophysicists.

Look, D. and Sauer, H. (1986). *Engineering Thermodynamics*. PWS Publishers, Boston.

Malinverno, A. and Ryan, W. (1986). Extension in the tyrrhenian sea and shortening in the apennines as result of arc migration driven by sinking of the lithosphere. *Tectonics*, **5**, 227–245.

Matasova, L., Mutaev, B., Plotnikova, L., Bossu, R., and Grasso, J. (1995). Peculiarities of seismotectonic deformations in a gas field are (Gazli, Usbekistan). In *IUGG XXI General Assembly Abstracts (Week A)*. International Union of Geodesy and Geophysics. Abstract number SA21E-5.

Menke, W. (1989). *Geophysical Data Analysis: Discrete Inverse Theory*, volume 45 of *International Geophysics Series*. Academic Press, Inc., San Diego, revised edition edition.

Minissale, A. (1991). The lardarello geothermal field: a review. *Earth-Science Reviews*, **31**, 133–151.

Montone, P., Amato, A., Chiarabba, C., Buonasorte, G., and Fiordelisi, A. (1995). Evidence of active extension in Quaternary volcanos of Central Italy from breakout analysis and seismicity. *Geophysical Research Letters*, **22**(14), 1909–1912.

Mori, H. (1985). Electrical update of japan. In *International Symposium on Geothermal Energy, International Volume*. Geothermal Resources Council.

Moritis, G. (1998). EOR oil production up slightly. *Oil and Gas Journal*, **96**(16), 49–56.

Moriya, H., Nagano, K., and Niitsuma, H. (1994). Precise source location of AE doublets by spectral matrix analysis of triaxial hodogram. *Geophysics*, **59**(1), 36–45.

Moriya, H., Niitsuma, H., and Kaieda, H. (1996). Identification of reservoir structure and stress state from hypocenter cloud in Ogachi HDR Field, Japan, by using triaxial doublet analysis. In *Proceedings of the 3rd International HDR Forum*, Santa Fe, New Mexico.

Muskat, M. (1981). *Physical Principles of Oil Production*. International Human Resources Development Corporation.

Nehring, R. (1991). Oil and gas resources. In A. Salvador, editor, *The Gulf of Mexico Basin*, volume J of *The Geology of North America*, chapter 1, pages 445–494. The Geological Society of America.

Nicholson, C. and Wesson, R. L. (1992). Triggered earthquakes and deep well activities. *Pure and Applied Geophysics*, **139**(3/4), 561–578. Special Issue on Induced Seismicity.

Niitsuma, H., Nakatsuma, K., Chubachi, N., Yokoyama, H., and Takanohashi, M. (1985a). Acoustic emission measurement of geothermal reservoir cracks in Takinoue (Kakkonda) field, Japan. *Geothermics*, **14**(4), 525–538.

Niitsuma, H., Nakatsuma, K., Takahashi, H., Chubachi, N., Yokoyama, H., and Sato, K. (1985b). Long-distance acoustic emission monitoring of hydraulically induced subsurface cracks in Nigorikawa geothermal field, Japan. *Geothermics*, **14**(4), 539–551.

Nolte, K. (1989). Fracturing-pressure analysis. In J. L. Gidley, S. A. Holditch, D. E. Nierode, and R. W. J. Veatch, editors, *Recent Advances in Hydraulic Fracturing*, volume Monograph 12 of *Henry L. Doherty Series*, chapter 1, pages 297–316. Society of Petroleum Engineers.

O'Connel, Daniel, R. and Johnson, L. R. (1982). Preliminary results of a velocity, attenuation, and source study of microearthquakes at the Geysers Geothermal Field, California. *EOS-Transactions of the American Geophysical Union*, **63**(45).

Pavlis, G. L. and Booker, J. R. (1983). Progressive multiple event location (PMEL). *Bulletin of the Seismological Society of America*, **73**(6), 1753–1777.

Pechmann, J. and Thorbjarnardottir, B. (1990). Waveform analysis of two preshock-main shock-aftershock sequences in Utah. *Bulletin of the Seismological Society of America*, **80**, 519–550.

Pechmann, J. C. and Kanamori, H. (1982). Wavefors and spectra of preshocks and aftershocks of the 1979 Iperial valley, California, earthquake evidence for fault heterogeneity. *Journal of Geophysical Research*, **87**(B13), 10579–10597.

Phillips, W., House, L., and Fehler, M. (1992). Vp/Vs and the structure of microearthquake clusters. *Seismological-Research-Letters*, **63**(1), 56–57.

Phillips, W., Fairbanks, T., Rutledge, J., and Anderson, D. (1995). Microearthquakes induced by hydraulic stimulation in the Austin Chalk. In *IUGG XXI General Assembly Abstracts (Week A)*. International Union of Geodesy and Geophysics. Abstract number SA21D-6.

Phillips, W., House, L., and Fehler, M. (1996). Detailed joint mapping at Fenton Hill, NM. In *Proceedings of the 3rd International HDR Forum*, Santa Fe, New Mexico.

Potter, R. and Dennis, B. (1974). Seismic and fluid pressure response from a series of hydraulic fractures in Granite. *EOS-Transactions of the American Geophysical Union*, **55**(4), 430.

Poupinet, G., Ellsworth, W., and Frechet, J. (1984). Monitoring velocity variations in the crust using earthquakes doublets: an application to the Calaveras Fault. *Journal of Geophysical Research*, **89**, 5,719–5,731.

Puxeddu, M. (1984). Structure and late cenozoic evolution of the upper lithosphere in southwest tuscany (italy). *Tectonophysics*, **101**, 357–382.

Puxeddu, M., Squarci, P., Rau, A., Tongiorgi, M., and Burgassi, P. (1977). Stratigraphic and tectonic study of the lardarello-travale basement rockes and its geothermal implications. *Geothermics*, **6**.

Rencher, A. C. (1995). *Methods of Multivariate Analysis*. John Wiley and Sons.

Riggs, S., Ellison Jr., S. P., Fisher, W., Galloway, W., Jackson, M., and Morton, R. (1991). Mineral resources and geopresured-geothermal energy. In A. Salvador, editor, *The Gulf of Mexico Basin*, volume J of *The Geology of North America*, chapter 1, pages 495–528. The Geological Society of America.

Rodi, W., Li, Y., and Cheng, C. (1993). Location of microearthquakes induced by hydraulic fracturing. In *Borehole Acoustics and Logging Consortium Annual Report*, pages 369–410. Massachussets Institute of Technology, Earth Resources Laboratory.

Rogers, A. M. and Malkiel, A. (1979). A study of earthquakes in the Permian basin of Texas-New Mexico. *Bulletin of the Seismological Society of America*, **69**(3), 843–865.

Roquemore, G. and Zellmer, J. (1982). Earthquake activity and deformation in the Coso Volcanic Field, California. *EOS-Transactions of the American Geophysical Union*, **63**(45).

Royden, L. (1993a). Evolution of retreating subduction boundaries formed during continental collision. *Tectonics*, **12**(3), 629–638.

Royden, L. (1993b). The tectonic expression slab pull at continental convergent boundaries. *Tectonics*, **12**(2), 303–325.

Royden, L., Patacca, E., and Scandone, P. (1987). Segmentation and configuration of subducted lithosphere in italy: An important control on thrust-belt and foredeep-basin evolution. *Geology*, **15**, 714–717.

Rutledge, J. T., Phillips, W., Fairbanks, T., and Anderson, D. (1995). Microseismicity associated with primary oil production in Clinton County, kentucky. In *IUGG XXI General Assembly Abstracts (Week A)*. International Union of Geodesy and Geophysics. Abstract number SA21D-2.

Salvador, A. (1991a). Introduction. In A. Salvador, editor, *The Gulf of Mexico Basin*, volume J of *The Geology of North America*, chapter 1, pages 1–12. The Geological Society of America.

Salvador, A. (1991b). Origin and development of the Gulf of Mexico Basin. In A. Salvador, editor, *The Gulf of Mexico Basin*, volume J of *The Geology of North America*, chapter 1, pages 389–444. The Geological Society of America.

Sasaki, S. (1995). Characteristics of microearthquakes induced during hydraulic fracturing at the Hijiori HDR site in Japan. In *IUGG XXI General Assembly Abstracts (Week A)*. International Union of Geodesy and Geophysics. Abstract number SA22D-10.

Sasaki, S. (1996). Characteristics of microearthquakes accompanying the 1995 circulation test at the Hijiori HDR site, Yamagata, Japan. In *Proceedings of the 3rd International HDR Forum*, Santa Fe, New Mexico.

Sato, Y. and Abé, H. (1996). Review of procedures of HDR reservoir creation at Hijiori from design methodology. In *Proceedings of the 3rd International HDR Forum*, Santa Fe, New Mexico.

Sawyer, D., Buffler, R., and Pilger, R. J. (1991). The crust under the Gulf of Mexico basin. In A. Salvador, editor, *The Gulf of Mexico Basin*, volume J of *The Geology of North America*, chapter 1, pages 55–72. The Geological Society of America.

Seber, G. A. F. and Wild, C. J. (1989). *Nonlinear Regression*. John Wiley and Sons.

Segall, P. (1989). Earthquakes triggered by fluid extraction. *Geology*, **17**, 942–946.

Sharp Jr., J. M., Kreitler, C. W., and Lesser, J. (1991). Groundwater. In A. Salvador, editor, *The Gulf of Mexico Basin*, volume J of *The Geology of North America*, chapter 1, pages 529–541. The Geological Society of America.

Simpson, D. W. and Leith, W. (1985). The 1976 and 1984 Gazli USSR, earthquakes-were they induced? *Bulletin of the Seismological Society of America*, **75**(5), 1465–1468.

Smith, A. and Woodcock, N. (1982). Tectonic synthesis of the alpine-mediterranean region: A review. In K. Hsu, editor, *Alpine-Mediterranean Geodynamics*, volume 7 of *Geodynamics Series*, pages 15–38. American Geophysical Union, Washington, D.C.

Spearing, D. (1991). *Roadside Geology of Texas*. Roadside Geology Series. Mountain Press Publishing Company.

Sprent, P. (1990). Some history of functional and structural relationships. In P. J. Brown and W. A. Fuller, editors, *Contemporary Mathematics: Proceedings from the 1989 Summer Conference on Statistical Analysis of Measurement Error Models and Applications*, volume 112. American Mathematical Society.

Stein, S. (1989). *Introduction to seismology, earthquakes, and earth structure*. Seth Stein.

Tapley, W. C. and Tull, J. E. (1991). *SAC - Seismic Analysis Code USERS MANUAL*. Lawrence Livermore National Laboratory, 3 edition.

Tezuka, K. and Niitsuma, H. (1995) Microseismic doublet analysis for fracture characterization in Hijiori HDR site. In *Proceedings of the 3rd SEGJ/SEG International Symposium on Geotomography and Fracture Imaging*. The Society of Exploration Geophysicists of Japan and The Society of Exploration Geophysicists.

Thain, I. (1985). Status report on the existing and planned utilization of geothermal energy in New Zealand. In *International Symposium on Geothermal Energy, International Volume*. Geothermal Resources Council.

Thorne, B. and Morris, H. (1988). Advances in borehole seismic fracture diagnostics. *SPE Formation Evaluation*, **3**(4), 711–715.

Thornjarnardottir, B. and Pechmann, J. (1987). Constraints on relative earthquake locations from cross-correlation of waveforms. *Bulletin of the Seismological Society of America*, **77**, 1,626–1,634.

Truby, L., Keck, R., and Withers, R. (1994). Data gathering for a comprehensive hydraulic fracturing diagnostic project: A case study. In *Proceedings of the 1994 IADC/SPE Drilling Conference*, pages 703–711, Dallas, TX. International Association of Drilling Contractors and the Society of Petroleum Engineers.

Veatch, R. W. J., Moschovidis, Z. A., and Fast, C. R. (1989). An overview of hydraulic fracturing. In J. L. Gidley, S. A. Holditch, D. E. Nierode, and R. W. J. Veatch, editors, *Recent Advances in Hydraulic Fracturing*, volume Monograph 12 of *Henry L. Doherty Series*, chapter 1, pages 1–38. Society of Petroleum Engineers.

Vinegar, H., Wills, P., DeMartini, D., Shlyapobersky, J., Deeg, W., Adair, R., Woerpel, J., Fix, J., and Sorrells, G. (1992). Active and passive seismic imaging of a hydraulic fracture in diatomite. *Journal of Petroleum Technology*, **44**(1).

Wallroth, T. and Dyer, B. (1996). A crosshole seismic survey of the inflated HDR reservoir in Fjällbacka, Sweden. In *Proceedings of the 3rd International HDR Forum*, Santa Fe, New Mexico.

Wetmiller, R. J. (1986). Earhtquakes near Rocky Mountains House, Alberta, and their relationship to gas production facilities. *Canadian Journal of Earth Science*, **23**, 172–181.

Willis-Richards, J., Kaieda, H., and Takahashi, H. (1996). The strange case of the Ogachi reservoir stimulations. In *Proceedings of the 3rd International HDR Forum*, Santa Fe, New Mexico.

Withers, R., Perkins, T., and Keck, R. (1996). *A Field Demonstration of Hydraulic Fracturing for Solids Waste Disposal, Part Two: Real-Time Passive Seismic Monitoring System and Data Analysis*. Academic Press.

Wolhart, S., Hill, D., and Smalley, E. (1998). Diffusion of advanced stimulation technology in the petroleum industry: A case history. *Journal of Petroleum Technology*, **50**(3), 32–35. Synopsis of SPE Paper number 38826.

Young, C.-Y. and Ward, R. (1977). Teleseismic mapping of anomalies associated with the Geysers KGRA. *EOS-Transactions of the American Geophysical Union*, **58**(12).